Studies of VHMS-related alteration: geochemical and mineralogical vectors to ore

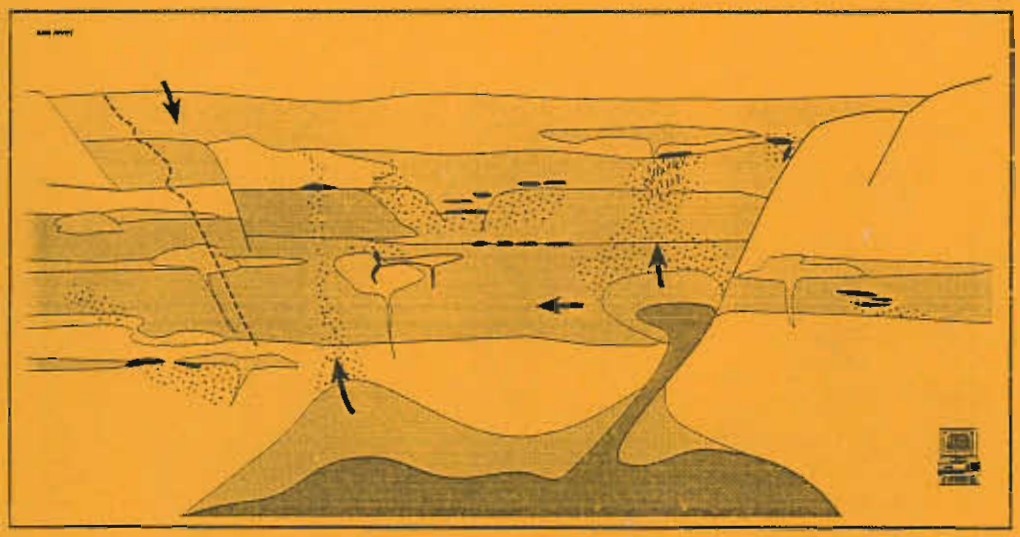

AMIRA/ARC project P439

Report 3
October 1996

Centre for Ore Deposit and Exploration Studies
University of Tasmania

Studies of VHMS-related alteration: geochemical and mineralogical vectors to ore

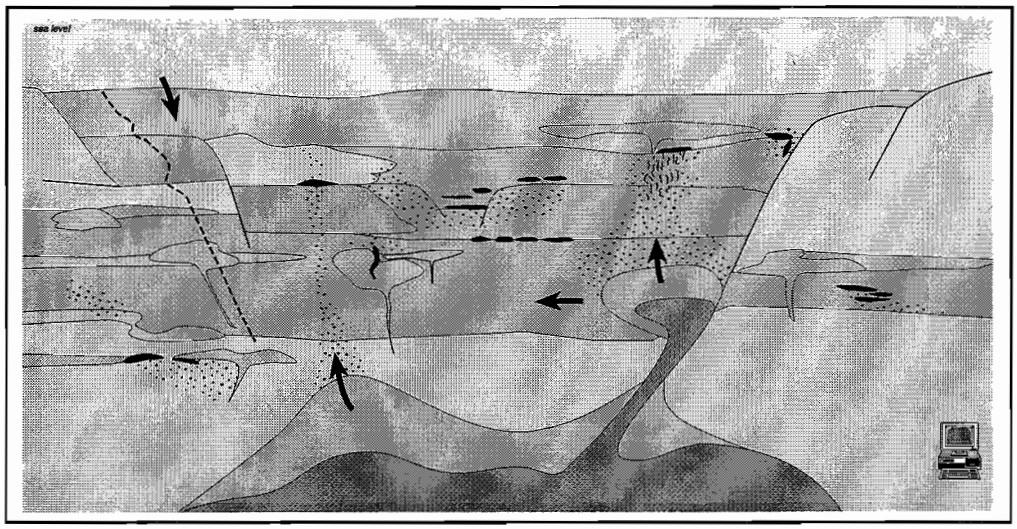

AMIRA/ARC project P439

Report 3
October 1996

Centre for Ore Deposit and Exploration Studies
University of Tasmania

Centre for Ore Deposit and Exploration Studies,
Geology Department,
University of Tasmania,
GPO Box 252-79,
Hobart, Tasmania,
Australia

http://www.geol.utas.edu.au/codes

another Pongratz Production 1996

Contents

Aims and framework of the project

Introduction

Volcanic-hosted massive sulphide deposits (VHMS) provide a significant contribution to the total zinc, copper, lead, silver and gold production in Australia and continue to be a major target for most base metal explorers. However, due to the geological complexity of ancient submarine volcanic terrains, new VHMS deposits are becoming extremely difficult to discover, especially deposits that are buried more than a few tens of metres below the surface. To complement the conventional multidisciplinary approach utilising geology, geophysics and geochemistry, a new attack to the problem is developed here which involves the integration of volcanic facies analysis with alteration geochemical and mineral chemical studies to develop a set of vectors to guide explorers toward ore-grade mineralisation. The research concentrates on three productive submarine volcanic belts in Australia: the Mount Read Volcanics (MRV) in western Tasmania, the Mount Windsor Volcanics (MWV) in northern Queensland, and the Archean Murchison volcanic province in western Australia.

Project objectives

1. To characterise the mineralogy and geochemistry for the various styles of hydrothermal alteration throughout the Mount Read Volcanics (MRV) and the Mount Windsor Volcanics (MWV). This will be based on mapping supported by whole-rock and trace element geochemistry, mineral chemistry, REE and stable isotope geochemistry.
2. To determine the relationship between geochemical alteration patterns and sub-volcanic intrusions that are coeval with VHMS formation.
3. To undertake case studies of alteration halos related to specific VHMS deposits with particular emphasis on hangingwall alteration, and the relationship between alteration patterns and volcanic facies.
4. To develop a set of vectors towards ore, based on the regional studies and ore deposit specific studies, that can be applied in the exploration for VHMS deposits in submarine volcanic sequences throughout Australia. The vector matrix will include whole-rock, trace element, mineral chemistry, REE, isotope and volcanic facies factors.

Research framework

The emphasis in this project involves a multidisciplinary approach utilising studies in volcanic facies analysis, volcanic petrology and geochemistry, with alteration and mineralisation to develop models for the nature, style and extent of alteration throughout submarine volcanic environments hosting VHMS deposits. The basis of this approach is outlined in the diagram below.

The combination of data and interpretation from these three subdisciplines will be used in the development of vectors to ore.

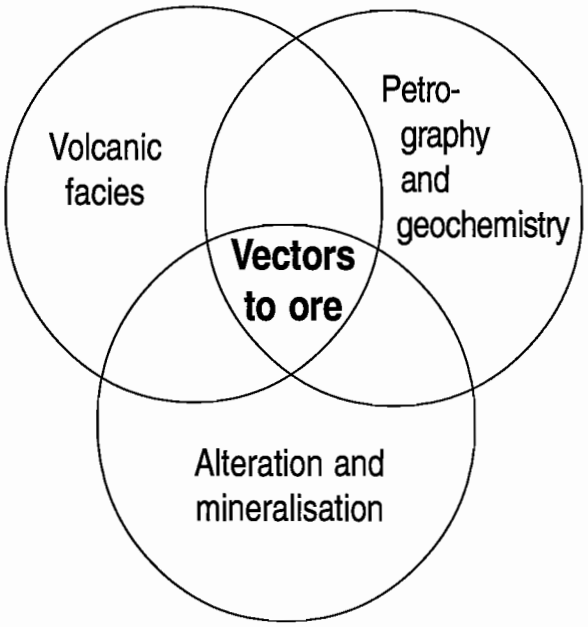

Relationship of subprojects

A schematic diagram showing the relationship between the various subprojects in the P439 program is shown in Figure 1. This diagram represents our working model for the various facies of alteration in a submarine volcanic belt and indicates the spatial relationships of subprojects within the model. Subprojects that feature in this report or will be visited during the field meeting are outlined in bold.

Regional studies

Aims
- To determine relationships between volcanic facies, petrography, geochemistry and intensity of alteration
- To determine criteria for diagenetic, hydrothermal and metamorphic alteration
- To build a chemical, mineralogical facies model for alteration through the volcanic belt.

Methods
- Multidisciplinary studies along selected traverses in MRV to include
  - volcanic facies mapping [1*]
  - petrography [1]
  - whole-rock, trace element and isotopic geochemistry [1]
- Traverses selected in MRV
  -Hall Rivulet Canal
  - Mt Black [2]
  - Hercules to Mt Read [3]
  - Red Hills–Selina [4]
  - Jukes Rd [5]

This report
- All traverses are reported upon in terms of volcanic facies and petrography
- Geochemical results are reported for all traverses
- Criteria for distinguishing between timing and chemistry of diagenetic, hydrothermal and metamorphic alteration are proposed and discussed.

Ore deposit studies

Aims
- To characterise the mineralogy and geochemistry of alteration halos (both FW and HW) to various VHMS deposits.
- To relate halo development to volcanic facies
- To develop chemical models to explain halo development
- To develop vectors to mineralisation

Methods
- Multidisciplinary studies of selected ore deposits to determine nature and extent of alteration halos in the HW, FW and along the ore position.
- Case studies include
  - Hellyer Zn–Pb–Ag [8, 9]
  - Rosebery Zn–Pb–Ag [10]
  - Hercules Zn–Pb–Ag [3]
  - Henty Au [11]
  - Mt Lyell (?) Cu–Au [12]
  - Thalanga Cu–Pb–Zn [14]
  - Highway–Reward Cu–Au [13]
  - Mt Windsor exhalites Fe [7]
  - Gossan Hill Cu–Zn [15]
- Isotopic, trace element and REE studies to complement volcanic facies and mineral vectors.
- Thermodynamic modelling of selected ore systems.

This report
- Hellyer — report Pearce element study and field visit
- Rosebery — report on timing of carbonate alteration and field visit
- Hercules — report on field traverse and field visit
- Henty — proposal for MSc research and field visit
- Mt Windsor — exhalite report

(*numbers refer to the subprojects in Figure 1)

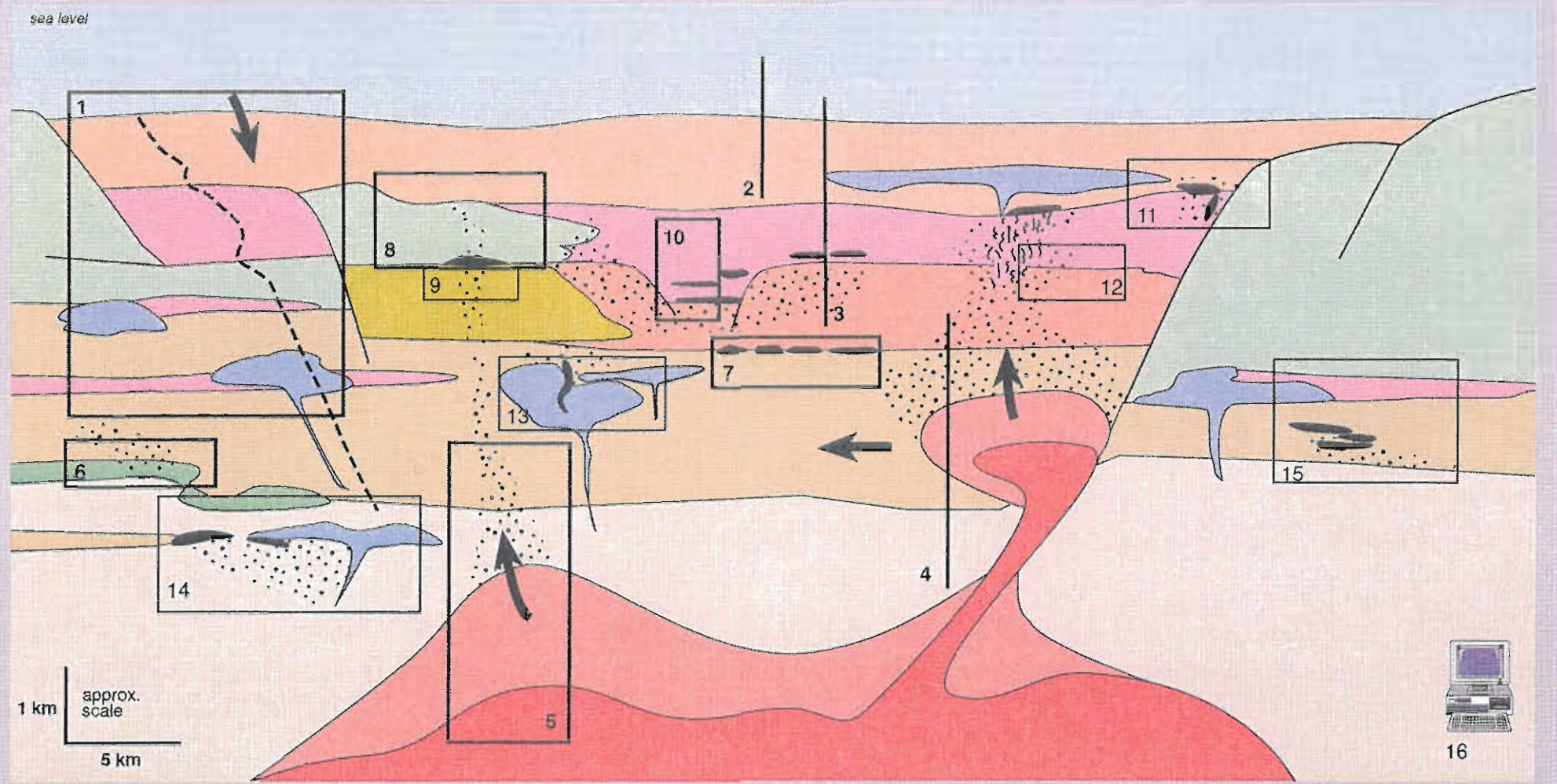

1. **Background diagenetic alteration and volcanic facies: JMcP, AJS, RLA, GD**
6. **Barren pyritic alteration, Gydgie: AJS, GD**
14. Thalanga alteration and facies: HP, JMcP, JBG
8. **Hellyer hangingwall alteration: RF, JBG**
9. Hellyer footwall: CS, JBG
5. **Syn-volcanic granite-related alteration: BW, RRL, DC, RLA**
10. **Rosebery carbonate alteration: RLA, RRL**
13. Highway–Reward Cu–Au system: MD, JMcP, RRL
7. **Exhalite chemistry and textures: GD, MD, AJS**
2. **Mt Black traverse: KG, AJS, JMcP, RLA**
3. **Hercules–Mt Read traverseL RLA, JMcP, RRL**
4. **Red Hills–Selina traverse: AJS, JMcP, RLA**
11. Henty Au alteration: TC, JS
12. Mt Lyell alteration system ?
15. Gossan Hill system: RS, JBG
16. Chemical modelling of fluid–rock interaction in alteration systems: DC

Figure 1
AMIRA Project P439 — Schematic working model of the relationship of project areas and topics (activity in this report shown in bold)

Summaries

'Barren' alteration systems: Example – Gydgie Central, Mt Windsor Volcanic Belt, North Queensland — Joe Stolz, Garry Davidson and Michael Blake

Studies have been undertaken of the petrography, major and trace element chemistry, oxygen and sulphur isotopes for volcanic rocks within the Gydgie central alteration system. These data indicate that, despite some anomalous base metal enrichment, the area was not a major focus for high-temperature hydrothermal fluids, and therefore is not likely to be directly associated with massive sulphide mineralisation. Four major styles of alteration have been distinguished in the area and their chemical characteristics are outlined. Sulphur isotope data for pyrites ($\delta^{34}S = 8$ to 15‰) are similar to values for the Thalanga deposit and indicate an origin from fluids with a relatively high-temperature (>200°C) history.

Whole-rock oxygen isotope data do not indicate a zone of depletion in heavy oxygen in the Gydgie area. However, the $\delta^{18}O$ values for the Gydgie rocks (8–11.8) have been modelled in terms of a two-stage history.

Volcanic influences in the formation of iron oxide-silica deposits in a volcanogenic-massive sulfide terrain, Mount Windsor Volcanic belt, Queensland — Mark Doyle

Careful elucidation of the volcanic facies and facies architecture has proven to be critical in unravelling the significance and emplacement processes of the iron oxide ± silica rocks in the Trooper Creek Formation. Deformation and metamorphism have modified ironstone textures but did not destroy facies relationships which allow for interpretation of ironstone geochemistry, depositional mechanisms and environments. Consideration of iron oxide ± silica rocks without attention to the character and emplacement processes of associated volcanic facies may obscure important textural and facies information that provide a framework for interpreting iron oxide-silica rocks and their significance in mineral exploration.

In the study area, ironstones are associated with differing volcanic facies whose physical properties, mineralogy and depositional environment vary. Quartz-hematite ironstone occurs as pods within coherent facies of lava domes and cryptodomes, as lenses which are the discontinuous facies equivalent of non-welded pumice breccia, and as pods and finely laminated beds in chert. Hematite-quartz ± carbonate also occurs as veins and seams in coherent rhyolite-dacite and as an alteration of the matrix in hyaloclastite and peperite along margins of lavas and cryptodomes.

Field relationships and relict volcanic textures indicate that many ironstone lenses are replacements of pumice breccia rather than seafloor exhalative deposits. The transition in mineralogy and textures passing from massive ironstone, through pyroclast-rich ironstone, into hematite altered pumice breccia record progressive stages in the alteration of the pumiceous precursor. Replacement occurred at or near the seafloor but was not excessively deep as clasts derived from the ironstone were incorporated into volcaniclastic mass flows overlying some ironstones.

The mineralogy, rare earth element geochemistry, and textures suggest that the ironstones deposited from oxidised, low temperature hydrothermal, alkaline to acid fluids. The ironstones are barren,

characterised by negative Eu anomalies, and distinct from ironstones flanking massive sulfide mineralisation at Thalanga.

The barren ironstones are interpreted to result from the development of short-lived, local hydrothermal systems in the proximal facies association of submarine- to littoral-volcanoes and around lavas and syn-sedimentary intrusions. Intrusion-extrusion of magma causes heating of pore water and convection of sea water in the enclosing volcanic package. Fluids leach Fe, Si and other elements during alteration of the glassy volcanic rocks and mix with magmatic fluids exsolved from the magma. The resulting fluids precipitate iron and silica by conductive cooling and mixing with seawater or pore fluids. Iron oxide-silica deposition can occur within the cooler glassy parts of the lava or intrusion(s) which is the heat engine for convection, in already cooled lavas or intrusions, or in the enclosing volcanic package. Hydrothermal fluids which reach the seafloor may accumulate at the vent after discharge or be dispersed in the water column from buoyant plumes.

Rosebery alteration study — Rodney Allen and Ross Large

Since the last report, drill core samples collected during the summer from seven drill holes have been prepared for geochemical analysis, thin rock slices of each sample have been polished for textural study, and thin sections have been made from about half the samples (100 thin sections). Detailed petrographic descriptions have been made on thin sections from drill hole 120R, which passes through K lens. Examples of the petrographic descriptions are provided in the appendix, and a geological log of drill hole 120R, showing sample locations, was provided in the May 1996 report.

The Hercules–Mt Read traverse: Relationships between volcanic mineralogy, alteration and geochemistry — Ross R. Large

Petrographic and geochemical studies of samples from the Hercules–Mt Read traverse allow the discrimination of samples into groups related to the intensity of alteration, mineralogy of alteration and geochemistry of alteration. Samples in the footwall pumice breccias at Hercules display a characteristic style and chemistry of alteration, distinct from the ore package samples and the hangingwall volcanic samples.

Alteration indices (Ishikawa AI, Chlorite/carbonate/pyrite Index and the Mn-carbonate Index) have proved useful in determining the facies of alteration and proximity to mineralisation.

Both strontium and the Ba/K_2O ratio are enriched in the volcanics surrounding the ore horizon, and require further evaluation as potential vectors to ore.

Road log of the Jukes Road and the Jukes Cu–Au Prospect with emphasis on petrography, alteration assemblages and preliminary geochemistry — Bill Wyman

Textural and mineralogical data appear to suggest that hydrothermal mineral assemblages can be distinguished from regional assemblages on the basis of four observations.

1. The widespread occurrence of alteration assemblages.
2. Intensity of chlorite alteration of feldspar phenocrysts. Sericite alteration of feldspar phenocrysts in weakly altered rocks can vary greatly but the appearance of chlorite appears to be an indicator of proximity to the hydrothermal system.
3. The presence or absence of accessory minerals such as pyrite, chalcopyrite, tourmaline or large amounts of magnetite/hematite.
4. Degree of textural destruction. Rocks with weakly moderate or greater textural destruction, in general, clearly show the effects of hydrothermal alteration. An exception to this appears to be the

albite alteration seen in the Jukes Road pumice breccia. This rock has undergone a great amount of textural destruction of the groundmass and is believed to have been altered under diagenetic conditions.

Hydrothermal alteration appears to have been controlled by fracture density. This is demonstrated by an increase in both fracture density, and increases in both chlorite and K-feldspar alteration of the columnar jointed rhyolite with increasing proximity to the Jukes Prospect. The primary indicator of alteration intensity is the degree of alteration of feldspar phenocrysts.

At the Jukes Prospect, two styles of hydrothermal breccias have been identified. The intimate association of magnetite, chlorite and tourmaline in the matrices, argues very strongly for a hydrothermal/magmatic origin. Breccias are classified according to their matrix type. The first contains various amounts of magnetite/hematite and tourmaline ± chlorite and the second chlorite and tourmaline ± magnetite/hematite. There is a possibility that the two breccias are related to each other and to the large magnetite bodies found both at the Jukes Prospect and farther south at Mt Darwin. Breccias are cut by faults but clearly predate fault-related tectonic fracturing.

Along the Jukes Road, two facies of the CVC have clearly been altered by hydrothermal solutions. The feldspar-phyric rhyolite and the quartz-feldspar porphyry both show varying hydrothermal alteration effects. The quartz-feldspar porphyry is not only altered by chlorite alteration but also by K-feldspar alteration. This suggests that the dykes were implaced prior to the hydrothermal event. The fact that the hydrothermal breccia follows the apparent boundary of a quartz-feldspar porphyry dyke suggests that the timing of the two events may not be too different.

Hellyer alteration study — Russell Fulton

Progress on the Hellyer hangingwall alteration study since the last meeting has concentrated on logging and sampling core, and attempting to map out the alteration from core logs provided by Aberfoyle. To date, the hangingwall basalt has been sampled in 11 holes with another three or four still to be looked at. Approximately 190 samples have been cut at 10 m intervals down through the basalt and at 5 m intervals near to the contact with the underlying hangingwall volcaniclastic suite (HVS). Samples are being used for whole rock geochemistry and thin sectioning for microprobe analysis of minerals. Holes have been chosen to sample both the most and least altered parts of the basalt and intermediate zones. For the Hellyer core shed visit, examples of intensely altered and relatively unaltered (hydrothermallly) basalt will be laid out and logs of the core are appended to this report.

PIMA-II spectral analysis of hydrothermal alteration associated with the Hellyer VHMS deposit: Progress report — K. Yang, J.F. Huntington, J.B. Gemmell and R. Fulton

This project is a combination of research efforts to compare the spectral data from the PIMA-II generated from AMIRA P435 with the detailed mineral chemistry and whole rock chemistry obtained from AMIRA P439.

The specific aims of the study at Hellyer are to (1) identify and (semi)quantify major phyllosilicate minerals and thus delineate alteration zoning and (2) identify any chemical variations of a particular mineral species, and determine their relationship to mineralisation. Samples from 10 diamond drill-holes, from within the Hellyer hydrothermal system and from unaltered host rocks, were measured with the PIMA II portable infrared spectrometer.

From the spectral data obtained in this portion of the study:

- Alteration zoning in the footwall can be better characterised than the hangingwall by the PIMA spectral data.
- White mica composition is a good index for mineralisation, with the Fe and/or Mg-rich mica being within or proximal, whereas the relatively Fe and Mg-poor mica peripheral, to the orebody.
- Chlorite composition, though also highly variable, does not appear to have a particular relationship with mineralisation, and therefore is less significant in directly indicating the mineralisation. The estimated Mg# of chlorite ranges from 0.7–0.2 for the altered footwall and 0.7–0.3 for hangingwall volcanics.
- Carbonate with minor chlorite could be the spectral signatures of the immediate host volcanics.

Mount Black Volcanics: Preliminary volcanic facies and alteration, petrography and geochemistry — Cathryn C Gifkins

The Mount Black Volcanic package is a conformable suite of coherent and clastic volcanics with a broad range of primary compositions, from rhyolitic to basaltic. The majority of samples have mineral assemblages which largely reflect these primary variations in composition. Ssilicic volcanics are dominated by sericite + chlorite + albite while the more mafic units are typically chlorite-epidote-carbonate rich. The package is weakly altered and many of the present mineral assemblages are typical of assemblages produced by diagenetic alteration and Greenschist facies metamorphism of glassy volcanics. Common alteration assemblages include chlorite + magnetite, sericite + chlorite, albite + quartz, epidote + chlorite, silicification and more rarely carbonate and hematite. The distribution of these alteration assemblages is largely controlled by available permeability. In coherent volcanics the fluid pathways include originally glassy flowbands, perlitic fractures, associated autoclastic debris and hydraulic breccias and fractures. In volcaniclastic deposits the alteration is controlled by the proportion of matrix to clasts and the amount of originally glassy material in the deposit. As different post-depositional processes effect the volcanics primary permeability may be destroyed or enhanced while new textures develop. In areas of intense alteration primary volcanic textures are generally destroyed.

Lithogeochemical exploration for metasomatic alteration zones using Pearce element ratios: Hellyer case study — Clifford R. Stanley and J. Bruce Gemmell

The Pearce Element ratio study intends to improve lithogeochemical exploration methods to enhance a geologist's ability to locate, identify and understand hydrothermal alteration zones, and thus improve their chances of discovering associated mineral deposits. This will be accomplished by: i) developing a numerical methodology, founded on simple yet sound theory, that may be used to quantify the metasomatism that accompanied the hydrothermal reactions responsible for the alteration zones and ii) investigate the Hellyer alteration system in order to test the lithogeochemical exploration methodology.

The study of the Hellyer VHMS deposit is broken down into two parts: I) previous data from both the footwall and hangingwall alteration zones will be interpreted to determine the systematics of the intense alteration and II) new samples and previous data from the immediate footwall and hangingwall lithologies away from the alteration zones will be analysed to determine vectors towards the alteration and mineralisation. Ninety new samples have been collected and whole rock analyses obtained from unaltered Hellyer basalt, Que River Shale and the footwall andesite in drill holes up to four kilometres away surrounding Hellyer.

From an initial analysis of the unaltered footwall plagioclase-phyric andesite, unaltered Que River Shale and footwall alteration whole rock data the significant findings are:

1. The new analyses of the unaltered footwall andesite and Que River Shale ("orientation data") are co-linear and plot along a background model lines. These data indicate the plagioclase phyric footwall andesite are cogenetic (derived from common parent that was at one time homogeneous). The data for the Que River Shale also indicates that they are cogenetic (they derive from a common parent that was at one time homogeneous - i.e. - the sediment source composition didn't change over time).
2. The altered samples show substantial variation from the background model lines. The deviation of the altered data from these lines indicates the degree of alteration and the direction of the deviation gives evidence as to the type and extent of the alteration processes.
3. Pearce element ratio analysis of the altered andesites in the immediate footwall indicate that they conatin significant amounts of both hydrolysis (sericite and chlorite) products and silicification (quartz).
4. Pearce element ratio analysis of the Que River Shale indicates a constant ratio of quartz : muscovite : chlorite for the majority of samples. Some samples have a over or under abundance of these minerals which may be due to some fractionation during the sorting of these minerals, or hydrothermalism may be responsible.

Petrographic and geochemical characteristics of alteration from the Hall Rivulet Canal–Mt Read–Red Hills–Anthony Dam traverse, Mt Read Volcanic Belt — Joe Stolz, Rod Allen, Cathryn Gifkins, Garry Davidson, Jocelyn McPhie and Michael Blake

Petrographic and geochemical studies of the samples from the Hall Rivulet Canal–Mt Read–Red Hills–Anthony Dam traverse indicate that diagenetic alteration of siliceous volcaniclastic sandstones involving albitisation and, less commonly, K-feldspar alteration is widespread. These styles of alteration produce distinctive chemical characteristics which are readily distinguishable from the more important and restricted hydrothermal alteration which produces the assemblage sericite ± pyrite ± chlorite. The chemical and mineralogical characteristics of the granitoid-related K–feldspar ± magnetite ± chlorite at Red Hills and Lake Selina are also documented and discussed.

'Barren' alteration systems: Example – Gydgie Central, Mt Windsor Volcanic Belt, North Queensland.

Joe Stolz, Garry Davidson and Michael Blake
Centre for Ore Deposit and Exploration Studies, Geology Department, University of Tasmania

Summary

Studies have been undertaken of the petrography, major and trace element chemistry, oxygen and sulphur isotopes for volcanic rocks within the Gydgie central alteration system. These data indicate that, despite some anomalous base metal enrichment, the area was not a major focus for high-temperature hydrothermal fluids, and therefore is not likely to be directly associated with massive sulphide mineralisation. Four major styles of alteration have been distinguished in the area and their chemical characteristics are outlined. Sulphur isotope data for pyrites ($\delta^{34}S = 8$ to 15‰) are similar to values for the Thalanga deposit and indicate an origin from fluids with a relatively high-temperature (>200°C) history.

Whole-rock oxygen isotope data do not indicate a zone of depletion in heavy oxygen in the Gydgie area. However, the $\delta^{18}O$ values for the Gydgie rocks (8–11.8) have been modelled in terms of a two-stage history.

Introduction

Within the Cambrian Mt Windsor Volcanic belt a number of areas of apparently prospective altered volcanic rock have been recognised, which after substantial exploration appear to have no obvious associated mineralisation. There are a number of possible explanations for the existence of these apparently barren alteration systems. Some of these include:

1. Mineralisation originally associated with the alteration system has been tectonically displaced or segregated from the focus of the alteration system.
2. Sedimentation rates were too high to enable concentrations of massive sulphides to accumulate on the sea floor. This is obviously not pertinent to sub-seafloor replacement massive sulphide bodies.
3. Fluid temperatures were not high enough to transport significant base metals.
4. There was insufficient focussing of hydrothermal fluids either due to the absence of suitable structural controls and/or because of the nature of the footwall lithology. Very porous and permiable volcaniclastic sequences may result in broad diffuse zones of sulphide development with associated hydrothermal alteration effects, but no significant sulphide accumulations.
5. The observed alteration effects represent the margins of a more intense zone nearby.
6. Fluid temperatures were too high for metals in solution to saturate and deposit base metal sulphides, forming only barren pyrite bodies.

Distinguishing between these possibilities is clearly very important when developing exploration models for the Mt Windsor belt in particular, but also for similar belts where such alteration systems are recognised. If mineralisation was originally present and has simply been structurally displaced from its alteration system, then structural models could be produced to predict the likely location to target drilling. However, if one of the other above scenarios is appropriate then it is vital to establish at an early stage in the exploration program the likely fertility of the alteration system being investigated.

This study concerns one such alteration system (Gydgie Central) within the Cambro-Ordovician Mt Windsor Volcanic belt (Fig. 1) that has been

extensively investigated by a number of companies including Esso, Pennaroya, Pancontinental Mining, and more recently RGC.

Regional geology and setting

The stratigraphy, structure and geochemistry of the Mt Windsor Volcanic belt have been discussed by Henderson (1985), Berry et al. (1992) and Stolz (1995). Briefly, the Mt Windsor subprovince is part of the early Palaeozoic Lolworth–Ravenswood block (Stolz, 1995) and it comprises a linear belt of volcano-sedimentary units which principally occur as a sub-vertical, south-facing limb of an east–west trending fold (Berry et al., 1992). The belt crops out discontinuously over a distance of about 160 km. It has been extensively intruded along its northern margin by Ordovician–Devonian granitoids of the Lolworth–Ravenswood batholith (Richards, 1980) and is covered to the south by Devonian to Carboniferous rocks of the Drummond basin and various ferricrete and alluvial deposits of Tertiary age.

The four major stratigraphic subdivisions in the Mt Windsor subprovince are

1. *Puddler Creek Formation* — a thick sedimentary package of mixed continental and volcanic provenance with minor mafic volcanics and intruded by abundant basaltic dykes.
2. *Mt Windsor Formation* — a thick sequence of rhyolitic volcanics and volcaniclastic rocks that overlies and is broadly conformable with the Puddler Creek Formation.
3. *Trooper Creek Formation* — a conformable, thinly intercalated sequence of basaltic to rhyolitic volcanic and volcaniclastic rocks.
4. *Rollston Range Formation* — a dominantly volcanic-derived sedimentary package largely devoid of primary volcanic units.

These volcanic and sedimentary units have experienced regional metamorphism ranging from prehnite–pumpellyite to greenschist facies with a contact metamorphic overprint related to the emplacement of granitoids at some localities along the northern margin of the belt (Berry et al., 1992).

The Gydgie alteration zone

The Gydgie alteration zone includes two prospects (Gydgie Central and Gydgie North) which are located within steeply dipping, intercalated rhyolitic to andesitic lavas, high-level intrusions and volcaniclastic units of the Trooper Creek Formation (Fig. 1). The altered appearance of the rocks is most evident in surface samples, from extensive iron staining and a bleached appearance reflected in substantial pyrite contents in the unweathered material. In addition, field mapping has delineated several gossanous zones over strongly "sericite-pyrite" altered volcaniclastic rocks.

Stream sediment sampling by Pennaroya indicated some weak base metal and precious metal anomalies which led to various follow-up RAB and RC drilling programs by Pennaroya and Pancontinental/Outokumpu. Base metal analyses of the bedrock RAB chip sample indicated a corridor of anomalous base metal concentrations which extends essentially continuously from the Gydgie North prospect in a southwesterly direction to the Gydgie Central prospect. This anomalous zone was initially interpreted as a likely feeder or footwall hydrothermal alteration pipe to a VHMS deposit. Consequently additional drilling was undertaken to locate the potentially mineralised horizon, or the contact between footwall and hangingwall packages based on changes in alteration style and intensity.

Objectives of this study

The principal objectives of this study are to:

1. Characterise the mineralogy and chemistry of the alteration;
2. Ascertain the relationships between alteration style and intensity to volcanic facies;
3. Determine the sulphur and oxygen isotope variations within the alteration zone; and
4. Assess the significance of the physical and chemical characteristics of the alteration in terms of the apparently 'barren' nature of this alteration style, and what distinguishes it from fertile alteration zones associated with mineralisation along strike.

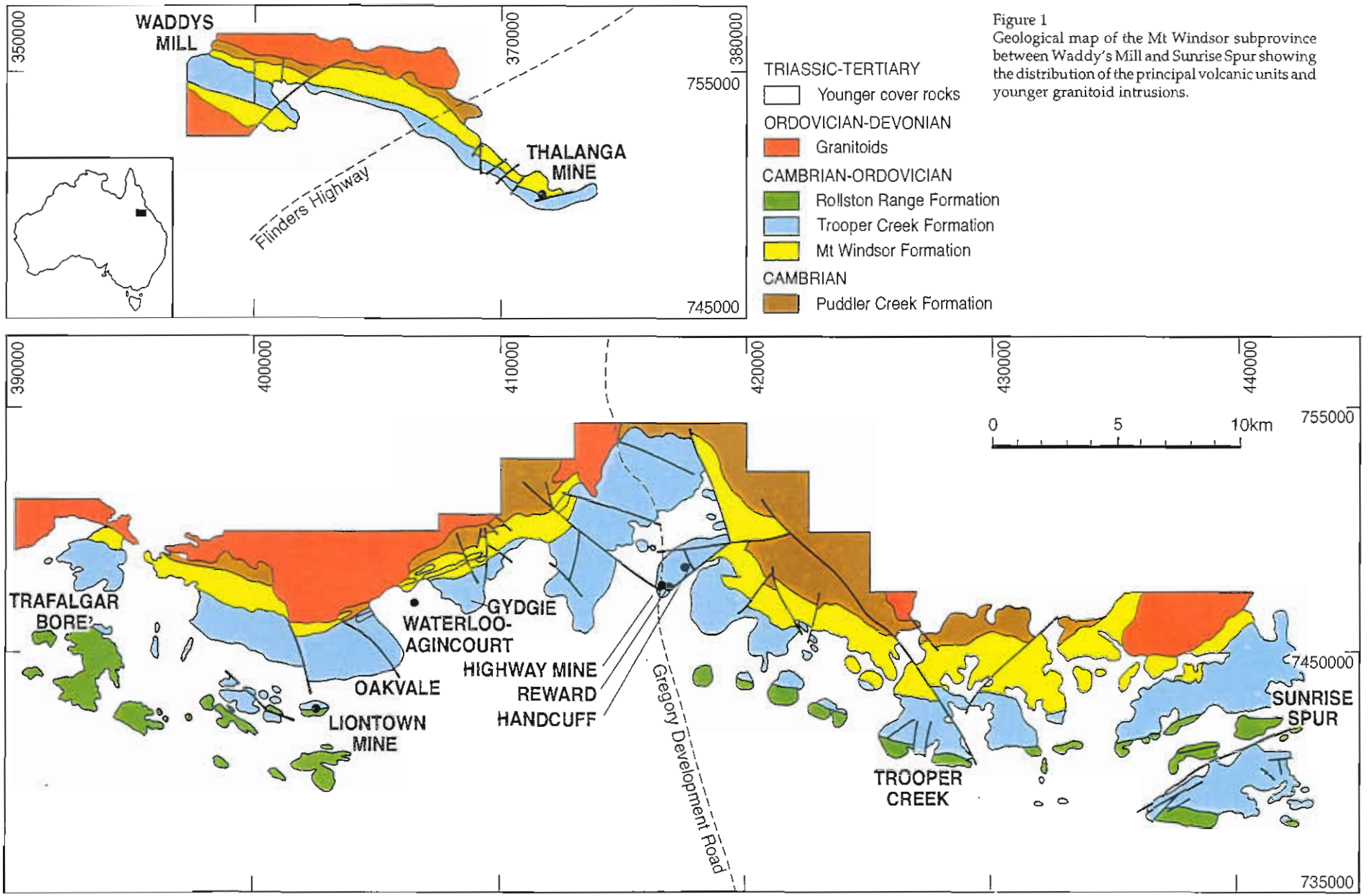

Figure 1
Geological map of the Mt Windsor subprovince between Waddy's Mill and Sunrise Spur showing the distribution of the principal volcanic units and younger granitoid intrusions.

Sampling strategy

The majority of samples for geochemical analysis were chips taken from the bottom of RAB holes drilled on a 50 m grid over the Gydgie Central prospect (Fig. 2). The RAB holes were generally stopped once they encountered unweathered bedrock and their depth varies somewhat but mostly exceeds 100 metres. These were supplemented by samples from RC holes and two diamond drill holes (GCDD1 and GCDD2). Samples for petrographic and sulphur isotope studies were derived both from outcrop and from the two diamond holes.

Lithologies

Examination of outcrop material indicated a predominance of volcaniclastic rocks within the study area with compositions ranging from andesitic to rhyolitic, and subordinate lavas and dykes with a similar range of compositions. The volcaniclastic rocks range from coarse volcanic lithic breccias and volcaniclastic sandstones to volcanic ash-rich siltstones.

Volcanic lithic breccias and pumice breccias

These are typically composed of abundant angular to subrounded fragments (up to 10's of cm diameter) of coherent and pumiceous rhyolitic to dacitic material, with subordinate fragments of andesitic lava (Figs. 3–6). The rhyolitic fragments are characterised by relatively large (2–3 mm), cracked and partly resorbed quartz phenocrysts and subhedral plagioclase phenocrysts in a very fine, recrystallised quartz-feldspar-rich groundmass which in some examples is spherulitic. Some of the surface breccia samples contain clasts (cm size) of Fe oxides after massive sulphide (Fig. 3E,). Fresh samples of similar breccia material (e.g. GCDD1/6, GCDD1/8, GCDD1/9 and GCDD1/10) contain clasts of massive pyrite (Fig. 3). The matrix of the breccias is composed of smaller lithic fragments, including tube pumice, abundant angular quartz and feldspar grains, and very fine quartz and feldspar which most likely represents recrystallised silicic ash. The matrix of these breccias exhibit variable amounts of sericite, which, in some cases, preferentially replaces the fine ash component, together with idiomorphic carbonate crystals, and disseminated cubes of pyrite (<0.1–0.5 mm).

Volcaniclastic sandstones

These are typically composed of abundant angular plagioclase grains (0.5–1.5 mm; albite twinned and unzoned) which display weak clay alteration, subordinate angular quartz grains and similar size lithic fragments composed mainly of fine recrystallised quartz and feldspar. Less common lithic fragments are andesitic in composition and may have sparse plagioclase phenocrysts in a fine groundmass of plagioclase microlites with interstitial chlorite. Tube pumice fragments display the characteristic banding defined by alternating layers of albite and chlorite (Fig. 5D). The matrix is composed of very fine recrystallised quartz and feldspar after silicic ash, and it exhibits variable replacement by sericite in veinlets, patchy aggregates of albite (Fig. 5), aggregates of idiomorphic carbonate crystals and disseminated pyrite (Fig. 4). Carbonate has also partly replaced some plagioclase grains (Fig. 6).

Siltstones

Composed of tiny angular quartz and feldspar grains in a very fine grained quartz-feldspar-rich matrix after recrystallised silicic ash (Fig. 3). Some of the angular grains are clearly shards. The matrix in some samples has a weak cleavage defined by fine muscovite which may , however, comprise only about 10% of the rock. Patchy carbonate occurs throughout and is characterised by aggregates of idiomorphic crystals which in some cases appear to be intergrown with sericite. Some ash-rich siltstones have relatively high pyrite contents (up to 10–15%) occurring as disseminated cubes (0.05–0.2 mm), whereas pyrite is sparse in other examples.

Rhyolitic and dacitic lavas

The rhyolitic lavas typically have euhedral, partly resorbed quartz phenocrysts ± subordinate plagioclase phenocrysts in a relatively homogeneous, very fine grained recrystallised groundmass that is commonly spherulitic. The groundmass displays

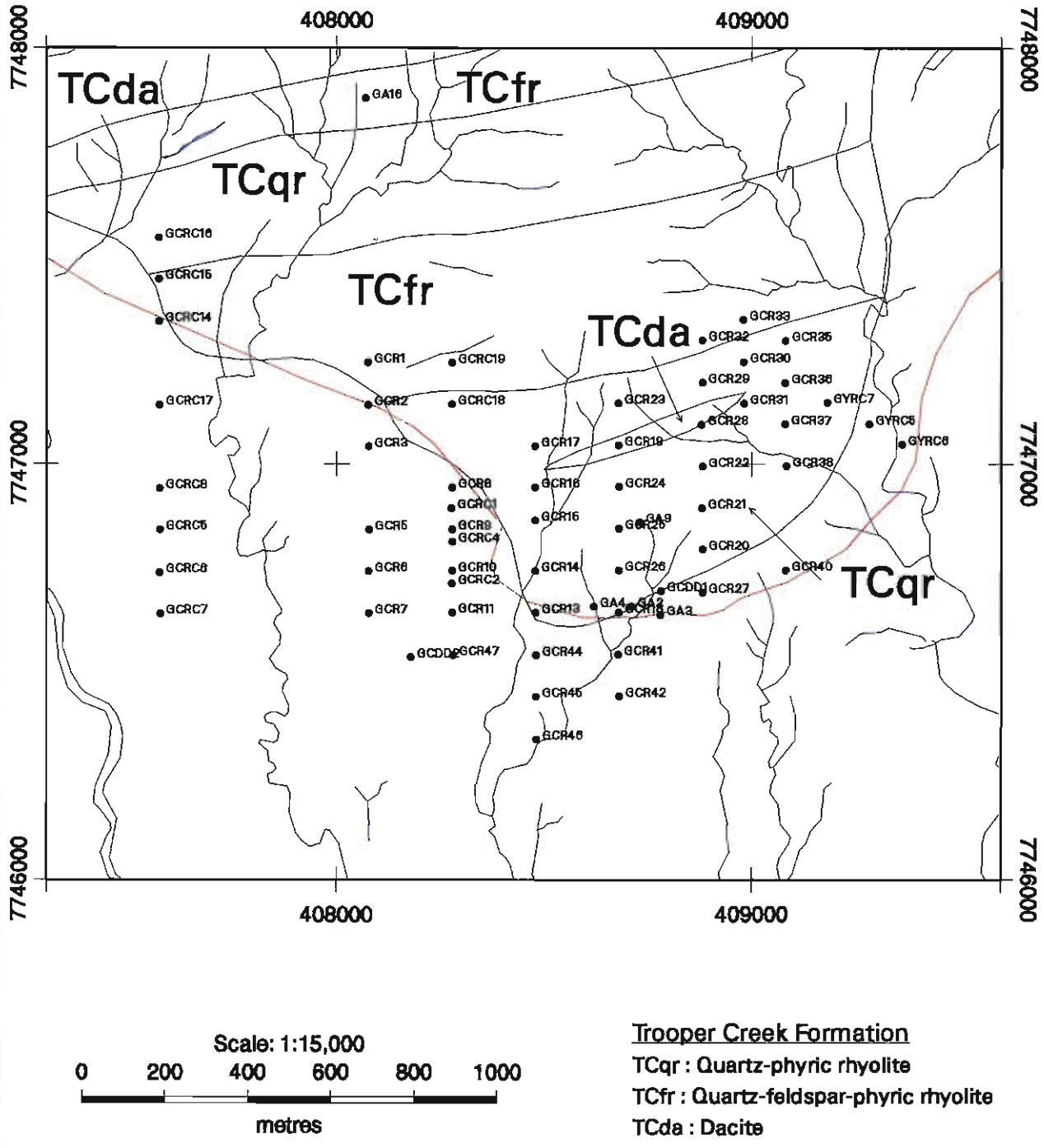

Figure 2
Map showing the area of the Gydgie Central prospect, together with the local geology and locations of drill holes and surface samples used in the study.

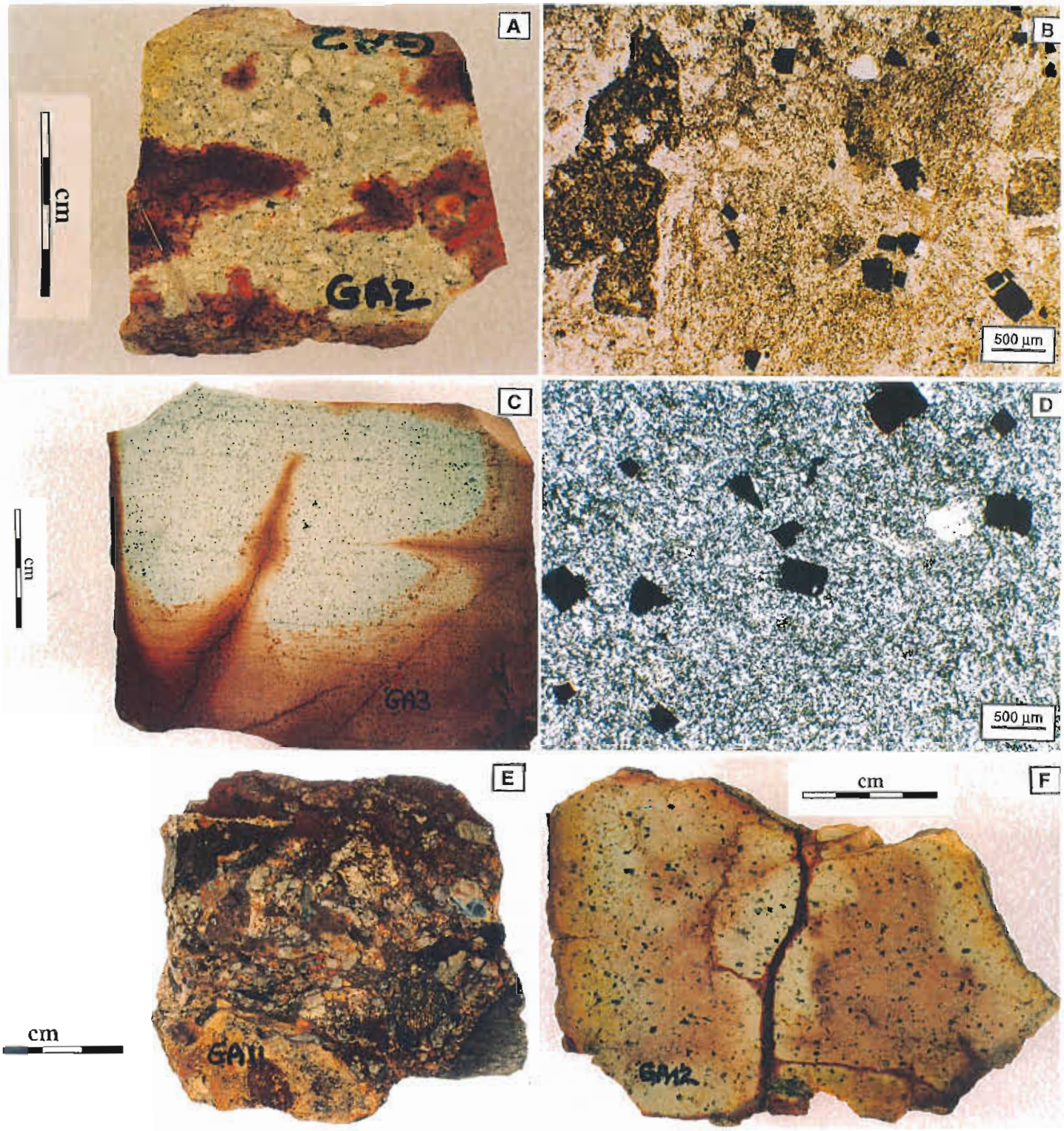

Figure 3
(A) Pumice breccia (GA2) with fine disseminated pyrite. (B) Photomicrograph of pumice breccia (GA2) showing siliceous pumice fragments and a more mafic clast with disseminated pyrite. (PPL) (C) Pyritic siliceous siltstone (GA3). (D) Photomicrograph of siliceous siltstone (GA3) showing a small unaltered albite grain in a very fine grained matrix of albite and quartz, and relatively coarse grained disseminated pyrite. (CPL). (E) Lithic breccia (GA11) with oxidised massive sulphide clast. (F) Quartz feldspar-phyric rhyolite (GA12) with oxidised pyritic veins.

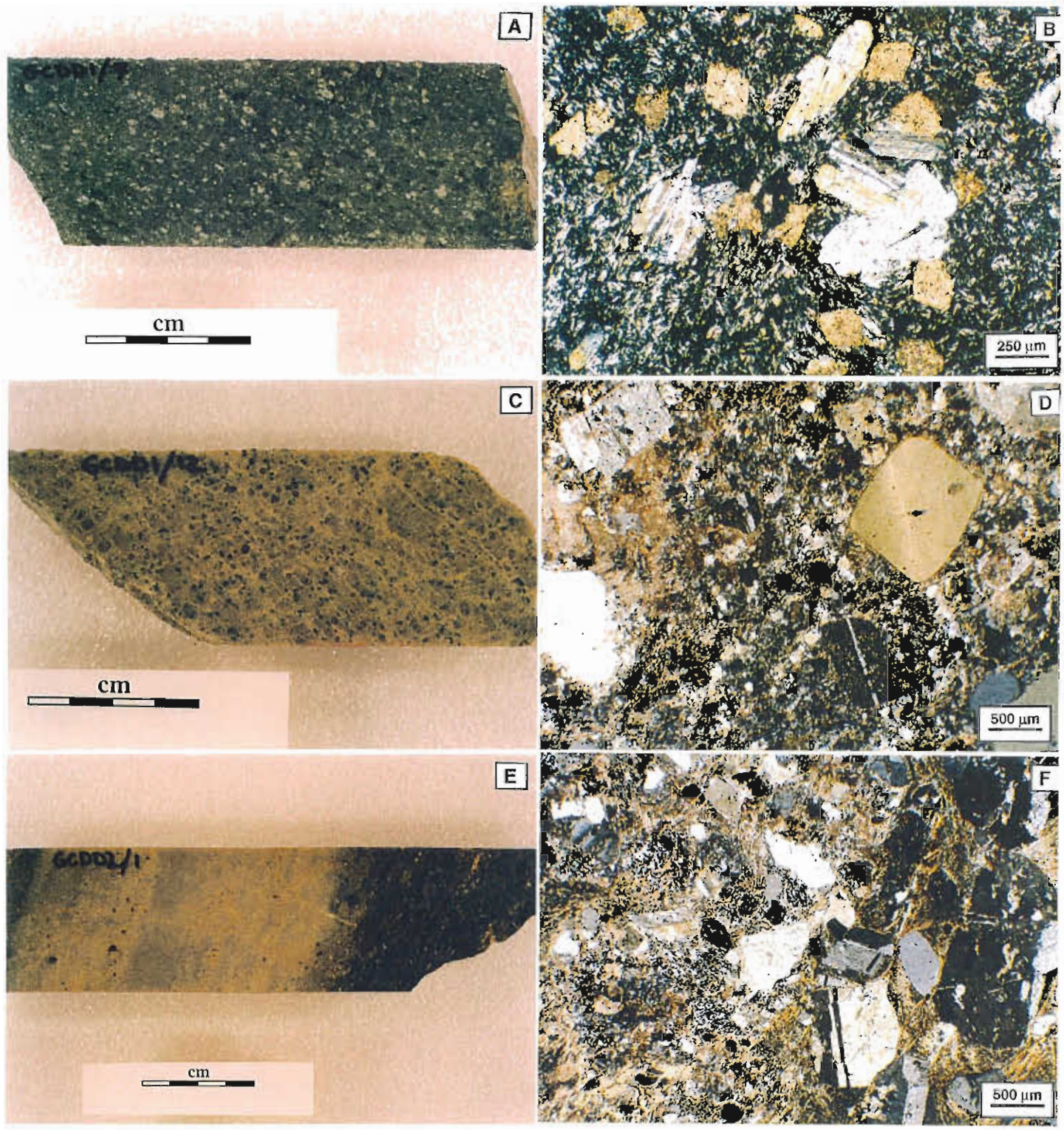

Figure 4
(A) Relatively unaltered plagioclase-phyric basalt (GCDD1/7) (B) Photomicrograph of basalt GCDD1/7 showing plagioclase phenocrysts, partly altered to carbonate in a groundmass of plagioclase laths with interstitial chlorite and disseminated carbonate grains. (CPL). (C) Relatively unaltered coherent quartz-feldspar-phyric rhyolite (GCDD1/12). (D) Photomicrograph of rhyolite GCDD1/12. (CPL). (E) Volcaniclastic sandsone (GCDD2/1) with chlorite-rich and chlorite-poor layers. (F) Photomicrograph of margin between chlorite-rich (relatively crystal-rich) layer and a chlorite poor (relatively ash-rich) layer in GCDD2/1). (CPL).

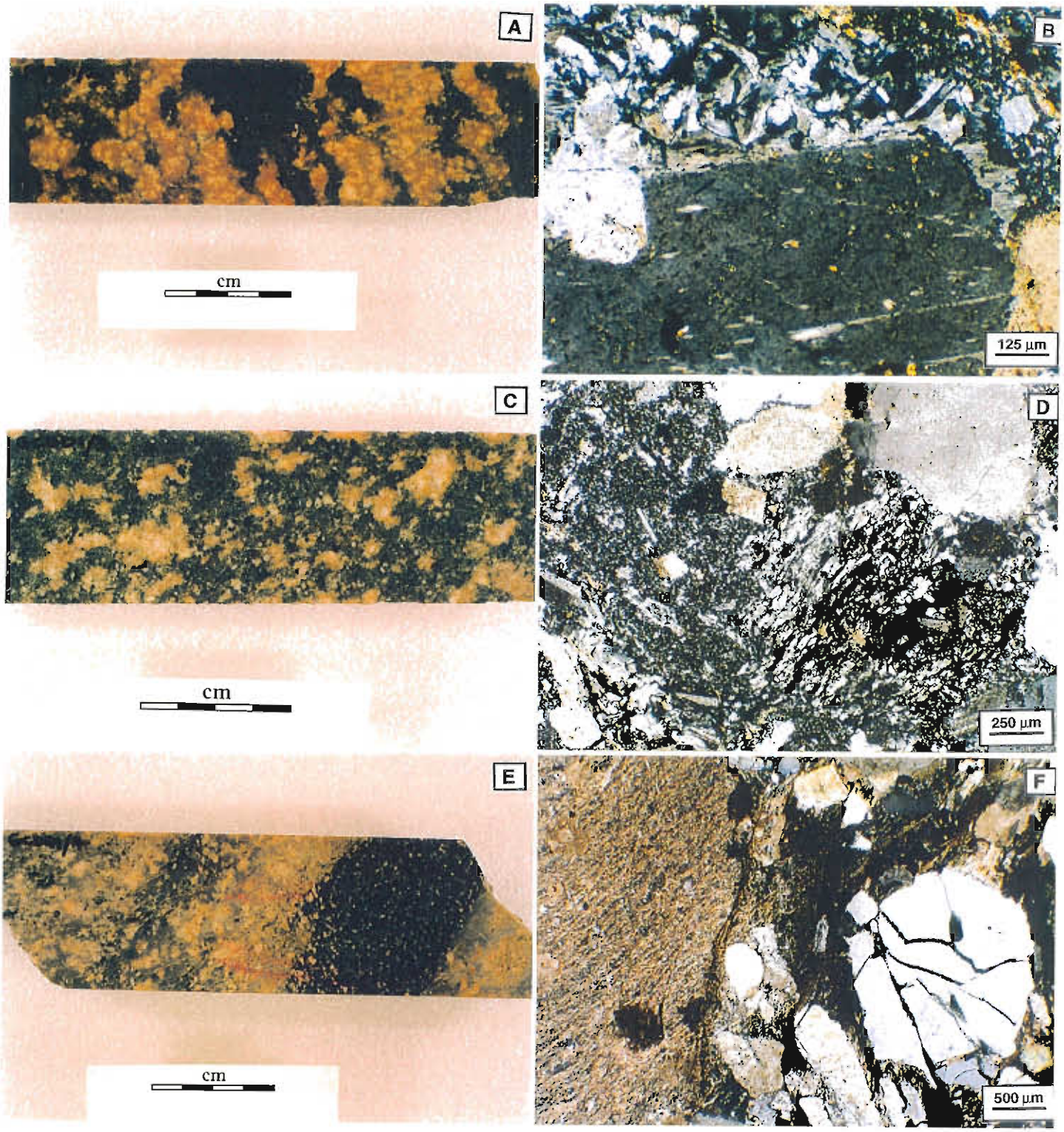

Figure 5
(A) Patchy albite-altered dacite (GCDD1/2) showing distinctive pink albite aggregates. (B) Photomicrograph of GCDD1/2 showing a plagioclase phenocryst with narrow marginal albite overgrowths and an adjacent aggregate of decussate laths of albite. (CPL). (C) Patchy pink albite alteration in lithic breccia GCDD1/3. (D) Photomicrograph of GCDD1/3 showing tube pumice fragment with alternating albite and chlorite layers. (CPL). (E) Volcaniclastic sandstone GCDD1/4 showing chlorite-rich patch. (F) Photomicrograph showing the margin between the crystal-rich and chlorite-rich patch and fine grained ash-rich matrix in sandstone GCDD1/4. (PPL)

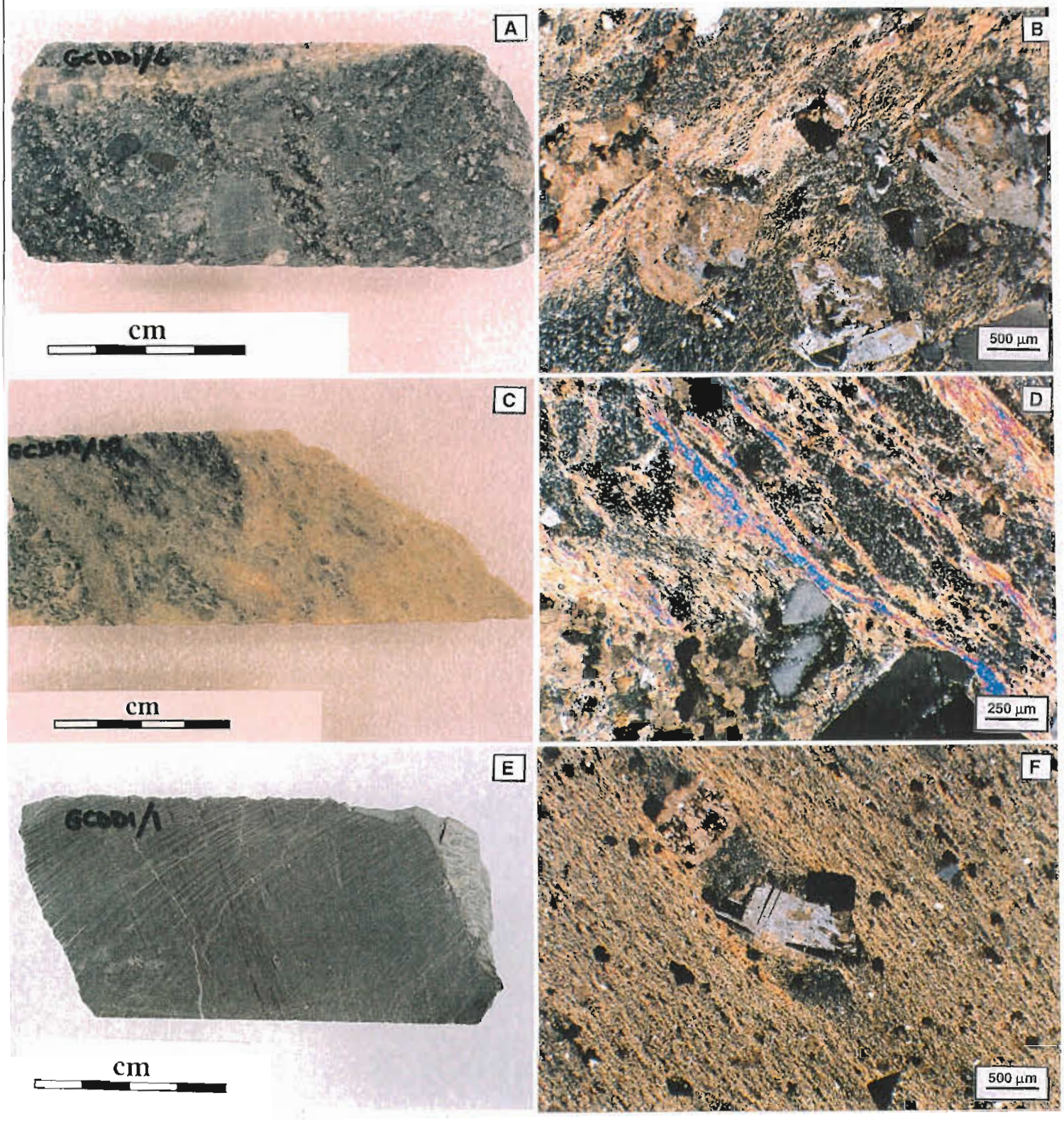

Figure 6
(A) Lithic breccia GCDD1/6 with abundant dacitic to andesitic clasts and a small pyrite clast. (B) Photomicrograph of GCDD1/6 showing plagioclase grains partly altered to carbonate, and partial alteration of the quartz-albite matrix to sericite. (CPL). (C) Quartz-phyric rhyolite GCDD1/10 showing variable sericitic alteration. (D) Photomicrograph showing sericite veinlets partly replacing the albite-quartz groundmass of rhyolite GCDD1/10. There is some patchy carbonate alteration but plagioclase phenocrysts are only partly altered. (CPL). (E) Pyritic siltstone GCDD1/1. (F) Photomicrograph of GCDD1/1 showing weakly carbonate altered plagioclase grains in a strongly sericite and pyrite altered matrix. (CPL).

variable alteration to sericite and a pale brown chlorite which may be dispersed or localised in veinlets and which define a weak cleavage. Patchy carbonate alteration is also common and widespread. Pyrite may occur concentrated in veinlets with carbonate, or weakly disseminated throughout the groundmass. The dacitic lavas are texturally similar although lack quartz as a phenocryst phase and have relatively abundant subhedral plagioclase phenocrysts.

Andesitic/basaltic lavas

These are characterised by sparse plagioclase phenocrysts, either unaltered or partly replaced by carbonate (Fig. 4), and elongate chlorite patches (probably after ferromagnesian phenocrysts) set in a fine groundmass composed of plagioclase laths, interstitial chlorite and fine granular opaques. These mafic units may occur as breccias, and some examples are vesicular with the vesicles filled by quartz, chlorite and carbonate. There is commonly a trace of sericite through the groundmass, some disseminated cubes of pyrite, and patchy carbonate alteration of the groundmass that may be extensive.

Alteration styles and intensity

There appear to be four main styles of alteration in the Gydgie rocks:

1. Disseminated and vein pyrite alteration
2. Albite alteration
3. Carbonate alteration
4. Sericite–chlorite–pyrite alteration

Disseminated and vein pyrite alteration

This is the most widespread and obvious alteration in the area and may vary from a trace to about 15% pyrite in some samples. The pyrite alteration commonly is not necessarily associated with significant sericite alteration, and the majority of these pyritic rocks contain unaltered feldspar both as phenocrysts and in the groundmass (Figs 3, 4). The pyrite typically occurs as cubes (0.1–0.5 mm) disseminated throughout the matrix of volcaniclastic sandstones and volcanic lithic breccias, and also throughout siltstones composed of recrystallised volcanic ash and carbonaceous siltstones. In the chloritised pyritic basalts the pyrite grains are elongate and aligned in the cleavage. There is also some remobilisation of pyrite into narrow (1 mm) veins in these rocks. The more coherent rhyolitic to dacitic rocks in the package typically have pyrite occurring in narrow veinlets (Fig. 3) rather than disseminated.

Albite alteration

Feldspar-dominated alteration is common in the volcaniclastic sandstones and lithic breccias, and in handspecimen these rocks often have a patchy pink–green colour (Fig. 5). The albite occurs as overgrowths on detrital plagioclase grains and ovoid patches of decussate, tabular, weakly twinned albitic plagioclase within the matrix or around plagioclase grains (Fig. 5). Chlorite is the principal ferromagnesian phase in these rocks, and epidote, which is relatively common in albite altered rocks from the Mt Read Volcanic belt, is absent. The available Ca appears to be in carbonate which is much more abundant in the Gydgie rocks than feldspar-altered MRV rocks.

Carbonate

This is widespread throughout the area and is commonly significant. Carbonate occurs replacing plagioclase grains and in patches or aggregates of idiomorphic crystals within the matrix usually closely associated with pyrite. Later remobilisaton of carbonate into cross-cutting veins is also widespread. No compositional data for the carbonates are available as yet.

Sericite–chlorite–pyrite

Some samples with abundant pyrite also display weak to moderate sericite–chlorite alteration. The most altered samples for which thin sections are available (e.g. GCDD1/1, GCDD1/6) exhibit substantial development of sericite and subordinate chlorite in the matrix, but detrital feldspar grains are generally only weakly altered to sericite and perhaps carbonate (Fig. 6). The absence of total feldspar destruction in these rocks is reflected in their bulk rock compositions and appears to be an important indication of the intensity of the hydrothermal alteration in the Gydgie area.

Geochemistry

Analytical methods

Major elements (SiO_2, TiO_2, Al_2O_3, ΣFe_2O_3, MnO, MgO, CaO, Na_2O, K_2O, P_2O_5, S) and most trace elements (Sc, V, Cr, Ni, Cu, Zn, Rb, Sr, Y, Zr, Nb, Ba, La, Ce, Nd, Pb, Th) were determined by XRF in the Geology Department at the University of Tasmania. Major elements were determined on glass discs prepared by a lithium metaborate fusion and the trace elements were measured on pressed pellets. A combination of international and in-house standards were used to monitor accuracy and precision of the analyses. Based on >>100 analyses of the in-house standard rocks, 1 sigma precision for the major elements is generally better than 2% (except for MnO, ± 5–7%), and the trace elements generally have a precision of 1–5%. Total carbon was determined by Analabs in Perth using the Leco technique which has a detection limit of 0.05 wt.%. Standard and duplicate analyses indicated that measured values were slightly higher (~10%) than the recommended values, but the precision was generally better than 5%.

An additonal suite of elements (As, Mo, Ag, Cd, Sb, Cs, Tl, Bi, Th, U) were determined on the same sample powders by Analabs in Perth using ICP-MS following a combined HF–HNO_3–$HClO_4$ acid digestion. This technique was adopted for these elements due to its greater sensitivity and lower detection limits compared with XRF. For example, Ag, Bi, Mo, Cd and Sb have a detection limit of 0.1 ppm, As (1 ppm), Tl (0.5 ppm), and Cs, Th and U (0.05 ppm). The accuracy and precision of these analyses were checked by inclusion of unidentified suites of standard rocks and by including a duplicate powder of every 10th sample. Comparison of the average values for the standards (Table 1) indicates the analyses were generally accurate within 5–10%, and the sample duplicates and standard replicates indicate precision generally better than 5–10%.

Major and trace element results

The major and trace element data for the Gydgie samples are presented in Table 2. Selected elements and element ratios have been plotted (Figs 7–30) using the GIS package ARCINFO to demonstrate the chemical variability over the Gydgie Central grid that has implications for alteration intensity and extent of enrichment in base and precious metals. To highlight element distributions the images are presented with the range of element concentrations and ratio values contoured using colours ranging from blue (lowest values) through various shades of green, yellow and orange to red for the highest values. The maximum values shown on the colour scales do not always indicate maximum concentrations in the rocks, but any values higher or lower than the maxima and minima on the scales are coloured red and blue, respectively. Colour distributions for the individual cells in the selection area are based on inverse distance weighted interpolated values determined using a linearly weighted combination of the sample points.

The images for Ti/Zr and total Fe as Fe_2O_3 clearly delineate some significant lithological variations at depth that are not evident from the surface geology. There are two andesitic to basaltic units (Ti/Zr = 80–95) that appear to strike NE–SW across the prospect, a trend that is consistent with the general strike indicated by the surface geology. These relatively mafic units also appear to exert a significant control on the distribution of sulphur and possibly carbonate during alteration as the maxima for these variables coincide closely with those on the Ti/Zr and total Fe images.

The images for Cu, Pb and Zn display well defined anomalies with Zn displaying a single strong anomaly in the centre of the grid and a smaller zone of enrichment in the northeastern corner. Cu and Pb show additional zones of enrichment in the eastern part of the grid. The distribution pattern for Cd mimics Zn, whereas Tl and Ag mimic Pb. Antimony and As display zones of enrichment which broadly coincide with those for Cu, Pb and Zn, but the maxima are more dispersed and there is an additional zone of enrichment in the northern part of the grid. The maximum concentrations of Bi in the area coincide broadly with this northern zone, but Bi and Mo also display enriched zones in the western part of the grid which correlate with enrichment zones of Cu, Fe and S. There are two small zones of anomalous

MnO concentrations which appear to broadly to correlate with the enrichment in base metals and S.

Zones of strong Na_2O and CaO depletion coupled with relative enrichment in K_2O and related elements bound in sericite (e.g. Ba, Cs, Rb) are well known features of focussed hydrothermal upflow zones associated with VHMS mineralisation. The Gydgie rocks display one zone of Na_2O depletion with values < 1wt.% Na_2O which coincides with a zone of enrichment in K_2O, Rb, Ba and Cs, however the area of Na_2O depletion is very restricted. The general lack of depletion, and indeed, enrichment in Na_2O in many of these rocks, is consistent with the petrographic observations which indicate plagioclase has remained stable and been added to through overgrowths of albite. The enhanced Rb concentrations for the most altered rocks are not anomalously high for rhyolitic rocks, although evidence from other studies indicates that where the albitisation process results in exchange of Na for K, Rb closely follows K and commonly is present at very low concentrations in the K-poor silicic rocks (e.g. <10ppm). In contrast, where K is strongly enriched relative to Na the Rb abundances are strongly elevated (~200ppm). Concentrations of Ba in the anomalous zones are substantially higher than expected levels in the rhyolitic rocks but these also appear to be modified by the alkali exchange effects associated with the albitisation. On the other hand, maximum Cs concentrations in the restricted anomalous zone (~ 4.5ppm) are probably lower than the concentrations in modern unaltered dacitic to rhyolitic rocks from island arc settings, but the enrichment has been superimposed on very low levels which resulted from the albitic alteration. The zone of strongest Na_2O depletion and metal enrichment correlate broadly with higher values for the alteration index of Ishikawa et al. (1976). However, the lack of very high values (i.e. >80) for this alteration index reflects the restricted Na depletion in the area. Similarly, the very low values of the alteration index for some samples (e.g. < 25–30) reflects the overall addition of Na_2O in the albitised rocks. Enrichment in total C expressed as CO_2 generally also occurs in the region of maximum base metal enrichment within the central part of the grid, but is a more widespread and diffuse zone.

Ratios of certain elements commonly better reflect processes than mapping of individual elements. For example, Th is a generally regarded as a relatively immobile element during alteration at low water/rock values, whereas U is typically quite mobile. The Th/U values for unaltered modern volcanics exhibit a very restricted range (~2 to 4) as magmatic processes are not capable of significantly fractionating these elements. It is only through weathering and other fluid-related proceses that the Th/U values are modified from this limited range of primary values. The distribution of Th/U values in the Gydgie area indicates a number of zones with slightly elevated values (i.e. >4) which might indicate some U loss during weak alteration, and one distinctive zone with a very high Th/U value that coincides with a zone of metal enrichment and stronger alteration. The distribution of Rb/Sr should also reflect zones of maximum alteration as these should be characterised by strong Sr depletion as a result of feldspar destruction and relative enrichment of Rb with K during sericite development. However, the range of Rb/Sr values in volcanics can vary from values of 0.2–0.3 for basaltic rocks to values of 1–10 in rhyoltic rocks, the higher values occurring in rhyolitic rocks that have experienced extensive feldspar fractionation. Although the Rb/Sr distribution in the Gydgie area displays maxima in the more altered zones which most likely reflect fluid-related processes, many of the values lie within the range of fractionated rhyolites. This ratio would be best suited to mafic volcanic packages which have low initial Rb/Sr values that are likely to be most severely modified by hydrothermal alteration processes.

(text continues on p. 75)

Table 1. Comparison of average values for standards analysed by ICP-MS with recommended values.

Detection limit	Ag	As	Bi	Mo	Cd
ppm	0.1	1	0.1	0.1	0.1
GSS1	0.2	45	1.2	2.7	4.9
expected	0.35+-0.03	33.5+-1.7	1.17+-0.06	1.4+-0.1	4.3+-0.2
GSS3	0.1	5	0.2	0.3	<0.1
expected	0.091+-.004	4.4+-0.3	0.17+-0.02	0.30+-0.04	0.059+-.009
GSD7	1.1	87	0.6	1.5	1.5
expected	1.05+-0.04	84+-3	0.66+-0.05	1.4+-0.07	1.05+-0.04
TASBAS (aver 8)	0.2	2.6	<0.1	7.5	0.2
expected	?	1.17	?	7.4	0.1
TASGRAN (aver 6)	<0.1	<1	<0.1	0.3	<0.1
expected	?	0.38	?	0.31	0.088
GSS5 (aver 6)	4.1	427	41	5.1	0.55
expected	4.4+-0.3	412+-8	41+-2	4.6+-0.2	0.45+-0.04
GSS6 (aver 4)	0.2	225	51	18.4	<0.1
expected	0.20+-0.01	220+-7	49+-3	18+-1	0.13+-0.02
GXR4/542 (aver 6)	2.9	107	18.9	311	1.3
expected	4.0+-1.0	98+-7	19+-4	310+-60	0.86+-0.60
TASDOL (aver 7)	<0.1	2	<0.1	1	0.3
expected	?	0.7	?	1.04, 1.77	0.12
GXR1/534	28.1	372	1270	15.6	2.6
expected	31.0+-4.0	427+-45	1380+-60	18.0+-6.0	3.3+-1.3
GXR2/527	16.4	26	0.1	1.3	4.7
expected	17+-3	25+-4	0.69+-0.42	2.1+-1.0	4.1+-0.7

Expected values for TASBAS, TASGRAN and TASDOL are based on ICP-MS and Spark Source Mass Spectrometry data from the Research School of Earth Sciences, ANU.

Sb	Cs	Tl	Th	U
0.1	0.05	0.5	0.05	0.05
1.5	8.25	1.4	not analysed	3.02
0.87+-0.12	**9.0+-0.4**	**1.0+-0.1**	**11.6+-0.4**	**3.3+-0.3**
0.5	2.48	<0.5	not analysed	0.99
0.45+-0.06	**3.2+-0.3**	**(0.48?)**	**6.0+-0.3**	**1.26+-0.18**
2.7	4.7	0.9	not analysed	3.4
2.6+-0.2	**5.9+-0.4**	**0.93+-0.10**	**12.6+-0.7**	**3.5+-0.2**
0.3	**0.98**	**<0.5**	**4.81**	**1.85**
0.1	**1.06, 1.22**	**?**	**4.76**	**1.86**
0.1	**11.5**	**1.5**	**19.9**	**2.88**
0.126	**13.21**	**1.2**	**19.0,19.5**	**3.21**
39.5	**13.70**	**2.3**	**24.0**	**6.52**
35.4+-2.4	**15.0+-0.6**	**1.6+-0.2**	**22.7+-0.8**	**6.5+-0.5**
61	**9.96**	**2.8**	**23.6**	**6.89**
60+-3	**10.8+-0.3**	**2.4+-0.3**	**23+-1**	**6.7+-0.5**
4.6	**2.49**	**3.5**	**21.6**	**5.59**
4.8+-0.4	**2.8+-0.3**	**3.2+-0.5**	**22.5+-1.6**	**6.2+-1.3**
0.3	**4.74**	**0.60**	**6.81**	**2.33**
0.332	**5.01, 6.45**	**0.44**	**6.68**	**2.29**
87.7	2.56	*3.3(high!)*	2.94	31
122+-18	**3.0+-0.6**	**0.39+-0.2**	**2.44+-0.19**	**34.9+-1.2**
31.8	*4.35*	*2.8*	9.1	2.66
49+-5	**5.2+-0.3**	**1.03+-0.23**	**8.8+-0.3**	**2.9+-0.06**

Table 2. Major and trace element analyses of volcanic rocks from the Gydgie Central prospect.

	GCR1	GCR2	GCR3	GCR5	GCR6	GCR7	GCR8	GCR9	GCR10	GCR11	GCR13	GCR14
SiO2	76.34	71.15	51.82	70.69		67.71				74.7	70.73	70.18
TiO2	0.23	0.49	1.26	0.62		0.34				0.23	0.33	0.2
Al2O3	13.38	12.08	15.11	11.56		12.65				12.69	12.1	9.59
Fe2O3#	1.99	5.1	12.27	5.59		3.4				1.81	3.17	3.7
MnO	<0.01	0.14	0.23	0.09		0.17				0.08	0.12	0.13
MgO	0.21	2.62	5.20	3.24		1.6				0.74	1.5	2.17
CaO	0.1	0.11	1.65	0.31		2.37				0.89	2.15	2.61
Na2O	3.11	1.01	4.27	1.28		4.48				3.47	0.97	1.33
K2O	1.38	2.1	0.31	2.42		1.4				2.48	3.45	2.06
P2O5	0.03	0.07	0.26	0.21		0.09				0.03	0.08	0.05
LOI	2.12	4.94	7.23	3.8		5.19				2.3	5.63	7.15
TOTAL	98.89	99.81	99.62	99.81		99.40				99.42	100.23	99.17
Tl/Zr	9.3	35.5	80.3	47.7		19.2				7.9	16.6	13.8
S	1.04	1.94	5.48	1.94		0.49				0.16	0.31	1.43
Total C	0.05	0.44	1.09	1.04	2.39	1.16	0.49	0.8	0.78	0.35	0.87	1.38
CO2	0.18	1.61	3.99	3.81	8.76	4.25	1.80	2.93	2.86	1.28	3.19	5.06
Alteration Index	33.1	80.8	48.2	78.1		30.5				42.5	61.3	51.8
Trace Elements (ppm)												
Sc	11	29	38	23	30	13	32	31	32	8	12	9
V	21	164	261	101	130	44	162	161	166	9	50	22
Cr	3	5	3	2	4	7	6	9	7	2	7	2
Ni	<1	4	3	<1	2	<1	14	3	3	<1	<1	2
Cu	14	9	188	148	29	16	474	192	110	5	65	23
Zn	14	209	113	861	103	70	3705	1143	2430	26	205	264
As	13	22	18	33	1	8	40	17	7	1	6	21
Rb	27	43	6	41	66	42	14	14	22	72	95	46
Sr	129	63	69	39	190	178	67	74	78	89	66	82
Y	17	15	24	17	28	18	26	20	22	23	18	12
Zr	149	83	94	77	110	106	78	80	100	174	119	87
Nb	6.9	4.4	5.8	4.6	6.1	5.8	5.1	4.5	5.1	8	6.2	4.5
Mo	0.5	0.4	0.4	3.5	0.3	0.7	1.1	0.8	0.2	0.1	1.6	2.4
Ag	<0.1	<0.1	<0.1	0.2	<0.1	<0.1	0.3	0.2	0.1	<0.1	0.4	0.1
Cd	<0.1	0.3	0.4	2.7	0.4	0.2	6.5	2.7	10.5	0.4	2.2	0.8
Sb	0.2	0.2	0.4	0.9	0.4	0.8	0.4	0.6	0.5	0.8	3.4	0.8
Cs	0.41	0.45	0.25	0.73	1.55	0.93	0.39	0.35	0.44	1.17	1.68	0.95
Ba	353	740	65	1119	763	845	136	186	823	944	1701	716
La	15	4	12	7	12	15	9	6	11	13	13	9
Ce	29	17	21	20	22	34	22	13	20	28	29	21
Nd	15	6	16	10	13	13	13	8	10	11	12	9
Tl	<0.5	<0.5	<0.5	0.6	<0.5	<0.5	0.6	0.8	<0.5	<0.5	0.7	0.8
Pb	4	7	4	7	4	4	123	105	5	6	85	83
Bi	0.9	3	3.8	0.1	<0.1	0.3	0.9	0.9	0.8	0.1	0.3	0.2
Th	8.09	4.01	2.33	2.14	2.61	5.39	2.73	2.46	2.59	8.84	6.38	4.75
U	1.58	1.71	0.77	0.97	0.81	1.38	0.72	0.71	0.7	2.15	1.62	1.22

Total Fe as Fe2O3; LOI = loss on ignition; Alteration Index = 100(MgO+K2O)/(MgO+K2O+CaO+Na2O)

Table 2. continued.

	GCR16	GCR17	GCR18	GCR19	GCR20	GCR21	GCR22	GCR23	GCR24	GCR25	GCR26	GCR27	GCR29
SiO2		54.35	64.73	72.46		74.18			65.67	87.65		70.05	
TiO2		0.54	0.52	0.29		0.22			0.86	0.17		0.43	
Al2O3		16.66	12.81	12.87		12.07			14.07	5.94		14.62	
Fe2O3#		7.67	7.25	2.46		1.66			4.98	1.96		3.6	
MnO		0.36	2.12	0.11		<0.01			0.31	0.31		0.04	
MgO		6.94	2.2	1.61		0.14			3.07	0.22		2.09	
CaO		1.20	1.12	0.85		0.04			0.87	0.11		0.17	
Na2O		4.13	0.22	3.97		1.08			4.73	1.61		2.88	
K2O		0.70	2.98	1.43		1.65			0.69	0.99		2.38	
P2O5		0.11	0.24	0.07		0.07			0.21	0.05		0.08	
LOI		6.94	4.96	2.34		8.03			3.4	0.89		2.71	
TOTAL		99.60	99.15	98.46		99.14			98.86	99.90		99.05	
Ti/Zr		37.6	27.5	14.5		15.2			38.6	19.5		20.5	
S		2.45	0.23	1.08		2.95			0.94	0.01		0.77	
Total C	0.04	0.7	0.49	0.3	0.6	0.09	0.34	0.04	0.28	0.07	0.56	0.24	0.09
CO2	0.15	2.56	1.80	1.10	2.20	0.33	1.25	0.15	1.03	0.26	2.05	0.88	0.33
Alteration Index		58.9	79.4	38.7		61.5			40.2	41.3		59.4	
Trace Elements (ppm)													
Sc	10	29	14	13	9	16	7	12	22	5	8	11	14
V	4	279	88	21	24	30	7	21	113	26	12	43	30
Cr	2	9	70	2	7	3	3	2	4	12	3	17	5
Ni	<1	8	<1	<1	5	3	<1	<1	<1	<1	1	<1	3
Cu	9	156	204	11	29	2398	41	62	20	32	42	51	12
Zn	29	310	126	132	127	153	220	58	108	84	140	71	604
As	7	22	66	17	5	51	5	12	13	19	10	21	16
Rb	17	14	105	28	34	38	35	28	14	24	37	42	63
Sr	99	187	91	148	90	167	44	101	132	80	108	151	36
Y	31	17	29	18	20	10	25	17	26	11	19	21	22
Zr	165	86	114	120	136	87	162	115	134	52	130	126	150
Nb	10.8	5.8	11.4	5.1	7.6	3.8	14.2	5.6	7.1	3.9	6.6	8	7.6
Mo	1.5	1.6	3.2	0.9	0.3	1.1	0.3	0.9	1.1	0.6	0.6	0.8	0.2
Ag	<0.1	<0.1	0.2	<0.1	0.1	0.8	0.1	<0.1	<0.1	0.1	0.2	0.1	<0.1
Cd	0.2	0.2	0.9	0.3	0.5	0.9	0.3	0.2	0.2	0.7	0.9	0.4	2.3
Sb	0.1	0.6	1.7	0.3	0.6	1	0.3	0.2	0.8	1.5	0.7	0.7	0.2
Cs	0.23	0.32	2.88	0.42	0.59	0.62	0.83	0.34	0.37	0.53	0.58	1.26	0.84
Ba	411	161	1477	399	588	384	510	315	318	377	413	436	487
La	28	10	22	9	21	11	23	8	12	11	15	20	22
Ce	51	23	52	25	46	28	43	20	27	21	35	38	47
Nd	23	10	19	12	18	15	17	11	15	8	15	17	22
Tl	<0.5	<0.5	1.1	<0.5	<0.5	2.6	<0.5	<0.5	<0.5	<0.5	0.5	<0.5	<0.5
Pb	3	8	97	4	10	699	5	4	6	46	100	29	15
Bi	0.6	0.8	1.4	0.9	0.3	0.2	0.5	1.7	<0.1	0.3	0.3	0.4	1.1
Th	7.58	4.69	14.7	6.01	8.63	4.38	13.6	6.08	5.54	3.89	7.76	8.62	11.2
U	1.91	1.03	3.04	1.33	2.1	1.49	3.01	1.4	1.32	0.92	1.93	1.9	0.86

Total Fe as Fe2O3; LOI = loss on ignition; Alteration Index = 100(MgO+K2O)/(MgO+K2O+CaO+Na2O)

Table 2. continued.

	GCR31	GCR32	GCR33	GCR35	GCR36	GCR37	GCR38	GCR40	GCR41	GCR42	GCR45	GCRC1
SiO2		73.59		71.76		75.71	81.15	79.1		71.69	68.92	74.44
TiO2		0.35		0.38		0.24	0.24	0.3		0.44	0.47	0.16
Al2O3		12.19		14.24		10.32	10.01	11.21		14.41	13.73	9.53
Fe2O3#		3.26		3.18		2.74	1.68	1.77		4.09	4.24	2.65
MnO		0.44		0.05		0.04	0.01	0.06		0.03	0.07	0.15
MgO		1.04		1.55		0.88	0.6	0.23		1.25	1.68	1.79
CaO		1.24		0.24		2.77	0.53	0.14		0.16	1.42	2.50
Na2O		3.74		4.99		2.77	3.71	5.05		2.5	2.53	3.34
K2O		1.55		1.23		1.13	0.73	0.63		2.62	2.79	0.87
P2O5		0.09		0.1		0.06	0.05	0.01		0.09	0.11	0.04
LOI		2.85		1.9		3.14	1.27	1.05		2.58	3.87	4.52
TOTAL		100.34		99.62		99.80	99.98	99.55		99.86	99.83	100.00
Ti/Zr		13.4		16.1		16.0	14.0	14.4		13.8	18.7	3.7
S		0.06		<0.01		<0.01	<0.01	<0.01		0.01	0.37	1.24
Total C	0.71	0.05	0.04	0.03	0.03	0.57	0.12	0.04	0.63	0.04	0.58	1.09
CO2	2.60	0.18	0.15	0.11	0.11	2.09	0.44	0.15	2.31	0.15	2.13	3.99
Alteration Index		34.2		34.7		26.6	23.9	14.2		59.3	53.1	31.2
Trace Elements (ppm)												
Sc	15	16	8	18	10	9	7	9	9	14	15	8
V	26	47	20	37	21	25	17	19	32	52	73	5
Cr	2	3	2	3	2	3	2	5	3	39	37	2
Ni	<1	<1	1	<1	<1		<1	4	<1	19	17	2
Cu	11	260	56	30	10	11	9	22	11	37	48	5
Zn	81	115	341	607	20	100	51	137	54	64	87	89
As	4	7	42	17	11	4	<1	5	3	12	16	12
Rb	27	56	71	27	90	25	21	19	67	99	102	21
Sr	163	54	21	136	60	80	115	139	112	112	160	133
Y	22	27	17	26	21	14	15	18	16	32	26	55
Zr	126	156	123	142	142	90	103	125	99	191	151	264
Nb	7	8.7	5.3	7	6.3	5.2	5.4	7.2	5.6	13.2	10.1	17
Mo	1.2	0.5	3.4	2.2	0.5	1.2	0.4	0.4	<0.1	0.2	1	0.4
Ag	<0.1	0.1	0.7	0.2	0.5	<0.1	<0.1	0.4	<0.1	<0.1	0.1	<0.1
Cd	0.2	0.3	17.5	0.8	0.2	1.1	1.3	0.4	0.3	0.5	0.6	0.5
Sb	0.3	0.3	1.2	0.6	1.6	0.4	0.2	0.4	0.2	0.3	0.9	0.5
Cs	0.65	0.65	0.44	1.05	0.55	0.35	0.28	0.94	1.24	4.5	4.85	0.56
Ba	557	559	1195	192	575	294	163	396	804	713	723	159
La	15	18	11	15	13	9	8	14	12	29	23	19
Ce	31	39	30	34	29	18	16	31	27	55	53	42
Nd	15	18	10	18	13	10	8	15	11	24	22	26
Tl	<0.5	<0.5	2.6	<0.5	0.9	<0.5	<0.5	<0.5	<0.5	0.6	0.8	0.5
Pb	30	10	1168	27	92	10	7	12	5	17	39	5
Bi	0.1	2	1.6	1	0.1	0.2	0.1	0.1	<0.1	0.3	0.7	0.1
Th	6.18	11.1	9.14	7.12	9.76	4.99	5.78	6.48	5.93	14.6	10.8	5.72
U	1.51	2.57	2.34	1.5	2.13	1.21	1.45	1.54	1.34	3.06	2.77	1.44

Total Fe as Fe2O3; LOI = loss on ignition; Alteration Index = 100(MgO+K2O)/(MgO+K2O+CaO+Na2O)

Table 2. continued.

	GCRC4	GCRC5	GCRC6	GCRC7	GCRC8	GCRC14	GCRC15	GCRC17	GCRC18-48/49	GCRC18-112/1	GCRC19	GA0/11000N10
SiO2	58.13	62.39	47.33	64.55	56.79	77.63		73.24	58.96	51.14		72.21
TiO2	0.63	0.79	0.42	0.65	1.19	0.2		0.25	0.56	1.56		0.26
Al2O3	14.21	12.41	16.23	12.97	13.97	11.32		12.07	11.06	13.05		12.25
Fe2O3#	7.01	7.54	15.03	6.42	10.86	1.33		4.68	12.40	13.60		2.4
MnO	0.71	0.12	0.55	0.26	0.39	0.03		0.08	0.24	0.19		0.18
MgO	5.87	4.90	7.79	2.68	5.79	0.71		2.12	4.58	6.11		1.54
CaO	1.86	0.87	1.21	2.13	1.91	1.11		0.21	0.79	1.04		1.2
Na2O	3.63	5.06	2.46	4.28	2.67	4.48		1.27	2.64	1.66		2.55
K2O	0.89	0.04	1.02	1.86	0.32	1.35		2.24	0.51	1.10		2.73
P2O5	0.16	0.30	0.07	0.20	0.29	0.06		0.06	0.06	0.35		0.06
LOI	6.46	5.39	7.66	3.73	5.06	2.03		3.24	7.93	9.24		3.74
TOTAL	99.57	99.81	99.77	99.73	99.24	100.25		99.46	99.73	99.04		99.12
Tl/Zr	47.6	35.8	62.1	44.2	77.7	7.2		13.7	82.9	94.8		7.9
S	1.93	4.75	4.56	1.88	0.71	0.13		1.51	7.12	7.08		1.5
Total C	0.77	0.09	0.50	0.36	0.37	0.42	0.5	0.05	0.22	0.32	0.03	0.5
CO2	2.82	0.33	1.83	1.32	1.36	1.54	1.83	0.18	0.81	1.17	0.11	1.83
Alteration Index	55.2	45.5	70.6	41.4	57.2	26.9		74.7	59.7	72.8		53.2
Trace Elements (ppm)												
Sc	29	27	38	26	31	10	11	11	30	34	11	15
V	183	124	206	140	238	2	3	26	239	202	25	7
Cr	5	10	51	2	3	2	2	2	9	4	2	1
Ni	3	3	14	2	4	<1	<1	<1	4	2	1	2
Cu	154	6	732	53	151	2	3	19	33	283	5	7
Zn	883	92	133	187	126	20	35	57	105	179	98	46
As	7	11	21	5	7	<1	3	3	157	121	16	55
Rb	20	<1	22	19	10	29	39	50	11	23	49	85
Sr	102	74	82	157	81	153	123	27	59	56	33	84
Y	20	37	10	19	26	23	26	14	19	29	19	28
Zr	79	133	41	88	92	166	157	110	40	98	154	197
Nb	4.9	7.3	2.8	5.5	6.2	8.6	7.5	5	2.8	5.6	7.4	8.5
Mo	0.4	0.7	0.7	1.2	0.3	<0.1	2.6	18.8	1.6	1.8	0.7	3.4
Ag	0.2	<0.1	0.3	0.1	<0.1	<0.1	<0.1	<0.1	0.1	0.2	<0.1	0.5
Cd	1.5	0.4	0.1	0.5	0.1	0.1	0.3	0.2	0.5	0.3	0.1	0.3
Sb	0.6	0.3	0.2	0.5	0.5	0.4	1.6	0.5	1.6	1	0.5	7.4
Cs	0.42	0.1	0.41	0.1	0.54	0.41	0.7	0.57	0.3	0.58	0.66	0.76
Ba	230	24	507	1018	69	168	217	520	119	190	501	897
La	13	14	5	12	9	13	14	13	8	10	11	18
Ce	23	29	9	26	17	29	31	26	12	19	24	36
Nd	12	19	4	13	11	15	16	11	7	13	11	16
Tl	0.7	<0.5	<0.5	<0.5	<0.5	<0.5	0.8	<0.5	<0.5	<0.5	<0.5	4
Pb	208	7	18	93	4	5	4	2	20	17	6	59
Bi	0.7	0.9	7.7	0.1	0.5	<0.1	0.3	2.2	4.6	4.5	1	0.2
Th	2.73	2.89	1.68	3.04	2.28	7.14	6.61	5.79	1.42	2.43	7.81	7.74
U	0.67	0.72	0.4	0.79	0.94	1.66	1.33	1.22	0.4	0.64	2.83	3.56

Total Fe as Fe2O3; LOI = loss on ignition; Alteration Index = 100(MgO+K2O)/(MgO+K2O+CaO+Na2O)

Table 2. continued.

400E	GA3	GA4	GA9	GA13	GA16	GCDD1/1	GCDD1/3	GCDD1/5	GCDD1/6	GCDD1/7	GCDD1/11	GCDD1/12
SiO2	73.31	81.4	82.39	68.01	85.8	68.55	70.35	71.57	63.43	47.86	68.12	77.17
TiO2	0.29	0.17	0.24	0.73	0.13	0.49	0.34	0.32	0.38	0.61	0.33	0.27
Al2O3	12.92	9.29	11.13	19.77	8.96	11.95	12.78	12.21	15.13	16.88	13.3	10.65
Fe2O3#	3.71	1.86	0.65	1.98	1.04	5.54	2.97	3.25	3.86	7.53	3.38	1.73
MnO	<0.01	<0.01	<0.01	<0.01	<0.01	0.14	0.08	0.07	0.09	0.17	0.09	0.03
MgO	0.07	0.04	0.24	0.09	0.38	2.14	1.07	1.37	2.57	3.06	2.09	0.56
CaO	0.13	0.05	0.04	0.03	0.01	1.05	1.89	1.96	2.74	7.77	3.06	1.70
Na2O	5.72	5.39	4.5	0.18	0.03	1.02	6.21	2.55	1.59	1.22	0.55	2.93
K2O	0.05	0.03	0.98	0.33	2.82	3.08	0.47	2.23	2.8	2.94	2.87	1.54
P2O5	0.02	0.01	0.02	0.06	0.02	0.18	0.07	0.06	0.08	0.26	0.05	0.04
LOI	3.64	1.15	0.89	8.69	1.47	5.06	3.04	4	6.62	11.46	6.19	3.19
TOTAL	99.85	99.39	101.08	99.87	100.62	99.20	99.27	99.59	99.29	99.76	100.03	99.79
Ti/Zr	5.7	8.1	10.3	46.0	3.8	24.5	22.0	11.4	15.6	43.8	13.6	14.2
S	2.97	1.47	0.02	0.05	0.01	0.5	0.09	0.21	0.89	0.01	0.01	0.02
Total C	0.03	0.01	0.03	0.02	0.03	0.83	0.67	0.78	1.08	2.54	1.21	0.64
CO2	0.11	0.04	0.11	0.07	0.11	3.04	2.45	2.86	3.96	9.31	4.43	2.34
Alteration Index	2.0	1.3	21.2	66.7	98.8	71.6	16.0	44.4	55.4	40.0	57.9	31.2
Trace Elements (ppm)												
Sc	11	5	8	18	14	12	10	14	13	16	12	8
V	<1.5	<1.5	10	150	<1.5	85	40	34	43	148	32	24
Cr	1	3	3	23	1	66	7	3	6	9	3	3
Ni	2	2	2	1	<1	36	3	2	2	3	1	<1
Cu	7	5	6	16	5	89	52	16	61	7	11	18
Zn	47	7	32	45	11	103	45	83	245	187	144	39
As	9	6	3	6	5	34	4	6	14	2	<1	<1
Rb	1	<1	32	6	86	95	11	65	70	80	69	37
Sr	101	44	180	189	13	58	154	116	116	213	159	135
Y	61	18	20	12	30	27	15	25	22	20	20	16
Zr	302	126	140	95	203	120	93	168	146	83	145	112
Nb	14.8	7.7	7	4.4	12.1	11.9	5.2	8.3	7.9	6.3	6.9	6
Mo	1.2	2.5	0.9	1.2	0.8	3.6	1	1.3	2.7	0.7	2.5	0.8
Ag	<0.1	<0.1	<0.1	<0.1	<0.1	0.2	<0.1	<0.1	<0.1	<0.1	<0.1	<0.1
Cd	0.3	0.2	0.2	<0.1	0.2	0.2	0.2	0.2	0.3	0.2	0.2	0.1
Sb	0.4	0.2	0.5	0.7	0.3	0.6	0.6	0.4	0.9	0.4	0.3	0.3
Cs	<0.05	<0.05	0.39	0.23	0.33	1.56	0.25	0.73	0.91	0.96	1.01	0.47
Ba	25	20	389	251	631	868	294	489	829	560	961	577
La	26	4	22	11	58	35	12	18	9	13	14	10
Ce	58	13	41	22	110	71	24	32	20	28	32	24
Nd	37	10	18	13	48	29	13	14	9	14	14	10
Tl	<0.5	<0.5	<0.5	<0.5	<0.5	0.7	<0.5	<0.5	0.9	0.7	0.7	<0.5
Pb	9	3	47	117	16	37	10	7	16	6	5	5
Bi	0.2	0.1	0.3	0.6	1.8	0.8	0.4	0.4	0.7	0.1	<0.1	0.1
Th	6.95	5.63	7.86	2.81	16	13	5.42	7.89	8.22	5.42	8.35	6.38
U	1.61	1.54	1.89	0.79	2.51	2.52	1.3	1.91	2.04	1.18	2.1	1.33

Total Fe as Fe2O3; LOI = loss on ignition; Alteration Index = 100(MgO+K2O)/(MgO+K2O+CaO+Na2O)

Table 2. continued.

	GCDD2/4	GCDD2/6	GCDD2/7	GCDD2/8	GCDD2/9	GYRC3	GYRC5	GYRC6	GYRC7
SiO2	47.13	68.93	48.03	67.5					
TiO2	1.90	0.34	1	0.63					
Al2O3	16.38	12.82	16.96	12.74					
Fe2O3#	13.17	2.76	8.38	3.39					
MnO	0.17	0.08	0.12	0.07					
MgO	5.43	1.07	3.07	1.03					
CaO	3.40	3.16	6.44	3.33					
Na2O	3.30	1.41	6.89	3.1					
K2O	1.42	3.34	0.41	2.56					
P2O5	0.44	0.06	0.28	0.22					
LOI	7.08	5.5	8.05	5.3					
TOTAL	99.80	99.47	99.63	99.87					
Tl/Zr	82.3	12.5	55.9	28.7					
S	0.14	0.02	0.53	0.05					
Total C	1.49	1.1	1.93	1.18	1.1	0.88	0.55	0.57	0.78
CO2	5.46	4.03	7.07	4.32	4.03	3.22	2.02	2.09	2.86
Alteration Index	50.6	49.1	20.7	35.8					
Trace Elements (ppm)									
Sc	34	13	33	18		9	13	9	8
V	224	45	189	55		21	37	24	21
Cr	4	5	2	6		3	3	2	2
Ni	3	2	2	2		1	1	<1	1
Cu	23	12	58	22		17	58	15	11
Zn	158	87	197	49		102	26	27	38
As	5	3	195	6	8	9	20	<1	<1
Rb	38	83	9	61		41	102	31	29
Sr	129	76	272	121		77	49	127	104
Y	41	25	30	28		16	24	15	16
Zr	138	163	107	132		104	150	100	103
Nb	7.4	8.1	6.1	7.2		5.8	8.8	4.9	5.1
Mo	0.5	0.6	0.9	1	0.4	4.2	0.8	1.4	1.2
Ag	<0.1	<0.1	0.2	<0.1	<0.1	<0.1	<0.1	<0.1	<0.1
Cd	0.2	0.2	0.3	0.3	0.2	0.1	0.1	0.1	0.2
Sb	0.7	0.8	1.6	0.8	0.9	0.5	0.9	0.3	0.3
Cs	0.51	1.29	0.23	0.83	0.67	0.64	1.55	0.39	0.4
Ba	178	995	72	270		387	1013	308	261
La	8	14	11	15		13	14	9	13
Ce	21	33	27	30		27	33	23	29
Nd	13	14	16	15		12	13	10	12
Tl	<0.5	1.1	1.1	0.9	<0.5	<0.5	0.8	<0.5	<0.5
Pb	8	4	10	4		14	19	6	5
Bi	<0.1	0.1	<0.1	<0.1	<0.1	0.3	2.2	0.5	0.4
Th	2.09	8.63	2.53	5.68	2.02	5.6	9.1	5.1	5.14
U	0.54	2.13	1.33	1.57	0.52	1.34	1.54	1.47	1.33

Total Fe as Fe2O3; LOI = loss on ignition; Alteration Index = 100(MgO+K2O)/(MgO+K2O+CaO+Na2O)

blank

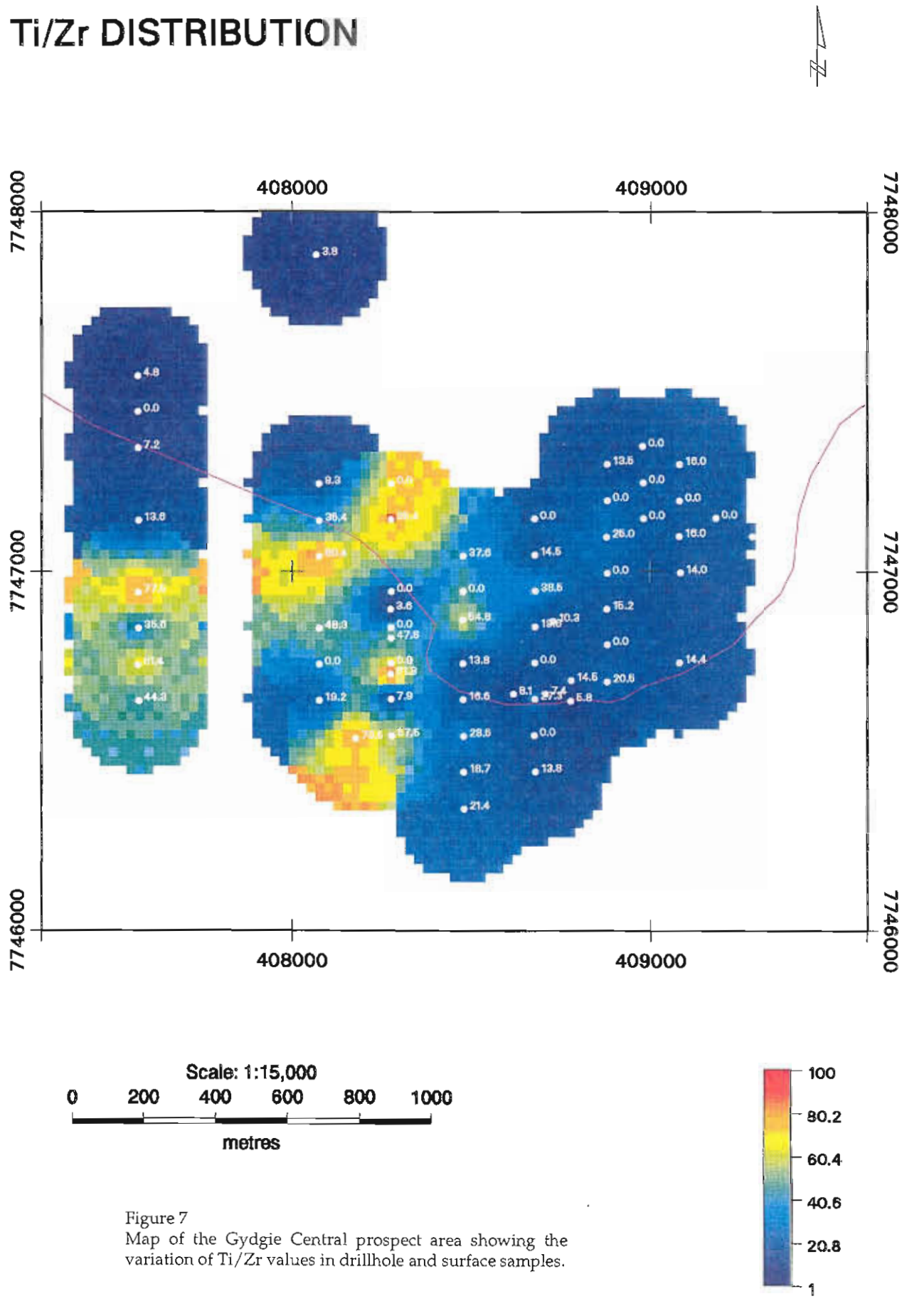

Figure 7
Map of the Gydgie Central prospect area showing the variation of Ti/Zr values in drillhole and surface samples.

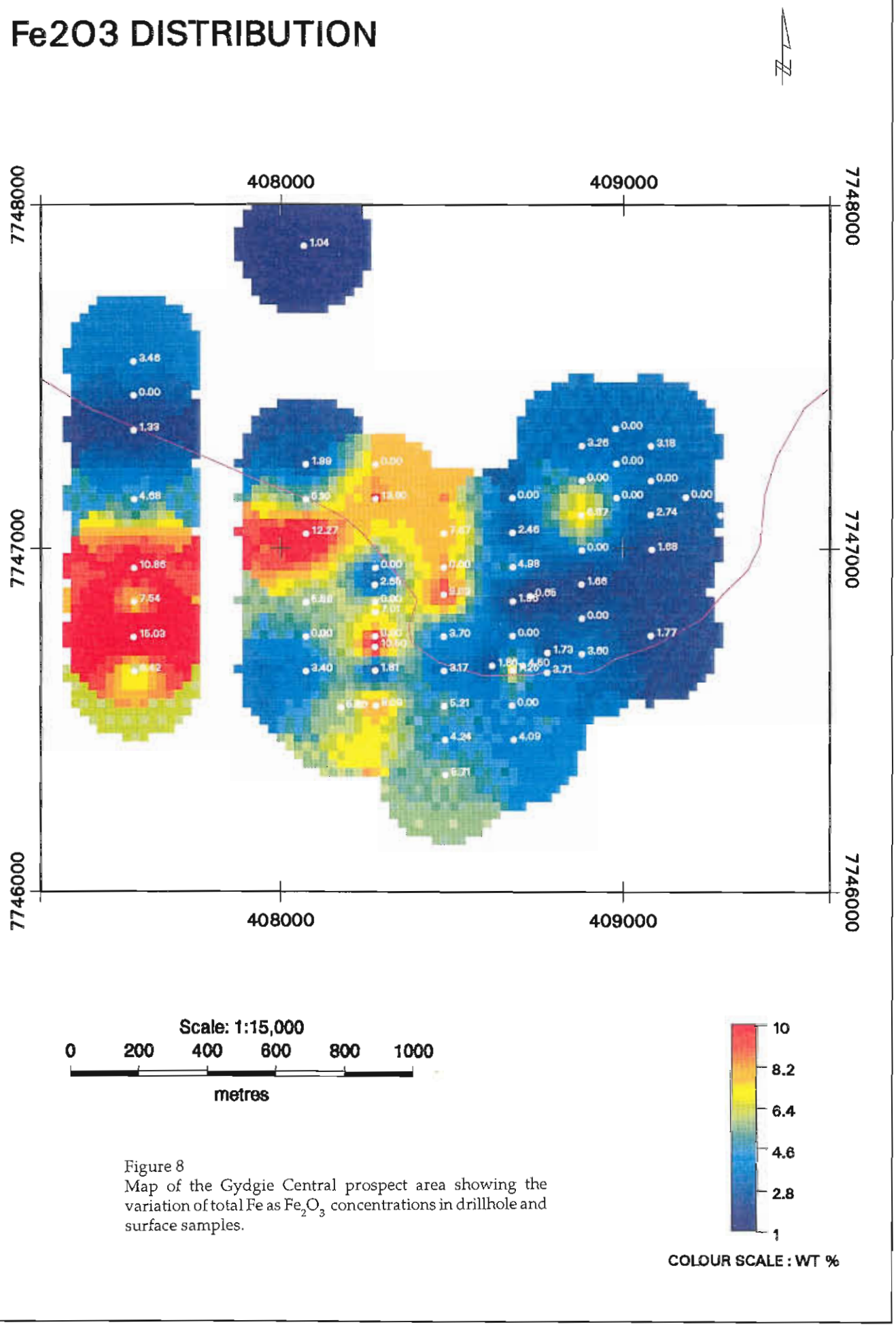

Figure 8
Map of the Gydgie Central prospect area showing the variation of total Fe as Fe_2O_3 concentrations in drillhole and surface samples.

S DISTRIBUTION

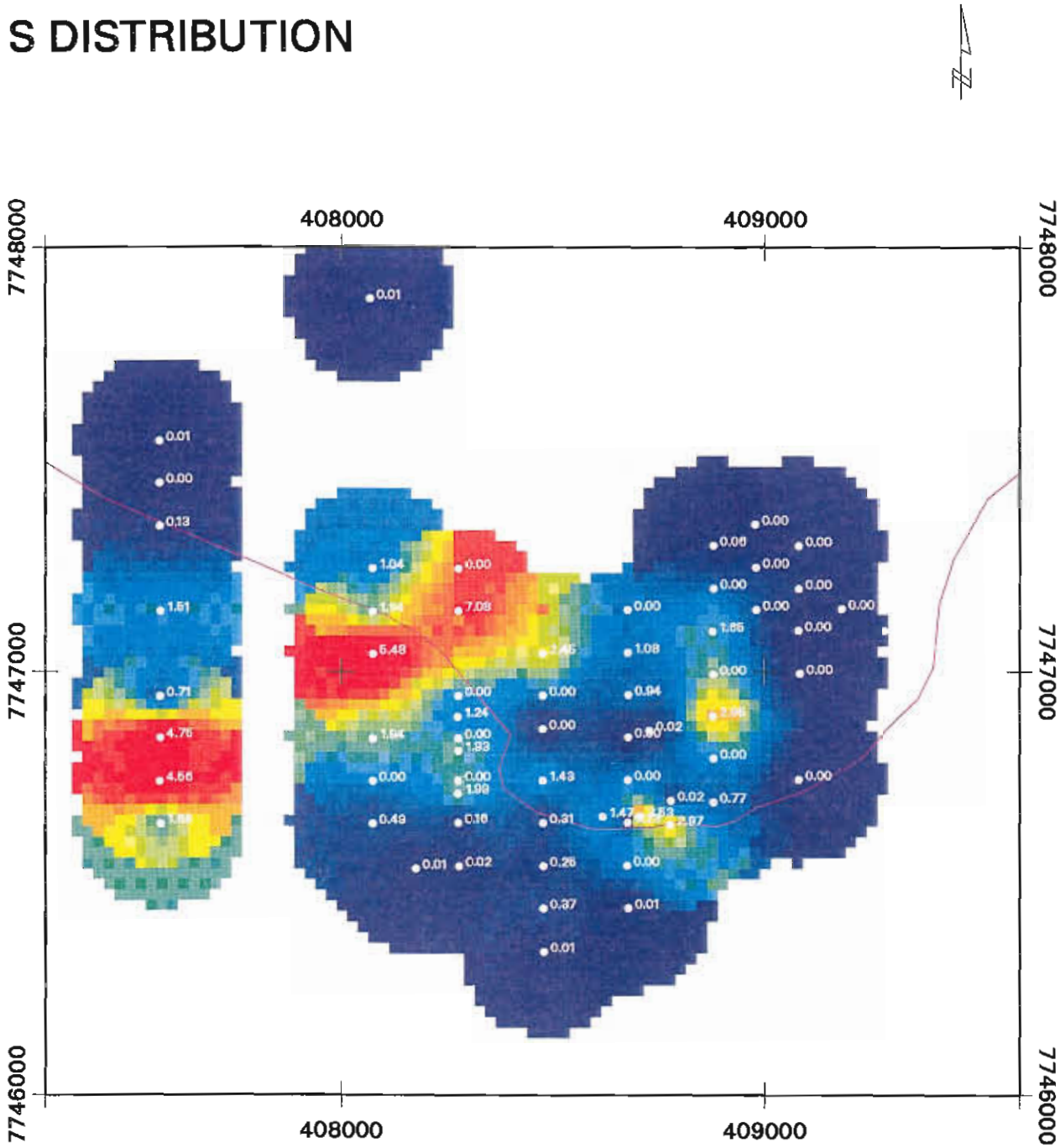

MT WINDSOR VOLCANICS - Gydgie Prospect

GEOCHEMISTRY

Figure 9

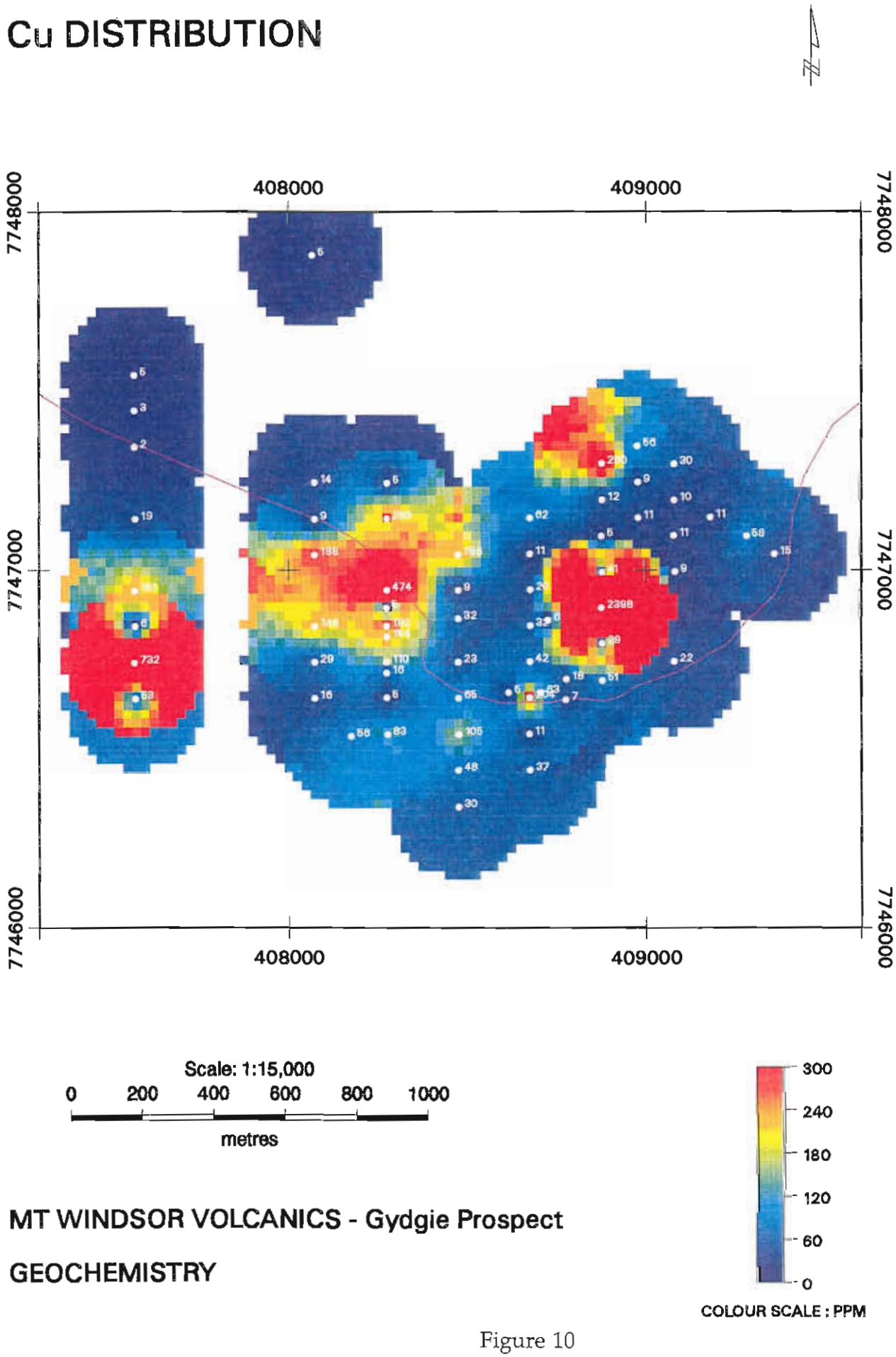
Cu DISTRIBUTION
408000
409000
7748000
7747000
7746000
Scale: 1:15,000
0 200 400 600 800 1000
metres
300
240
180
120
60
0
COLOUR SCALE : PPM
MT WINDSOR VOLCANICS - Gydgie Prospect
GEOCHEMISTRY

Figure 10

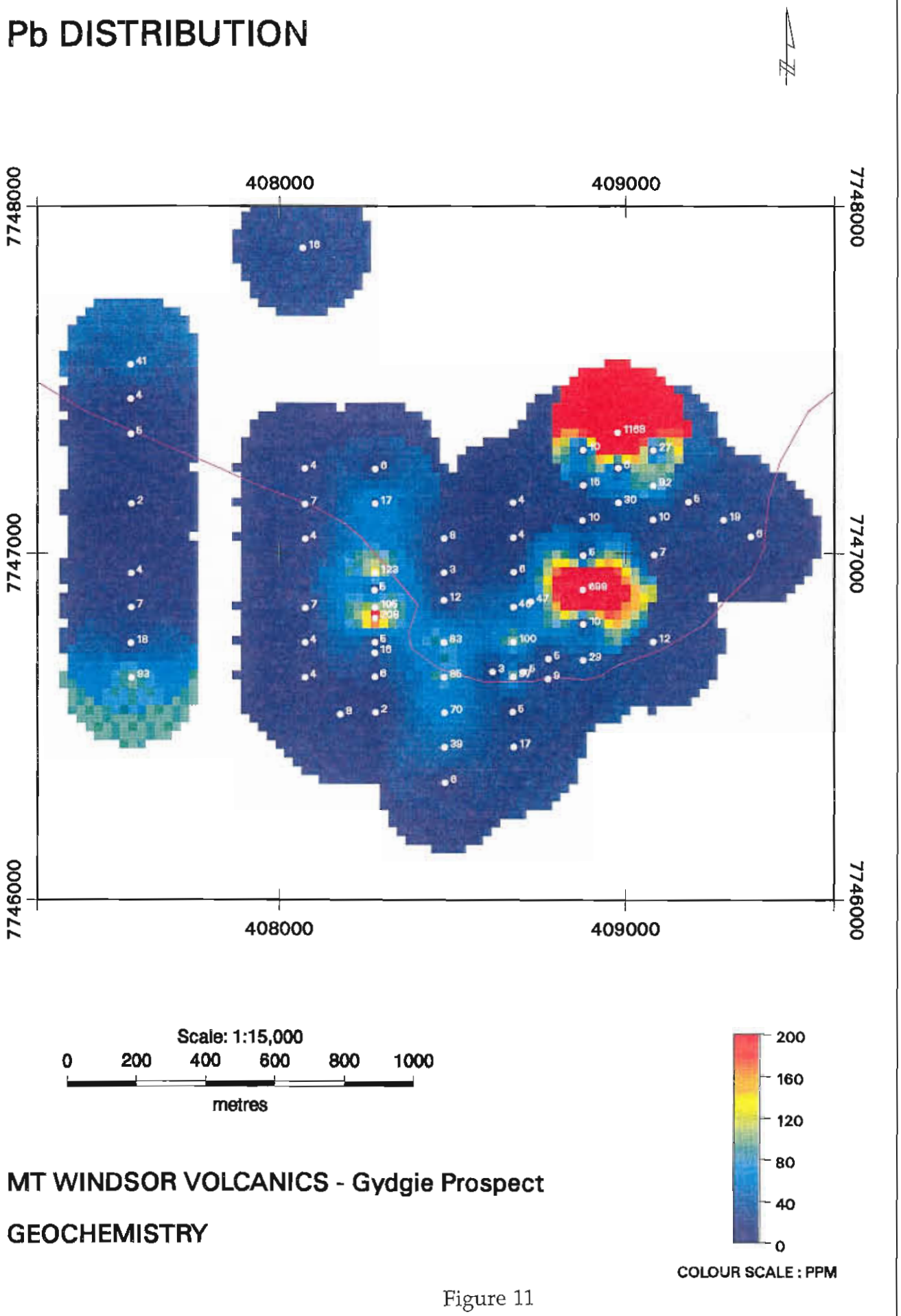

MT WINDSOR VOLCANICS - Gydgie Prospect

GEOCHEMISTRY

Figure 11

Zn DISTRIBUTION

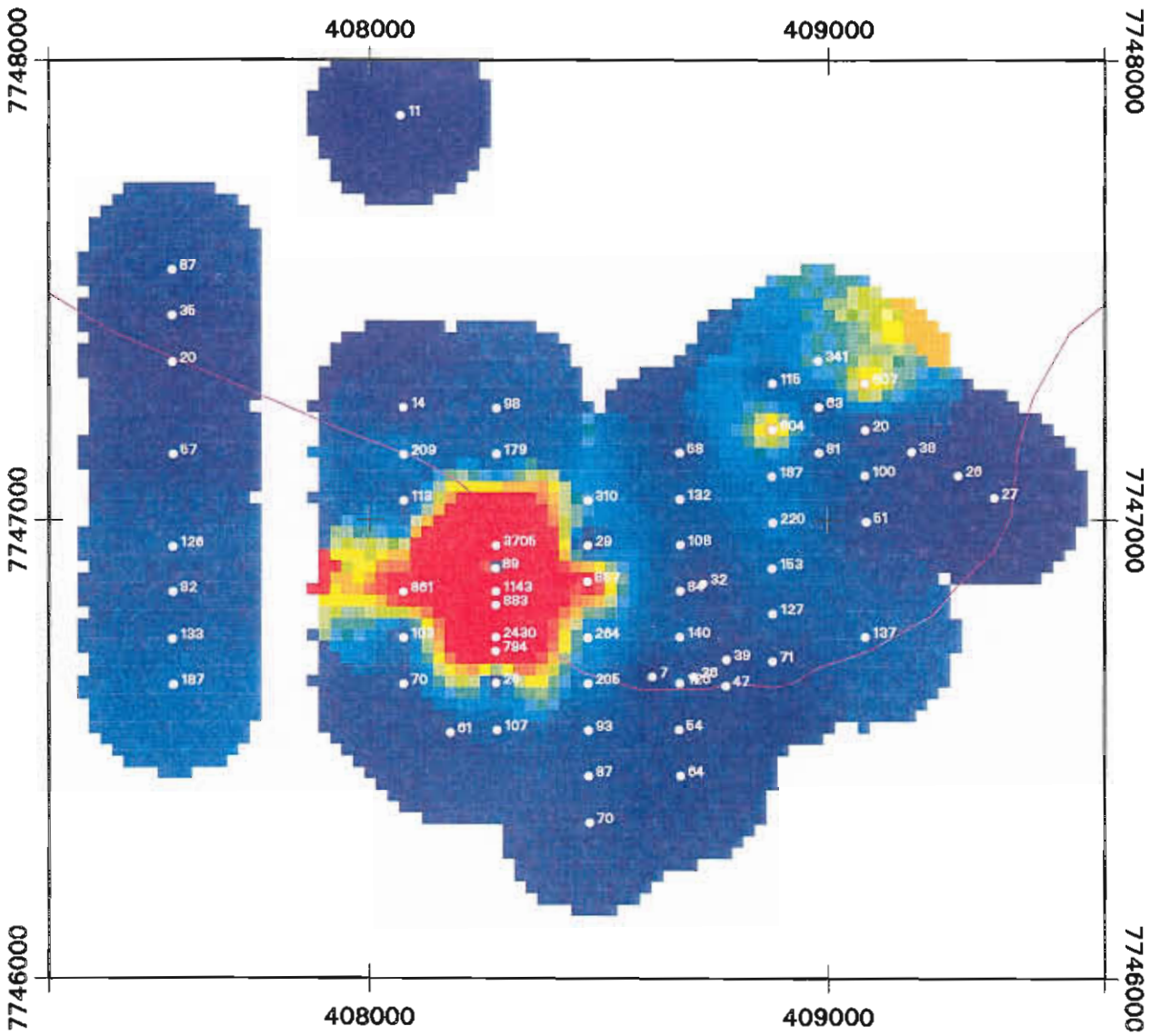

Scale: 1:15,000

0 200 400 600 800 1000

metres

800
640
480
320
160
0

COLOUR SCALE : PPM

MT WINDSOR VOLCANICS - Gydgie Prospect

GEOCHEMISTRY

Figure 12

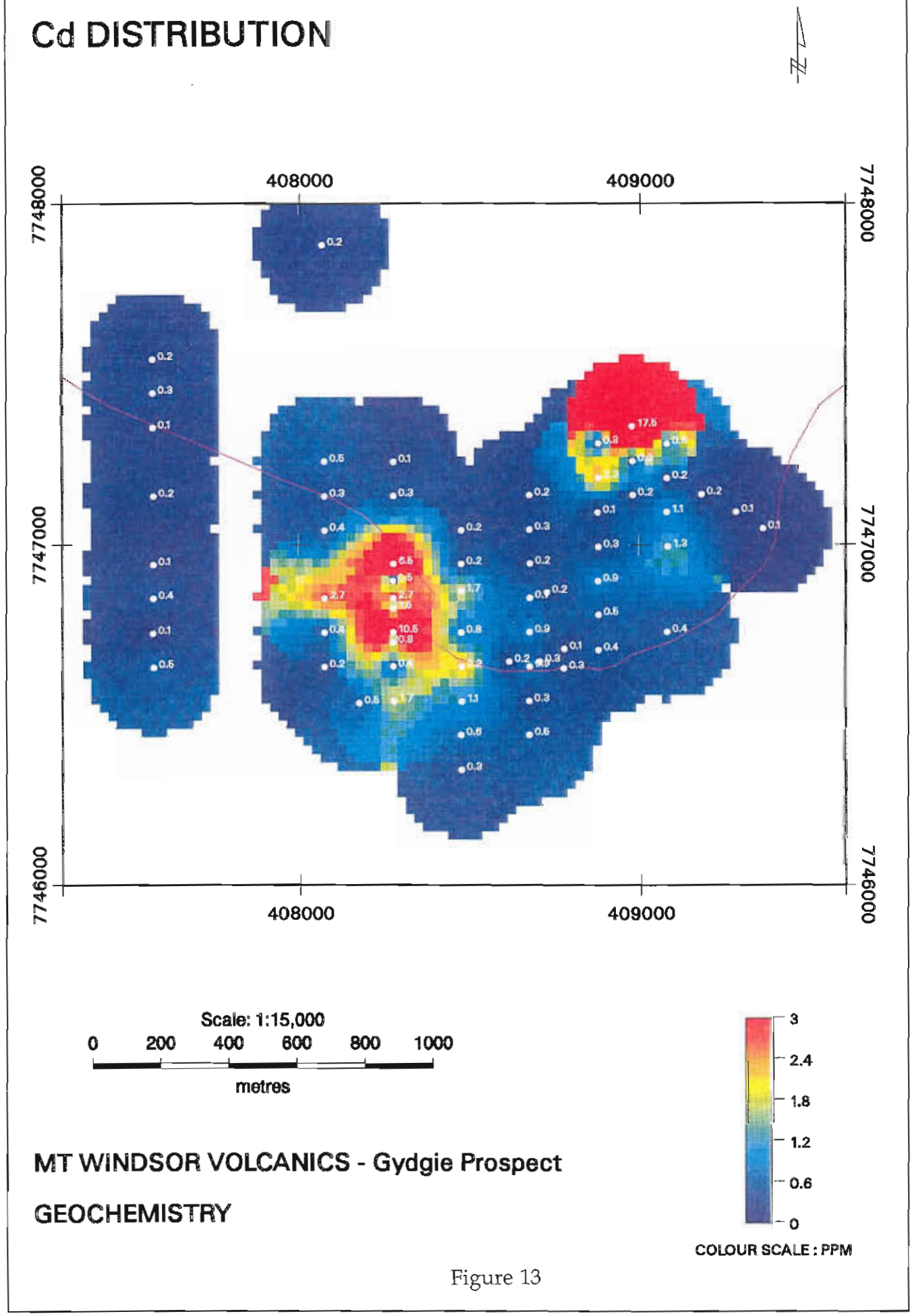
Cd DISTRIBUTION
408000
409000
7748000
7747000
7746000
Scale: 1:15,000
0 200 400 600 800 1000
metres
MT WINDSOR VOLCANICS - Gydgie Prospect
GEOCHEMISTRY
3
2.4
1.8
1.2
0.6
0
COLOUR SCALE : PPM

Figure 13

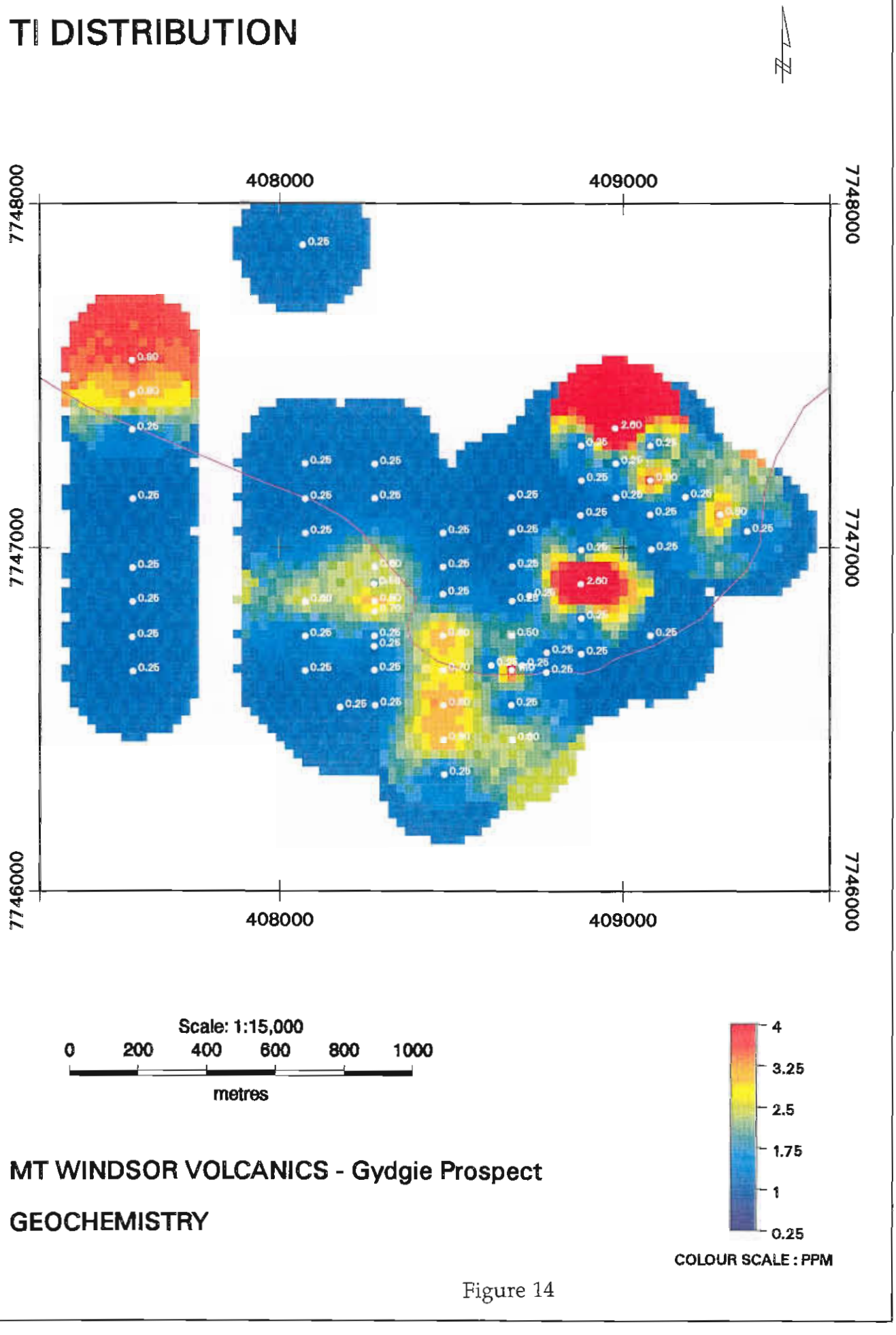
TI DISTRIBUTION
408000
409000
7748000
7747000
7746000
Scale: 1:15,000
0 200 400 600 800 1000
metres
4
3.25
2.5
1.75
1
0.25
COLOUR SCALE : PPM
MT WINDSOR VOLCANICS - Gydgie Prospect
GEOCHEMISTRY

Figure 14

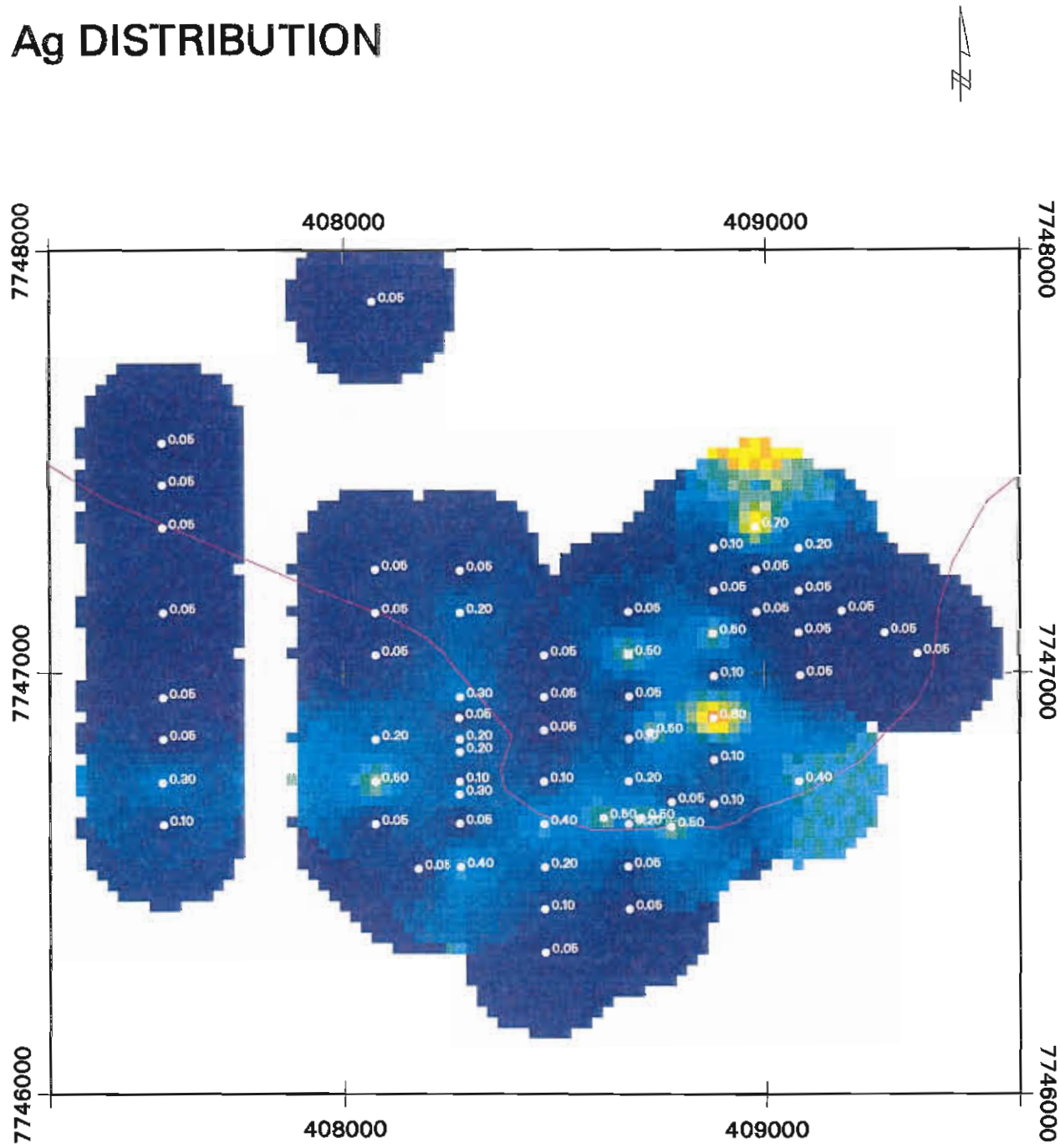
Ag DISTRIBUTION
N
408000
409000
7748000
7747000
7746000
Scale: 1:15,000
0 200 400 600 800 1000
metres
MT WINDSOR VOLCANICS - Gydgie Prospect
GEOCHEMISTRY
1
0.8
0.6
0.4
0.2
0
COLOUR SCALE : PPM

Figure 15

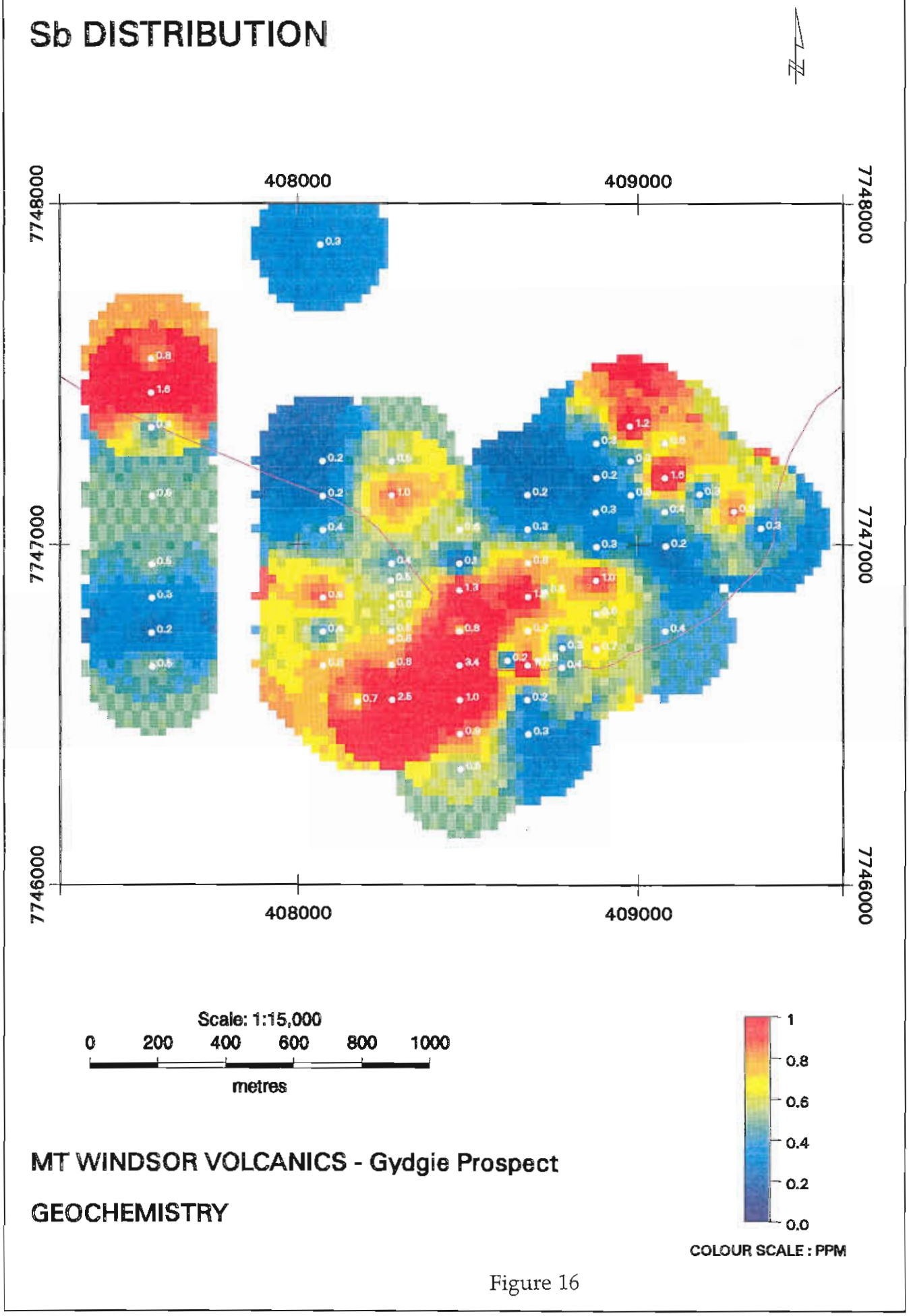
Sb DISTRIBUTION
408000
409000
7748000
7747000
7746000
Scale: 1:15,000
0 200 400 600 800 1000
metres
MT WINDSOR VOLCANICS - Gydgie Prospect
GEOCHEMISTRY
1
0.8
0.6
0.4
0.2
0.0
COLOUR SCALE : PPM

Figure 16

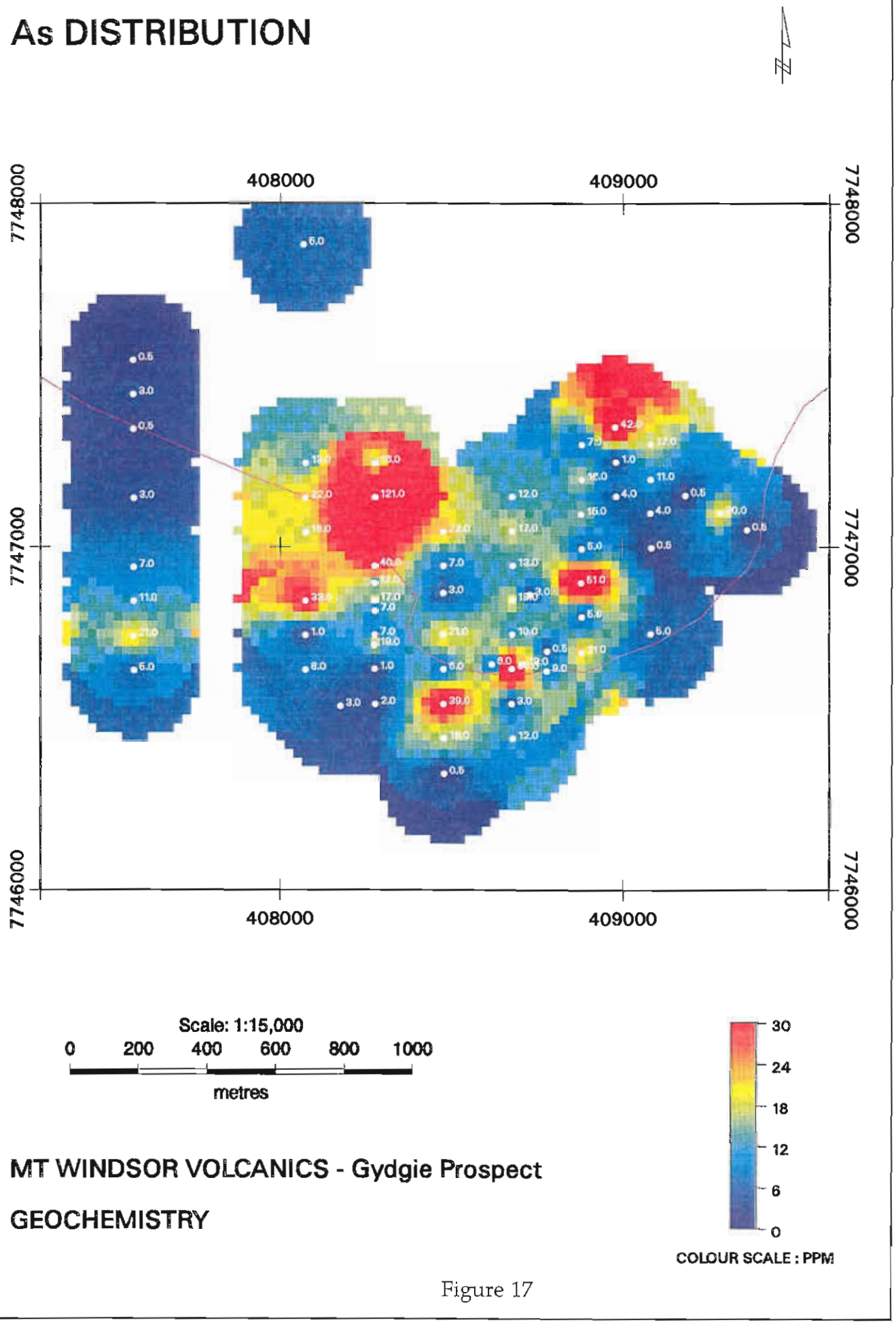
As DISTRIBUTION
N
408000
409000
7748000
7747000
7746000
Scale: 1:15,000
0 200 400 600 800 1000
metres
30
24
18
12
6
0
COLOUR SCALE : PPM
MT WINDSOR VOLCANICS - Gydgie Prospect
GEOCHEMISTRY

Figure 17

Bi DISTRIBUTION

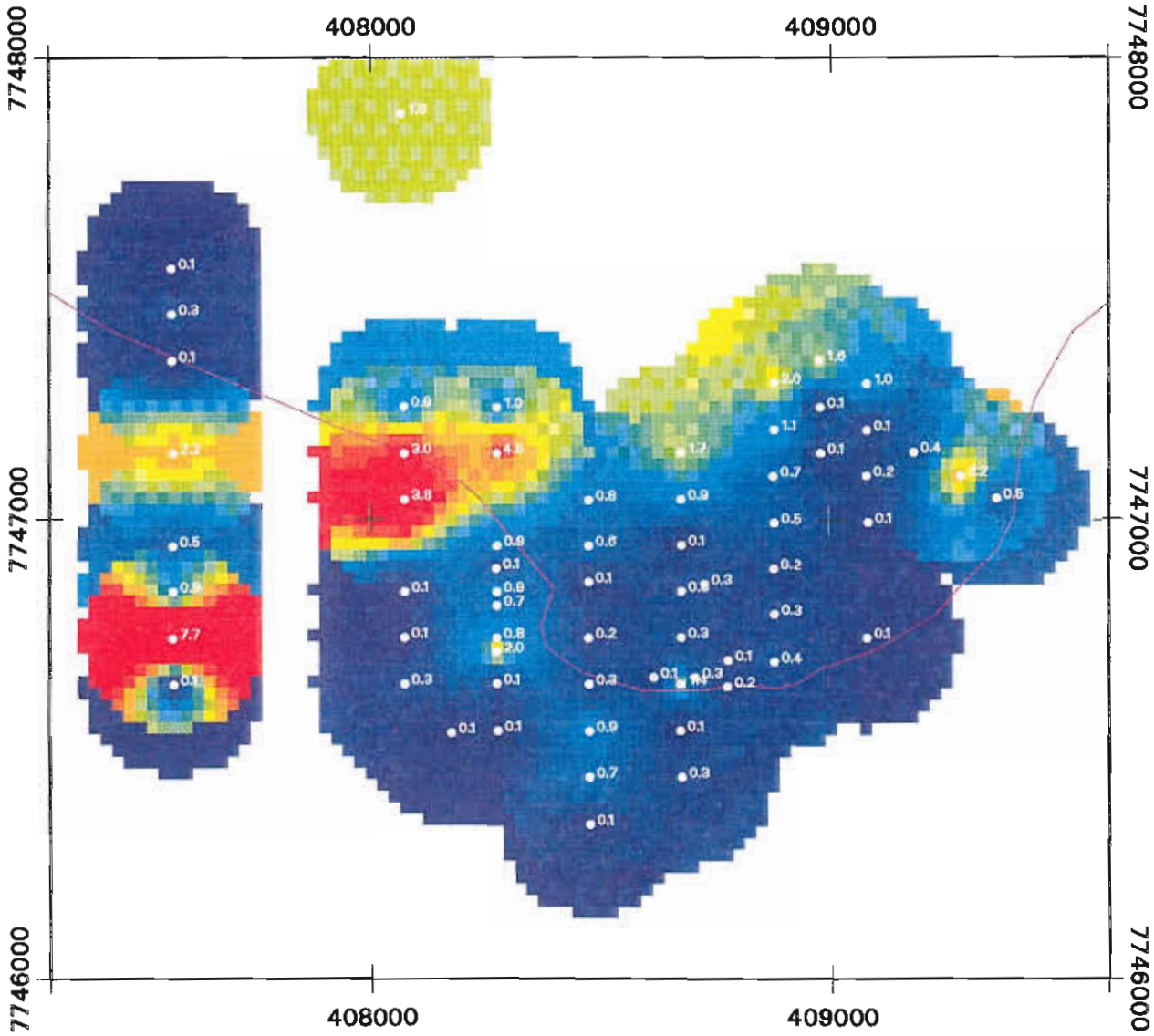

Scale: 1:15,000

0 200 400 600 800 1000

metres

3
2.4
1.8
1.2
0.6
0

COLOUR SCALE : PPM

MT WINDSOR VOLCANICS - Gydgie Prospect

GEOCHEMISTRY

Figure 18

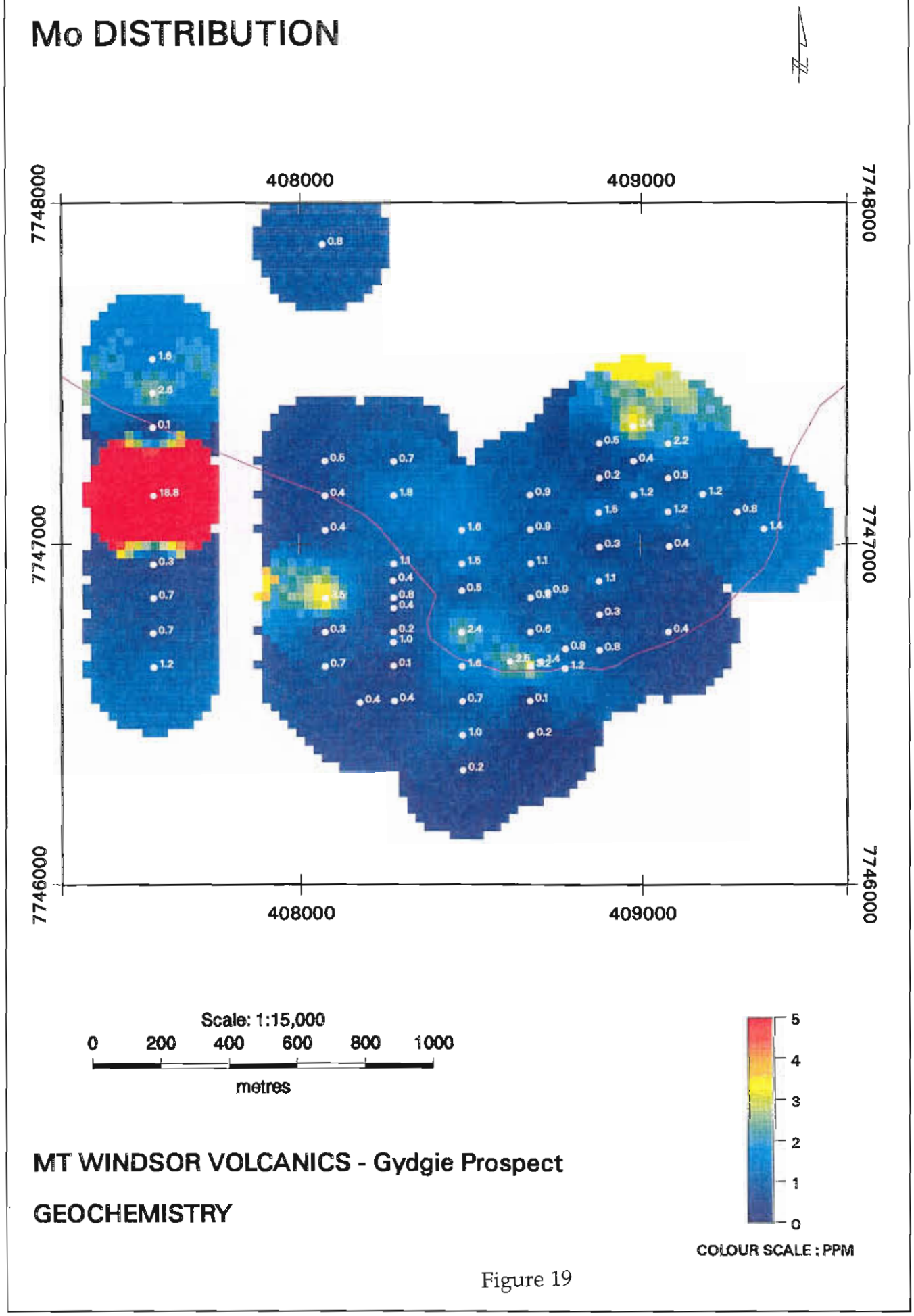
Mo DISTRIBUTION
408000
409000
7748000
7747000
7746000
Scale: 1:15,000
0 200 400 600 800 1000
metres
MT WINDSOR VOLCANICS - Gydgie Prospect
GEOCHEMISTRY
5
4
3
2
1
0
COLOUR SCALE : PPM

Figure 19

MnO DISTRIBUTION

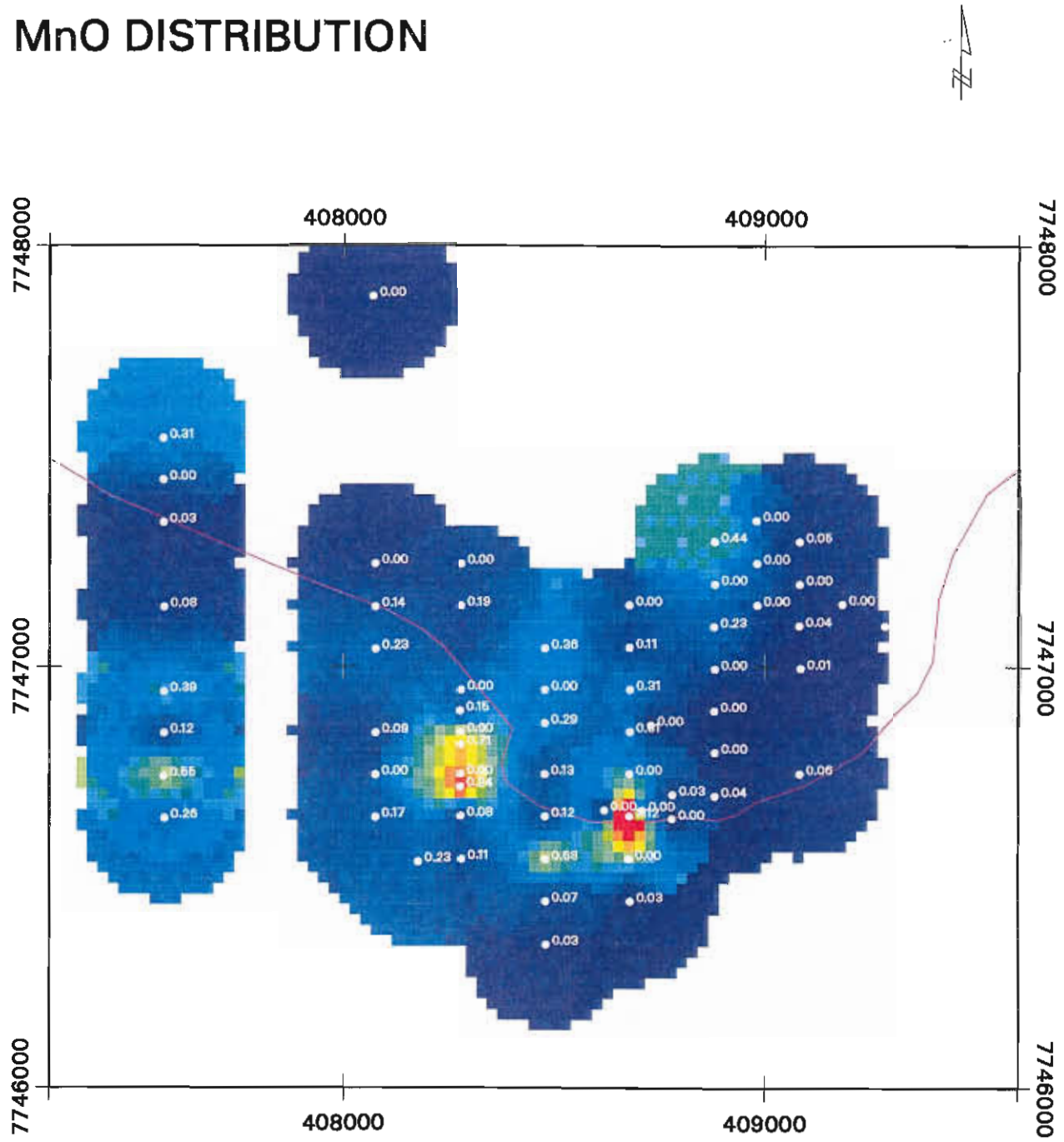

MT WINDSOR VOLCANICS - Gydgie Prospect

GEOCHEMISTRY

Figure 20

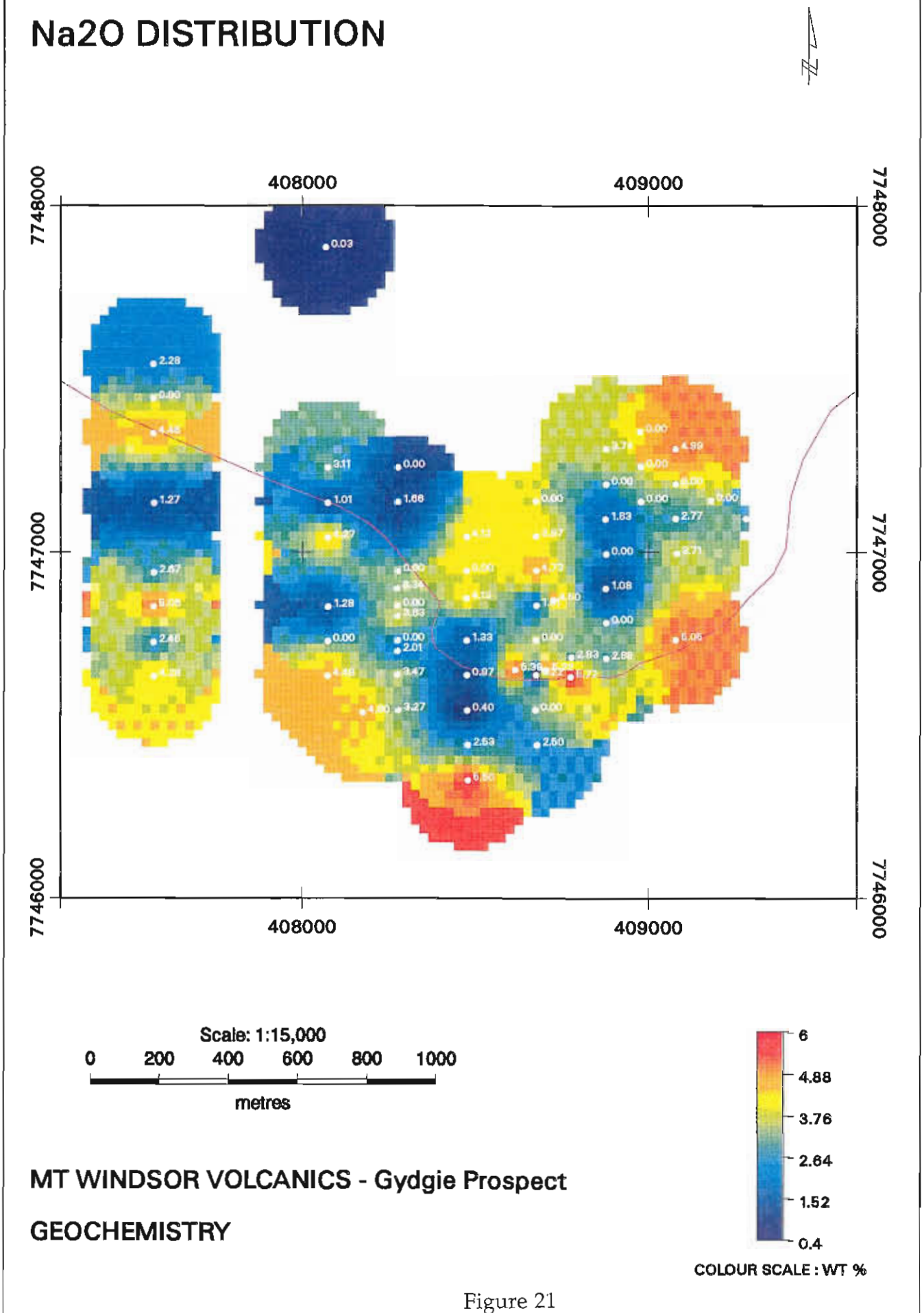
Na2O DISTRIBUTION
408000
409000
7748000
7747000
7746000
Scale: 1:15,000
0 200 400 600 800 1000
metres
MT WINDSOR VOLCANICS - Gydgie Prospect
GEOCHEMISTRY
6
4.88
3.76
2.64
1.52
0.4
COLOUR SCALE : WT %

Figure 21

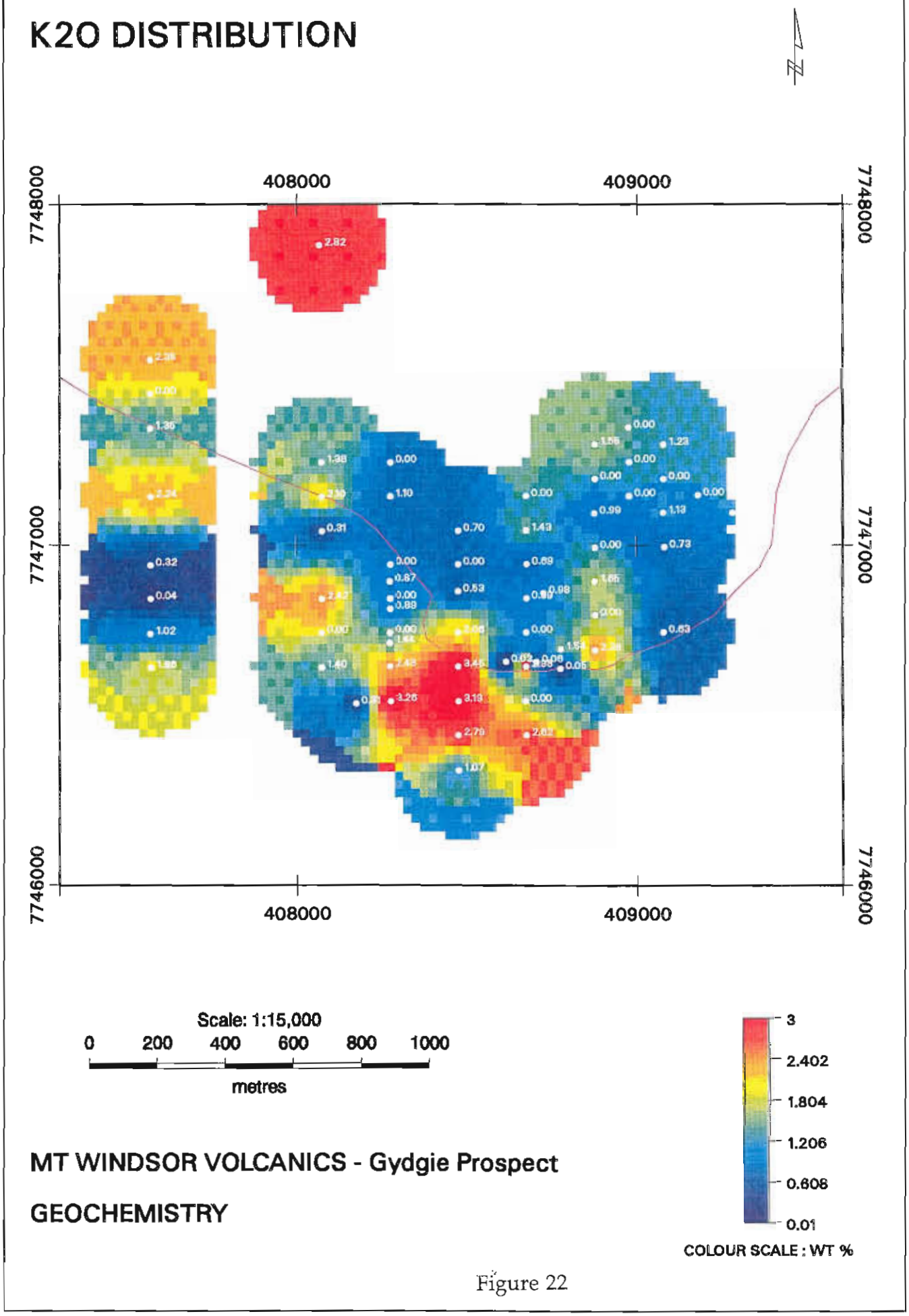
K2O DISTRIBUTION
N
408000
409000
7748000
7747000
7746000
Scale: 1:15,000
0 200 400 600 800 1000
metres
MT WINDSOR VOLCANICS - Gydgie Prospect
GEOCHEMISTRY
3
2.402
1.804
1.206
0.608
0.01
COLOUR SCALE : WT %

Figure 22

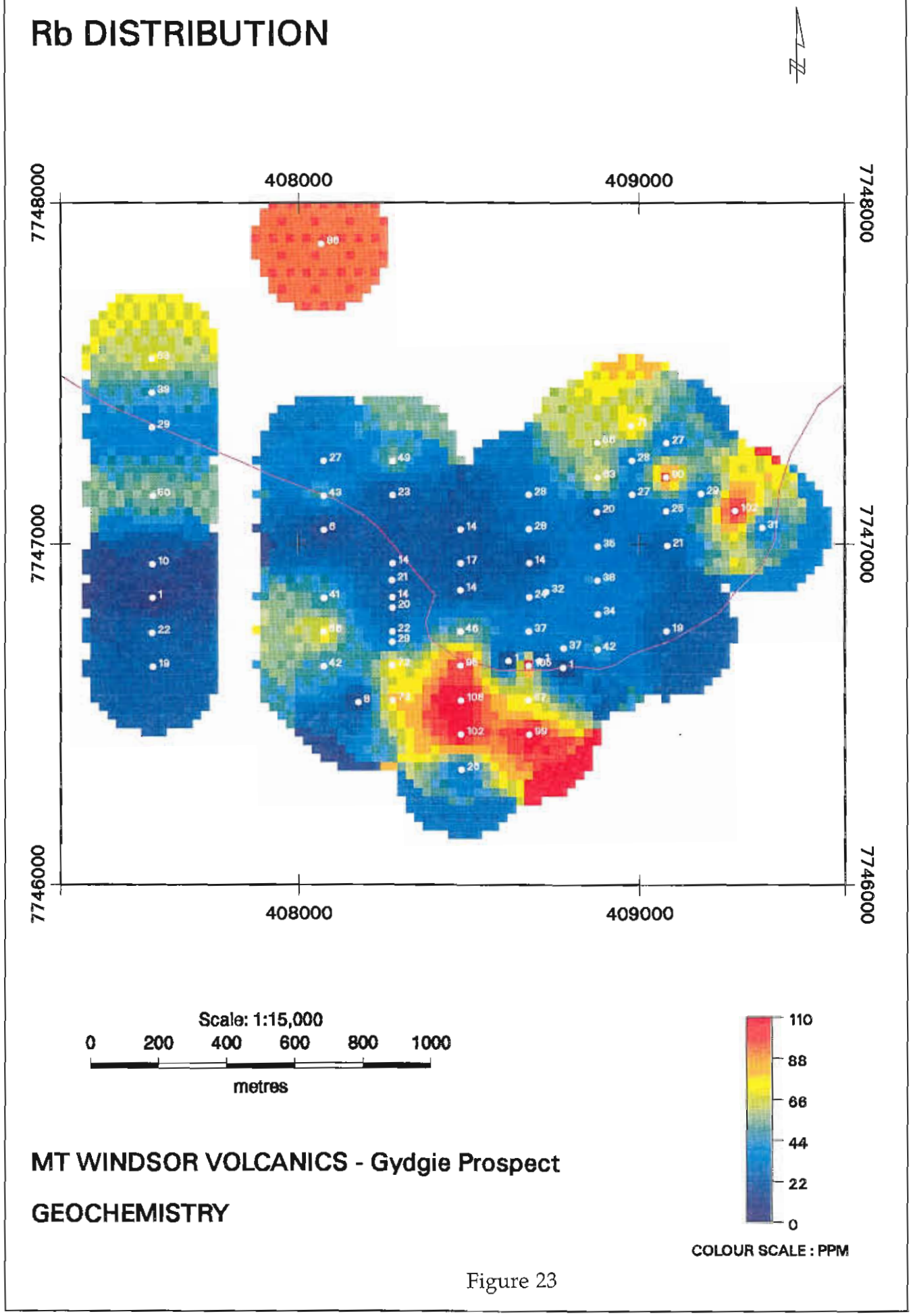
Rb DISTRIBUTION
N
408000
409000
7748000
7747000
7746000
Scale: 1:15,000
0 200 400 600 800 1000
metres
110
88
66
44
22
0
COLOUR SCALE : PPM
MT WINDSOR VOLCANICS - Gydgie Prospect
GEOCHEMISTRY

Figure 23

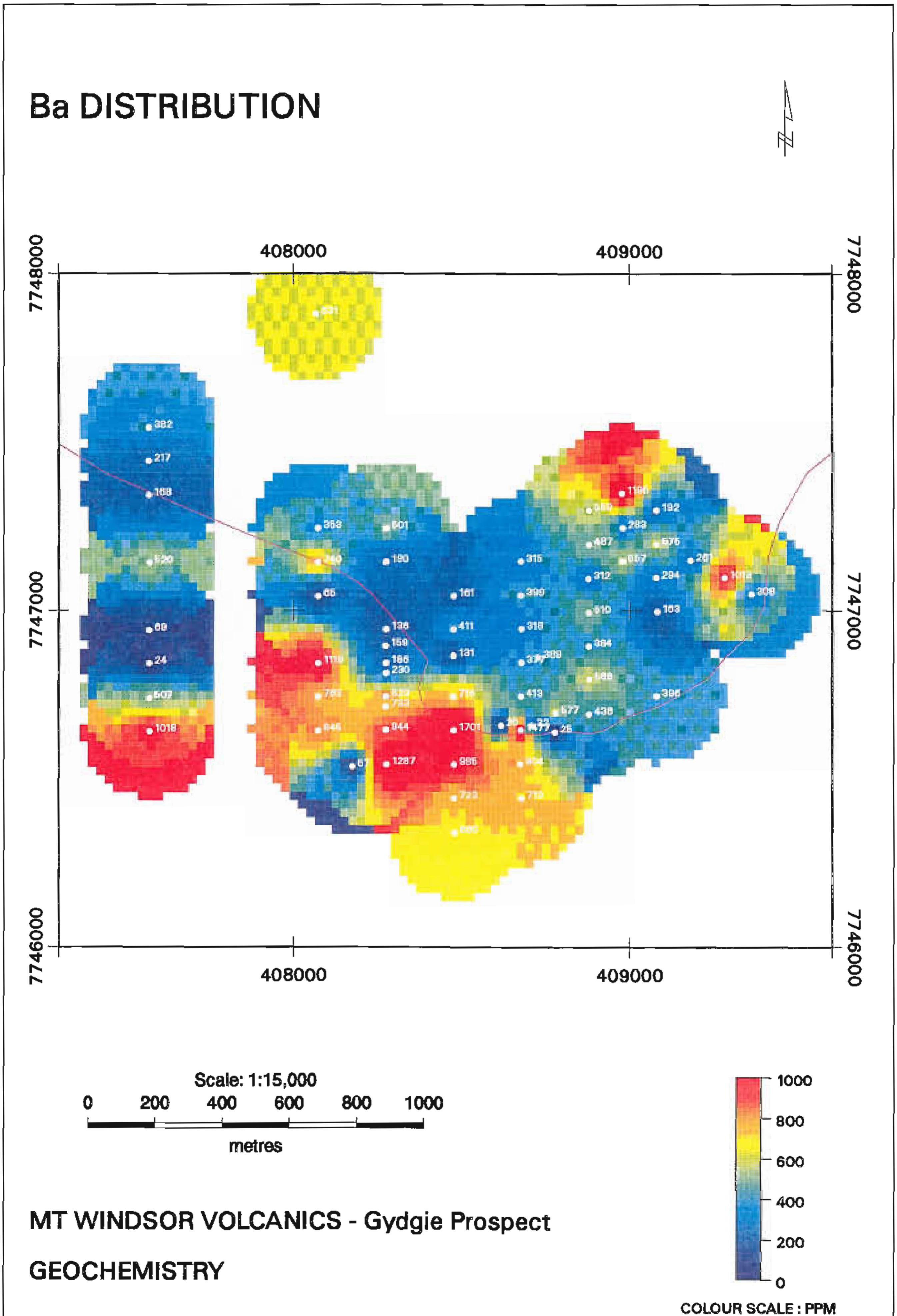
Ba DISTRIBUTION
408000
409000
7748000
7747000
7746000
Scale: 1:15,000
0 200 400 600 800 1000
metres
1000
800
600
400
200
0
COLOUR SCALE : PPM
MT WINDSOR VOLCANICS - Gydgie Prospect
GEOCHEMISTRY

Figure 24

Cs DISTRIBUTION

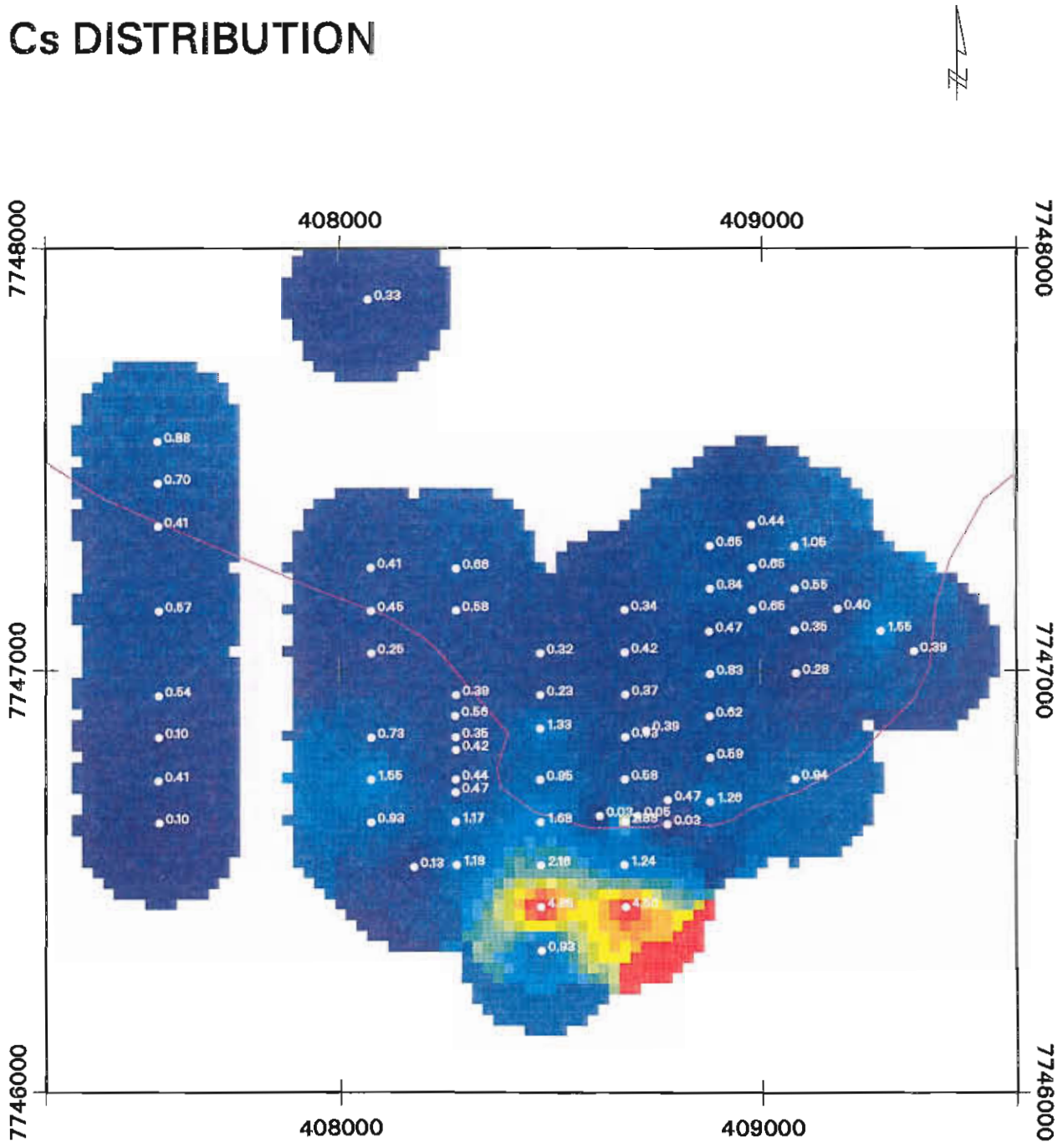

Scale: 1:15,000

0 200 400 600 800 1000

metres

5
4
3
2
1
0

COLOUR SCALE : PPM

MT WINDSOR VOLCANICS - Gydgie Prospect

GEOCHEMISTRY

Figure 25

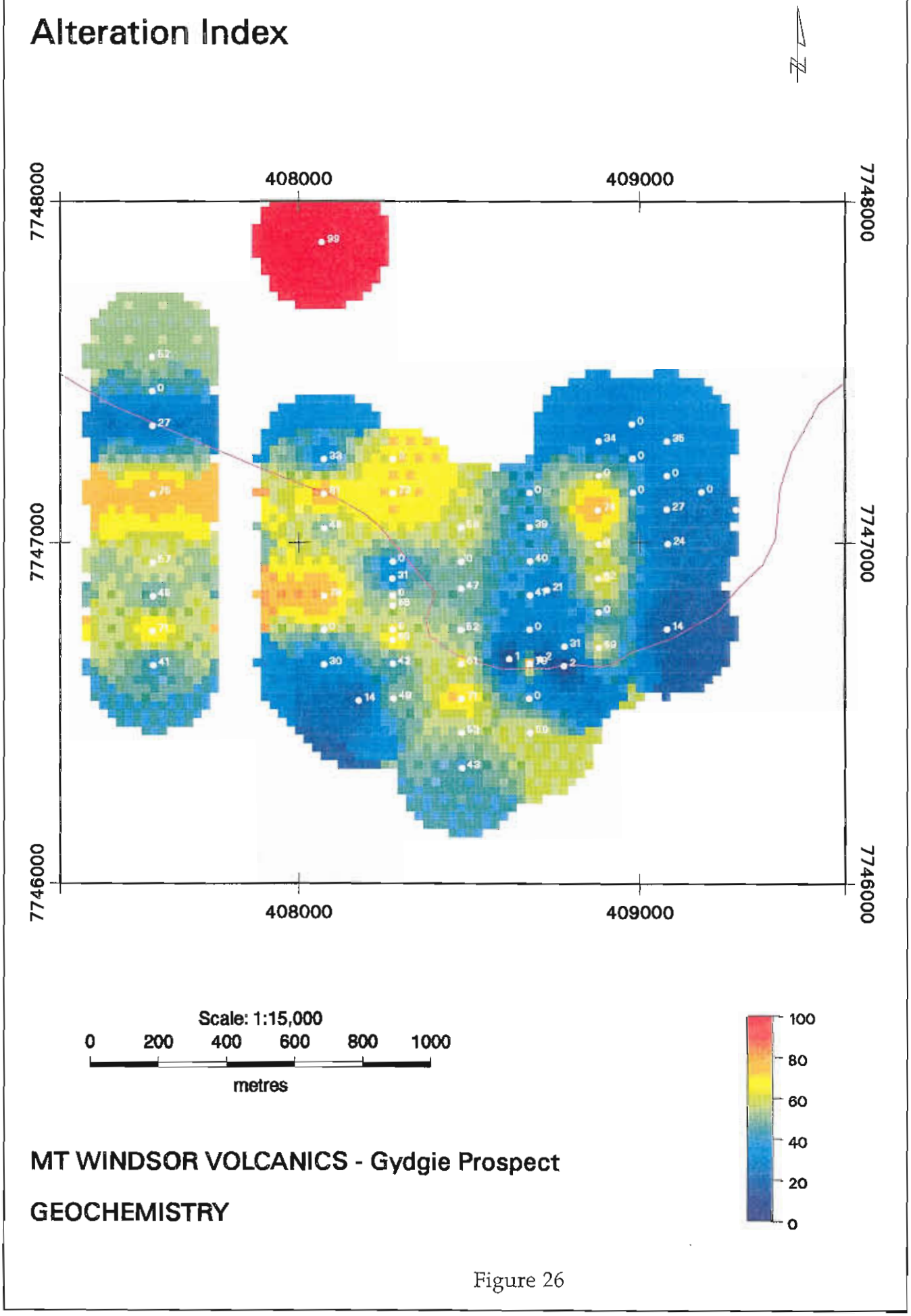
Alteration Index
N
408000
409000
7748000
7747000
7746000
Scale: 1:15,000
0 200 400 600 800 1000
metres
100
80
60
40
20
0
MT WINDSOR VOLCANICS - Gydgie Prospect
GEOCHEMISTRY

Figure 26

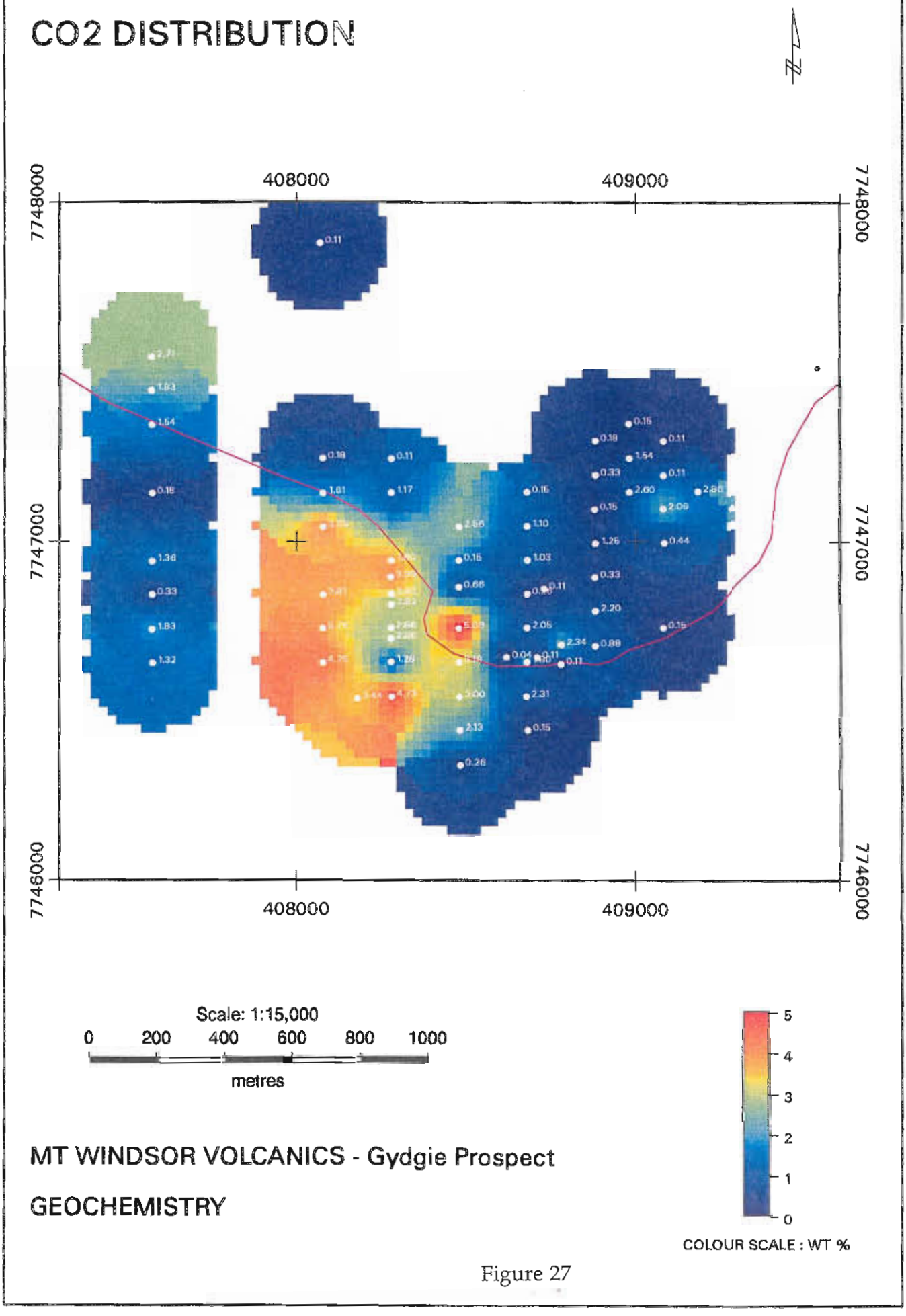
CO2 DISTRIBUTION
408000
409000
7748000
7747000
7746000
Scale: 1:15,000
0 200 400 600 800 1000
metres
MT WINDSOR VOLCANICS - Gydgie Prospect
GEOCHEMISTRY
5
4
3
2
1
0
COLOUR SCALE : WT %

Figure 27

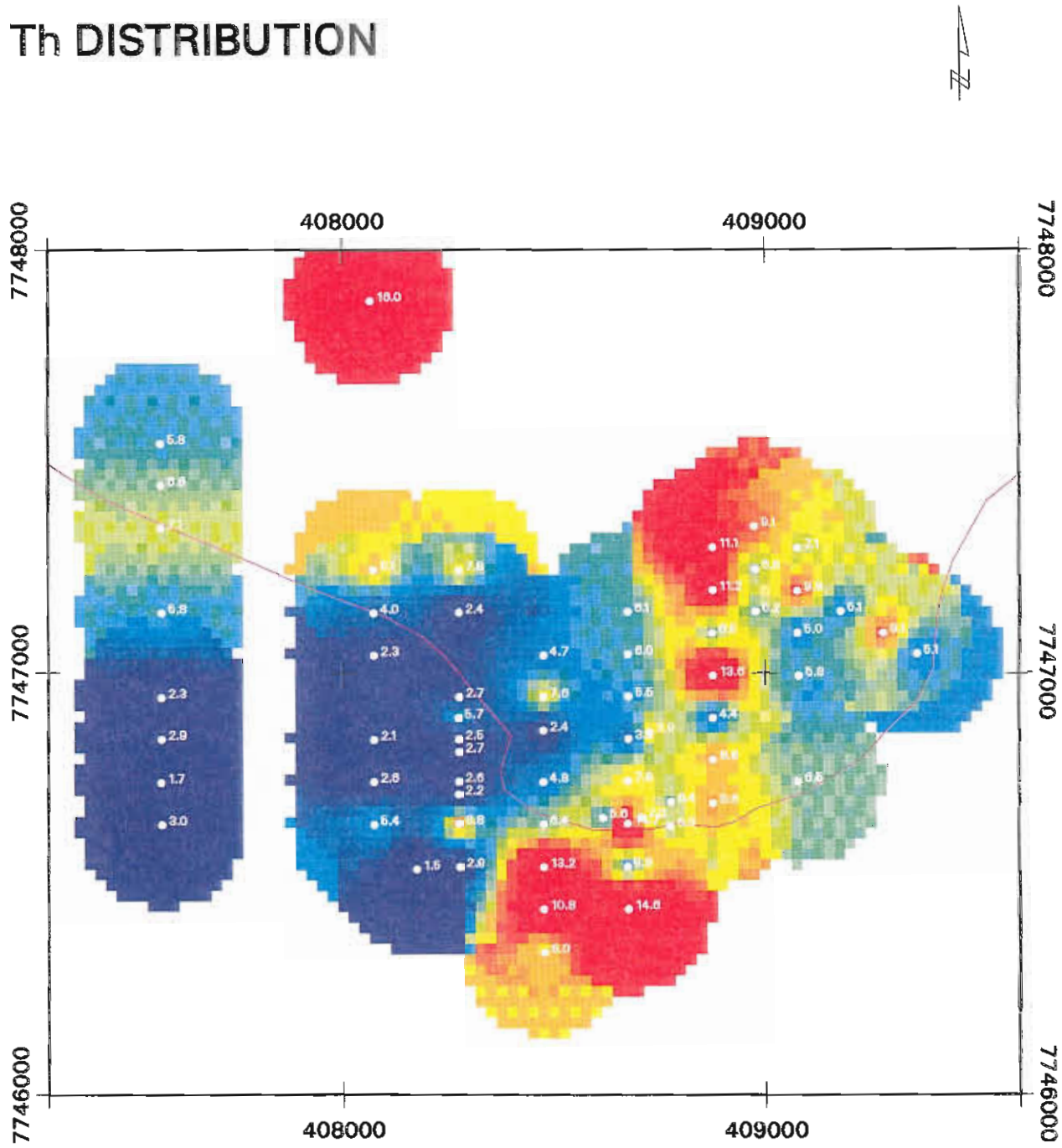
Th DISTRIBUTION
408000
409000
7748000
7747000
7746000
Scale: 1:15,000
0 200 400 600 800 1000
metres
MT WINDSOR VOLCANICS - Gydgie Prospect
GEOCHEMISTRY
10
8.6
7.2
5.8
4.4
3
COLOUR SCALE : PPM

Figure 28

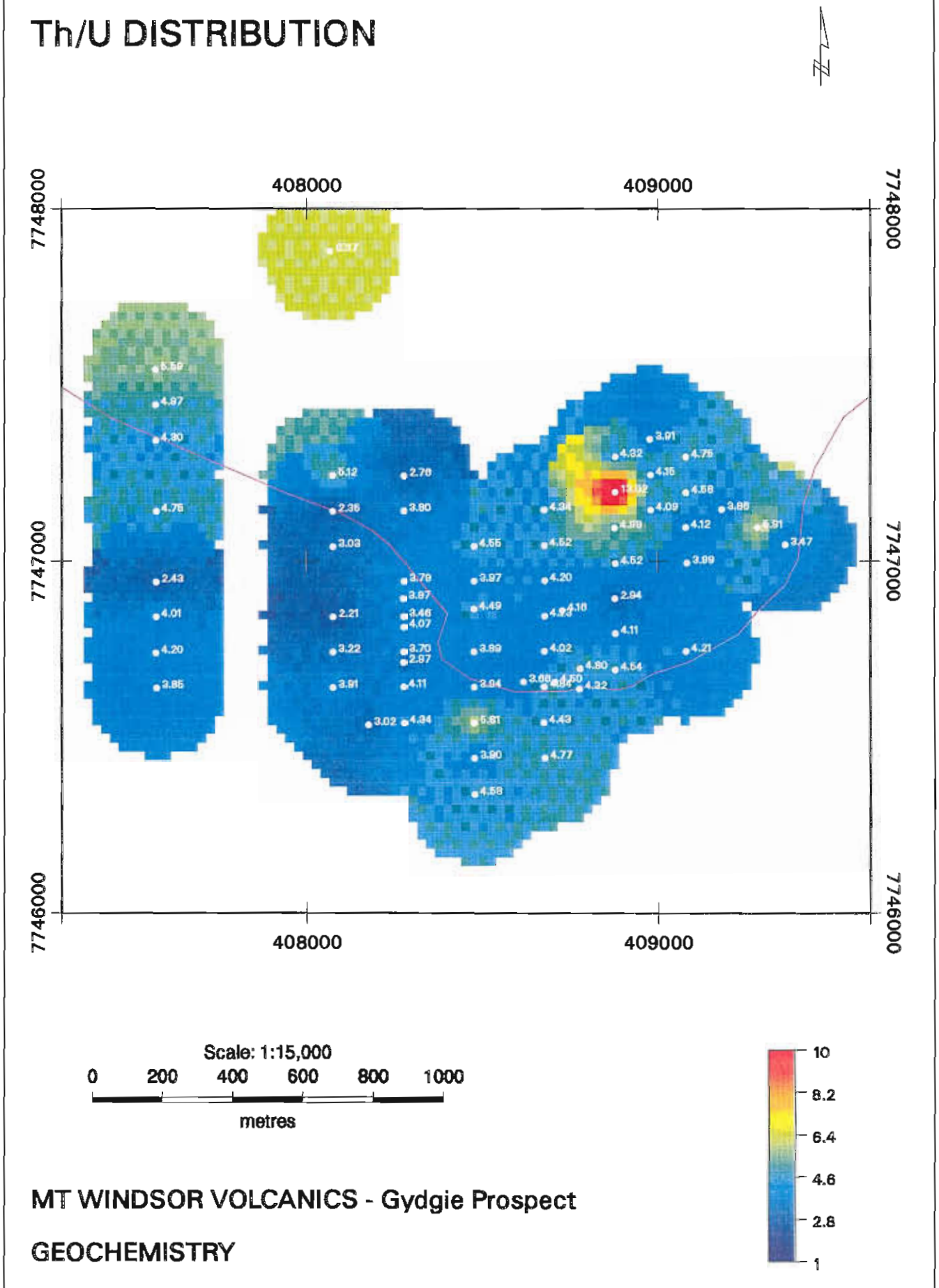
Th/U DISTRIBUTION
408000
409000
7748000
7747000
7746000
Scale: 1:15,000
0 200 400 600 800 1000
metres
10
8.2
6.4
4.6
2.8
1
MT WINDSOR VOLCANICS - Gydgie Prospect
GEOCHEMISTRY

Figure 29

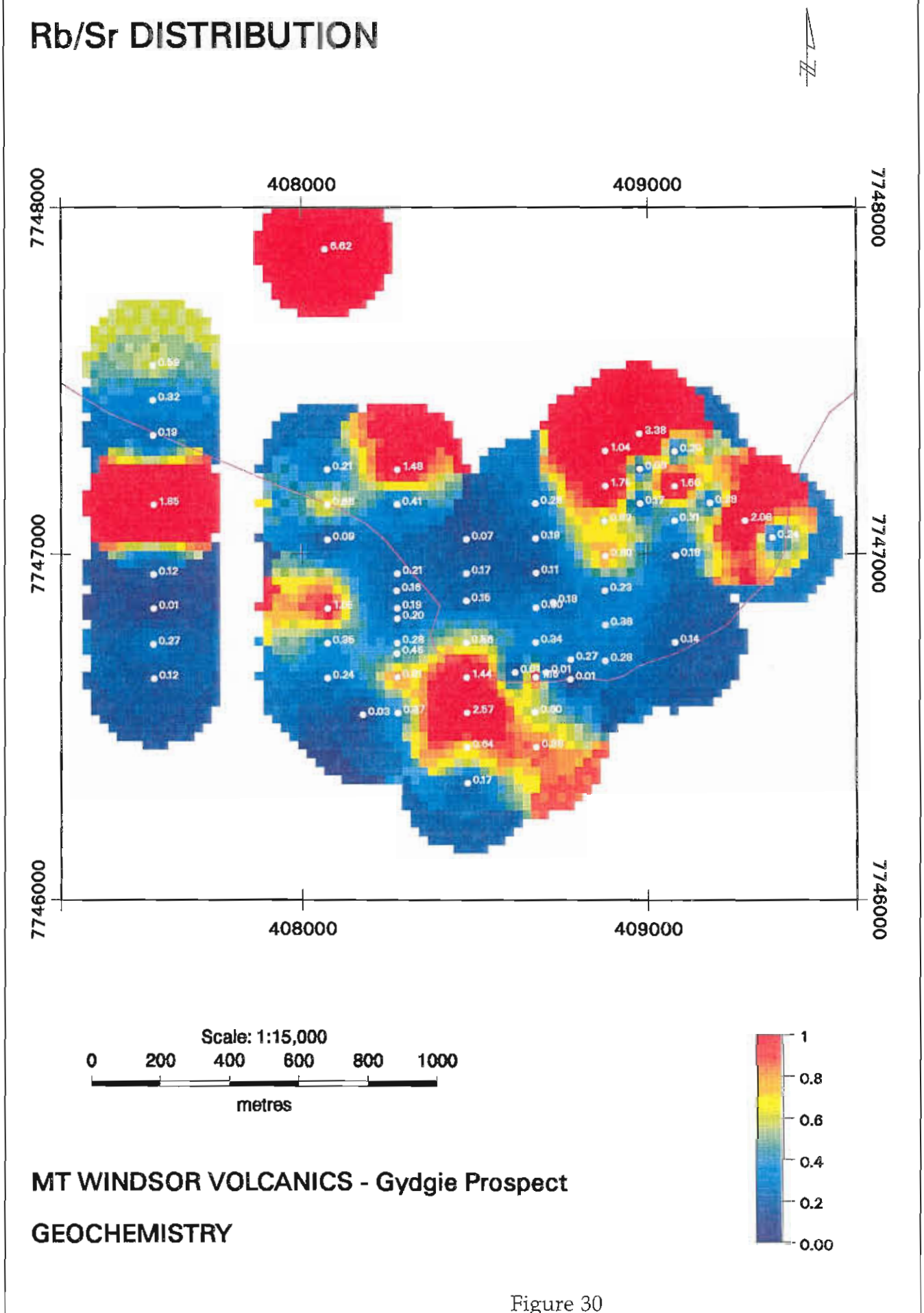
Rb/Sr DISTRIBUTION
N
408000
409000
7748000
7747000
7746000
Scale: 1:15,000
0 200 400 600 800 1000
metres
1
0.8
0.6
0.4
0.2
0.00
MT WINDSOR VOLCANICS - Gydgie Prospect
GEOCHEMISTRY

Figure 30

Oxygen isotopes

Zones of depletion in heavy oxygen (^{18}O) relative to light oxygen (^{16}O) are a feature of many hydrothermal upflow systems associated with massive sulphide mineralisation, and reflect interaction of the rocks with relatively high temperature fluids (300–400°C). If the Gydgie alteration was related to high temperature hydrothermal fluid activity this may be indicated by the O isotope data. Whole-rock oxygen isotope analyses were determined on 10 Gydgie samples (Table 4) along a NW–SE transect that passes from the least altered samples with background concentrations of base metals, through the anomalous metal enriched zone and back into background rocks.

In addition, a suite of the freshest available coherent volcanic samples from the Trooper Creek Formation and Mt Windsor Formation were analysed to provide an indication of likely $\delta^{18}O$ values in the precursor 'unaltered' volcanics. These least altered rocks are all characterised by unaltered feldspar phenocrysts, and have very low loss on ignition values (generally <1 wt.%, Table 3). However, despite these characteristics the silicic rocks display a very broad range of Na_2O/K_2O values (0.2–36.4) which most likely reflect low-temperature alkali exchange with seawater. A plot of $\delta^{18}O$ versus Na_2O (Fig. 31) shows that all of the dacitic to rhyolitic rocks from the Trooper Creek Formation have higher Na_2O and Na_2O/K_2O than the majority of the rhyolites from the Mt Windsor Formation, although one MWF sample is relatively Na-rich and K-poor. Nevertheless the $\delta^{18}O$ values for samples from both Formations show substantial overlap within the range 7.6 to 12.1‰ and no systematic variation of alkali content with oxygen isotope composition. Diagrams showing the variations of $\delta^{18}O$ with Na_2O, Zn and alteration index along the traverse (Fig. 32A–C) indicate a slight decrease in $\delta^{18}O$ coupled with decreased Na_2O and increased alteration index at about the 600m mark. However, the remainder of the traverse shows an increase in $\delta^{18}O$ at lower Na_2O contents and higher alteration index values. The maximum Zn concentration coincides with the lowest $\delta^{18}O$ values, but also relatively high Na_2O (~3.5 wt.%) and an alteration index of approximately 55.

Sulphur isotopes

Sulphur isotope analyses (Table 4) were undertaken on pyrite from the Gydgie alteration zone for comparison with pyrite data for the Waterloo–Agincourt and Thalanga deposits. Some sulphur isotope studies indicate that there is a zonation in the alteration haloes around massive sulphide systems from relatively heavy sulphur enriched in the

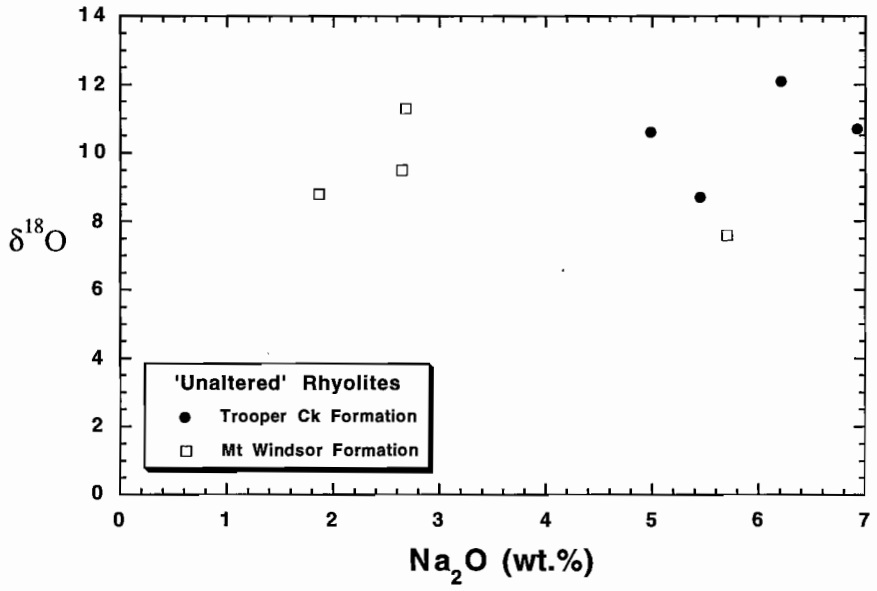

Figure 31
Plot of Na_2O (wt.%) versus $\delta^{18}O$ (‰) for the least altered rhyolitic rocks from the Trooper Creek Formation and Mt Windsor Formation.

Table 3. $\delta^{18}O$ values and other data for Gydgie Prospect and "unaltered" Mt Windsor Volcanics.

Sample	SiO_2	Na_2O	K_2O	LOI	$\delta^{18}O$
Gydgie					
GCR1	76.34	3.11	1.38	2.12	9.2
GCR2	71.15	1.01	2.10	4.94	8.0
GCR3	51.82	4.27	0.31	7.23	6.1
GCRC1	74.44	3.34	0.87	4.52	9.5
GCRC4	58.13	3.63	0.89	6.46	7.8
GCR14	70.18	1.33	2.06	7.15	10.4
GCR13	70.73	0.97	3.45	5.63	10.7
GCR44	68.61	0.40	3.19	5.28	10.6
GCR45	68.92	2.53	2.79	3.87	11.7
GCR46	66.01	5.50	1.07	2.52	10.6
Mt Windsor Formation					
HW26	73.06	1.86	9.65	0.45	8.8
HW35	77.66	2.64	6.09	0.64	9.5
WT27	79.44	5.70	0.33	0.90	7.6
WT44	78.02	2.68	5.21	0.83	11.3
Trooper Ck Formation					
HW1	75.28	6.92	0.19	0.96	10.7
HW10	73.38	5.45	1.75	1.18	8.7
WT11B	76.39	4.98	1.37	0.85	10.6
WT14A	72.95	6.21	0.20	1.39	12.1

Table 4. Sulphur isotope data for pyrites from the Gydgie prospect.

Sample	Description	$\delta^{34}S$
GCDD1/8	pyrite clast	5.85
GCDD1/9	pyrite clast	5.66
GCDD1/10	pyrite clast	5.44
GCDD2/1	diss pyrite in epicalstic	10.54
GCDD2/2	qtz vein + pyrite in epiclastic	13.33
GCDD2/4	pyrite in siltstone	20.97
GCDD2/4	pyrite in siltstone	22.46
GCDD2/3 (1) laser	pyrite in qtz vein	21.16
GCDD2/3 (2) "	Disseminated pyrite in volcaniclastic	13.53
GCDD2/3 (3) "	Disseminated pyrite in volcaniclastic	13.55
GA3 (1) "	Disseminated pyrite in silicic ash	13.5
GA3 (2) "	Disseminated pyrite in silicic ash	10.68
GA3 (3) "	Disseminated pyrite in silicic ash	12.69
GA4 (1) "	Disseminated pyrite in silicic ash	9.16
GA4 (2) "	Disseminated pyrite in silicic ash	9.26
GA4 (3) "	Disseminated pyrite in silicic ash	12.62
GA17 (1) "	Disseminated pyrite in siliceous ironstone	13.5
GA17 (2) "	Disseminated pyrite in siliceous ironstone	15.08
GA17 (3) "	Disseminated pyrite in siliceous ironstone	16.55

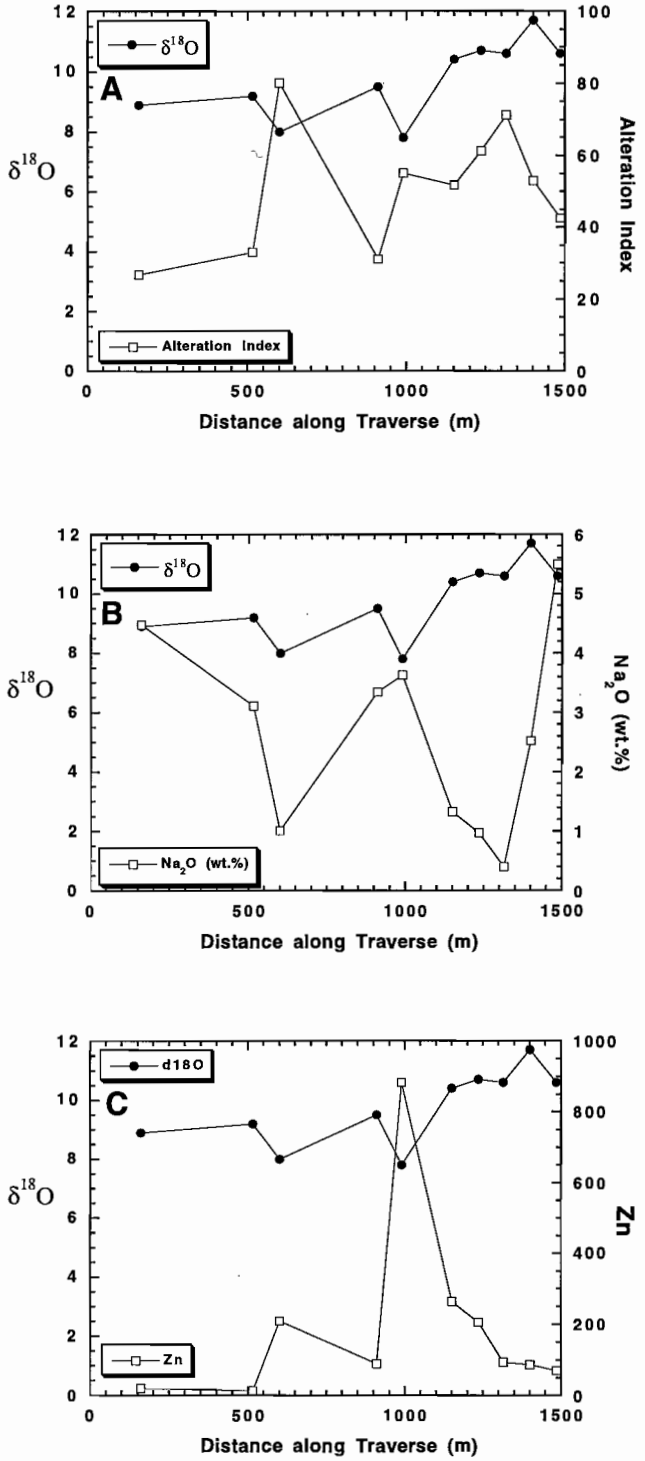

Figure 32
Diagrams comparing the variation of whole-rock $\delta^{18}O$ ‰ values across the Gydgie prospect with variations of (A) Alteration Index, (B) Na_2O (wt.%) and (C) Zn (ppm).

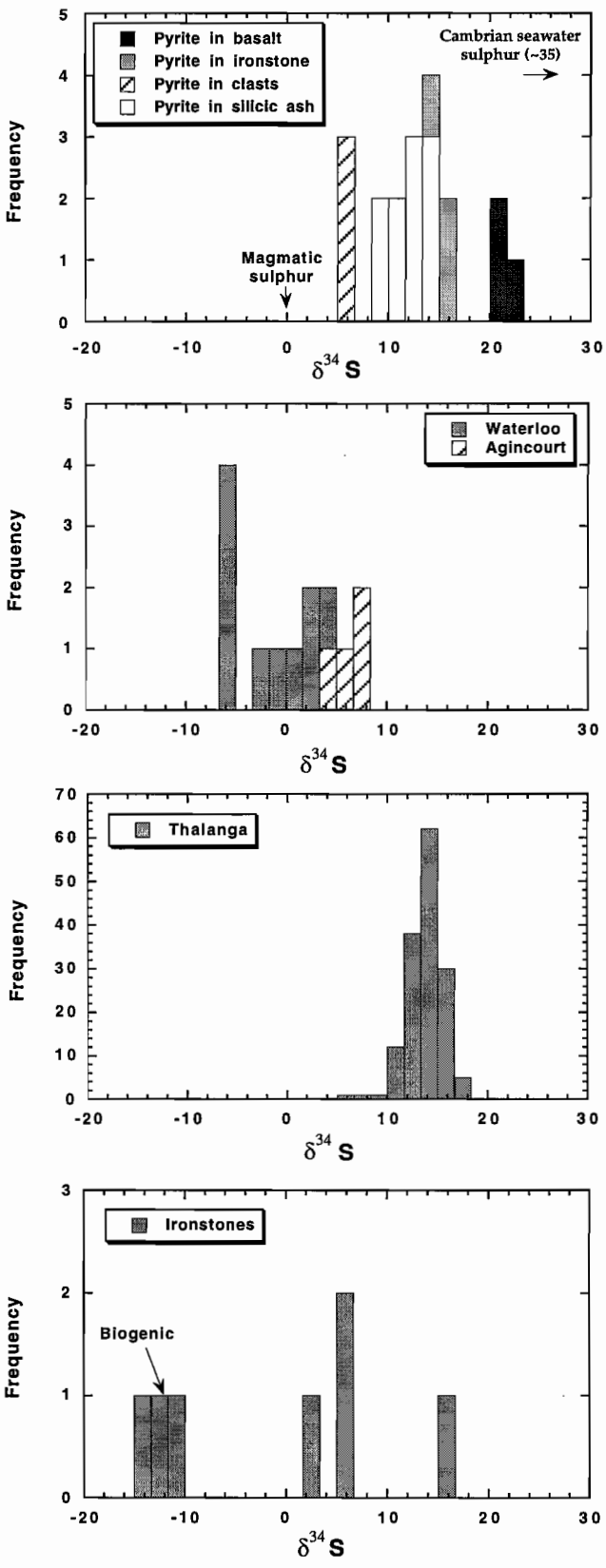

Figure 33
Histograms comparing sulphur isotope data ($\delta^{34}S$ ‰) for pyrite from various lithologies within the Gydgie area with pyrite data from the Waterloo-Agincourt mineralisation, the Thalanga deposit and from various ironstone bodies in the Mt Windsor Volcanic belt.

peripheral zones to relatively light sulphur enriched in the hotter parts of the system (Gemmell and Large, 1993).

Conventional analyses were performed on relatively coarse pyrite drilled from disseminated material in volcaniclastic sandstones and metabasalts, and also from several pyrite clasts in the sandstones. The very fine disseminated pyrite which is common in the siliceous ash-rich units in the Gydgie system was analysed by Robina Sharpe using the laser ablation system at the University of Tasmania Central Science Laboratory.

The data indicate three distinct populations of sulphur isotope compositions that span a relatively large range of $\delta^{34}S$ values (5.4 to 22.5‰). These are plotted in a frequency histogram and compared with other relevant data from the Mt Windsor belt in Figure 33. The pyrites from the sulphide clasts have the lowest $\delta^{34}S$ values (5.4 to 5.9‰) and are most similar to pyrites from the Waterloo and Agincourt mineralisation that occurs some 2 km west along strike. The sulphur isotope composition of these massive sulphide bodies is quite distinctive compared with, for example, the Thalanga deposit (average $\delta^{34}S$ ~ 12‰, Fig. 33), and has been interpreted as indicating either a significant magmatic or volcanic-derived sulphur component in the Agincourt mineralisation, and in the case of Waterloo, sulphide deposition from relatively oxidised fluids (Huston et al., 1995). The clasts in the Gydgie volcaniclastic sandstones and breccias therefore are likely to have been derived from these systems and incorporated in mass-flows sourced from that area. The disseminated pyrite in silicic ash deposits from the Gydgie system have $\delta^{34}S$ values that are more similar to the Thalanga pyrite with an average $\delta^{34}S$ ~ 11‰. Disseminated pyrite from a siliceous ironstone just to the north of the Gydgie Central alteration system also has similar $\delta^{34}S$ values (Fig. 33). The third compositional group are pyrites occurring in a basaltic unit from drillhole GCDD2 which have very high $\delta^{34}S$ values (21 to 22.5‰) trending toward the inferred value for Cambrian seawater ($\delta^{34}S$ ~ 35‰).

Discussion

A major control on the alteration in the Gydgie area appears to have been the predominance of volcaniclastic over coherent units with which meteoric and hydrothermal fluids have interacted. The volcaniclastic rocks, including the fine grained silicic ash-rich units and the coarse pumiceous and lithic sandstones and breccias, show more intense alteration (whether albitic, pyritic or sericite–pyrite alteration) than coherent rocks from the same sequence reflecting enhanced porosity and permeability.

The precise mechanism for the formation of the relatively low temperature albitic alteration which appears to have affected all of the rocks in this sequence is difficult to constrain. Some inferences can be drawn from studies of diagenetic alteration of silicic ash-dominated sediments in the Nankai Trough, Japan that were undertaken at site 808 ODP (Ocean Drilling Project) leg 131 (Masuda et al., 1992). They found with progressive depth below the seafloor the principal alteration minerals of rhyolitic glass changed from smectite at 200 mbsf (20°C), to clinoptilolite at 646 mbsf (65°C) and analcite at 810 mbsf (75°C). They also analysed the porewaters isolated from the sediment column and found systematic changes in the fluid compositions which complemented the mineralogical changes. It seems likely that relative enrichment of Na_2O in the altered glass portion of the silicic volcaniclastic deposits would result from exchange with porewaters and stabilisation of analcite during relatively deep burial diagenesis. This procedure appears to very effectively result in exchange of potassium group elements i.e. K_2O, Rb, Cs, and Ba by Na as is evident from the low concentrations of these elements in the Na-rich samples.

Chemical changes associated with the different alteration styles

Pyritic and albitic alteration

The albitisation appears to be the earliest alteration which has been overprinted by the pyrite, carbonate and sericite–pyrite–chlorite alteration. Comparisons between unaltered modern volcanics and their

variably altered ancient equivalents (Stolz et al., 1996) indicated that volcanics with >6 wt.% Na_2O are extremely rare and that ancient rocks with similar or higher concentrations must have experienced Na_2O addition. Petrographic examination of the Gydgie rocks indicates that albite overgrowths of plagioclase occur in rocks with > 4.5 to 5 wt.% Na_2O suggesting that some addition of sodium has also occurred in these rocks. Consequently, rocks with > 5 wt.% Na_2O are regarded as albitised, and those with < 2 wt.% Na_2O are regarded as having experienced some loss of sodium by reaction with relatively hot, acid fluids. In plots of alteration index versus the chlorite index and manganese carbonate index of Large et al. (1996) (Fig. 34), the Na_2O-rich rocks plot close to the albite end-member, reflecting their low K_2O and MgO, but some samples have relatively high values for the chlorite index which reflects their relatively high pyrite and sulphur contents (Fig. 35). Neither the albitisation nor pyrite development (in the absence of sericite) appears to have resulted in enrichment of Pb, Zn, As, Sb, Bi or Tl significantly above expected background values (Figs 35, 36). The maximum values in modern arc volcanics shown on these diagrams are taken from Noll et al. (1996) and Stolz (unpublished data).

Carbonate alteration

The effects of carbonate alteration are difficult to isolate from those of the sericite–pyrite–chlorite alteration with which it is most commonly associated. The albitised rocks mostly have low CO_2, although there are several exceptions (Fig. 35). There is a strong positive correlation between CaO and CO_2 (Fig. 37a) and, to a lesser extent, between total Fe as Fe_2O_3 and CO_2 (not shown) suggesting that the carbonate is mainly calcite. There are no obvious correlations between CO_2 and the various trace metals suggesting that carbonate deposition was not necessarily related to the metal enrichment event.

Sericite–pyrite–chlorite alteration

The moderate intensity of this alteration is evident in the plot of alteration index versus chlorite index (Fig. 34) where the maximum values for the Ishikawa alteration index are ~80 and the relatively Na_2O-depleted rocks trend toward the chlorite composition rather than sericite. This is in marked contrast to the

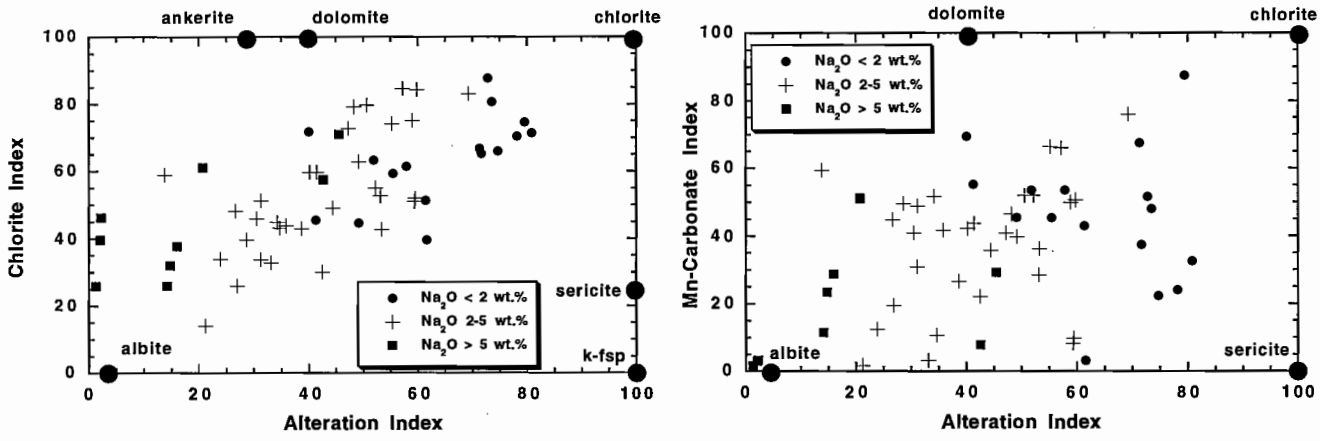

Figure 34
Plots of Chlorite Index and Mn-Carbonate Index (Large et al., 1996) versus the Alteration Index of Ishikawa et al. (1976) for the Gydgie rocks grouped on the basis of their Na_2O contents.

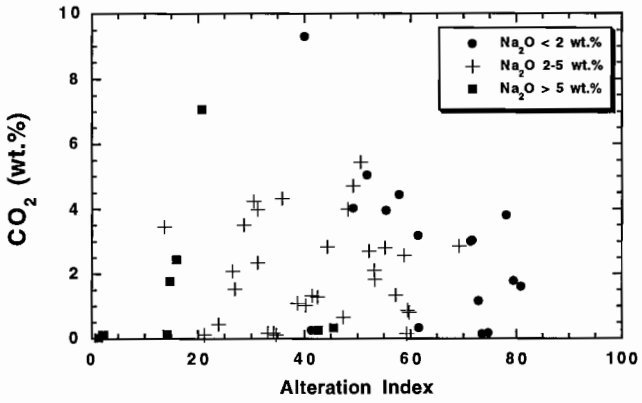

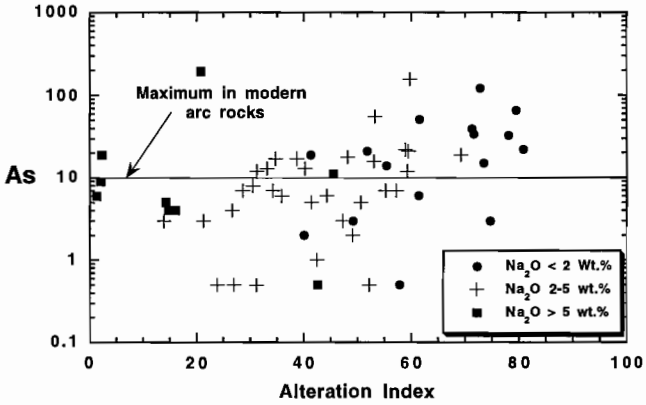

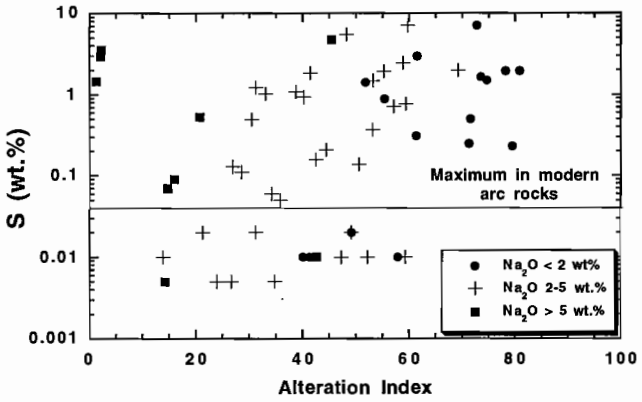

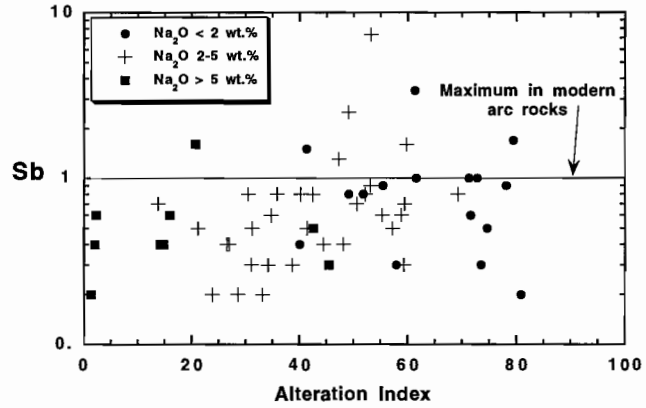

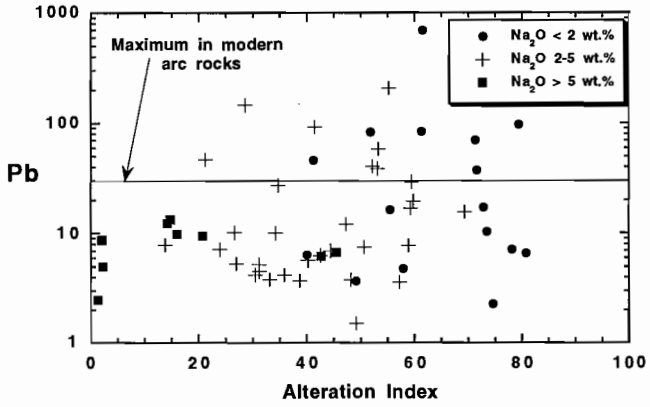

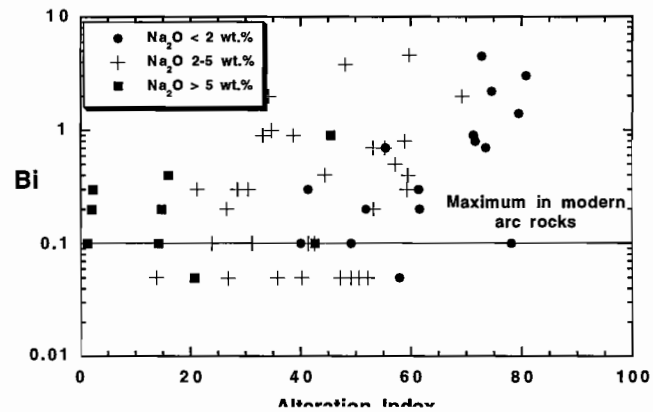

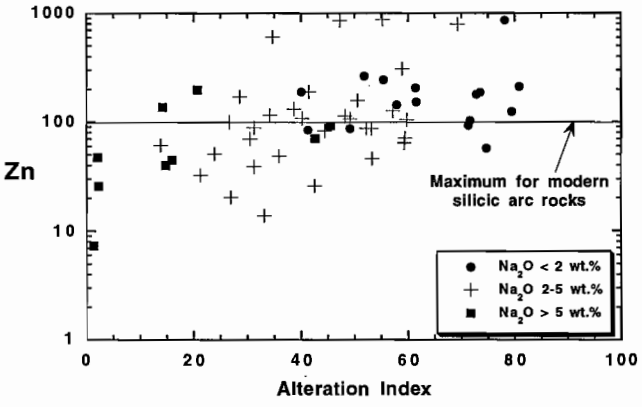

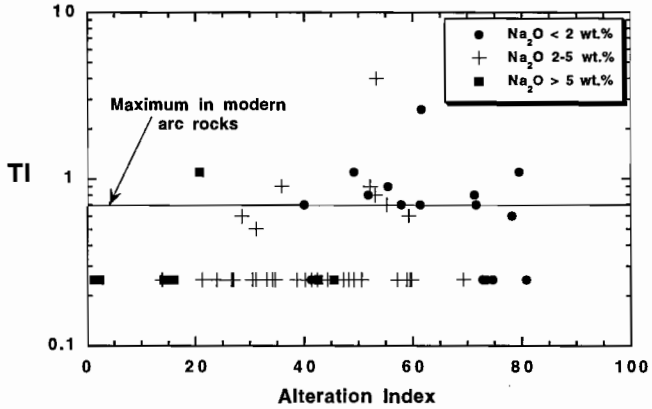

Figure 35
Plots of CO_2, S, Pb and Zn against Alteration Index for the Gydgie rocks.

Figure 36
Plots of As, Sb, Bi and Tl against Alteration Index for the Gydgie rocks.

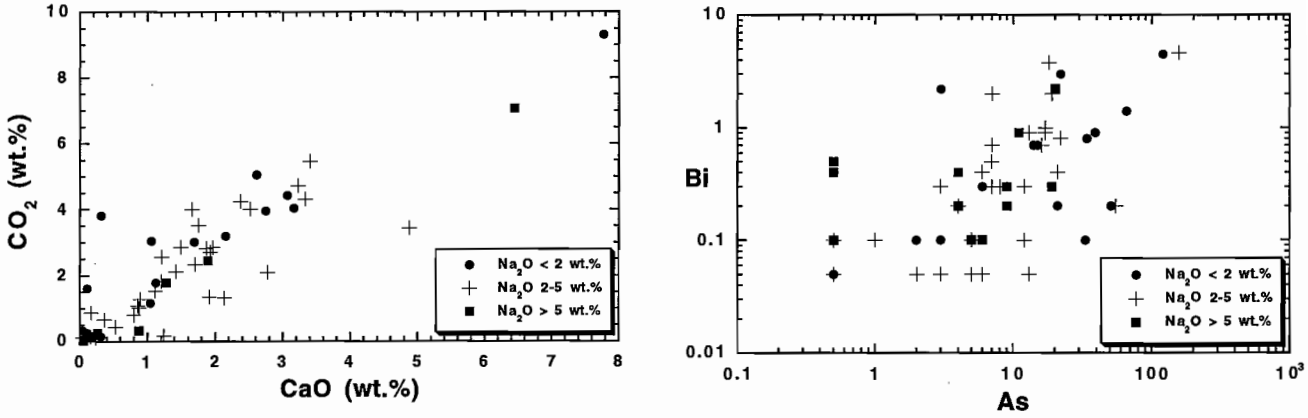

Figure 37
Plots showing correlations between (A) CaO and CO_2 and (B) Bi and As in the Gydgie rocks.

trend displayed by altered Mt Read Volcanics and probably reflects pyrite alteration rather than chlorite as the latter is not a major phase in these rocks. The majority of rocks with this alteration assemblage display elevated CO_2 and S, and variable enrichment in base metals (Figs. 35 and 36), particularly As, and Bi which display a moderate positive correlation (Fig. 37).

Sulphur isotope patterns

The effectiveness of sulphur isotopes in fingerprinting barren hydrothermal systems will depend on the characteristics of the system. The following scenerios may result in recognisable sulphur isotope signatures:

Local hydrothermal circulation — Local circulation may be initiated by small, high level intrusions, but the resulting fluids may be <200° C, the critical temperature for sulphate reduction by ferrous minerals at realistically efficient rates for reduced sulphur formation (Ohmoto and Lasaga, 1982). The system could still produce wall-rock alteration, but most sulphur would derive from leaching of wall-rock sulphur, and hence would have isotopic values similar to the bulk host-rock. In Cambrian systems, in which most VHMS deposits range from $\delta^{34}S$ = 7 to 15‰, this is a mechanism inferred to produce values of –5 to +8, the predominant range for igneous rocks in submarine arc settings. An example is the Boco Siding, 13 km northeast of Rosebery (Green and Taheri, 1992), Mount Read Volcanic Belt, in which disseminated and exhalative pyrite has $\delta^{34}S$ = –1.2 to +4.7‰. Green and Taheri (1992) also suggest that the MRV-hosted Basin Lake, Chester and Cattley Prospects all fall into this category.

Shallow seawater convection, anhydrite deposition, and conversion to pyrite — Seawater descends and readily flows laterally through porous volcaniclastic rocks and clastic sediments. It has been shown that in many submarine volcanic terrains where these rocks are common, the shallowly circulating waters experience heating, which results in widespread deposition of anhydrite within zeolite facies alteration (Ohmoto et al., 1983), forming a distinct and widespread zone of low temperature hydrothermal recharge. In areas where this facies is subsequently fluxed with high temperature fluids, it is possible that anhydrite may be converted to pyrite by reduction of hydrothermal Fe, at temperatures > 200°C. The isotopic composition of this pyrite should approach that of prevailing seawater sulphate, if most of the anhydrite is reduced *in situ* to sulphide, but

the specific isotopic value will be a function of the ratio of the resulting fluid. Such zones may broadly underlie or border massive sulphide deposits (e.g. Gemmell and Large, 1993), or if temperatures were only 200–250°C, may not be associated with significant base metals at all because of limited base-metal transport in this temperature range.

Oxygen isotope zonation

Alteration zones that are associated with VHMS deposits consistently exhibit distinctly lower oxygen isotope compositions than those of surrounding volcanics (Green et al., 1983; Urabe et al., 1983; Green and Taheri, 1992). Classically these systems are modelled as forming by the interaction of seawater with $\delta^{18}O = 0‰$ and volcanic rock ($\delta^{18}O = 5$ to $10)‰$ at varying water/rock values. Surprisingly, few researchers use the measured isotopic value of waters from acid volcanic-hosted seafloor hydrothermal systems to constrain their modelling. These values diverge markedly from the isotopic value of unmodified seawater. Where the subsurface is experiencing diagenetic alteration of glass to zeolites and smectites in the upper ~2 km (Cathles, 1983), water decreases from 0‰ at surface to $\delta^{18}O = -5$ to $-10‰$, and even lower (Pisutha-Arnond and Ohmoto, 1983), due to preferential uptake of ^{18}O by alteration phases in a closed system at moderate to low temperatures, a process which leaves the remaining water ^{18}O-depleted. Additionally, the isotopic value of venting high temperature waters has been calculated to be $\delta^{18}O = 0$ to $+5‰$ in some ancient felsic-hosted systems (Pisutha-Arnond and Ohmoto, 1983), although the enrichment above cold seawater is only 0.4 to 2.2‰ in modern mid-ocean ridge systems (Bohlke and Shanks, 1993). It is clear from this that the isotopic value for the mineralising or altering fluid in particular systems should be calculated from the isotopic values of minerals precipitated in equilibrium within the hydrothermal system, rather than by assuming the unaltered seawater value.

Many workers also assume that the pre-mineralisation host-rock had the isotopic value of unaltered igneous material. The selection of this value implicitly assumes that the mineralisation event occurs in a single stage, with unaltered host-rock being successively altered to form recognisable shells of alteration all in one event. However, there is abundant evidence that low-grade hydrothermal alteration is widespread in the burial environment, and that this process may significantly isotopically modify the host-rocks prior to their interaction with an ore fluid. For instance, in the Kuroko district, extensive zeolite alteration of volcaniclastic-rich rocks surrounding the VHMS-deposits has $\delta^{18}O = 16$ to $25‰$ (Green et al., 1983).

The relationship between different alteration zones in time and space is partly model-driven, but is very important to consider when modelling oxygen isotopes. The selection of the isotopic value of the host-rock, and of the altering fluid, is particularly important for barren hydrothermal systems, because their conditions of formation are not yet well understood compared with mineralised systems.

Applications to the Gydgie system

Geochemical analysis of the "unaltered" coherent rocks in the Mt Windsor Volcanic Belt indicates that they have been partly altered to fine-grained albite-only or K-feldspar-only assemblages with $\delta^{18}O = 7.4$ to $12.2‰$. Fresh rocks in similar tectonic settings have $\delta^{18}O \sim 6$ to $8‰$, suggesting that the MWVB rocks have experienced oxygen exchange. Given that the MWVB response was in coherent rocks that were selected because they were the least-altered samples, the associated volcaniclastic rocks probably experienced stronger regional alteration. This suggests that cryptic low-grade alteration is widespread throughout the belt, but unlike the zeolite-grade alteration of unmetamorphosed belts such as the Hokuroko Basin, hosting Japan's Kuroko deposits, low grade regional alteration is manifested as fine grained feldspar. This feldspar may have been deposited as a primary alteration product, or more likely, may be metamorphosed analcime and adularia/microcline alteration. Pisutha-Arnond and Ohmoto (1983) favour the formation of analcime from the breakdown of mordenite and clinoptilolite at 50–200°C in volcanic sediments. Further study is required to determine the conditions of formation of the Mt Windsor

Volcanics regional feldspar alteration. However, in either interpretation large-scale low to medium temperature diagenetic or hydrothermal alteration was widespread in the MWVB.

Altered rocks from the Gydgie system have $\delta^{18}O$ = 8 to 11.8‰, completely overlapping the value of regional rocks discussed above. At first analysis, this similarity might downgrade the mineralising potential of the Gydgie system. However, in Fig. 38 the oxygen isotope modelling of Green et al. (1983) is adapted to the Mount Windsor Volcanics, and the result indicates that alteration with $\delta^{18}O$ = 6 to 12‰ is the likely product of moderately high temperature alteration of typical MWVB lithologies. In a two-stage model, the Gydgie area experiences regional analcime-alteration by typical diagenetic fluids ($\delta^{18}O_w$ = –8‰) under closed-system conditions, forming albite and K-feldspar alteration with $\delta^{18}O$ = 6 to 12‰. Pore fluids typically obtain a value of $\delta^{18}O$ = -8‰ at ~600m below the ocean floor (Gieskes and Lawrence, 1981). The Gydgie prospect was subsequently subjected to high temperature alteration by fluids with $\delta^{18}O$ = 0‰, the lower end of compositions found for seafloor ore forming solutions. In this situation the Gydgie isotopic range of $\delta^{18}O$ = 8 to 11.8‰ corresponds to a temperature range of 170–300° C (Stage II, Fig. 38), which would encompass acceptable ore fluids. Under the limitations of the two-stage model, no strong isotopic depletion would occur if the high temperature alteration was tightly

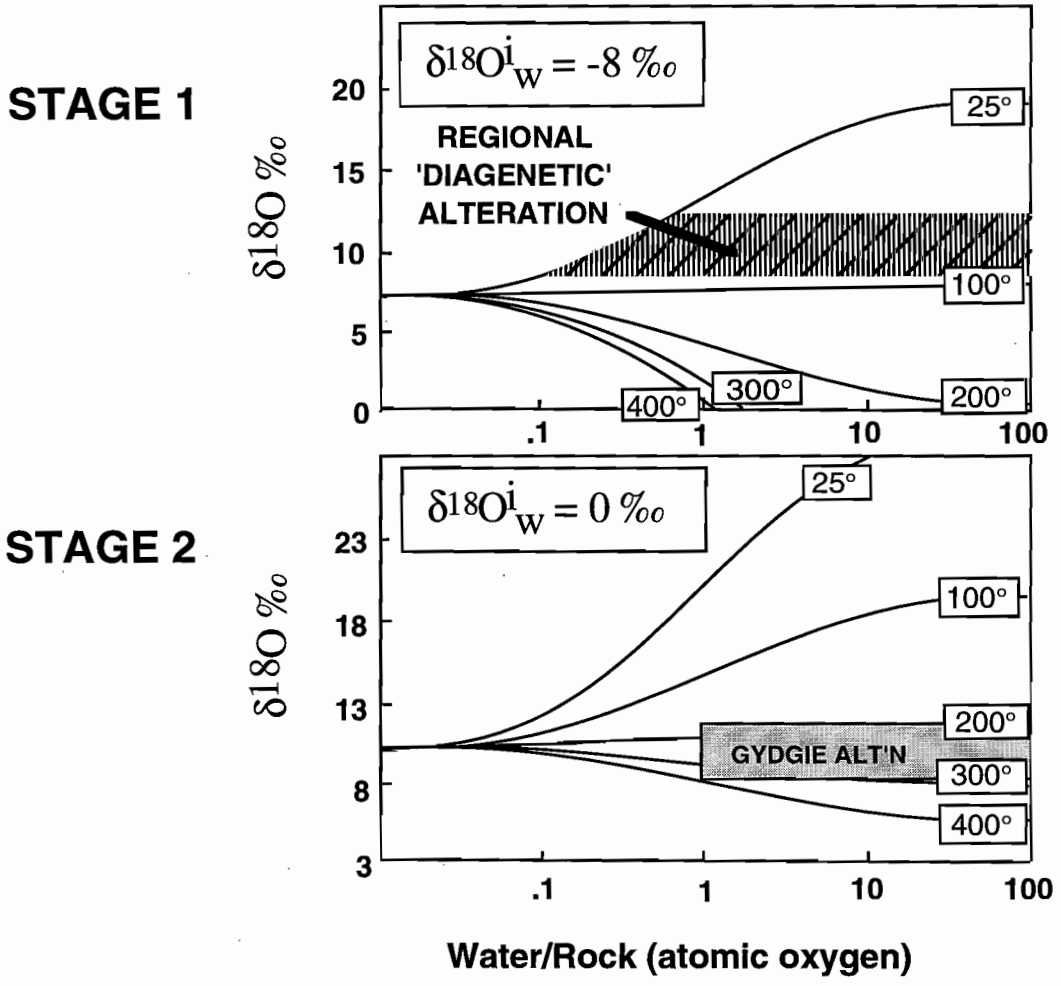

Figure 38
Potential whole rock oxygen isotope history of the Gydgie area. In Stage 1, the regional albite/K-spar alteration is formed by interaction of diagenetic volcanic pore-waters with fresh glass at 25–80°C. In stage 2 the diagenetically altered rocks are reacted with deep hot hydrothermal waters at 180–300°C, forming the $\delta^{18}O$ = 8–11.8‰ alteration (sericite/chlorite).

focussed, i.e. did not possess a significant halo of lower temperature fluids, which would have produced surrounding ^{18}O enrichment.

The purpose of this exercise was to determine if the oxygen isotope evidence can conclusively indicate the prospectivity of the Gydgie site. In this instance it is concluded that the lack of depletion does not necessarily downgrade the prospectivity because the "unaltered background" is ~10‰ as a result of earlier low temperature alteration. However, this interpretation will be tested by determining the temperature of formation of phases in the alteration.

In terms of sulphur isotope values, the Gydgie pyrites in silicic ash are unlikely to have formed from a local hydrothermal system <200° C, because they have $\delta^{34}S$ = 8 to 15‰, higher than likely values for igneous sulphur. The approach of these values towards Cambrian seawater sulphate (~35‰) indicates that temperatures were >200°C at some point in the system, to enable sulphate reduction, and this is viewed as a positive feature for the system. The similarity of the values to those of Thalanga is also a positive feature. The dissimilarity to the light values of Agincourt and Waterloo (–6 to +8‰) along strike is not necessarily a negative feature, because the Waterloo values in particular are unusual for Cambrian massive sulphide systems, and strongly imply sulphate-rich fluids, or a post-depositional seafloor oxidation history for the deposit which altered its sulphur isotope signature. For instance, the value of "igneous" sulphide in some MOR basalts decreases significantly during seafloor weathering, when pyrrhotite is leached and secondary pyrite deposited (Alt et al., 1989); this process may also occur if seafloor massive sulphide bodies interact with seawater but are not completely oxidised.

Conclusions

- Petrographic observations, coupled with the geochemical and isotopic data indicate that the Gydgie Central alteration system was not a major focus for high-temperature hydrothermal fluids, and accordingly is not likely to be directly associated with massive sulphide mineralisation.
- There are four major styles of alteration recognisable in the volcanic sequence. These are (1) albite, (2) pyrite, (3) carbonate, and (4) sericite–pyrite–chlorite. The albitic alteration appears to be a product of diagentic processes involving the formation of analcite which was converted to albite during deeper diagenesis (>150°C) or subsequent regional metamorphism. Pyrite alteration (without sericite) and carbonate alteration are both locally important and appear to post-date the albitic alteration. None of these alteration styles appear to be associated with significant enrichment of base metals above background concentrations.
- The zones of anomalous base metal and Ba concentrations coincide with areas of strongest alteration of the silicic volcaniclastic rocks to sericite-pyrite bearing assemblages. However, the absence of extreme sodium depletion in these rocks (mostly > 1% Na_2O) reflecting incomplete plagioclase destruction, and alteration indices generally <75–80 indicates that hydrothermal fluid activity was characterised by relatively low water/rock values (probably less than ~10). Water/rock values >100 are probably typical of intense alteration systems associated with significant base metal mineralisation.
- Sulphur isotope data for disseminated pyrites from within the system ($\delta^{34}S$ = 8 to 15‰) are similar to values for the Thalanga deposit and indicate an origin from fluids with a relatively high-temperature (>200°C) history.
- Whole-rock oxygen isotope data do not indicate a zone of depletion in heavy oxygen in the Gydgie area. However, the $\delta^{18}O$ values for the Gydgie rocks (8 to 11.8) have been modelled in terms of a two-stage history which involved an initial increase in $\delta^{18}O$ during diagenesis, followed by a decrease to their present values by interaction with a relatively high-temperature fluid (~200°C) with $\delta^{18}O$ = 0.

- Collectively these data suggest that the Gydgie alteration system may have been a short-lived satellite system that was peripheral to, and temporally related to the Waterloo-Agincourt mineralising event.

References

Alt, J.C., Anderson, T.F. and Bonnell, L., 1989, Geochemistry of sulfur in a 1 km section of hydrothermally altered oceanic crust. Geochim. Cosmochim. Acta 53: 1011–1023.

Bohlke, J.K. and Shanks, W.C. III, 1993, Stable isotope study of hydrothermal vents at Escanaba Trough: observed and calculated effects of sediment–seawater interaction. In USGS Bull. 2022.

Cathles, L.M., 1983, An analysis of the hydrothermal system responsible for massive sulfide deposition in the Hokuoku Basin of Japan. Econ. Geol. Mon. 5, 439–487.

Gemmell J.B. and Large R.R., 1993, Evolution of a VHMS hydrothermal sytstem, Hellyer deposit, Tasmania, Australia: sulphur isotope evidence. Resource Geology Special Issue 17: 108–119.

Green G.R. and Taheri J., 1992, Stable isotopes and geochemistry as exploration indicators. Bull. Geol. Surv. Tasmania 70: 84–91.

Green, G.R., Ohmoto, H., Date, J., and Takahashi, T., 1983, Whole rock oxygen isotope distribution in the Fukazawa–Kosak area, Houroko district, Japan, and its potential application to mineral exploration. Econ. Geol. Mon. 5, 395–411.

Gieskes J.M. and Lawrence, J.R., 1981, Alteration of volcanic matter in deep sea sediments: evidence from the chemical composition of interstitial waters from deep sea drilling cores. Geochim. Cosmochim. Acta 45, p. 1687–1703.

Huston, D.L., Kuronen, U. and Stolz, A.J., 1995. Waterloo and Agincourt prospects, northern Queensland: contrasting styles of mineralisation within the same volcanogenic hydrothermal system. Aust. J. Earth Sci., 42, 203–221.

Ishikawa, Y., Sawaguchi, T., Iwaya, S. and Horiuchi, M., 1976. Delineation of prospecting targets for Kuroko deposits based on modes of volcanism of underlying dacite and alteration haloes. Mining Geology, 26, 105–117.

Large, R.R., Stolz, J. and Duhig, N., 1996, Preliminary assessment of MRV geochemical database in terms of possible vectors to ore. CODES - AMIRA Project P439 Report , May, p197–209.

Masuda, H., Tanaka, H., Gamo, T., O'Neil, J.R., Peacor, D.R. and Jiang, W.-T., 1992, Formation of authigenic smectite and zeolite and associated major element behaviour during early diagenesis of volcanic ash in the Nankai Trough, Japan, ODP leg 131, in, Kharaka and Maest (eds.) Water-Rock Interaction, Balkema, Rotterdam, p1659–1662.

Noll, P.D., Newsom, H.E., Leeman, W.P. and Ryan, J.G., 1996, The role of hydrothermal fluids in the production of subduction zone magmas: Evidence from siderophile and chalcophile trace elements and boron. Geochim. Cosmochim. Acta, 60, 587–611.

Pisutha-Arnond, V. and Ohmoto, H., 1983, Thermal history and chemical and isotopic compositions of the ore-forming fluids responsible for the Kuroko massive sulfide deposits in the Hokuroku district of Japan. Econ. Geol. Mon. 5, 523–558.

Stolz, J., Large, R.R. and Duhig, N., 1996, Progress report on the utilisation of the Mount Read Volcanics database. CODES - AMIRA Project P439 Report , May, p181–196.

Urabe, T., Scott, S.D. and Hattori, K., 1983, A comparison of footwall-rock alteration and geothermal systems beneath some Japanese and Canadian volcanogenic massive sulfide deposits. Econ. Geol. Mon. 5, 345–386.

Volcanic influences in the formation of iron oxide-silica deposits in a volcanogenic-massive sulfide terrain, Mount Windsor Volcanic belt, Queensland

Mark Doyle
Centre for Ore Deposit and Exploration Studies, Geology Department, University of Tasmania

7.1 Introduction

Iron oxide-silica rocks form the ore equivalent horizon or favourable stratigraphic position within the host volcanic pile to many volcanic-hosted massive sulfide (VHMS) deposits and have long been considered a potential marker horizon for mineral exploration (e.g. Large, 1977, 1992). Hematitic siltstones, maroon hematitic jaspers and quartz-hematite ± magnetite rocks mark the ore equivalent horizon of many Australian VHMS deposits including Mount Chalmers (Large and Both, 1980; Hunns, 1994a,b), Mount Morgan (Taube, 1988; Taube and Messenger, 1994, Messenger and Taube, 1994) Scuddles and Gossan Hill (Ashley et al., 1988; Barley, 1992), Thalanga (Duhig et al., 1992) and Captains Flat (Davis, 1975). The iron oxide-silica rocks may be the lateral equivalent of massive sulfide or ore equivalent volcano-sedimentary units (e.g. Thalanga), occur as veins and massive replacement of volcanic rock in the hostrocks to mineralisation (e.g. Highway-Reward), or occur within or just above the level of mineralisation (e.g. Mt Morgan). In many cases iron oxide-silica rocks are not restricted to the ore position but are developed within a 10 to 50 metre thick stratigraphic package which includes the ore horizon (Large, 1992). The iron oxide-silica rocks are sometimes spatially separated from mineralisation by a few tens to hundreds of metres laterally (e.g. Duhig et al., 1992a,b) and not all iron oxide-silica occurrences are associated with mineralisation. The genetic significance of these iron oxide-silica rocks may vary from that of thin volcano-sedimentary units enriched in products from hydrothermal exhalations which mark the ore equivalent horizon of some Canadian volcanic-hosted massive sulfide (VHMS) deposits (e.g. Ridler, 1971), and Japanese Kuroko deposits (Kalogeropoulos and Scott, 1983).

Recent observations of the sea floor confirm the presence of a variety of Fe- and Si- enriched hydrothermal precipitates. They may occur as either chimneys, thin sediment blankets, irregularly shaped mounds, small patches, or fill fractures within lava flows (Hekinian et al., 1993). Many iron oxide-silica deposits are the product of hydrothermal exhalation concurrent with massive sulfide deposition. Youthful submarine iron oxide ± silica-rich sediments associated with actively venting sulfide mounds at mid-ocean ridge spreading centres have been mapped at the East Pacific Rise (Barrett et al., 1988; Juniper and Fouquet, 1988; Boyd et al., 1993; Hekinian and Fouquet, 1985; Hekinian et al., 1993; Alt et al., 1987; Janecky and Seyfried, 1984), the FAMOUS site on the Mid-Atlantic Ridge (Juniper and Fouquet, 1988), the Juan de Fuca Ridge (e.g. Normark et al., 1983; Tivey and Delaney, 1986; Hannington and Scott, 1988) and the Galapagos Spreading Centre (Herzig, 1988). Similar iron oxide ± silica deposits have been recorded from the Valu Fa Ridge, Lau Basin (Fouquet et al., 1993), the Japanese spreading centre, western Pacific (Adachi et al., 1986), the Okinawa Trough (Juniper and Fouquet, 1988) and submarine hotspot volcanoes of the Society Islands, South Pacific (Boyd et al., 1993; Hekinian et al., 1993). Others are associated with silicic-intermediate submarine volcanic settings including the PACMANUS site, western Woodlark basin (Binns et al., 1993; Boyd et al., 1993).

There is clearly a spectrum of iron oxide-silica deposits/rocks in host sequences to massive sulfide

mineralisation. Important insights into hydrothermal and mineralisation processes might be gained by investigating the complex relationships between iron oxide-silica rocks, mineralisation and volcanic facies, so it is important that complexities are recorded. Here I describe iron oxide ± silica rocks and alteration in silicic to intermediate volcano-sedimentary host sequences to massive sulfide mineralisation in the Mount Windsor Volcanic belt (Fig. 7.1). Duhig et al. (1992a,b) described the mineralogy, textures and geochemistry of quartz-hematite ± magnetite rocks associated with the Thalanga VHMS deposit and compared these with samples from other parts of the Mount Windsor Volcanic belt. They interpreted the ironstones to have formed from the mixing of hydrothermal fluids and seawater at the sea-floor. At some sites iron-oxide secreting bacteria and/or fungi were interpreted to have been important by providing a framework for the precipitation of Fe and silica. In the current study, quartz-hematite lenses in the area between Coronation homestead and Trooper Creek prospect (Fig. 7.1) are reinterpreted in the light of detailed volcanic facies analysis which demonstrate that many of the iron oxide ± silica rocks are sub-seafloor replacements of permeable pumiceous units, stromatolitic and oncolitic sandstone, massive rhyolite-dacite and peperite. In particular, terminology is reviewed, the involvement of iron oxide secreting micro-organisms in ironstone deposition is assessed, and the critically important role of volcanic facies and volcanism on iron oxide ± silica precipitation and distribution is discussed.

7.2 Terminology and the description of iron oxide ± silica rocks/deposits

Iron oxide ± silica rocks and alteration in volcanic successions have been variably termed exhalite, ironstone, jasper, jaspilite, chemical sediment, ochre, umber and ferruginous chert. The term tuffaceous exhalite has been used for iron oxide ± silica rock which overlies some of the Noranda deposits in Canada (e.g. Kalogeropoulos and Scott, 1983) and tetsusekiei (literally iron quartz) which overlies some Kuroko deposits (e.g. Kalogeropoulos and Scott, 1989) in recognition of the important contribution of volcaniclastic material to these deposits. Exhalite (Ridler, 1971) is a genetic interpretive term and is not suitable for the description of iron oxide ± silica rocks for which the relationships with the enclosing volcano-sedimentary facies do not clearly demonstrate an exhalative origin. In sedimentary classifications, an ironstone is a rock containing > 15 wt% Fe (James, 1954). In the current study, the term ironstone has been used to refer to massive or laminated silica and iron-oxide rich rock with or without a sedimentary or volcanic component. The term tuffaceous ironstone is adopted for ironstones which contain a recognisable volcaniclastic component (e.g. shards, pumice, scoria, crystals) or alteration products of a former volcaniclastic component.

Small zones of intense pervasive hematite alteration occur at the margins of the Highway-Reward massive sulfide deposit, as stratiform zones beneath some ironstones, as discontinuous pods in andesite lithic-scoria breccia, and at the margins of lava domes and cryptodomes. Iron contents of greater then 10 wt% are approaching those of sedimentary ironstones but use of the term ironstone is avoided as the hematite is clearly the product of hydrothermal alteration. The term iron oxide ± silica alteration/ rock is adopted here as a non-genetic descriptive term incorporating iron oxide altered volcanic rock, ironstone and tuffaceous ironstone.

7.3 Stratigraphic distribution

Small discontinuous lenses and pods of quartz-hematite or magnetite are common in the Mount Windsor Volcanic belt (Duhig et al., 1992; Berry et al., 1992). In the area west of Thalanga mine, ironstones occur in three distinct stratigraphic positions (Duhig et al., 1992); at the contact between the Puddler Creek Formation and rhyolites of the Mount Windsor Formation (MWF); within the Thalanga ore horizon at the contact between the MWF and the overlying Trooper Creek Formation (TCF) and; within the TCF 80-100 m above the Thalanga ore position.

Elsewhere in the Mount Windsor Volcanic belt, ironstones are largely restricted to the TCF or occur

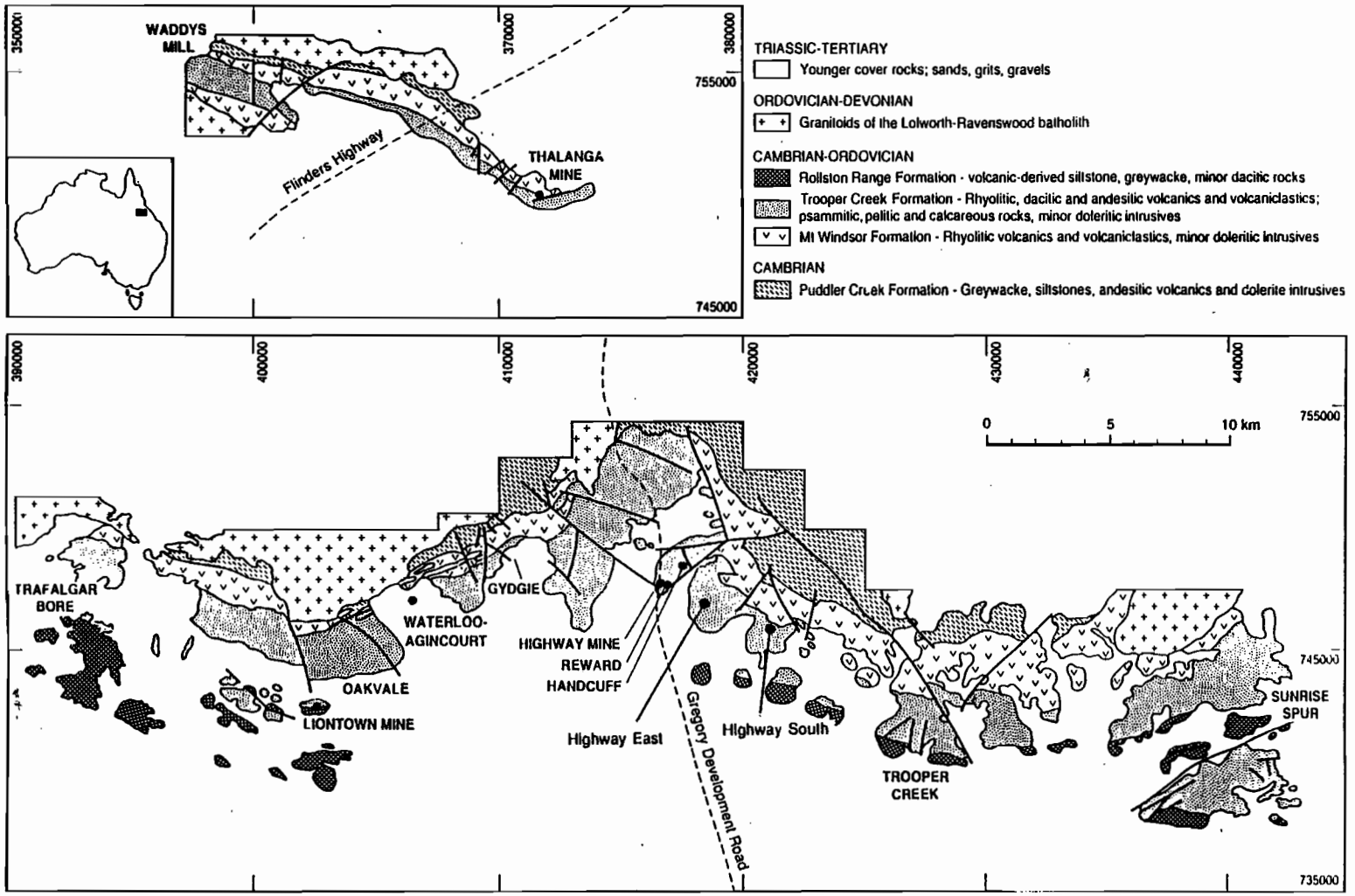

Figure 1: Simplified geological map of the Mt Windsor subprovince between Waddy's Mill and Sunrise Spur showing the distribution of the principal units and younger granitoids. Modified from Berry et al. (1992).

at the contact between the TCF and the overlying Rollston Range Formation (Fig. 1; Duhig et al., 1992; Berry et al., 1992; Doyle, 1994a,b). In the area between Coronation homestead and Trooper Creek prospect ironstones are restricted to the middle and upper TCF, cropping out at Trooper Creek prospect and in laterally equivalent sequences to the west, north of Trooper Creek prospect, at Highway East and at Handcuff (Fig. 7.1). At Highway-Reward veins and patches of quartz-hematite rock and hematite alteration occur in drill core, and semi-massive quartz-hematite rock crops out in the base of the Highway pit.

7.4 Occurrence and volcanic facies

In the study area, ironstones are associated with differing volcanic facies whose physical properties, mineralogy, geochemistry, and depositional environment vary. Four principal facies are important:

(1) Massive coherent quartz and feldspar phyric rhyolite and dacite.

(2) A range or syn-eruptive juvenile volcaniclastic deposits sourced from explosive eruptions in shallow subaqueous or subaerial environments. Two main facies are recognised. One is dominated by lithic-scoria breccia containing bomb fragments and was deposited by subaqueous mass flows and by fallout from subaqueous eruption columns and fire fountains. The second type contains abundant pumice produced from explosive silicic eruptions and deposited as water-settled fallout and from high-concentration turbidity currents.

(3) Occurrences of coarsely feldspar phyric dacite with peperitic upper margins that suggests they were emplaced into wet unconsolidated sediment as a cryptodome. Other iron oxide-silica rocks are hosted by lava domes and flows.

(4) Massive and thinly planar laminated cherty siltstone

7.4.1 Ironstone associated with pumiceous sandstone-breccia

Pumice-rich sandstone-breccia characterised by fractured quartz and feldspar overlies and underlies a thin poorly exposed pod of massive ironstone at Highway East prospect around 7747500mN, 419900mE (AMG). Perlitically fractured and finely flow banded dacite clasts are a minor component in the breccia beneath the ironstone. Parts of the breccia along the top contact of the ironstone contain small quartz-hematite spots.

At Trooper Creek Prospect lenses of ironstone occupy the contact between andesite scoria breccia and underlying units of pumice breccia, forming a discontinuous stratigraphic horizon (horizon 1) approximately 500 m in length. These lenses range in thickness from 1-2 cm to 10 m and although mostly 10 to 20 m in exposed (actual ?) length, one occurrence crops out continuously over a strike length of approximately 116 m. Detailed mapping of the best exposed sections of horizon 1 ironstone (Figs. 7.2-7.4A) confirms that the lenses are a discontinuous facies equivalent of non-welded, diffusely stratified dacite pumice breccia consisting of pumice shreds and a matrix of sub-millimetre shards, crystals and crystal fragments. The breccias-sandstones contain rare scattered trachytic andesitic lithic fragments, comprising interlocking sanidine microphenocrysts in a formerly glassy chloritic groundmass. Ironstone occurs at the base, top or is enclosed by the pumice breccia. Top contacts of the ironstone lenses are sharp however, bottom contacts vary from sharp to gradational with massive siliceous ironstone passing through tuffaceous ironstone with remnant diffuse lamination into purple sericite-hematite altered pumice breccia or scoria breccia (Fig. 5). Tuffaceous ironstone is a texturally complex mixture of juvenile volcanic particles and non-volcanic quartz and hematite. Quartz-hematite rich patches and bands in tuffaceous ironstone alternate with quartz dominant pyroclast-rich patches and bands accentuating the primary laminated fabric. Pumice breccia both beneath and between ironstone lenses is purple due to pervasive sericite-hematite alteration. The intensity of hematitic alteration increases upward passing

through a thin (45 cm) zone of quartz-hematite nodule bearing pumice breccia into massive and/or tuffaceous ironstone a few centimetres to metres thick and overlain by thinly planar laminated grey to purple cherty siltstone. One segment of horizon 1 ironstone is stromatolitic and oncolitic (Fig. 7.2 — section B). In situ growth position stromatolites occur as domed biostromes 1-3 cm thick built upon and intergrown with tuffaceous- and oncolitic-sandstone. Microbialites in the ironstone are now quartz-hematite whereas pumice is pervasively silicified and outlined by fine grained hematite.

A poorly exposed 28.7 m thick sequence of thinly planar laminated cherty siltstone and polymictic pumice-lithic breccia separates horizon 1 ironstone from a second thin stromatolitic and oncolitic tuffaceous ironstone horizon (horizon 2, Fig. 7.3 — section B). The polymictic lithic breccia contains clasts of dacite, laminated siltstone and massive ironstone supported in a pumiceous matrix. Strong patchy hematite alteration of the matrix to the upper part of the breccia is texturally destructive. The deposit is weakly normally graded suggesting deposition from a mass-flow which incorporated ironstone at the source, or from deposits on or below the sea floor during transport.

Horizon 2 ironstone is a very poorly exposed, texturally complex mixture of volcanic detritus, oncolites and stromatolite. In situ stromatolites occur as domed bioherms 6-7 cm high and up to 8 cm in diameter. The intercolumn material is a mixture of unaltered crystal fragments, lithic fragments and silicified pumice shreds. The biostromes are overlain by pervasively hematite altered siltstone and are built upon fine grained sandstone, granular sandstone and pebble conglomerate. Sandstones are dominated by pumice and crystal fragments or consist of grain-supported aggregates of sand- to granule-sized oncolites, stromatolite fragments and volcanic fragments. Breccias are clast- to matrix-supported frameworks of stromatolite fragments to 12 cm long separated by a matrix of smaller fragments, oncolites, pumice, shards, crystal fragments and minor lithic fragments. Hematite and lesser quartz have completely replaced the oncolites and stromatolites, whereas the volcanic component and beds are more quartz-rich and hematite-poor.

Diffusely laminated dacite pumice breccia (horizon 3) intercalated with cherty siltstone and hematite altered mixed dacite-siltstone breccia overlies horizon 2 ironstone. Intense pervasive purple hematite alteration of the lower 2 m of horizon 3 pumice breccia has destroyed most primary textures in this part of the unit and suggests that fluids selectively moved along the contact between the breccia and underlying siltstone.

Horizon 4 ironstone at Trooper Creek prospect overlies the fine grained top of a normally graded andesite scoria breccia characterised by abundant fluidly shaped variably vesicular bomb fragments (Fig. 7.3 — section D). The ironstone has a granular sandy texture in which dark maroon hematite-rich patches 1 to 5 mm long are separated by hematite-poor, quartz-rich material which resembles a matrix. Thin sections reveal rare patches of poorly preserved shards. Scoria breccia beneath the ironstone lens is intensely quartz-hematite altered within a metre of the contact and variably sericite-hematite altered to 130 m below the contact. Hematite alteration is most intense within 26 m of the ironstone obscuring clast margins and generating an apparent fine grained breccia-sandstone.

7.4.2 Ironstone and andesite lithic-scoria breccia

Stratigraphically below and west of horizon 4 ironstone at Trooper Creek prospect, quartz-hematite forms a matrix to scoria clasts in a small 1 m sized pod in the breccia (95-321).

At Highway East prospect around (7747350mN, 420000mE) andesite scoria breccia that has been pervasively altered to a sericite-hematite assemblage. Strong hematite alteration and cleavage development have made recognition of the original textures and character of the rocks very difficult. Although ironstone is not exposed, the intensity of hematite alteration is similar to that associated with known ironstones at Trooper Creek prospect, and the alteration may be a lateral or vertical equivalent of an unexposed, poorly developed, or infantile ironstones.

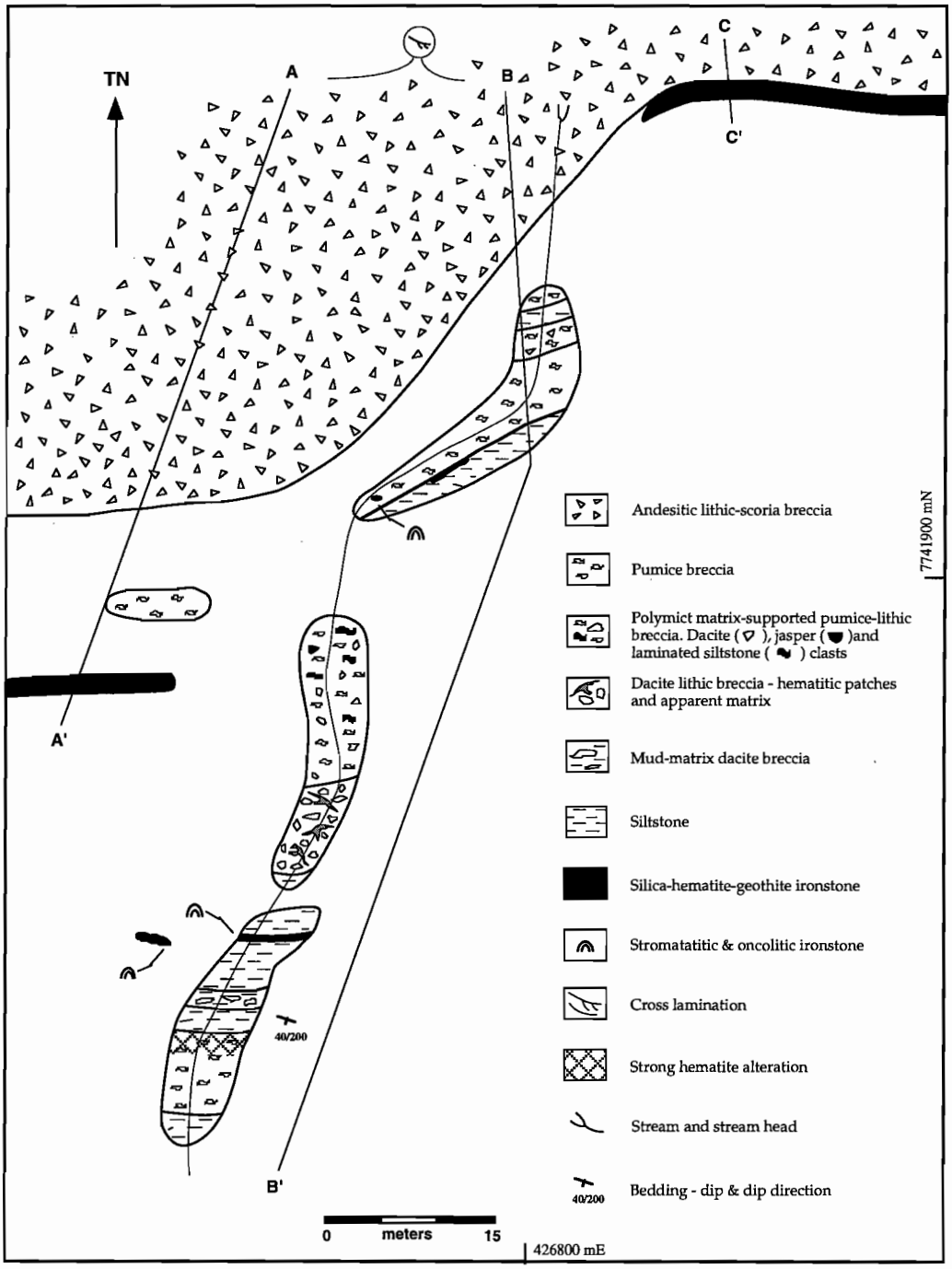

Figure 7.2 — Outcrop map showing the distribution of ironstone lenses and volcanic facies at Trooper Creek prospect in the area around 7741900mN, 426800mE. Section lines (A-C) mark the positions of lithological logs illustrated in figure 7.3.

Figure 7.3: Measured sections presented as graphic logs for major lithologies in the Trooper Creek Formation in the area of the Trooper Creek Prospect. Locations of sections 1A-C are illustrated in Fig 7.2.

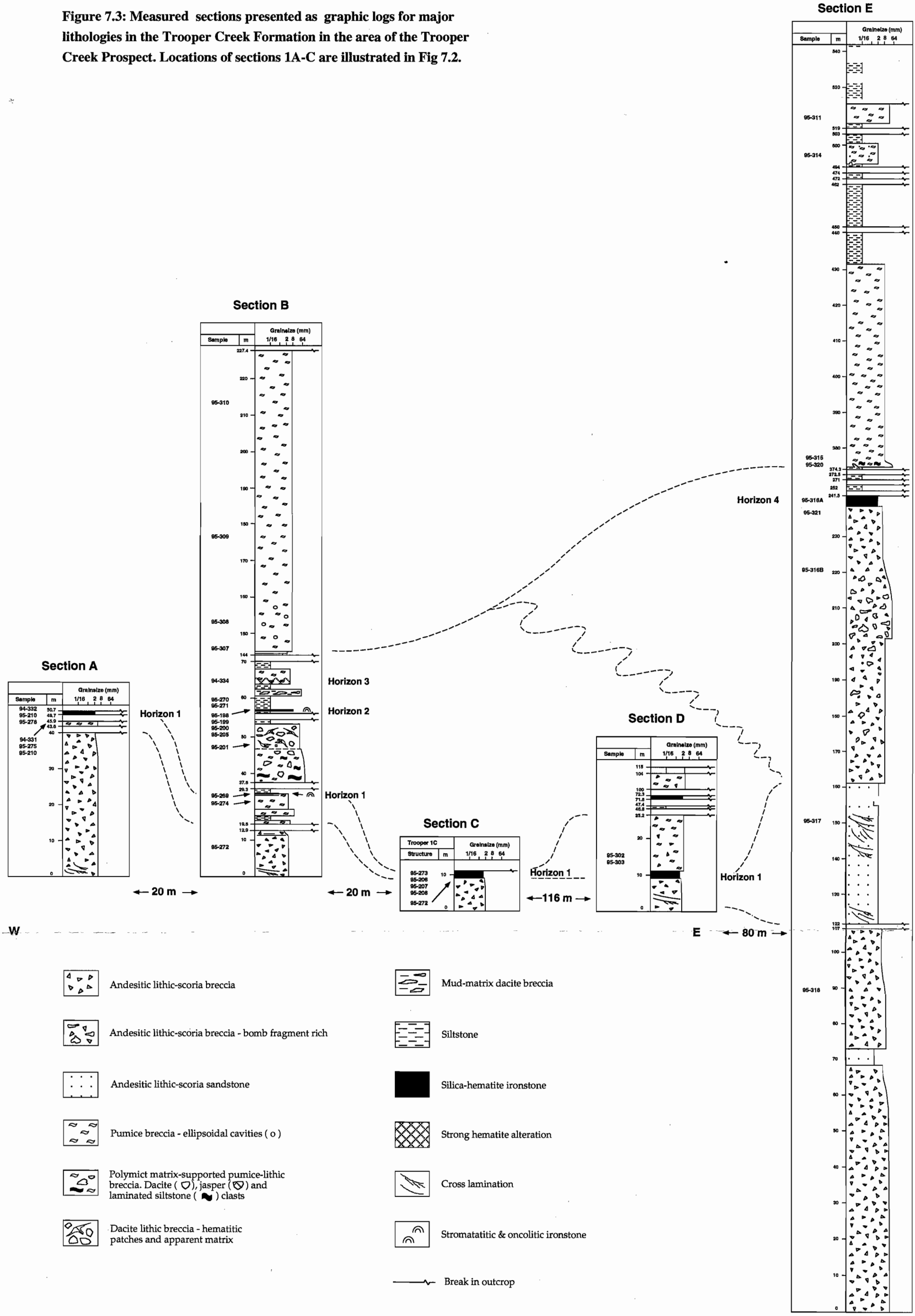

Andesitic lithic-scoria breccia

Andesitic lithic-scoria breccia - bomb fragment rich

Andesitic lithic-scoria sandstone

Pumice breccia - ellipsoidal cavities (o)

Polymict matrix-supported pumice-lithic breccia. Dacite ( ), jasper ( ) and laminated siltstone ( ) clasts

Dacite lithic breccia - hematitic patches and apparent matrix

Mud-matrix dacite breccia

Siltstone

Silica-hematite ironstone

Strong hematite alteration

Cross lamination

Stromatatitic & oncolitic ironstone

Break in outcrop

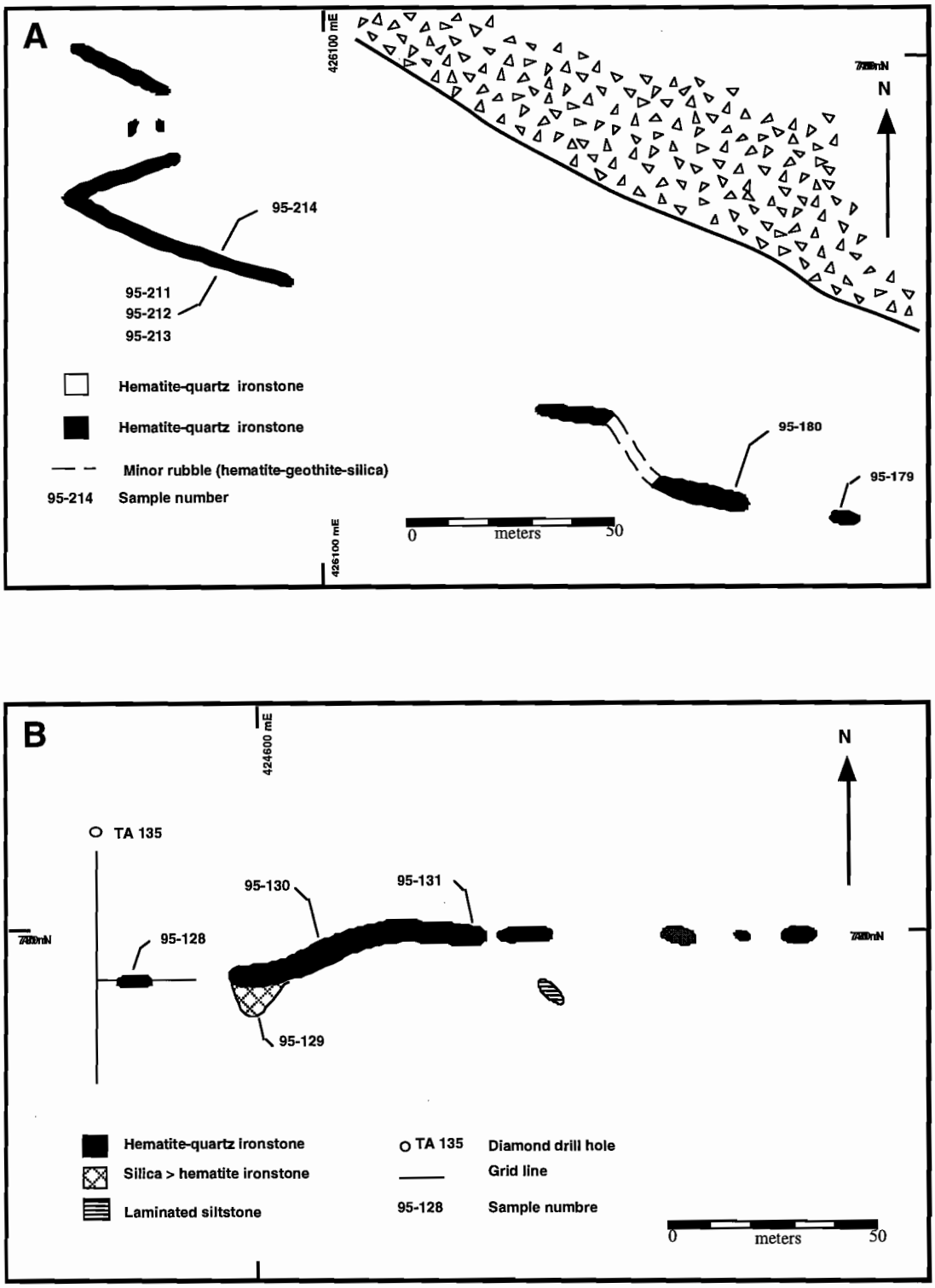

Figure 7.4 — Outcrop map showing the discontinuous nature of ironstone lenses and relationship to volcanic facies. (A) Horizon 1 ironstone (western lenses) in the western part of the Trooper Creek prospect. (B) Ironstone lenses to the west of Trooper Creek around 7743700 mN, 424600 mE (cattle yard).

7.4.3 Ironstone related to coherent, autoclastic and peperitic rhyolite

Occurrences of ironstone northwest of Trooper Creek prospect (AMG 7743700mN, 424600mE) display contact relationships which suggest they are pods enclosed in massive coherent rhyolite. Pods are only a few metres across and have sharp margins. The ironstones have an apparent clast in matrix texture in which equant, irregular and ovoid oncolite-like hematite-rich "grains" are enclosed in a hematite-poor quartz-rich apparent matrix. Parts of the ironstone 2 to 10 cm across are devoid of the apparent clastic texture and are massive quartz-hematite. Rhyolite surrounding the ironstones is purple in colour due to pervasive hematite alteration and contrasts with sericite-chlorite altered rhyolite of the remainder of the body. Quartz-hematite veins cut the rhyolite along contacts with the ironstone. The rhyolite is quartz and feldspar (sanidine, plagioclase) phyric, and consists almost entirely of coalescing radial fibrous spherical spherulites. Partial recrystallisation to interlocking anhedral quartz and feldspar has destroyed some microstructures in many of the spherulites. A mosaic of anhedral quartz and feldspar (possibly after recrystallised micro-spherulites), with subordinate feldspar crystallites occurs between the spherulites. Cuspate areas of very fine grained granular hematite occur between some coalescing spherulites and along the margins of quartz and feldspar grains in the groundmass. The hematite has replaced former remnant glass between spherulites or an earlier alteration mineral of glass.

Field relationships and some drill hole sections in the Handcuff area around (grid 11700N, 10700E) show that some ironstone lenses and flow banded quartz-feldspar porphyry are spatially, and possibly genetically, related. Ironstone lenses are enclosed by thinly planar laminated and massive cherty siltstone at the peperitic margin of the rhyolite. Massive ironstone contrasts with lenses in which quartz-hematite rich bands alternate with cherty siltstone bands (laminae?). The rhyolite is mostly sericite-chlorite and silica altered but along some contacts near ironstone lenses both the rhyolite and siltstone are purple, hematitic and contain fine grained disseminated pyrite. In diamond drill hole HDD 012, small veinlets of quartz-hematite are associated with patchy weak silicic alteration overprinting massive chlorite-sericite-silica altered rhyolite (at 25m down hole) and peperite at contacts with the underlying siltstone (at 99 m).

7.4.4 Iron oxide-silicate assemblages and dacite

At Handcuff prospect, quartz-hematite occurs as veins cutting massive coherent dacite (grid 12100N, 10160E; HDD 007, 402-410 m) and as veins or matrix between clasts in dacite lithic breccia (e.g. HDD 007, 372.5-400 m; HDD 022, 262-275 m). Breccias are unstratified monomictic clast to matrix-supported frameworks of angular blocky fragments. Clast shapes and gradations between brecciated and coherent facies indicate that the breccias are hyaloclastite formed through quench fragmentation at the top of a partly emergent cryptodome. Clasts in the hyaloclastite are mostly altered to sericite and chlorite but some clasts and all of the matrix have been silicified and locally replaced by patchy quartz-hematite.

Peperite is a rock formed through the mixing of magma or lava and wet unconsolidated sediment, and commonly forms along the base of flows and around the margins of syn-sedimentary intrusions. In the top of diamond drill hole REW 803 (31.55-130 m) at Highway-Reward, dacite includes irregular bifurcating seams of siltstone, or is present as jigsaw-fit aggregates of clasts separated by siltstone, and gradational into massive and flow banded coherent facies. Siltstone in the peperite is locally quartz-hematite-rich and seams of quartz-hematite ± carbonate without siltstone dissect the core. A silicic halo up to 4 cm wide surrounds some of the seams suggesting that they are replacements of the dacite and are not sediment which mixed with the dacite during fragmentation. Continuity of flow banding between "clasts" and euhedral feldspar phenocrysts in apparent matrix domains support the interpretation that the silica-hematite-carbonate assemblage postdates fragmentation. Two phase alteration of coherent or weakly brecciated dacite has formed an apparent breccia in which quartz ± hematite ±

carbonate forms an apparent matrix between sericite-chlorite altered apparent clasts.

At Handcuff around (grid 11000N, 10450E), peperite along the top contact of a partly emergent cryptodome provides evidence for mixing of dacite and wet unconsolidated iron oxide-rich siltstone. Jigsaw-fit dacite clasts in the peperite are sericite altered and separated by maroon iron oxide-rich siltstone. Siltstone has penetrated even the finest fractures, and between millimetre sized fragments in the peperite, demonstrating that the iron oxide phase was fixed in the siltstone component during mixing with the dacite and is not a later alteration phase.

7.4.5 Ironstone as lenses in cherty siltstone

Massive and weakly planar laminated cherty siltstone north of the Handcuff prospect around (grid 10200E, 12050N to 10450E, 12350N) includes lenses of ironstone to 30 m in length. Ironstone lenses are enclosed in the siltstone and together define a bedding parallel horizon in the hinge zone of a steeply SSW plunging syncline. Single ironstone lenses are oriented perpendicular to probable bedding. Ironstone lenses are separated by, and subordinate to, finely laminated pale, creamy green siltstone containing diffusely bound patches of iron oxide-silicate from 5 to 20 cm in size. The ironstone lenses are sometimes massive, blood red and contain cubic pits after ?pyrite. More often light grey and green-grey chert bands alternate with, or enclose, iron oxide-rich patches with irregular ragged, round, and ellipsoidal shapes. Patches define thin, discontinuous bedding parallel bands in the chert and some lenses include thin (2-3 mm) semi-continuous iron oxide-silicate-rich bands (? laminae).

At Handcuff prospect around (grid 10500E, 11600N) massive and finely laminated chert includes subordinate thin (2-5 mm), dark red, iron oxide-silicate laminae (Fig. 7.5).

7.4.6 Indeterminate facies relationships

In a limited number of cases relationships between ironstone lenses and volcanic facies are indeterminable due to poor exposure. To the west of Trooper Creek around (7743700mN, 414600mE) a series of massive ironstone lenses crop out discontinuously over a strike length of 175 m (Fig. 7.4B). At Highway East prospect around (7746600mN, 418250mE) ironstone lenses occur near outcrops of rhyolite but contacts are unexposed.

7.5 Ironstone mineralogy and textures

The mineral assemblages associated with massive ironstone and tuffaceous ironstone are different. Petrography combined with X-ray diffraction, show that quartz, hematite and occasionally very fine grained magnetite are the principal components of massive ironstone. In addition to quartz, hematite and magnetite various assemblages of epidote, sericite, chlorite, albite, calcite, sanidine and plagioclase feldspar are present in tuffaceous ironstone and stromatolitic-oncolitic ironstone. The mineral assemblages in tuffaceous ironstone are the lower greenschist grade metamorphosed and foliated equivalent of syn-volcanic assemblages, which by analogy with recent volcanic deposits probably originally comprised combinations of clays, zeolites, micas, feldspars, quartz and carbonate.

Ironstones contain textures which can be subdivided into three main groups: (1) those reflecting a volcanic input or precursor; (2) textures recording biological activity in the depositional environment; (3) non-volcanic and non-biological textures, here defined as hydrothermal textures. Many ironstones are characterised by textures from more than one group, and by different textures from the same group. Textures in ironstones associated with each of the principal volcanic facies can be similar but others are unique to a given facies association or ironstone outcrop. During metamorphism and tectonic deformation earlier mineral assemblages were recrystallised or replaced by coarse metamorphic mineral, destroying or modifying primary (volcanic, biological, hydrothermal) textures.

7.5.1 Volcanic textures

Hydrothermal processes and products accompanying ironstone deposition have modified or destroyed volcanic textures in the ironstones. In most cases the primary mineralogy of the volcanic component has

Figure 7.5
Outcrop and hand specimen photographs of ironstone from the Trooper Creek Formation.

(A) Resistant lens of massive hematite-quartz ironstone from Trooper Creek prospect western lenses (774150 mN, 426100 mE).

(B) Tuffaceous ironstone comprising maroon hematite-rich bands and patches separated by light quartz-rich domains with minor sericite. Trooper Creek prospect western lenses (774150 mN, 426100 mE).

(C) Pervasively hematite altered planar laminated pumice breccia. Planar lamination and mantle bedding suggest the pumice breccia is a water-settled fall deposit. The pumice breccia underlies and is laterally continuous with massive and tuffaceous ironstone a few metres to the west. Trooper Creek prospect (7741900 mN, 426800 mE).

(D) This sample of stromatolitic ironstone comes from horizon 2 at Trooper Creek prospect. At the base of the photograph, in situ stromatolites occur as domed biostromes built upon and intergrown with pervasively hematite-altered and silicified tuffaceous sandstone. The biostrome is overlain by matrix-supported, polymictic breccia. The breccia comprises clasts of stromatolite supported by smaller fragments, pumice, shards, crystal fragments and minor lithic fragments. Hematite and lesser quartz have completely replaced the oncolites and stromatolites, whereas the pumice and shards have altered to quartz, sericite, and minor hematite.

(E) Ironstones which occurs as pods in rhyolite have an apparent clastic texture. Equant, irregular and ovoid hematite-rich "clasts" are surrounded by a hematite-poor, quartz-rich "matrix". Occasional relict spherules suggest that the matrix has formed through recrystallisation of chalcedony spherules. North of Trooper Creek prospect (7743500 mN, 428160 mE).

(F) These four samples are from an altered, quench fragmented rhyolite lava from the hangingwall of the Reward massive sulfide deposit. Weakly brecciated rhyolite comprised angular blocky chlorite-sericite altered fragments separated by small amounts of silicified matrix (core a). The hyaloclastite passes gradationally down into peperite comprising clasts of rhyolite supported in a matrix of pumice shreds (core b,c). Pumice shreds and clasts in the breccia have been silicified, sericitised and hematite altered (core c). Pumice breccia away from the contact (core d) is sericite-quartz altered. (DDH HMO 52, 146-160 m).

(G) This example of peperite occurs at the top of a dacitic cryptodome where it intruded purple hematitic siltstone. Clasts in the breccia are sericite altered, often display jigsaw-fit fabric, and are intimately mixed with the siltstone. Lamination in the siltstone is disrupted and contorted around the contact. Handcuff prospect (grid 11000N, 10450E).

(H) Finely laminated quartz-hematite ironstone. Handcuff prospect (grid 11600N, 10500E).


A


B


C

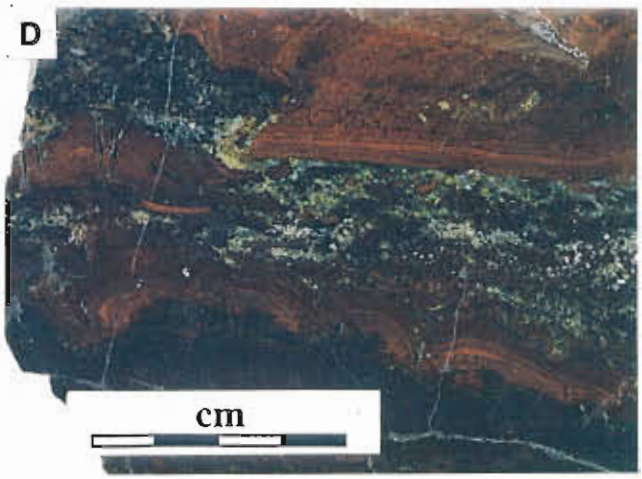
D
cm


E
cm

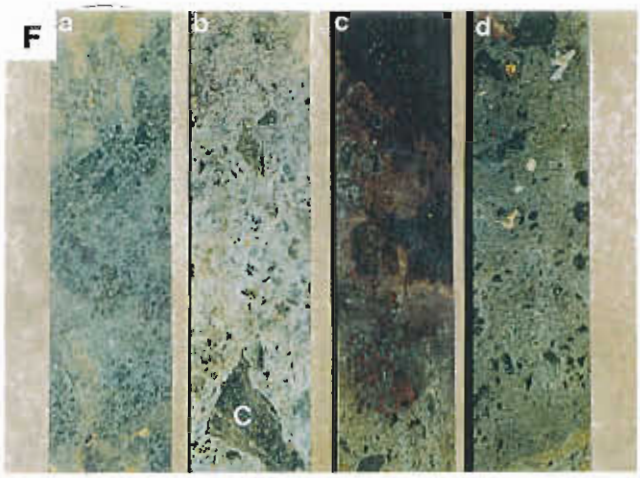
F
a
b
c
d
C


G


H

Table 1: Significant ironstone occurrences in the Trooper Creek Formation between Coronation homestead and Trooper Creek prospect.

Prospect	Locality	Grid reference	Occurrence	Character	Sample number(s)
Trooper Ck eastern lenses	Horizon 1B	7741900 mN, 426800 mE	dacite pumice breccia	massive ironstone	**95-206**, 95-207, 95-208, **95-210**, **95-273**, **95-276**
				tuffaceous ironstone	95-209, **95-275**
				stromatolitic & tuff	95-202, **95-217**
				hematitic pumice bx	**95-274**, 95-203
				andesite breccia	**95-272**
	Horizon 1A		dacite pumice bx	tuffaceous	95-269
	Horizon 2	7741900 mN, 426800 mE	stromatolitic-oncolitic dacite pumice breccia	stromatolitic & tuffaceous	95-198, 95-199, **95-200**, 95-205
	Horizon 3	7741900 mN, 426800 mE	dacite pumice bx	hematite altered pumice breccia	**94-334**
	Horizon 4	7741700 mN, 427000 mE	andesite lithic-scoria breccia	massive lens	**95-316** **95-317B, 95-318**
Trooper Ck western lenses	Loc 527	AMG 7742000 mN, 426100 mE	unexposed, overlies andesite lithic scoria bx	massive ironstone lenses	95-179, 95-180, 95-211, 95-213
				tuffaceous ironstone	**95-212, 95-214, 94-327**
Trooper Ck cattle yard	Loc. 911	AMG 7743700 mN, 424600 mE	unexposed; ? andesitic lithic scoria breccia	massive ironstone lenses	95-128, 95-129, **95-130**, 95-131
Trooper Ck north	Loc. 946	AMG 7743500 mN, 428160 mE	massive rhyolite	massive pods	95-149, **95-150**
Highway East	Loc. 439	7746600 mN, 418250mE	unexposed. Adjacent to rhyolite	massive ironstone	94-197
Highway East	Loc. 544	7747500mN, 419900mE	rhyolite pumice breccia	massive ironstone pod	**94-246**
Highway	REW 803	10150N, 10515E (mine grid)	peperitic dacite	veins & ? matrix	REW 803, 38.77m REW 803, 117m
Handcuff	HDD 012		coherent & peperitic rhyolite	veinlets	
Handcuff	Loc. 69, 72	11710N, 10720E 11640N, 10770E	contact >< rhyolite & chert	sericitic Fe-oxide with	**94-25**
	Loc. 52	11290N, 10660E		disseminated pyrite	**94-18**
Handcuff	HD 007 HDD 022	11571N, 10740E	hyaloclastite & coherent dacite	veins, replacement of matrix in bx	HDD 007, 444.3m
Handcuff	Loc. 150	12090N, 10130E	coherent dacite	veins	94-61
Handcuff	Loc. 98	12310N, 10400E	massive-laminated chert	aligned patches in chert	**94-401**,
Handcuff / Truncheon	Loc. 76	11620N, 10510E	laminated chert	planar laminae in chert	

been lost and replaced by quartz, hematite ± magnetite, sericite, epidote or chlorite. Because the distribution of minerals and the textures produced during replacement are strongly related to the initial textural and permeability patterns of the volcanic component, hydrothermal textures in volcanic components are discussed here.

Pumice and shards: Tube pumice in the ironstones has rough ragged ends and planar smooth margins, characteristic of woody pumice. Most of the glass shards have cuspate and microvesicular pumice shapes, but a few platy shards occur. Hydrothermal and metamorphic minerals have faithfully preserved vesicular pumice textures or else destroyed them completely. In areas of phyllosilicate alteration, pumice and shards have been replaced by mechanically weak sericite (± quartz), and consequently are strongly compacted (e.g. 95-204). Former tube-vesicles in pumice are recorded by thin discontinuous trails of iron oxide granules which prior to compaction lined vesicle walls. In quartz-rich domains, relicts of uncompacted tube-vesicle and round-vesicle pumice and shards are preserved as quartz, and sometimes hematite and sericite, have infilled vesicles and replaced formerly glassy vesicle walls. The pumice shreds, shards and in some cases the ovoid vesicles within them are outlined by fine opaque hematite. Some vesicle fills are zoned with an outer hematite zone passing into quartz and/or sericite zones (e.g 95-203). Hematite has replaced in from the margins of some phyllosilicate (e.g. 95-204) and quartz has altered pumice shreds obscuring the margin of large pumice shreds and completely replacing some small pumice fragments. Thick oxide coatings generate pumice clasts with apparent blocky or prismatic shapes bound by planar to curviplanar surfaces. Some equant oxide patches are replacements of single pumice shreds in which internal vesicular textures are not preserved but cuspate margins, which are in part the former walls of vesicles, are sharp and "unmodified" (e.g. 95-203). Other oxide patches are replacements of pumice- and shard-rich domains with relict vitriclasts replaced by quartz and coated with hematite (e.g. 95-210). Margins of pumice shreds and vesicle walls without oxide coatings are obscured or unidentifiable due to texturally destructive replacement by quartz (e.g. 95-200) or sericite (e.g. 95-203). Many phyllosilicate altered pyroclasts are deformed around competent quartz-hematite altered pumice and feldspar crystals, defining a bedding parallel compaction foliation. Trails of Fe-oxide defining former vesicle walls are more closely spaced in more compacted segments of single shreds or domains.

Crystals and crystal fragments: In tuffaceous ironstone, sanidine and plagioclase feldspar crystal fragments and phenocrysts in pumice shreds are largely unaltered or only weakly altered. Sericite has partially replaced feldspar in a few samples, and rarely (e.g. 95-200) polycrystalline quartz pseudomorphs a tabular mineral which may have been feldspar. Epidote pseudomorphs angular fragments of an unidentifiable former mafic mineral.

7.5.2 Biological textures

Stromatolites and oncolites: Oncolites in the ironstones are elliptical to spherical in shape and vary from 0.5 to 1.5 cm across. The component laminae are arranged around a central nucleus and can be concentric or comprise discontinuous overlapping shells. Laminae are typically very thin (8-15 μm) and are alternately quartz-rich and hematite-rich. Nuclei include single volcanic fragments (principally crystal fragments or pumice), fragments of stromatolite, or smaller oncolites. Stromatolites are characterised by an internal structure of relatively flat laminae and may be columnar or non-columnar. Non-columnar varieties have flat-laminated, undulatory, pseudo-columnar, cumulate or columnar layered forms. Columnar stromatolites have digitate, coalesced and anastomosed branched forms with upright to inclined, uniform, slender to stubby shapes and steeply convex laminae. Laminae in stromatolites are 8-70 μm thick and now comprise alternating dark brown to opaque hematite-rich laminae and lighter quartz-rich laminae with sub-millimetre sized granular hematite. In some thick quartz-rich laminae, thin films of hematite outline relict tube-vesicle pumice and shards. Quartz comprising oncolites and stromatolites is very fine

grained (5-20 μm) but in patches has recrystallised to coarser grains with 120 ° triple junctions. In some samples, medium grained quartz fills cracks which either follow or cut across the constituent laminae.

Evidence for microbes forming the stromatolites and oncolites in the ironstones has largely been destroyed as the laminae are now quartz and hematite. However, branching networks of filaments are preserved in the cores of oncolites and between grains in samples (95-198; 95-200) of stromatolitic and oncolitic tuffaceous breccia. The filaments have cylindrical cross-sections, 5-8 μm in diameter and are 10-200 μm long. Filament walls are outlined by very fine grained hematite and cryptocrystalline quartz fills the remaining space. Similar filaments occur in ironstone without oncolites or stromatolites. These include samples of quartz-hematite veins in dacite (94-61), examples of massive ironstone replacing horizon 1 pumice breccia (95-206, 95-212), and in tuffaceous ironstone (95-214) underlying massive horizon 1 ironstone. Filaments in the different ironstone facies are similar to those described by Duhig et al. (1992) from other parts of the Trooper Creek Formation and interpreted as microaeropilic chemolithotrophic bacteria or fungi.

Other biological structures: Fragments of trilobites are preserved in one sample of stromatolitic and oncolitic breccia. Other microfossils include possible sponge spicules, a single gastropod, and a possible brachiopod (95-200). The fossils are now cryptocrystalline quartz ± hematite and are outlined by very fine grained hematite.

7.5.3 Hydrothermal textures

Spheroidal textures: Spheroidal textures in the ironstones display a variety of forms which are classified on the basis of the relative proportions and distribution of quartz to hematite, as well as internal structure. The eight principal morphologies recognised are defined as types 1-8 and their characteristics are summarised in Table 2 and figure 7.7. Type 1A,B spherules are composed only of quartz or albite, whereas the other spherules types are fine intergrowths of quartz and hematite. Radial fibrous texture in type 2 and 3 spherules reflect variation in the abundance and packing of very fine granules and flecks of hematite intergrown with quartz. Hematite granules and flecks radiate out from the centre of these spherules. Similar radial fibrous textures characterise the core (type 4 spherules), or rim (types 4, 5 &6) of spherules which are zoned. Cores are opaque or near opaque and hematite is more abundant than quartz, whereas rims are quartz-rich and hematite is present as single granules and flecks or these are arranged in trails. Neither the hematite core or thin quartz rim of type 7 spherules are radially fibrous. In some instances (type 8), the cores of spherules are concentrically zoned with alternating quartz-rich and hematite-rich bands, and rims are radially fibrous.

Spherules typically have diameters of 50-200 μm. Isolated spherules are commonly spherical. Adjacent spherules may impinge on each other, producing elongate single or branching trains and coalescing patches. Areas of opaque hematite occur between coalescing spherules and have cuspate shapes. Fan- to sheaf-shaped bundles of radial quartz and hematite fibres occur around the outer margin of some domains of coalescing spherules and project into large cuspate hematite patches, suggesting that the bundles are filling space in the ironstone. Similar bundles of fibres radiate out from a line forming axiolite-like structures in some samples (e.g. 95-179).

Spherulites display progressively stages of recrystallisation. Initially, radial fibrous textures are obscured as the centres of spherules recrystallise to interlocking anhedral quartz and in some cases radial segments of the spherules become coarser grained. Further recrystallisation produces mosaics of interlocking coarse grained anhedral quartz without fibrous textures, or only small segments of a few spherules are preserved.

Botryoidal texture: Botryoidal texture in ironstone comprise alternating concentric dark hematite-rich bands and light hematite-poor, quartz-rich bands. Bands are a few to ten microns wide and are semi-continuous or discontinuous. In some instances, bands nucleate around single tube-pumice shreds (e.g. 95-204), feldspar crystal fragments (e.g. 95-203) or opaque hematite patches with equant

Figure 7.6
Photomicrographs of ironstone textures.

(A) Coalescing type 1 spherules surrounding a cuspate patch of hematite. Fans of fibres (arrow) project out from the margin of spherules into the hematite patch suggesting that both the bundles of fibres and the hematite are space filling. Sample 95-210; Trooper Creek prospect.

(B) Coalescing type 8 spherules with characteristic hematite cores and quartz rims. Cuspate patches of hematite separate some spherules. Sample 95-206; Trooper Creek prospect.

(C) Occasional pumice and shards are preserved in this sample of massive ironstone. The pumice shreds (P) are now quartz and are outlined by hematite. Hematite has completely replaced pumice in some parts of the sample. 95-273; Trooper Creek prospect.

(D) In this sample of massive ironstone, patches of spherules (S) and hematite are separated by an apparent matrix of fine grained recrystallised quartz (R). Occasional relict domains of spherules are identifiable in some parts of the apparent matrix. Sample 95-210; Trooper Creek prospect.

(E) Pumice and shards in this sample are now fine grained quartz and are outlined by hematite. The pyroclasts have compacted and deformed around a large quartz nodule which grew within the pumice breccia during replacement by quartz and hematite. Sample 95-212; Trooper Creek prospect.

(F) Botryoidal texture in tuffaceous ironstone. Alternating concentric quartz and hematite laminae nucleate out from a hematite core. The remainder of the photomicrograph comprises hematite patches separated by finely crystalline quartz. Sample 95-275; Trooper Creek prospect.

(G) Thin sections of pumice breccia associated with ironstone reveal abundant uncompacted pumice shreds. The pumice grains and ovoid vesicles (v) within them are outlined by hematite. The vesicles and formerly glassy walls are now sericite. Apart from pumice shreds, the pumice breccia contains hematite patches. Sample 95-204; Trooper Creek prospect.

(H) This sample comes from a ironstone pod in rhyolite. Relict coalescing spherules separated by cuspate hematite patches are preserved. Many spherule domains have recrystallised to fine grained quartz. Sample 95-150, north of Trooper Creek prospect.

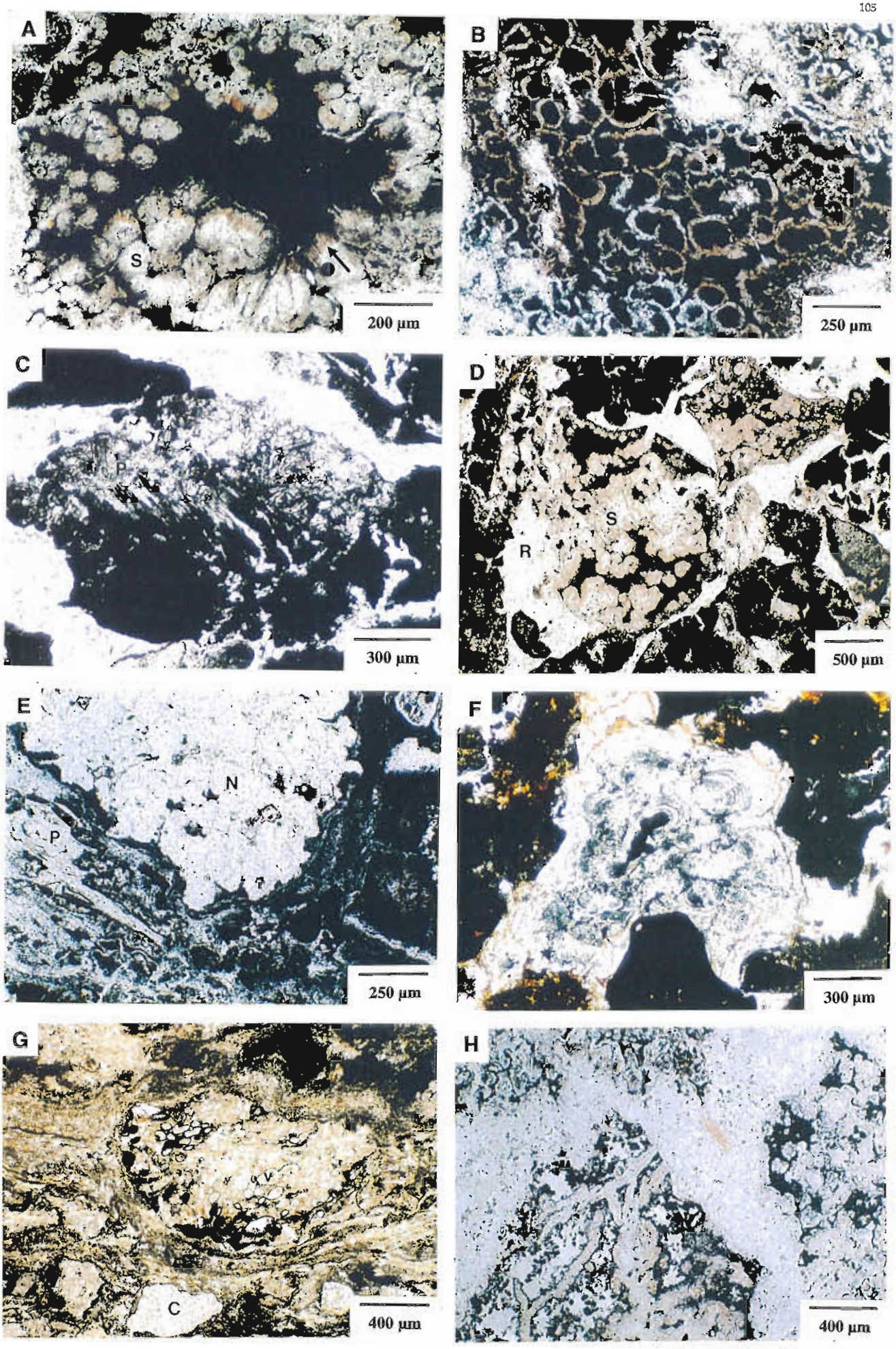
A
S
200 µm
B
250 µm
C
P
300 µm
D
S
R
500 µm
E
N
P
250 µm
F
300 µm
G
C
400 µm
H
400 µm

blocky or bulbous shapes. Groups of equant opaque patches separated by finely crystalline quartz display jigsaw-fit texture and form the nucleus to other botryoidal structures. Botryoidal structures have a simple round concentric banded texture or have bulbous colloform-like arrangements of bands.

Iron oxide patches and granules: Hematite is mostly present as equant blocky to irregular patches surrounded by quartz. Wedge-shaped quartz-filled fractures extend in from margins of patches and are similar to cracks described in cherts and attributed to internal volume loss via the syneresis or dewatering of silica gel (Schubel and Simonson, 1990). Single Fe-oxide patches contrast with those which form jigsaw-fit aggregates separated by quartz and others which have elongate ragged shapes and are connected along mutual boundaries by thin stems. Magnetite occurs as small acicular crystals, 5 μm long (e.g. 95-316) in a few hematite patches. Some iron oxide patches are replacements of blocky pumice shreds in which internal vesicular textures are destroyed but margins, which are in part the former walls of vesicles, are partly preserved. Most iron oxide patches are not replacements of single pyroclasts, and what is controlling their distribution is not obvious. Cuspate Fe-iron-oxide patches in spherule domains are clearly space filling or replacing a precursor space filling mineral phase(s).

Occasional chloritic patches in ironstone contain small (5 μm) round hematite "globules" (e.g. 95-273). In detail, the globules comprise smaller aggregates of very fine grained "granular" hematite. Granular hematite is also present as a fine dissemination in many quartz or hematite dominated mosaics between pyroclasts, within hematite patches, and as hematite bands in botryoidal structures. Hematite outlining the margins and vesicles of pyroclasts is also granular.

Quartz: Quartz is the principal component of the ironstones and displays a range of different morphologies (Kneller et al., 1968; Duhig et al., 1992). The following quartz polymorphs are adopted from Duhig et al. (1992). Megaquartz is clear, equant to tabular, and greater than 200 μm across. Chalcedony is optically fibrous quartz which forms radial fibres, mostly around 100 μm long, in spherules or fan- to sheaf-shaped bundles. Microcrystalline quartz is equant, 1 to 100 μm across and displays undulatory extinction and pinpoint birefringence. Cryptocrystalline quartz appears isotropic under cross polars, and is less than 1 μm in grain size. Microcrystalline quartz and cryptocrystalline quartz often are yellowy brown to pink in colour, possibly due to a very fine dusting of iron oxide, and is sometimes difficult to distinguish from albite using optical microscopy.

7.6 Ironstone textures and volcano-sedimentary facies

7.6.1 Ironstone, tuffaceous ironstone and pumice breccia

Cross-sectional profiles through ironstone associated with dacite pumice breccia show that ironstone textures vary passing from massive hard quartz-hematite ironstone, through pyroclast-rich ironstone, down into hematite altered pumice breccia with iron oxide-silica spots. In massive ironstone, clear fine to coarsely crystalline quartz has replaced formerly glassy pumice and shards in much of the rock, thereby forming a continuous matrix domain. Only locally are delicate volcanic textures preserved (95-273). Microcrystalline quartz replacing pyroclasts and forming the "matrix" domain shows patchy texturally destructive recrystallisation to coarse grained megaquartz. Quartz separates small irregular patchy domains of coalescing type 2 and occasional type 6 spherules, equant to cuspate patches of iron oxide, and rare botryoidal structures. The result in hand specimen is a finely granular texture. In samples of horizon 1 ironstone from Trooper Creek prospect, relict patches of calcite cement occur between patches of hematite, spherules, and calcite with fine granular hematite. Very fine light and dark bands in the calcite conform to contacts with the patches. Elemental maps from microprobe analysis show that zoning in the calcite is due to thin trails of very fine grained (1-2 μm) anhedral quartz (Fig. 7.6). Recrystallisation to clear quartz-free calcite along the margins of patches destroys original textures in the earlier calcite generation.

Table 2: Distinguishing characteristics of the eight spherule types recognised in ironstone in the study area.

Spheroid texture	Size	Core	Rim
Type 1A		Core & rim absent. Radially fibrous quartz or albite crystals nucleate out from centre.	
Type 1B	50-60 μm	Core & rim absent. Finely crystalline quartz spherules.	
Type 2	70-80 μm	Absent. Sometimes "core" is quartz dominant.	Increasing density of radially distributed hematite flecks & granules towards Fe-oxide poor margin.
Type 3	50 μm	Granules of hematite form ring in from margin.	Trails of hematite extend in from jagged spherule margin.
Type 4	100 μm ?	Radially fibrous hematite flecks & granules. As wide as rim.	Clear quartz rim with minor hematite granules.
Type 5A	50-60 μm	Opaque hematite nucleus smaller than rim.	Radial arrangement of quartz and hematite flecks and granules.
Type 5B	50-60 μm	Opaque hematite nucleus. Smaller than rim.	Radial arrangement of hematite flecks & granules between nucleus & thin clear quartz rind.
Type 6		Black isotropic nucleus. Thicker than rim.	Radial extinction of component anhedral quartz crystals.
Type 7	100-250 μm	Spherical, ellipsoidal to cuspate. Granular hematite ± minor quartz. Larger than rim (to 200 μm)	Clear crystalline quartz with weak hematite dissemination.
Type 8	50-100 μm	Concentrically arranged hematite-poor and radially fibrous Fe-oxide-rich bands. Smaller than rim.	Quartz dominant with radially arranged Fe-oxide flecks & granules.

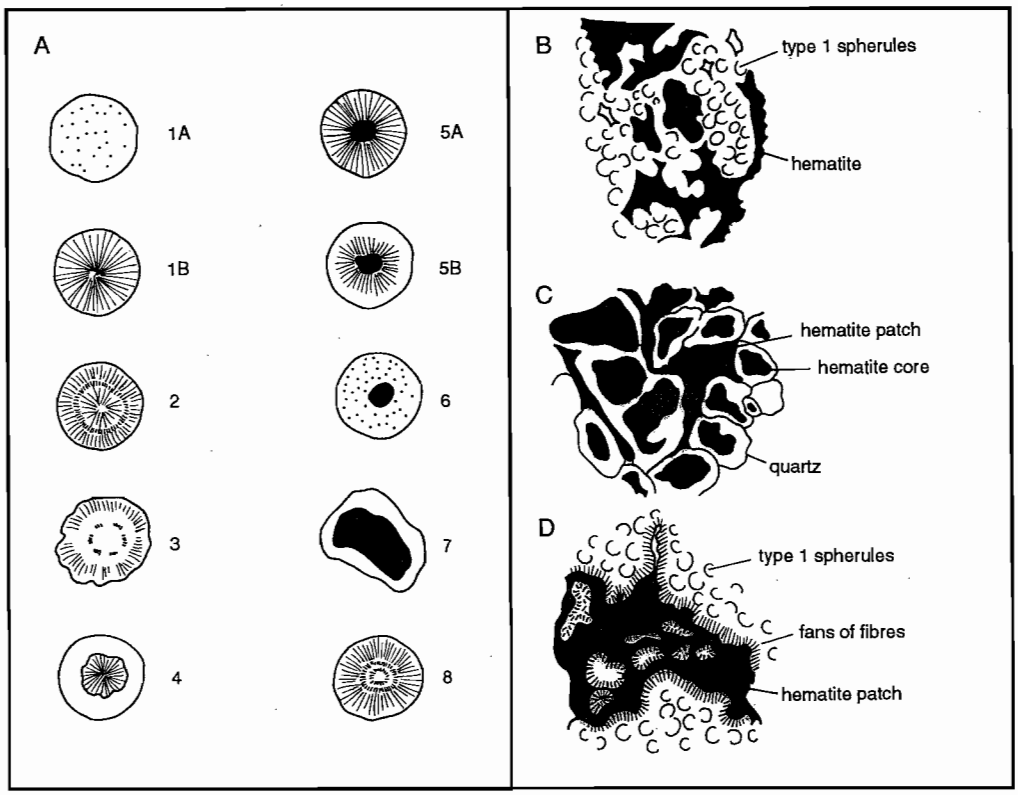

Figure 7.7
(A) Different spherule types (1-8) identified in ironstone. (B) Coalescing, variably recrystallised type 1 spherules separated by space filling patches of hematite. (C) Coalescing type 8 spherules. (C) Fans of quartz-hematite fibres projecting out from the margins of type 1 spherules into a cuspate patch of space filling hematite.

Massive ironstone with only very rare pumice or crystal fragments (e.g. 95-179, 95-180) has a different texture. Patchy domains of spherules (type 1B, 5B, 6, 7 or 8), some separated by cuspate opaque patches, dominate these samples. The role of each spherule type as enclosing or enclosed by the other varies. Many spherule patches are separated by clear or yellow (? fine oxide dissemination) coloured quartz which is a recrystallisation of types 2 spherules. Axiolite-like bundles of quartz and hematite fibres separated by finely crystalline (5 μm) clear quartz form complex networks in some patches of a few samples (95-179). Samples of horizon 4 ironstone from Trooper Creek prospect are dominated by patches of types 1A and 3B spherules but include remnant patches of tube pumice and shards. Recrystallisation of the spherules to interlocking medium grained (25 μm) or coarse grained (400 μm) quartz has destroyed microstructures in many spherules, forming large textureless patches. Pyroclasts are now composed of medium grained (35 μm) anhedral quartz and occasional small type 1A spherules (e.g. 95-316). Pumice, shards, and vesicles, are outlined by fine grained granular hematite. Quartz and fine granular hematite fills the space between the pyroclasts. Spherules at the margins of these domains cut across pumice, shards and the vesicles within them. Relict segments of shards occur in the space between coalescing spherules.

In pyroclast-rich tuffaceous ironstone (95-212, 95-214), pumice is poorly preserved in quartz-rich patches and bands but is distinct where thin oxide films coat or partially replace pyroclast margins and vesicle walls. Compaction of pumice and shards around coarsely crystalline (25 um) quartz nodules with fine bulbous margins suggests that the nodules formed early prior to diagenetic compaction. Coalescing type 2 spherules occur as patches in quartz dominant bands/patches which were possibly formerly pyroclast rich. Discrete and interconnected iron oxide patches separated by finely crystalline quartz are the dominant component of iron oxide-rich bands in the ironstone. Only rarely are botryoidal or filamentous structures present. One sample (e.g. 95-214), contains branching networks of iron oxide filaments around 200 μm long. Fibres extend out from the margins of iron oxide patches or are enclosed by clear quartz. Isolated single iron oxide globules at the ends of fibres may be cross-sections through filaments.

Pumice breccia beneath tuffaceous ironstone contains small iron oxide patches and nodules ranging from 400 μm to 5 mm across. Some oxide patches have bulbous margins and are massive with opaque cores and thin more quartz-rich margins containing a fine dissemination of iron oxide. A few nucleate around partially sericitised feldspar crystals and sericite altered tube pumice. Nodules are large (2-5 mm) and comprise a fine grained mosaic of hematite and quartz. Sericitised tube pumice in the breccia is deformed around the more competent nodules, silica-sericite altered uncompacted pumice shreds, and feldspar crystals.

7.6.2 Stromatolitic-oncolitic ironstone

Stromatolites and oncolites in ironstones are red in handspecimen as they are replaced by massive opaque hematite or comprise alternating hematite-rich and quartz-rich laminae. Finely crystalline quartz and subordinate disseminated granular hematite has replaced pumice and shards trapped and bound between stromatolites and forming the matrix between clasts and oncolites. Relics of uncompacted tube- and round-vesicle pumice outlined by thin hematite films are present in parts of some samples but recrystallisation to medium grained (20-50 μm) anhedral quartz has destroyed many primary textures. Hematite films defining pumice margins are mostly preserved even where recrystallisation has destroyed all internal vesicular textures in the shreds. Opaque hematite has replaced in from the margins of some pumice shreds and completely replaced other pumices, forming equant opaque hematite patches. Other hematite patches have irregular shapes and are an alteration of fine grained pumice and ash. Fine grained quartz patches without volcanic textures sometimes enclose hematite-rich botryoidal structures. Clasts of tuffaceous siltstone in the breccias are now fine grained mosaics of quartz and granular hematite without vitriclastic texture

and some have opaque hematite-rich margins. Feldspar crystal fragments are mostly unaltered but a few are pseudomorphed by polycrystalline quartz. Epidote replaces fragments of a former mafic mineral (olivine ?). In the tuffaceous sandstone matrix of sample 95-218, polycrystalline quartz pseudomorphs rare lozenge-shaped gypsum crystals. Spherule texures are absent in stromatolitic ironstone.

7.6.3 Iron oxide pods in andesitic lithic-scoria breccia

Horizon 3 ironstone at Trooper Creek is underlain by andesite scoria breccia which includes a small pod of hematite-matrix-rich breccia. Hematite occurs between clasts as fine grained granules intergrown with minor quartz, as small patches within clasts, and as thin films outlining margins and vesicle walls of other clasts. Spherules, botryoidal structures and filaments are absent.

7.6.4 Ironstone pods in rhyolite

Ironstone pods in rhyolite have a clast in matrix texture in which hematite-rich "grains" are separated by a clear quartz apparent matrix. Coalescing spherules (types 2A, 6 or 8) separated by cuspate patches of opaque hematite are the principal component of most "grains". Some patches are zoned with a marginal zone of coalescing spherical and fan- to sheaf-shaped spherules enclosing a hematite-rich core with single spherules or branching trains of spherules. The remaining grains comprise equant jigsaw-fit groups of opaque hematite patches separated by quartz, or spongy intergrowths of hematite and quartz. The areas between oxide-rich patches locally show remnant spherule textures and clear quartz partially replaces many spherules at the margins of some patches and has completely replaced all spherules in other patches. In these patches, bulbous margins along contacts with hematite, or remnant cuspate patches of opaque hematite, are the only indication that the quartz-rich "matrix" originally consisted of spherules. The areas between patches comprises fine grained (25 μm) clear quartz which has locally recrystallised to coarse grained (300 μm) megaquartz.

7.6.5 Quartz-hematite ± carbonate veins in dacite

Textures in carbonate-hematite-quartz (e.g. REW 803, 117.2 m) and quartz-hematite (94-61) veins are different. In the former, hematite occurs as thin rinds (20 μm) around coarse grained polycrystalline quartz patches (150-300 μm across) with blocky shapes bound by curviplanar or irregular margins. Single and groups of quartz patches are separated by carbonate with abundant isolated hematite pseudomorphs of euhedral apatite (50 μm across). In a few cases, only small segments or the margins of albite crystals have been altered. Along vein margins, subrounded hematite patches comprising smaller coalescing spherical hematite globules are intergrown with carbonate or occur in quartz.

In quartz-hematite veins, hematite occurs as opaque patches with bulbous margins or as fan- and sheaf-shaped bundles of fibres which may be isolated in quartz, radially arranged around a opaque hematite nucleus, or radiate from elongate ellipsoidal hematite patches. Hematite fibres, patches and radial spherule-like structures cut across boundaries between interlocking anhedral quartz crystals. Quartz is 20-200 μm across and weakly peppered with fine grained hematite. Occasional filamentous structures are preserved.

7.6.6 Ironstone in chert

Many ironstone lenses in chert comprise patchy domains of finely crystalline quartz and hematite separated by larger domains of coarsely crystalline quartz (e.g. 94-401). In iron oxide-rich patches, quartz is outlined by thin trails of very fine grained (2.5 μm) granules of hematite which locally coalesce forming small (40-100 μm) opaque patches. Quartz in the chert occurs as interlocking crystals with 120° triple point junctions which suggest strong recrystallisation by metamorphism. Massive hematite-rich ironstone lenses have a similar texture but is sometimes diffusely banded (e.g. 94-18). Dark red and near opaque bands comprise euhedral and fine grained (5 μm) granular hematite intergrown with subordinate fine grained quartz. Light coloured bands are more quartz-rich and enclose small patches of coarsely recrystallised (100 μm) quartz.

7.7 Ironstone geochemistry

Detailed definition of the volcanic facies and the mineralogical and textural characteristics of ironstones provide a framework for geochemical studies using whole rock major, minor, trace and rare earth element (REE) analyses. Major and trace element analyses were determined by standard X-ray fluorescence techniques on fused disks and pressed pellets, respectively (Norrish and Hutton, 1969; Norrish and Chappell, 1977). Ag and REE were determined by ICP-MS at ANALABS facilities in Perth.

7.7.1 Major and trace element geochemistry

Ironstone samples from the Trooper Creek Formation are principally composed of silica and Fe_2O_3. All other oxides constitute less than 1 wt% with the exception of Al_2O_3 which is high in some samples of massive, tuffaceous and stromatolitic ironstone. Single samples of tuffaceous ironstone from Trooper Creek prospect contain elevated K_2O (94-327) or MgO (95-275). The transition from massive ironstone into tuffaceous and stromatolitic ironstone is generally marked by a systematic decrease in SiO_2 and Fe_2O_3 (Fig. 7.8A). Ratios of $SiO2/Fe_2O_3$ are generally higher in massive ironstone, decrease passing into tuffaceous and stromatolitic ironstone, but increase again in hematite altered dacite pumice breccia (95-274) and the unaltered equivalent (95-308). Increasing concentrations of TiO_2, P_2O_5 and Al_2O_3 characterise the transition from massive ironstone into the least altered equivalent (Fig. 7.8B,C). Ti/Zr ratios for ironstone associated with pumice breccia at Trooper Creek prospect range between 16-40 but are mostly between 18-20, similar to the least altered pumice breccia (95-308). Variation in ratios between samples may reflect initial compositional differences in the volcaniclastic precursor. Ironstone enclosed in rhyolite (95-150) has a very low Ti/Zr ratio, suggesting that provided Ti/Zr have remained immobile, the ironstones contain little volcanic material.

Major element patterns for ironstone associated with pumice breccia, chert and rhyolite are similar (Fig. 7.9A). TiO_2 is low in ironstone associated with rhyolite and massive ironstone associated with pumice breccia contains elevated MgO. Trace element abundances vary between ironstone facies. Concen trations of Ba are higher in ironstone associated with chert than ironstone from other facies associations. Cu, Pb and Zn vary considerably between ironstone facies. One sample of ironstone associated with chert (95-401) contains high concentrations of Cu, Pb and Zn however, high values also occur in hematite altered pumice breccia in the immediate footwall of horizon 1 ironstone (95-274) and from horizon 3 (94-334). V, Cr and Ni show a covariance with Fe (Fig. 7.10A-C). The highest values (V 1.3 wt%; Cr 26 ppm; Ni 18 ppm) occur in hematite altered pumice breccia (94-334). Fe shows a negative correlation with Mn and both Fe and Mn show a covariance with Ni (Fig. 7.10D). Sc, Sb, Bi and Ag are consistently low and mostly below detection limits.

Compared with ironstones from the ore horizon and Trooper Creek Formation at Thalanga, ironstones associated with pumice breccia at Trooper Creek prospect are enriched in MgO and K_2O and depleted in Na_2O (Fig. 7.9B). Ironstone associated with rhyolite is enriched in CaO and depleted Na_2O and K_2O compared with ironstones at Thalanga. Ironstone associate with chert contains less Na_2O than ironstone at Thalanga. Major element patterns of massive ironstone associated with dacite pumice breccia at Trooper Creek prospect are similar to those of chemical layers in ironstone associated with the Kuroko and Noranda massive sulfide deposits (Fig. 7.11A, B). Variation in the concentration of MgO, CaO, Na_2O, K_2O and P_2O_5 in tuffaceous ironstone from the different districts suggests differences in the original chemical composition of the volcanic component in the ironstones. The major element pattern of Trooper Creek prospect ironstone is distinct from those of modern seafloor deposits (Fig. 7.11C).

Adachi et al. (1986) demonstrated that compared to non-hydrothermal cherts, hydrothermal cherts are characterised by a low ratio of Al/(Al+Fe+Mn). All ironstones analysed from the Trooper Creek Formation plot within the hydrothermal field defined on a Fe-Al-Mn plot by Adachi et al. (1986) (Fig. 7.12).

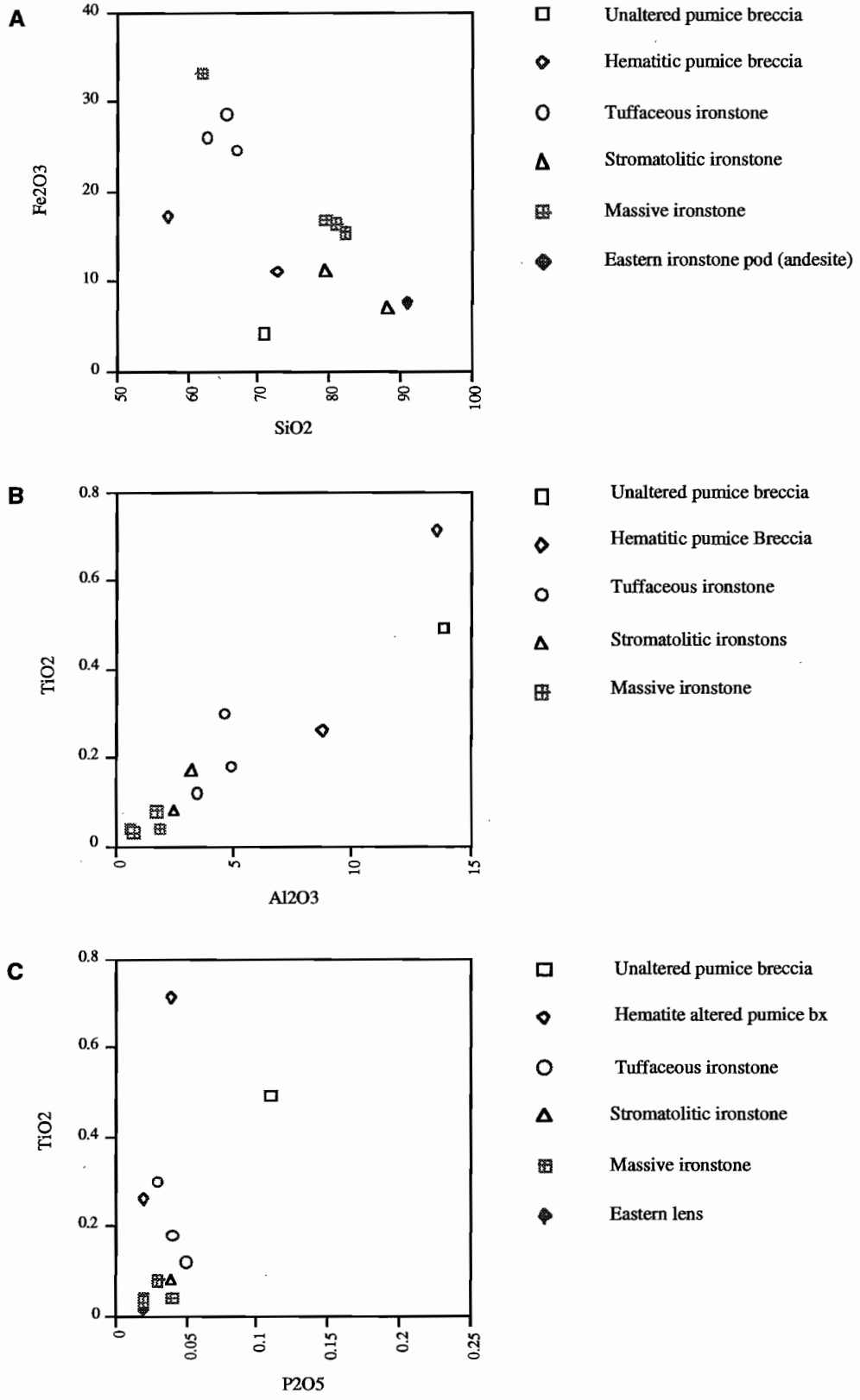

Figure 7.8 — Major element plots for ironstone associated with pumice breccia at Trooper Creek prospect. Elemental concentrations vary systematically passing from hematite altered pumice breccia, through tuffaceous ironstone, into massive ironstone. (A) Fe2O3 vs. SiO2; (B) TiO2 vs. Al2O3; (C) TiO2 vs. P2O5.

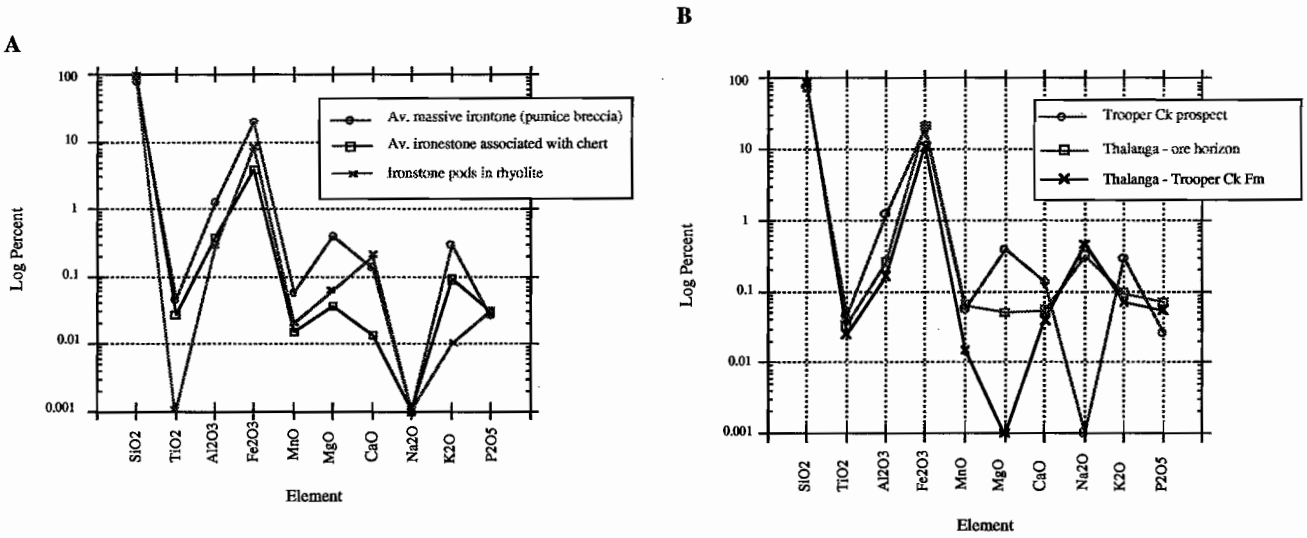

Figure 7.9 — Major element concentrations. (A) Comparison of ironstone associated with dacite pumice breccia at Trooper Creek Prospect, ironstone associated with chert from Handcuff, and ironstone enclosed in rhyolite from Trooper Creek North; (B) Elemental patterns for the average composition of massive ironstone at Thalanga and associated with pumice breccia at Trooper Creek prospect.

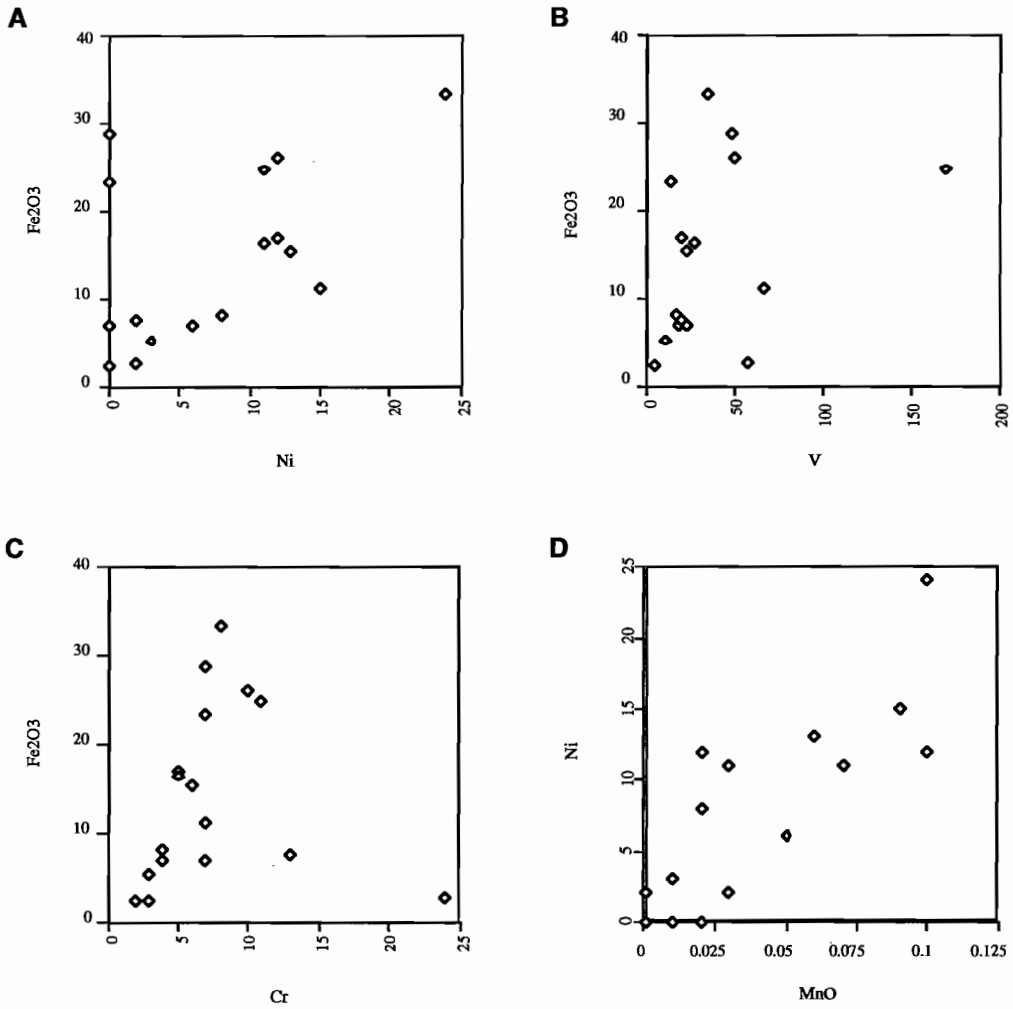

Figure 7.10 — Selected trace element vs. major element plots for ironstones from the Trooper Creek Formation in the area between Coronation homestead and Trooper Creek prospect. (A) Fe2O3 vs. Ni; (B) Fe2O3 vs. V; (C) Fe2O3 vs Cr; (D) Ni vs MnO.

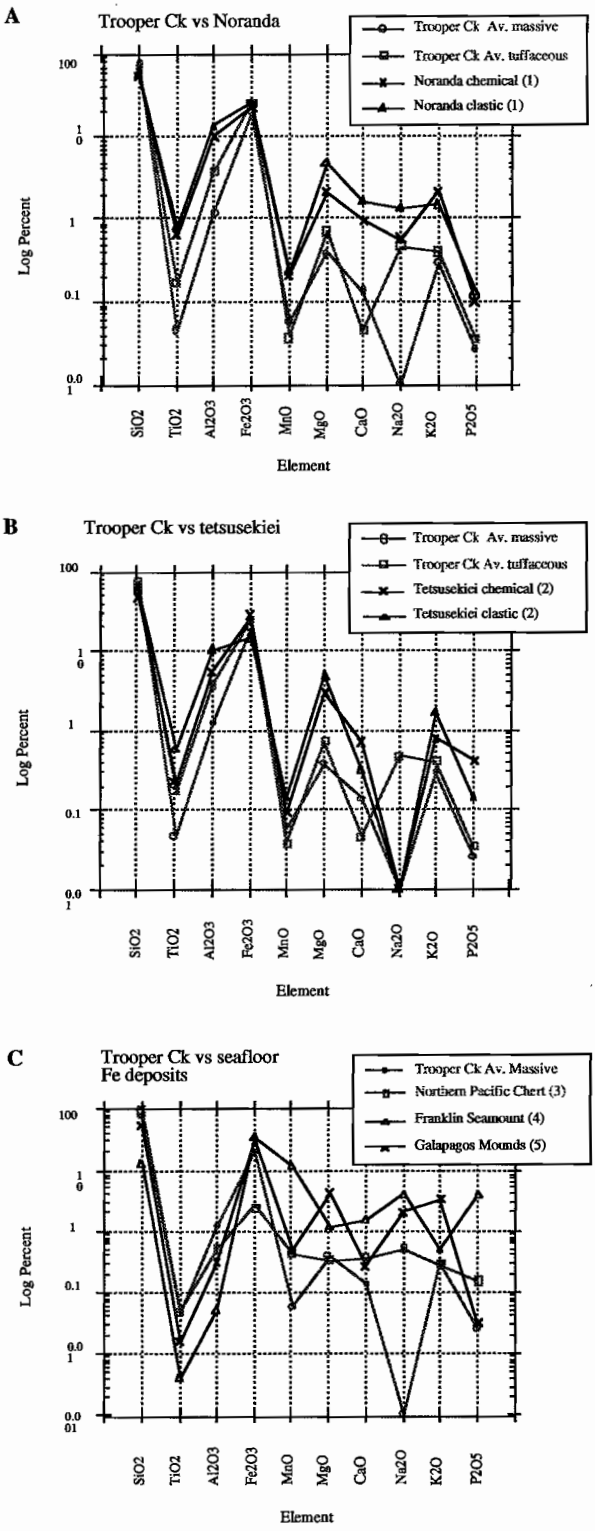

Figure 7.11 — Major element concentrations of ironstone associated with dacite pumice breccia at Trooper Creek Prospect and (A) Noranda chemical and clastic layers; (B) Tetsusekiei clastic and chemical layers; (C) modern seafloor deposits. Data from (1) Kalaogeropoulos and Scott, 1989; (2) Kalogeropoulos and Scott, 1983; (3) Adachi et al., 1986; (4) Binns et al., 1993; (5) Barrett et al., 1988.

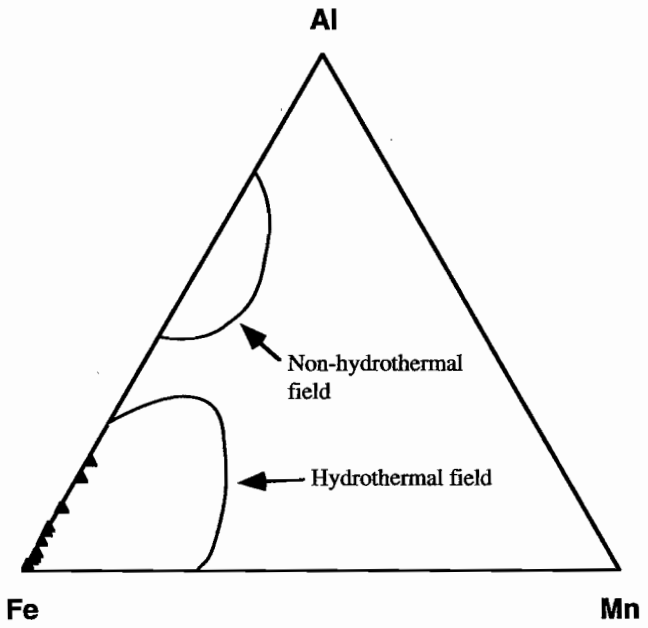

Figure 7.12 — Al-Fe-Mn plot for ironstones from the Trooper Creek Formation in the study area. Samples (n=14) plot in the hydrothermal field for Fe-Mn-Si oxides defined by Adachi et al. (1986).

7.7.2 Isocon analysis

Bulk chemical compositions of tuffaceous ironstone at Trooper Creek prospect cannot be equated with the composition of their precursor volcaniclastics, because of major addition and/or depletion of Si, Fe, and other elements. To determine the overall chemical changes with increasing alteration, a least altered dacite pumice breccia (95-308) from the stratigraphic section was compared with the average of each of its altered equivalents. The isocon method (Grant, 1986; Huston, 1988, 1993) provides a graphical method to determine compositional changes during alteration. In these calculations elements are ordered so that those usually considered immobile are evenly dispersed, and each element is assigned an integer (ni) in ascending order (e.g. SiO2 =1, Fe2O3=2). The scaled concentration of a particular element ($C^s i$) can be calculated from:

$$C^s i = ni * C^A i / C^o i \qquad (1)$$

where $C^A i$ is the concentration of element in the altered rock for the corresponding integer value ni, and $C^o i$ = the concentration of element in the unaltered equivalent for the corresponding integer value ni. The scaled values are plotted on the Y-axis against the corresponding integer, which for ease of interpretation is replaced by the corresponding element symbol.

Once plotted the isocon can be determined by fitting a line through the immobile elements (Al, Ti, Zr, Nb and Y) and the isocon slope (m) calculated. The net mass change (ΔM^A) relative to the "unaltered" equivalent can be calculated using:

$$\Delta M^A\ (\%) = 100\ (1/m-1) \qquad (2)$$

Relative mass changes for each element can be estimated from the isocon. Elements that gained mass through alteration plot above the isocon, and those that lost mass plot below the isocon. The relative mass change for particular elements can be calculated by the relationship:

$$\Delta C^A i\ (\%) = 100\ [CAi/(mCUi)-1] \qquad (3)$$

where $\Delta C^A i$ (%) is the relative mass change for the element corresponding to the integer ni.

The absolute mass change has not been calculated because the present density of the least altered equivalent is different to that when it was unaltered, uncompacted, and glassy. The interpretation of the isocon has several limitations (Huston 1988, 1993): (1) relative gains and losses are calculated using a least altered equivalent which was sourced from a different eruption than that hosting the ironstone, and so may have a different chemistry; (2) the altered and unaltered rock types are resedimented pyroclastic deposits and so will have internal variations in chemical composition unrelated to alteration; (3) the original composition of the precursor pumice breccia has been strongly modified during alteration and compaction. The significance of the former is probably limited as the altered samples and least altered equivalent have similar immobile element concentration and the Ti/Zr ratios. The average of multiple samples has been used in calculations where possible to limit the effect of the second limiting factor (e.g. Huston 1988, 1993).

The relative gains and losses in the transition from massive ironstone (95-210, 95-276) through tuffaceous ironstone (95-275), into hematitic pumice breccia (95-274) have been calculated for horizon 1 (Fig. 2,3 — section A,B). Massive ironstone displays substantial enrichment in Si, Fe, Cr, Cu, Pb and Mn relative to the least altered equivalent (Fig. 7.13A). Zn, Mg, Ca, P and Ba are also enriched but less so. Sr, Rb, Na and K show minor depletion while the immobile elements vary little from the least altered equivalent. Tuffaceous ironstone displays similar elemental trends to massive ironstone however, the relative gains in Si, Cr, Cu, Pb and Mn are less substantial (Fig. 7.13B). Tuffaceous ironstone is enriched in Mg compared to massive ironstone. Sr, Rb, Ca and K are depleted relative to the least altered equivalent but have similar concentrations to samples of massive ironstone. Hematite altered pumice breccia is enriched in Fe, Zn and Pb but much less so than overlying ironstone facies (Fig. 7.14A). Cu and Ba are also depleted relative to the least altered equiva-

lent. The net mass changes (ΔM^A) relative to the unaltered equivalent is 1044.2 % for massive ironstone, 199 % for tuffaceous ironstone, and -15 % for hematite altered pumice breccia.

Results from section B are compared with stromatolitic ironstone from horizon 2 (Fig. 2, 3 — section B; 95-200) tuffaceous ironstone exposed in lenses to the west (95-212, 95-214, 95-327) and to horizon 4 massive ironstone to the east (Fig. 2,3 — section E; 95-316). Samples of stromatolitic ironstone are less enriched in those elements which have been added to massive- and tuffaceous-ironstone during alteration (Fig. 7.14B). In contrast to massive- and tuffaceous ironstone Zn and Mg are depleted in stromatolitic ironstone, in addition to Rb, Na and K. The net mass change during alteration of stromatolitic tuffaceous ironstone is equal to a 270 % addition. Because stromatolitic ironstone varied in mineralogy from the unaltered equivalent prior to alteration direct comparison of results is not possible. Massive ironstone from horizon 4 has similar trends of elemental enrichment when compared with massive ironstone from section B (Fig. 7.15A) but is enriched in Mn and depleted in Nb and Zn relative to both the least altered equivalent and massive ironstone from section B. A net mass gain of 5570 % is indicated. Tuffaceous ironstone cropping out to the west of section B has similar patterns of enrichment and depletion compared with tuffaceous ironstone. However, the western lenses are less enriched in Cu and Pb and depleted in Zn, Mn and Mg compared to the equivalent further to the east (7.15B).

Interpretation

The low concentration of element other than SiO_2 and Fe_2O_3 reflects the dominance of quartz and hematite in samples of ironstone associated pumice breccia. The decrease in the concentration of TiO_2, P_2O_5 and Al_2O_3 in the transition from massive ironstone, through tuffaceous ironstone, into hematite altered pumice breccia records depletion in those elements during replacement of the volcanic component by addition of quartz and hematite. The covariance between Fe and Ni, Cr and V is tentatively interpreted to reflect adsorption by iron oxides. Ni abundances may indicate a seawater input (Davidson, 1996). Isocon analysis identifies those elements which have been added by the hydrothermal fluid (and seawater) during alteration of the pumice breccia. These include Si, Fe, Cr, Cu, Zn, Pb, Mn, Mg and P. Cr may have been derived during passage of the hydrothermal fluid through the underlying package of andesitic lithic-scoria breccia deposits. Alteration of pyroclasts in the pumice breccia resulted in mobilisation of Sr, Rb, Na, and K.

7.7.3 Rare Earth Elements

Chondrite normalised (Boynton, 1984) rare earth element concentrations for ironstone samples from the study area are mostly relatively high (Fig. 7.16). Ironstones with incomplete REE patterns have high LREE concentrations and HREE below detection limits (Fig. 7.17B-C). These include samples of massive ironstone associated with pumice breccia from Highway East prospect (94-246) and massive ironstone from east of Trooper Creek (95-130).

Samples of ironstone associated with pumice breccia are characterised by relatively steep negative slope with notable light rare earth element (LREE) enrichment and negative Eu anomalies (Fig. 7.16A). Single samples of massive ironstone (95-316), tuffaceous ironstone (95-212) and hematite altered pumice breccia also display negative Ce anomalies (Fig. 7.16B-C). The transition from hematite altered pumice breccia, through tuffaceous and stromatolitic ironstone, into massive ironstone is marked by a decrease in the concentration of both LREE- and HREE-elements. The different ironstone types mostly have similar REE patterns and slopes (Fig. 7.16A). Massive ironstone with the smallest component of volcanic detritus (95-316) has the lowest concentration of REE, greatest negative Ce anomaly, and Eu is below the detection limit. Overall the REE patterns of the ironstones associated with pumice breccia is similar to that of least altered rhyolites and dacites from the Trooper Creek Formation around Highway mine (Fig. 7.17A). The rhyolites have relatively flat to slightly LREE enriched patterns with shallower slopes than ironstone associated with pumice breccia.

Ironstone from pods enclosed in rhyolite is enriched in LREE and depleted in HREE, Ce and Eu (Fig 7.17B). The REE pattern of this sample (95-150)

is nearly parallel with those of massive and tuffaceous ironstone. Massive ironstone associated with chert displays a variety of different patterns. Sample 94-25 shows slight LREE enrichment and a negative Ce anomaly. The pattern for sample 94-18 displays a U-shaped pattern with slight light- and heavy-REE enrichment, and a weak positive Eu anomaly (Fig. 7.17C). Ironstone dominated by chert (94-401) is characterised by a relatively flat LREE pattern, positive Eu anomaly and HREE depletion.

Interpretation of rare earth elements

Oxide deposits with light REE enriched patterns and positive Eu anomalies are currently forming around hydrothermal vents on the modern sea floor (e.g. Michard et al., 1983; Michard and Albarede, 1986). The REE patterns of these deposits contrast with the surrounding sea water which is characterised by HREE enrichment, and negative Ce anomalies (e.g. Alt, 1988). REE patterns characteristic of purely hydrothermal deposits have also been recognised in some ancient ironstones associated with massive sulfide mineralisation, including ironstones at Thalanga (Duhig et al., 1992b). Other ironstones in both modern and ancient settings result from the mixing of seawater and hydrothermal fluids and display REE patterns which reflect input form these different sources (e.g. Graf, 1977). REE distribution patterns for these samples often show both negative Ce anomalies, characteristic of sea water, and positive Eu anomalies, typical of hydrothermal vent fluids. Examples include hydrothermal precipitates from the Mid-Atlantic Ridge (German et al., 1990) and Southern Explorer Ridge, northeastern Pacific (Barrett et al., 1990). Initial hydrothermal signatures can be masked by post depositional scavenging of sea water derived elements by Fe-Mn hydroxide phases (e.g. German et al., 1990; Olivarez and Owen, 1991). Barrett et al. (1990), studying hydrothermal precipitates on the Southern Explorer Ridge, demonstrated that iron oxyhydroxide deposits at the vent have positive Eu anomalies, recording a hydrothermal input, whereas distal precipitates have seawater modified Eu patterns. REE/Fe ratios in suspended particles in the TAG hydrothermal field, on the Mid-Atlantic Ridge increase with increasing distance from their hydrothermal source (German et al., 1990). German et al. (1990) attributed this to progressive scavenging of REE from seawater as hydrothermal particles are dispersed through the water column, and more importantly, after hydrothermal particles have settled to the seafloor. Burial rates limit the degree to which hydrothermal precipitates scavenge REE. Post-depositional scavenging will be limited under high sedimentation rates (Olivarez and Owen, 1991).

Positive Eu patterns for hydrothermal precipitates reflect deposition from divalent Eu enriched fluids and thus either temperatures higher than 250 °C or reducing fluid conditions (Sverjensky, 1984; Lottermoser, 1989; Michard, 1989). Positive Eu anomalies are largely controlled by the break down of Eu enriched feldspar during alteration of the source rock although hornblende, sphene, pyroxene and garnet may also contribute to an Eu anomaly (Rollinson, 1993; Barrett et al., 1990).

Several ironstone samples associated with pumice breccia have pronounced negative Eu anomalies. Although REE are largely immobile the concentration of LREE, HREE and Eu may be significantly modified during metamorphism, hydrothermal alteration, and seafloor weathering (e.g. McLennan and Taylor, 1979; Campbell et al., 1984; Lottermoser, 1990; Schandl and Gorton, 1991). Feldspar in tuffaceous ironstone and hematite altered pumice breccia is largely unaltered suggesting that Eu depletion is not related to the differential mobilisation of divalent Eu during breakdown of feldspar. Although feldspar is largely absent in samples of massive ironstone, negative Eu anomalies are not always pronounced, suggesting limited mobility of Eu even under the most intense conditions of alteration. On the basis of their distinct negative Eu anomalies and hematite-rich composition the ironstones associated with rhyolite and pumice breccia are interpreted to have deposited from oxidised and possibly low temperature hydrothermal fluids. Samples with distribution patterns showing LREE enrichment and negative Eu and Ce anomalies indicate that the rare earth elements in these hydrothermal precipitates come from both hydrothermal vent fluid and seawater sources.

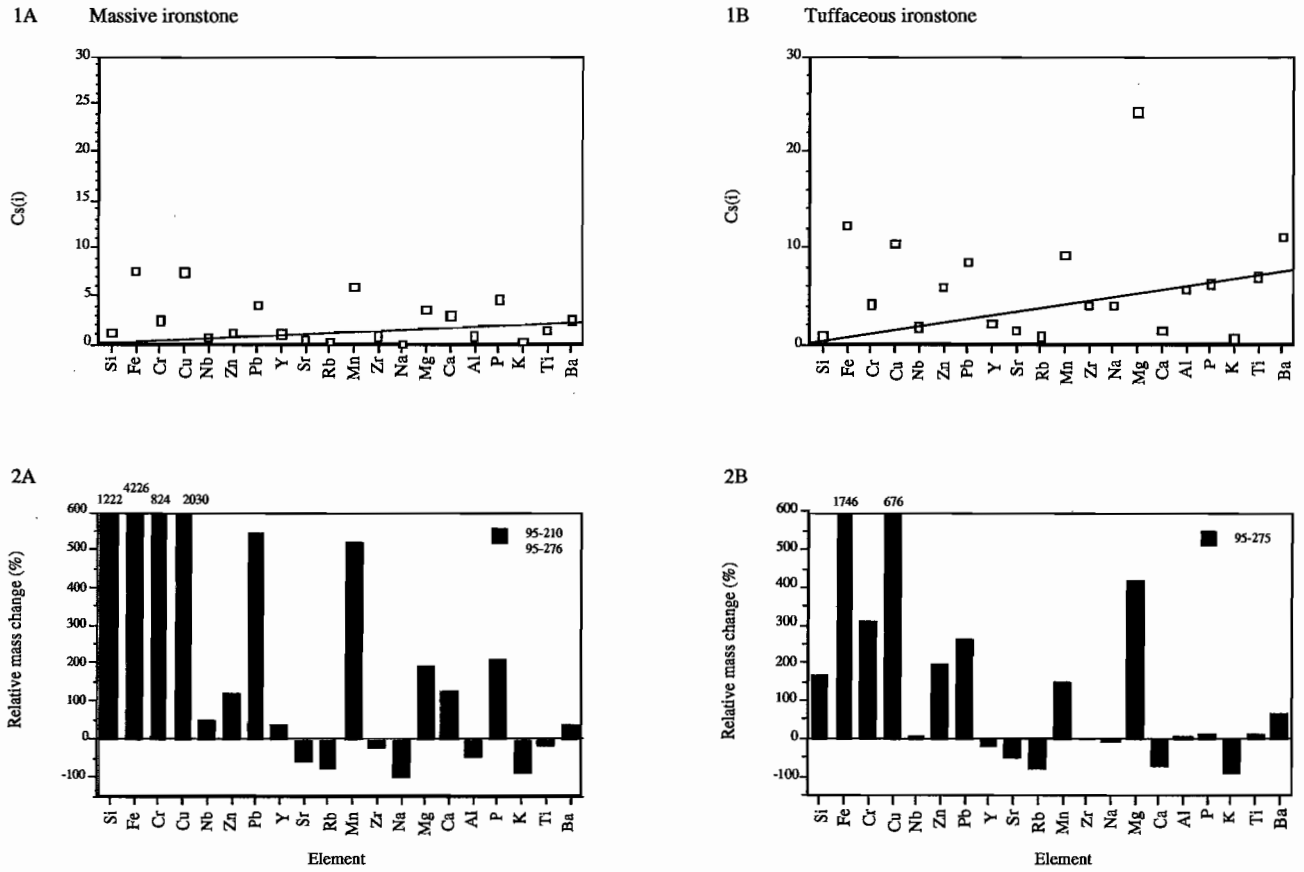

Figure 7.13 — Isocon diagrams illustrating scaled concentrations of particular elements (1) and relative mass change for each element (2) in (A) massive ironstone and (B) tuffaceous ironstone.

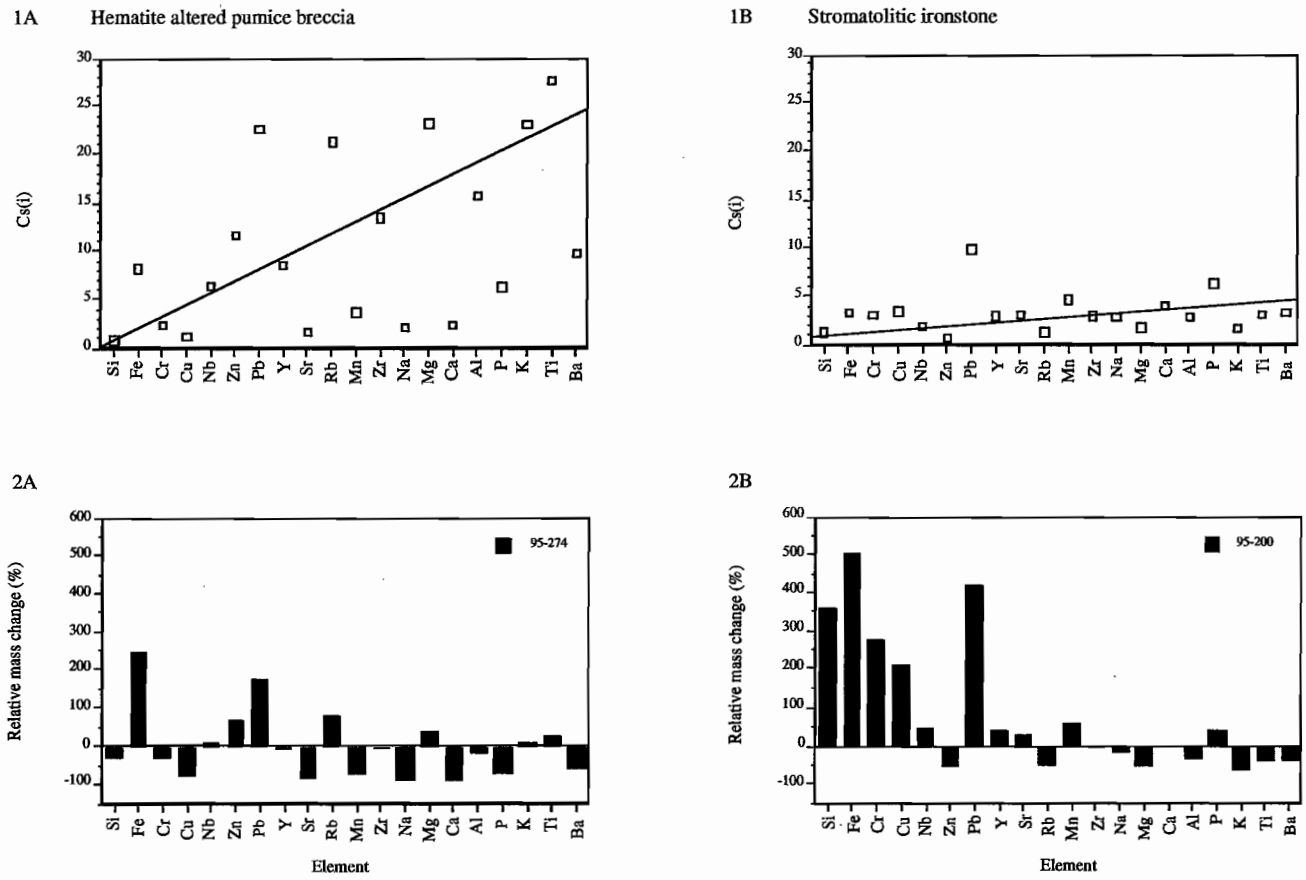

Figure 7.14 — Isocon diagrams illustrating scaled concentrations of particular elements (1) and relative mass change for each element (2) in (A) hematitic pumice breccia and (B) stromatolitic ironstone.

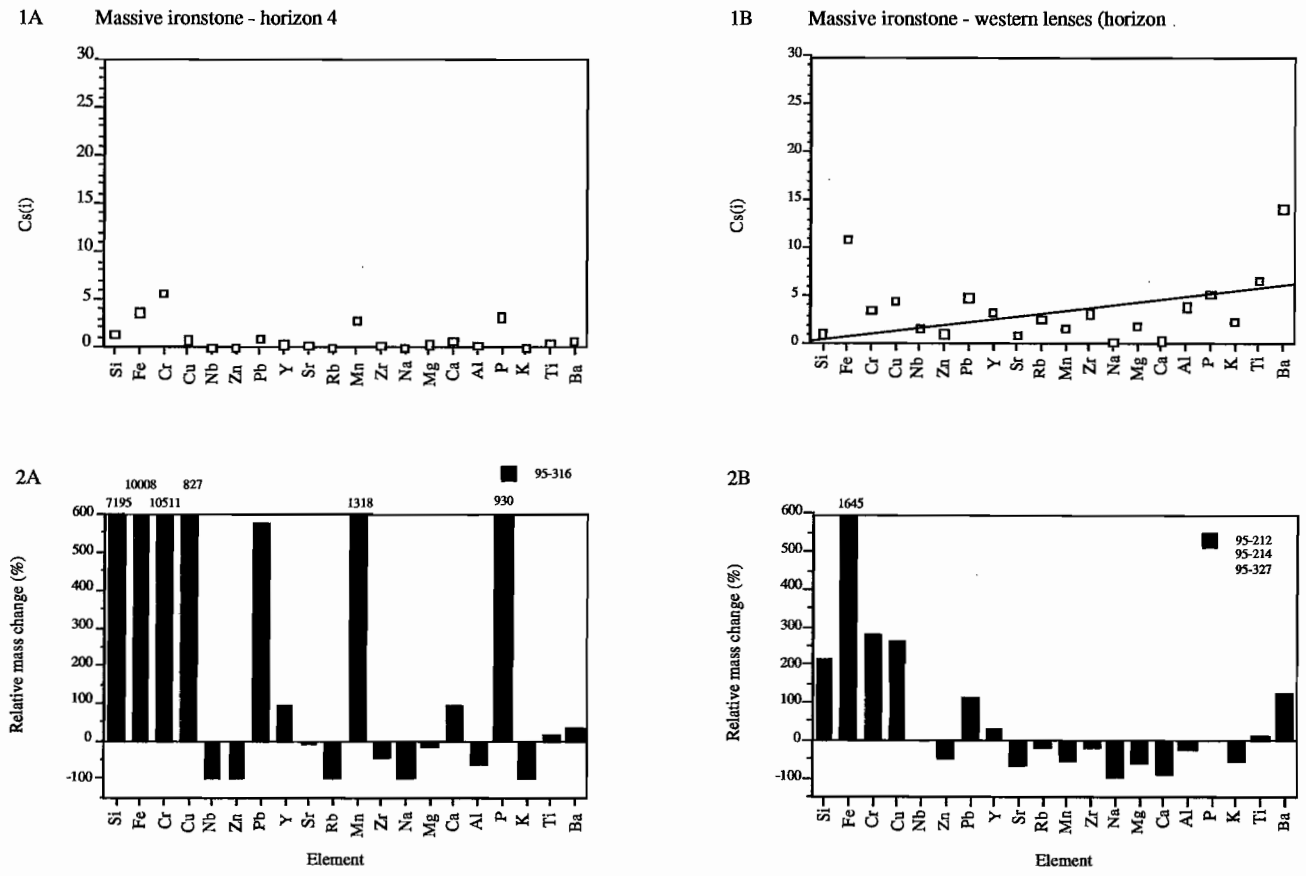

Figure 7.15 — Isocon diagrams illustrating scaled concentrations of particular elements (1) and relative mass change for each element (2) in (A) massie ironstone from horizon 4, Trooper Creek prospect and (B) tuffaceous ironstone from the western lenses of horizon 1, Trooper Creek prospect.

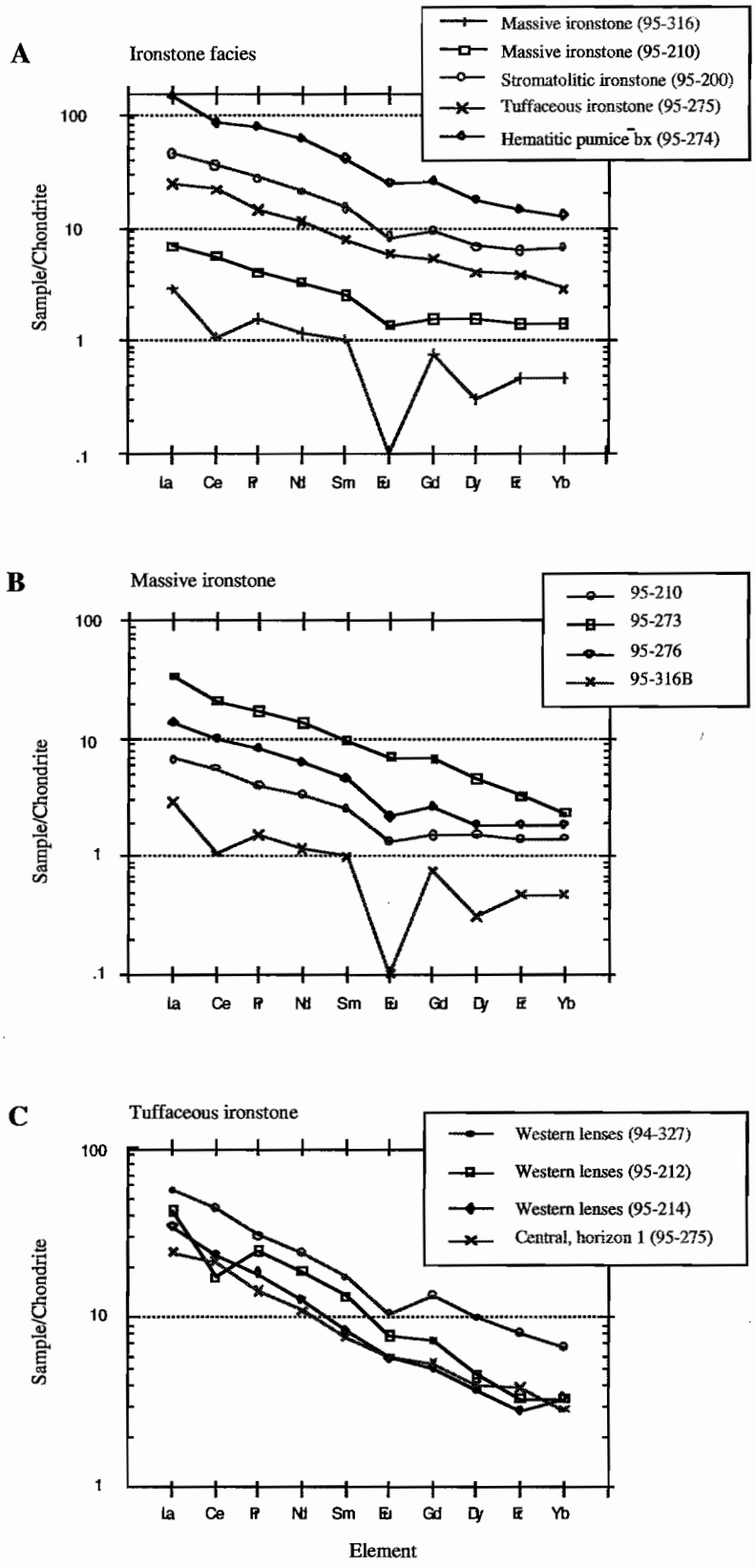

Figure 7.16 — Rare earth element plots of ironstone from the Trooper Creek prospect normalized to the chondritic values of Boynton (1984). (A) Massive, tuffaceous and stromatolitic ironstone and hematite altered pumice breccia from the central and eastern lenses. (B) Massive ironstone from the eastern and central lenses. (C) Tuffaceous ironstone from the central and western lenses.

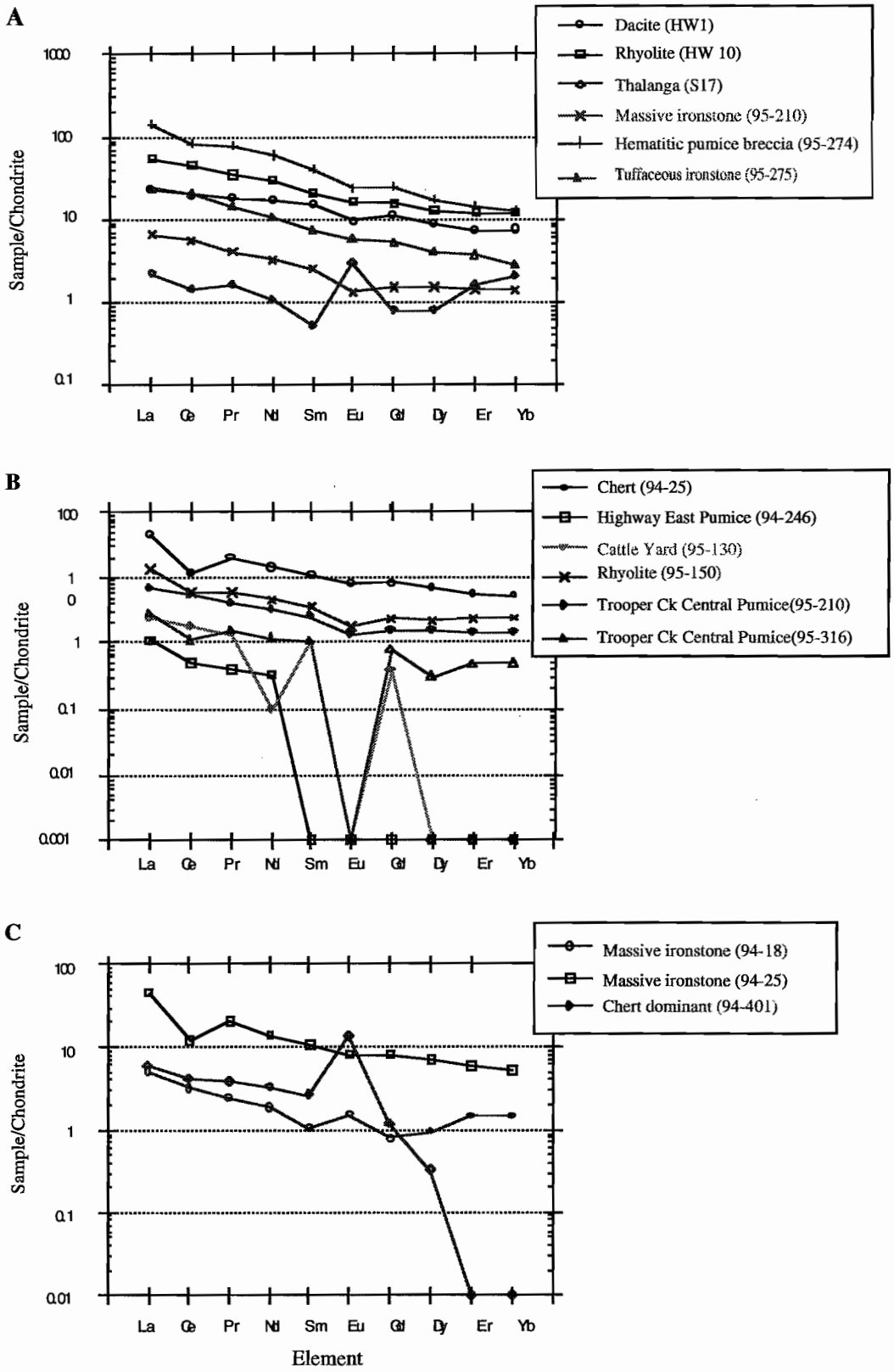

Figure 7.17 — Rare earth element patterns normalized to chondritic values of Boynton (1984). (A) Ironstone associated with chert at Handcuff, rhyolite from Trooper Creek prospect and dacite pumice breccia at Trooper Creek Prospect central and Trooper Creek cattle yard. (B) Ironstone associated with chert. (C) Comparison of ironstones from Trooper Creek prospect, Thalanga ore horizon (data from Duhig et al., 1992) and rhyolite-dacite from the Trooper Creek Formation (data from Stolz, 1991).

The LREE enriched patterns of the ironstones associated with pumice breccia compared to that of least altered rhyolites and dacites from the Trooper Creek Formation is consistent with modification of primary volcanic REE patterns by hydrothermal fluids in equilibrium with feldspar. REE concentrations in ironstone associated with pumice breccia decrease passing from hematite altered pumice breccia, through tuffaceous ironstone, into massive ironstone. Although there is depletion in REE element concentrations, REE patterns are similar in the different ironstone types. Depletion is interpreted as a response to progressive dilution of REE (original and hydrothermal) by gradational addition of Si and other REE-poor minerals during replacement of a precursor pumice breccia. In addition, diagenetic compaction in hematite altered pumice breccia may have increased the concentration of REE relative to massive ironstone and tuffaceous ironstone which altered early and remained uncompacted. Post depositional scavenging of sea water derived REE may have been important. Textural evidence indicating a sub-seafloor replacement origin for some ironstones lenses associated with pumice breccia suggest a sea water signature might also come from pore water in the unconsolidated volcaniclastic precursor or through shallow circulation of seawater near the sea floor. Post depositional scavenging of elements from seawater might also have been important.

Ironstone associated with chert show a range of REE patterns. Sample 94-25 displays a pattern of slight LREE enrichment and Eu depletion, and negative Ce anomaly indicating that the REE in these samples were derived from both sea water and hydrothermal sources. The patterns for the remaining samples (94-18, 94-401) display positive Eu anomalies suggesting deposition from relatively hot and/or reduced hydrothermal fluids. The weak enrichment in HREE in sample 94-18 may reflect a sea water input.

7.8 Discussion

7.8.1 Mechanisms and conditions of quartz-hematite deposition

In the Trooper Creek Formation ironstones, the presence of hematite and the absence of significant barite suggests that the Fe-Si depositing fluids were oxidised and unable to transport significant Ba. Negative Eu anomalies in REE plots support the interpretation of deposition from oxidised and possibly low temperature hydrothermal fluids. Furthermore, textures in the ironstones (e.g. syneresis cracks and spherules; Fournier, 1985) and in some cases preservation of primary volcanic textures (delicate pumice and shards) suggest precipitation from low temperature solutions (<100°C) of amorphous silica rather than quartz. This is consistent with the temperatures and mineralogy of currently forming hydrothermal deposits.

Amorphous silica precipitates in sea floor hydrothermal systems associated with active mid-ocean spreading centres at low temperatures (15-100°C). The fluids evolve from mixing of relatively high-temperature (175-350°C), silica-saturated hydrothermal fluids and cold seawater (Janecky and Seyfried, 1984; Tivey and Delaney, 1986; Alt et al., 1987; Hannington and Scott, 1988). Herzig et al. (1988) demonstrate for the Galapagous Rift at 86°W, that deposition of non-sulfidic amorphous silica chimneys occurs at low temperatures (32-40°C), whereas amorphous silica intergrown with sulfides formed at 100°C. Tsutumi and Ohmoto (1983) demonstrated, using oxygen isotope analyses, that tetsusekiei ores associated with Kuroko deposits in the Hokuroku district of Japan were deposited from hydrothermal fluids with a temperature of ≤ 100°C. Most studies conclude that deposition of amorphous silica proceeds by conductive cooling (e.g. Tivey and Delaney, 1986) or conductive cooling and mixing with seawater (e.g. Hannington and Scott, 1988; Herzig et al., 1988; Janecky and Seyfried, 1984) of either a pure hydrothermal fluid or hydrothermal fluid-seawater mixture. Hekinian and Fouquet (1985) examining massive sulfide fields on the East Pacific Rise near 13°N suggest silica deposition during the

waning stage of hydrothermal activity solely by mixing of low temperature (<100 °C) silica-rich solutions with seawater.

Silica solubility increases as solutions become more basic and with increasing temperature and pressure (Williams and Crerar, 1985). A sharp drop in pH, temperature, or volume of fluid (by evaporation) will cause the solution to become rapidly supersaturated with respect to silica (Fournier, 1985; Williams and Crerar, 1985). The formation of amorphous silica is facilitated by the presence of Fe-O-OH ions which induce polymerisation of mutually repelling silica colloids or substrates in acid to neutral pH solutions (Williams and Crerar, 1985). Adsorption of silica by clays, iron oxides and other impurities can also remove silica from solution (Williams et al., 1985). In ironstones associated with pumice breccia, the high surface area of reactive glassy pumice and shards may have provided nuclei for the precipitation of silica (and hematite) from the mineralising fluid (cf. Ohmoto et al., 1993). Early deposited alteration minerals (e.g. clay, zeolite, hematite) were probably also present, promoting deposition of amorphous silica. Reaction of silica saturated fluids with glassy parts of lavas or intrusions might also have promoted ironstone deposition. Ironstones with negative Ce anomalies suggest that silica precipitation did not occur solely in response to conductive cooling (cf. Barrett et al., 1990) and mixing with seawater or pore water was important.

Theoretical modeling by Janecky and Seyfield (1984) suggests that quartz can deposit directly from high temperature (350°C) fluids by mixing with cool seawater, but this is inconsistent with observations from the seafloor. The sluggish nucleation kinetics of quartz below 200°C inhibits precipitation from rapidly cooled fluids (Rimstidt and Barnes, 1980; Janecky and Seyfried, 1984). Alt et al. (1987) identified significant quartz in hydrothermal oxide deposits on seamounts near 21°N, East Pacific Rise. However, quartz here is a recrystallisation of amorphous silica in response to reheating of opal-rich material within the growing sulfide deposit. Amorphous silica has a high surface area, is relatively unstable, and so readily transforms to more stable silica polymorphs (cristobalite, opal-CT, chalcedony or quartz). The time required for the transformations decreases as temperature increases and in the presence of solutions with high pH, high salinity or containing dissolved Mg (Fournier 1985). In the Trooper Creek ironstones, the conversion of amorphous silica to quartz probably began early during the period of hydrothermal activity (cf. Renaut and Owen, 1988). Good evidence comes from ironstone replacing pumice breccia at Trooper Creek prospect. At this locality had lithification been late clasts of ironstone could not have been ripped up and incorporated into mass flow deposits which overlie horizon 1 ironstone. Preservation of pumice and shards with delicate margins and vesicles also implies rapid replacement.

In many Trooper Creek Formation ironstones, quartz spherules crystallised from the viscous, possibly colloidal, amorphous silica precursor (cf. Oehler 1976a,b). Iron oxide bands and nuclei are characteristic of many spherule types. Coatings of iron minerals on the surface of some spherule types are interpreted to be due to surface adsorption effects or to exclusion of iron-rich impurities during spherule growth. Concentric bands of iron oxide are impurities that were entrapped during growth. The bands provide evidence for the co-precepitation of iron oxide and silica. In some cases hematite acted as crystallisation nucleation centres. Similar textures have been recorded from some Precambrian ironstones (e.g. Oehler, 1976b). Oehler (1976b) demonstrated experimentally that chalcedonic spherules crystallise from a silica gel until the concentration of dissolved silica decreases below a critical value, following which euhedral quartz crystallised from the remaining silica depleted solution. In the Trooper Creek Formation ironstones, interlocking anhedral quartz which fills pore space in some ironstone samples may have deposited by the same mechanism.

At the time of deposition spherules comprised chalcedony (cf. Oehler, 1976b) but many progressively transformed to more stable quartz. Recrystallisation probably began early but was most texturally destructive during metamorphism. Recrystallisation has destroyed or obscured radially

fibrous textures of spherules, converting many to interlocking mosaics of anhedral quartz. In some cases, recrystallisation has not been pervasive and regions of quartz spherules grade into domains of interlocking anhedral quartz grains, and some spherules have only been partially converted to anhedral quartz.

In the broad spectrum of currently active iron-silica depositing hydrothermal systems Fe deposits as iron oxyhydroxides (e.g. Alt et al., 1987; Hekinian and Fouquet, 1985; Holm, 1987). Hematite characterises some depositional settings (e.g. Soufrière volcano, Sigurdsson, 1977) and may have been the primary oxide phase in the Trooper Creek ironstones. Alternatively, iron oxyhydroxide (e.g. geothite) may have formed an unstable precursor which later converted to more stable hematite. REE analysis and textures are consistent with deposition of the Fe-oxide at low temperatures, consistent with observations from the sea floor. For example, Fe-oxidising bacteria in Fe-rich muds at Santorini suggest that iron-hydroxides deposited at between 12-30°C (Holm, 1987). In the Trooper Creek Formation ironstones, iron oxide patches were hydrated, but less so than the enclosing amorphous silica, as evidenced by syneresis cracks along some margins. Textural evidence suggests that hematite outlining pumice shreds and forming patches with equant shapes deposited prior to the growth of chalcedony sherules. Cuspate patches of hematite filling space between coalescing spherules deposited during and/or after growth of the spherules.

7.8.2 Preservation of pumice and shards

Relict volcanic textures indicate that ironstone lenses at Trooper Creek prospect and Highway East prospect are mostly replacements of dacitic clast-supported pumice breccia, rather than seafloor precipitates. Incorporation of water settled pumice into the ironstone concurrent with seafloor exhalation is inconsistent with several lines of evidence. Firstly, planar lamination in hematite altered pumice breccia continues into the laterally equivalent tuffaceous ironstone. Secondly, the thickness of ironstone is similar to the thickness of the laterally equivalent pumice breccia. Thirdly, the thickness of the pumice fall deposit and absence of intervening deposits suggest that the pumice breccia deposited rapidly concurrent with explosive volcanism. Replacement may have occurred at or below the seafloor, but was not excessively deep because: (1) clasts of ironstone were incorporated into overlying subaqueous mass-flow deposits; (2) pumice breccia has been altered without producing veins. After lithification, alteration of pumiceous deposits is mostly fracture controlled (McPhie et al., 1993).

Pumiceous deposits were originally highly porous and permeable aggregates of easily compactable glassy fragments (pumice and shards). These primary textural characteristics greatly influenced the distribution of alteration minerals and textures. The original high permeability and porosity allowed rapid alteration of the units. Hydrothermal and diagenetic alteration were possibly both involved in the dissolution, replacement and precipitation of minerals along fluid pathways in the breccias during ironstone deposition. Assemblages of sericite, chlorite and albite are typical of diagenetic alteration of volcanic glass (e.g. Allen and Hunns, 1990; Doyle et al., 1993; McPhie et al., 1993; Doyle, 1994). In the ironstones, quartz and hematite record the flooding of pumiceous units by hydrothermal fluids. The transition in mineralogy passing from massive ironstone (quartz-hematite), through tuffaceous ironstone (hematite>quartz), down into pumice breccia (sericite>hematite) may records a decreasing involvement of hydrothermal fluids to diagenetic fluids in alteration/replacement. As a consequence, textures in each ironstone facies have evolved along different paths. In all cases fine grained hematite outlines vesicle walls and pyroclast margin. As both vesicles and pumice/shard walls are now phyllosilicate or quartz, an early phase of hematite alteration is probably recorded. Hematite probably replaced the margins of glassy fragments or an earlier alteration mineral of the glass (e.g. zeolite, clay). Alternatively, the edges of the pumice and shards may have been oxidised or reacted with sea water and/or pore water prior to or following deposition. Similar oxide films coating pumice have been observed in non-welded ignimbrite (e.g.

Ongatiti ignimbrite, New Zealand) and in pumiceous volcanosedimentary deposits (e.g. Taupo Volcanic Centre, New Zealand).

Preservation of pumice and shards requires simultaneous dissolution of glass and crystallisation of silica. In massive ironstone, amorphous silica filled vesicles and replaced glassy bubble walls of pumice and shards outlined by earlier deposited iron oxide. Transformation of amorphous silica to chalcedony and quartz occurred rapidly, and probably concurrent with replacement. Single chalcedony ± oxyhydroxide (now hematite) spherules or interlocking anhedral quartz replaced some pumice and shard walls preserving the primary volcanic texture. More often, coalescing spherules cut across pumice and shards without displacing them but destroying primary textures (Fig. 7.18A). Coarsely crystalline quartz with hematite globules fills other voids and may be primary or recrystallisation product of earlier void filling amorphous silica or chalcedony. Later recrystallisation destroyed spherule textures generating an apparent matrix domain between relict patches of spherules, pumice, and hematite (Fig 7.18B).

In pyroclast-rich tuffaceous ironstone amorphous silica and/or hematite (or a precursor oxyhydroxide) replaced pumice and shards. Hematite replaced single pumice shreds or pumiceous domains in the breccia forming irregular to equant hematite patches. Amorphous silica in areas between hematite patches rapidly transformed to coalescing spherules destroying many vitriclastic textures. Relict pumice and shards are now fine grained (2-5 μm) quartz but may once have comprised chalcedonic microspherules. Rarely, nucleation and coalescence of spherules formed nodules which displaced pumice and shards in the surrounding hydrous gel. Botryoidal structures record the inorganic precipitation of iron oxyhydroxide (or hematite) and silica around feldspar crystals and other impurities during the transformation of the amorphous silica gel. Areas between spherules and remaining pore spaces were filled with hematite.

A different style of alteration occurred in quartz-hematite-sericite altered pumice breccia beneath ironstone lenses. The silica-hematite alteration was restricted to single pumice shreds and small domains in the breccia leaving large areas of glassy material which was altered to sericite and chlorite during subsequent diagenetic alteration. Many phyllosilicate-rich pumice were flattened during diagenetic compaction and deformed around the more competent quartz-hematite altered pumice, hematite patches, and feldspar crystals. Diffuse trails of hematite define the former vesicle walls and fragment margins in sericitised pumice shreds. There are no indications that spherules formed in the breccia, although recrystallisation to fine grained quartz may have destroyed any microspherule texture. Hematitic pumice breccia unassociated with ironstone (horizon 3, Trooper Creek prospect) has a similar textural history. Hematite patches are smaller and less abundant suggesting the hydrothermal system was smaller or short lived.

It is unclear whether quartz, hematite and sericite were the first alteration minerals of the pumiceous units or, instead, even earlier minerals such as zeolite, albite, clay or carbonate were present. In one sample, relict patches of zoned carbonate show incomplete replacement by recrystallised anhedral quartz. Zoning in the calcite conforms to contacts with hematite patches suggesting that calcite deposition postdates hematite alteration, and may represent a cavity fill. Recrystallisation of the calcite is indicated by uniform extinction across growth zones and by quartz free calcite which has precipitated along some grain boundaries.

The transition from massive ironstone with well preserved spherule texture, through tuffaceous ironstone with variably abundant spherules, into pumice breccia without spherule texture are interpreted as primary and not a function of later recrystallisation and spherule destruction. Decreasing pore space due to early diagenetic compaction and increasing impurities may have also combined to inhibit spherule growth in tuffaceous ironstone and hematite altered pumice breccia. In contrast to pyroclast-rich tuffaceous ironstone, feldspar crystals are rare in massive ironstone suggesting that feldspar was originally absent or was unstable at the

conditions of quartz-hematite deposition and was consumed. The transition implies either a change from sub-seafloor mineralisation to partially exhalative ironstone deposition, or a change in fluid chemistry from acidic to alkaline.

7.8.3 Palaeodepositional depths:

At the Trooper Creek prospect, incorporation of stromatolites and oncolites into the ironstones, sedimentary structures consistent with wave agitation in a dominantly quiet water environment. Lateral facies variations indicate ironstone deposition in a shallow shelf environment. Regional context favours deposition is a submarine rather than lacustrine setting. The remaining ironstone deposits are hosted by volcanic and sedimentary facies which imply deposition in a relatively deep (below storm wave base) environment.

7.8.4 Role of micro-organisms in ironstone formation

The recognition of microbialites and filamentous structures in some ironstones suggests that iron and silica precipitation may have been regulated directly or indirectly by microbial activities. That microbialtic ironstone is laterally continuous with ironstone lenses without microbialites suggests none or a limited role for micro-organisms in iron oxide deposition. Rather the microbial structures may have provided only a framework for iron oxide (or oxyhydroxide) minerals to deposit and played no more a direct role in mineral deposition than crystal and vitric particles in the ironstone. Because the microbialites and associated pumice shreds show no evidence of compaction, it is likely that deposition of silica and hematite occurred very early, and possibly concurrent with growth of some of the microbes.

There is no evidence to determine whether the microbes forming stromatolites and filamentous networks were algae or bacteria (e.g. Park, 1977), and in some cases whether these organisms were iron-loving micro-organisms or phototropic microbes. In both modern and ancient terrains, stromatolites and oncolites are composed primarily of cyano-bacteria. By analogy, stromatolites and oncolites in ironstone from the Trooper Creek Formation probably comprised similar micro-organisms. Networks of filaments similar to those described by Duhig et al. (1992), and interpreted as iron secreting algae or fungi, are also present in some stromatolitic samples. Similar filaments have been identified in quartz-hematite veins in dacite, and in massive- and tuffaceous ironstone replacing pumice breccia. Recognition of filaments in ironstone without stromatolites or oncolites suggests that the filaments may be iron secreting algae or fungi. Filaments in veins and within tuffaceous ironstone suggests that the organisms were able to colonise the sub-seafloor environment during ironstone deposition. The role of seafloor Fe-oxidising microaerophilic bacteria in precipitation of iron oxide around hydrothermal vents is well documented (Holm 1987, 1989; Alt et al., 1987; Alt, 1988; Duhig et al., 1992). Algae have also been implicated in iron oxide deposition (e.g. Trudinger and Mendelsohn, 1976). Microaerophilic chemolithotrophic bacteria metabolise in oxygen-poor environments and are solely dependent on the immediate geochemical environment. The bacteria use energy liberated during the oxidation of Fe^{+2} to Fe^{+3} to secrete a mucus sheath composed of Fe-oxyhydroxides, which diagenetically alter to more stable hematite. Hydrothermal ferruginous sediments precipitated by the activity of microaerophilic chemolithotrophic bacteria have been identified in both shallow- and deep-marine hydrothermal fields. For example, Holm (1987, 1989), studying active shallow water hydrothermal fields at Santorini, Greece and Reykjanes peninsula, Iceland, established that actively depositing ferruginous sediments consist almost entirely of biogenic Fe-oxyhydroxide formed on the stalks of Galionella ferruginea, a type of Fe-oxidising bacteria. The sediments are up to a few metres thick, and with depth biogenic Fe-oxide-hydroxide transform to goethite and hematite through diagenesis.

7.8.5 Ironstone associated with rhyolite and chert

To the north of Trooper Creek prospect, a rhyolitic cryptodome contains pods and veins of quartz-

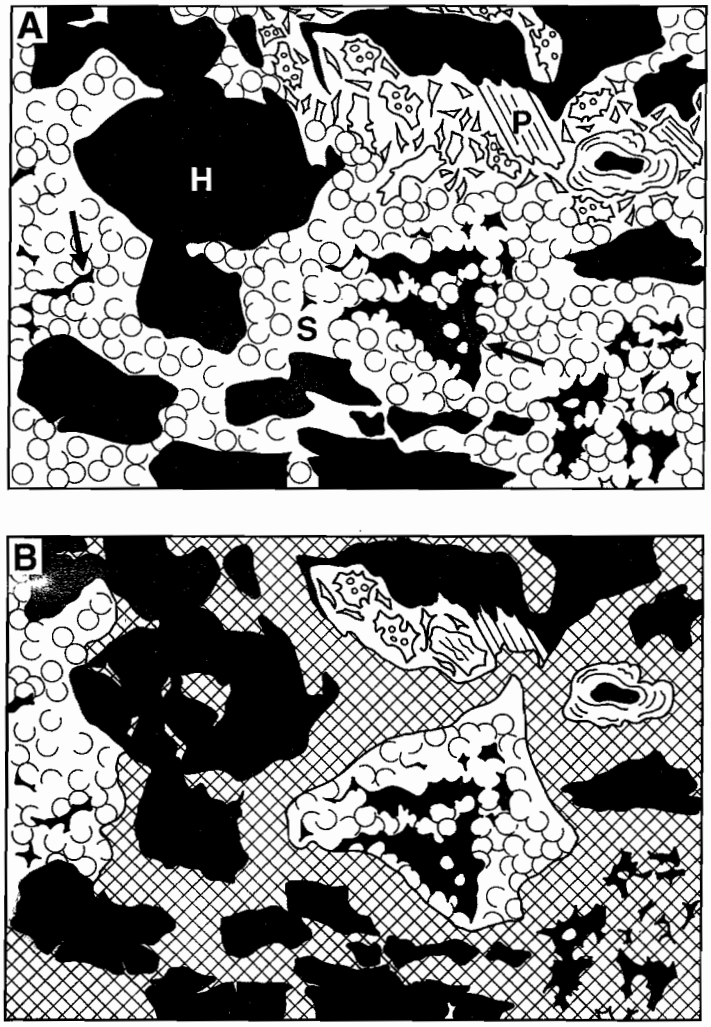

Figure 7.18 — Evolution in texture during the replacement of pumice breccia by iron oxide-silica depositing hydrothermal fluids. A — Replacement of glassy pumice (P) by amorphous silica and subsequent crystallisation of chalcedony spherules between hematite patches (P). Infilling of voids between coalescing spherules by late hematite (arrow). B — Recrystallisation of spherules to fine quartz (hatching) generating an apparent matrix between relict patches of spherules, pumice breccia, and hematite.

hematite. Quartz-hematite veins at the margins of the pod within massive coherent rhyolite suggest that the ironstone pods are not sediment that was mixed with the rhyolite during intrusion. Spherulites in hematite altered rhyolite surrounding the ironstone pods demonstrate that the rhyolite was formerly glassy. Iron and silica depositing solutions may have replaced small glassy domains in the rhyolite following intrusion. As for ironstone which replaced pumice breccia, chalcedonic spherules and syneresis cracks along the margins of equant hematite patches imply initial deposition from solutions of an amorphous Fe-Si-O-OH gel. Iron oxide-silica veins in rhyolite and dacite have similar texture to massive ironstone in rhyolite, and can be considered feeders for Fe and Si transporting solutions.

Primary textures in ironstone associated with chert have been destroyed by recrystallisation during greenschist phase regional metamorphic. Silica has recrystallised to granoblastic quartz and granular hematite has migrated into triple point junctions and grain boundaries. In the absence of primary textures, the mechanisms of silica hematite deposition are conjectural. In better preserved cherty ironstones, amorphous silica precipitation is interpreted to preceded transformation to chalcedonic spherules and quartz (e.g. Adachi et al., 1986). In the Trooper Creek Formation, chert with thin planar hematite-rich and quartz-rich laminae may have deposited as an amorphous gel following exhalation of hydrothermal fluids onto the seafloor. In other examples, hematite-rich domains in chert are patchy and discontinuous and inconsistent with deposition of Fe minerals and silica from a hydrothermal plume. In these cases, a patchy distribution of iron oxide and silica may record the diffuse passage of hydrothermal fluids through earlier deposited material.

7.8.6 Environment, volcanism and ironstone deposition

The mere presence of ironstone does not necessarily indicate the existence of quiescent conditions for the accumulation of, in some cases, significant thicknesses of chemical precipitates. Selective replacement of permeable horizons at or below the sea floor by convecting hydrothermal fluids may continue uninterrupted as younger deposits are emplaced from concurrent volcanic activity. The preservation potential of ironstones formed by replacement may be more viable than exhalative deposits, particularly in shallow water environments, where volcanism and currents can disrupt and disperse exhaling hydrothermal plumes or erode poorly consolidated gels. However, replacement may be restricted to near seafloor horizons as the decrease in porosity and permeability, and changes in mineralogy accompanying diagenetic compaction may limit the ability of hydrothermal fluids to diffuse though volcanic deposits.

In volcanic terrains ironstone deposition may record periods of heightened volcanic activity, as for example was recorded by deposition of Fe-rich sediments during the 1971-72 Soufriere eruption on St. Vincent (Sigurdsson, 1977). Similarly, the Michipicoten ironstones, Canada hydrothermal activity followed a period of highly explosive volcanic activity (Goodwin, 1962). Iron oxide ± quartz veins and lenses at the margins of lavas, domes and cryptodomes suggest establishment of small local hydrothermal systems during and/or immediately following magma emplacement. Exhalation of iron rich fluids into subaqueous environments in intrusive-extrusive dominated volcanic centres are a source of Fe and Si during ambient sedimentation. At Handcuff, dacite intrudes Fe-rich siltstone which was probably deposited from exhaling Fe-rich fluids focused above the intrusion or associated nearby rhyolite domes and intrusions. At Trooper Creek prospect, cycles of iron oxide ± silica deposition consistently follow the emplacement of syn-eruptive pumiceous deposits. The iron oxide ± silica units probably record the establishment of shallow water hydrothermal systems in periods between explosive silicic volcanism associated with a nearby subaerial or shallow marine volcanic centre. These exhalations may not only have supplied the essential ironstone components but probably generated fluctuating physiochemical conditions in the restricted shallow water environment (shelf ?) they were emplaced.

Each incursion may have acted in the direction of increasing Ph, and in some cases possibly decreasing Eh (biological activity). The countervailing marine influence was probably in the direction of higher Eh and decreasing pH. The Trooper Creek prospect ironstone is associated with a developing hydrothermal system as indicated by the abundance of syn-depositional volcanic rocks.

Volcanic processes and deposits play a major role in shaping and physically modifying depositional environments. For example water depth, gradient and relief can vary rapidly in response to explosive eruptions, extrusion or intrusion of magma, or tectonism concurrent with volcanism. Volcanism, particularly explosive volcanism, has the potential to release large volumes of volcaniclastic material into depositional environments, interrupting or terminating ambient sedimentation, sea floor hydrothermal systems and exhalative ironstone deposition. Lavas and intrusions can generate seafloor topography which may be important for the concentration of mineral depositing hydrothermal solutions vented onto the seafloor.

Volcanic deposits range widely in physical properties such as density, porosity, permeability, and chemical stability. For example, pyroclasts and large parts of some lavas and cryptodomes are glassy and are easily altered or replaced during the passage of hydrothermal fluids. Experimental studies show that volcanic glass readily contributes silica and iron to circulating hydrothermal solutions and feldspar is a source of Eu (e.g. Fournier, 1985; Sigurdsson, 1977). The shapes, dimensions and viability of hydrothermal circulation important for iron oxide ± silica deposition will be strongly dependent on the volcanic facies and their properties. The current study suggests that distinct or genetically related iron oxide ± silica deposits that involve different facies may contrast markedly in texture, structure and geochemistry.

7.8.7 Models for ironstone emplacement

Despite the large volume of literature on the genesis of volcanic-hosted massive sulfide deposits, relatively few studies have examined the distribution of iron oxide-silica deposits in subaqueous volcanic terrains and their significance to massive sulfide mineralisation. The spectrum of iron oxide deposit styles depicted in figure 7.19, and their departure from the classic blanket style exhalative ironstone associated with some massive sulfide deposits (e.g. Kalogeropulos and Scott 1983,1989), is attributed to variation in the chemistry of hydrothermal fluids, different volcanic facies, the facies architecture, and the character of the seafloor. Several different models have been proposed for Fe-oxide deposits, many based on observations of the seafloor.

Diffuse fluid flow and white smokers

Diffuse venting of low temperature hydrothermal solutions occurs during the waxing and waning stages of massive sulfide mineralisation and by peripheral hydrothermal flow. Mineral precipitates are typically thin and consist of amorphous Fe-oxyhydroxides, Mn-oxides, clay and silica. Fluids may vent from fractures in volcanic rock or from white-smoker chimneys on the massive sulfide mound. White smoker chimneys may grow throughout the history of a mound, during early, low temperature venting, when the fluids are not hot enough to transport significant metals, or alternatively during the high-temperature stage of mound growth (Hannington et al., 1995). Observations from the seafloor indicate that as a mound matures and becomes less permeable replacement of previous sulfides by higher temperature mineral assemblages is accompanied intramound cooling of hydrothermal fluids. Low temperature fluids discharge through the outer surface crust depositing barite, silica and minor pyrite, and forming white-smoker-type chimneys (e.g. Tivey and Delaney, 1986; Alt et al., 1987; Lydon, 1988).

Hydrothermal plume model

The inefficiency of mineral accumulation from a buoyant hydrothermal plume, as demonstrated by the modern black smokers, may allow for accumulation of thin deposits of Fe oxide-rich sediments around seafloor massive sulfide deposits (e.g. Hannington et al., 1995). Some of the larger sulfides that precipitate in the buoyant plume during mixing

with seawater are deposited near the vent but most are rapidly oxidised (Feeley et al., 1994). As the buoyant plume looses its vertical momentum and starts to spread out laterally, Fe and Mn oxy-hydroxides precipitate and are dispersed over distances of several kilometres from the vent (e.g. Lilley et al., 1995).

Ferriferous exhalations have been proposed as the delivery mechanism for extensive iron-rich chemical sedimentary rocks forming iron formations (e.g. Kimberley, 1989a,b). Among those who support exhalative models, thermal convection and seismic pumping are invoked as the driving mechanism for fluid generation.

Oxidised brine pool model

Solomon et al (1990) suggested that sheet-like massive sulfide deposits (termed "Rosebery-type deposits") form from dense brine accumulations in topographic depressions on the seafloor. As outlined by Sato (1972) and Large (1977) highly saline hydrothermal solutions whose densities are greater than cold sea water (Type 1 and 2 solutions, Sato 1972) may move away from the vent along the seafloor and become trapped in seafloor depressions. Depending on the initial seafloor topography, massive sulfide mineralisation which precipitates from the brine pool may be displaced from the hydrothermal conduit or pool above it (e.g. Large, 1992). Magnetite ± hematite ± pyrite ironstone or chert may provide a link between massive sulfide mineralisation at the feeder zone and distal mineralisation (Large 1977). Solomon et al. (1990) site the Rosebery and Woodlawn VHMS deposits in Australia, and Bathurst camp deposit from New Brunswick, Canada as examples of examples of this deposit style. Iron oxide rocks are not reported from Woodlawn (McKay and Hazeldene, 1987). At Rosebery deposit pyrite-hematite-magnetite ± chalcopyrite lenses occur above the massive sulfide orebody and within, and at the edges of, barite lenses above the Pb-Zn ore (e.g. Green and Iliff, 1989; Green et al., 1981). The lenses have been compared with ironstones associated with the Kuroko deposits (Brathwaite, 1974).

A clear example of ore genesis by brine pool accumulation comes from Atlantis II Deep in the Red Sea. Here, iron oxyhydroxide and silica deposits are the lateral equivalent of Cu-Zn-rich metalliferous sediments precipitated from the brine pool (Pottorf and Barnes, 1983). The Atlantis deposit is widespread, laterally continuous and confined to the fault-bound limits of the depocentre.

Sub-seafloor replacement of permeable volcanic horizons

Ohmoto et al. (1983) concluded, based on the kinetics of quartz precipitation, that tetsusekiei associated with Kuroko deposits formed by the mixing of hydrothermal fluids and seawater in wet unconsolidated sediment. Ironstone at Trooper Creek prospect display critical textural evidence to support a sub-seafloor replacement model for some silica and iron oxide deposits. A model for sub-seafloor ironstone deposition has been constructed based on ironstones at Trooper Creek prospect.

Large volumes of iron oxide and silica depositing fluid must have passed through the pumice breccia in order to precipitate thick ironstone deposits at Trooper Creek prospect. This was achieved by replenishment of hydrothermal fluid lost to the sea floor by diffuse flow (Fig. 7.20A). Another possible mechanism for depositing sheet style ironstone is by strata-bound replacement of favourable volcanic horizons adjacent to faults acting as fluid pathways for mineralising fluids (Fig. 7.20B). Ironstones deposited by this mechanism may be less laterally continuous than those fed by a series of local hydrothermal vents above a zone of poorly focussed discharge.

Hydrothermal fluid or hydrothermal fluid/seawater mixtures diffuse through the pore space in the permeable volcaniclastic units and cool by interaction with pore water. Hydrothermal fluids may migrate down slope within the confines of the permeable host unit. Initial pore space is supplemented by permeability that develops through the dissolution of glass. Conductive cooling and mixing of the hydrothermal fluid with seawater in pore space allows for deposition of amorphous silica. The

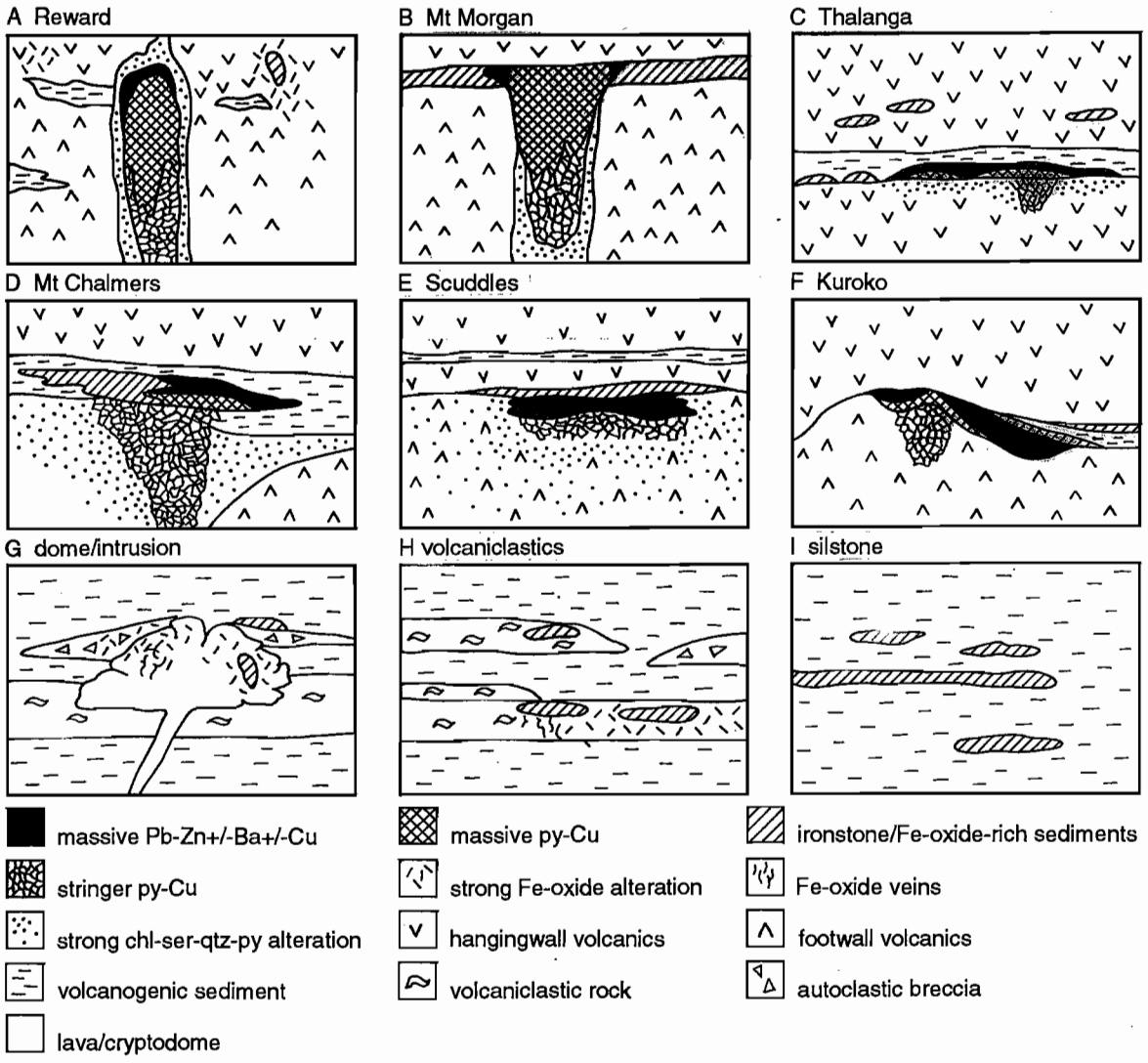

Figure 7.19 — (A-E) Schematic representation of the distribution of ironstone lenses in several Australian VHMS deposits. (F-H) Schematic representation of the succession of facies hosting barren ironstones in the study area.

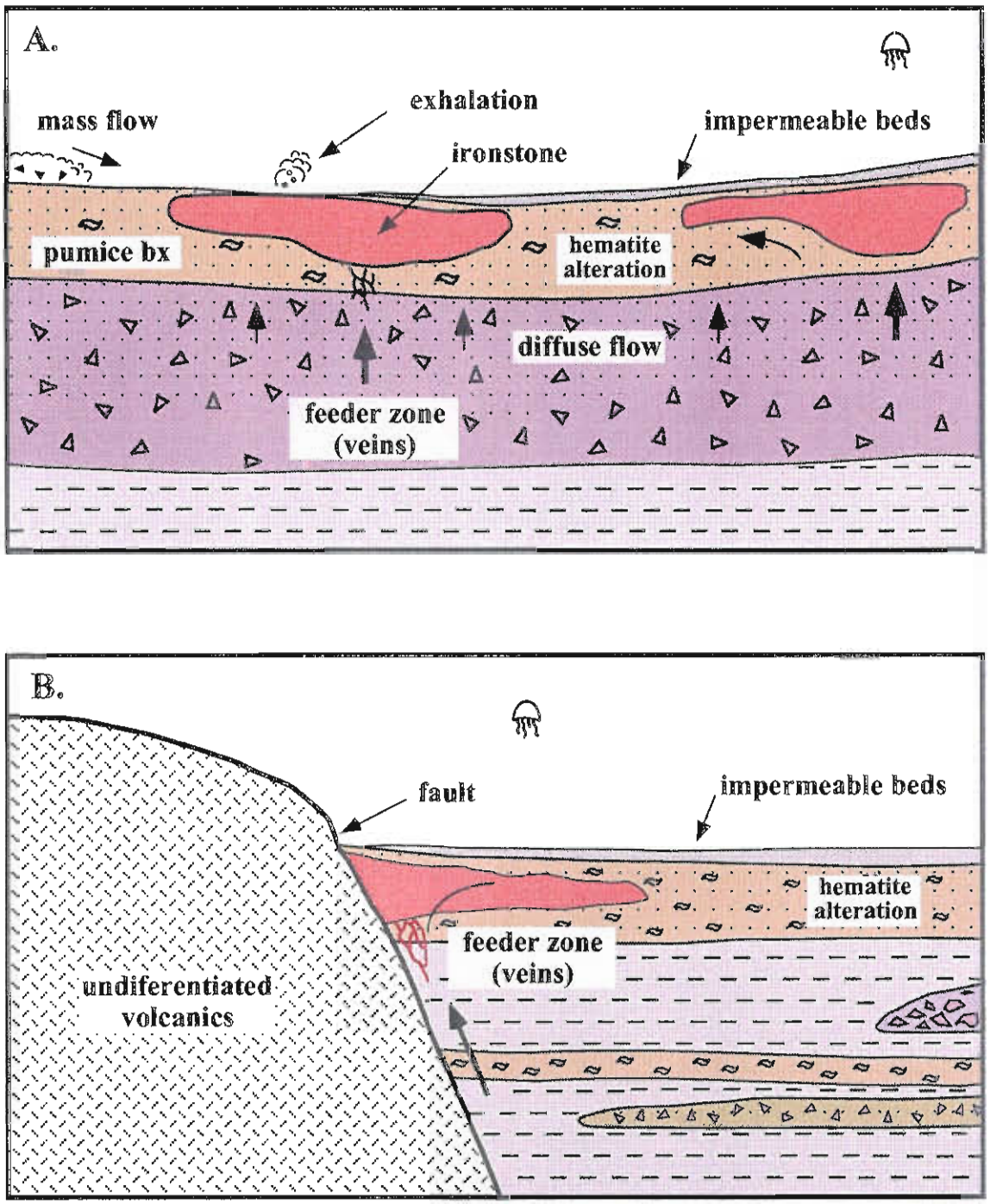

Figure 7.20 — Models for the sub-seafloor replacement of permeable volcaniclastic units by Fe-Si depositing hydrothermal fluids. (A) Fluids progress towards the seafloor by diffuse fluid flow and deposit by replacement and exhalation. (B) Hydrothermal fluids are focussed along growth faults within the volcanic package. See text for detail.

hydrothermal precipitates decrease the permeability of the volcaniclastic deposits. Defocussing of hydrothermal discharge by cementation of volcaniclastics over the original fluid conduit promotes conductive cooling, mixing with pore water, and silica-oxyhydroxide precipitation in unaltered parts of the host unit. It is possible that a low-permeability zone may develop in the upper part of a host unit, where more pore water is available to induce mineral precipitation, causing fluids to circulate and progressively replace down as well as laterally into the host. The cap might also act as an insulator promoting the transformation of amorphous silica to more stable silica polymorphs (Oehler 1976a,b). This model for ironstone growth is similar to that for generation of massive sulfide mounds, where a low-permeability crust causes higher temperature fluids to circulate in the mound. This results in the upward migration of isotherms, and so remobilisation and replacement of early sulfides by higher temperature mineral assemblages (zone refinement; e.g. Large, 1992).

The upward termination of the ironstone lenses at Trooper Creek prospect indicates that the hydrothermal system was self sealing or that hydrothermal activity was confined to the time interval between deposition of the pumice breccia and the deposition of the overlying siltstone. Alternatively the siltstone may have acted as an aquitard. Weak hematite alteration of siltstone overlying some ironstone lenses suggests this was important. Intense silica-hematite alteration of units in the immediate footwall to some ironstone lenses may represent poorly confined feeder zones for mineralising hydrothermal solutions. Marginal to the feeder zones diffuse fluid flow deposited weak-moderate disseminated hematite in poorly silicified pumice breccia and andesite scoria breccia. There is clear evidence for topography on the Cambrian surface of the pumice breccia hosting horizon 1 ironstone. Rather than occupying the topographic lows, ironstone lenses replaced pumice breccia mantling palaeotopographic highs. Along with textures and discontinuous nature the ironstone lenses this evidence suggests the lenses are not deposits from brine pool accumulations. Replacement may have been promoted by flow of hydrothermal fluids down gradients within the pumice breccia, but mineralisation was dominantly a sub-seafloor process.

Ironstones related to cryptodomes and domes

In the dome/cryptodome model for iron oxide-silicate deposits, it is proposed that the mineralising fluids originate as pore waters in the volcano-sedimentary package and/or as seawater (Fig. 7.21). Intrusion or extrusion of magma causes heating the fluids along geothermal gradients. Depending on the permeability of the host lithologies, short lived, narrow, convection cells may develop around the cooling magma bodies. Fluids moving along fractures in the brecciated carapace of the lavas/intrusions attain Fe, Si and other elements by the leaching of glass and mixing with magmatic fluids. The resulting mild-low temperature, oxidised fluids precipitate iron and silica by conductive cooling and mixing with cooler seawater or pore fluids. Iron oxide ± silica deposition may occur within the cooler glassy and/or brecciated parts of intrusions which are the heat engine for convection, in already cooled domes or intrusions, or in the enclosing volcanosedimentary package. Hydrothermal fluids which access syn-volcanic faults may reach the seafloor and accumulate near the vent after discharge or be dispersed in the water column from buoyant plumes. The resulting deposit are likely to be thin and possibly laterally continuous.

That mineralising hydrothermal systems develop around syn-volcanic intrusions is supported by recent observations of the seafloor. For example, hydrothermal mineralisation within the rift floor of the Guyamus Basin, Gulf of California, results from short-lived exhalations of pore water following emplacement of shallow basaltic intrusions (Einsele et al., 1980; Einsele, 1986). Similar hydrothermal systems can develop around lavas. For example, during the 1971-72 eruption of Soufriere volcano leaching of hot disintegrating glassy lava extruded subaqueously into a crater lake sourced ferrous irons to the lake waters. Precipitation of hematite in the sediments on

the crater floor followed oxidation of the convecting fluids (Sigurdsson, 1977).

7.9 Significance of ironstones to mineral exploration

Stratiform and discordant ironstone lenses occur throughout the Mount Windsor Volcanic belt. As illustrated in figure 22, ironstones may be genetically related to massive sulfide mineralisation (type 1; Fig 7.22A) or they may relate to localised, low temperature, sea water circulation around lavas and intrusions or explosive volcanic centres (type 2; Fig 7.22B). Type 2 ironstones are characterised by positive Eu anomalies and anomalous Zn, Ba, and Au. They are the deposits of high temperature, reduced fluids from large scale hydrothermal cells. Type 2 ironstones are characterised by negative Ce anomalies and although they may contain some Pb, Zn, and Cu, they are low in Ba. These ironstones deposit from oxidised, low temperature fluids, which are in equilibrium with feldspar (alkaline).

As some styles of massive sulfide mineralisation are hosted in the proximal facies association submarine volcanic centres type 2 ironstones are likely to be represented in these environments. This is the case at Highway-Reward. The Highway and Reward volcanogenic massive sulfide deposit are hosted by a volcano-sedimentary package dominated by syn-sedimentary intrusions, partly emergent cryptodomes, lava domes, and associated in situ and resedimented autoclastitic deposits. These facies represent a proximal facies association from intrabasinal, intrusive/extrusive, non-explosive mamgatism. Quartz-hematite replacing the matrix of hyaloclastite and peperite, and occurring as lenses in the host sequence to mineralisation, is interpreted to be the deposits from type 2 fluids related to emplacement of the lavas and intrusions. Intense pervasive hematite alteration occurs in small domains within the host volcanic sequence. This style of alteration is widespread in the Mount Windsor Volcanic belt and often occurs along the margins of lavas and intrusions. It is likely that this alteration style is unrelated to mineralisation but records the passage of a type 2 fluid through the volcanic rocks.

7.10 Conclusions

Careful elucidation of the volcanic facies and facies architecture has proven to be critical in unravelling the significance and emplacement processes of the iron oxide ± silica rocks in the Trooper Creek Formation. Deformation and metamorphism modify ironstone textures but do not destroy facies relationships which allow for interpretation of ironstone geochemistry, depositional mechanisms and environments. Consideration of iron oxide ± silica rocks without attention to the character and emplacement processes of associated volcanic facies may obscure important textural and facies information that provide a framework for interpreting iron oxide-silica rocks and their significance in mineral exploration.

In the study area, ironstones are associated with differing volcanic facies whose physical properties, mineralogy and depositional environment vary. Quartz-hematite ironstone occurs as pods within coherent facies of lava domes and cryptodomes, as lenses which are the discontinuous facies equivalent of non-welded pumice breccia, and as pods and finely laminated beds in chert. Hematite-quartz ± carbonate also occurs as veins and seams in coherent rhyolite-dacite and as an alteration of the matrix in hyaloclastite and peperite along margins of lavas and cryptodomes.

Field relationships and relict volcanic textures indicate that many ironstone lenses are replacements of pumice breccia rather than seafloor exhalative deposits. The transition in mineralogy and textures passing from massive ironstone, through pyroclast-rich ironstone, into hematite altered pumice breccia record progressive stages in the alteration of the pumiceous precursor. Replacement occurred at or near the seafloor but was not excessively deep as clasts derived from the ironstone were incorporated into volcaniclastic mass flows overlying some ironstones.

The mineralogy, rare earth element geochemistry, and textures suggest that the ironstones deposited from oxidised, low temperature hydrothermal, alkaline to acid fluids. The ironstones are barren, characterised by negative Eu anomalies, and distinct

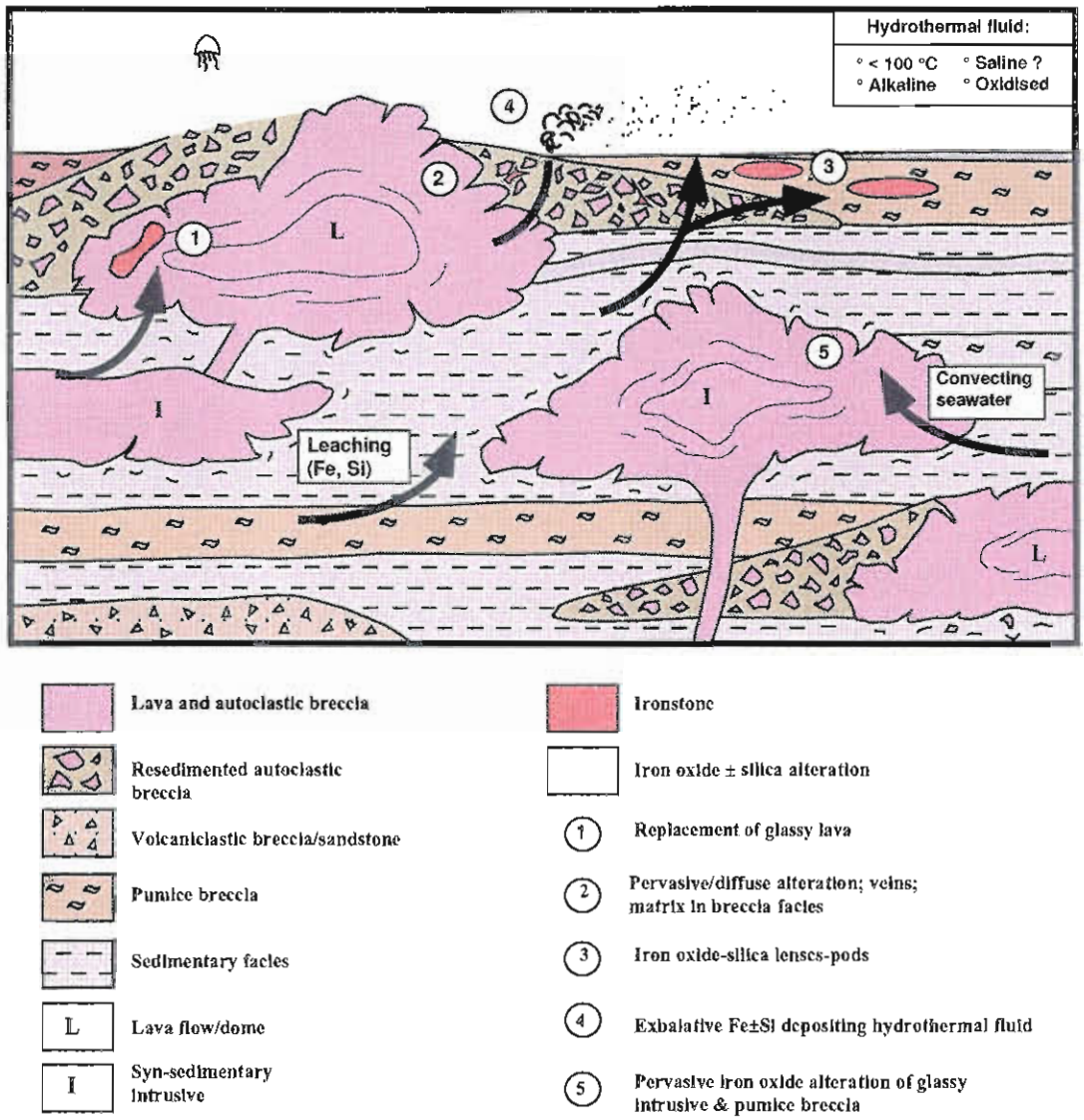

Figure 7.21 Dome/cryptodome model for ironstone emplacement. Convection of seawater and pore-water around a lava domes and cryptodomes. Circulating fluids leach Fe and Si from the surrounding volcanic pile. The hydrothermal fluid precipitates Fe and Si by mixing with seawater and conductive cooling. Ironstones may be deposited at the margin of the cooling intrusion-extrusion, within the enclosing volcanic package, or discharge onto the seafloor.

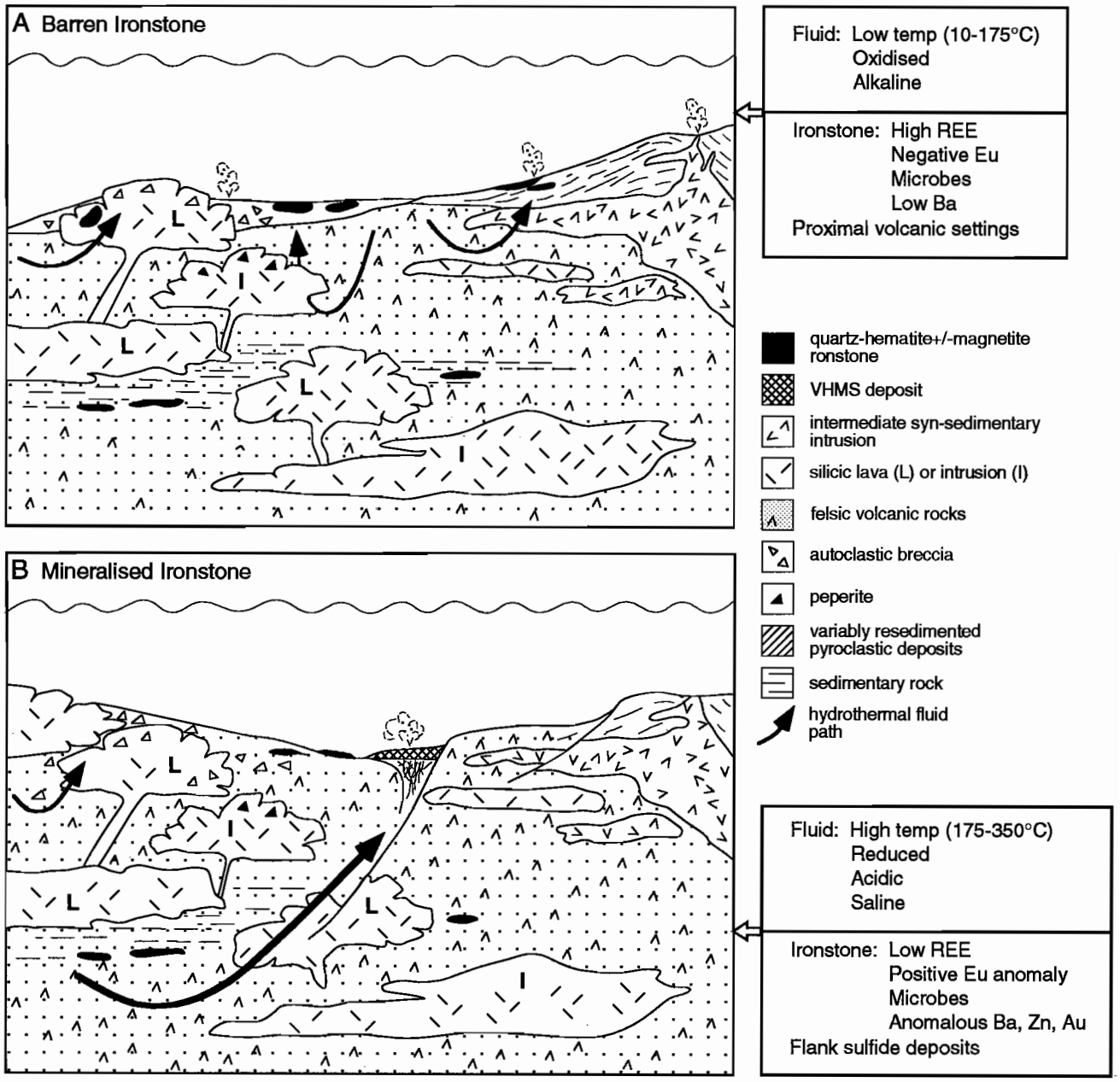

Figure 7.22 — Summary models for the formation of ironstones in the Mount Windsor Volcanic belt. (A) Barren ironstones related to the development of local hydrothermal cells at shallow levels in the volcanic pile. These are interpreted to form in response to convection of seawater and pore water driven by shallow intrusion-extrusion of magma. (B) Ironstones associated with VHMS mineralisation form in response to the development of larger scale hydrothermal cells. Those spatially associated with mineralisation are characterised by a distinct geochemical signature. Barren ironstones may form during the waxing and waning stages of mineralisation and in response to volcanism.

from ironstones flanking massive sulfide mineralisation at Thalanga.

The barren ironstones are interpreted to result from the development of short-lived, local hydrothermal systems in the proximal facies association of submarine- to littoral-volcanoes and around lavas and syn-sedimentary intrusions. Intrusion-extrusion of magma causes heating of pore water and convection of sea water in the enclosing volcanic package. Fluids leach Fe, Si and other elements during alteration of the glassy volcanic rocks and mix with magmatic fluids exsolved from the magma. The resulting fluids precipitate iron and silica by conductive cooling and mixing with seawater or pore fluids. Iron oxide-silica deposition can occur within the cooler glassy parts of the lava or intrusion(s) which is the heat engine for convection, in already cooled lavas or intrusions, or in the enclosing volcanic package. Hydrothermal fluids which reach the seafloor may accumulate at the vent after discharge or be dispersed in the water column from buoyant plumes.

References

Adachi M., Yamamoto K. and Sugisaki R., 1986. Hydrothermal chert and associated siliceous rocks from the northern Pacific: their geological significance. Sedimentary Geology, 47: 125-148.

Allen R.L. and Hunns S.R., 1990. Excursion Guide E1. The Mount Read Volcanics and related ore deposits. In: 10th Aust Geol Conv, Hobart, 15-27.

Alt J.C., 1988. The chemistry and sulfur isotope composition of massive sulfide and associated deposits on Green Seamount, eastern Pacific. Econ. Geol., 83: 1026-1033.

Alt J.C., Lonsdale P., Haymon R. and Muehlenbachs K., 1987. Hydrothermal sulfide and oxide deposits on seamounts near 21¡ N, East Pacific Rise. Geol. Soc. Am. Bull., 98: 157-168.

Barley M.E., 1992. A review of Archean volcanic-hosted massive sulfide and sulfate mineralisation in Western Australia. Econ. Geol., 87: 855-872.

Barrett T.J., Jarvis I. and Jarvis K.E., 1990. Rare earth element geochemistry of massive sulfide-sulfates and gossans on the Southern Explorer Ridge. Geology, 18: 583-586.

Barrett T.J., Jarvis I., Longstaffe F.J. and Farquhar R., 1988. Geochemical aspects of hydrothermal sediments in the Eastern Pacific Ocean. Canadian Mineralogist, 26: 841-858.

Bauld J., D'Amelio E. and Farmer J.D., 1992 Modern microbial mats. In: Schopf, J. and Klein, C. (eds.) The Proterozoic biosphere - A multidisciplinary study. Cambridge University Press, 261-269.

Berry R.F., Huston D.L., Stolz A.J., Hill A.P., Beams S.D., Kuronen U. and Taube A., 1992. Stratigraphy, structure, and volcanic-hosted mineralisation of the Mount Windsor Subprovince, north Queensland, Australia. Econ. Geol., 87: 739-763.

Binns R.A., Scott S.D., Bogdanov Y.A., Lisitzin A.P., Gordeev V.V., Gurvich E.G., Finlayson E.F., Boyd T., Dotter L.E., Wheller G.E. and Muravyev K., 1993. Hydrothermal oxide and gold-rich deposits of Franklin Seamount, Western Woodlark Basin, Papua New Guinea. Econ. Geol., 88: 2122-2153.

Boyd T., Scott S.D. and Hekinian R., 1993. Trace element patterns in Fe-Si-Mn Oxyhydroxides at three hydrothermally active seafloor regions. Resource Geology Special Issue, 17: 83-95.

Boynton W.V., 1984 Geochemistry of the rare earth elements: meteorite studies. In: Henderson, P. (eds.) Rare earth element geochemistry. Elsevier, 63-114.

Braithwaite R.L., 1974. The geology and origin of the Rosebery ore deposit, Tasmania. Econ. Geol., 69: 1086-1101.

Burne R.V. and Moore L.S., 1987. Microbialites: Organosedimentary deposits of benthic microbial communities. PALAIOS, 2: 241-254.

Campbell I.N.H., Lesher C.M., Coad P., Franklin J.M., Gorton M.P. and Thurston P.C., 1984. Rare-earth element mobility in alteration pipes below massive Cu-Zn sulfide deposits. Chem. Geol., 45: 181-202.

Davidson G., Stolz A.J. and Eggins S.M., 1996. Exhalite geochemistry: A preliminary geochemical documentation of two barren ferruginous chert bodies in the Mount Windsor Volcanics. CODES, University of Tasmania.

Davis E.E. and Villinger H., 1992. Tectonic and thermal structure of the Middle Valley Sedimented Rift, Northern Juan De Fuca Ridge. Proc ODP, Initial Reports, 139: 9-41.

Davis L.W., 1975. Captains Flat lead-zinc orebody. Australasian Inst Mining Metallurgy Mon, 5: 694-700.

Doyle M.G., 1994 Facies architecture of a submarine volcanic centre: Highway-Reward, Mount Windsor Volcanics, Canbro-Ordovician, Northern Queensland. In: Henderson, R. A. and Davis, B. K. (eds.) New developments in geology and matallogeny: Northern Tasman Orogenic Zone. EGRU Contribution, 50: 149-150.

Doyle M.G. and McPhie J., 1994. A silicic submarine syn-sedimentary intrusive-dome-hyaloclastite host sequence to massive sulfide mineralisation: Mount Windsor Volcanics, Cambro-Ordovician, Australia. In: International Volcanological Congress, IAVCEI, Ankara, Turkey, Theme 10.

Duhig N.C., Davidson G.J. and Stolz J., 1992. Microbial involvement in the formation of Cambrian sea-floor silica-iron oxide deposits, Australia. Geology, 20: 511-514.

Duhig N.C., Stolz J.S., Davidson G.J. and Large R.R., 1992. Cambrian microbial and silica gel textures in silica iron exhalites from the Mount Windsor Volcanic Belt, Australia: Their petrography, chemistry, and origin. Econ. Geol., 87: 764-784.

Einsele G., 1986. Interaction between sediments and basalt injections in young Gulf of California-type spreading centres. Geol. Rund., 75: 197-208.

Einsele G., Gieskes J.M., Curray J., Moore D.M., Aguayo E., Aubry M.P., Fornari D., Guerreo J., Kaster M., Kelts K., Lyle M., Mato Y. and others, 1980. Intrusion of basaltic sills into highly porous sediments, and resulting hydrothermal activity. Nature, 283: 441-445.

Fouquet Y., Stackelberg U.v., Charlou J.L., Erzinger J., Herzig P.M., Muhe R. and Wiedicke M., 1993. Metallogenesis in back-arc environments: The Lau Basin example. Econ. Geol., 88: 2154-2181.

Fournier R.O., 1985. The behaviour of silica in hydrothermal solutions. Reviews in Economic Geology, 2: 45-61.

German C.R., Klinkhammer G.P., Edmond J.M., Mitra A. and Elderfield H., 1990. Hydrothermal scavenging of rare-earth elements in the ocean. Nature, 345: 516-518.

Graf J.L., 1977. Rare earth elements as hydrothermal tracers during the formation of massive sulfide deposits in volcanic rocks. Econ. Geol., 72: 527-548.

Grant J.A., 1986. The isocon diagram-A simple solution to Gresens' equation for metasomatic alteration. Econ. Geol., 81: 1976-1982.

Green G.R. and Iliff G., 1989. Rosebery. In: Burrett, C. and Martin, E. (ed.) Geology and Mineral Resources of Tasmania. Geological Society of Australia Special Publication, Hobart, 132-137 pp.

Green G.R., Solomon M. and Walshe J.L., 1981. The formation of the volcanic-hosted massive sulfide ore deposit at Rosebery, Tasmania. Econ. Geol., 304-338:

Hannington M.D., Jonasson I.R., Herzig P.M. and Peterson S., 1995 Physical and chemical processes of seafloor mineralisation at Mid-Ocean Ridges. In: Humphries, S., Zierenberg, R., Mullineaux, L. and Thomson, R. (eds.) Seafloor hydrothermal systems: physical, chemical, biological, and geological interactions. Geophysical Monograph 91, 115-157.

Hannington M.D. and Scott S.D., 1988. Mineralogy and geochemistry of a hydrothermal silica-sulfide-sulfate spire in the caldera of axial seamount, Juan De Fuca Ridge. Canadian Mineralogist, 26: 603-625.

Hekinian R. and Fouquet Y., 1985. Volcanism and metallogenesis of axial and off-axial structures on the East Pacific Rise near 13¡N. Econ. Geol., 80: 221-249.

Hekinian R., Hoffert M., Larque« P., Chemine«e« J.L., Stoffers P. and Bideau D., 1993. Hydrothermal Fe and Si oxyhydroxide deposits from South Pacific intraplate volcanoes and East Pacific Rise axial and off-axial regions. Econ. Geol., 88: 2099-2121.

Herzig P.M., Becker K.P., Stoffers P., Backer H. and Blum N., 1988. Hydrothermal silica chimney fields in the Galapagos spreading centre at 86° W. Earth and Planetary Science Letters, 89: 261-272.

Holm N.G., 1987. Biogenic influences on the geochemistry of certain ferruginous sediments of hydrothermal origin. Chem. Geol., 63: 45-57.

Holm N.G., 1989. The $^{13}C/^{12}C$ ratios of siderite and organic matter of a modern metalliferous hydrothermal sediment and their implications for banded iron formations. Chem. Geol., 77: 41-45.

Hunns S.R., 1994b Geology of the Mount Chalmers volcanic-hosted massive sulfide, and implications for its formation. In: Holcombe, R., Stephens, C. and Fielding, C. (eds.) 1994 Field Conference: Capricorn region central coastal Queensland. Geological Society fo Australia, Queensland division, 80-92.

Hunns S.R., Zaw K., Large R.R., Dean J.A., Ryan C.G. and McPhie J., 1994a Preliminary geochemical results constraining the formation of the Mount Chalmers volcanic-hosted massive sulfide deposit. In: Henderson, R. and Davis, B. (eds.) New developments in geology and metallogeny: Northern Tasman Orogenic Zone. EGRU Contribution 50, 117-124.

Huston D.L., 1988. Aspects of the geology of massive sulfide deposits from the Balcooma district, Northern Queensland and Rosebery, Tasmania: Implications for ore genesis [Unpublished Ph.D thesis]. University of TAsmania, 380 pp.

Huston D.L., 1993. The effect of alteration and metamorphism on wall rocks to the Balcooma and Dry River South volcanic-hosted massive sulfide deposits, Queensland, Australia. Journal of Geochemical Exploration, 48: 277-307.

James H.L., 1954. Sedimentary facies of iron formations. Econ. Geol., 49: 235-293.

Janecky D.R. and Seyfried W.E.J., 1984. Formation of massive sulfide deposits on oceanic ridge crests: Incremental reaction models for mixing between hydrothermal solutions and seawater. Geochim Cosmochim Acta, 48: 2723-2738.

Juniper S.K. and Fouquet Y., 1988. Filamentous iron-silica deposits from modern and ancient hydrothermal sites. Canadian Mineralogist, 26: 859-869.

Kalogeropoulos S.I. and Scott S.D., 1983. Mineralogy and geochemistry of tuffaceous exhalites (Tetsusekiei) of the Fukazawa mine, Hokuroku district, Japan. Economic Geology Monograph, 5: 412-432.

Kalogeropoulos S.I. and Scott S.D., 1989. Mineralogy and geochemistry of an Archean tuffaceous exhalite: the Main Contact Tuff, Millenbach mine area, Noranda, Quebec. Can. J. Earth Sci., 26: 88-105.

Kimberley M.M., 1989. Exhalative origins of iron formations. Ore Geology Reviews, 5: 13-145.

Knoll A.H. and Simonson B., 1981. Early Proterozoic microfossils and penecontemporaneous quartz cementation in the Sokoman Iron Formation, Canada. Science, 211: 478-480.

Large R.R., 1977. Chemical evolution and zonation of massive sulfide deposits in volcanic terrains. Econ. Geol., 72: 549-572.

Large R.R., 1992. Australian volcanic-hosted massive sulfide deposits: features, styles, and genetic models. Econ. Geol., 87: 471-510.

Large R.R. and Both R.A., 1980. The volcanogenic ores at Mount Chalmers, eastern Queensland. Econ. Geol., 75: 992-1009.

Lilley M.D., Feely R.A. and Trefry J.H., 1995 Chemical and biochemical transformations in hydrothermal plumes. In: Humphris, S., Zierenberg, R., Mullineaux, L. and Thomson, R. (eds.) Seafloor hydrothermal systems: physical, chemical, biological and geological interactions. Geophysical Monograph, 91: 369-391.

Lottermoser B.G., 1989. Rare earth element study of exhalites within the Willyama Supergroup, Broken Hill Block, Australia. Mineral. Deposita, 24: 92-99.

Lydon J.W., 1988. Ore deposit models #14. Volcanogenic massive sulphide deposits, Part 2: Genetic models. Geoscience Canada, 15: 43-65.

McKay W.J. and Hazeldene R.K., 1987. Woodlawn Zn-Pb-Cu sulfide deposit, New South Wales, Australia: An interpretation of ore formation from field observations and metal zoning. Econ. Geol., 82: 141-164.

McLennan S.M. and Taylor S.R., 1979. Rare earth element mobility associated with uranium mineralisation. Nature, 282: 247-250.

McPhie J., Doyle M.G. and Allen R.L., 1993. Volcanic Textures. CODES, University of Tasmania, Hobart, 198 pp.

Messenger P.R. and Taube A., 1994 The northern part of the Calliope Volcanic Assemblage, Mt Morgan-Dee Range area. In: Holcombe, R., Stephens, C. and Fielding, C. (eds.) 1994 Field Conference: Capricorn region, central coastal Queensland. Geological Society fo Australia, Queensland division, 46-63.

Michard A., 1989. Rare earth element systematics in hydrothermal fluids. Geochemica et Cosmochimica acta, 53: 745-750.

Michard A. and Albarde F., 1986. The REE content of some hydrothermal fluids. Chem. Geol., 55: 51-60.

Michard A., Albarde F., Michard G., Minister J.F. and Chalou J.L., 1983. Rare-earth elements and uranium in high-temperature solutions from the East Pacific Rise hydrothermal vent field (13¡N). Nature, 303: 795-797.

Norish K. and Hutton J.T., 1969. An accurate X-ray spectrographic method for analysis of a wide range of geologic samples. Geochim Cosmochim Acta, 33: 431-454.

Norrish K. and Chapell B.W., 1977 x-ray fluorescence spectrography. In: Zussman, J. (eds.) Physical methods in determinative mineralogy. New York, Academic Press, 161-214.

Oehler J.H., 1976a. Experimental studies in Precambrian paleontology: Structural and chemical changes in blue-green algae during simulated fossilization in synthetic chert. Geol. Soc. Am. Bull., 87: 117-129.

Oehler J.H., 1976b. Hydrothermal crystallization of silica gel. Geol. Soc. Am. Bull., 87: 1143-1152.

Ohmoto H., Mizukami M., Drummond S.E., Eldridge C.S., Pisutha-Arnond V. and Lenagh T.C., 1983 Chemical processes of Kuroko Formation. In: Ohmoto, H. and Skinner, B. (eds.) The Kuroko deposits and related volcanogenic massive sulfide deposits. Economic Geology Monograph, 5: 433-438.

Olivarez A.M. and Owen R.M., 1991. The europium anomaly of seawater: implications for fluvial versus hydrothermal REE inputs to the oceans. Chem. Geol., 92: 317-328.

Pottorf R.J. and Barnes H.L., 1983 Mineralogy, geochemistry, and ore genesis of hydrothermal sediments from the Atlantis II Deep, Red Sea. In: Ohmoto, H. and Skinner, B. (eds.) The Kuroko and related volcanogenic massive sulfide deposits. Economic Geology Monograph 5, 198-223.

Renaut R.W. and Owen R.B., 1988. Opaline cherts associated with sublacustrine hydrothermal springs at Lake Bogoria, Kenya Rift valley. Geology, 16: 699-702.

Ridler R.H., 1971. Analysis of Archean volcanic basins in the Canadian Shield using the exhalite concept. Canadian Mining and Metallurgy Bulletin, 64: 20.

Rimstidt J.D. and Barnes H.L., 1980. The kinetics of silica-water reactions. Geochim Cosmochim Acta, 44: 1683-1699.

Rollinson H., 1993. Using geochemical data: evaluation, presentation, interpretation. Longman scientific and technical, 352 pp.

Sato T., 1972. Behaviours of ore-forming solutions in seawater. Mining Geology, 22: 31-42.

Schandl E.S. and Gorton M.P., 1991. Postore mobilisation of rare earth elements at Kidd Creek and other Archean massive sulfide deposits. Econ. Geol., 86: 1546-1553.

Sigurdsson H., 1977. Chemistry of the crater lake during the 1971-72 Soufri_re eruption. J. Volcanol. Geotherm. Res., 2: 165-186.

Solomon M., Walshe J.L. and Heinrich C.A., 1990. The formation of Rosebery-type volcanogenic massive sulfide deposits. In: Geological Society of Australia Abstracts

Stolz A.J., 1991 Stratigraphy and geochemistry of the Mt Windsor Volcanics and associated exhalites. In: Pongratz, J. and Large, R. (eds.) Geological controls on VMS mineralisation in the Mt Windsor Volcanic Belt-Research Report N0. 2. Centre for Ore Deposit and Exploration Studies, University of Tasmania, 23-83.

Sverjensky D.A., 1984. Europium equilibria in aqueous solutions. Earth and Planetary Science Letters, 67: 70-78.

Taube A., 1986. The Mount Morgan gold-copper mine and environment, Queensland: A volcanogenic massive sulfide deposit associated with penecontemporaneous faulting. Econ. Geol., 81: 1322-1340.

Taube A. and Messenger P., 1994 Volcanic stratigraphy of the Dee Range: a new prospective on Mt Morgan. In: Henderson, R. and Davis, B. (eds.) New developments in geology and metallogeny: Northern Tasman Orogenic Zone. 85-87.

Tivey M.K. and Delaney J.R., 1986. Growth of large sulfide structures on the Endeavour segment of the Juan de Fuca Ridge. Earth and Planetary Science Letters, 77: 303-317.

Tsutsumi M. and Ohmoto H., 1983 A preliminary oxygen isotope study of Tetsusekiei ores associated with the Kuroko deposits in the Hokuroku district, Japan. In: Ohmoto, H. and Skinner, B. (eds.) The Kuroko deposits and related volcanogenic massive sulfide deposits. Economic Geology Monograph, 5: 433-438.

Walter M.R. and Hoffman H.J., 1983 The paleontology and palaeoecology of Precambrian iron-formations. In: Trendall, A. and Morris, R. (eds.) Iron Formations: Facts, problems. Elsevier, 373-400.

Williams L.A. and Crerar D.A., 1985. Silica Diagenesis, II. General mechanisms. J. Sediment. Petrol., 55: 312-321.

Williams L.A. and Parks G.A., 1985. Silica Diagenesis, I. Solubility controls. J. Sediment. Petrol., 55: 301-311.

Rosebery alteration study

Rodney Allen and Ross Large

Volcanic Resources Limited, Stavanger, Norway and Centre for Ore Deposit and Exploration Studies, Geology Department, Univerity of Tasmania.

Introduction

The aims of the project are to determine the physical character, timing relationships, and geochemistry of carbonate alteration along drill hole traverses through A-B and K ore lenses at the north end of the Rosebery mine (Figure 1). The alteration and geological context of the alteration are to be studied in the footwall, hangingwall, ore zone and along strike, in order to establish physical, geochemical and isotopic vectors to ore. Other details of the project were reported previously (November 1995, May 1996). Due to a request from Pasminco Exploration the Rosebery alteration study has been reduced in size, and partly in scope. Currently it is anticipated that 9 or 10 drill holes from the north end of the mine will be logged and sampled (Figure 1).

Work completed to date

Since the last report, drill core samples collected during the summer from seven drill holes have been prepared for geochemical analysis, thin rock slices of each sample have been polished for textural study, and thin sections have been made from about half the samples (100 thin sections). Detailed petrographic descriptions have been made on thin sections from drill hole 120R, which passes through K lens. Examples of the petrographic descriptions are provided in the appendix, and a geological log of drill hole 120R, showing sample locations, was provided in the May 1996 report.

The physical character and timing relationships of the carbonate alteration will be documented in detail once the remaining drill cores and thin sections have been studied. However, some brief preliminary results are given below.

Carbonate textures

Table 1 provides a summary of carbonate textures in the Rosebery–Hercules area. This compilation is based on results from this study, previous observations (e.g. Allen and Hunns, 1990), and the results of Hill and Orth (1995). This is very much work in progress and will be modified and expanded in the future.

One very important set of timing relationships that is confirmed from the current drill core logging and petrographic work is that the nodular carbonate alteration that is closely associated with ore at both Rosebery and Hercules, pre-dates the earliest known diagenetic and tectonic fabrics in the rocks (S1 bedding-parallel, stylolitic foliation). The earliest event recorded in the rocks is clay/phyllosilicate alteration of the surfaces of undeformed glass shards and pumice clasts. The remainder of the partly altered shards and pumice was then replaced, infilled and enclosed by the nodular or spotty carbonate (see descriptions in the Appendix). The carbonate nodules and spheroids behaved as very competant domains during subsequent deformation, with the result that the shards and pumice within the carbonate nodules are now still undeformed, even in otherwise strongly foliated rocks. If the carbonate nodules developed late in the diagenetic history of the rocks, or during compressional deformation, then the delicate, metastable glass shards would show the texturally destructive effects of this history. These results

confirm the conclusion first made by Allen (1989, 1991) that the carbonate nodules have replaced pumiceous debris at the top of the footwall volcanic pile, almost directly after deposition, and prior to all compressional diagenetic and tectonic deformation. The clear, direct relationship between the nodular carbonate alteration and the ore, therefore implies that the ore also formed during early diagenesis of the volcanic pile.

Subsequent carbonate generations such as rhombic overgrowths and recrystallization, and most carbonate veins, represent: (1) redistribution of the early nodular carbonate alteration during further hydrothermal and tectonic events, (2) redistribution of carbonate components within the hangingwall black slates and mass flow units, and (3) the possible net influx of new carbonate during deformation and metamorphism.

Chemical differences between the various carbonate textural types and generations, and chemical changes with distance from ore are at present unknown, but will be studied in the future.

Future plans

The next step is to finish geological logging and sampling of the remaining 2-3 drill holes. This should be completed in November. Following this the thin sections from all holes will be studied, and whole rock, trace element and carbonate analyses will be carried out. Polished rock slices, thin sections and geochemical samples have all been taken from the same samples so that the physical and chemical features of the alteration can be correlated.

References

Allen, R.L., 1989. Unpublished geological plans and sketches filed with Pasminco Mining Rosebery (partly reproduced in Allen and Hunns, 1990).

Allen, R.L., 1991. Stratigraphy, structure, volcanology and ore genesis of the Rosebery–Hercules ZnPbCuAu massive sulphide district, Tasmania. Unpublished report to Pasminco Exploration, Melbourne Australia. 3 volumes.

Allen, R.L. and Hunns, S.R., 1990. Geology of the Hercules and South Hercules orebodies, and Hercules excursion stops. *In* Corbett, K. & Large, R. (Eds): Excursion guide E1 - The Mount Read Volcanics and associated ore deposits. 10th Australian Geological Convention, Hobart: 15-27.

Hill, A., and Orth, K., 1995. Textures and origins of carbonate associated with the volcanic-hosted massive sulphide deposit at Rosebery, Tasmania. AMIRA-ARC project P439, Report 1, November 1995, p. 129-141.

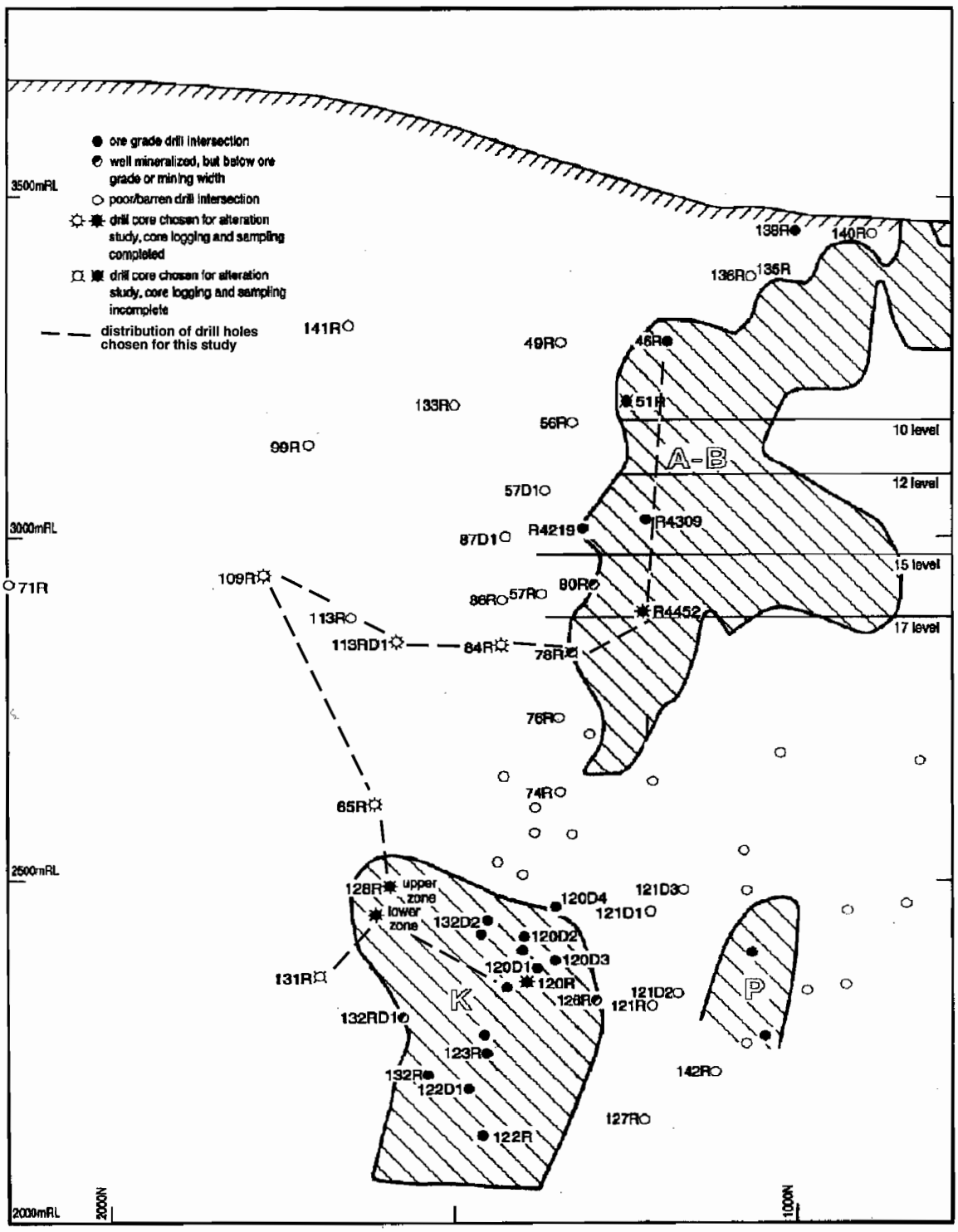

Figure 1
Longitudinal section of the north end of Rosebery mine, showing the location of A-B, K and P ore lenses, drill core intersections of the ore stratigraphic position, and drill cores selected for this study.

Table 1
Carbonate alteration textures in the Rosebery-Hercules area (work in progress).

Texture		Variations	Internal structure variations	Examples
Nodular or spotty				
Large nodules	(1 cm - 2 m diameter nodules)	- Dispersed - Intergrown	- Massive granular, or - Concentric layering	Hercules 4-level road
Spheroidal	(0.2 mm - 1 cm diameter spheroids of anhedral grains)	- Dispersed, distinct spheroids - Close-packed, intergrown	- Distinct fine concentric layering - Faint concentric layering	Rosebery 120R 1361.4m Rosebery + Hercules
Spheroidal-rhombic	(0.5 mm - 1 cm diameter spheroids composed entirely of, or with rim of radiating rhombs)	as above	as above	
Rhombic	(0.2 mm - 1 cm rhombs)	- Dispersed - Random intergrowth	- Concentric zoning - Unzoned	
Lozenge	(0.2 mm - 1 cm lozenge-shaped grains)	- Dispersed - Close-packed, intergrown	- Concentric zoning	Rosebery 120R 1364.4m
Platey	(5 mm - 3 cm tabular laths or plates ?after anhydrite, gypsum)	- Dispersed - Interlocking network	- Massive	Hercules E of M-Lode
Blebby	(≤ 10 cm irregular patches)	- Dispersed - Interconnected	Not massive, no distinct spheroidal texture	
Massive	(irregular compact granular masses 5 cm - 2 m)	- Anhedral grains - Close-packed rhombs - Close-packed spheroids with carbonate-filled interstices	- Concentric zoned grains - Unzoned grains	
Impregnation	(filling or replacement of matrix within non-carbonate rock)	- Irregular patches - Pervasive over several metres	- anhedral, unzoned grains	Rosebery: base of hanging-wall mass flow unit 2a
Vein	(carbonate ± quartz veins and their alteration selvages)	- pre-S2 cleavage - syn-S2 - post-S2		Rosebery hangingwall
Limestone	(fine grained, compact, calcitic carbonate)	- Layer, bed - Clasts in mass flows	- Massive to foliated - Fossiliferous	- Thin beds in black slates - Clasts: HW unit 3a

Appendix

Example rock and thin section descriptions of some samples from drill hole 120R (see drill core log and sample locations given in the last report (Report 2, May 1996)

Sample number: **96-120R-1**

Rock and thin section description

Location: Drill hole 120R 1068.5 m; north end Rosebery mine

Hand specimen and summary: Upper part of Hangingwall Unit 3a pumice breccia mass flow unit. Plagioclase»qtz phenocrysts set in non-welded pumice clasts. Bleached, moderate q-ser-carb altered. Alteration comprises mosaics of fine grained feld-qtz»ser-carb enclosing strongly ser»carb altered feld phenocrysts and patches of ser»carb alteration. The rock has abundant fine qtz veinlets and lesser carb veinlets, despite the apparent paucity of veins in hand specimen.

Mineral percentages in thin section:

plagioclase	?50%	)__ 75%
quartz	?25-30%	)
sericite	15%	
carbonate	5%	
sphene-leucox	1%	
apatite, opaques	<1%	

Primary textures: Plagioclase phenocrysts (15-20%) » 1-2 % subhedral (subrounded, embayed) qtz phenocrysts, enclosed by moderately preserved, non-welded, round-vesicle pumice and glass shards. Couple of poorly feld-porphyritic rhyolite lithic clasts with faint relict perlitic texture.

Tectonic fabrics: One moderate foliation expressed by orientation of matrix sericite and elongation and partial transposition of pumice texture. Qtz crystals have undulose extinction and weak-moderate subgrain development.

Alteration, veins: 1% ≤0.2mm subplanar slightly wavy carb veins; appear post-S2; these cut two generations of qtz veins. Second is very fine grained, slightly murkey qtz>ser with 5% ?apatite, carb and ≤10% opaque ?sulphides. First generation qtz veinlets are cleaner, coarser grained with 2-5% tiny euhedral carb rhombs and subrounded high relief ?apatite. These qtz veinlets are moderately deformed, locally have ?S2 foliation, and are recrystallized; suggests syn-tectonic. Carbonate comprises medium brown carbonate (?Fe/Mn-bearing) and lesser pale brown to colourless carbonate.

Pumice porosity and original bubble walls are replaced by interpenetrating-twinned plagioclase (probably albite?), in turn variably replaced by sericite»carb in ser-carb-rich areas, and extensively by fine grained feld-qtz mosaic in siliceous, ser-carb-poor areas. Feldspar phenocrysts extensively, incompletely replaced by ser»carb. Many feldspar phenocrysts have relict plagioclase rims, partly replaced (but much less so than the phenocrysts) by very fine grained feld±qtz mosaics and to lesser extent by ser»carb. Plagioclase of the rims is commonly in optical continuity with the plagioclase of the phenocryst.

Interpretation/important relationships: Fine grained feld-qtz and ser»carb alterations post-date feldspar replacement of pumice. Ser»carb alteration is pre- or syn-S2 foliation. Ser»carb alteration has replaced feldspar phenocrysts more intensely than matrix feldspar, suggests a compositional control and that phenocryst feldspar is different composition to matrix secondary (alteration) feldspar.

Sample number: **96-120R-3**
Rock and thin section description

Location: Drill hole 120R, 1094.5 m; north end Rosebery mine

Hand specimen and summary: Lower crystal-lithic-rich part of Hangingwall Unit 3a pumice breccia mass flow unit. Plagioclase»qtz phenocrysts and lithic clasts enclosed by moderately-poorly preserved pumice and glass shards. Weak-moderate q-ser and biot-chl alteration. Disseminated Sp. Alteration mainly comprises extensive mosaic of fine grained feld>qtz»ser-carb-clinoz, and weak ser-altered feld phenocrysts. Biot ?overprints ser. The rock has minor qtz>carb veinlets.

Mineral percentages in thin section:

plagioclase	?50%	)__ 75%
quartz	?25%	)
sericite	7-10%	
biot	5%	
chlorite	3%	
carbonate	3-5%	
sphene-leucox	3%	
opaques (sp)	1%	
zircon	trace	

Primary textures: 35% 1.5 mm plag » qtz crystals, and several lithic clasts, enclosed by pumice-glass shard matrix. Pumice and shard textures only locally well preserved. One fine-grained, siliceous, aphyric rhyolite lithic with 5% streaky amygdales. One feld-biot-ser-rich, 10% feld-porphyritic, relict perlitic, felsic lava lithic. This lithic contains a few 0.12mm zircons.

Tectonic fabrics: One strong foliation expressed by orientation of matrix sericite and clinozoisite, beard pressure shadow growths on phenocrysts, and folding, elongation and partial transposition of pumice texture. Qtz crystals have undulose extinction and moderate subgrain development.

Alteration, veins: Rock has similar secondary feldspar alteration to that described in samples 96-120R-1 and 2, however, the fine grained recrystallization of originally coarse secondary feldspar is more advanced. Plagioclase phenocrysts are relatively well preserved, with only weak replacement by sericite » carb. Pale brown biot occurs in sericitic areas, including in the matrix and within the feldspar phenocrysts, and appears to replace sericite. The biot is commonly intergrown with chl and appears altered/retrograded to the chl. Minor, deformed, foliated, ≤0.5mm qtz>carb»ser veinlets.

Sphene is abundant, and is both irregularly disseminated throughout, and occurs as diffuse stylolitic "veins" (S1 foliation), which are strongly foliated and folded by S2-F2.

Carbonate is clean, almost clear (?Fe/Mn-poor).

Opaques are mainly irregular dissemination/impregnation of streaky (foliated) sphalerite. Sp appears pre- to early-S2.

Interpretation/important relationships: Sphalerite is disseminated rather than vein related, and appears pre-S2. Fine grained feld±qtz and ser alterations post-date feld replacement of pumice. Earliest preserved feld replacement of pumice is untwinned optically continuous feld; this replaced/recrystallized to twinned coarse grained plag (albite), then in turn changes to fine grained plag±qtz mosaics. Minor carbonate is scattered throughout, but is concentrated in qtz-carb veinlets. Biotite-chl alteration appears to be the latest alteration stage, and could be Devonian granite-related.

Sample number: **96-120R-4**
Rock and thin section description

Location: Drill hole 120R, 1100.3 m; north end Rosebery mine

Hand specimen and summary: Lower crystal-lithic-rich part of Hangingwall Unit 3a pumice breccia mass flow unit. Intense carb-qtz alteration comprising veins and irregular patches (impregnations). Plagioclase»qtz phenocrysts and lithic clasts are well preserved and enclosed by extensively carb-replaced, originally pumice-rich "matrix". Alteration assemblages have strong S2 foliation.

Mineral percentages in thin section:

plagioclase	?35%	)__ 65%
quartz	?30%	)
carbonate	25%	
sericite	7%	
chlorite	1-2%	
sphene-leucox	2%	
opaques (sp)	1%	

Primary textures: 40% Feld»qtz crystal-rich and lithic-rich pumice breccia similar to 96-120R-3. Feldspar phenocrysts are multiple-twinned plag » simple-twinned Kspar. Primary feldspars well preserved, but pumiceous matrix texture very poorly preserved due to replacement by carbonate and strong foliation. Two ser>chl-rich lenses are strongly foliated fiamme, or pseudofiamme of ser-chl-altered and foliated pumice.

Tectonic fabrics: One strong foliation expressed by orientation of carb, coarse grained qtz, ser-chl, and elongation and partial transposition of matrix ?perlite texture in the lithics. Qtz crystals locally have undulose extinction, but subgrain development is minor. The fiamme-like lenses are strongly S2 foliated and oriented mainly parallel to S2, but locally diverge from S2 orientation, and in these areas are crenulated by S2.

Alteration, veins: Very abundant (40-50%) coarse grained veins, up to several mm wide, both of qtz » carb and carb»qtz. Carb is very pale brown to clear, and twinned (?Fe/Mn-poor ?calcite-dolomite). The carbonate is common in carb-rich veins and as irregular carb-rich patches. Most carb crystals show strong preferred orientation parallel to S2, and consequently are inferred to have grown synchronous with S2. The irregular carb alteration patches occur preferentially in the pumiceous matrix, which is extensively obliterated by the carb. Interestingly, plag phenocrysts are only weakly ser-carb altered; more weakly altered than the samples further up-hole. Qtz in the q veins is moderately deformed and recrystallized to smaller aggregates of grains with strong preferred orientation parallel to S2. Chl is intergrown with ser, and the greatest concentration of both ser and chl is in the fiamme-like lenses. Sphene ± clinozoisite is abundant in one of these lenses, and is also disseminated through most of the rock, except the qtz-rich veins.

Many feldspar phenocrysts preserve thin relict rims, and internal fracture-fill veinlets, of untwinned secondary feldspar. The part of the matrix that is not extensively replaced by carbonate, comprises a fine grained mosaic of feld-qtz with lesser carb and ser.

Interpretation/important relationships: The strong S2 fabric in the carb and qtz alteration and veins, indicates growth (or recrystallization) of these minerals during S2 development. The qtz and carb alteration must therefore be pre- or syn-S2. The fiamme-like lenses are probably S1-parallel fiamme that are strongly transposed into the S2 foliation.

Sample number: **96-120R-9**

Rock and thin section description

Location: Drill hole 120R, 1229.3 m; north end Rosebery mine

Hand specimen and summary: Lower part of upper of two black slate units; Unit 1 of hangingwall succession. Fine parallel syn-tectonic qtz-carb veining. Strong S2 foliation.

Mineral percentages in thin section:

sericite	35%	
plagioclase	?5%	)__ 40%
quartz	?35%	)
carbonate	10%	
graphite/carbon	10%	
sphene-leucox	2%	
opaques (pyrh-py-sp)	2%	

Primary textures: Rare: local relict primary lamination at high angle to cleavage; comprises 0.5-1mm bands of coarser grained qtz-feld-opaques-sphene-leucoxene.

Tectonic fabrics: One strong pervasive slatey cleavage = S2. Locally there is a faint but distinct S1 foliation parallel to bedding (primary lamination). The qtz-carb veins are boudinaged (veins have strong pinch and swell morphology) and foliated by S2. The cleavage is slightly oblique to

the veins, and has a moderately anastomosing style. The veins are planar, whereas the faint primary lamination is folded (by F2-S2).

Alteration, veins: Similar to 96-120R-8, but more veinlets and more carb, and there is a subordinate synchronous qtz-carb vein set oblique to the main set. 35% of the rock comprises thin (≤5mm, average 0.4mm), parallel, qtz>carb»ser-sulphide veinlets and carb>qtz»ser-sulphide veinlets. Qtz in the veins is mainly fine grained anhedral mosaics, recrystallized from original larger qtz grains. Almost all sulphides occur as coarse euhedral crystals and blebs within the veins. Most or all of the carb appears to be in the veins. The carbonate is white calcitic in handspecimen, and pale non- to very weakly pleochroic in plane polarised light in thin section.

Interpretation/important relationships: Most likely the qtz-carb veins developed early during the S2-F2 deformation, and were themselves deformed by S2.

Sample number: 96-120R-10
Rock and thin section description

Location: Drill hole 120R, 1237.2 m; north end Rosebery mine

Hand specimen and summary: Upper part of upper interval of TSV (host rocks), between black slate units. Very strong carb>ser>chl alteration, mainly of matrix to phenocrysts. Strong S2 foliation.

Mineral percentages in thin section:

carbonate	40%
plagioclase	30%
sericite	15%
quartz	?7%
chlorite	3%
sphene-leucox	1-2%
opaques (py-pyrrh)	3%

Primary textures: The rock has the relict primary texture of a moderate to well sorted, feld crystal-lithic sandstone. Crystals: 60-70% of rock originally; average1.2mm; all plagioclase, commonly with concentric zoning (this zoning much more prominent than in hangingwall sequence). Lithics: 7% of rock; all same textural and compositional type; probably andesitic; <5% small phenocrysts (≤1mm) of feld » ilmenite/magnetite; fine granular feld-microlitic to micropoikilitic devitrified, feldpar-rich groundmass, with 2-5% fine dusting of opaques (?mag, ilmen, sphene, py) and ≤10% very fine chl laths; similar to lithics in the Rosebery-Hercules footwall pumice breccia.

Tectonic fabrics: One strong pervasive foliation-lineation expressed by orientation of carb, ser, chl, and beard growths on phenocrysts. Cross-cutting carb>qtz veins are less deformed.

Alteration, veins: Very strong carb>ser alteration comprising: Feld crystals moderately to strongly ser≥carb altered. Lithics have only weak ser-chl-carb alteration. Matrix and local larger patches (i.e. including feld crystals) have intense carb > ser > chl replacement. This cut by younger coarse grained carb»qtz veins with little or no foliation (much less than the alteration they cut). The carb is commonly foliated (occurs as elongate grains parallel to the foliation), and has only faint brownish tinge/dustgin (?Fe/Mn-poor ?calcite-dolomite). Sphene-leucoxene and opaques (sulphide) occur disseminated throughout, and in spaced, foliated, anastomosing stylolitic trails.

Interpretation/important relationships: Groundmass carb grew and/or recrystallized during S2 foliation development. Cross-cutting carb>qtz veins are younger than groundmass carb>ser alteration.

Sample number: 96-120R-17
Rock and thin section description

Location: Drill hole 120R, 1356.9 m; north end Rosebery mine

Hand specimen and summary: Top of spotty carbonate zone in top of footwall feldspar-phyric pumice breccia, above K lens mineralization. Intense carbonate>ser alteration. Moderate S2 foliation.

Mineral percentages in thin section:

carbonate	80%
sericite	11%
quartz	3%
opaques: py	5%
sp	<1%
sphene-leucox	1%

Primary textures: Primary textures obliterated except for faint, poorly preserved, probable round-vesicle pumice texture within a few of the earlier carbonate spheroids.

Tectonic fabrics: There is one moderate intensity, pervasive foliation-lineation (S2-L2) expressed by orientation of matrix ser, and beard growths on some carbonate spheroids. There is also weak development of an anastomosing S1 stylolitic foliation expressed by concentration of sphene-leucoxene and opaques. S1 clearly overprinted by S2.

Alteration, veins: Intense carbonate>sericite alteration, comprising three distinct types:

(1) Moderately deformed (S2), close-packed to moderately dispersed (matrix-supported), carbonate spheroids, with interstitial foliated (by S2) sericite and trails of py>sphene-leucoxene. The latter are subparallel to, and foliated by S2, and could be deformed S1-parallel bands. The carb spheroids are fractured, moderately dismembered and weakly foliated in response to S2 deformation. Fractures and interstices are filled with sericite. Extinction pattern of the deformed carbonate spheroids varies from radial to radial-mosaic to irregular mosaic extinction, and gradations between these styles occur. Most of the pyrite occurs in these domains as thin stringers with sphene-leucoxene and sericite.

(2) Two, 1-1.5 cm wide lenses (or veins) of massive intergrown spheroidal carbonate. These are pre-S2 (local beard growths), but are only weakly deformed. They preserve superb radial cross extinction. Most of the sphalerite and a minor part of the pyrite occurs in these domains as irregular anhedral blebs within carbonate.

(3) Veins or patches of very coarse grained carbonate with simple/normal extinction, and local abundant inclusions of small carbonate rhombs, qtz grains and sericite. These indicate the large carbonate grains grew over earlier formed grains. Growth could be pre- and/or syn-S2.

Most carbonate in all domains is dusty pale brown with pale carbonate-brown birefringence (only minor areas of bright colours in centre of some spheroids), and is probably Mn-Fe-bearing ?rhodocrositic carbonate.

Interpretation/important relationships: The gradations between radial, mosaic and simple/normal carbonate extinction suggest that they represent the various stages of increasing recrystallization (partly or mainly due to deformation) of originally fine-grained concretionary carbonate with radial extinction. The radial extinction probably reflects an original radial spherulitic growth pattern (formed during concretionary growth). The deformed carbonates, which contain most of the sulphide mineralization are pre-S2 in timing, and probably pre- to syn-S1.

Sample number: 96-120R-19 a, b
Rock and thin section description

Location: Drill hole 120R, 1364.4 m; north end Rosebery mine

Hand specimen and summary: Lower part of spotty carbonate zone in top of footwall feldspar-phyric pumice breccia, just above K lens mineralization. Intense carbonate-ser alteration. Strong S2 foliation.

Mineral percentages in thin section:

carbonate		60%
sericite		30%
quartz		4%
opaques:	py>sp	5%
sphene-leucox		1%

Primary textures: Completely undeformed glass shard and pumice textures are extremely well preserved in some of the carbonate spheroids. No primary textures are preserved outside the spheroids. These relict textures indicate that the primary character of the rock was a massive, uncompacted, vitric pyroclastic deposit with small

bubble-wall glass shards > round-vesicle pumice clasts > tube pumice. The shards and pumice are preserved by fine sericite alteration of their rims/surfaces. The cores of the thicker shards and pumice walls, and the fine vitric dust between the shards and pumices, and within the vesicles of the pumice, are all replaced by massive to faintly concentric banded carbonate.

Tectonic fabrics: There is one strong, pervasive foliation-lineation (S2-L2) expressed by orientation of matrix sericite, and beard growths on carbonate spheroids. There is also a weak foliation at a high angle to S2, expressed as an alignment of small carbonate spheroids and the sericite septa between the spheroids. This foliation could be S1. Carbonate spheroids are commonly fractured, dismembered and stretched in the S2-L2 fabric. Fractures are filled by sericite or new carbonate. The carbonate behaved as extremely competant bodies during deformation, in contrast to the readily foliated sericite.

Alteration, veins: Close-packed to dispersed, large (1-3 mm) carbonate spheroids, with faint concentric layering, set in a finer matrix of carbonate and foliated sericite. The spheroids have radial to radial-mosaic extinction. The carbonate of the "matrix" varies in texture, and includes:

(1) Close-packed to dispersed, small (0.2-0.8 mm), lozenge-shaped carbonate grains with internal concentric layering. The carbonate grains are separated by foliated sericite.

(2) Close-packed to dispersed, small (0.25 mm), spheroidal carbonate grains with internal concentric layering.

(3) Close-packed to dispersed, small (0.25 mm), rhombic carbonate grains with internal concentric layering.

Carbonate spheroids and matrix carbonate are pink-cream coloured in hand specimen and dusty pale brown with pale carbonate-brown birefringence in thin section (only minor areas of bright colours in centre of some spheroids). They are probably Mn-Fe-bearing ?rhodocrositic carbonate. Pyrite occurs as diffuse stringers subparallel to S2. Carbonate veins are minor, and are composed of paler carbonate as in sample 120R-18.

Interpretation/important relationships: The deformation style of the carbonate spheroids indicates they are pre-S2 in timing. The fine concentric layering of the spheroids indicates very early, concretionary growth in a very low stress environment. They must have grown during early diagenesis. The radial extinction probably reflects an original radial and concentric growth pattern (formed during concretionary growth). The amazingly well preserved glass shard and pumice textures, confined to within carbonate spheroids also indicate that the spheroids grew prior to any compaction of the strata and prior to S1 foliation. Carbonate spheroid growth was preceded by clay/phyllosilicate alteration of the surfaces of the glass shards and pumice. The shard-rich, relatively pumice poor character of the rock suggests it could be part of the fine, graded top of a coarser pumice breccia bed.

The Hercules–Mt Read traverse: Relationships between volcanic mineralogy, alteration and geochemistry

Ross R. Large
Centre for Ore deposit and Exploration Studies, Geology Department, University of Tasmania

Summary

Petrographic and geochemical studies of samples from the Hercules–Mt Read traverse allow the discrimination of samples into groups related to the intensity of alteration, mineralogy of alteration and geochemistry of alteration. Samples in the footwall pumice breccias at Hercules display a characteristic style and chemistry of alteration, distinct from the ore package samples and the hangingwall volcanic samples.

Alteration indices (Ishikawa AI, Chlorite/carbonate/pyrite Index and the Mn-carbonate Index) have proved useful in determining the facies of alteration and proximity to mineralisation.

Both strontium and the Ba/K_2O ratio are enriched in the volcanics surrounding the ore horizon, and require further evaluation as potential vectors to ore.

Introduction

Thirty-two rock samples were collected at regular intervals along a 5 km traverse crossing the Hercules VHMS deposit (Fig. 1), as part of our study of the relationship between volcanic facies, alteration and geochemistry surrounding massive sulphide deposits. This traverse was chosen because of the excellent outcrop through both the footwall and hangingwall volcanic sequences at Hercules. Locations of the samples, numbered MR96-46 to MR96-77 are shown in Figure 1. The samples have been analysed for major and trace elements and the results are presented in Table 1. A description of the volcanic facies and alteration textures will be provided in a subsequent report by Rod Allen. This report covers the alteration mineralogy and geochemistry. Previous alteration and oxygen isotope studies in the Hercules region are contained in Green and Taheri (1992).

Primary volcanic facies and composition

The traverse includes rhyolitic and dacitic volcanics of the Central Volcanic Complex. Rocks sampled to the west of Hercules, in the footwall sequence, are composed of altered rhyolitic pumice breccias while volcanics to the east of Hercules, and on Mt Read, comprise a complex volcanic facies association including rhyolitic pumice breccias (e.g MR96-63), intrusive quartz-feldspar ± biotite porphyries (e.g. MR96-67, 71), flow banded rhyolite lavas (e.g. MR96-71), rhyolitic volcaniclastics (e.g. MR96-73a) and feldspar phyric rhyolites (e.g. MR96-76). All the volcanic lithologies sampled are feldspar phyric and rare examples are quartz-feldspar phyric (e.g. MR96-71).

Due to the extensive hydrothermal alteration it is not possible to be certain about the primary volcanic composition of each sample. However, a study of the immobile elements Ti and Zr allows some preliminary interpretation. Previous studies (Large et al., 1989) have divided the CVC coherent volcanics into the following categories based on Ti/Zr ratios:

	Ti/Zr
Rhyolite	4 to 12
Dacite	12 to 20
Andesite	20 to 60
Basalt	60 to 120+

In Figure 2 it is apparent that all the traverse samples have a Ti/Zr ratio between 5 and 20. The footwall pumice breccias have a fairly constant ratio of 7 to 8 while the hangingwall facies show considerable variation from 5 to 19. Thus, the footwall sequence has a uniform rhyolitic composition, while the hangingwall sequence varies over the range rhyolite–rhyodacite–dacite. Samples immediately adjacent to the ore horizon (Fig. 2) show a higher Ti/Zr ratio of 12 to 15, possibly indicating a dacitic precursor lithology. However, these rocks are highly altered, and the possibility of mobility of Ti and/or Zr, leading to a spurious ratio, cannot be ignored.

Alteration mineralogy and geochemistry

Summary sheets highlighting the major features of the alteration mineralogy and geochemistry of each traverse sample are given in the Appendix. These sheets are designed to rapidly communicate to the reader the key features associated with volcanic alteration: alteration intensity, style, mineralogy, texture, alteration index (AI), chlorite index (CI), AI-CI box plot, and critical geochemical profiles of AI and Zn ppm.

In assessing the intensity, style and mineralogy of alteration, emphasis has been placed on the alteration of the groundmass ***and*** alteration of the plagioclase phenocrysts.

In simple terms, the alteration mineralogy along the traverse can be summarised as follows:

Lithology	Alteration
Footwall pumice	strong to intense sericite–breccias quartz ± chlorite ± pyrite (both groundmass and feldspar phenocrysts are replaced)
adjacent to ore zone	intense carbonate–chlorite–sericite–sulphides
hangingwall rhyolitic facies	weak to moderate sericite ± minor carbonate and chlorite restricted to groundmass alteration. Feldspar phenocrysts generally unaltered

In detail, the alteration is more complex than this and the reader is referred to the summary sheets for the alteration features of individual samples.

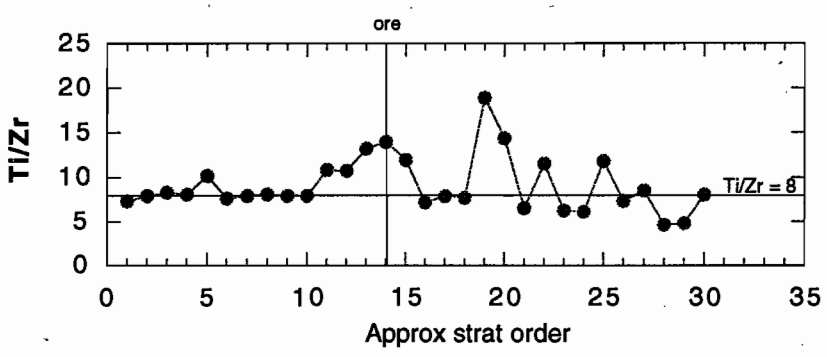

Figure 2
Ti/Zr ratio plot for samples along the Hercules–Mt Read Traverse. Note that the footwall pumice breccia has a consistent Ti/Zr ratio of 8.

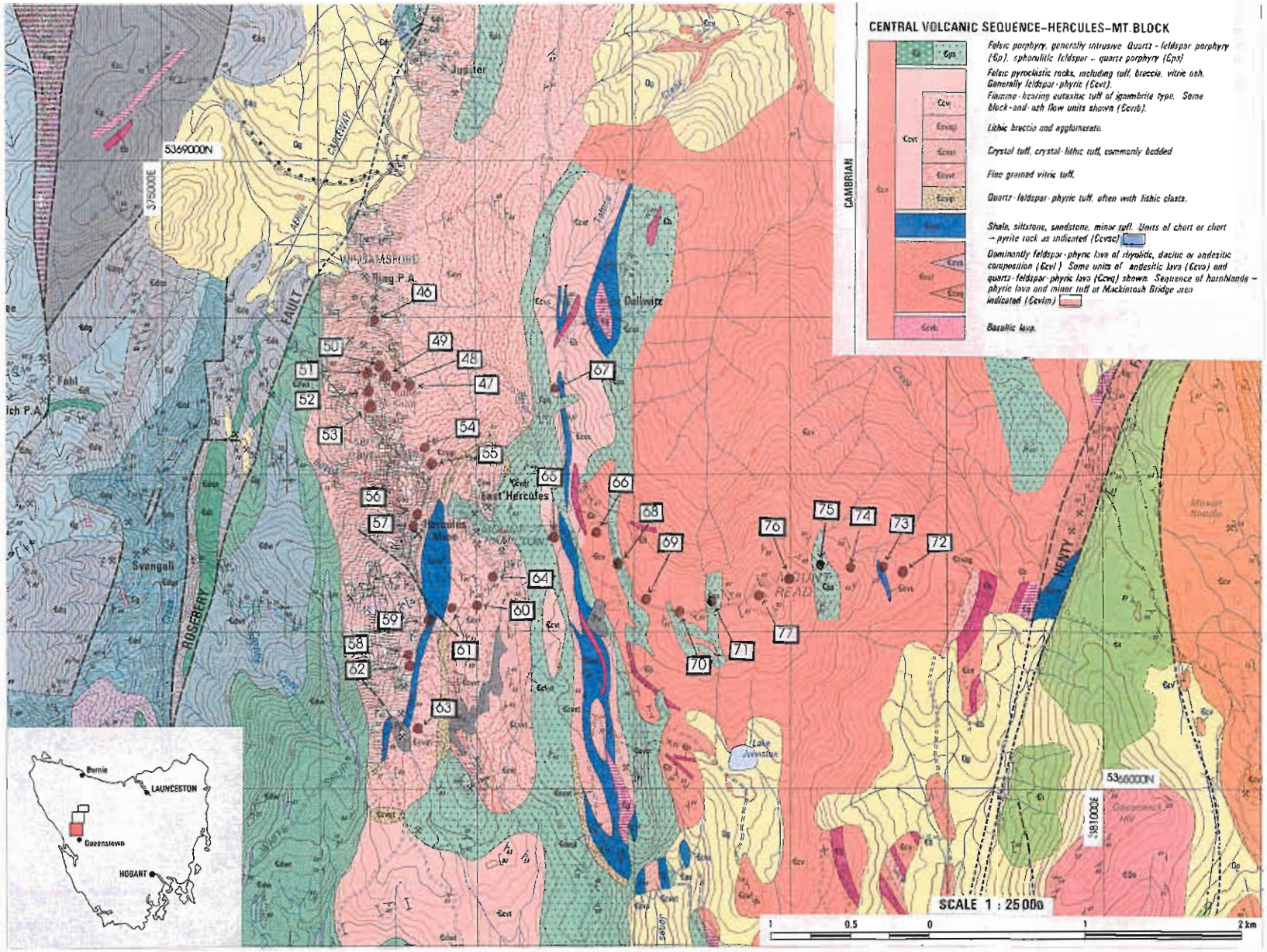

Figure 1
Location of samples along the Hercules–Mt Read Traverse. Base geology from Map 3, MRT, Mt Read Project.

Table 1. Major and trace element analyses of the foot wall and hanging wall volcanics to the Hercules deposit.

	MR96-46	MR96-47	MR96-48	MR96-49	MR96-50	MR96-51	MR96-52	MR96-53	MR96-54	MR96-55	MR96-56
SiO2	74.85	67.93	73.04	72.46	76.19	72.42	57.91	72.58	70.47	73.45	44.31
TiO2	0.32	0.42	0.29	0.30	0.22	0.30	0.32	0.29	0.39	0.35	0.51
Al2O3	14.22	16.78	12.76	13.42	8.55	12.22	11.34	12.95	15.81	14.09	14.87
Fe2O3#	1.09	2.71	2.32	2.46	5.03	5.70	18.57	5.86	2.65	2.36	1.77
MnO	0.01	0.03	0.27	0.62	0.09	0.18	0.82	0.17	0.04	0.04	0.92
MgO	1.36	1.38	1.14	2.19	1.11	1.39	4.43	1.10	1.30	0.96	8.14
CaO	0.01	0.02	1.40	0.10	0.03	0.01	0.01	0.01	0.76	0.62	10.52
Na2O	0.07	0.21	0.96	0.03	0.05	0.03	0.05	0.03	2.76	3.89	0.11
K2O	5.41	7.25	4.33	4.87	3.08	3.67	0.65	3.67	3.49	2.31	3.28
P2O5	0.02	0.05	0.05	0.05	0.04	0.04	0.02	0.05	0.06	0.05	0.12
LOI	2.30	2.56	3.26	3.03	3.78	3.23	5.77	2.83	2.28	1.56	15.23
Total	99.62	99.34	99.82	99.53	97.94	99.14	99.88	99.50	100.01	99.69	99.78
S	0.01	0.01	0.29	0.24	3.26	1.53	2.68	0.72	0.01	0.01	0.45
Total C	0.02	0.05	0.31	0.20	0.02	0.02	0.02	0.02	0.03	0.01	2.79
CO2	0.07	0.18	1.14	0.73	0.07	0.07	0.07	0.07	0.11	0.04	10.22
Alteration Index	98.8	97.4	69.8	98.2	98.1	99.2	98.8	99.2	57.6	42.1	51.8
Trace Elements (ppm)											
Sc	5	7	5	4	2	4	4	4	6	4	14
V	6	16	10	10	4	9	10	9	14	11	38
Cr	2	2	2	2	2	2	3	3	3	3	4
Ni	2	2	2	2	1	2	1	1	1	1	1
Cu	3	4	5	5	1093	55	248	608	6	15	12
Zn	49	51	54	403	11667	155	651	111	53	60	79
As	3	4	3	8	33	25	23	6	3	2	45
Rb	227	278	215	258	150	191	35	194	171	105	176
Sr	4	20	40	5	2	5	3	8	228	228	172
Y	34	34	32	32	26	26	52	33	51	57	40
Zr	263	312	221	225	130	230	232	230	296	267	286
Nb	13.3	14.2	11.9	12.3	7.0	11.6	12.8	11.7	14.9	12.8	14.5
Mo	0.2	0.3	0.2	1.1	7.4	6.3	1.3	0.5	0.2	0.2	0.8
Ag	0.5	0.3	0.4	0.2	9.2	2	1.8	3.9	0.2	0.1	2.6
Cd	0.2	0.2	0.2	0.8	39.1	0.7	0.5	0.3	0.4	0.4	0.4
Sb	0.9	1.2	1.1	1.5	1.7	1.2	1.7	1.2	1.1	1.5	8.9
Cs	2.26	5.53	3.98	3.78	1.99	1.74	0.39	1.82	5.37	3.78	3.37
Ba	1267	1047	1308	908	1072	1018	220	1284	1017	721	2317
La	45	34	41	42	25	37	23	35	56	61	52
Ce	98	72	88	89	58	77	48	75	111	97	116
Nd	41	30	36	37	21	32	20	31	54	67	46
Tl	1	1.3	1	1.3	1.2	1.6	<0.5	1.5	1	0.8	16.7
Pb	30	3	20	67	999	52	54	94	7	13	109
Bi	<0.1	0.1	0.3	<0.1	22.9	7.3	4.7	10.5	0.3	0.2	0.2
Th (XRF)	23.4	22.2	19.2	19.3	11.7	19.4	21.4	20.1	26.2	22.2	21.7
Th (ICP)	23.6	24.1	20.4	20.6	12.1	17.8	20.9	18.4	23.7	19.8	20.3
U	5.7	5.96	5.23	5.42	4.21	4.5	3.9	5.06	5.81	4.32	5.35

Total Fe as Fe2O3; LOI = loss on ignition; Alteration Index = 100(MgO+K2O)/(MgO+K2O+CaO+Na2O)

Table 1. continued

	MR96-57	MR96-58	MR96-59	MR96-60	MR96-61	MR96-62	MR96-63	MR96-64	MR96-65	MR96-66	MR96-67
SiO2	29.42	81.26	61.94	75.81	73.97	13.27	75.49	71.22	62.55	76.27	69.14
TiO2	0.34	0.33	0.55	0.30	0.31	0.26	0.31	0.33	0.71	0.26	0.43
Al2O3	10.12	9.41	17.39	12.44	14.36	7.86	13.29	13.74	16.48	12.40	15.08
Fe2O3#	2.82	2.07	3.39	2.86	2.02	6.27	1.91	4.11	5.34	1.80	4.36
MnO	2.66	0.02	0.62	0.21	0.05	20.70	0.08	0.47	0.12	0.05	0.16
MgO	14.87	0.65	2.87	1.24	0.60	3.43	0.45	0.97	1.89	0.36	1.00
CaO	17.24	0.13	1.59	0.04	0.17	4.88	0.71	0.66	1.69	0.49	0.14
Na2O	0.03	0.03	0.47	2.62	3.28	0.05	3.64	1.37	3.64	4.57	2.91
K2O	0.06	3.10	4.17	2.38	2.92	2.01	2.51	4.01	3.26	2.32	3.00
P2O5	0.12	0.08	0.11	0.04	0.05	0.09	0.04	0.06	0.21	0.04	0.09
LOI	21.61	2.59	5.71	1.82	1.75	23.95	1.49	2.62	3.44	1.21	2.66
Total	99.30	99.64	98.81	99.76	99.48	97.98	99.97	99.56	99.32	99.78	98.99
S	0.27	1.72	1.69	0.01	0.12	9.42	0.02	0.27	0.02	0.01	0.02
Total C	4.16	0.03	0.40	0.05	0.04	4.50	0.05	0.16	0.26	0.09	0.05
CO2	15.24	0.11	1.47	0.18	0.15	16.49	0.18	0.59	0.95	0.33	0.18
Alteration Index	46.4	95.9	77.4	57.6	50.5	52.5	40.5	71.1	49.1	34.6	56.8
Trace Elements (ppm)											
Sc	13	8	14	5	5	4	5	5	15	4	10
V	30	14	100	11	7	11	10	11	74	7	64
Cr	4	2	18	2	3	3	2	2	11	2	6
Ni	1	1	30	1	1	1	1	1	4	1	1
Cu	7	231	17	10	5	*3500*	7	139	7	3	28
Zn	139	2848	3676	187	31	*87000*	107	124	194	28	198
As	77	51	77	<1	4	577	3	3	<1	<1	<1
Rb	3	151	193	127	122	105	113	222	155	79	107
Sr	253	9	110	32	216	12	272	31	130	107	114
Y	48	20	56	31	33		40	36	40	33	29
Zr	192	150	278	227	261	112	237	260	227	240	181
Nb	10.2	6.7	15.1	11.3	13.7	3.3	12.3	12.4	12.7	13.1	10.2
Mo	0.4	9	4.5	1.7	0.2	19.9	0.5	0.2	0.3	0.3	0.3
Ag	163?	91.9?	1.9	1.1	0.3	92.3	1.1	0.5	0.2	<0.1	0.2
Cd	0.2	6.3	2	0.2	0.3	203	0.2	0.6	0.4	0.3	1.1
Sb	13.4	7.3	20.1	1	1.5	315	5.3	1.5	0.8	0.8	0.6
Cs	0.48	3.11	4.5	1.89	3.37	2.4	2.65	2.76	1.76	1.21	2.07
Ba	117	2103	2320	1168	1095	2514	786	933	1011	665	1291
La	36	14	68	39	60	30	47	42	77	67	41
Ce	74	41	150	77	124	84	89	81	101	81	80
Nd	32	14	64	33	49	5	46	37	62	47	33
Tl	8	6.8	17	0.7	0.6	53.1	1.5	1.5	1.2	0.5	0.8
Pb	28	1457	58	155	7	*35000*	66	31	18	5	3
Bi	0.2	0.1	0.4	3.1	0.1	0.7	0.2	1.5	0.2	<0.1	0.3
Th (XRF)	16.5	10.8	22.4	20.8	23.8		20.6	22.8	22.3	20.4	19.1
Th (ICP)	13.7	12.6	23	21.6	23.7	12.2	18.5	20.5	19.4	19.4	17.5
U	5.56	3.95	18.8	5.26	6.21	5.71	4.76	5.42	5.09	5.53	3.99

Total Fe as Fe2O3; LOI = loss on ignition; Alteration Index = 100(MgO+K2O)/(MgO+K2O+CaO+Na2O)

Table 1. continued

	MR96-68	MR96-69	MR96-70	MR96-71	MR96-72	MR96-73	MR96-74	MR96-75	MR96-77
SiO2	71.43	73.51	76.37	70.81	71.37	79.55	76.17	71.78	72.08
TiO2	0.47	0.27	0.23	0.40	0.35	0.17	0.16	0.34	0.21
Al2O3	14.54	13.39	11.65	14.21	14.18	11.47	11.63	13.33	10.95
Fe2O3#	3.55	1.79	2.02	3.33	2.90	1.66	2.08	2.50	2.77
MnO	0.07	0.04	0.15	0.10	0.06	0.02	0.07	0.05	0.14
MgO	0.81	0.36	0.49	1.06	0.55	0.47	0.73	0.64	0.65
CaO	0.08	1.03	1.35	0.15	0.89	0.04	1.55	1.46	3.86
Na2O	1.98	3.80	3.84	3.48	3.79	3.72	1.29	3.07	3.66
K2O	4.42	3.71	1.71	3.65	3.68	1.71	3.17	4.50	1.35
P2O5	0.09	0.04	0.04	0.09	0.07	0.01	0.02	0.06	0.04
LOI	2.13	1.82	2.10	1.93	1.90	1.19	2.72	2.03	4.06
Total	99.58	99.86	99.95	99.19	99.75	100.01	99.58	99.78	99.78
S	0.01	0.01	0.01	0.01	0.01	0.01	0.01	0.01	0.01
Total C	0.06	0.20	0.24	0.02	0.14	0.06	0.30	0.23	0.70
CO2	0.22	0.73	0.88	0.07	0.51	0.22	1.10	0.84	2.56
Alteration Index	71.8	45.7	29.8	56.5	47.5	36.7	57.9	53.2	21.0
Trace Elements (ppm)									
Sc	11	4	2	8	5	2	3	6	4
V	42	7	7	46	11	1.5	1.5	10	7
Cr	3	3	2	3	2	2	2	2	3
Ni	2	1	1	2	1	1	1	1	1
Cu	4	4	2	4	7	2	5	5	4
Zn	94	28	46	54	23	27	46	33	63
As	3	<1	<1	<1	2	<1	3	<1	<1
Rb	162	105	77	120	116	69	137	144	63
Sr	76	118	68	118	131	94	88	185	111
Y	41	33	32	38	42	31	40	37	36
Zr	247	260	227	205	264	214	209	241	173
Nb	13.5	14.6	12.2	11.6	15.1	13.7	13.9	12.9	12.5
Mo	1.3	0.2	0.2	0.2	0.7	0.1	0.5	0.2	0.1
Ag	<0.1	0.2	0.1	<0.1	<0.1	<0.1	0.2	0.2	<0.1
Cd	0.4	0.4	0.4	0.3	0.3	0.3	<0.1	0.2	0.2
Sb	1	0.9	0.4	1.2	0.8	0.4	0.6	0.6	0.3
Cs	3.16	1.08	1.02	2.32	3.21	1.35	2.7	3.14	1.09
Ba	1184	1092	302	987	1149	496	713	1131	237
La	44	36	74	66	52	24	44	47	28
Ce	95	78	83	105	100	60	80	93	51
Nd	41	30	52	55	46	21	34	40	22
Tl	1	0.6	<0.5	0.6	0.7	<0.5	0.6	0.7	<0.5
Pb	9	8	6	14	4	3	15	6	4
Bi	<0.1	<0.1	<0.1	<0.1	<0.1	<0.1	0.1	0.4	<0.1
Th (XRF)	21.7	21.5	19.1	21.4	21.5	18.9	21.2	22.1	19.8
Th (ICP)	20.9	18.5	17.7	20	19.8	17.5	17.6	20.3	16.3
U	3.76	4.45	4.42	3.38	4.49	4.48	4.72	5.12	3.72

Total Fe as Fe2O3; LOI = loss on ignition; Alteration Index = 100(MgO+K2O)/(MgO+K2O+CaO+Na2O)

Alteration intensity

Alteration intensity along the traverse is reflected in the degree of replacement of the volcanic groundmass and the degree of replacement of the feldspar phenocrysts. Figures 3 and 4 are a series of photomicrographs showing the effects of increasing hydrothermal alteration on the various rhyolitic volcanic facies at Hercules.

Stages in the alteration intensity are outlined below:

- The least altered volcanics (Fig. 3A, B) have only suffered diagenetic alteration followed by metamorphism. The original glassy groundmass shows up to 20% alteration by sericite whereas the feldspar phenocrysts remain fairly pristine (less than 10% alteration by sericite or carbonate). Alteration index varies 20 to 35.
- Weak alteration leads to increased replacement of groundmass by sericite ± chlorite (Fig. 3C, D), involving 20–50% groundmass replacement generally following pumice outlines (e.g. Fig. 3C) or perlitic cracks. Feldspars show 10–30% sericite flecks or patchy carbonate alteration. Alteration index has increased from 40 to 60. It is difficult to interpret whether weak alteration of this type is related to strong diagenetic/metamorphic alteration or weak hydrothermal alteration.
- Moderate hydrothermal alteration (Figs 3E, F; 4A, B) causes partial to complete breakdown of phenocryst feldspars with 30–100% replacement by sericite, quartz or carbonate. Groundmass replacement by sericite and quartz also increases (50–100%). Chlorite alteration of selected pumice or groundmass patches becomes more common. Alteration index increases from 50 to 80.
- Strong to intense hydrothermal alteration (Fig. 4C, D, E, F), leads to the total replacement of all original components in the volcanic rock. However, outlines of original feldspar phenocrysts are normally evident and some groundmass texture may be preserved. In strongly deformed zones, these altered rocks become schists (e.g. Fig. 4d, f). Feldspar phenocrysts may be replaced by quartz (Fig. 4D), by sulphides (Fig. 4C) by carbonate (Fig. 4A, F), or by a mixture of these minerals (Fig. 4E). Alteration index is normally in the range 95–100, although carbonate-rich samples show high CI and low AI (e.g. Fig. 4F).

Figure 3 (opposite)
Photomicrographs of rhyolitic volcanic rocks displaying increasing intensity of alteration from (A) to (F).
(A, B) Feldspar phyric rhyolite with minimal alteration of groundmass and plagioclase phenocrysts (hangingwall volcanics);
(C) Rhyolitic pumice breccia with weak and patchy alteration of pumice and feldspars (hangingwall pumice breccia);
(D) Moderate pervasive sericite chlorite alteration of groundmass to pumice breccia. Feldspar phenocrysts show patchy carbonate, epidote, chlorite alteration (hangingwall pumice breccia);
(E) Strong carbonate alteration of groundmass and feldspar phenocrysts (20 m below massive sulphide lens);
(F) Strong sericite alteration of groundmass and feldspar phenocrysts. Fine albite alteration occurs in zones surrounding sericitised plagioclase.

** Figure 4 (page 163)
Photomicrograph of rhyolitic volcanic rocks displaying increasing intensity of alteration from (A) to (F).
(A) Strong sericite–silica alteration of groundmass and carbonate–quartz alteration of feldspar phenocrysts (footwall pumice breccia);
(B) Strong patchy sericite–chlorite altered groundmass and carbonate ± epidote–quartz alteration of phenocrysts;
(C) Intense quartz–sericite alteration of groundmass with pyrite–quartz–carbonate–sphalerite alteration of feldspar phenocrysts;
(D) Intense sericite–quartz pyrite alteration of groundmass with replacement of feldspar phenocrysts by quartz (footwall schist);
(E) Intense quartz–chlorite–sericite alteration. Note the composite replacement of feldspar phenocrysts by quartz–carbonate–chlorite;
(F) Chlorite carbonate schist in near footwall position. Original feldspar phenocrysts in volcanics are replaced by aggregates of carbonate.

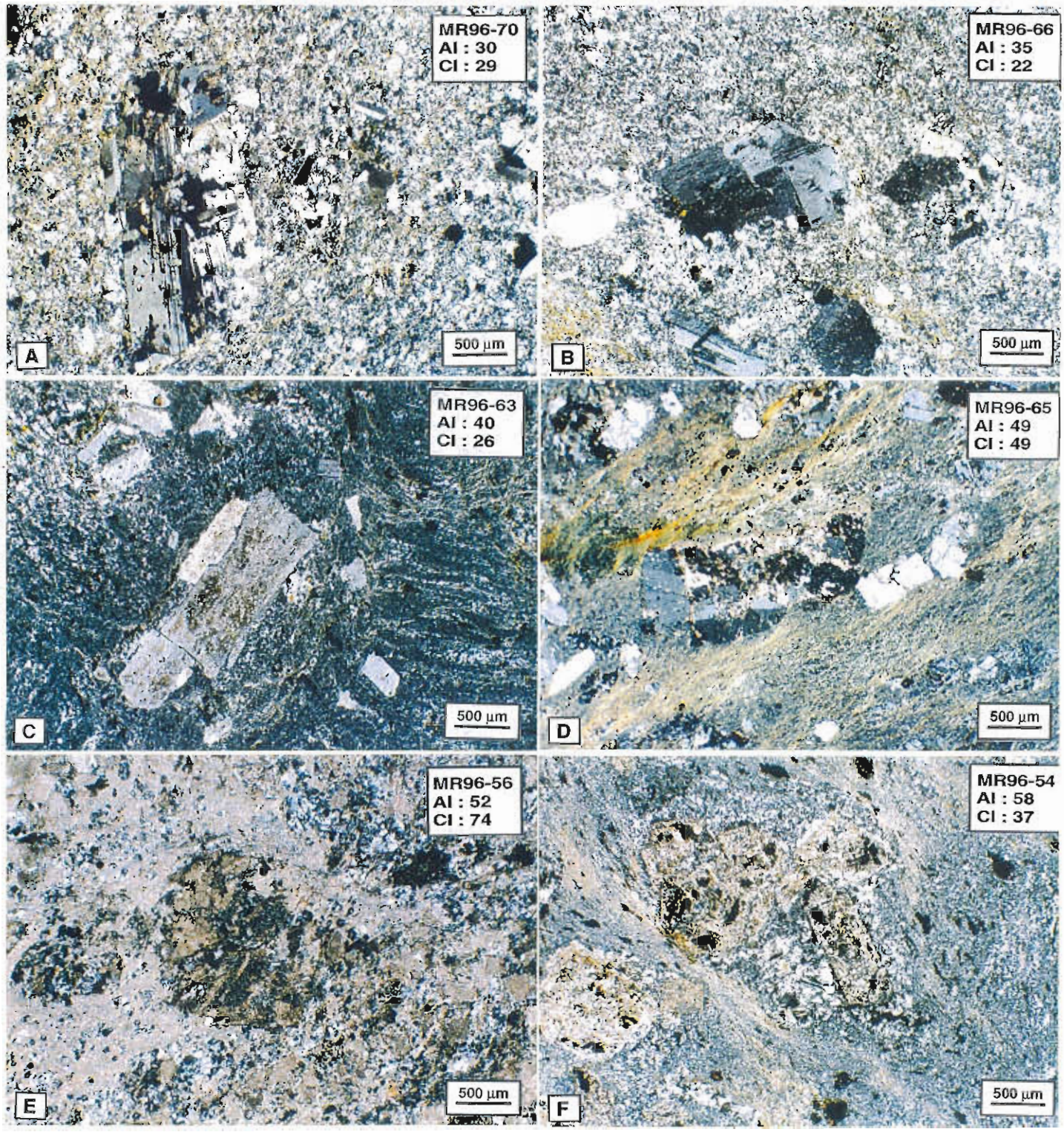
MR96-70
AI : 30
CI : 29
500 µm
A
MR96-66
AI : 35
CI : 22
500 µm
B
MR96-63
AI : 40
CI : 26
500 µm
C
MR96-65
AI : 49
CI : 49
500 µm
D
MR96-56
AI : 52
CI : 74
500 µm
E
MR96-54
AI : 58
CI : 37
500 µm
F

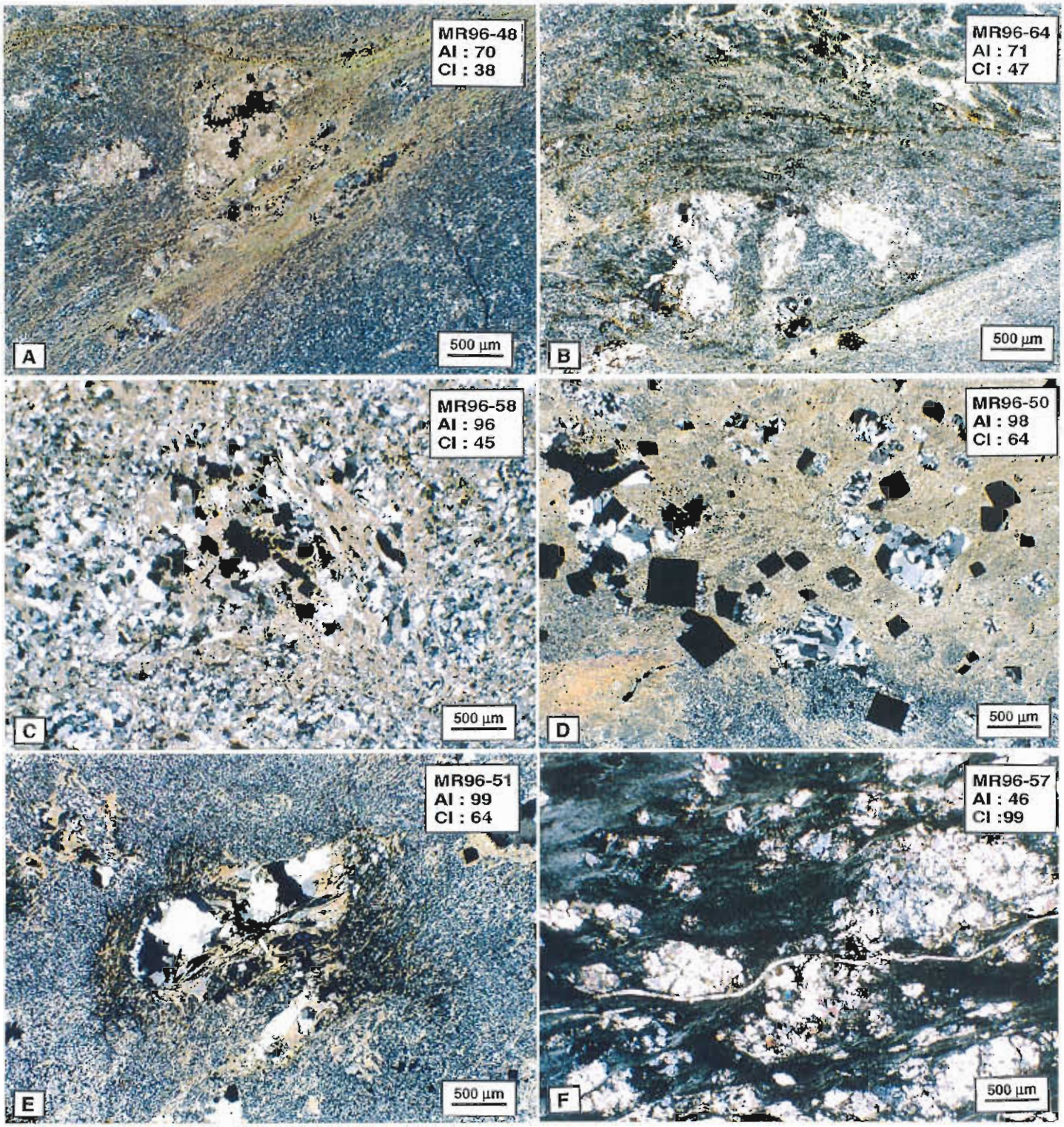
MR96-48
AI : 70
CI : 38
500 µm
A
MR96-64
AI : 71
CI : 47
500 µm
B
MR96-58
AI : 96
CI : 45
500 µm
C
MR96-50
AI : 98
CI : 64
500 µm
D
MR96-51
AI : 99
CI : 64
500 µm
E
MR96-57
AI : 46
CI :99
500 µm
F

Feldspar altered volcanics

One footwall pumice breccia sample displays K-feldspar alteration and two other samples display albite alteration. The K-feldspar alteration of plagioclase phenocrysts in sample MR96-47 is accompanied by intense sericite and quartz alteration of the groundmass. The K-feldspar is interpreted to be part of the footwall hydrothermal alteration assemblage in this instance.

The two pink albite altered samples occur in the "footwall" pumice breccia immediately northwest of Hercules (MR96-54 and MR96-55, Fig. 1). The albite occurs as small crystal clusters surrounding sericite altered plagioclase phenocrysts (see summary alteration sheets in the Appendix). The albite-rich volcanics exhibit moderate groundmass alteration but low alteration index and no pyrite development compared to other footwall pumice breccia samples. These features suggest that MR96-54 and MR96-55 are from a fault block of weakly altered hangingwall volcanics, rather than part of the footwall hydrothermal system. The question remains unresolved as to whether the albite alteration is an early diagenetic event or part of the hangingwall hydrothermal alteration associated with the ore deposit.

An alternative interpretation is that the albite altered volcanics are part of the footwall alteration system that have been protected from intense alteration due to early diagenetic albite formation causing permeability destruction and consequent low water–rock interaction. These alternatives will be investigated by further research.

Alteration geochemistry

Geochemical plots of selected major and trace elements are given in Figures 5 to 8. The data has been arranged in approximate stratigraphic order from footwall (west) to hangingwall (east) along the traverse. However, the stratigraphic order of samples selected is open to interpretation, due to the complex nature of the geology in the Hercules area. For example footwall pumice breccia may have been thrust over the Hercules host rock package along the Mt Hamilton fault (Allen, 1994). This geological complexity makes it difficult to assess the likelihood of hangingwall alteration to the Hercules VHMS deposit.

Base metals and sulphur variation (Fig. 5)

Two anomalous zones of base metal (Cu, Pb, Zn, Mn) and sulphur occur along the traverse, one deep in the footwall altered zone (MR96-50) and the other at the Hercules ore position (MR96-62). The subtle decrease in Zn, Pb, Cu and Mn values in the hangingwall volcanics passing east from the ore position **may** represent a very weak hangingwall dispersion halo.

The marked difference in sulphur content between the footwall package and the hangingwall package is not in keeping with the interpretation that footwall volcanics have been thrust over the ore horizon at Mt Hamilton.

Major elements

Selected major elements that show significant trends are outlined in Figure 6.

Na_2O: most of the footwall altered rocks show sodium depletion (< 1.0 % Na_2O) compared to hangingwall volcanics, which range from 1 to 5% Na_2O. The "footwall" albite altered zone (sample positions 7 to 10) are clearly evident on the plot (Fig. 6).

K_2O shows considerable variation along the traverse, representing variable sericite alteration that exhibits no clear relationship to the ore position.

CO_2 is enriched in the immediate footwall and hangingwall sequence related to carbonate alteration surrounding the ore deposit.

Trace elements

A selection of trace elements that show trends related to mineralisation are shown in Figures 7 and 8.

As, Mo and Cd exhibit anomalous values coincident with Zn, Pb and Cu outlining the ore position and the intense alteration system deep in the footwall pumice breccias (Fig. 7).

Sb and Tl exhibit anomalous values one to two orders of magnitude above background enveloping the ore position. No anomaly is present over the intensely altered footwall zone (Fig. 7).

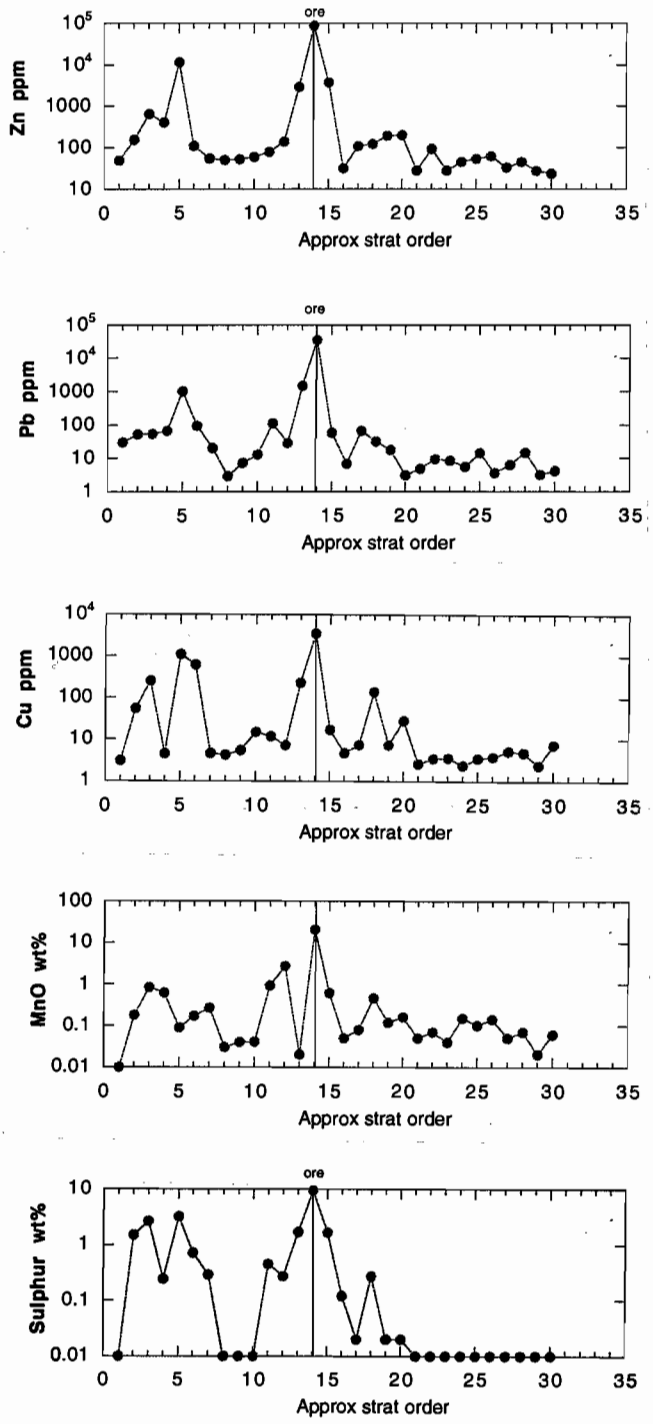

Figure 5
Variation in Zn, Pb, Cu, MnO and S along the Hercules–Mt Read Traverse.

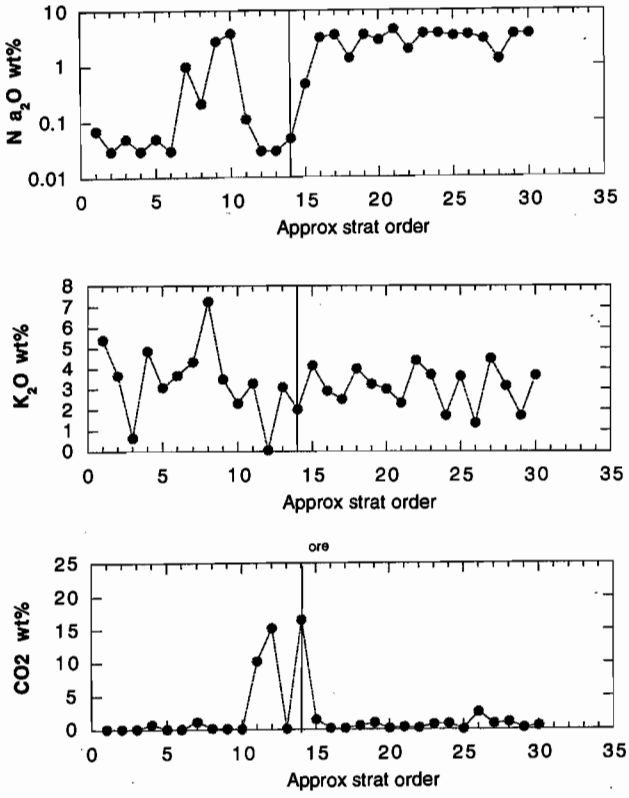

Figure 6
Variation in Na_2O, K_2O and CO_2 along the Hercules–Mt Read Traverse.

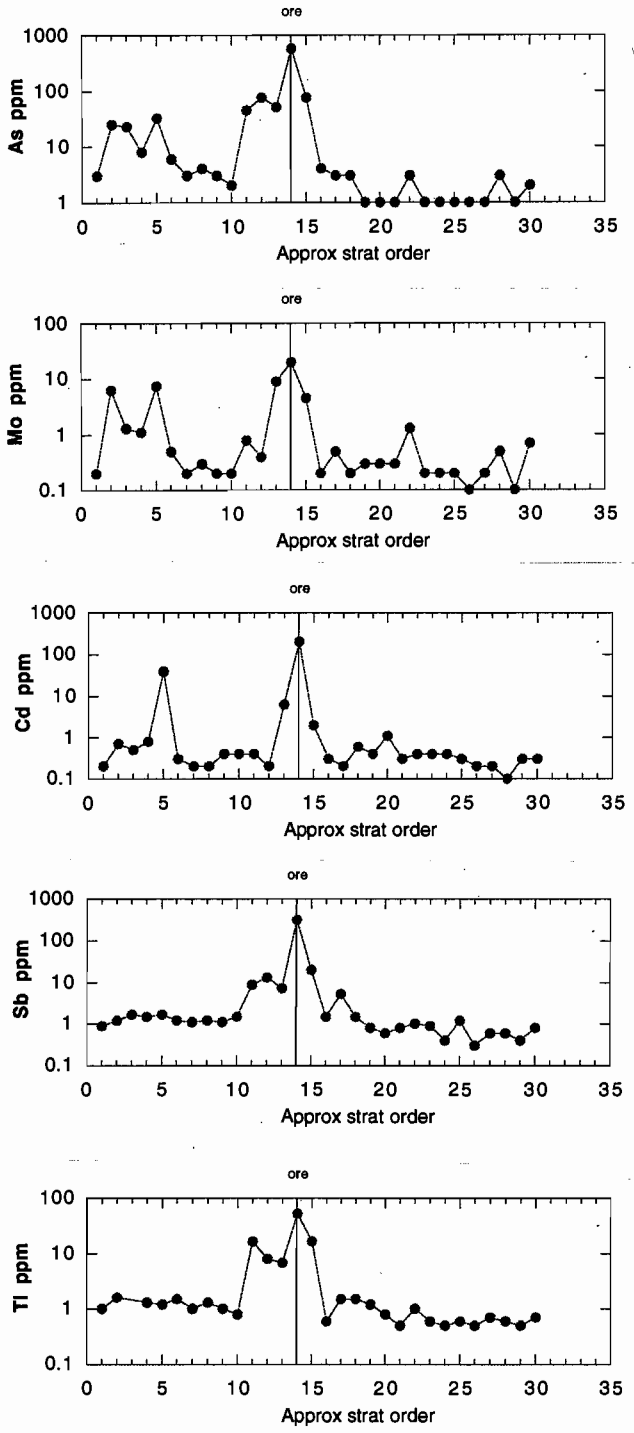

Figure 7
Variation in As, Mo, Cd, Sb and Tl along the Hercules–Mt Read Traverse.

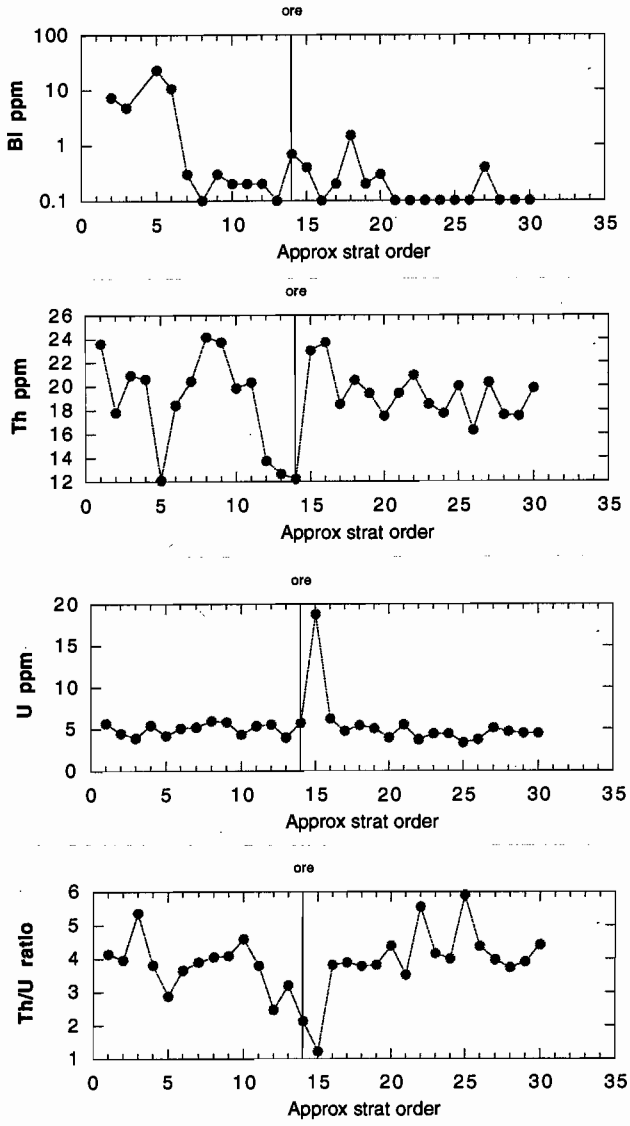

Figure 8
Variation in Bi, Th, U and Th/U ratio along the Hercules–Mt Read Traverse.

Bi: anomalous values > 5 ppm are confined to the intense footwall altered zone and are lacking from the ore position (Fig. 8).

Th and U: thorium is depleted in the immediate ore environment compared with the footwall and hangingwall volcanics. Uranium is very consistent (3–6 ppm) except for one sample in the immediate hangingwall shale. The Th/U ratio decreases (< 3) in the ore environment.

Strontium (Fig. 9) shows anomalously high values in the volcanics up to approximately 100 m on either side of the ore horizon at Hercules. This element appears to be one of the best geochemical indicators of the ore environment. Sr is most likely substituting for Ca in the alteration carbonates, but shows greater dispersion than the CO_2 alteration (Fig. 6). The intensely altered deep footwall volcanics exhibit Sr depletion, whereas the remote hangingwall volcanics have normal background Sr values for rhyolites (60–150 ppm).

Barium (Fig. 9) is enriched in the ore environment (> 2000 ppm) compared to both footwall and hangingwall volcanics (100–1500 ppm). A plot of Ba/K_2O ratio indicates that away from the ore environment Ba content is controlled by K_2O content (i.e. Ba substitutes for K in sericite). However, around the orebody $(Ba/K_2O)10^4$ ratios of greater than 500 suggest that the Ba occurs as barite. This data indicates that the Ba/K_2O ratio is a more useful vector than Ba alone.

Phosphorous (Fig. 9): P_2O_5 appears to be leached from the deep footwall volcanics (< 0.05 wt % P_2O_5) compared with the hangingwall sequence. P_2O_5 enrichment around the ore position is not apparent from the data, unlike the P_2O_5 anomaly at Mt Lyell (Large et al., 1996).

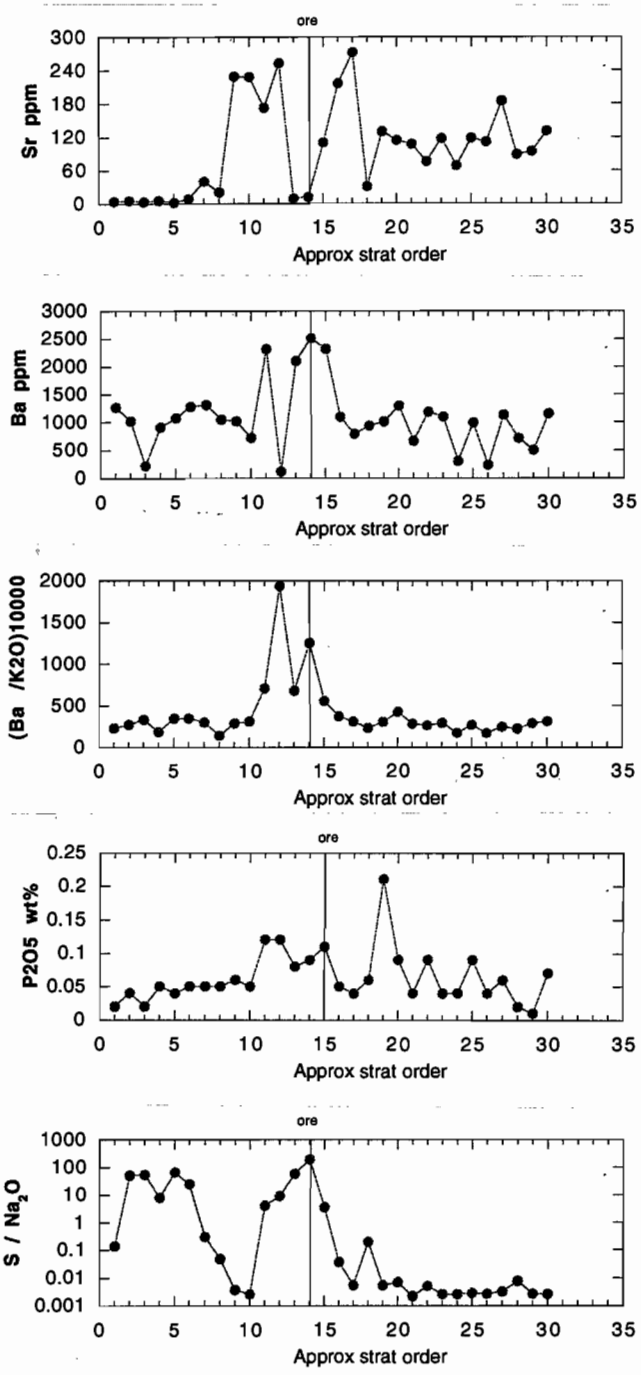

Figure 9
Variation in strontium, barium, $(Ba/K_2O)10000$ ratio and P_2O_5 along the Hercules–Mt Read Traverse.

Alteration indices

Plots of the Ishikawa alteration index and previously defined chlorite index and Mn-carbonate index (Large et al., 1996) are given in Figure 10. The formulae for these indices are:

$$\text{Alteration Index (AI)} = \frac{100\,(K_2O + MgO)}{(K_2O + MgO + Na_2O + CaO)}$$

$$\text{Chl/carb/py Index (CI)} = \frac{100\,(MgO + FeO)}{(MgO + FeO + Na_2O + K_2O)}$$

$$\text{Mn-carbonate Index (MI)} = \frac{100\,(CaO + 10MnO)}{(CaO + 10MnO + Na_2O + K_2O)}$$

Alteration Index

The quartz–sericite–pyrite altered pumice breccias deep in the Hercules footwall show high AI values (> 95) consistent with the intense hydrothermal alteration visible in these rocks. However, the albite altered footwall rocks show intermediate AI values (40–80). The hangingwall volcanics display variable AIs from 20 to 80, and a general decrease in the rolling mean value (Fig. 10b) passing higher into the hangingwall sequence. This pattern suggests the possibility of a weak hangingwall alteration halo at Hercules.

Chl/carb/py Index

This index, which measures the degree of chlorite, carbonate and/or pyrite alteration in volcanics, shows two anomalous zones, one deep in the footwall and another around the ore position. These two anomalies coincide with the Zn, Pb, Cu and S anomalies (Fig. 5).

Mn-Carbonate Index

Peaks in the MI correspond with the CI and basemetal anomalies.

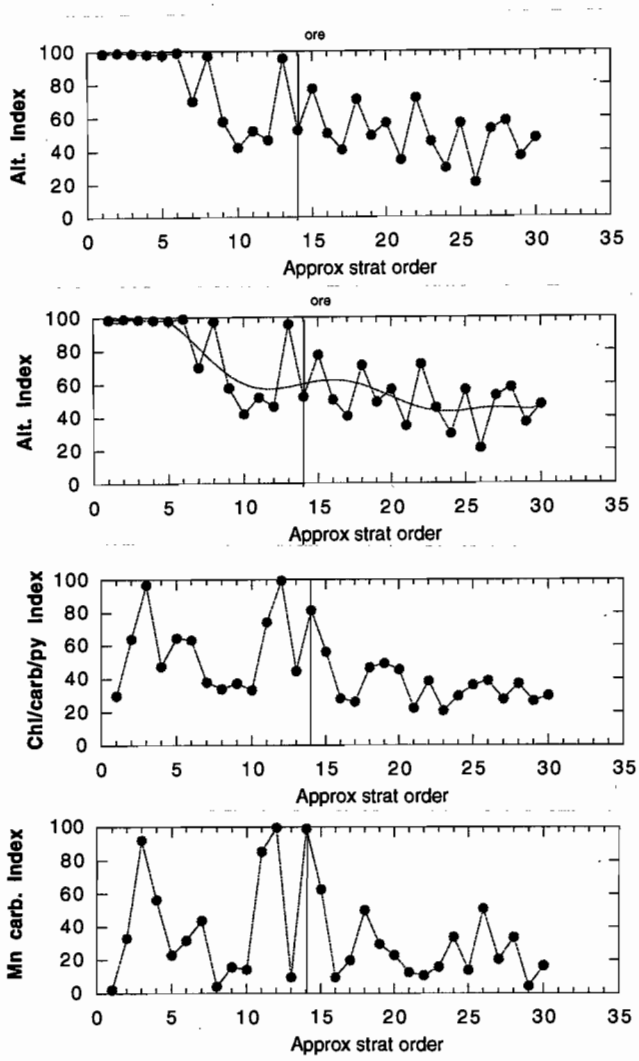

Figure 10
Variation in alteration index (AI), chlorite/carbonate/pyrite index (CI) and Mn-carbonate index (MI) along the Hercules–Mt Read Traverse.

Correlation between Zn and alteration indices

There is a general positive correlation between the alteration indices and zinc content of traverse samples. From Figure 11 it is apparent that samples with background AI values of 20–50 and CI values of 15–40 generally contain background zinc values of less than 100 ppm. The correlation is best developed between Zn and the chl/carb/py index (CI) were most of the data fall along a corridor between the background box ($20 < CI < 40$; $10 < Zn < 100$ ppm). The reason for this good correlation is that zinc deposition in the ore environment at Hercules is accompanied by an increase in at least one of the minerals (chlorite, carbonate or pyrite) that make up the CI index.

Further work will be required to determine whether the linear data trend on the CI vs Zn diagram can be used as a discriminator for samples in the ore environment of VHMS deposits.

AI vs CI box plot

The AI vs CI box plot is a plot of Ishikawa Alteration Index against the chlorite/carbonate/pyrite index (Large et al., 1996b). The plot is used on the summary alteration sheets in the Appendix to track the relationship between alteration geochemistry and mineralogy in the traverse samples.

A summary plot for the complete traverse data set is shown in Figure 12. Samples of least altered pumice breccia and rhyolite lava plot toward the centre of the diagram with $25 < AI < 50$ and $18 < CI < 35$. Increasing diagenetic alteration and/or weak hydrothermal sericite–chlorite alteration (typical of hangingwall alteration) leads to an increase in AI (50–80) and CI (30–50).

Intense alteration, typical of the footwall alteration zone, results in samples plotting along the sericite–chlorite ± pyrite vertex with $AI > 95$ and CI from 30 to 100. Samples adjacent to the ore horizon plot along a corridor linking sericite and dolomite.

This diagram enables:

- a visual geochemical determination of the intensity of alteration
- an estimate of the major alteration mineral assemblage

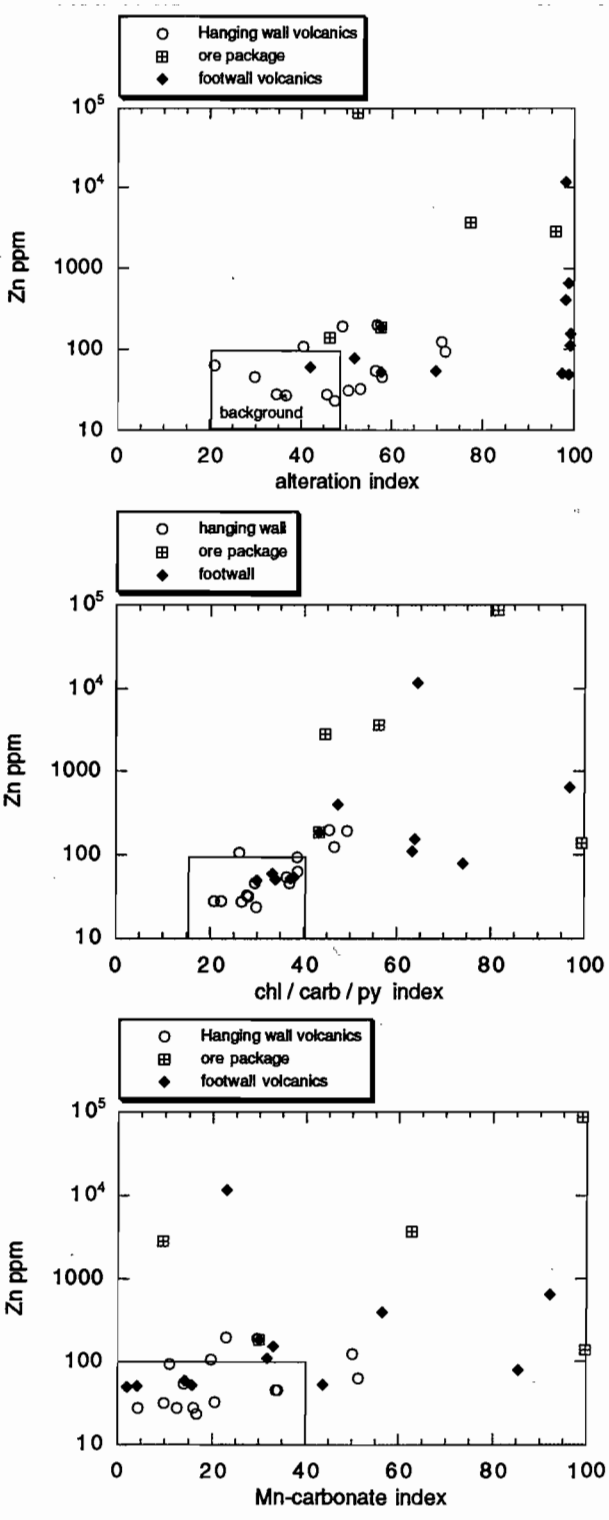

Figure 11
Correlation between zinc and the three alteration indices for the Hercules–Mt Read Traverse samples. The box on each plot represents the background values for "unaltered" samples. Note the good correlation between Zn and the chl/carb/py index (CI) for most of the data.

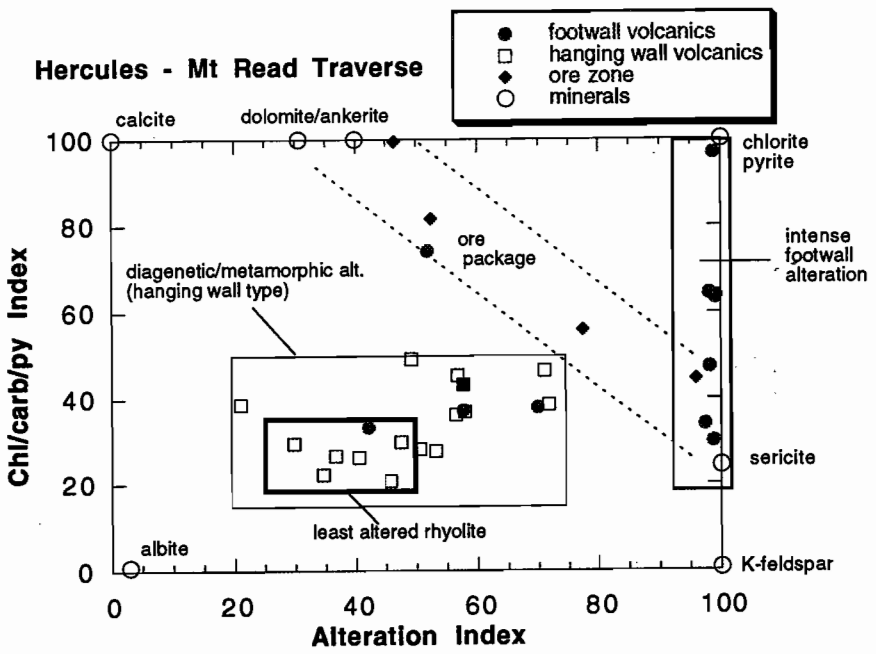

Figure 12
AI vs CI box plot showing the fields for least altered volcanics, diagenetic/metamorphic alteration, intense footwall alteration and the ore package alteration.

- classification of the likely facies of alteration, i.e. hangingwall alteration, footwall alteration or ore horizon alteration

Geochemical associations

The data outlined in Figures 5 to 12 enables some preliminary interpretation of the geochemical associations that characterise volcanics relative to the Hercules ore position.

1. Intensely altered footwall pumice breccias show positive anomalies in AI, CI, MI and sulphur accompanied by enrichments in the trace elements Cu, Zn, Pb, Mn, As, Mo, Cd, Bi.

2. The ore environment is characterised by anomalies in CI, MI, CO_2 and sulphur accompanied by enrichments in Cu, Pb, Zn, Mn, As, Mo, Cd, Sb, Tl and Ba/K_2O ratio.

3. The weakly altered hangingwall volcanics are characterised by generally low AI, CI, MI, S and CO_2 accompanied by high levels of Na_2O (>2 wt%)

4. Geochemical parameters that are diagnostic of the ore environment ***only*** are:
   Thallium > 5 ppm
   Sb > 5 ppm
   CO_2 > 5 wt %
   $(Ba/K_2O)10^4 > 500$
   Th/U < 2.5

5. Geochemical parameters that are diagnostic of the footwall alteration system ***only*** are:
   AI > 95
   Bi > 5 ppm
   CaO < 0.1 wt %

6. Geochemical parameters that are diagnostic of the less altered hangingwall volcanics are:
   S < 0.01 wt %
   Na_2O > 1.0 wt %
   $S/Na_2O < 0.01$

Conclusions

The following conclusions can be drawn from this study:

- The footwall pumice breccias at Hercules exhibit strong to intense hydrothermal alteration of sericite–quartz ± chlorite ± pyrite with AI from 95 to 100.
- Zones of albite alteration in the pumice breccias may be part of the hangingwall alteration system, and exhibit low AI values (from 40 to 70) and low S content.
- Alteration surrounding the ore zone is dominated by carbonate–chlorite–sericite with AI values from 40 to 100.
- The hangingwall volcanic facies is composed of lavas, volcaniclastics and intrusives which exhibit weak to moderate groundmass alteration but negligible feldspar phenocryst alteration. AI values vary from 20 to 70.
- There is a good correlation between alteration index and intensity of feldspar destruction in both the pumice breccia and coherent rhyolites.
- Box plots of AI vs CI allow a classification of the intensity, mineralogy and likely facies of alteration associated with Rosebery style alteration systems.
- A suite of elements and indices has been developed that is diagnostic of footwall alteration, hangingwall "alteration" and the ore environment at Hercules.

References

Allen, R.L., 1994: Volcanic Facies analysis indicates large pyroclastic eruptions, sill complexes, syn-volcanic grabens, and subtle thrusts in the Cambrian CVC, volcanic centre, western Tasmania. *In* Cooke, D. and Kitto, P. (Eds): *CONTENTIOUS ISSUES IN TASMANIAN GEOLOGY.* GSA Tas. Div., Hobart 1994: 31–34.

Green, G.R. and Taheri, J., 1992: Stable isotopes and geochemistry as exploration indicators. *AN ISLAND OF POTENTIAL. Tasmanian Geological Survey Bulletin* 70: 84–91.

Ishikawa, Y., Sawaguchi, T., Iwaya, S. and Horiachi, M., 1976. Delineation of prospecting targets for Kuroko deposits based on modes of volcanism of underlying dacite and alteration halos. *Mining Geology* 26: 105–117 (in Japanese with English abstract).

Large, R. R., Doyle, M., Raymond, O., Cooke, D., Jones, A. and Heasman, L., 1996a. Evolution of the role of Cambrian granites in the genesis of world class VHMS deposits in Tasmania. *Ore Geology Reviews* 10: 215–238.

Large, R.R., Stolz, A.J. and Duhig, N., 1996b: Preliminary assessment of MRV geochemical database in terms of possible vectors to ore. *AMIRA Project P439,* May 1996, pages 197 - 209.

Large, R.R., Crawford, A.J., Adrichem, S., 1989: Primary alteration chemistry of the Mount Read Volcanics. *AMIRA Project P210,* November 1986: 38–45.

Appendix

(pages 173–234)

Alteration summary sheets for Hercules–Mt Read traverse

Sample no.: MR96-46
Group/Formation: MRV-CVC
Location: Hercules traverse
AMG: 376395.6E:5367958N

Field description:
Quartz sericite schist

Ti/Zr = 7

Alteration:

Intensity	☐ weak	☐ moderate	☐ strong	☒ intense
Style	☐ patchy	☒ pervasive	☐ veined	☐ cleavage controlled

Mineralogy: Groundmass alteration: **sericite** 100 % altered

Feldspar alteration: **quartz, sericite ± K-feldspar** 100 % altered

Interpretation: ☐ diagenetic ☐ metamorphic ☒ hydrothermal

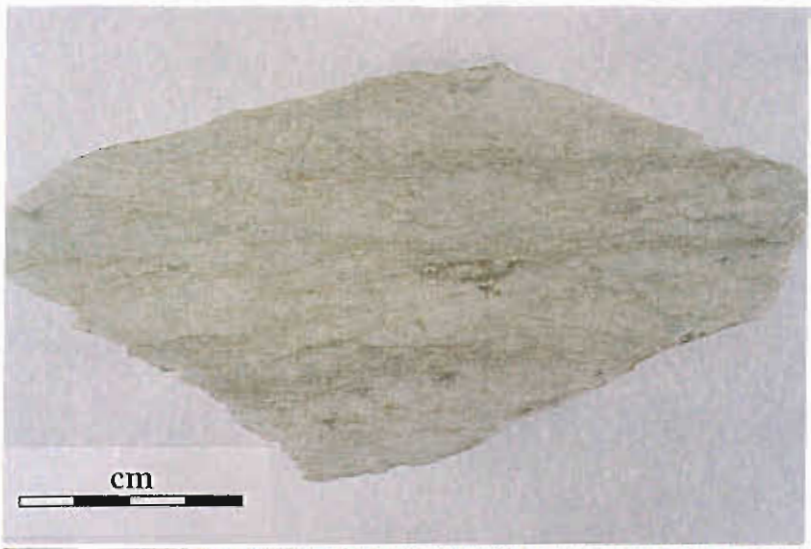

Alteration Index
AI = 99

Chlorite/carb/py Index
CI = 30

Na_2O % = 0.07
Zn ppm = 49
Pb ppm = 30
S % = 0.01
$\delta^{18}O$ =

Whole-rock analysis:

SiO2	74.85
TiO2	0.32
Al2O3	14.22
Fe2O3	1.09
MnO	0.01
MgO	1.36
CaO	0.01
Na2O	0.07
K2O	5.41
P2O5	0.02
S	0.01
CO2	0.07
Total	99.62

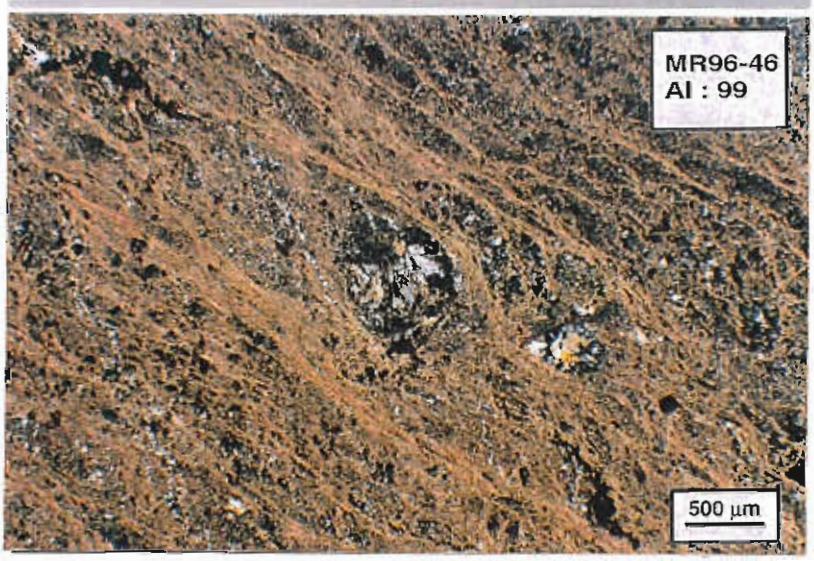

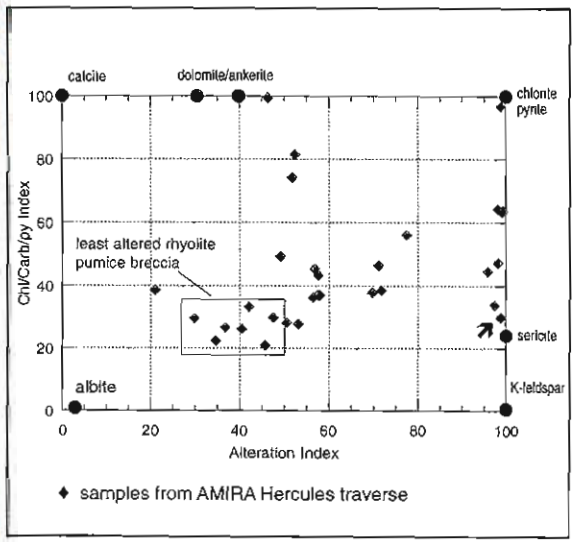

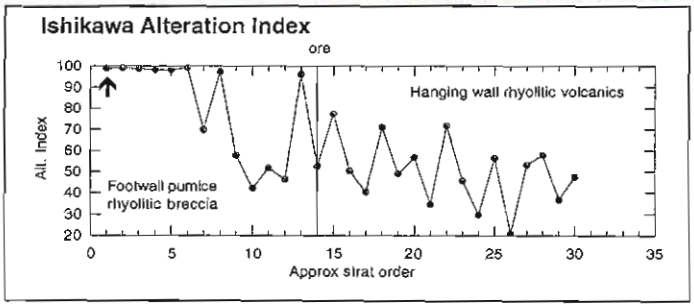

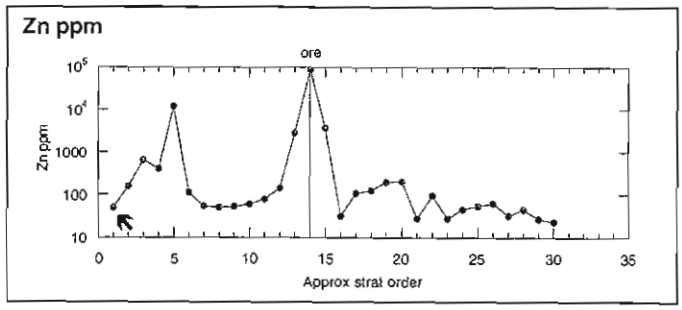

Sample no.: MR96-47
Group/Formation: MRV-CVC
Location: Hercules Traverse
AMG: 376584.3E:5367576N

Field description:
Sericite-carbonate alterred rhyolitic pumice breccia

Ti/Zr = 8

Alteration: Intensity ☐ weak ☐ moderate ☐ strong ☒ intense
Style ☐ patchy ☒ pervasive ☐ veined ☐ cleavage controlled

Mineralogy: Groundmass alteration: **sericite, quartz**
Feldspar alteration: **plag → K-feldspar**

Interpretation: ☐ diagenetic ☐ metamorphic ☒ hydrothermal

Alteration Index
AI = **97**

Chlorite/carb/py Index
CI = **34**

Na_2O % = 0.21
Zn ppm = 51
Pb ppm = 3
S % = 0.01
$\delta^{18}O$ =

Whole-rock analysis:

SiO2	67.93
TiO2	0.42
Al2O3	16.78
Fe2O3	2.71
MnO	0.03
MgO	1.38
CaO	0.02
Na2O	0.21
K2O	7.25
P2O5	0.05
S	0.01
CO2	0.18
Total	99.34

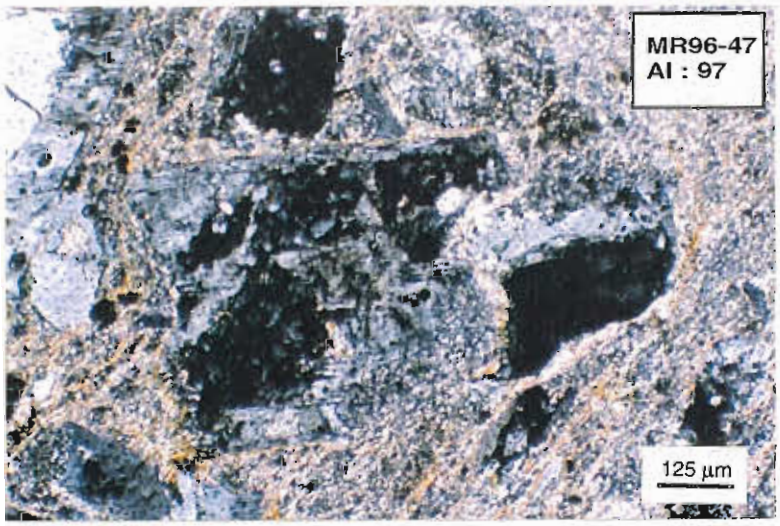

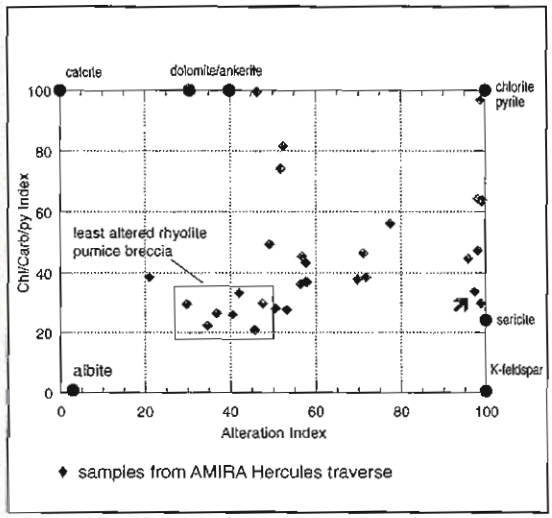

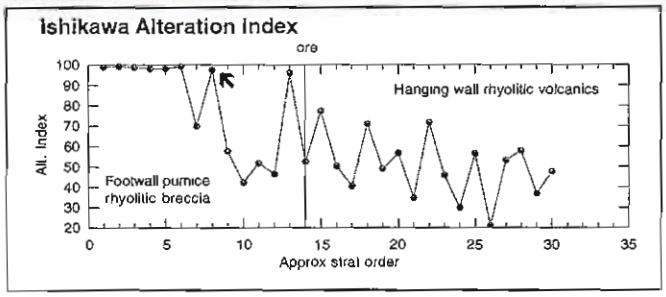

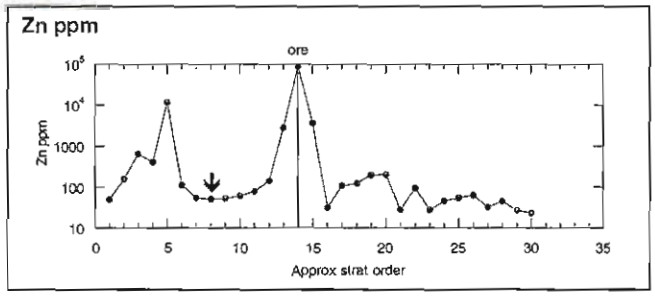

Sample no.: MR96-48
Group/Formation: MRV-CVC
Location: Hercules traverse
AMG: 376525.8E:5367568N

Field description:
Quartz-sericite altered rhyolitic pumice breccia

Ti/Zr = 8

Alteration:

Intensity	☐ weak	☐ moderate	☒ strong	☐ intense
Style	☒ patchy	☒ pervasive	☐ veined	☐ cleavage controlled

Mineralogy:

Groundmass alteration:	**sericite, with quartz veining**	80 % altered
Feldspar alteration:	**carbonate, quartz**	80 % altered

Interpretation: ☐ diagenetic ☐ metamorphic ☒ hydrothermal

Alteration Index
AI = 70

Chlorite/carb/py Index
CI = 38

Na_2O % = 0.96
Zn ppm = 54
Pb ppm = 20
S % = 0.29
$\delta^{18}O$ =

Whole-rock analysis:

SiO2	73.04
TiO2	0.29
Al2O3	12.76
Fe2O3	2.32
MnO	0.27
MgO	1.14
CaO	1.40
Na2O	0.96
K2O	4.33
P2O5	0.05
S	0.29
CO2	1.14
Total	99.82

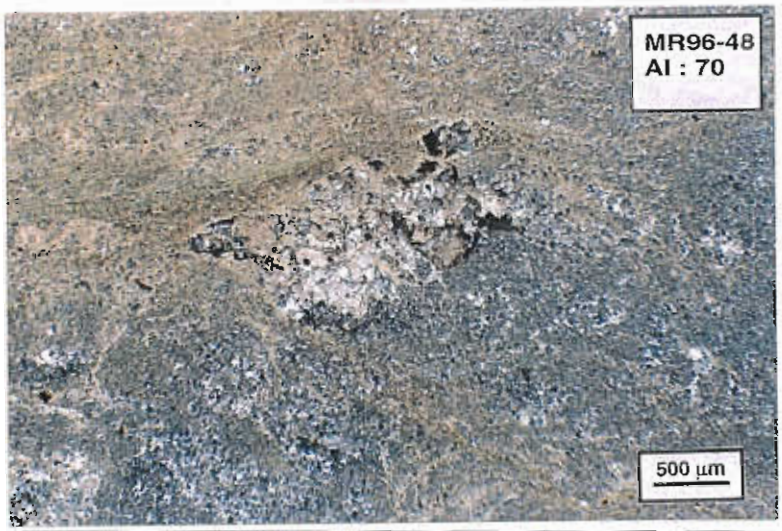

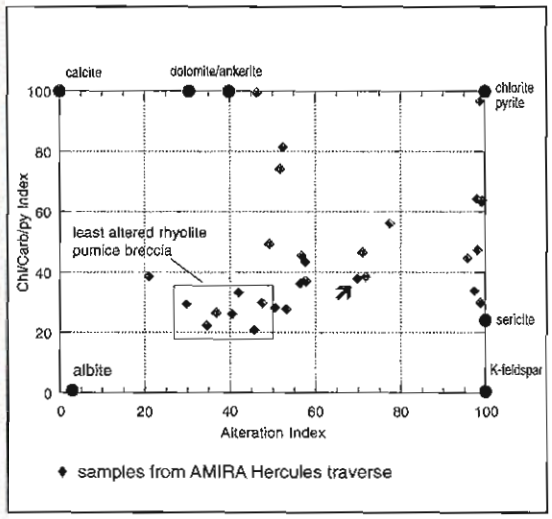

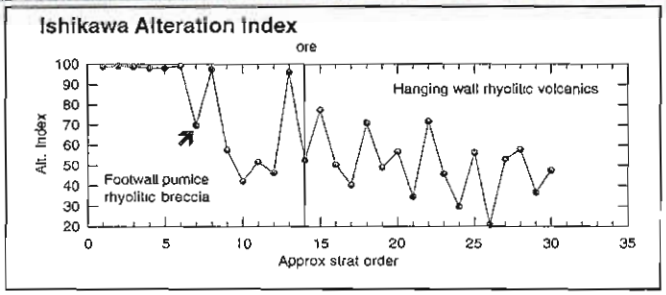

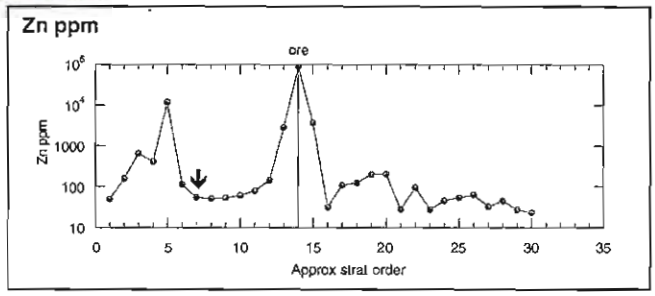

Sample no.: MR96-49
Group/Formation: MRV-CVC
Location: Hercules traverse
AMG: 376473.3E:5367589N

Field description:
Chlorite-sericite altered rhyolitic pumice breccia

Ti/Zr = 8

Alteration: Intensity: [ ] weak [ ] moderate [X] strong [ ] intense
Style: [X] patchy [X] pervasive [ ] veined [ ] cleavage controlled

Mineralogy: Groundmass alteration: **sericite, with chlorite lenticles** 90 % altered
Feldspar alteration: **sericite, quartz, opaque gunge** 100 % altered

Interpretation: [ ] diagenetic [ ] metamorphic [X] hydrothermal

Alteration Index
AI = 98

Chlorite/carb/py Index
CI = 47

Na_2O % = 0.03
Zn ppm = 403
Pb ppm = 67
S % = 0.24
$\delta^{18}O$ =

Whole-rock analysis:

SiO2	72.46
TiO2	0.30
Al2O3	13.42
Fe2O3	2.46
MnO	0.62
MgO	2.19
CaO	0.10
Na2O	0.03
K2O	4.87
P2O5	0.05
S	0.24
CO2	0.73
Total	99.53

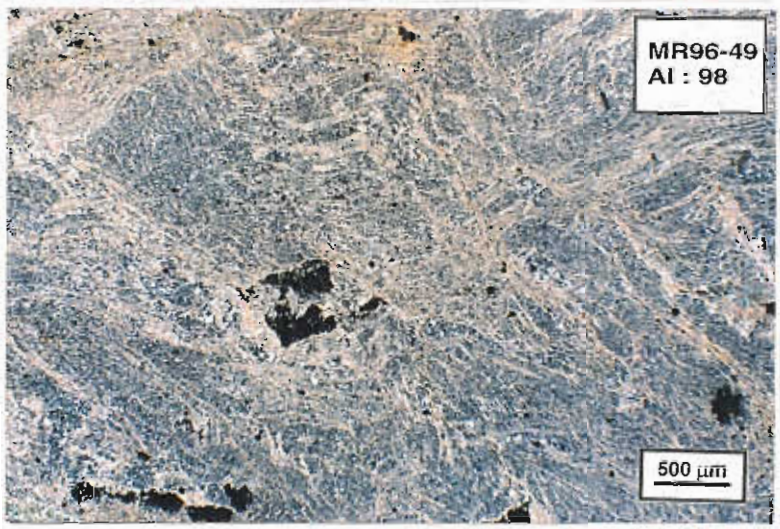

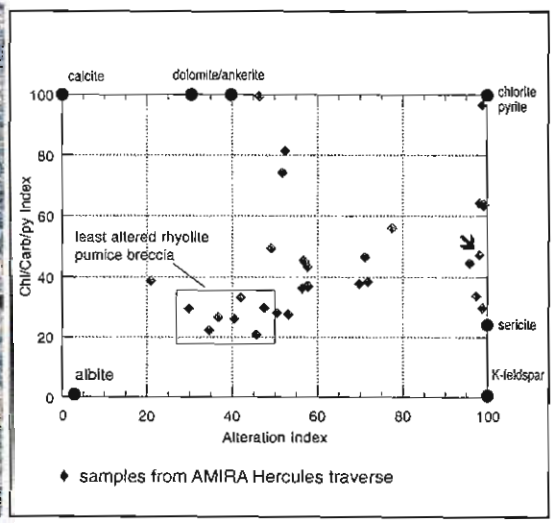

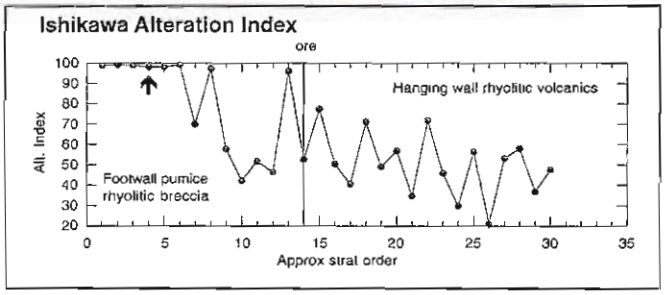

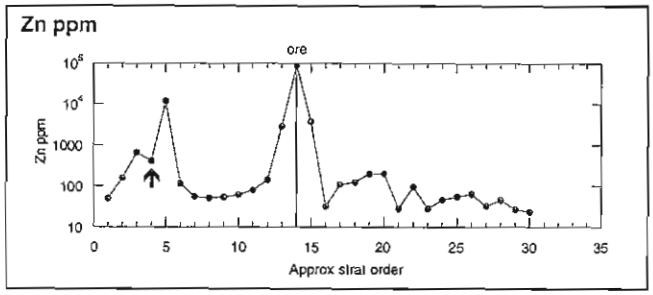

Sample no.: MR96-50
Group/Formation: MRV-CVC
Location: Hercules traverse
AMG: 376414.4E:5367654N

Field description:
Quartz-sericite schist with disseminated py-sp

Ti/Zr = 10

Alteration: Intensity ☐ weak ☐ moderate ☐ strong ☒ intense
Style ☐ patchy ☒ pervasive ☐ veined ☐ cleavage controlled

Mineralogy: Groundmass alteration: **sericite, quartz** 100 % altered
Feldspar alteration: **quartz** 100 % altered

Interpretation: ☐ diagenetic ☐ metamorphic ☒ hydrothermal

Alteration Index
AI = 98

Chlorite/carb/py Index
CI = 64

Na_2O % = 0.05
Zn = 1.2%
Pb ppm = 1000
S % = 3.26
$\delta^{18}O$ =

Whole-rock analysis:

SiO2	76.19
TiO2	0.22
Al2O3	8.55
Fe2O3	5.03
MnO	0.09
MgO	1.11
CaO	0.03
Na2O	0.05
K2O	3.08
P2O5	0.04
S	3.26
CO2	0.07
Total	97.94

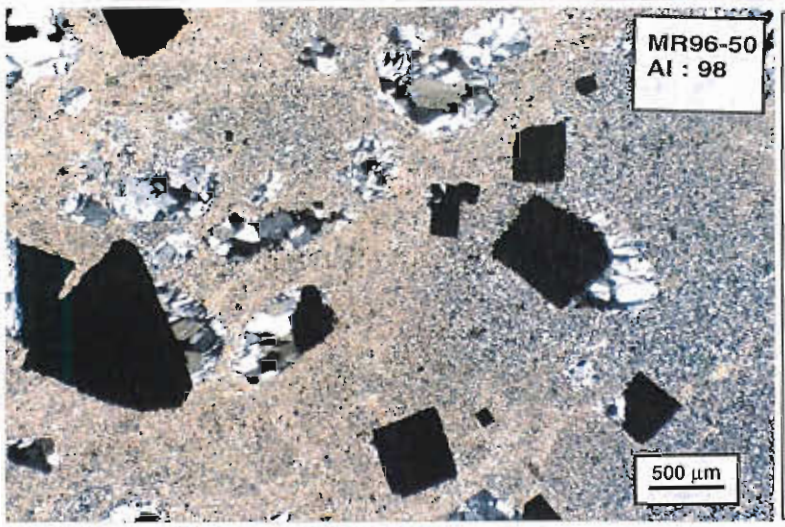

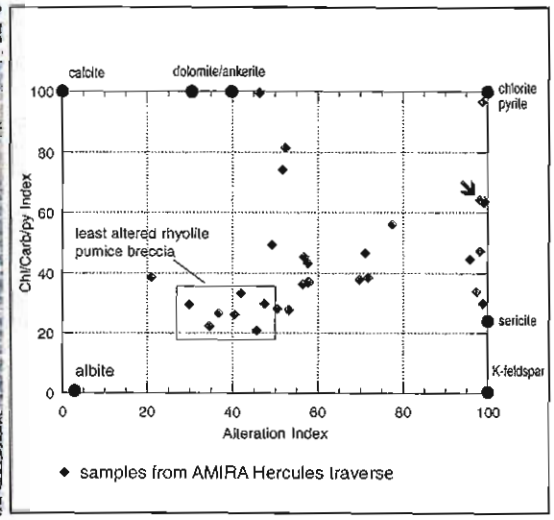

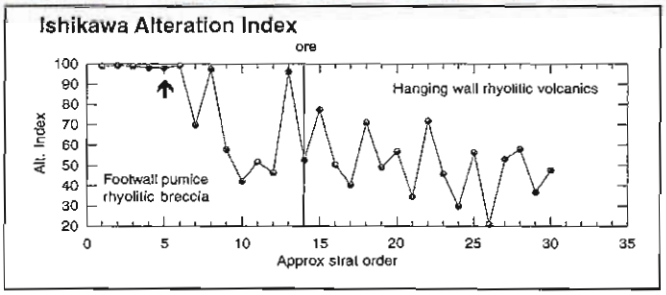

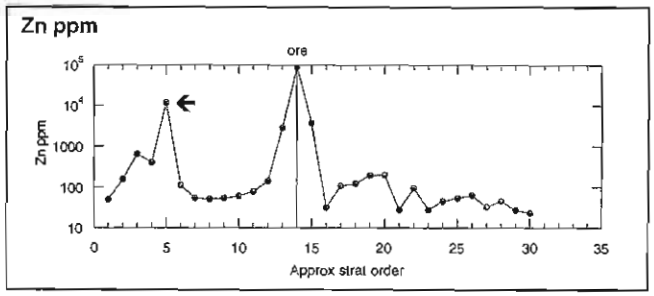

Sample no.: MR96-51
Group/Formation: MRV-CVC
Location: Hercules traverse
AMG: 376329.9E:5367642N

Field description:
Quartz-chlorite-sericite-pyrite schist

Ti/Zr = 8

Alteration:

Intensity	☐ weak	☐ moderate	☐ strong	☒ intense
Style	☐ patchy	☒ pervasive	☐ veined	☐ cleavage controlled

Mineralogy:

Groundmass alteration: **quartz,sericite, patchy chlorite** 100 % altered

Feldspar alteration: **quartz,chlorite, sericite** 100 % altered

Interpretation: ☐ diagenetic ☐ metamorphic ☒ hydrothermal

Alteration Index
AI = 99

Chlorite/carb/py Index
CI = 64

Na_2O % = 0.03
Zn ppm = 155
Pb ppm = 52
S % = 1.53
$\delta^{18}O$ =

Whole-rock analysis:

SiO2	72.42
TiO2	0.30
Al2O3	12.22
Fe2O3	5.70
MnO	0.18
MgO	1.39
CaO	0.01
Na2O	0.03
K2O	3.67
P2O5	0.04
S	1.53
CO2	0.07
Total	99.14

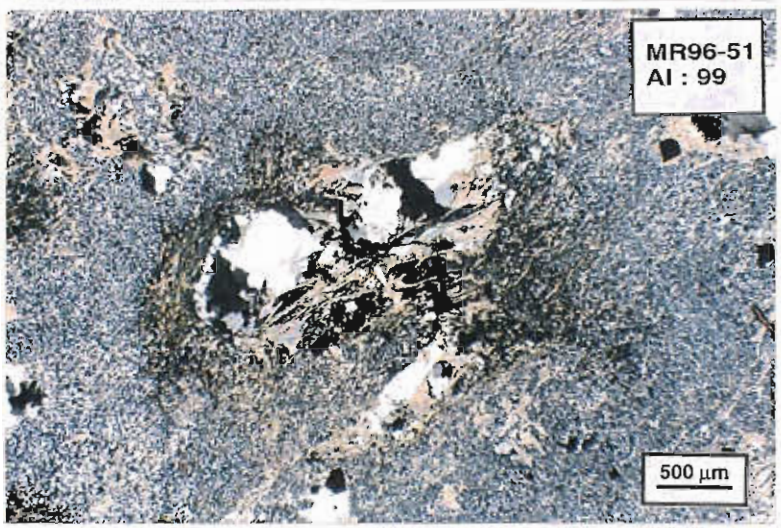

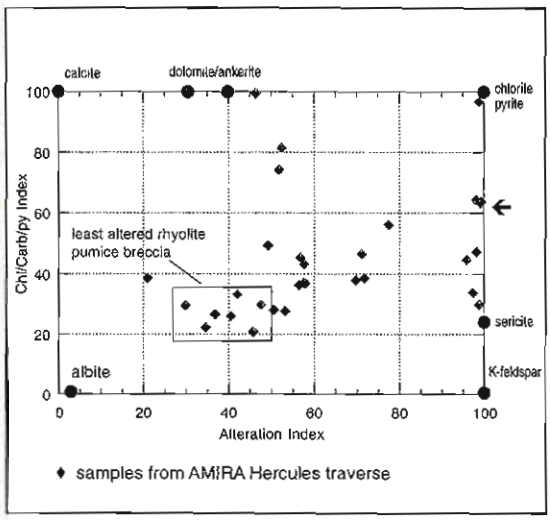

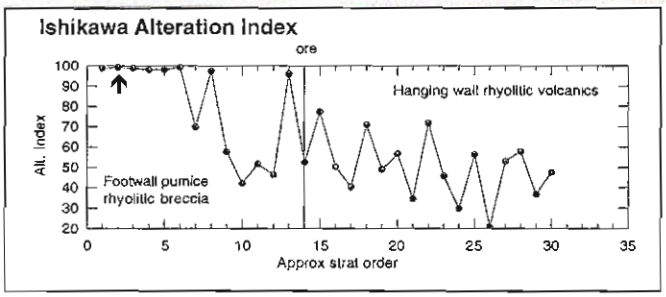

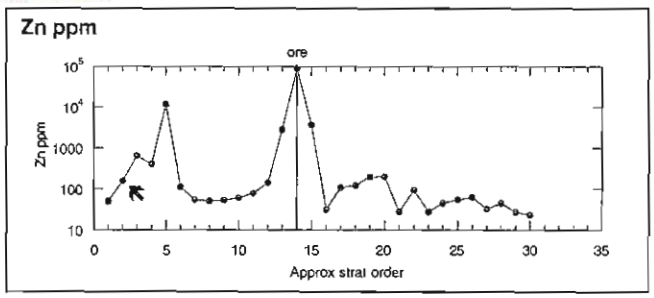

Sample no.: MR96-52
Group/Formation: MRV-CVC
Location: Hercules traverse
AMG: 376324.7E:5367547N

Field description:
Chlorite-pyrite vein in quartz chlorite-sericite schist

Ti/Zr = 8

Alteration:

Intensity	☐ weak	☐ moderate	☐ strong	☒ intense
Style	☐ patchy	☒ pervasive	☐ veined	☐ cleavage controlled

Mineralogy:

Groundmass alteration:	**quartz, chlorite, pyrite**	100 % altered
Feldspar alteration:	**quartz**	100 % altered

Interpretation: ☐ diagenetic ☐ metamorphic ☒ hydrothermal

Alteration Index
AI = **99**

Chlorite/carb/py Index
CI = **97**

Na_2O % = 0.05
Zn ppm = 650
Pb ppm = 54
S % = 2.68
$\delta^{18}O$ =

Whole-rock analysis:

SiO2	57.91
TiO2	0.32
Al2O3	11.34
Fe2O3	18.57
MnO	0.82
MgO	4.43
CaO	0.01
Na2O	0.05
K2O	0.65
P2O5	0.02
S	2.68
CO2	0.07
Total	99.88

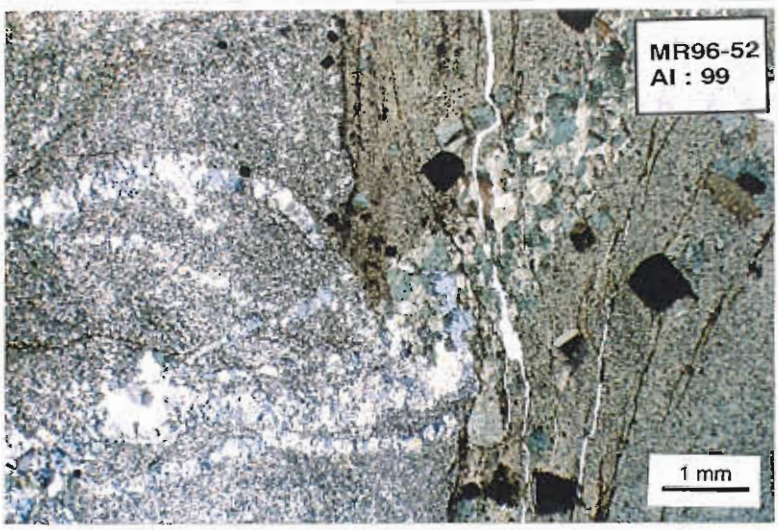

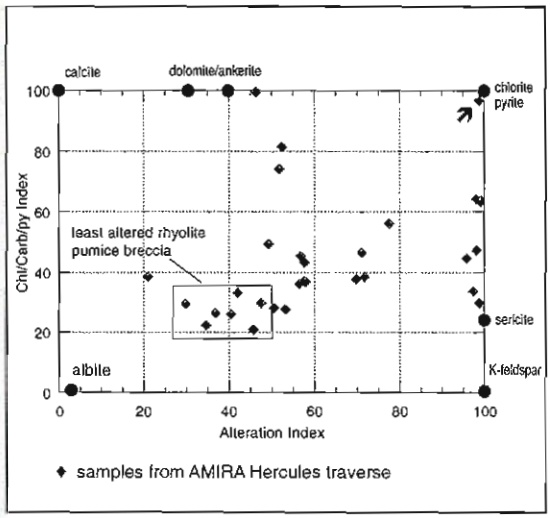

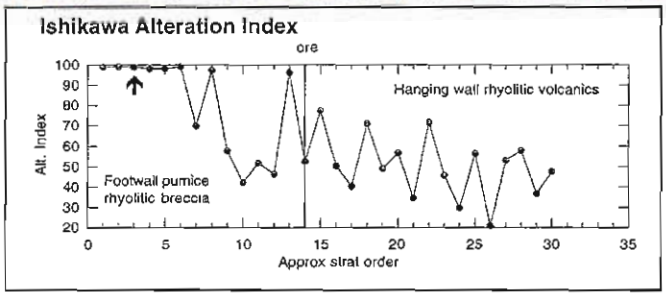

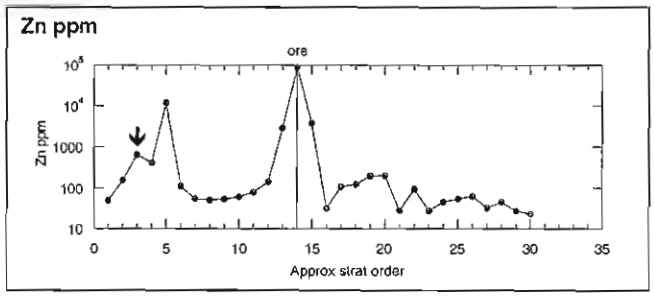

Sample no.: MR96-53
Group/Formation: MRV-CVC
Location: Hercules traverse
AMG: 376329.4E:5367457N

Field description:
Chlorite-sericite altered rhyolitic pumice breccia

Ti/Zr = 8

Alteration:
Intensity: ☐ weak ☐ moderate ☐ strong ☒ intense
Style: ☒ patchy ☒ pervasive ☐ veined ☐ cleavage controlled

Mineralogy:
Groundmass alteration: **sericite, quartz, chlorite** 100 % altered
Feldspar alteration: **quartz, sericite** 100 % altered

Interpretation: ☐ diagenetic ☐ metamorphic ☒ hydrothermal

Alteration Index
AI = 99

Chlorite/carb/py Index
CI = 63

Na_2O % = 0.03
Zn ppm = 111
Pb ppm = 94
S % = 0.72
$\delta^{18}O$ =

Whole-rock analysis:

SiO2	72.58
TiO2	0.29
Al2O3	12.95
Fe2O3	5.86
MnO	0.17
MgO	1.10
CaO	0.01
Na2O	0.03
K2O	3.67
P2O5	0.05
S	0.72
CO2	0.07
Total	99.50

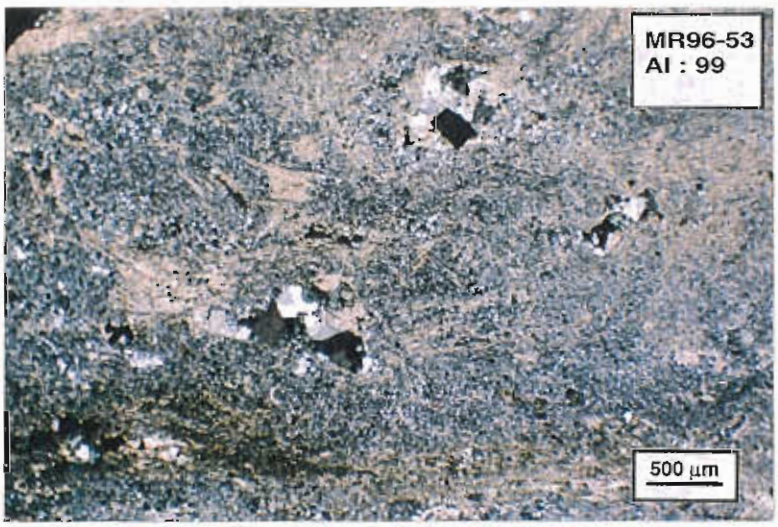

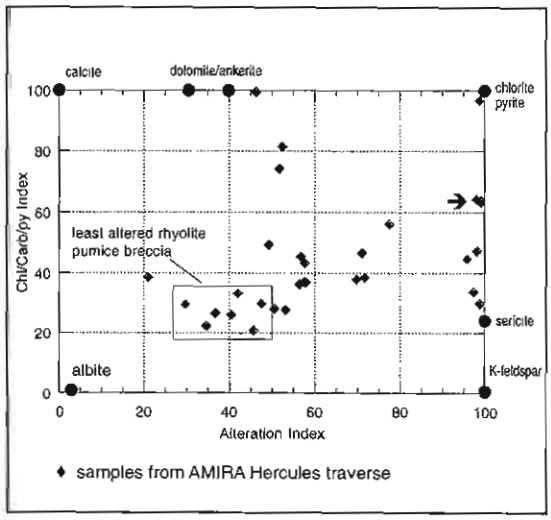

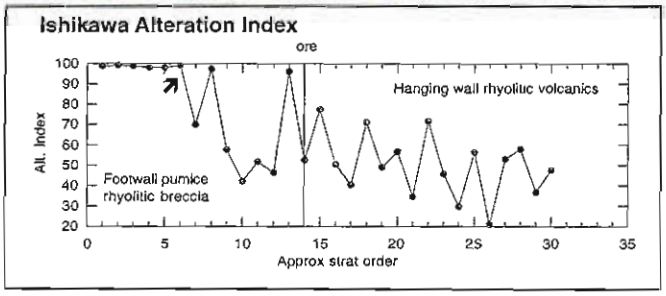

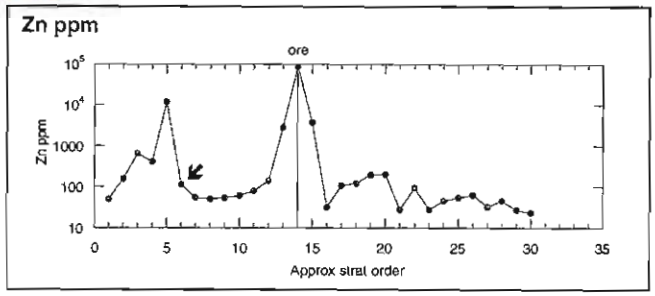

Sample no.: MR96-54
Group/Formation: MRV-CVC
Location: Hercules traverse
AMG: 376690.4E:5367164N

Field description:
Albite sericite altered rhyolitic pumice breccia

Ti/Zr = 8

Alteration:
Intensity: ☐ weak ☐ moderate ☐ strong ☒ intense
Style: ☐ patchy ☒ pervasive ☐ veined ☐ cleavage controlled

Mineralogy:
Groundmass alteration: **sericite, quartz** 100 % altered
Feldspar alteration: **sericite with albite overgrowths** 80 % altered

Interpretation: ☒ diagenetic ☐ metamorphic ☒ hydrothermal

Alteration Index
AI = 58

Chlorite/carb/py Index
CI = 37

Na_2O % = 2.76
Zn ppm = 53
Pb ppm = 7
S % = 0.01
$\delta^{18}O$ =

Whole-rock analysis:

SiO2	70.47
TiO2	0.39
Al2O3	15.81
Fe2O3	2.65
MnO	0.04
MgO	1.30
CaO	0.76
Na2O	2.76
K2O	3.49
P2O5	0.06
S	0.01
CO2	0.11
Total	100.01

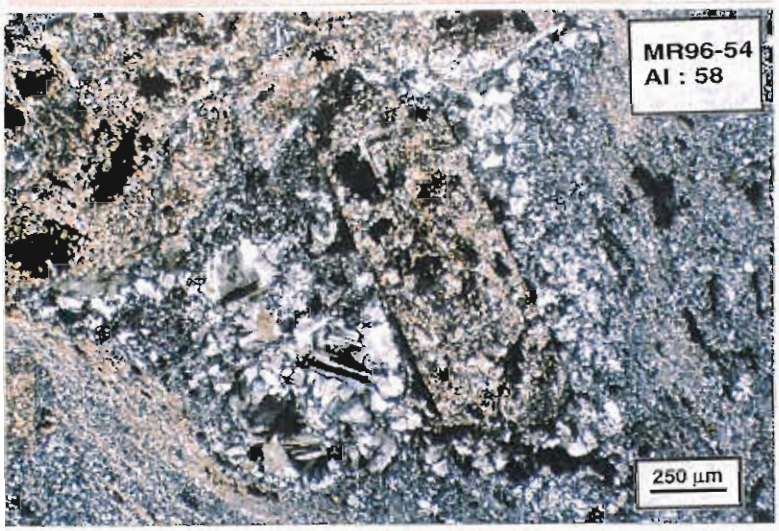

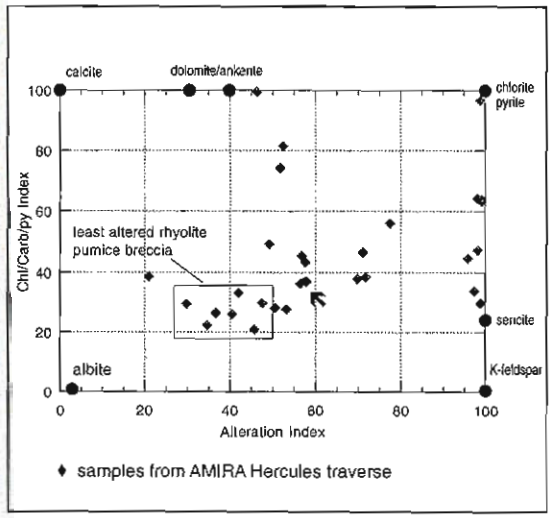

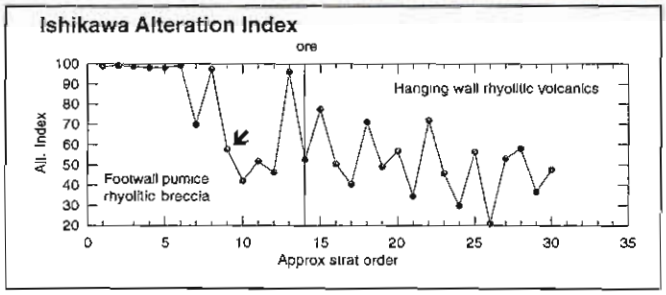

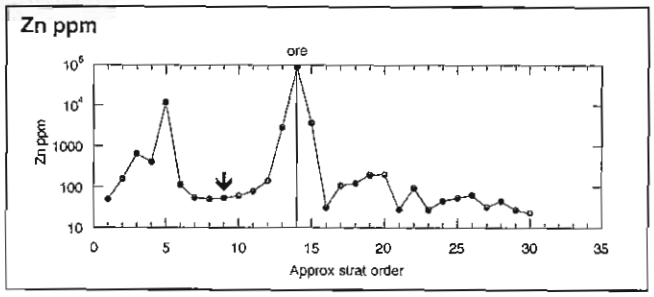

Sample no.: MR96-55
Group/Formation: MRV-CVC
Location: Hercules footwall
AMG: 376718.7E:5367093N

Field description:
Albite altered rhyolitic pumice breccia

Ti/Zr = 8

Alteration:
Intensity: ☐ weak ☐ moderate ☒ strong ☐ intense
Style: ☒ patchy ☒ pervasive ☐ veined ☐ cleavage controlled

Mineralogy:
Groundmass alteration: **sericite, quartz, albite** — 100 % altered
Feldspar alteration: **sericite with albite overgrowths** — 50 % altered

Interpretation: ☒ diagenetic ☐ metamorphic ☒ hydrothermal

Alteration Index
AI = 42

Chlorite/carb/py Index
CI = 33

Na_2O % = 3.89
Zn ppm = 60
Pb ppm = 13
S % = 0.01
$\delta^{18}O$ =

Whole-rock analysis:

SiO2	73.45
TiO2	0.35
Al2O3	14.09
Fe2O3	2.36
MnO	0.04
MgO	0.96
CaO	0.62
Na2O	3.89
K2O	2.31
P2O5	0.05
S	0.01
CO2	0.04
Total	99.69

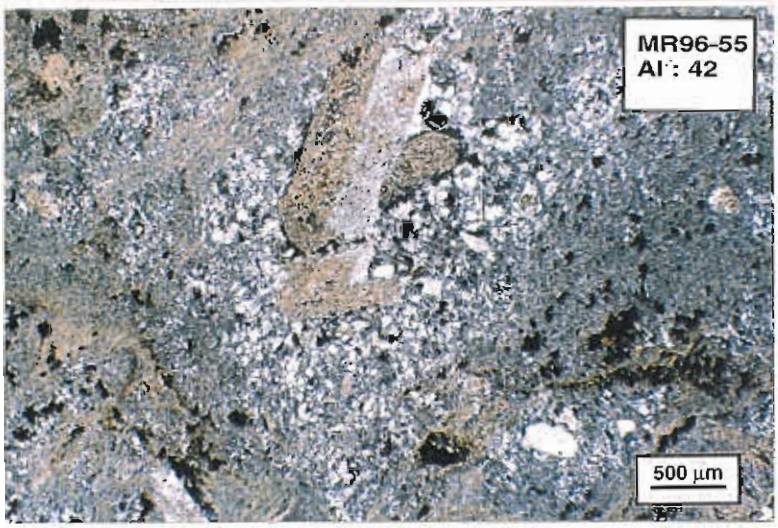

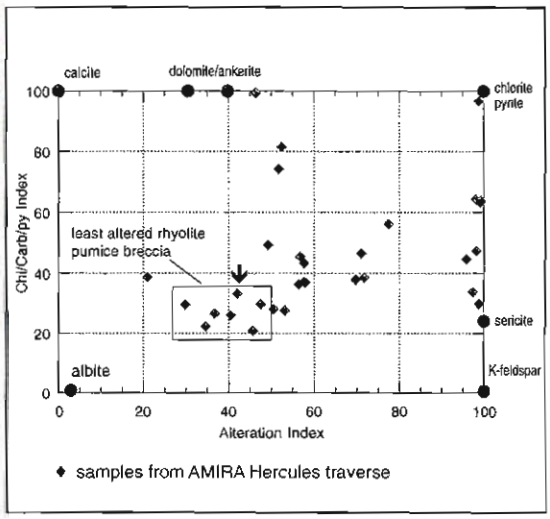

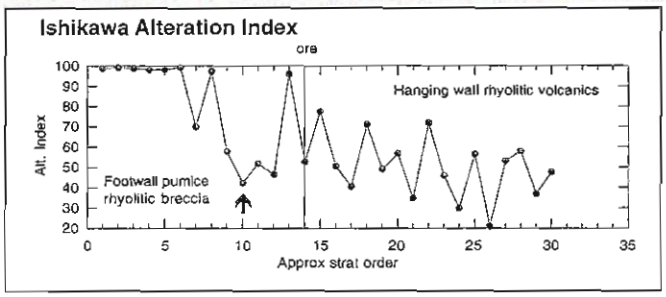

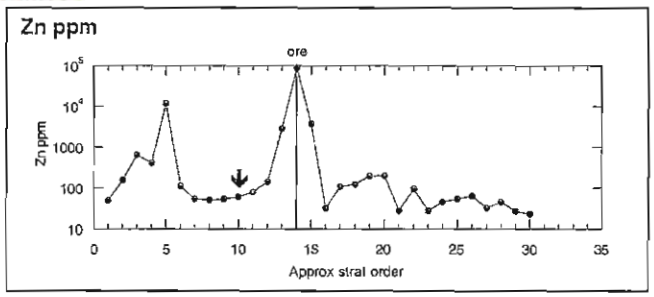

Sample no.: MR96-56
Group/Formation: MRV-CVC
Location: Hercules footwall
AMG: 376623.4E:5366722N

Field description:
Carbonate-sericite altered volcanics, 20 m below massive sulphide lens

Ti/Zr = 11

Alteration:

Intensity	☐	weak	☐	moderate	☐	strong	☒ intense
Style	☐	patchy	☒	pervasive	☐	veined	☐ cleavage controlled

Mineralogy:

Groundmass alteration:	**carbonate, quartz, sericite (?)**	100 % altered
Feldspar alteration:	**carbonate**	100 % altered

Interpretation: ☐ diagenetic ☐ metamorphic ☒ hydrothermal

Alteration Index
AI = 52

Chlorite/carb/py Index
CI = 74

Na_2O % = 0.11
Zn ppm = 79
Pb ppm = 109
S % = 0.45
$\delta^{18}O$ =

Whole-rock analysis:

SiO2	44.31
TiO2	0.51
Al2O3	14.87
Fe2O3	1.77
MnO	0.92
MgO	8.14
CaO	10.52
Na2O	0.11
K2O	3.28
P2O5	0.12
S	0.45
CO2	10.22
Total	99.78

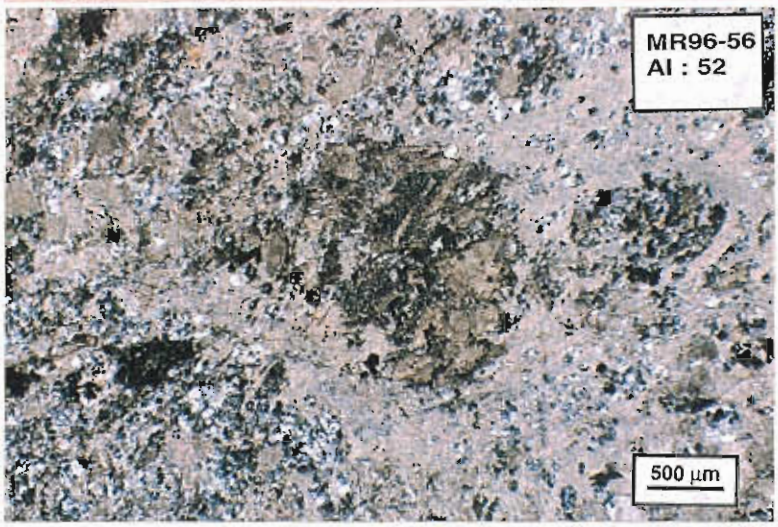

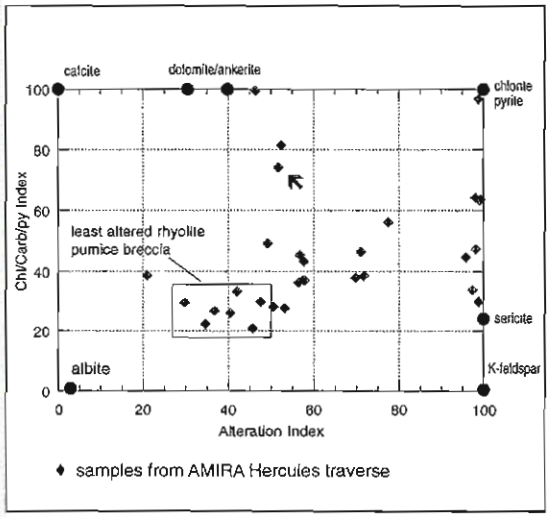

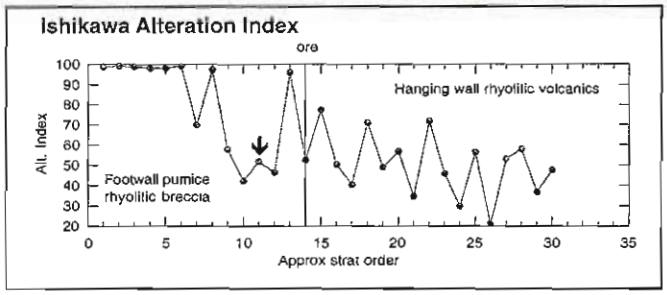

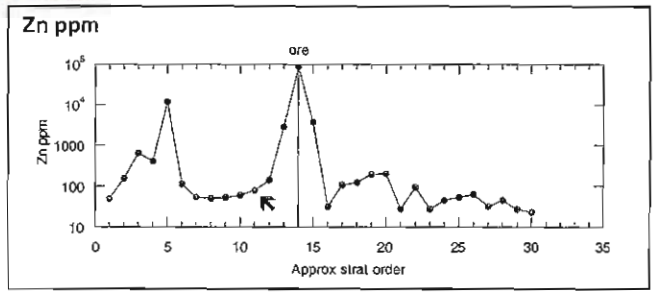

Sample no.: MR96-57
Group/Formation: MRV-CVC
Location: Hercules footwall
AMG: 376596.9E:5366659N

Field description:
Siliceous carbonate-chlorite altered rhyolitic pumice breccia

Ti/Zr = 11

Alteration: Intensity ☐ weak ☐ moderate ☐ strong ☒ intense
Style ☐ patchy ☒ pervasive ☐ veined ☐ cleavage controlled

Mineralogy: Groundmass alteration: **chlorite, carbonate** 100 % altered
Feldspar alteration: **carbonate, quartz, chlorite** 100 % altered

Interpretation: ☐ diagenetic ☐ metamorphic ☒ hydrothermal

Alteration Index
AI = 46

Chlorite/carb/py Index
CI = 99

Na_2O % = 0.03
Zn ppm = 139
Pb ppm = 28
S % = 0.27
$\delta^{18}O$ =

Whole-rock analysis:

SiO2	29.42
TiO2	0.34
Al2O3	10.12
Fe2O3	2.82
MnO	2.66
MgO	14.87
CaO	17.24
Na2O	0.03
K2O	0.06
P2O5	0.12
S	0.27
CO2	15.24
Total	99.30

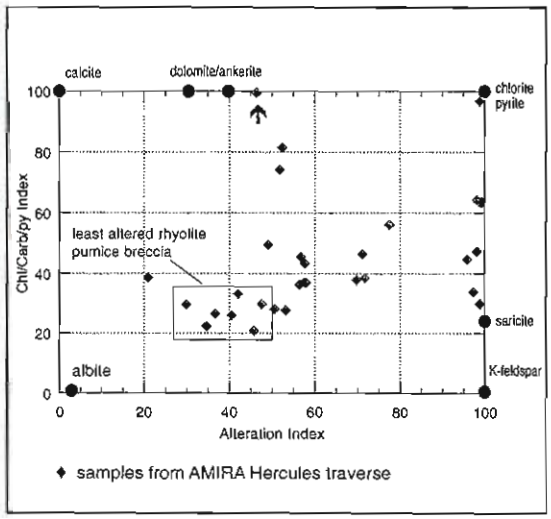

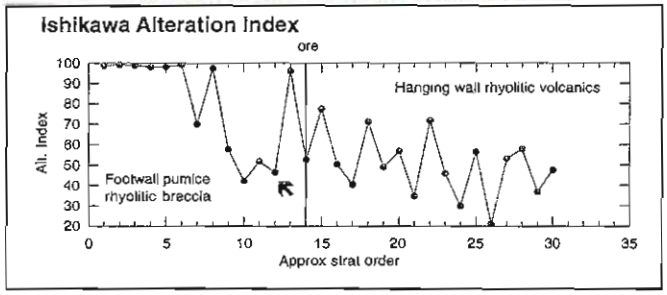

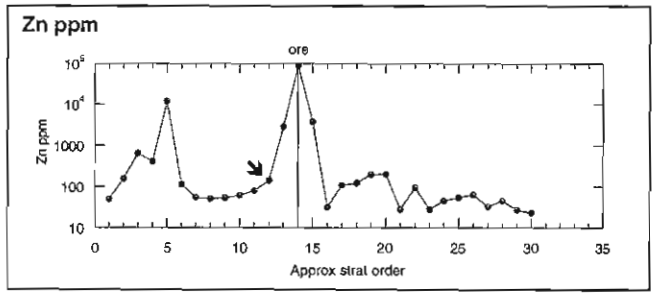

Sample no.: MR96-58
Group/Formation: MRV-CVC
Location: Footwall of Hercules ore
AMG: 376542.6E:5366044N

Field description:
Siliceous altered zone in M lode open cut. <10 m from ore

Ti/Zr = 13

Alteration:

Intensity	☐	weak	☐	moderate	☐	strong	☒ intense
Style	☐	patchy	☒	pervasive	☐	veined	☐ cleavage controlled

Mineralogy:
Groundmass alteration: **quartz, sericite** — 100 % altered
Feldspar alteration: **quartz, sericite, pyrite, sphalerite** — 100 % altered

Interpretation: ☐ diagenetic ☐ metamorphic ☒ hydrothermal

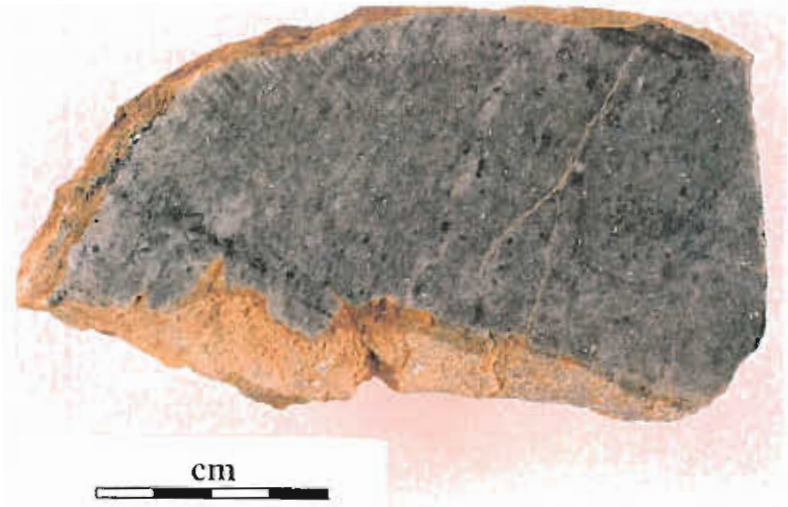

Alteration Index
AI = 96

Chlorite/carb/py Index
CI = 45

Na_2O % = 0.03
Zn ppm = 2800
Pb ppm = 1500
S % = 1.72
$\delta^{18}O$ =

Whole-rock analysis:

SiO2	81.26
TiO2	0.33
Al2O3	9.41
Fe2O3	2.07
MnO	0.02
MgO	0.65
CaO	0.13
Na2O	0.03
K2O	3.10
P2O5	0.08
S	1.72
CO2	0.11
Total	99.64

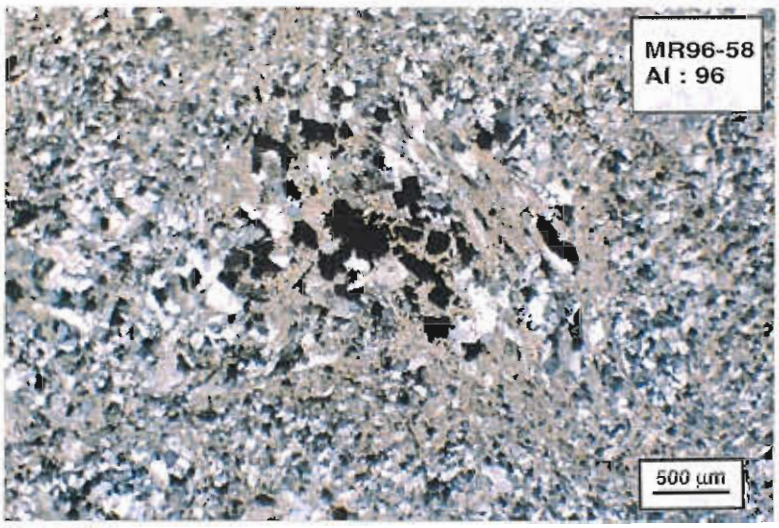

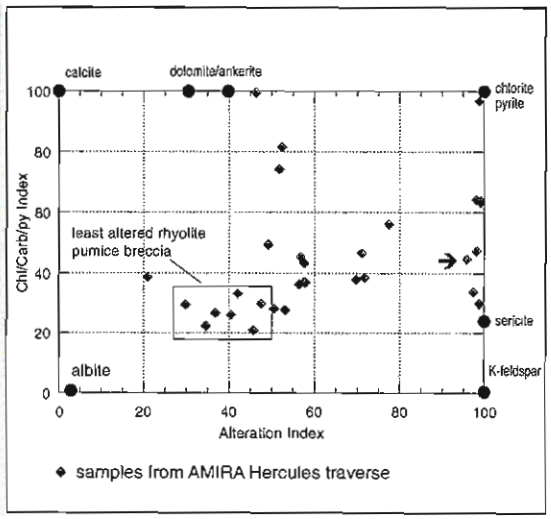

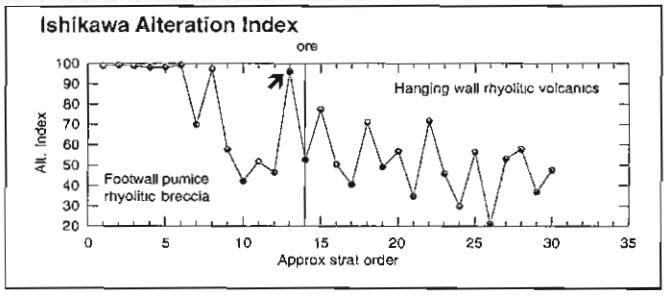

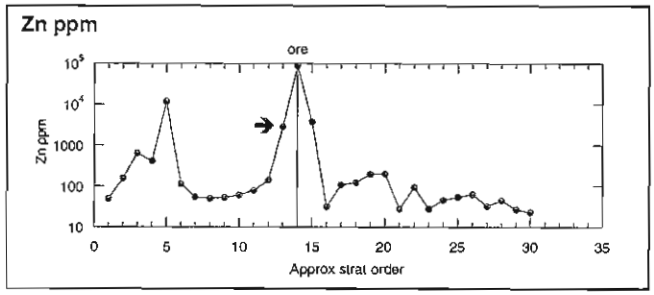

Sample no.: MR96-59
Group/Formation: MRV-CVC
Location: Hercules mine
AMG: 376654.6E:5366165N

Field description:
Cleaved banded dark shale
— Hercules host rock

Ti/Zr = 12

Alteration:
Intensity: ☐ weak ☐ moderate ☐ strong ☒ intense
Style: ☐ patchy ☒ pervasive ☐ veined ☐ cleavage controlled

Mineralogy:
Groundmass alteration: **carbonate, sericite, chlorite** — 100 % altered
Feldspar alteration: **carbonate, relict albite (?)** — 80 % altered

Interpretation: ☐ diagenetic ☐ metamorphic ☒ hydrothermal

Alteration Index
AI = 77

Chlorite/carb/py Index
CI = **56**

Na_2O % = 0.47
Zn ppm = 3700
Pb ppm = 58
S % = 1.69
$\delta^{18}O$ =

Whole-rock analysis:

SiO2	61.94
TiO2	0.55
Al2O3	17.39
Fe2O3	3.39
MnO	0.62
MgO	2.87
CaO	1.59
Na2O	0.47
K2O	4.17
P2O5	0.11
S	1.69
CO2	1.47
Total	98.81

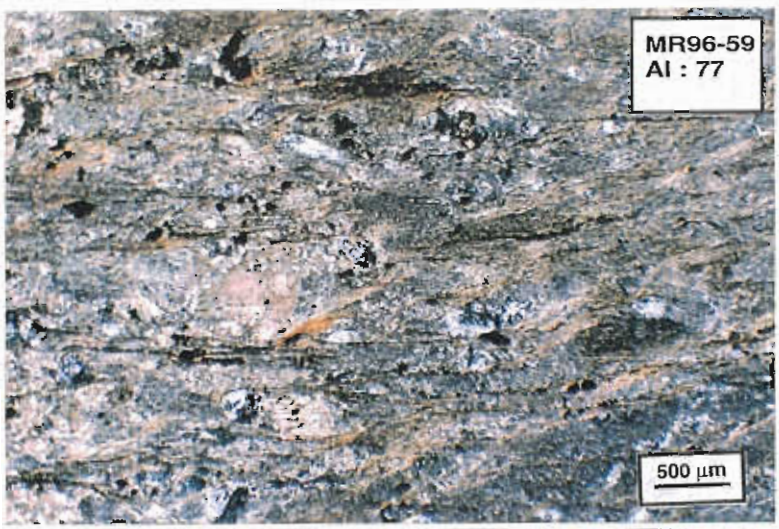

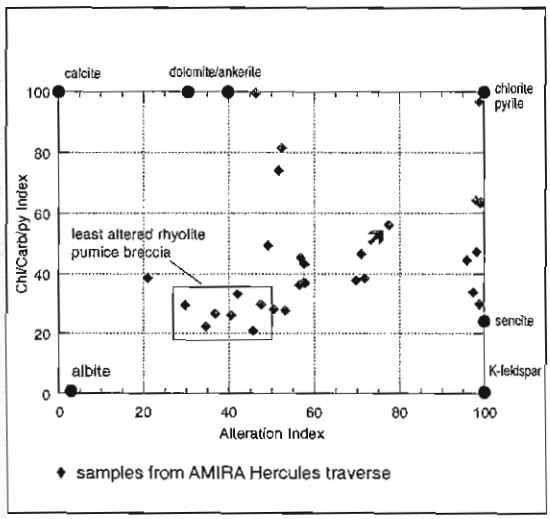

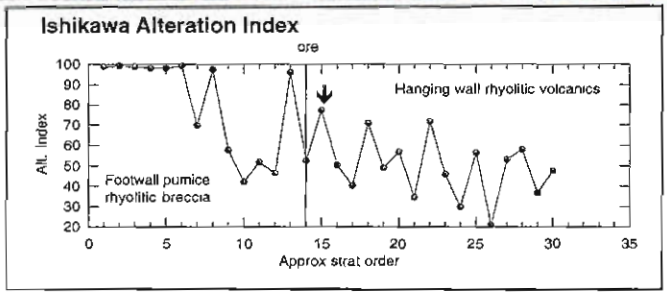

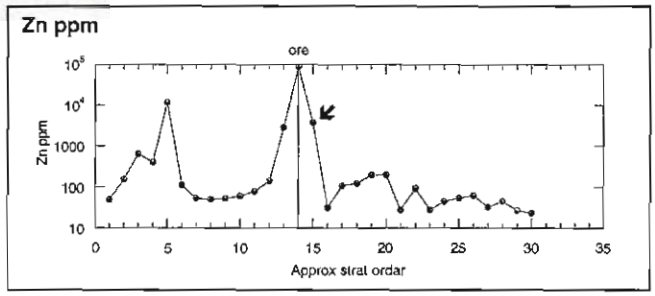

Sample no.: MR96-60
Group/Formation: MRV-CVC
Location: Hercules hangingwall
AMG: 376980.9E:5366161N

Field description:
Weakly altered rhyolitic pumice breccia

Ti/Zr = 7.9

Alteration:
Intensity: [X] weak [ ] moderate [ ] strong [ ] intense
Style: [X] patchy [ ] pervasive [ ] veined [ ] cleavage controlled

Mineralogy:
Groundmass alteration: **sericite, chlorite** — 30 % altered
Feldspar alteration: **unaltered, minor albite overgrowths** — 10 % altered

Interpretation:
[ ] diagenetic [X] metamorphic [ ] hydrothermal

Alteration Index
AI = 58

Chlorite/carb/py Index
CI = 43

Na_2O % = 2.62
Zn ppm = 187
Pb ppm = 155
S % = 0.01
$\delta^{18}O$ =

Whole-rock analysis:

SiO2	75.81
TiO2	0.30
Al2O3	12.44
Fe2O3	2.86
MnO	0.21
MgO	1.24
CaO	0.04
Na2O	2.62
K2O	2.38
P2O5	0.04
S	0.01
CO2	0.18
Total	99.76

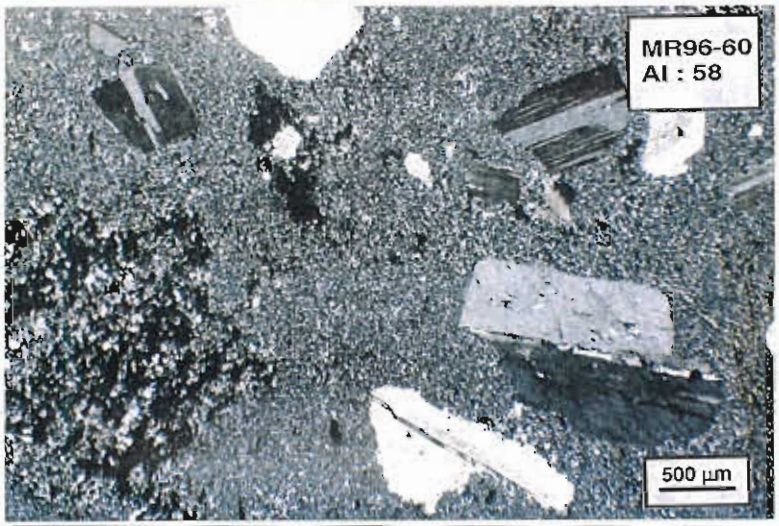

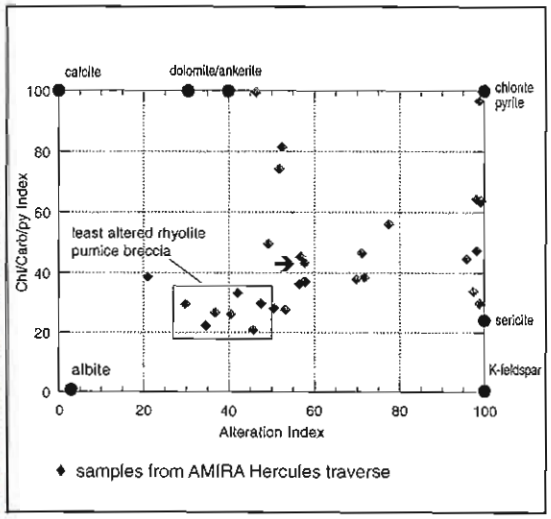

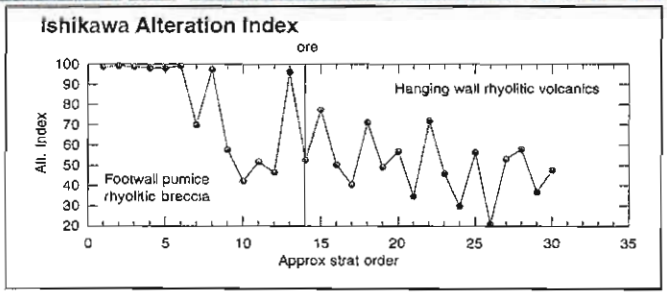

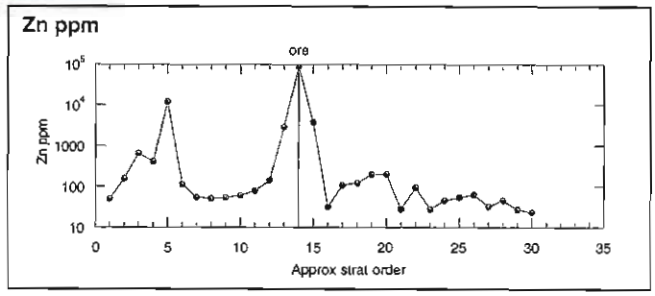

Sample no.: MR96-61
Group/Formation: MRV-CVC
Location: Hercules hangingwall
AMG: 376850.8E:5366151N

Field description:
Fine siliceous volcaniclastic pumice breccia with quartz-chlorite veins

Ti/Zr = 7

Alteration:

Intensity	☐ weak	☒ moderate	☐ strong	☐ intense
Style	☐ patchy	☒ pervasive	☒ veined	☐ cleavage controlled

Mineralogy:
Groundmass alteration: **sericite, chlorite** — 50 % altered
Feldspar alteration: **weak sericite** — 20 % altered

Interpretation: ☐ diagenetic ☐ metamorphic ☒ hydrothermal

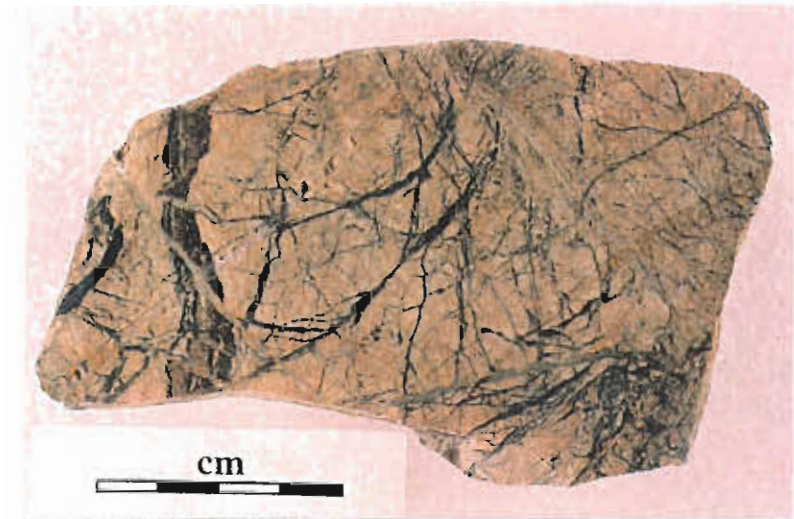

Alteration Index
AI = 51

Chlorite/carb/py Index
CI = 28

Na_2O % = 3.28
Zn ppm = 31
Pb ppm = 7
S % = 0.12
$\delta^{18}O$ =

Whole-rock analysis:

SiO2	73.97
TiO2	0.31
Al2O3	14.36
Fe2O3	2.02
MnO	0.05
MgO	0.60
CaO	0.17
Na2O	3.28
K2O	2.92
P2O5	0.05
S	0.12
CO2	0.15
Total	99.48

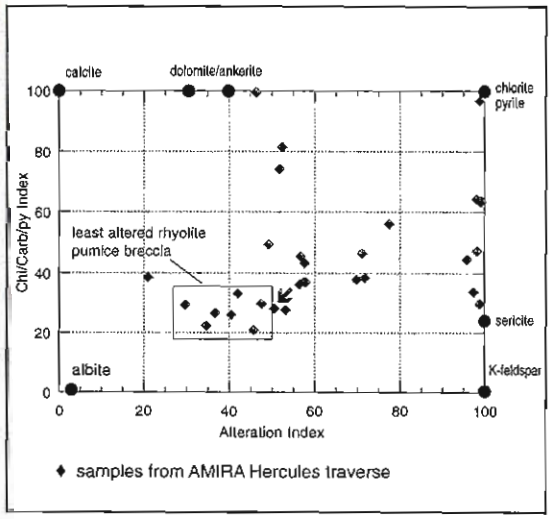

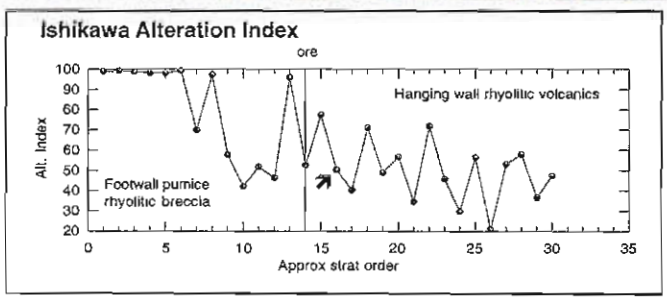

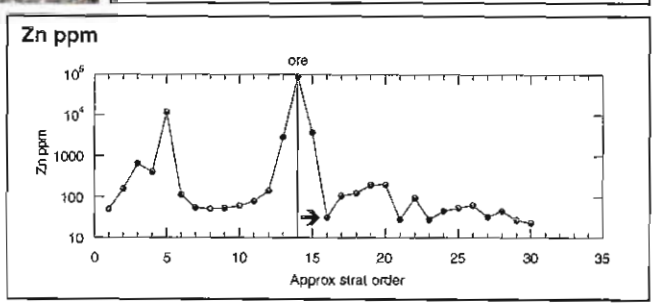

Sample no.: MR96-62
Group/Formation: MRV-CVC
Location: Hercules mine
AMG: 376555E:5366011N

Field description:
Carbonate-sphalerite ore from M lode

Ti/Zr = 14

Alteration: Intensity ☐ weak ☐ moderate ☐ strong ☒ intense
Style ☐ patchy ☒ pervasive ☐ veined ☐ cleavage controlled

Mineralogy: Groundmass alteration: **radial and colloform carbonate** ☐ % altered
Feldspar alteration: ☐ % altered

Interpretation: ☐ diagenetic ☐ metamorphic ☒ hydrothermal

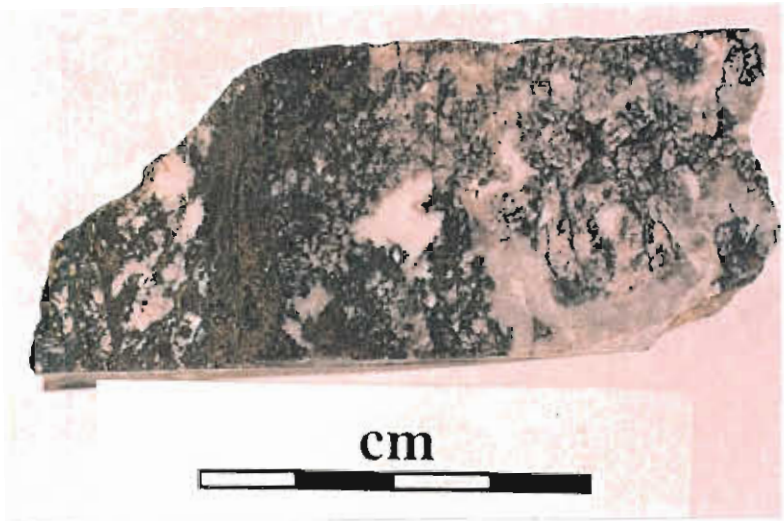

Alteration Index
AI = 53

Chlorite/carb/py Index
CI = 82

Na_2O % = 0.05
Zn ppm= 87,000
Pb ppm= 35,000
S % = 9.42
$\delta^{18}O$ =

Whole-rock analysis:

SiO2	13.27
TiO2	0.26
Al2O3	7.86
Fe2O3	6.27
MnO	20.70
MgO	3.43
CaO	4.88
Na2O	0.05
K2O	2.01
P2O5	0.09
S	9.42
CO2	16.49
Total	97.98

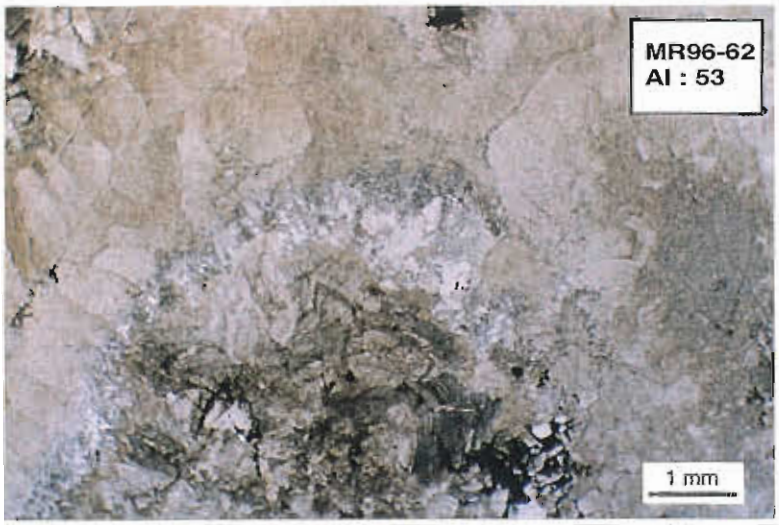

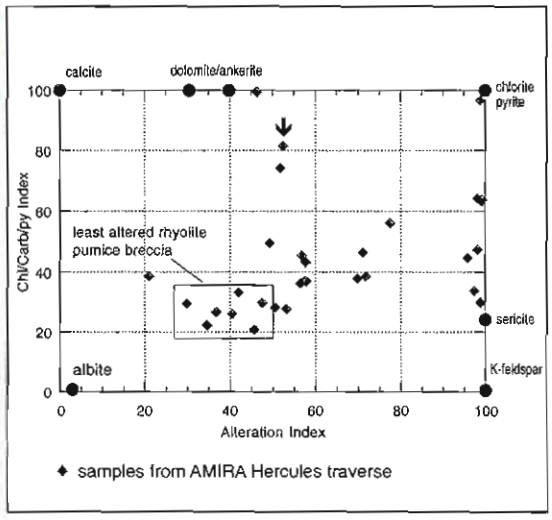

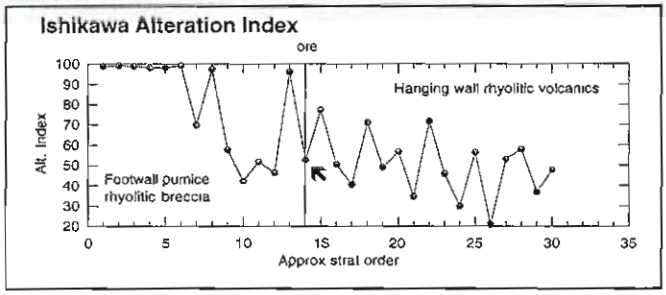

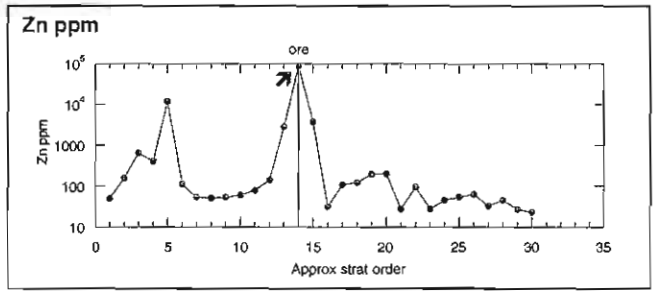

Sample no.: MR96-63
Group/Formation: MRV-CVC
Location: Hercules hangingwall
AMG: 376635E:5365373N

Field description:
Rhyolitic pumice breccia (least altered)

Ti/Zr = 8

Alteration: Intensity [x] weak [ ] moderate [ ] strong [ ] intense
Style [x] patchy [ ] pervasive [ ] veined [ ] cleavage controlled

Mineralogy: Groundmass alteration: **very minor sericite, chlorite** 20 % altered
Feldspar alteration: **flecky sericite** 10 % altered

Interpretation: [ ] diagenetic [x] metamorphic [ ] hydrothermal

Alteration Index
AI = **40**

Chlorite/carb/py Index
CI = **26**

Na_2O % = 3.64
Zn ppm = 107
Pb ppm = 66
S % = 0.02
$\delta^{18}O$ =

Whole-rock analysis:

SiO2	75.49
TiO2	0.31
Al2O3	13.29
Fe2O3	1.91
MnO	0.08
MgO	0.45
CaO	0.71
Na2O	3.64
K2O	2.51
P2O5	0.04
S	0.02
CO2	0.18
Total	99.97

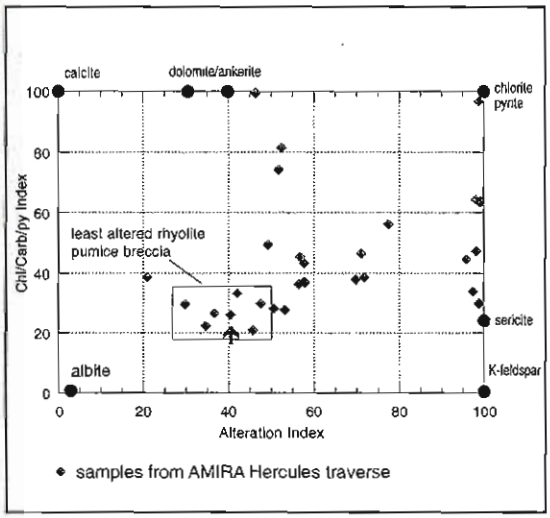

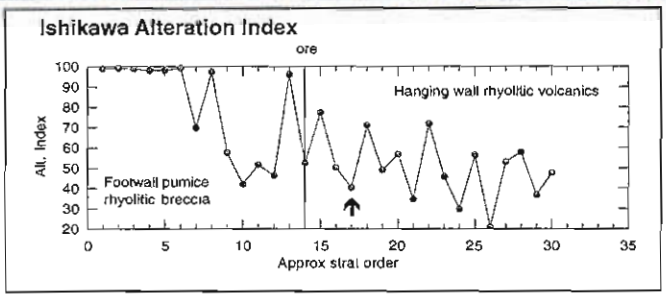

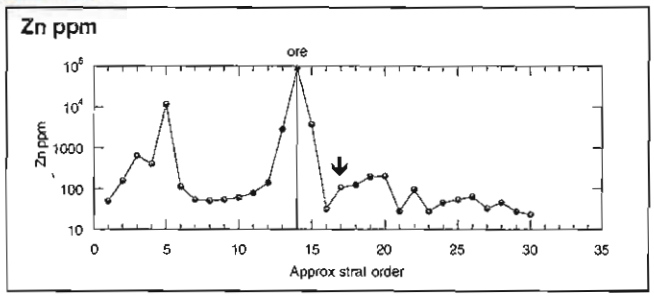

Sample no.: MR96-64
Group/Formation: MRV-CVC
Location: Hercules hangingwall
AMG: 377067.9E:5366308N

Field description:
Sericite-chlorite pumice breccia

Ti/Zr = 8

Alteration: Intensity [ ] weak [ ] moderate [x] strong [ ] intense
Style [x] patchy [ ] pervasive [ ] veined [ ] cleavage controlled

Mineralogy: Groundmass alteration: **sericite, quartz, chlorite** 70 % altered
Feldspar alteration: **carbonate, epidote, quartz** 80 % altered

Interpretation: [ ] diagenetic [ ] metamorphic [x] hydrothermal

Alteration Index
AI = 71

Chlorite/carb/py Index
CI = 47

Na_2O % = 1.37
Zn ppm = 123
Pb ppm = 31
S % = 0.27
$\delta^{18}O$ =

Whole-rock analysis:

SiO2	71.22
TiO2	0.33
Al2O3	13.74
Fe2O3	4.11
MnO	0.47
MgO	0.97
CaO	0.66
Na2O	1.37
K2O	4.01
P2O5	0.06
S	0.27
CO2	0.59
Total	99.56

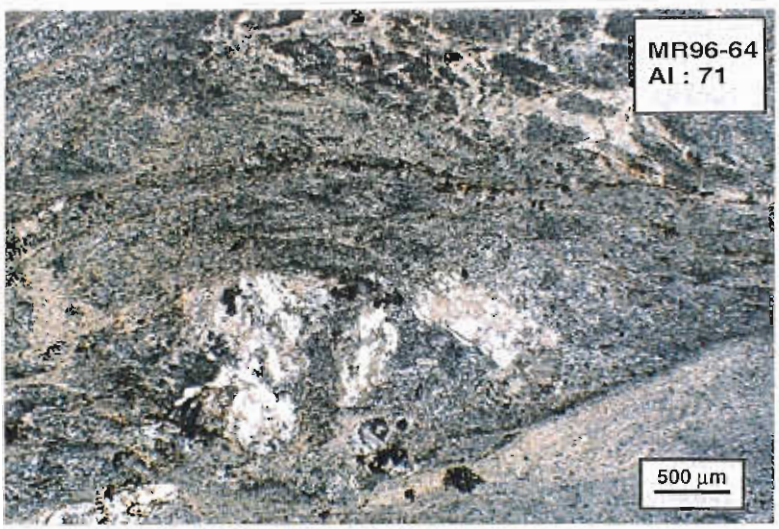

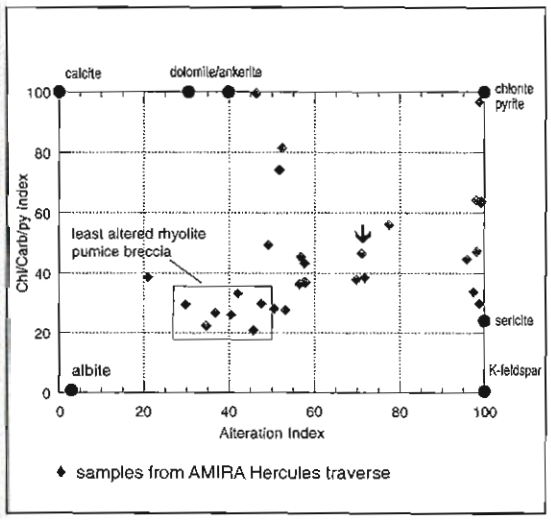

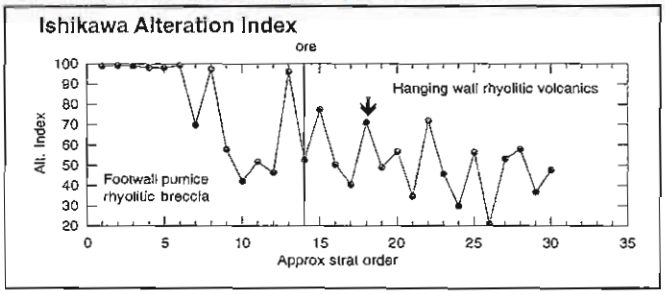

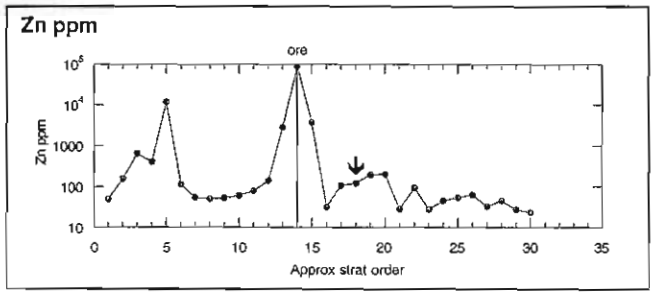

Sample no.: MR96-65
Group/Formation: MRV-CVC
Location: Hercules hangingwall
AMG: 377511.2E:5366607N

Field description:
Weakly altered rhyolitic pumice breccia

Ti/Zr = 19

Alteration:

Intensity	☐ weak	☐ moderate	☒ strong	☐ intense
Style	☒ patchy	☒ pervasive	☐ veined	☐ cleavage controlled

Mineralogy:
Groundmass alteration: **sericite, chlorite** — 80 % altered
Feldspar alteration: **weak carbonate ± epidote ± chlorite** — 30 % altered

Interpretation: ☐ diagenetic ☒ metamorphic ? hydrothermal

cm

Alteration Index
AI = 49

Chlorite/carb/py Index
CI = 49

Na_2O % = 3.64
Zn ppm = 194
Pb ppm = 18
S % = 0.02
$\delta^{18}O$ =

Whole-rock analysis:

SiO2	62.55
TiO2	0.71
Al2O3	16.48
Fe2O3	5.34
MnO	0.12
MgO	1.89
CaO	1.69
Na2O	3.64
K2O	3.26
P2O5	0.21
S	0.02
CO2	0.95
Total	99.32

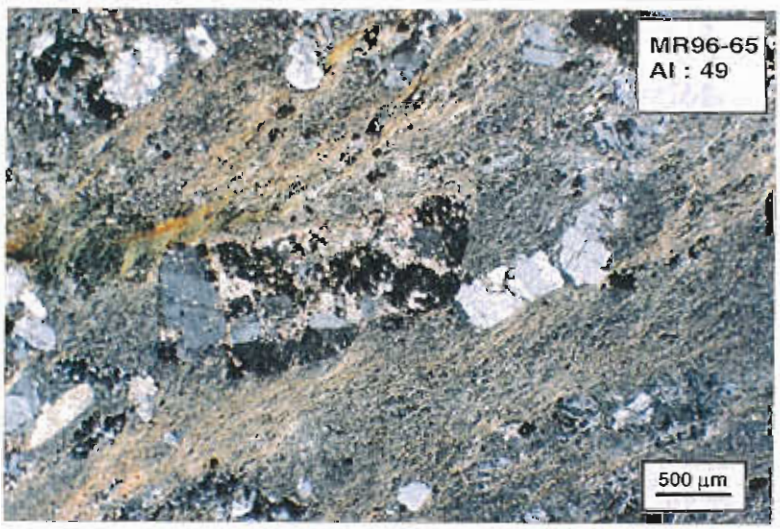

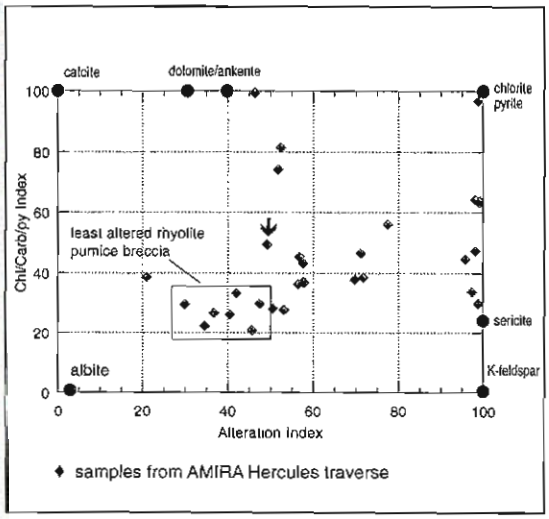

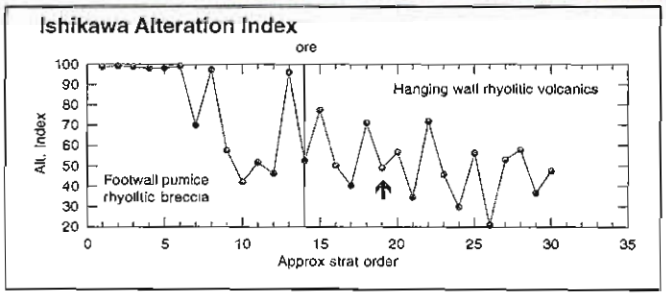

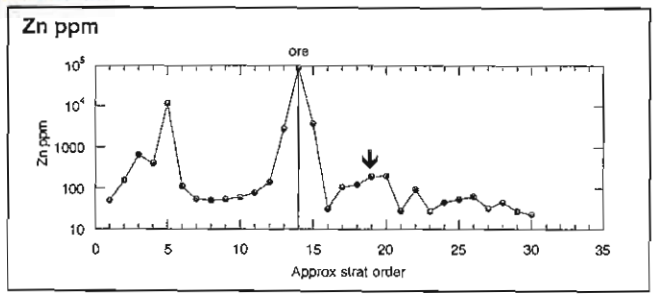

Sample no.: MR96-66
Group/Formation: MRV-CVC
Location: Hercules hangingwall
AMG: 377780.3E:5366605N

Field description:
Flow banded rhyolite lava

Ti/Zr = 7

Alteration:

Intensity	[x]	weak	[ ]	moderate	[ ]	strong	[ ] intense
Style	[x]	patchy	[ ]	pervasive	[ ]	veined	[x] cleavage controlled

Mineralogy:
Groundmass alteration: **weak sericite** — 20 % altered
Feldspar alteration: **nil to very weak** — 5 % altered

Interpretation: [ ] diagenetic [x] metamorphic [ ] hydrothermal

Alteration Index
AI = 35

Chlorite/carb/py Index
CI = 22

Na_2O % = 4.57
Zn ppm = 28
Pb ppm = 5
S % = 0.01
$\delta^{18}O$ =

Whole-rock analysis:

SiO2	76.27
TiO2	0.26
Al2O3	12.40
Fe2O3	1.80
MnO	0.05
MgO	0.36
CaO	0.49
Na2O	4.57
K2O	2.32
P2O5	0.04
S	0.01
CO2	0.33
Total	99.78

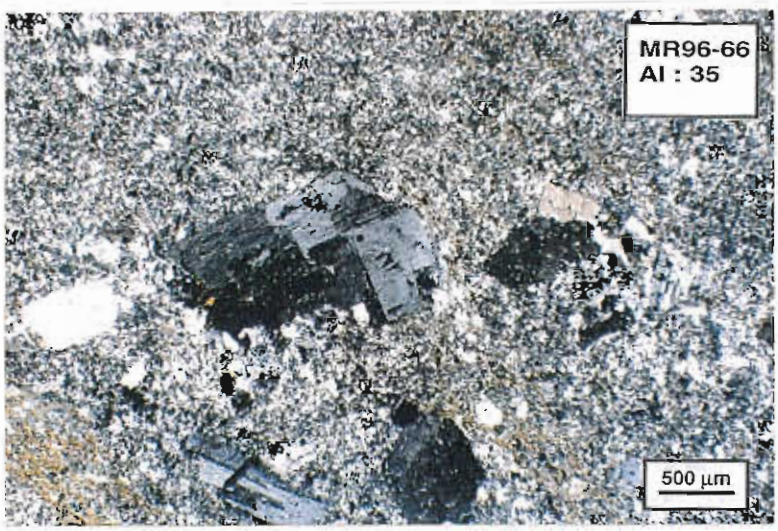

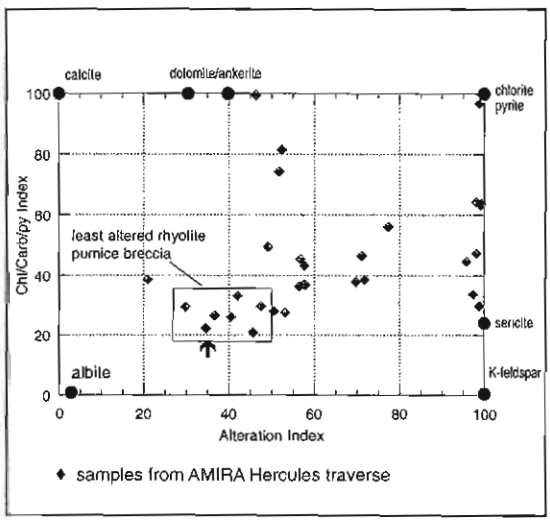

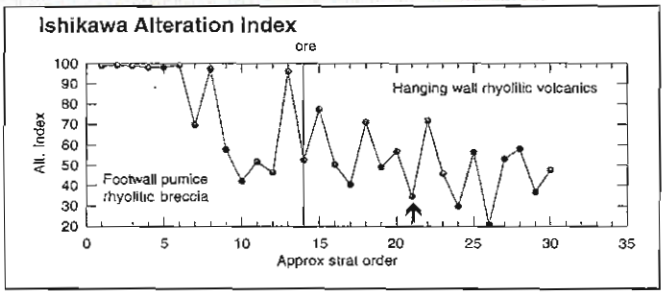

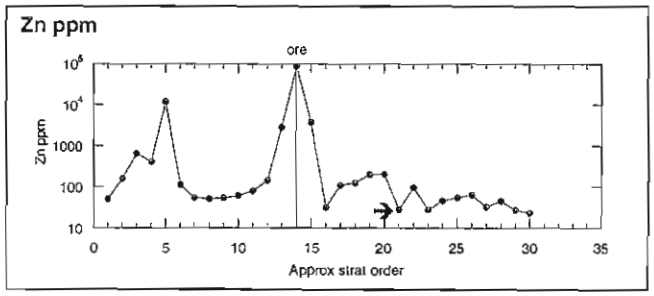

Sample no.: MR96-67
Group/Formation: MRV-CVC
Location: Hercules hangingwall
AMG: 377546.3E:5367449N

Field description:
Quartz-feldspar porphyry

Ti/Zr = 14

Alteration:

Intensity	[x]	weak	[x]	moderate	[ ]	strong	[ ] intense
Style	[ ]	patchy	[x]	pervasive	[ ]	veined	[x] cleavage controlled

Mineralogy:
Groundmass alteration: **sericite and FeO_x** — 50 % altered
Feldspar alteration: **very weak flecky sericite** — 5 % altered

Interpretation: [x] diagenetic [x] metamorphic [ ] hydrothermal

Alteration Index
AI = 57

Chlorite/carb/py Index
CI = 45

Na_2O % = 2.91
Zn ppm = 198
Pb ppm = 3
S % = 0.02
$\delta^{18}O$ =

Whole-rock analysis:

SiO2	69.14
TiO2	0.43
Al2O3	15.08
Fe2O3	4.36
MnO	0.16
MgO	1.00
CaO	0.14
Na2O	2.91
K2O	3.00
P2O5	0.09
S	0.02
CO2	0.18
Total	98.99

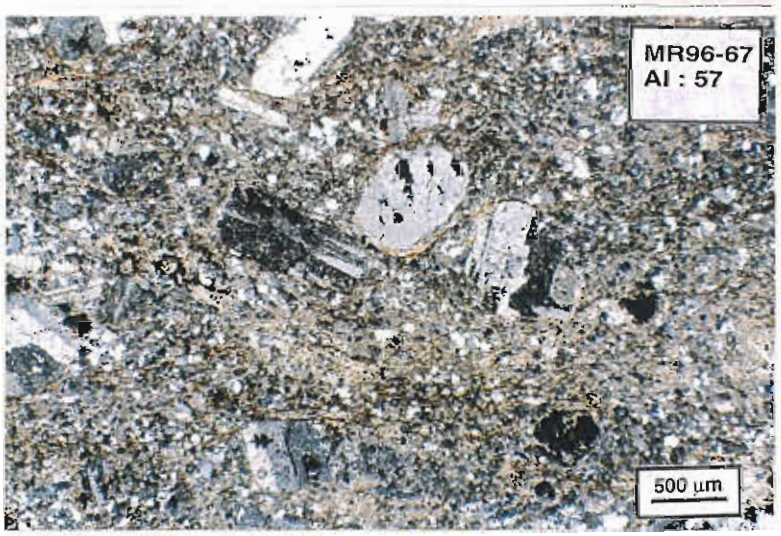

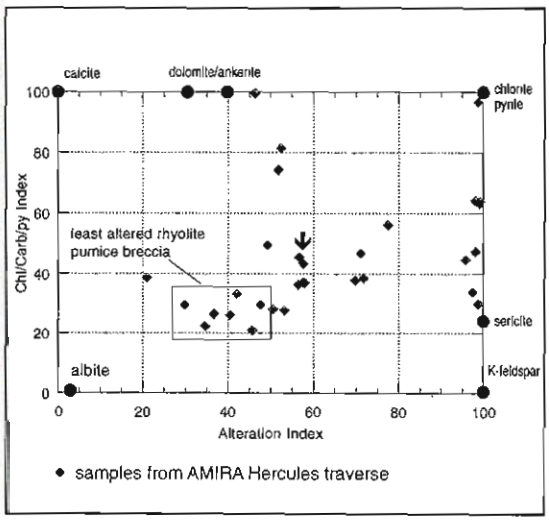

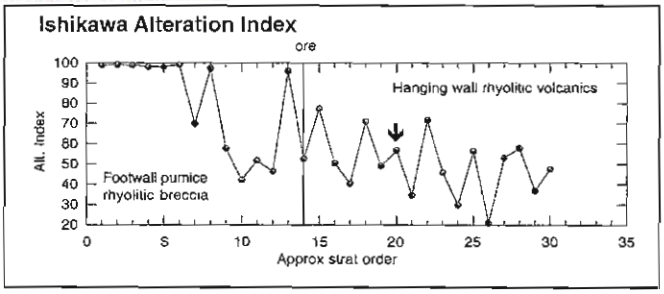

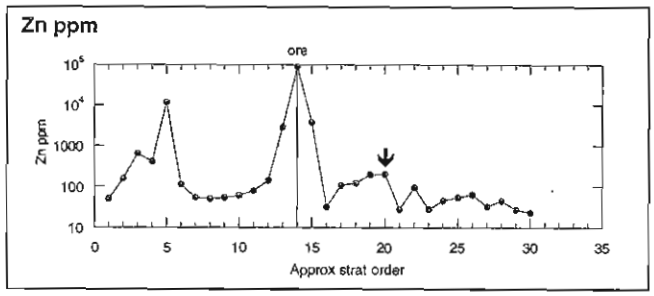

Sample no.: MR96-68
Group/Formation: MRV-CVC
Location: Hercules hangingwall
AMG: 377938.7E:5366359N

Field description:
Sphaleritic rhyolite

Ti/Zr = 12

Alteration: Intensity ☐ weak ☒ moderate to ☒ strong ☐ intense
Style ☒ patchy ☐ pervasive ☐ veined ☐ cleavage controlled

Mineralogy: Groundmass alteration: **sericite** 30 % altered
Feldspar alteration: **sericite** 30 % altered

Interpretation: ☒ diagenetic ☒ metamorphic ? hydrothermal

Alteration Index
AI = 72

Chlorite/carb/py Index
CI = 39

Na_2O % = 1.98
Zn ppm = 94
Pb ppm = 9
S % = 0.01
$\delta^{18}O$ =

Whole-rock analysis:

SiO2	71.43
TiO2	0.47
Al2O3	14.54
Fe2O3	3.55
MnO	0.07
MgO	0.81
CaO	0.08
Na2O	1.98
K2O	4.42
P2O5	0.09
S	0.01
CO2	0.22
Total	99.58

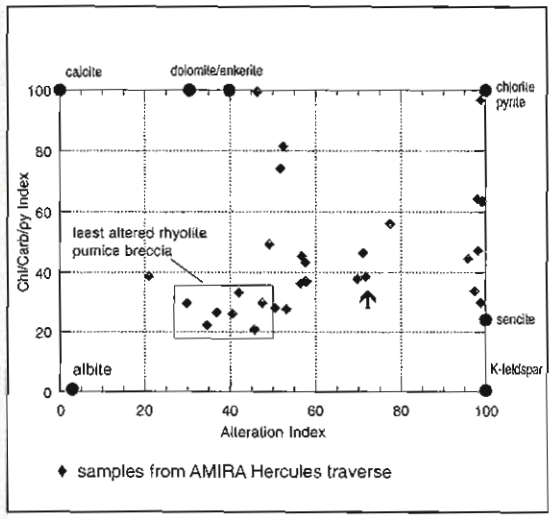

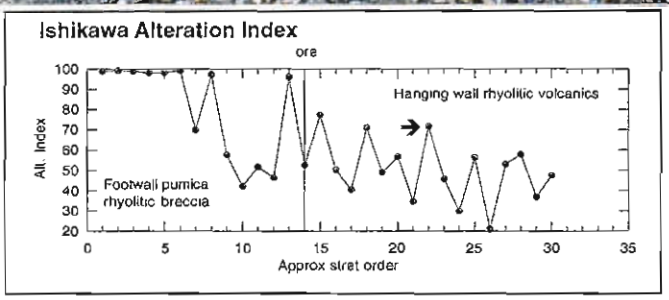

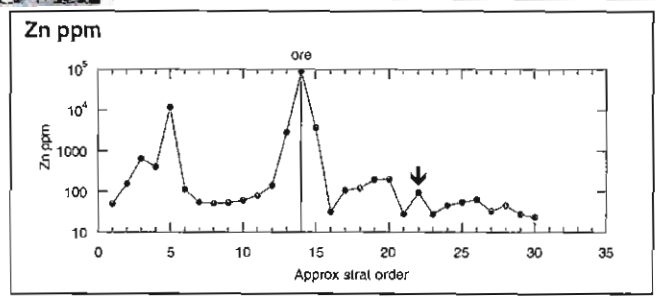

Sample no.: MR96-69
Group/Formation: MRV-CVC
Location: Mount Read
AMG: 378053.7E:5366199N

Field description:
Flow banded coherent rhyolite

Ti/Zr = 6

Alteration:
Intensity: ☐ weak ☒ moderate ☐ strong ☐ intense
Style: ☒ patchy ☒ pervasive ☐ veined ☐ cleavage controlled

Mineralogy:
Groundmass alteration: **sericite** — 60 % altered
Feldspar alteration: **minor carbonate ± sericite** — 20 % altered

Interpretation:
☒ diagenetic ☒ metamorphic ☐ hydrothermal

Alteration Index
AI = 46

Chlorite/carb/py Index
CI = 21

Na_2O % = 3.80
Zn ppm = 28
Pb ppm = 8
S % = 0.01
$\delta^{18}O$ =

Whole-rock analysis:

SiO2	73.51
TiO2	0.27
Al2O3	13.39
Fe2O3	1.79
MnO	0.04
MgO	0.36
CaO	1.03
Na2O	3.80
K2O	3.71
P2O5	0.04
S	0.01
CO2	0.73
Total	99.86

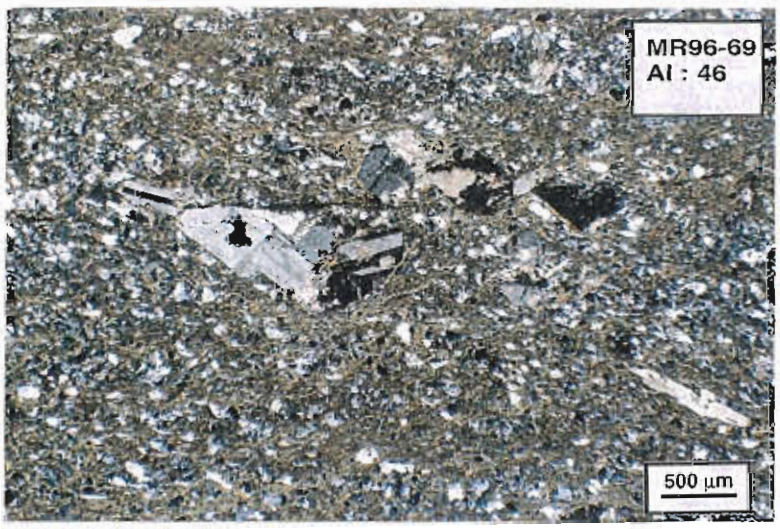

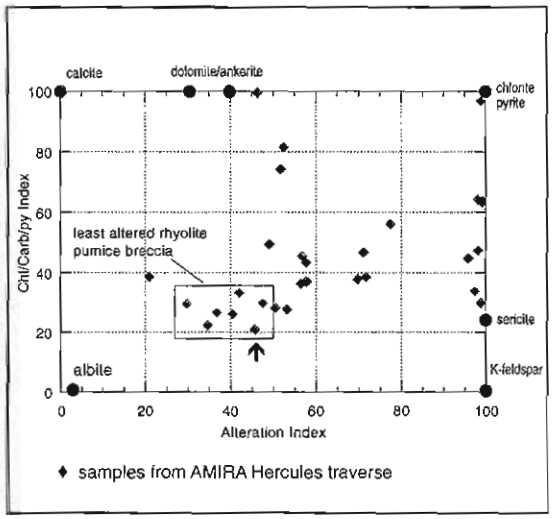

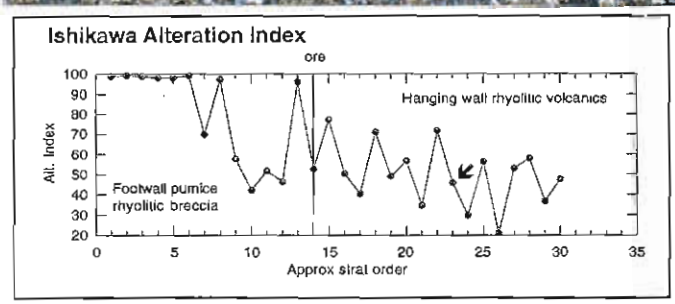

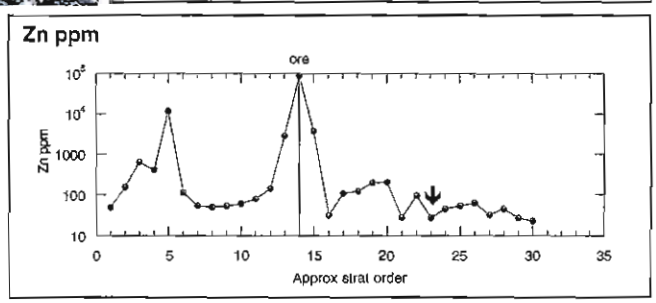

Sample no.: MR96-70
Group/Formation: MRV-CVC
Location: Mount Read
AMG: 378330.2E:5366122N

Field description:
Feldspar phyric rhyolite

Ti/Zr = 6

Alteration:
Intensity: [X] weak [ ] moderate [ ] strong [ ] intense
Style: [X] patchy [ ] pervasive [ ] veined [ ] cleavage controlled

Mineralogy:
Groundmass alteration: **weak sericite, chlorite** — 20 % altered
Feldspar alteration: **very weak carbonate** — 10 % altered

Interpretation:
[X] diagenetic [X] metamorphic [ ] hydrothermal

cm

Alteration Index
AI = 30

Chlorite/carb/py Index
CI = 29

Na_2O % = 3.84
Zn ppm = 46
Pb ppm = 6
S % = 0.01
$\delta^{18}O$ =

Whole-rock analysis:

SiO2	76.37
TiO2	0.23
Al2O3	11.65
Fe2O3	2.02
MnO	0.15
MgO	0.49
CaO	1.35
Na2O	3.84
K2O	1.71
P2O5	0.04
S	0.01
CO2	0.88
Total	99.95

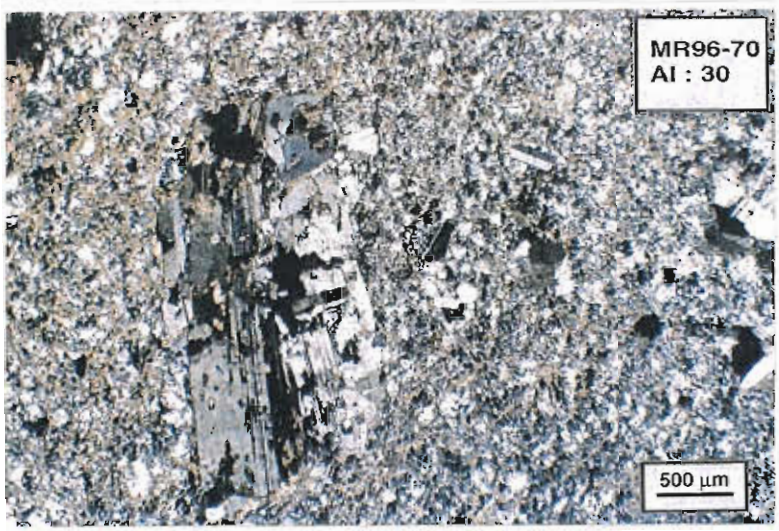

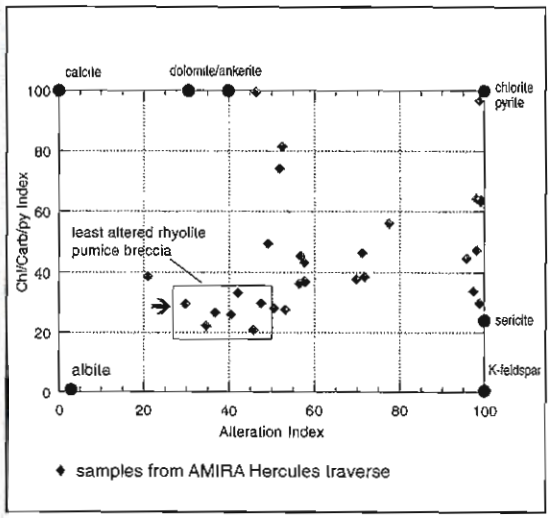

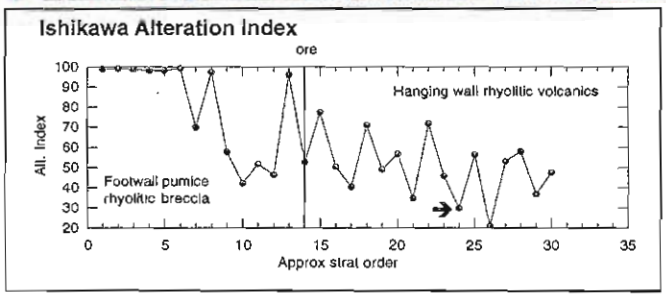

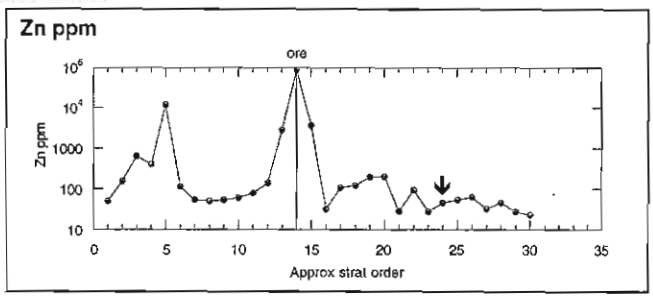

Sample no.: MR96-71
Group/Formation: MRV-CVC
Location: Mount Read
AMG: 378483.7E:5366186N

Field description:
Quartz-feldspar phyric intrusive with mafic clots (after biotite)

Ti/Zr = 12

Alteration:
Intensity: [x] weak [ ] moderate [ ] strong [ ] intense
Style: [ ] patchy [x] pervasive [ ] veined [ ] cleavage controlled

Mineralogy:
Groundmass alteration: **weak sericite** 20 % altered
Feldspar alteration: **weak sericite** 10 % altered

Interpretation:
[x] diagenetic [x] metamorphic [ ] hydrothermal

Alteration Index
AI = 56

Chlorite/carb/py Index
CI = 36

Na_2O % = 3.48
Zn ppm = 54
Pb ppm = 14
S % = 0.01
$\delta^{18}O$ =

Whole-rock analysis:

SiO2	70.81
TiO2	0.40
Al2O3	14.21
Fe2O3	3.33
MnO	0.10
MgO	1.06
CaO	0.15
Na2O	3.48
K2O	3.65
P2O5	0.09
S	0.01
CO2	0.07
Total	99.19

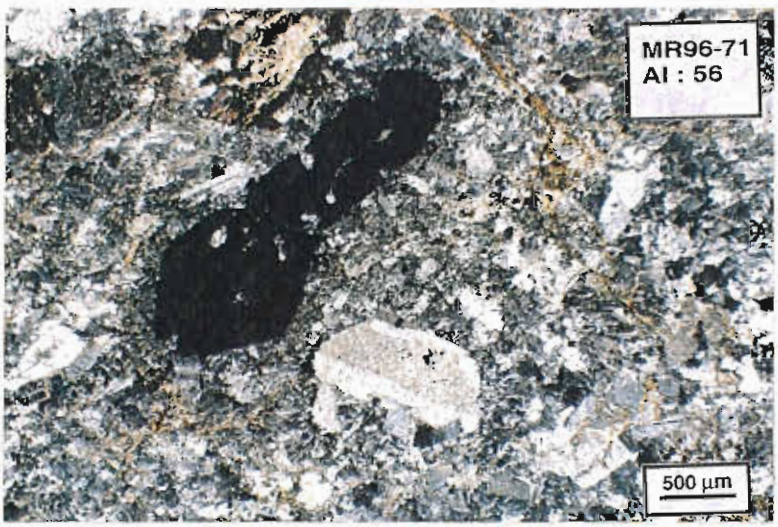

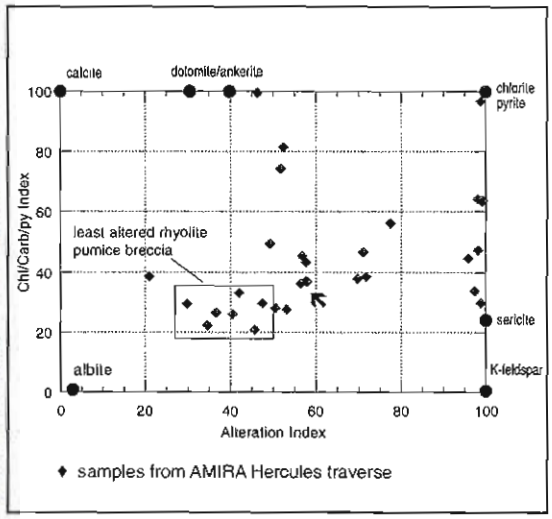

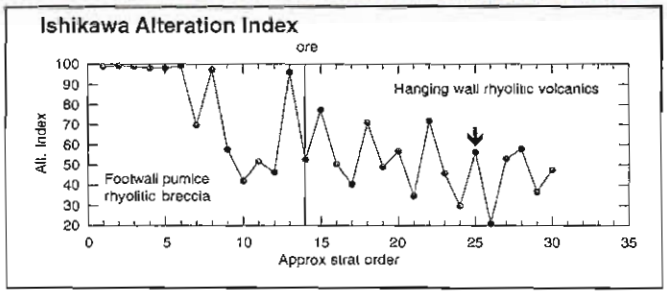

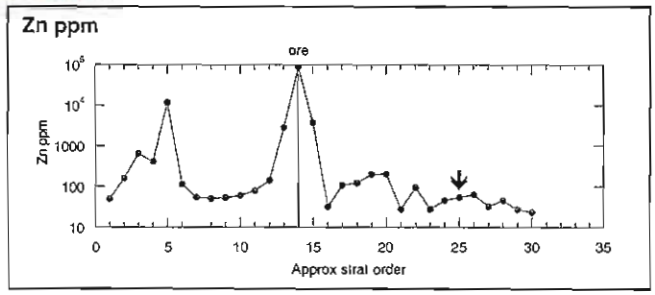

Sample no.: MR96-72
Group/Formation: MRV-CVC
Location: Mount Read
AMG: 379683.9E:5366325N

Field description:
Feldspar phyric rholite

Ti/Zr = 8

Alteration:
Intensity: [X] weak [ ] moderate [ ] strong [ ] intense
Style: [X] patchy [ ] pervasive [ ] veined [ ] cleavage controlled

Mineralogy:
Groundmass alteration: **very weak, patchy sericite, chlorite** 10 % altered
Feldspar alteration: **weak carbonate, sericite** 10 % altered

Interpretation:
[X] diagenetic [X] metamorphic [ ] hydrothermal

Alteration Index
AI = 47

Chlorite/carb/py Index
CI = 30

Na_2O % = 3.79
Zn ppm = 23
Pb ppm = 4
S % = 0.01
$\delta^{18}O$ =

Whole-rock analysis:

SiO2	71.37
TiO2	0.35
Al2O3	14.18
Fe2O3	2.90
MnO	0.06
MgO	0.55
CaO	0.89
Na2O	3.79
K2O	3.68
P2O5	0.07
S	0.01
CO2	0.51
Total	99.75

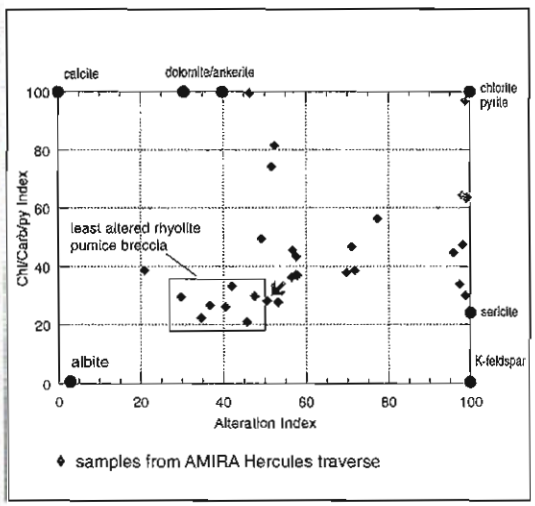

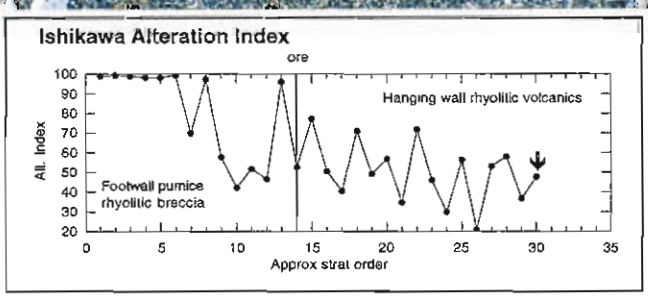

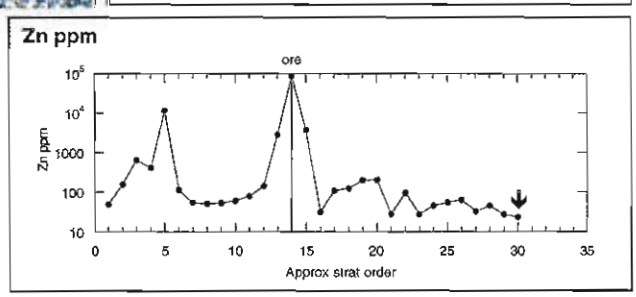

Sample no.: MR96-73A
Group/Formation: MRV-CVC
Location: Mount Read
AMG: 379621.9E:5366361N

Field description:
Fine bedded silicic volcaniclastic

Ti/Zr = 5

Alteration:
Intensity ☐ weak ☐ moderate ☐ strong ☐ intense
Style ☐ patchy ☐ pervasive ☐ veined ☐ cleavage controlled

Mineralogy:
Groundmass alteration: nil ☐ % altered
Feldspar alteration: nil ☐ % altered

Interpretation: ☐ diagenetic ☐ metamorphic ☐ hydrothermal

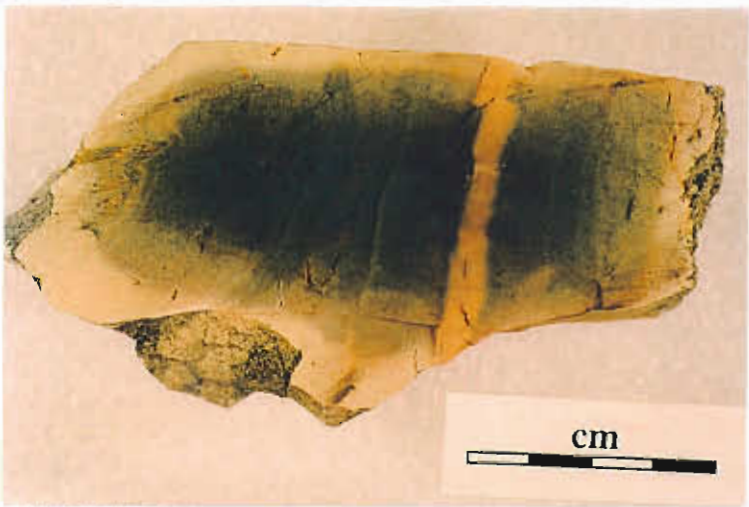

Alteration Index
AI = 37

Chlorite/carb/py Index
CI = 27

Na_2O % = 3.72
Zn ppm = 27
Pb ppm = 3
S % = 0.01
$\delta^{18}O$ =

Whole-rock analysis:

SiO2	79.55
TiO2	0.17
Al2O3	11.47
Fe2O3	1.66
MnO	0.02
MgO	0.47
CaO	0.04
Na2O	3.72
K2O	1.71
P2O5	0.01
S	0.01
CO2	0.22
Total	100.01

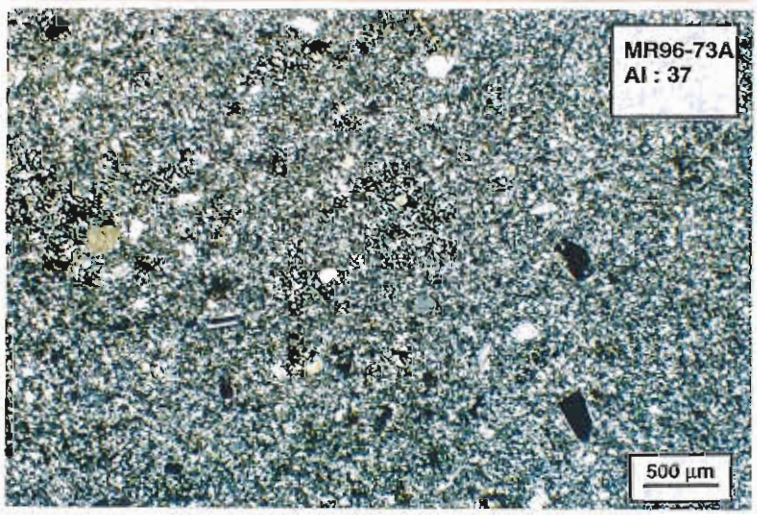

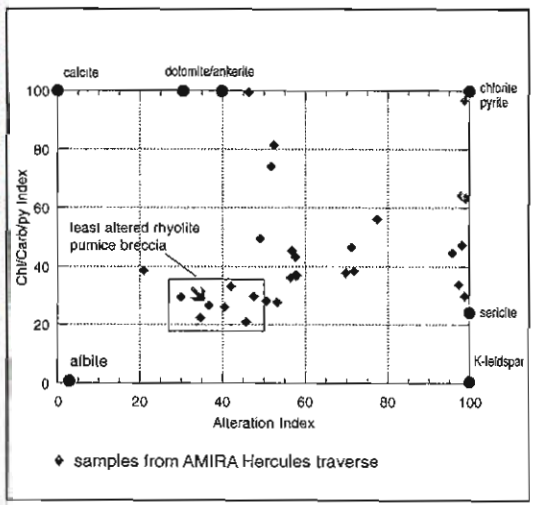

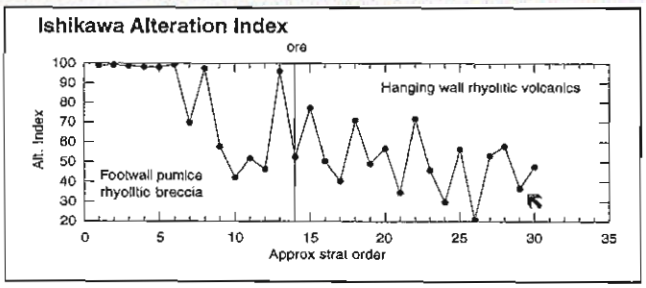

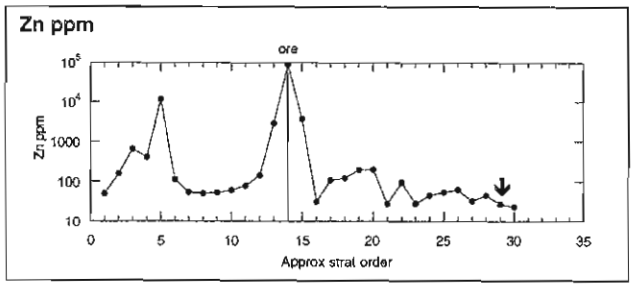

Sample no.: MR96-73B
Group/Formation: MRV-CVC
Location: Mount Read
AMG:

Field description:
Coarse rhyolitic pumiceous breccia

Ti/Zr = 5

Alteration: Intensity [X] weak [ ] moderate [ ] strong [ ] intense
Style [X] patchy [ ] pervasive [ ] veined [ ] cleavage controlled

Mineralogy: Groundmass alteration: **sericite** **20** % altered
Feldspar alteration: **unaltered** **0** % altered

Interpretation: [ ] diagenetic [X] metamorphic [ ] hydrothermal

Alteration Index
AI = 37

Chlorite/carb/py Index
CI = 27

Na_2O % = 3.72
Zn ppm = 27
Pb ppm = 3
S % = 0.01
$\delta^{18}O$ =

Whole-rock analysis:

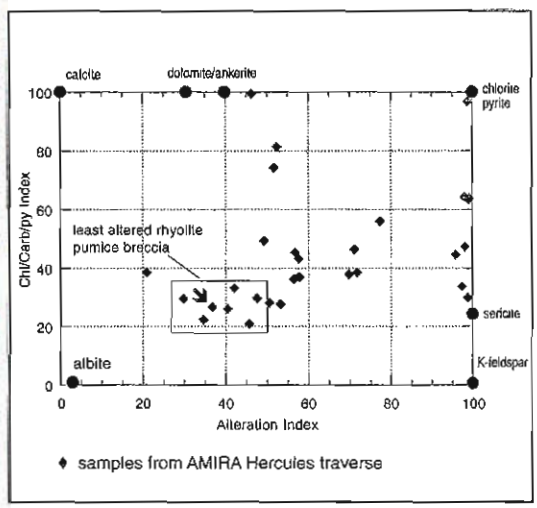

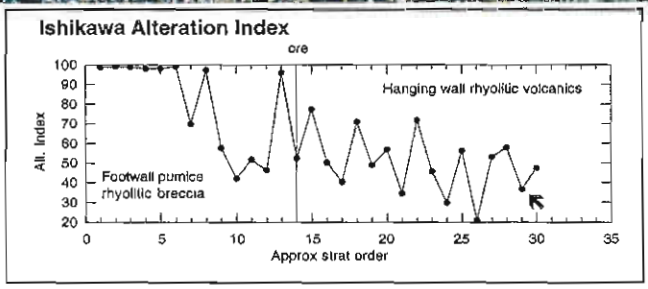

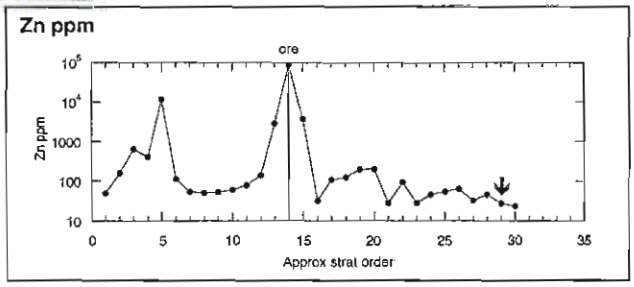

Sample no.: MR96-74
Group/Formation: MRV-CVC
Location: Mount Read
AMG: 379424.5E:5366379N

Field description:
Flow banded rhyolite

Ti/Zr = 5

Alteration:
Intensity: [x] weak [x] moderate [ ] strong [ ] intense
Style: [x] patchy [ ] pervasive [ ] veined [ ] cleavage controlled

Mineralogy:
Groundmass alteration: **carbonate, sericite** 30 % altered
Feldspar alteration: 40 % altered

Interpretation:
[ ] diagenetic [x] metamorphic [ ] hydrothermal

Alteration Index
AI = 58

Chlorite/carb/py Index
CI = 37

Na_2O % = 1.29
Zn ppm = 46
Pb ppm = 3
S % = 0.01
$\delta^{18}O$ =

Whole-rock analysis:

SiO2	76.17
TiO2	0.16
Al2O3	11.63
Fe2O3	2.08
MnO	0.07
MgO	0.73
CaO	1.55
Na2O	1.29
K2O	3.17
P2O5	0.02
S	0.01
CO2	1.10
Total	99.58

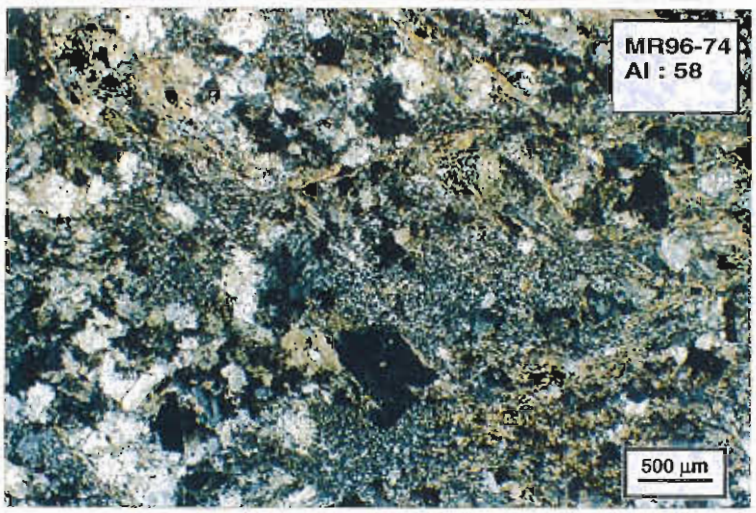

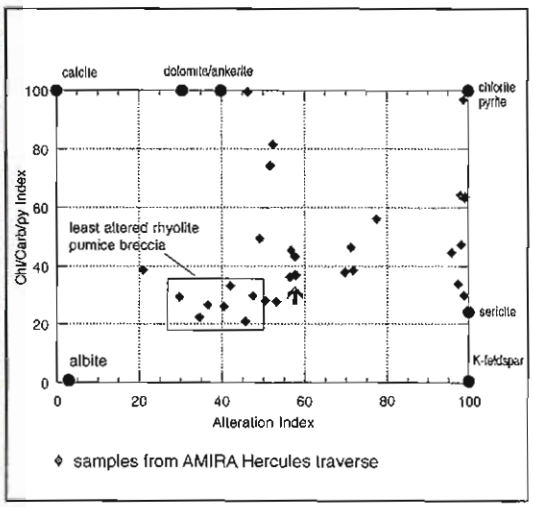

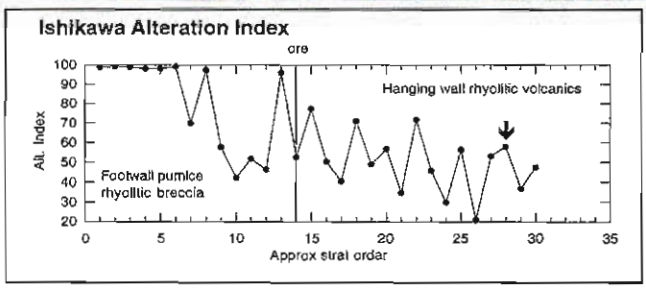

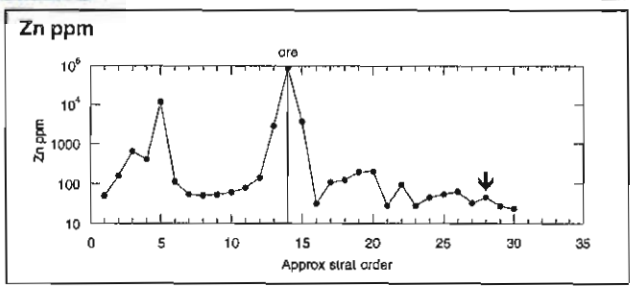

Sample no.: MR96-75
Group/Formation: MRV-CVC
Location: Mount Read
AMG: 379238.4E:5366365N

Field description:
Spherulitic rhyolite

Ti/Zr = 9

Alteration:
Intensity: [X] weak [ ] moderate [ ] strong [ ] intense
Style: [X] patchy [ ] pervasive [ ] veined [ ] cleavage controlled

Mineralogy:
Groundmass alteration: **weak sericite, carbonate** 20 % altered
Feldspar alteration: **flecky sericite** 10 % altered

Interpretation:
[ ] diagenetic [X] metamorphic [ ] hydrothermal

Alteration Index
AI = 53

Chlorite/carb/py Index
CI = 28

Na_2O % = 3.07
Zn ppm = 33
Pb ppm = 6
S % = 0.01
$\delta^{18}O$ =

Whole-rock analysis:

SiO2	71.78
TiO2	0.34
Al2O3	13.33
Fe2O3	2.50
MnO	0.05
MgO	0.64
CaO	1.46
Na2O	3.07
K2O	4.50
P2O5	0.06
S	0.01
CO2	0.84
Total	99.78

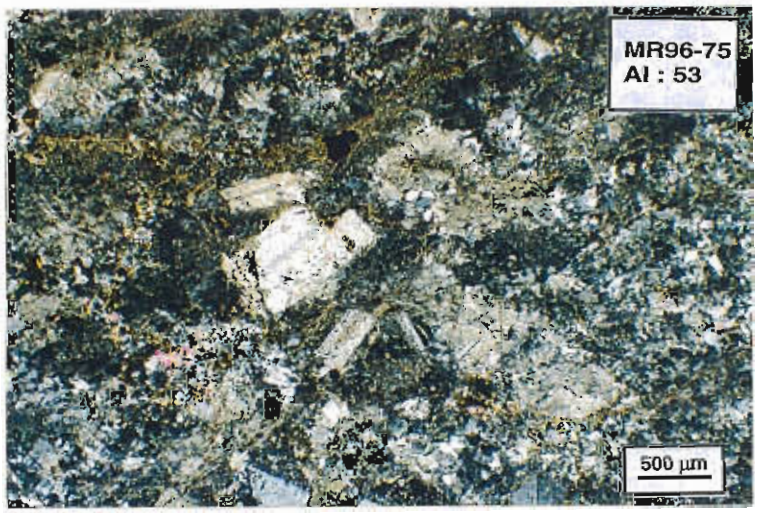

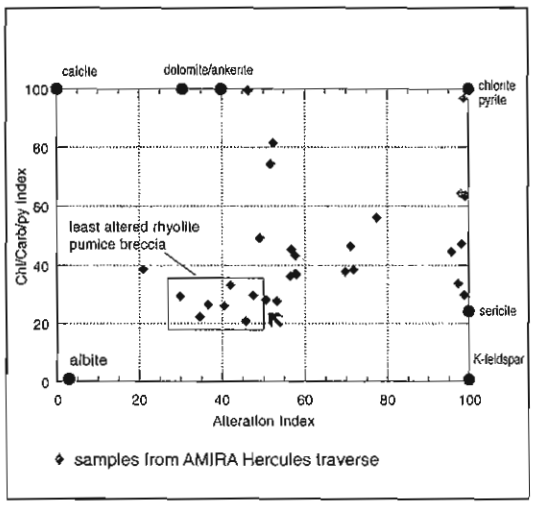

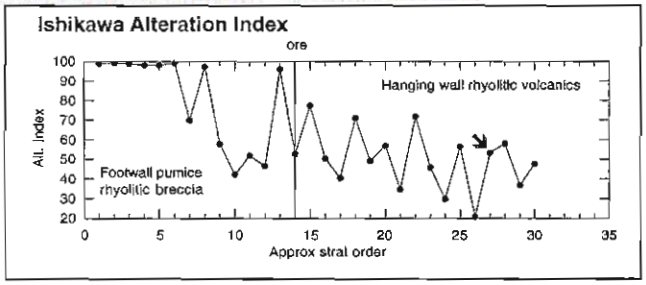

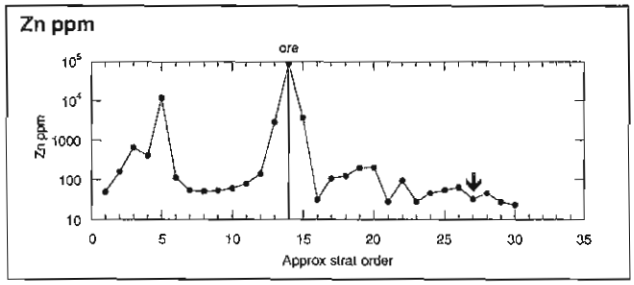

Road log of the Jukes Road and the Jukes Cu–Au Prospect with emphasis on petrography, alteration assemblages and preliminary geochemistry

Bill Wyman

Centre for Ore Deposit and Exploration Studies, Geology Department, University of Tasmania

Summary

Textural and mineralogical data appear to suggest that hydrothermal mineral assemblages can be distinguished from regional assemblages on the basis of four observations.

1. The widespread occurrence of alteration assemblages.
2. Intensity of chlorite alteration of feldspar phenocrysts. Sericite alteration of feldspar phenocrysts in weakly altered rocks can vary greatly but the appearance of chlorite appears to be an indicator of proximity to the hydrothermal system.
3. The presence or absence of accessory minerals such as pyrite, chalcopyrite, tourmaline or large amounts of magnetite/hematite.
4. Degree of textural destruction. Rocks with weakly moderate or greater textural destruction, in general, clearly show the effects of hydrothermal alteration. An exception to this appears to be the albite alteration seen in the Jukes Road pumice breccia. This rock has undergone a great amount of textural destruction of the groundmass and is believed to have been altered under diagenetic conditions.

Hydrothermal alteration appears to have been controlled by fracture density. This is demonstrated by an increase in both fracture density, and increases in both chlorite and K-feldspar alteration of the columnar jointed rhyolite with increasing proximity to the Jukes Prospect. The primary indicator of alteration intensity is the degree of alteration of feldspar phenocrysts.

At the Jukes Prospect, two styles of hydrothermal breccias have been identified. The intimate association of magnetite, chlorite and tourmaline in the matrices, argues very strongly for a hydrothermal/magmatic origin. Breccias are classified according to their matrix type. The first contains various amounts of magnetite/hematite and tourmaline ± chlorite and the second chlorite and tourmaline ± magnetite/hematite. There is a possibility that the two breccias are related to each other and to the large magnetite bodies found both at the Jukes Prospect and farther south at Mt Darwin. Breccias are cut by faults but clearly predate fault-related tectonic fracturing.

Along the Jukes Road, two facies of the CVC have clearly been altered by hydrothermal solutions. The feldspar-phyric rhyolite and the quartz-feldspar porphyry both show varying hydrothermal alteration effects. The quartz-feldspar porphyry is not only altered by chlorite alteration but also by K-feldspar alteration. This suggests that the dykes were implaced prior to the hydrothermal event. The fact that the hydrothermal breccia follows the apparent boundary of a quartz-feldspar porphyry dyke suggests that the timing of the two events may not be to different.

Introduction

Jukes Road is located approximately 9 km south of Queenstown and cuts through sections of the Western Sequence (Yolande River Sequence), Central Volcanic Complex (CVC) and Eastern Sequence (Eastern Quartz Phyric Sequence (EQP) and Tyndall Group) (Fig. 1). The Jukes Pty. Cu–Au prospect is located along the Jukes Road and has been the subject of research by others most recently being Doyle (1990), and White (1975). Road cuttings along Jukes Road provide an excellent opportunity to examine a variety

of alteration assemblages in Central Volcanic Complex rocks as well as alteration associated with the Jukes Prospect.

As part of AMIRA project P.439, over 100 ten-metre-long chip samples were collected along a 5.7 km traverse along the Jukes Road in early 1995. Rock chip and whole rock samples were collected at 500 m intervals outside the Jukes prospect and at 10 m intervals within the prospect.

Descriptions of volcanic facies and preliminary alteration assemblages were presented in Wyman et al. (1996). This paper presents some of the results of detailed petrographic examinations made on rocks collected during the previous traverses. Additional petrographic descriptions and alteration assemblages are presented in a Road Log format to correspond to a field excursion planned along the Jukes Road as part of the Spring 1996 AMIRA Meeting. Where appropriate, geochemical data is used to support some of the interpretations.

The Jukes Road meterage system was established in the spring 1995 traverse by Nathan Duhig and Andrew Jones when they collected the first 100 or so 10 m chip samples. This meterage system has been maintained since and is a very useful tool for locating features along the road. The meterage system begins in the East, at 8100, and runs along the road in a westerly direction through 13800. Point 10000 is located on a large rock approximately 200 m up the road from the contact between the CVC and EQP contact. Point 13800 is located 4 km along the road past the King River bridge. This Road Log will begin in the west at 13800 and run up the road in an easterly direction to the Jukes prospect. The traverse will explore the various volcanic facies as well as the various alteration relationships in the field and support those observations by presenting petrographic descriptions and photomicrographs as necessary.

Petrology of the Jukes Road rocks

Rocks of the Western Sequence (Yolande River Sequence), Central Volcanic Complex (CVC) and Eastern Sequence (Eastern Quartz Phyric Sequence and Tyndall Group) are all well exposed along Jukes Road. For the purposes of this traverse, rocks of the Western sequence were not examined, and rocks of the Tyndall group were only briefly examined and not sampled. Neither unit will be described in this paper. Figure 1 shows a simplified geological map of the Jukes Road area and sample locations for samples studied as part of this study. A graphic log depicting the more detailed geology of the entire Jukes Road as well as the Jukes Prospect is shown as Figure 2a, b. The Eastern Quartz-Phyric Sequence (EQP) lies between Tyndall Group volcaniclastic rocks to the east, and CVC rocks to the west. The dominant facies in the EQP is quartz-feldspar phyric volcaniclastics, with subordinate quartz-feldspar phyric lavas. The eastern contact between the EQP and the Tyndall Group is not exposed. The western contact between the EQP and the CVC rocks is a major fault visible on the ground and on aerial photographs. Rocks of the CVC appear to interfinger with rocks of the Yolande River Sequence to the west in an apparently conformable contact. Rocks of the CVC along Jukes Road are dominantly feldspar-phyric lavas and pumiceous volcaniclastics and mass-flow deposits with a minor tuffaceous/sedimentary facies. In the following sections, facies of the EQP and CVC will be discussed in more detail. These rocks will be described in a West to East direction. This order approximately corresponds to the order in which they will be viewed on the field trip at the AMIRA field meeting in late October 1996.

Central Volcanic Complex

CVC, feldspar phyric rhyolitic volcaniclastic and mass-flow deposits

Rhyolitic volcaniclastic rocks dominate the western part of the CVC in the Jukes Road area. These rocks include tube pumice breccias, pumiceous mass-flow deposits and finer grained rhyolitic volcaniclastic rocks. This succession of volcaniclastic rocks appears to underlie the fine-grained sedimentary facies of the CVC and forms an apparent conformable and gradational contact with the poorly exposed Yolande River sequence. Plate 1 (Plates follow page XX) shows an outstanding example of a mass flow deposit. Typical volcaniclastic rocks contain 10 to 20% feldspar **

WESTERN TASMANIA

Jukes Road and Jukes Prospect Area

Simplified Geology and Sample Location Map

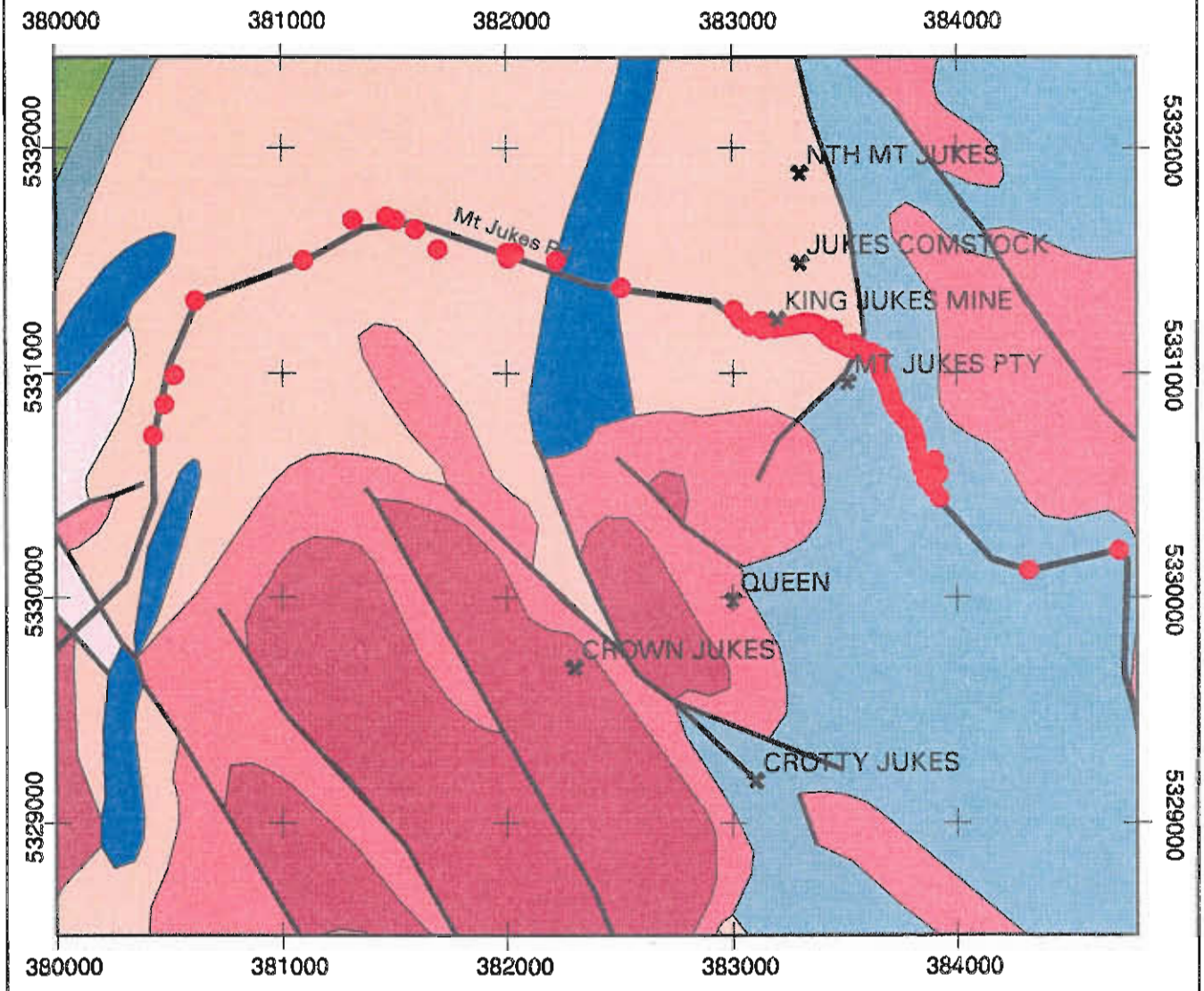

OWEN CONGLOMERATE : UPPER SANDSTONE
OWEN CONGLOMERATE (UNDIFF.)
EASTERN QUARTZ-PHYRIC SEQUENCE
CVC FELDSPAR-PHYRIC VOLCANICS AND VOLCANICLASTICS
CVC TUFFACEOUS SANDSTONES, SILTSTONES AND MINOR TUFFS
YOLANDE RIVER SEQUENCE VOLCANICANICS AND VOLCANICLASTICS
YOLANDE RIVER SEQUENCE FELSIC PORPHYRY

Scale: 1:30,000
0 200 400 600 8001000
metres

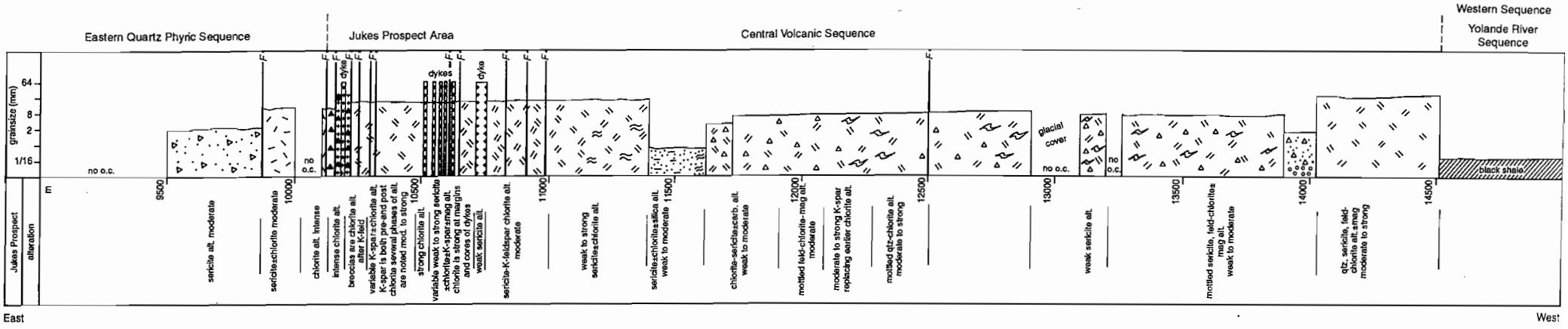

Figure 2a: Graphic presentation of the geology and alteration along the Jukes Road

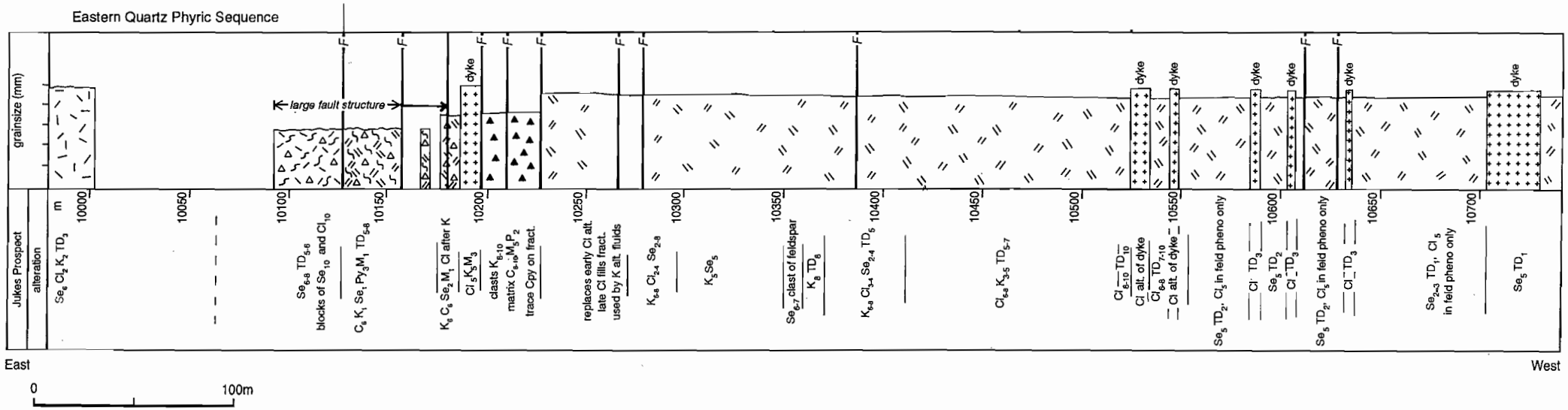

Eastern Quartz Phyric Sequence

- coherent quartz-feldspar dacite porphyry
- brecciated and sheared quartz-feldspar dacite porphyry, alteration varies from Se_{5-10} to Cl_{5-10}

Central Volcanic Sequence

- brecciated, sheared feldspar phyric rhyolite
- brecciated, feld-phyric rhyolite breccia contains rounded clasts of quartz porphyry dyke rx
- quartz ± feld porphyry dyke
- probable polylithic hydrothermal breccia matrix to clast supported clasts almost always K_{8-10}, matrix usually Cl_{8-10} M_5 Py_{2+}, clasts angular, little transport
- feldspar phyric (± quartz) rhyolite columnar jointing well developed in least altered areas

Figure 2b: Graphic presentation of the geology and alteration at the Jukes Prospect

phenocrysts up to 2 mm in length. Relict feldspar-phyric pumice clasts formed well developed fiamme-like lenses and undeformed pumice textures are rare.

Regional cleavage is well developed in this facies due to pervasive sericite and chlorite development. A well-developed metamorphic foliation is developed in the groundmass due to alignment of sericite. This foliation is very easily seen around coarser phenocrysts and crystals. Sericite forms a mottled texture overprinting earlier quartz.

Sericite alteration occurs in the feldspar phenocrysts and is weak to moderate. Sericite alteration of the plagioclase crystals is uniform, pervasive and often follows and defines cleavage surfaces. Sericite also occurs as small micro-veinlets cross-cutting the groundmass as well as individual crystals. Chlorite is visible as a very minor component in the groundmass. Chlorite also occurs as small blebs in the crosscutting quartz veins. Epidote occurs as rare euhedral to subhedral crystals to 1 mm in association with minor magnetite. Carbonate alteration is very common in this unit but is currently believed to be post deformational.

Coarse-grained rhyolitic volcaniclastic rocks (13800–11700 m)

Stop 1, 13800 m

The coarser-grained rhyolitic volcaniclastic rocks are composed of quartz, plagioclase, K-feldspar, sericite, with minor chlorite, pyrite and epidote. In addition, XRD results indicate the presence of significant kaolinite (10–15%) in some rocks (Appendix A). The typical groundmass is almost entirely very fine-grained (< 0.1–0.5 mm) quartz and feldspar forming a fine mosaic of interlocking crystals. Sericite and kaolinite are common in the groundmass. Small angular quartz fragments up to 2 mm are found scattered throughout the rock. Quartz and feldspar crystals are broken with some jigsaw fits. At 11800 m numerous pristine euhedral zoned feldspar phenocrysts 0.25–1 mm are found. Well developed glomerocrysts of plagioclase may also be either a primary texture or possibly indicate very little transport. Subhedral prismatic plagioclase phenocrysts up to 3.5 mm are abundant and often occur in glomocrysts. The plagioclase composition was determined to be of two types, andesine and labradorite, by the Michael Levy method. K-feldspar phenocrysts are less abundant and typically smaller in size. Euhedral and subhedral pyrite is disseminated throughout as 1–1.5 mm size crystals. Some of the pyrite has altered to magnetite and is associated with wispy coarse chlorite and quartz in pressure shadows of pyrite grains. Relict glass shards, now fine-grained quartz-feldspar-sericite mosiacs, make up to 20–30% of the rock. The fine-grained quartz-feldspar-sericite mosiacs are most probably a devitrification texture. In addition to pumice and glass lithic clasts, clasts with well developed granophyric textures are found and may have been derived from primary lavas.

A well developed metamorphic foliation is developed in the groundmass due to alignment of sericite. This foliation is very easily seen around coarser phenocrysts and crystals. Sericite forms a mottled texture overprinting earlier quartz. Rare wispy relict pumice shards as well as tube pumice and devitrification textures are seen. Relict perlitic fractures were seen around one large glomocryst. Small quartz veins up to 0.06 mm wide predate deformation as they are deformed by slippage along the cleavage surfaces in the sericite.

Alteration of feldspars to sericite is intense in the groundmass. Sericite alteration of the feldspars in the glomocrysts and in individual feldspar phenocrysrts is weak to moderate. Cores of both quartz and feldspars are replaced and sericite has replaced 20–30% of individual feldspar crystals. Sericite also occurs as small micro-veinlets cross-cutting both the groundmass as well as individual crystals. Chlorite is visible as a very minor component in the groundmass but is common as wispy deformed crystals in pressure shadows of pyrite grains and in fractures in glomerocrysts. Chlorite also occurs as small blebs in the crosscutting quartz veins. Epidote occurs as rare euhedral to subhedral crystals to 1 mm in association with minor magnetite.

Jukes Road pumice breccia (12450–12700 m)

Stop 2, 12600 m

Stop 3, 12450 m

One horizon in this sequence is distinct from all of the others due to its pink and green banding (Plate 2). It contains excellent tube pumice breccia textures and altered pumice and lithic clasts in a matrix feldspar and quartz. These rocks appear to be similar to the Rosebery–Hercules feldspar-phyric pumice breccias, except for the presence of more lithic clasts. Mineralogically the rocks are composed of quartz, plagioclase, sericite, chlorite, and carbonate with traces of pyrite and magnetite. Quartz commonly occurs as fine (0.02–0.1 mm) interlocking mosaics with feldspars (albite?) in the groundmass. Euhedral to subhedral plagioclase is most common in the in 1–5 mm size lithic clasts of tube pumice and vesicular pumice. The plagioclase composition of the phenocrysts was determined to be oligoclase by the Michael Levy method. Euhedral zircons are rare but are seen scattered throughout the groundmass and as inclusions in feldspars.

Shards of tube pumice and vesicular pumice are preserved and fine-grained mosiacs of quartz and feldspar are probably relict glass shards (Plate 3 and Plate 4). The tube pumice is preserved as small 1–7 mm sized wispy very fine-grained mosaics of quartz and feldspar with the long dimension of the tubes defined by alignment of small chlorite and sericite blebs and patches. Shards are randomly oriented in the sample. Vesicular or spherulitic shards are well represented in the rock and compositionally make up about 30% of the shards seen. Circular and semi-circular spherulites or vesicles are common and are filled with interlocking aggregates of recrystallised twinned feldspar (albite?) and quartz. Relict perthitic fractures are common in some shards.

Metamorphic or deformationally related textures are weak and locally defined by sericite alignment forming a weak foliation.

The pink and green banding seen in the rock is due to irregular distribution of feldspar alteration, presumably albite, in the groundmass. The albite altered areas form the pink domains, while the green domains are formed by a chlorite dominant groundmass. Albite alteration in the groundmass is pervasive to almost absent. Plate 5 and Plate 6 show two photomicrographs of the same rock. Notice the differences in the groundmass alteration. In Plate 5, albite has almost totally replaced and recrystallised the groundmass into fine to medium-grained aggregrates of interlocking crystals. Faint twinning in groundmass sized feldspar crystals is common. Chlorite occurs as patches and blebs. The albite is clearly post sericite alteration as seen in feldspar phenocrysts where albite alteration halos occur around fractures within the feldspar phenocryst. This style of alteration is characteristic of diagenetic alteration seen elsewhere in the CVC (White, 1996), and is also described by Allen and Cas (1990).

Sericite alteration occurs in the feldspar phenocrysts but is very weak. Sericite alteration of the plagioclase crystals is uniform, pervasive and often follows and defines cleavage surfaces. Chlorite occurs as coarse aggregrates in fractures in the feldspars, in pressure shadows of feldspars in the coarse lithic clasts, in the groundmass of the tube pumice shards and as an almost total replacement of groundmass feldspars. Plate 6 shows typical chlorite alteration of the groundmass and weak sericite alteration of the feldspar phenocrysts. Chlorite can very in abundance in various shards possibly indicating differences in the original composition of the shards. Rare pyrite has altered to magnetite.

Carbonate alteration is very common in this unit but is currently believed to be post deformational. Plagioclase crystals in the coarse pumice shards are broken and coarse carbonate alteration has invaded the open space. The carbonate alteration most commonly occurs at high angles to the twinning planes in the feldspars and is most abundant in the most broken crystals. The carbonate–plagioclase contact is ragged and shows clear evidence of external invasion. Carbonate also occurs as blebs and irregular patches of various sizes within the groundmass.

Tuffaceous ash/sandstone facies (11450–11700 m)

Stop 4, 11500 m

The tuffaceous ash/sandstone facies includes thin tuffaceous ash horizons interbedded with thin tuffaceous-sandstone and pumiceous volcaniclastic horizons (Plates 7, 8). The unit as a whole is exposed for approximately 230 m along Jukes Road. Graded bedding is preserved in some of the thin sandstone horizons and facing directions can be interpreted. Regional cleavage is variably developed in this unit and is subparallel or slightly oblique to bedding. Cleavage is best developed in the more sericitic or chloritic units.

This facies is most altered to sericite, with only local chlorite alteration. Silicification is weak in most samples, however in some of the more tuffaceous horizons, silicification has produced light pink or light green cherts.

CVC, columnar jointed feldspar-phyric rhyolite (11450–10100 m)

Stops 5, 7, 8, 9, 10, 11, 12 and 13

Columnar jointed feldspar-phyric rhyolite is the primary host unit to the Jukes Cu–Au Prospect. This unit is exposed for roughly 1 km along Jukes Road. The rocks are locally spherulitic (Plate 9), and contains 5–7% feldspar crystals in a fine-grained groundmass. Locally small amygdales, lithophysae and tuff/ash inclusions can be found. Well developed columnar joints are common (Plate 10). This unit is interpreted to be a single sill or flow.

The feldspar-phyric rhyolite is composed of quartz, plagioclase, K-feldspar, sericite, and chlorite with minor amounts of magnetite and pyrite. Scattered subhedral and euhedral 0.02 mm zircons are also found. Grain boundaries in the groundmass are generally serrated but were formally cuspate or curved. Quartz most commonly occurs as individual anhedral grains from 0.2–0.4 mm, which form a micropoikilitic texture (Plates 9, 11a, 11b). This granular texture is defined by irregular boundaries between quartz grains outlined by sericite. "Birdseye" texture in the quartz cores of micropoikilitic quartz is caused by embayments of feldspar commonly replaced by sericite and/or chlorite. These embayments also form micrographic and granophyric textures (Plate 12) that impart a "worm burrow" appearance to many of the groundmass quartz and feldspar grains. "Unaltered" quartz cores are optically continuous with the rest of the quartz grain. The quartz cores may represent an initial stage in the formation of granophyric texture or the nucleation point of the larger quartz grain. Plagioclase and K-feldspar occur typically as 0.1–0.2 mm size subhedral to anhedral lathlike crystals in the groundmass, although K-feldspar laths may be euhedral and show good carlsbad twinning. Plagioclase and K-feldspar also form euhedral to subhedral phenocrysts from 1–5 mm in size. K-feldspar phenocrysts are much less abundant than plagioclase phenocrysts and are usually smaller in size. K-feldspar is preserved in the groundmass in weakly altered rocks and carlsbad twinning is occasionally seen. K-feldspar is generally less replaced by sericite than plagioclase.

Relict perlitic textures are found in some of the least altered rocks and are defined by alignment of sericite and or chlorite around the rims of relict fractures. All perlitic texture is destroyed by increasing alteration effects. This is probably due to the easy access of fluids to the rock via perlitic fractures.

Regional metamorphic cleavage is poorly developed in unaltered rocks but is developed in rocks with chlorite alteration. Sericite rich rocks around 10800 (600 **m** northwest of Jukes) show well developed crenulations crosscutting other textures in the altered rocks. These crenulations form a wide-spaced cleavage in the rock. This cleavage becomes weakly developed although some distortion of phenocrysts is seen.

Weak to moderate cleavage offsets microfractures related to hydrothermal alteration and is therefor post fracture. Metamorphic cleavage is frequently, but not always, oblique to the fractures. Where the cleavage is parallel to the fractures, movement along the fractures is demonstrated by alignment of the sericite and chlorite parallel to the direction of movement. Where oblique, fractures are cut off sharply. Sericite in the groundmass commonly aligns

itself parallel to this cleavage and forms a weak foliation.

Alteration effects in the columnar jointed feldspar-phyric rhyolite vary from weak to almost complete. A complete transition from weakly altered rhyolite, with good textural preservation, to rocks with almost totally new mineralogy, related to the hydrothermal event, is expressed along the Jukes Road. The descriptions below will begin with least altered rocks in the west (around 11200 m) and transition inward to the core of the hydrothermal system at around 10100 m. It is worth keeping in mind that the alteration mineralogy and textures are imprinted on a single fairly homogeneous rhyolitic sill or flow unit with little variability in its original composition, texture and mineralogy. The alteration is also irregularly distributed in the rocks several hundred meters away from the center of the mineralisation. Rocks with locally intense alteration are found sandwiched between rocks exhibiting weaker degrees of alteration. Alteration intensity appears to be controlled by fracture density, therefore it is suggested that altered fracture systems radiate outward from the core of the mineralised system for several hundred metres.

Stop 5, 11200 m: Weakly altered columnar jointed rhyolite

10800 m: This rock is the least altered of the feldspar-phyric rhyolite unit. The groundmass is weakly altered by sericite (Plate 11a, b). Grain boundaries are often defined by small sericite grains and rarely a weak foliation will be defined. Feldspar phenocrysts are plagioclase and albite twinning in the feldspar is frequently preserved. Replacement of phenocrysts by sericite varies from 20–50% with lesser amounts of chlorite and carbonate (Plate 13a, b). XRD results indicate that sericite is 15–25%, and chlorite is less than 5% of the rock (Appendix A). Carbonate is less abundant than chlorite. Carbonate alteration is very irregular in its distribution. Replacement can vary from almost complete, in some selected phenocrysts to absent. Carbonate is always accompanied by lesser amounts of sericite and occasionally chlorite. Few if any fractures.

Stop 7, 10470 m: **Fracture controlled K-feldspar alteration**

10750 to 10420 m: The alteration is similar in style and intensity to that described above but the intensity of carbonate alteration become progressively less . By 10700 carbonate alteration is only visible in trace amounts and by 10420 is completely absent. A few small scattered <0.04 mm quartz veins. They are offset by movement on cleavage therefore predate it. Low fracture density, alteration is moderate sericite.

10420 m: Feldspar phenocrysts are intensely altered to very fine-grained mosiacs of sericite and quartz. Chlorite and carbonate are absent. In the groundmass, sericite has entirely replaced the microphyric texture in the feldspars and forms cores of the "birdseye" textures in micropoikilitic quartz (Plate 14a, b). Sericite replacement of the feldspar phenocrysts is incomplete and typically less than 50%. In crossed polars the shape, size and relict extinction of the feldspars remains although relict twinning is often obscured. In plane polarized light the alteration appears almost total. Sericite forms a very weak foliation in the rock.

10370–10390 m: The groundmass alteration is expressed by weak chlorite development but two types of phenocryst replacement are seen. First is almost complete replacement by sericite (Plate 15a and Plate 15b). Sericite is 70–90%. Second is intense replacement of phenocrysts by sericite and chlorite (Plate 16a, b). These rocks are shattered by numerous chlorite/tourmaline ± magnetite veins and numerous stages of quartz, quartz/sericite, quartz/chlorite ± tourmaline veins. A large (1 cm) late crosscutting quartz, chlorite carbonate vein pinches out to nothing. Increasing fracture density. Plate 17 shows some of the complex interrelationships of veining and brecciation at this location. High vein density of thin quartz/sericite veins with random orientations (Plate 18).

Stop 8, 10360 m: **Sericite alteration in the columnar jointed rhyolite. This zone of sericite alteration is within the hydrothermal halo of the Jukes system.**

10350 m: Feldspar phenocrysts are intensely altered to mosiacs of sericite and chlorite. The green colour of chlorite gives the rock an overall greenish appearance although dominant alteration mineral is sericite. Phenocrysts are replaced by two distinct domains of mineralogies. One is a fine mesh of interlocking sericite (70%) and chlorite (30%) (Plate 19a, b). The second is 80% or more chlorite with minor sericite (Plate 20a, b). The chlorite dominant domain is common in the smaller phenocrysts and may represent selective replacement of the K-feldspar phenocrysts in a different manner than the larger plagioclase phenocrysts. Alteration in the groundmass is dominated by sericite > chlorite > carbonate (trace). Chlorite forms distinct crystals (up to 0.04 mm) and small crystal aggregates, probably as replacement of the small feldspar laths. This is the last occurrence of carbonate alteration as the mineralisation is approached. No fractures seen, low density, alteration moderate sericite/chlorite.

Stop 9, 10345 m: **Sericite altered matrix and chlorite altered phenocrysts. "Chlorite Disease"**

10330 m: Both the phenocrysts and the groundmass are intensely altered by sericite and phenocrysts frequently contain one or two bits of skeletal magnetite. Twinning is destroyed in the phenocrysts but sometimes is faintly visible in groundmass feldspars. Alteration of at least some of the phenocrysts took place along cleavage surfaces. Chlorite occurs as irregularly distributed patches (0.02–0.1 mm) but most commonly occurs with sericite as 0.002 mm sized blebs in the groundmass and phenocrysts. XRD results indicate sericite (mica) at 15–25%, chlorite at 10–15% and K-feldspar at 5–10% (Appendix A). Three domains of chlorite: (1) Irregular blebs in the groundmass (0.02–0.05 mm) with some larger masses to 0.2 mm. (2) Irregular masses in phenocrysts with sericite. (3) Large irregular masses as cores of magnetite and iron oxides, and four domains of sericite: (1) Veins, ± chlorite or quartz, (2) Intergrain boundaries with irregular orientation, (3) Intercrystalline patches and replacements in groundmass feldspars and quartz. (4) Almost total replacement of feldspar phenocrysts. Small K-feldspar phenocrysts are totally replaced by sericite. Two sets of roughly aligned small fractures. One is quartz only and the other is quartz and sericite.

10310 m: Phenocrysts are >80% replaced by sericite/chlorite (Plate 21a, b). Chlorite occurs as more abundant coarse patches and irregular coarse masses frequently associated with replaced feldspar phenocrysts. Alteration is irregularly dispersed throughout the rock with some areas more chlorite rich and others more sericite rich. An alteration front is visible in the thin section with small chlorite altered groundmass feldspars and micropoikilitic feldspar on one side and relatively unaltered groundmass feldspars on the other. This is shown in Plates 22, 23 and 24. Much higher fracture density than 10330 (Plate 25). Veins and veinlets of quartz (<0.01 mm), quartz + chlorite (0.01–0.04 mm), and chlorite + sericite ± quartz.

10300 m: The groundmass is altered to K-feldspar, sericite and chlorite. Small groundmass K-feldspar phenocrysts are totally replaced by sericite. Chlorite occurs as individual irregular masses of anhedral crystals in the groundmass. Both sericite and chlorite occur as embayments in micropoikilitic quartz replacing feldspar. Phenocryst boundaries are ragged and are 95–100% replaced by sericite or sericite and chlorite. Sericite replacement of plagioclase phenocrysts may selectively replace along individual crystallographic axis giving the resultant sericite a common extinction. Four domains of sericite are found in these rocks. (1) Veins ± chlorite or quartz, (2) Intergrain boundaries with irregular orientation, (3) Intercrystalline patches and replacements in groundmass feldspars and quartz. (4) Almost total replacement of feldspar phenocrysts. Four domains of chlorite are also found. (1) Irregular blebs in the groundmass (0.02–0.05 mm) with some larger masses to 0.2 mm. (2) Irregular masses in phenocrysts with sericite. (3) Large irregular masses as cores of magnetite and iron oxides. (4) Veins ± quartz. Fracture density as in 10330. Microfractures are common with

two styles, sericite + chlorite (0.05 mm wide), and smaller microfractures of sericite + quartz (<0.01–0.01 mm wide).

Stop 10, 10290 m: **Remobilised mineralisation in post Devonian fault.**

10290 m: K-feldspar alteration is the dominant alteration style. Most of the rock is black and white under crossed polars but under plane light the rock looks pink-reddish (Plate 26a, b). The dominant alteration style in the groundmass is K-feldspar. Small K-feldspar laths and cores of micropoikilitic quartz show a complete transition in alteration from very weak sericite alteration to complete chlorite alteration in a K-feldspar altered rock (Plates 26a, 27 and 28). Chlorite forms alteration cores in some phenocrysts (K-feldspar ??), while plagioclase phenocrysts are completely altered to sericite + chlorite ± quartz. Intense fracture density of several crosscutting veinlets. At a magnification of 2.5 there are usually at least 4–5 veins per field of view. Veinlets are frequently offset by later minor movement possibly related to the formation of weak cleavage in some of the lesser altered rocks. Some veinlets pinch from 0.4–0 mm across the section. Several vein types are recognised. Quartz fills fractures (0.02–0.08 mm) with rare accessory minerals although there is a trace of chlorite in some including one with 20% chlorite. Veins with quartz and chlorite or quartz and sericite are cut by quartz only veins. A Vein with quartz and K-feldspar (?) is cut by a vein of quartz + chlorite. These veins appear responsible for the potassic (K) alteration. Fractures with quartz and K-feldspar are annealed and recrystallised and are the earliest veins in the section.

Stop 11, 10280 m

Alteration is K-feldspar–sericite. Stockwork vein control of K-feldspar alteration. Fractures are reused by later chlorite. Parallel to subparallel quartz–chlorite veins with pyrite and chalcopyrite.

10270 m: Chlorite and sericite alteration in phenocrysts. Small K-feldspar laths are altered to chlorite. K-feldspar is the dominant alteration mineral in the groundmass. Scattered pyrite and lesser magnetite. Dense occurrence of microfractures forms small stockworks. Microfractures vary in size from much less than 0.01 mm to 0.1 mm. Microfractures of quartz + chlorite and sericite + quartz are common.

10250 m: K-feldspar and sericite occur in approximately equal amounts with lesser chlorite in the groundmass, and disseminated pyrite and magnetite are common. Sericite is the dominant alteration phase in the phenocrysts at approximately 20–90%. Some of the least altered phenocrysts are only weakly sericite altered and/or only have a trace of chlorite. Sericite occurs along twinning boundaries in the plagioclase phenocrysts and twinning is often preserved (Plate 29a, b). Microfracture density is low and is dominated by sericite + quartz.

Stop 12, 10245 m: **K-feldspar and sericite alteration are fracture controlled and are post sericite–chlorite alteration.**

10230 m (MJ-96-6): Quartz is partially replaced by an alteration assemblage of K-feldspar + sericite + chlorite. Quartz "Birdseyes" are partially replaced. K-feldspar and sericite are approximately and are much more common that chlorite. Rims around the "birdseye" quartz are altered to sericite + K-feldspar. Quartz cores are also approximately 10% replaced by sericite and K-feldspar. Phenocrysts are altered to either a sericite or a sericite (70%) + chlorite (30%) assemblage. Disseminated magnetite is common. High microfracture density throughout. Microfractures of quartz, quartz + chlorite and sericite only are seen. Sizes range from <0.01–0.1 mm. Some of the larger fractures may represent later post alteration remobilisation. These contain ladder like quarts and bright green chlorite with minor iron oxides (Plate 30).

10220 m: Phenocrysts are altered to mosiacs of coarser chlorite and finer sericite (Plate 31a, b). The groundmass is mostly K-feldspar and lesser sericite altered. Some domains of sericite are overprinted by K-feldspar (??). Chlorite occurs as four domains. (1) Irregularly spaced small masses in the groundmass, (2) Fine crystals after the small K-feldspar laths, (3) veins and (4) in phenocrysts. Pyrite is disseminated throughout and also occurs in veins with chalcopyrite

(Plate 32a, b). Microfracture with quartz, K-feldspar and minor pyrite and chalcopyrite (Plate 33) are common. Some fractures are "zoned" from a core of quartz outward to pyrite and chalcopyrite on the edges. This may represent relict banding in the veinlet. Chalcopyrite occurs as anhedral to subhedral masses and crystals. These veinlets are later cut by quartz only microfractures.

Quartz–feldspar biotite porphyry dykes

Dykes of quartz–feldspar–biotite porphyry crosscut the columnar jointed feldspar–phyric rhyolite at numerous localities. Seven dykes have been mapped along Jukes Road. Contacts with the feldspar-phyric rhyolite are sharp and some have been intensely chloritised. Two distinct phases of the quartz-feldspar biotite porphyry dykes exist. The first contains up to 30% quartz phenocrysts, 5–10% plagioclase phenocrysts and 2–3% biotite phenocrysts set in a very fine-grained groundmass (Plate 34). The second contains 15% plagioclase phenocrysts, 5% quartz phenocrysts and 2–3% biotite phenocrysts set in a medium-grained groundmass (Plate 35).

Quartz–feldspar biotiteporphyry dykes: Type 1

Stop 14, 10195 m: **Quartz-feldspar phyric dyke cutting hydrothermal breccia. Breccia matrix is magnetite–tourmaline and chlorite.**

Subhedral to anhedral quartz and feldspar phenocrysts make up fully 30–40% of the rock. Quartz phenocrysts compose up to 20–30% of the rock, vary in size from 0.2 to 8 mm. Some show rounding of the grains and excellent embayed textures while others can be angular, the result of being broken. Frequently quartz phenocrysts show non-uniform extinction that is interpreted to be evidence of strain. Feldspar phenocrysts compose up to 15–20% of the rock, vary in size from 0.1–0.5 mm to 6 mm, are generally euhedral to subhedral, and are usually sericitically or chloritically altered. Both quartz and feldspar phenocrysts show a complete gradation in size from microphenocrysts through to their maximum size. Biotite phenocrysts are variable in size from 0.1–0.4 mm to 2 mm and are almost completely replaced by chlorite. The groundmass is composed of 0.005–0.01 mm quartz and altered feldspars and 2–3% uniformly disseminated magnetite. One dyke, however has a much finer groundmass averaging 0.005 mm. Zircons to 0.01 mm vary from common to rare. Grainsize of the groundmass is 0.01–0.02 mm. Magnetite may be up to 5% of the rock. Carbonate is rare in the dykes farthest from the Jukes Prospect and absent in those near the center of the hydrothermal system. Pyrite, magnetite and occasionally chalcopyrite are accessory opaques.

Quartz phenocrysts are rounded and many show excellent embayments. Feldspar phenocrysts are also embayed and in some dykes show a preferred orientation aligning themselves parallel to the walls of the dykes. The groundmass varies from unfoliated to moderately well foliated and has a seriate texture.

Plagioclase phenocrysts are almost totally altered to sericite or a combination of sericite and chlorite. Alteration in the phenocrysts was clearly controlled by cleavage in the original feldspar (Plate 36a, b). Sericite replaces a previously K-feldspar altered groundmass (Plate 37a, b). Chlorite is up to 5% of the rock, and occurs as rims and embayments in the biotite phenocrysts and as irregularly distributed 0.02–0.1 mm patches and blebs throughout the groundmass. Chlorite occasionally is up to 30% of the groundmass. Two types of chlorite are suspected. One has typical green to greenish-brown interference colors and the other has very distinct blue–green interference colours (Plate 38a, b). What the difference is at this time is unknown. One dyke at 10520 m has both K-feldspar and chlorite alteration in the groundmass. Pyrite occurs with sericite in altered plagioclase feldspars and in very close proximity to broken sericitically altered feldspars.

Quartz–feldspar biotite porphyry dykes: Type 2

Stop 6, 10520 m

Quartz-feldspar phyric dyke cutting the columnar jointed rhyolite. Intense chlorite alteration is seen along the edges of the dyke. The groundmass of the dyke is both K-feldspar and chlorite altered.

Some Type 2 dykes are well within the alteration

halo of the Jukes hydrothermal system. Compositionally Type 2 is similar to Type 1, however there are two distinct differences. The grainsize of the groundmass is much coarser averaging 0.01–0.1 mm. Quartz phenocrysts can be up to 5–10% of the rock and plagioclase phenocrysts make up about 15% and biotite phenocrysts are rare.

Initial replacement of the feldspar phenocrysts appears to have been by sericite, leaving relict unaltered cores and patches. Relict cores of feldspar are occasionally found surrounded by sericite. In some phenocrysts the cores of feldspars are replaced by later chlorite (Plate 39). This is interpreted as representing a second late preferential replacement of the remaining unaltered feldspar by chlorite. Chlorite replaces biotite and also occurs as small randomly scattered blebs throughout the groundmass. Feldspar phenocrysts are 30–40% altered by sericite. Replacement occurs along cleavage and unaltered feldspar shows uniform and shadowy extinction.

Several fracture sets have been identified cutting through the quartz-feldspar–biotite porphyry dykes. They include veins, veinlets and microveinlets that contributed to the alteration as well as veins and veinlets that are clearly post hydrothermal event and are probably the result of metamorphic remobilisation.

Breccia bodies

Stop 13, 10200–10220 m

Main hydrothermal breccia body. There are both magnetite–tourmaline and chlorite tourmaline matrices in this location. Sulfides are not uncommon. Clasts are dominated by K-feldspar altered rhyolite.

At the Jukes Prospect, two styles of breccias have been identified that appears to be of hydrothermal origin. These breccias were previously identified by Doyle (1990) as pseudobreccias however the intimate association of magnetite, chlorite and tourmaline in the matrices, argues very strongly for a hydrothermal origin. The breccias are predominately clast supported (60–90% clasts) although localized areas of matrix supported breccias are found. The breccias often form a fine crackle breccia with jigsaw fits. Wall rocks adjacent to the breccias are commonly marked by zones of crackle breccia ranging from one to several metres in width. Within these zones, proximity to the breccias is marked by an increase in fracture density and, near the contact, some rotation of the clasts. The main body of the breccias is matrix supported and contains milled breccia clasts and abundant rock flour. Clasts in the breccia are dominated by angular to subangular blocks of intensely K-feldspar altered feldspar–phyric rhyolite. Rare rounded clasts of porphyry dyke rocks are also found in the breccia, indicating that they were disrupted and transported during breccia formation. Breccias are classified according to their matrix type. The first contains various amounts of magnetite/hematite and tourmaline ± chlorite and the second chlorite and tourmaline ± magnetite/hematite as shown in Plate 40 and Plate 41. Fragments vary in size from <1 mm to > 20 cm. There is a possibility that the two breccias are related to each other and to the large magnetite bodies found both at the Jukes Prospect and further south at Mt Darwin. Breccias are cut by faults but clearly predate fault-related tectonic fracturing. The two types of breccias will be described separately below.

Disseminated pyrite ± chalcopyrite mineralisation occurs irregularly throughout the breccias. Best grades of chalcopyrite mineralisation are found in the post-breccia faults, most likely as a result of later remobilization and concentration.

Magnetite–tourmaline breccias

Magnetite dominates the matrix of the magnetite–tourmaline breccias and can form from 10 to 50–60% of the rock or more (Plate 41). Magnetite occurs as euhedral to subhedral interlocking crystals and frequently forms exsolution lamellae with ilmenite (Plate 42). Magnetite and ilmenite are often seen in roughly equal amounts. Microveinlets of magnetite radiate outward from larger veins forming both diffuse random arrays and disseminated halos. Tourmaline occurs throughout the magnetite matrix as euhedral to subhedral crystals of variable dimension(0.08 x 0.4 mm to 0.4 x 1 mm). Tourmaline crystals typically grow between and around pre-

existing euhedral magnetite. Tourmalines are randomly oriented and cross-sections, perpendicular to the long axis, often show good zoning (Plate 43). Tourmaline typically makes up less than 1 to 5% of the matrix but is almost always present. In addition to tourmaline, the matrix may contain variable amounts of chlorite (0.2 mm), milled rock flour and very fine quartz. Most commonly the clasts show little rotation and appear to form jigsaw and pseudo jigsaw fit textures. Clasts are typically very angular with very corroded margins.

Magnetite–tourmaline breccias are clearly cross-cut by quartz and quartz–chlorite veins (Plate 44). These are in turn broken and bent within the breccia by later movement (Devonian ??) and are therefor interpreted as Cambrian in age and related to part of the hydrothermal event.

Chlorite–tourmaline breccias

The primary breccia matrix is chlorite (70–100%) with variable amounts of tourmaline and accessory magnetite and pyrite. The chlorite/tourmaline matrix appears to have been forcefully emplaced as evidenced by both jigsaw fit and rotational domains of clasts (Plate 10-31). Tourmaline occurs as up to 30% of the matrix in small (<0.005–0.05 x 0.025 mm sized crystals) aggregrates and masses (Plate 45a, b). Magnetite has two modes of occurrence. One is as apparent pseudomorphs after an elongate bladed mineral (Plate 46). The second magnetite occurrence is as evenly distributed 0.02–0.06 mm sized euhedral crystals throughout the rock. This includes both the groundmass of the breccia matrix and the clasts. This may indicate a late origin to the second mode of occurrence of magnetite. Carbonate occurs as occasional patchy anhedral masses (Plate 47) and may postdate the hydrothermal event.

Quartz microveins crosscut the K-feldspar altered clasts (Plate 48). These veinlets do not cut through the breccia matrix and clasts with these veinlets appear to have been slightly rotated. This is taken as evidence that they were emplaced earlier than the breccia formation. Other small veins of quartz clearly cut both the clasts as well as the breccia matrix indicating that there was another later quartz veining episode (Plate 49). Post breccia veins range in size to 0.1 mm and appear more abundant than the pre-breccia quartz veinlets. The breccia matrix is later cut by sericite filled microfractures either formed during a later part of the hydrothermal event or during later metamorphic remobilisation.

Eastern quartz–phyric sequence (EQP)

Quartz–feldspar–phyric dacite

Quartz–feldspar–phyric dacite is exposed along Jukes Road for approximately 200 m (from 9900 to 1100), in an area immediately adjacent to the fault between the CVC and EQP sequence. Quartz–feldspar–phyric dacites have well developed tectonic cleavage and contain up to 30% quartz and feldspar phenocrysts. Compositionally the rocks contain feldspar, quartz, biotite, relict ferromagnesian minerals (now chlorite), muscovite (sericite) and minor magnetite. Average quartz crystal size is 0.1 to 5 mm. Average plagioclase crystal size is 0.5 to 4 mm. The groundmass is very very fine grained and foliated. Composition is difficult to determine optically but appears to be composed of quartz muscovite (sericite), chlorite and relict feldspar. Average grainsize is 0.001–0.002 mm but some coarser areas are found. Much of the coarser ground mass is composed of a mash of feldspar (now sericite), quartz, chlorite and minor magnetite as randomly oriented angular interlocking crystals and masses rotated by movement along cleavage. These masses may be relict glassy lithic clasts or recrystallised glassy shards and often form thin flattened and deformed rod and spine shapes (Plate 50). Some of the relict lithic clasts appear to have been pumiceous and are now replaced by sericite and chlorite, Iron oxides are common along cleavage surfaces. This unit is interpreted to be a volcaniclastic rock.

Quartz phenocrysts are euhedral to subhedral and embayed. Many are broken and have rounded corners. Plagioclase phenocrysts are broken and many margins are corroded. Some are stretched by foliation/cleavage development into small augens. Some quartz shows excellent granophyric intergrowths with feldspar. Relict spherulites are also common and defined by radial growth from a central

point (Plate 51, b). The original mineralogy of the spherulites was replaced by feldspar and quartz and later by sericite.

Plagioclase phenocrysts are replaced by up to 50% sericite and to a lesser extent chlorite (5–20%). Albite twinning is preserved in many of the phenocrysts. Replacement appears to follow cleavage surfaces. Magnetite occurs as a replacement of a planer mineral in small rounded to subrounded masses with quartz. Cores of the magnetite's often show second order interference colors. Within a given rock or outcrop the alteration style can vary greatly due to very irregular distribution. Both sericite and chlorite alteration are variable in intensity from moderate to strong.

Quartz–feldspar–phyric rhyolite porphyry

The quartz–feldspar–phyric rhyolite porphyry facies of the EQP is only exposed for a short distance along Jukes Road where it is sandwiched between the quartz–feldspar–phyric dacite described above and the quartz–feldspar–phyric rhyolitic volcaniclastic described below.

The quartz–feldspar–phyric rhyolite porphyry facies is interpreted to be coherent lava. The groundmass is a very fine grained (0.03–0.06 mm) pseudo-micropoikilitic interlocking mosaic of quartz and finer feldspar. Probably the result of recrystallised and devitrified glass. Quartz phenocrysts range in size from 0.5–8 mm and comprise up to 30% of the porphyry. Feldspar phenocrysts are much rarer, range in size from 0.5 to 5 mm, and make up only about 5 % of the rock. The unit contains a few scattered spherulitic rhyolite clasts. Tectonic cleavage is weakly developed but has dismembered many crystals and a weakly developed foliation is defined by sericite (Plate 52a, b).

Alteration is dominated by sericite with subordinate chlorite. Feldspar phenocrysts are moderately to strongly altered to sericite and chlorite (Plate 53a, b). The recrystallised groundmass is only weakly altered to sericite and relict feldspar is preserved.

Quartz–feldspar–phyric rhyolitic volcaniclastic

Quartz–feldspar–phyric rhyolite is the dominant lithology in the EQP. It is exposed along Jukes Road for over 1 km, in an area between the quartz–feldspar–phyric rhyolite porphyry described above and Tyndall Group rocks. The rocks contain quartz (60%), mica (25%), Kaolinite (10–15%), chlorite (5%), and K-feldspar (5%) as determined by XRD analysis (Appendix A). Accessory minerals are carbonate and magnetite. Zircons are occasionally found. The groundmass has a sandy texture. Phenocrysts of feldspar and quartz make up 20–30% of the rock. Phenocrysts have a complete gradation in size from 0.5 to 5 mm but feldspar phenocrysts are usually smaller than those of quartz. Quartz phenocrysts can be euhedral, rounded broken or embayed. Lithic clasts are common and are typically millimeter scale but are occasionally much larger (Plate 54). Lithic clasts are of several types, fine mosiacs of quartz and feldspar were formerly glassy shards, now devitrified and recrystallised. Clasts with relict perlitic textures defined by sericite, are also preserved. Some clasts were vesicular. Lithic clasts of quartz-feldspar–phyric volcanic rocks are common. This unit is interpreted to be a massive, moderately crystal rich volcaniclastic sediment or mass flow.

Quartz–feldspar–phyric rhyolites have weak to moderately well developed foliation defined by development of sericite (Plate 55a, b). Cleavage development is weakly to moderately well developed in some rocks.

The rhyolites are altered to sericite with minor potassium feldspar (K-feldspar) chlorite, magnetite, pyrite and carbonate. Sericite or sericite–chlorite alteration in the groundmass is usually moderate and post alteration tectonism has produced a well defined foliation in most rocks. Plagioclase phenocrysts can be replaced variable amounts of sericite, carbonate or a combination of sericite and chlorite. Alteration varies from weak to complete. Alteration of the feldspar phenocrysts occurs selectively along cleavage planes within the crystals and is shown by both sericite and/or carbonate alteration. In weakly altered rocks, relict twinning in the feldspar is

preserved. Both lithic clasts as well as the groundmass and phenocrysts are altered.

Alteration assemblages

Along the Jukes Road, styles of hydrothermal alteration and intensities are dependent upon fluid access to the rock via a series of well defined fracture networks. Some of these are presumably related, at least in part, to the development of the hydrothermal breccias described in Section 2.3. Several overlapping vein types have been identified and reconstruction of a vein paragenesis is part of the ongoing work. Several observations can be made based on the examinations so far. One, there are both early, pre and post hydrothermal breccia micro-quartz veins. Many of the veins have been reopened and reused several times by different solutions including some by post mineralisation Devonian veins.

At 10180 m, in the heart of the hydrothermal system, an excellent paragenesis is shown by an extensive network of microfractures that clearly cut and have altered a quartz–feldspar porphyry dyke. Diffuse replacement of a previously K-feldspar altered groundmass by sericite is seen around one veinlet with a sericite selvage and a chlorite/quartz core (Plate 37a, b). The vein has a sharp contact with the surrounding rock. Microfractures of sericite finger outward throughout the groundmass in ever decreasing size until they are intergranular to groundmass crystals. Another indication of the complexity of the vein and breccia relationships is shown in the rocks at 10390 where quartz veins are reused by later chlorite/tourmaline breccias and pinch out into chlorite veins (Plate 17).

Veins that appear to be of post hydrothermal event origin typically contain quartz and bright green or bright blue–green chlorite and often well developed rhombohedral carbonates. Plate 10–15 is a late vein, probably Devonian, with spectacular quartz, chlorite and spar carbonate cutting intensely K-feldspar altered rhyolite. The quartz usually forms ladder like structures and the chlorite forms as clean interlocking fine-grained < 0.01 mm mosiacs in large openspace between and around quartz grains. Late crosscutting veins may also have other accessory minerals such as sericite, magnetite and rare sulfides. At 10200 m, a late quartz (with ladder like structure), chlorite, sericite vein (0.04–0.5 mm wide) with no alteration along its margins, crosscuts the rock, deforming quartz phenocrysts but not breaking them.

Six styles of alteration assemblages have been identified along the Jukes Road. Each of these will be discussed below in more detail. In almost every case, there is extreme variability within the assemblage in terms of a range of intensities of the various mineral phases. The alteration assemblage seen at any one locality is frequently a combination of two or more styles with complex overprinting relationships. The six dominant assemblages are: sericite, chlorite, potassium feldspar (K or K-feldspar), carbonate, albite and silica. Of the six dominant types of assemblages, sericite, chlorite and K-feldspar assemblages are the most common and most easily identified. Carbonate, albite and silica assemblages are minor.

Accessory minerals include pyrite, magnetite, hematite, goethite, chalcopyrite and rarely apatite. Magnetite and pyrite are, by far, the most abundant accessory phases.

Sericitic dominant assemblages

Sericite is widespread throughout the Mt. Read volcanic belt and it is likely that most of the sericite is of metamorphic origin. Currently all white to light-green fine-grained mica is classified as sericite, although to be technically correct, almost all of the mica is to coarse-grained and should be, more correctly, called muscovite. However, to remain consistent with other workers in the region, the sericite terminology will be retained. Sericite is almost always accompanied by chlorite in either lesser or greater amounts, and occasionally by carbonate, K-feldspar, epidote and magnetite.

Sericite alteration assemblages are the most common alteration assemblages found in rocks along the Jukes Road. They occur in all sequences from the Eastern Quartz-Phyric through to the Yolande River Sequence. Sericite at the Jukes Prospect is, however more intensely developed and texturally destructive. Intensity and textural destruction are taken as

evidence of a hydrothermal origin for at least some of the sericite in the prospect area.

Four domains of sericite are found in the Jukes Road rocks. (1) Veins, ± chlorite or quartz, (2) small individual grains of sericite along intergrain boundaries with irregular orientation, (3) intercrystalline patches and replacements in groundmass feldspars and quartz. These are usually irregularly distributed within the groundmass crystals and are independent of any foliation in the rock. (4) replacement of feldspar phenocrysts. Intensities range from very weak to intense. Sericite rarely occurs alone without the presence of other minor accessory minerals, most typically, chlorite. Sericite–chlorite typically replaces the fine-grained groundmass. In volcaniclastic rocks, sericite–chlorite often occurs in both the lithic clasts and host rock with equal intensity. Mafic minerals and quartz appear to have been unaffected by weak sericite or sericite–chlorite alteration, but mafic minerals were destroyed during the formation of the intense alteration assemblages, usually by alteration to chlorite. Feldspar phenocrysts in feldspar-phyric rocks vary from unaltered to almost total replacement by light-green sericite. Many phenocrysts are only weakly altered, whereas the groundmass can have been almost totally replaced by sericite or sericite and chlorite. Other rocks contain feldspar phenocrysts that have been almost totally replaced by sericite leaving only pseudomorphed crystal shapes. Textural destruction of the groundmass is typically moderate, however most textures are generally preserved in rocks with sericite alteration assemblages.

Sericite only

Sericite alteration of groundmass is typically weak to moderate. Sericite forms small aggregates as replacements of groundmass feldspar and often outlines interlocking groundmass grains. Sericite can also occur as small micro-veinlets cross-cutting both the groundmass as well as individual phenocrysts. Sericite is typically seen as the first sign of alteration in feldspar phenocrysts. It typically replaces the feldspar along cleavage plains or via fractures. Cores and blebs of unaltered relict feldspar with preserved twinning are typical. In intense alteration of the feldspar phenocrysts, the feldspar is converted to an interlocking mass of sericite and quartz. In the Jukes Prospect area, the initial replacement often appears to have been by sericite and then later overprinted by other assemblages.

Sericite–chlorite

Three domains of sericite with lesser chlorite are found. (1) Irregular blebs in the groundmass (0.02–0.05 mm) with some larger masses to 0.2 mm. (2) Irregular masses in phenocrysts. (3) in veins with quartz or other minor accessories. Chlorite is most common as an accessory in phenocryst replacement where it can form coarse aggregrates related to fractures or fine interlocking mosiacs with sericite. Sericite–chlorite alteration is common in rocks with moderate to intense alteration. Phenocryst replacement is destructive to crystallographic structure, twinning is not preserved. In outcrop and hand specimen, weak sericite–chlorite alteration is easily confused with stronger chlorite alteration due to the strong greenish color given to the rock by even minor amounts of chlorite.

Sericite–chlorite alteration is only weakly developed in most of the EQP rocks and is typically confined to weak groundmass alteration in the coherent quartz- feldspar-phyric rhyolite/dacite facies. This sericite–chlorite alteration is probably metamorphic in origin.

Chlorite dominant assemblages

Chlorite dominant alteration assemblages are perhaps the most texturally destructive style of alteration developed along Jukes Road. Previously, Wyman et al. (1996) described two phases of hydrothermal chlorite along the Jukes Road. In addition, early pre-mineralisation as well as post-mineralisation chlorite assemblages were recognised. This paper further subdivides the chlorite alteration assemblages into six domains. These six domains are related to various timing events and phases of hydrothermal activity and post mineral deformation. The six domains are described below.

1. Early pre-mineralisation chlorite–sericite assemblage: This assemblage replaces both the groundmass and plagioclase and ferromagnesian mineral phenocrysts, as well as glassy and pumaceous shards. Chlorite is accompanied by lesser to equal amounts of sericite. This alteration is interpreted to be related to diagenesis and/or metamorphism. Feldspar twinning is generally preserved in phenocrysts and intensities are typically weak to moderate.

2. Early hydrothermal chlorite–sericite assemblage: Chlorite occurs as irregular blebs of varying size in the groundmass that is previously sericite or chlorite–sericite altered. Complete groundmass replacement is uncommon. This alteration is related to increased fracture density and early hydrothermal activity. Chlorite and sericite replace plagioclase, biotite and other ferromagnesian mineral phenocrysts. Chlorite is typically the dominant replacement mineral although sericite is a common accessory and is in part, probably overprinted by this later event. This phase of alteration is pre K-feldspar alteration and generally accompanied by only one additional accessory mineral, magnetite. Evidence for the timing of this alteration includes, chlorite veins that have cut sericite/chlorite altered rhyolites. These veins show diffuse chlorite alteration boundaries with chlorite replacing sericite/chlorite altered volcanics. Generally these veins occur on the centimeter scale with the diffuse boundary being limited to a few centimeters. Feldspar twinning is weakly preserved to completely destroyed and intensities are typically moderate to intense.

3. Chlorite only: Chlorite replaces small groundmass size feldspar laths. This alteration overprints previously sericite and/or K-feldspar altered groundmasses that did not alter the fine groundmass feldspar laths. This alteration is seen behind small solution fronts and is in part post K-feldspar alteration.

4. Chlorite only: Large irregular masses of chlorite occur as cores of magnetite and iron oxides. This appears to be a phase of magnetite replacing large masses of chlorite, or the chlorite may have pseudomorphed an early mineral or relict mineral after the magnetite.

5. Chlorite ± sericite ± quartz ± tourmaline: This assemblage occurs in hydrothermal veins with quartz ±sericite. Other minor accessories include sulfides. This phase of chlorite alteration is post K-feldspar timing and includes the presence of tourmaline, sulfides, and magnetite. Fluids infiltration during this phase of alteration appears to have been associated with hydrothermal brecciation. New fracture systems were formed and old fracture systems were reopened. Chlorite occurs as both matrix (along with varying amounts of magnetite and tourmaline) and fracture fillings. Chlorite in the matrix surrounds angular blocks of strong to intensely K-feldspar altered volcanic clasts. In strong to intensely K-feldspar altered zones, fractures that were clearly used by K-feldspar altering fluids are now filled with chlorite ± pyrite, and may show diffuse boundaries.

6. Chlorite–quartz–carbonate veins: These veins occur in post mineral fractures and faults with quartz, carbonate and some remobilised sulfides. Pyrite is the principal sulfide, but chalcopytite occurs in minor amounts and has locally been significantly remobilised and concentrated in post-mineral faults. Some of these fractures are several centimeters wide and occur in en echelon vein sets. Most are flat lying.

K-feldspar alteration assemblage

Hydrothermal K-feldspar appears to be confined to the area near Jukes Prospect, is typically moderate to intense and texturally destructive and turns the rocks pink. Phenocrysts in the intensely K-feldspar altered rocks are typically sericite–chlorite, or chlorite–sericite altered. K-feldspar alteration is almost always associated with weak chlorite alteration and is believed to have overprinted it. K-feldspar alteration

only occurs without other alteration assemblages in the groundmass of the most intensely altered rocks. The most common accessory alteration assemblages found in association with K-feldspar alteration in order of abundance are chlorite, sericite and silica. Sulfides are only found in post K-feldspar alteration fractures in the presence of chlorite.

K-feldspar alteration is clearly later than the first phase of hydrothermal chlorite alteration. Fractures within chloritically altered feldspar-phyric rhyolites exhibiting chlorite disease are filled with K-feldspar. This alteration extends outward with decreasing intensity away from the fractures. Commonly, intense textural destruction is observed within a few cm of the fractures while farther from the fracture, chlorite-replaced phenocrysts are still preserved.

K-feldspar alteration in the EQP is rare, and appears to only have affected the groundmass feldspar and mafic minerals; phenocrysts are unaffected.

Albite alteration assemblage

Albite alteration is generally texturally destructive to the groundmass, and is believed to be diagenetic or metamorphic in origin. This regional style of alteration would have intensities controlled by fluid/rock ratios during diagenesis or metamorphism. In the pink/green mottled rocks at 12500, moderate to strong albite alteration of the groundmass appears to have overprinted earlier weak chlorite alteration. Evidence includes chloritic cores in albite altered pumice clasts. Albite has replaced both the groundmass and lithic clasts, and appears to be conformable to bedding.

Albite–chlorite

Albite has almost totally replaced and recrystallised the groundmass into fine to medium-grained aggregrates of interlocking crystals. Faint twinning in groundmass sized feldspar crystals is common. Chlorite occurs as patches and blebs. The albite is clearly post sericite alteration as seen in feldspar phenocrysts where albite alteration halos occur around fractures within the feldspar phenocryst.

Silica alteration assemblage

Silica alteration in the form of silicification occurs to a limited extent in the CVC and EQP sequences. Silicification is typically weak and appears to always be accompanied by weak K-feldspar alteration. K-feldspar alteration, conversely, is not always accompanied by silicification. Silica alteration is only a minor phase of alteration along Jukes Road. It is significant only in localized areas at Jukes Prospect, where it occurs with K-feldspar alteration in weak to moderate intensities. Silicification has resulted in flooding of the groundmass by silica. Typically, the groundmass is light pink to light green, slightly translucent and dense and hard. Silica alteration is texturally destructive to the groundmass mineralogy.

Carbonate alteration assemblage

Carbonate alteration occurs along the Jukes Road. It typically occurs as weakly disseminated blebs and patches in the groundmass of sericite or chlorite altered rocks. Replacement, accompanied by sericite, can vary from weak to almost complete replacement of selected phenocrysts. Carbonate is almost always found with sericite and lesser amounts of chlorite except in the albite altered rocks at 12500 where it is found overprinting albite. Coarser carbonate occurrences also are found in late crosscutting veins with quartz ± chlorite. Carbonates identified to date are calcite, dolomite (Doyle, 1990), ankerite ($CaFe(CO_3)_2$) and siderite ($FeCO_3$).

Carbonate alteration is currently believed to be post deformational, however a case can be made that it appears to become less intense as the main Jukes system is approached. Carbonate is not seen as an alteration phase in the presence of K-feldspar alteration except as clearly post alteration deformation related veins. Plagioclase crystals in the coarse pumice shards are broken and coarse carbonate alteration has invaded the open space. Carbonate alteration most commonly occurs at high angles to the twinning planes in the feldspars and is most abundant in the most broken crystals. The carbonate–plagioclase contact is ragged and shows clear evidence of external invasion.

Geochemistry

Presented here are some of the basic geochemical results observed so far. Figure 3a, b, c and Figure 4a, b, c are presented to show a comparison of some of the major elements as well as Cu and Au in relation to the geology as depicted along Jukes Road. Figure 3a-c show the entire length of the road section in relation to K_2O, Na_2O and CaO, MgO, MnO and Fe_2O_3 and the Ti/Zr Ratio and the Alteration Index. Figure 4a, b show details of the same elements in relation to the rocks at the Jukes Prospect Appendix B includes a summary of the data used in preparing this report. A few broad statements appear to be valid based on observations of the data so far. They are: Geochemically, intensely altered rocks from the Jukes Prospect area show a clear trend of potassium enrichment in relation to weaker regional sericite and chlorite altered rocks. Hydrothermal chlorite development in the feldspar phyric rhyolite unit is associated with a corresponding increase in total iron and manganese in the rocks. Weak regional chlorite alteration does not appear to show effects of added iron or magnesium. Geochemically the regional feldspar alteration does not appear to have involved addition of potassium when compared to other hydrothermally altered rocks from the Jukes prospect but clearly shows an increase in Na_2O. This supports the conclusion that the alteration seen at 12450–12600 is albite alteration.

The Ti/Zr ratio is relatively consistent in the CVC rocks as shown on Figure 3c where it is plotted in relation to the geology. The range of values in EQP rocks is 7.7–14.4 but is very consistent in the 9–11 range. The average EQP Ti/Zr ratio is 10.98. The range of values in CVC rocks is 5.0–12.3 but is very consistent in the 6–7 range. The average CVC Ti/Zr ratio is 7.3. The Ti/Zr data is included with the geochemistry in Appendix B.

The Alteration Index was calculated for the rocks along the Jukes Road. Figure 3c shows the Alteration Index plotted against distance. Higher values indicate greater degrees of alteration. All of the CVC rocks along the traverse have values >60 and show some evidence for gain or loss of sodium. The rocks near 12500 are albite altered, appear to have added sodium, and according to this index would be the least altered rocks along the traverse. Further work with the alteration index will hopefully help explain these issues.

The distribution of Cu and Au is presented in relationship to the geology of the Jukes Prospect in Figure 4c. Closer examination of the Cu–Au data suggests a relationship between higher Cu values and higher Au values. This increase in Au appears to be limited, however to about a maximum of 2 ppm Au.

Discussion

The textural and mineralogical data outlined above is preliminary and detailed paragenetic and geochemical work is continuing. Work to date suggests that hydrothermal mineral assemblages can be distinguished from regional assemblages on the basis of four observations:

1. Widespread occurrence. Widespread occurrence of weak alteration strongly suggests a diagenetic or metamorphic origin.
2. Intensity of chlorite alteration of feldspar phenocrysts. Sericite alteration of feldspar phenocrysts in weakly altered rocks can vary greatly but the appearance of chlorite appears to be an indicator of proximity to the hydrothermal system.
3. The presence or absence of accessory minerals such as pyrite, chalcopyrite, tourmaline or large amounts of magnetite/hematite.
4. Degree of textural destruction. Rocks with weakly moderate or greater textural destruction, in general, clearly show the effects of hydrothermal alteration. An exception to this appears to be the albite alteration seen in the Jukes Road pumice breccia. This rock has undergone a great amount of textural destruction of the groundmass and is believed to have been altered under diagenetic conditions.

Hydrothermal alteration appears to have been controlled by fracture density. This is demonstrated by an increase in both fracture density, and increases in both chlorite and K-feldspar alteration of the columnar jointed rhyolite with increasing proximity to the Jukes Prospect. The primary indicator of

alteration intensity is the degree of alteration of feldspar phenocrysts.

At the Jukes Prospect, two styles of hydrothermal breccias have been identified. The intimate association of magnetite, chlorite and tourmaline in the matrices, argues very strongly for a hydrothermal/magmatic origin. Breccias are classified according to their matrix type. The first contains various amounts of magnetite/hematite and tourmaline ± chlorite and the second chlorite and tourmaline ± magnetite/hematite. There is a possibility that the two breccias are related to each other and to the large magnetite bodies found both at the Jukes Prospect and further south at Mt. Darwin. Breccias are cut by faults but clearly predate fault-related tectonic fracturing.

Along the Jukes Road, two facies of the CVC have clearly been altered by hydrothermal solutions. The feldspar-phyric rhyolite and the quartz–feldspar porphyry both show varying hydrothermal alteration effects. The quartz–feldspar porphyry is not only altered by chlorite alteration but also by K-feldspar alteration. This suggests that the dykes were implaced prior to the hydrothermal event. The fact that the hydrothermal breccia follows the apparent boundary of a quartz–feldspar porphyry dyke suggests that the timing of the two events may not be to different.

References

Allen, R.L. and Cas, R.A.F., 1990, The Rosebery Controversy: distinguishing prospective submarine ignimbrite in the Rosebery–Hercules Zn Cu Pb massive sulfide district, Tasmania. Geological Society of Australia Abstracts 25: 31–32

Doyle, M. G., 1990. The geology of the Jukes Proprietary prospect, Mt. Read Volcanics: Unpubl. Honours Thesis, Univ. Tas.: 114p.

White, M., 1996. Volcanic facies correlations in the Tyndall Group. Unpubl. PhD thesis, Univ. Tas.

Wyman, B, Allen, Rod, and Duhig, Nathan, 1996, Jukes Road: Preliminary Volcanic Facies analysis and Alteration petrography, Unpublished AMIRA Report, project P.439

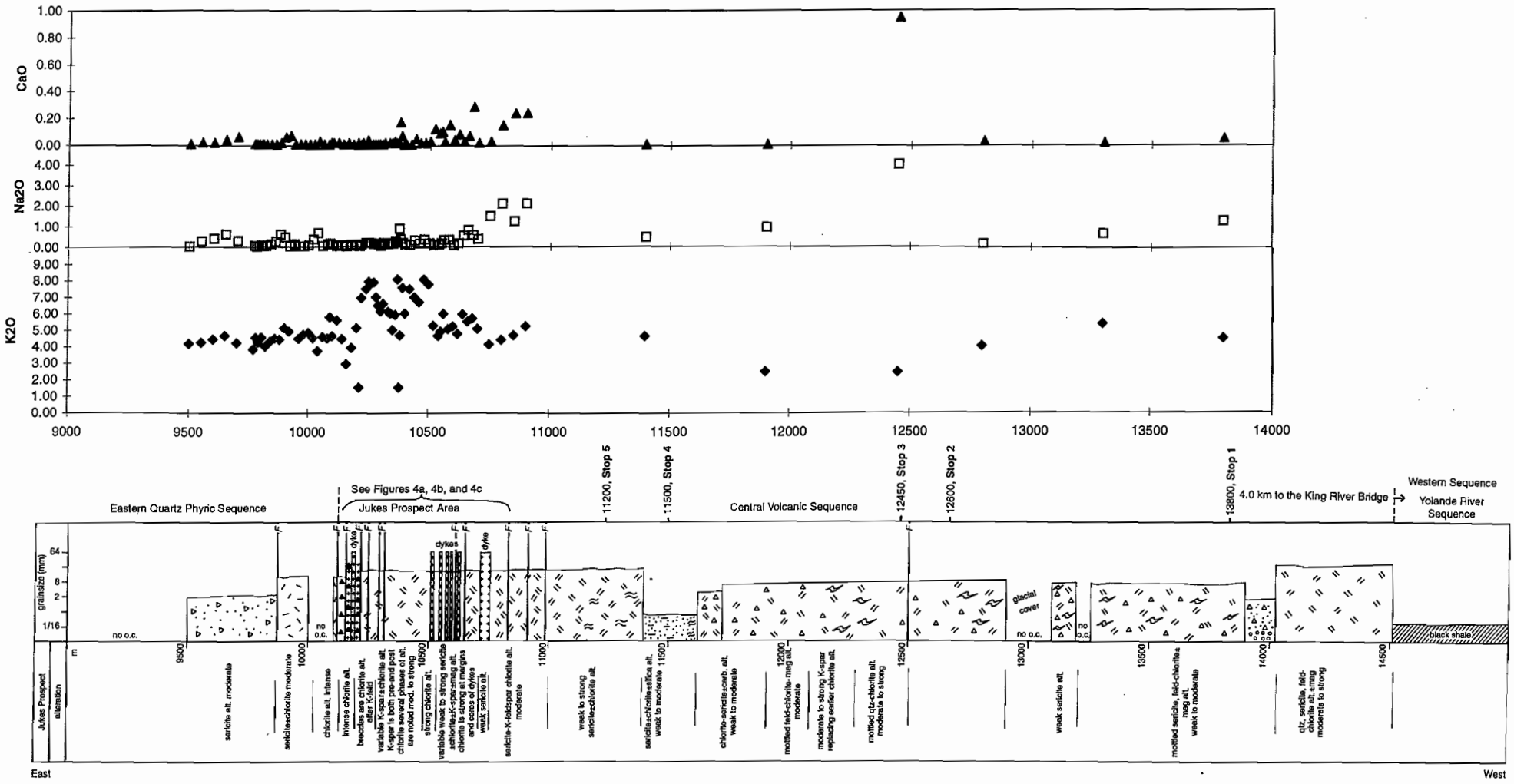

Figure 3a: K20, Na2O and CaO plotted against distance on a graphic presentation of the geology and alteration along the Jukes Road

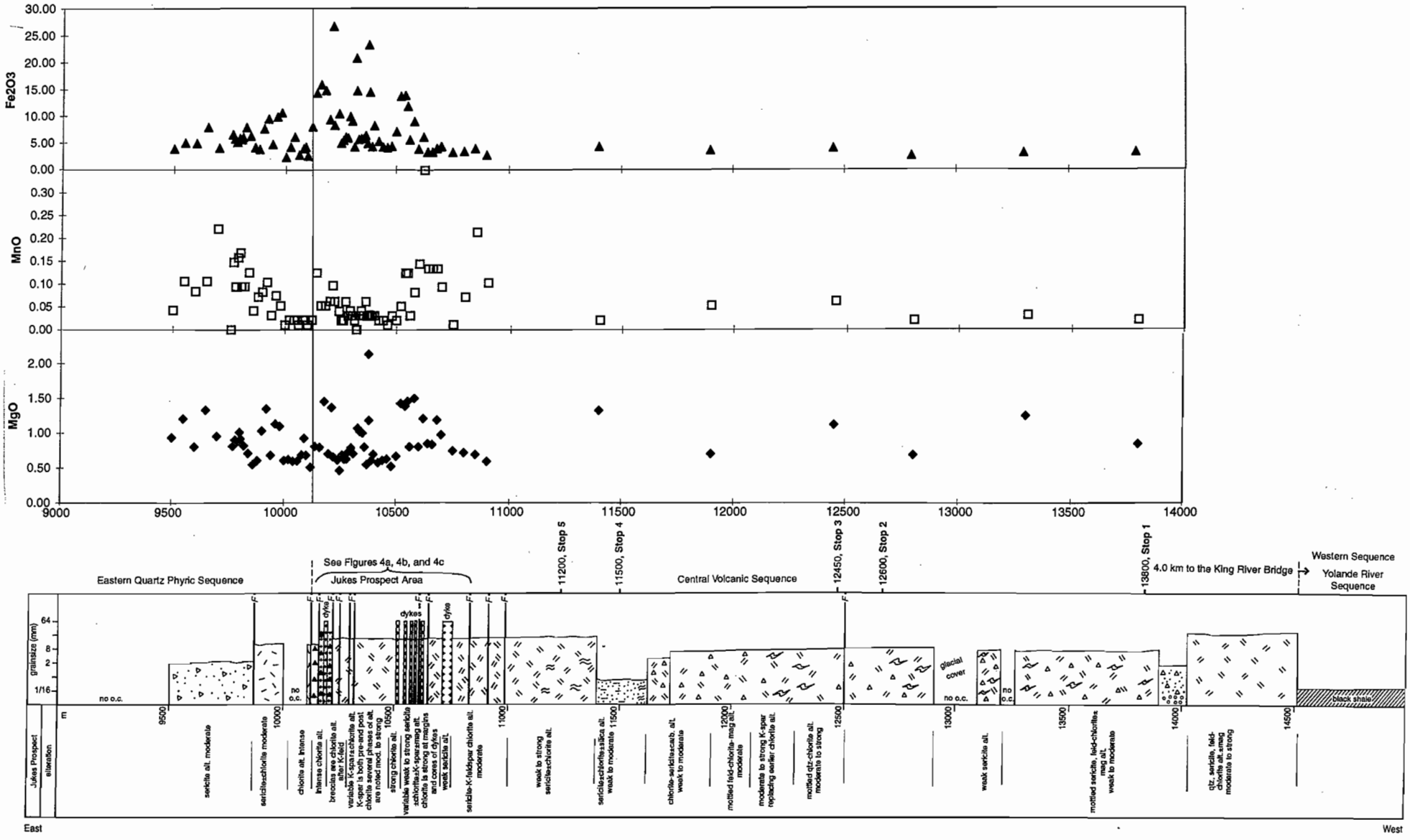

Eastern Quartz Phyric Sequence

- crystal-rich volcaniclastic sediment or pyroclastic flow deposit, quartz phyric
- coherent quartz-feldspar phyric dacite porphyry

Central Volcanic Sequence

- hydrothermal breccia - chlorite ±magnetite± sulphide matrix, clasts all intensely chlorite or K-feldspar altered, varies from clast to matrix supported
- quartz porphyry intrusive - intensely chlorite altered groundmass, quartz phenocrysts to 5mm
- feldspar phyric columnar jointed rhyolite massive fine to medium grained
- interbedded volcaniclastic sandstone and fine tuffaceous horizons, ash-sandstone sequence, occasional pumice, rich clastic horizons
- lithic-rich feldspar phyric volcaniclastic breccias frequently containing pumice clasts and often well developed lithic-rich pumice breccias, lithic clasts from 1cm to 3m
- lithic-rich mass flows with rounded lava clasts in well-defined bottoms

flow banding

Figure 3b: MgO, MnO and Fe2O3 plotted against distance on a graphic presentation of the geology and alteration along the Jukes Road

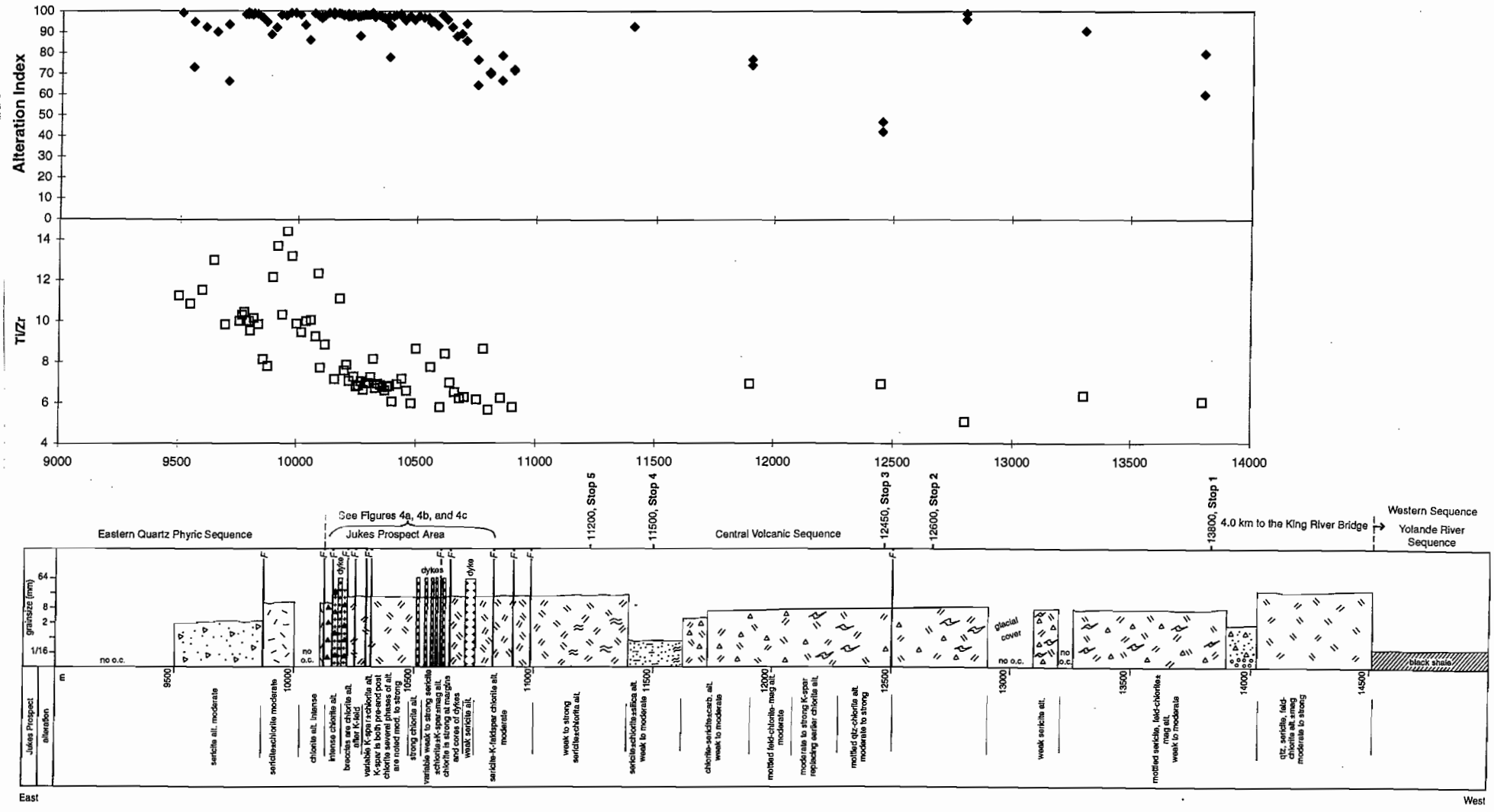

Figure 3c: Ti/Zr and the Alteration Index (AI) plotted against distance on a graphic presentation of the geology and alteration along the Jukes Road

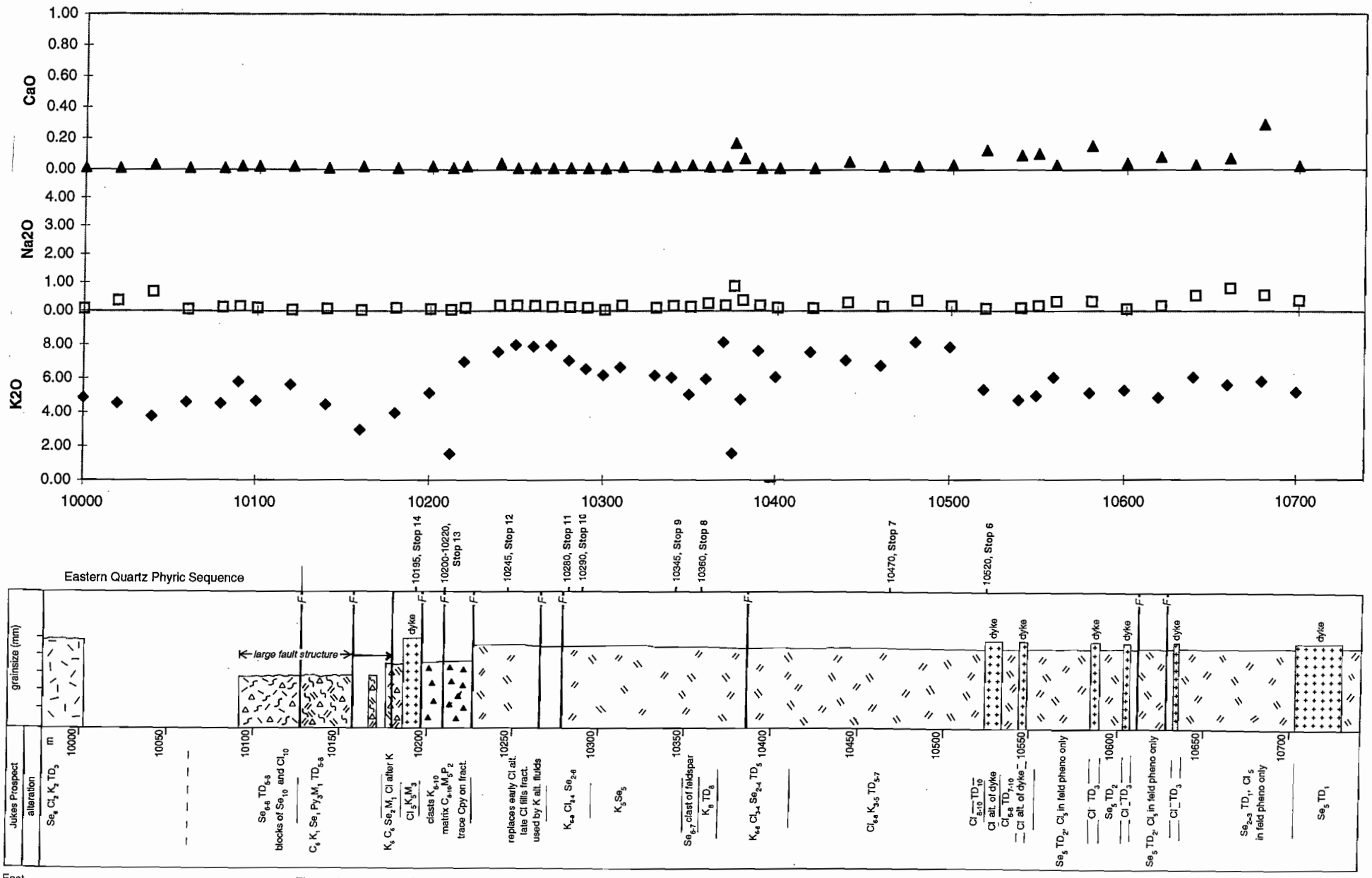

Figure 4a: K20, Na2O and CaO plotted against distance on a graphic presentation of the geology and alteration at the Jukes Prospect

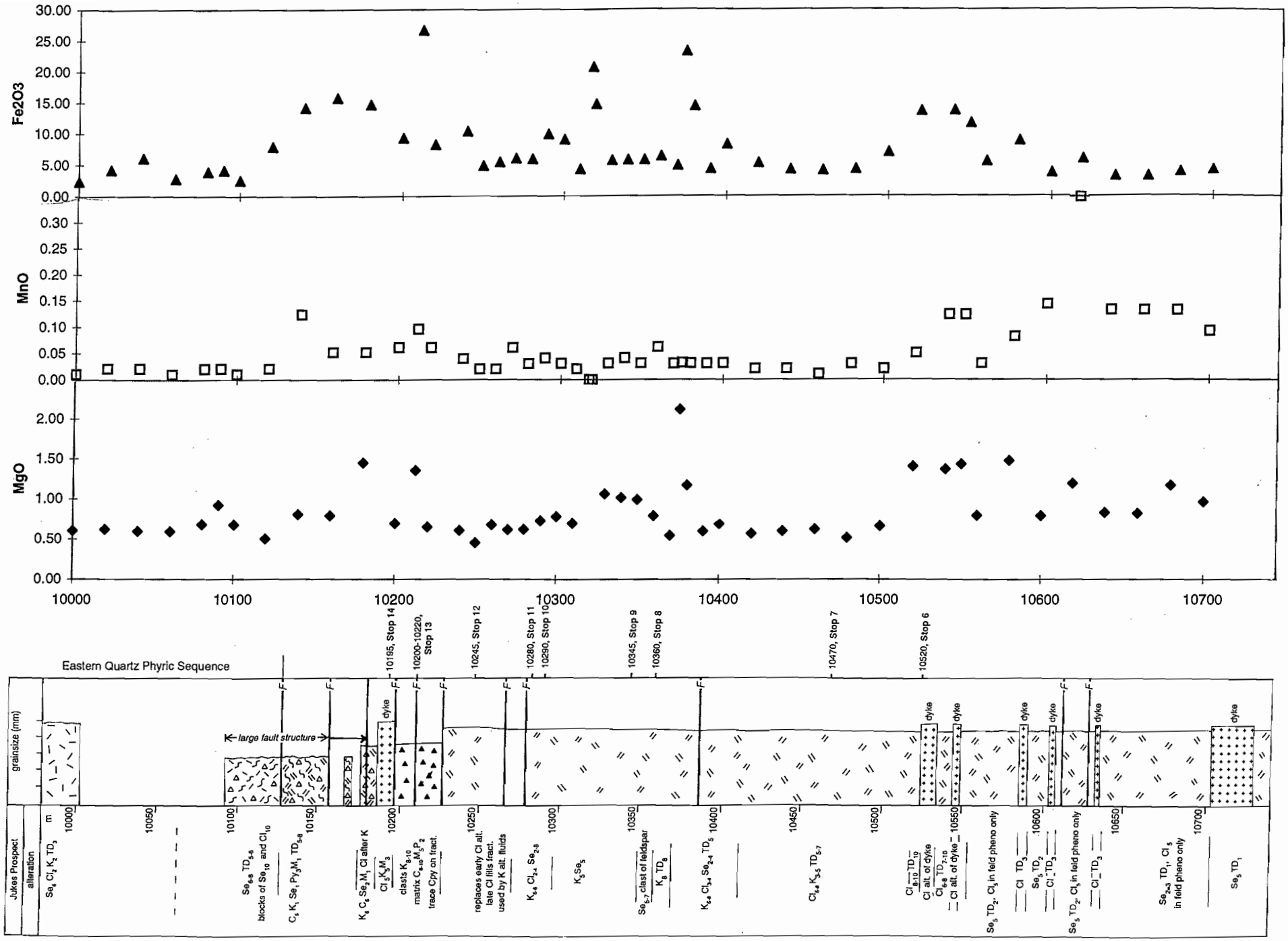

Figure 4b: MgO, MnO and Fe2O3 plotted against distance on a graphic presentation of the geology and alteration at the Jukes Prospect

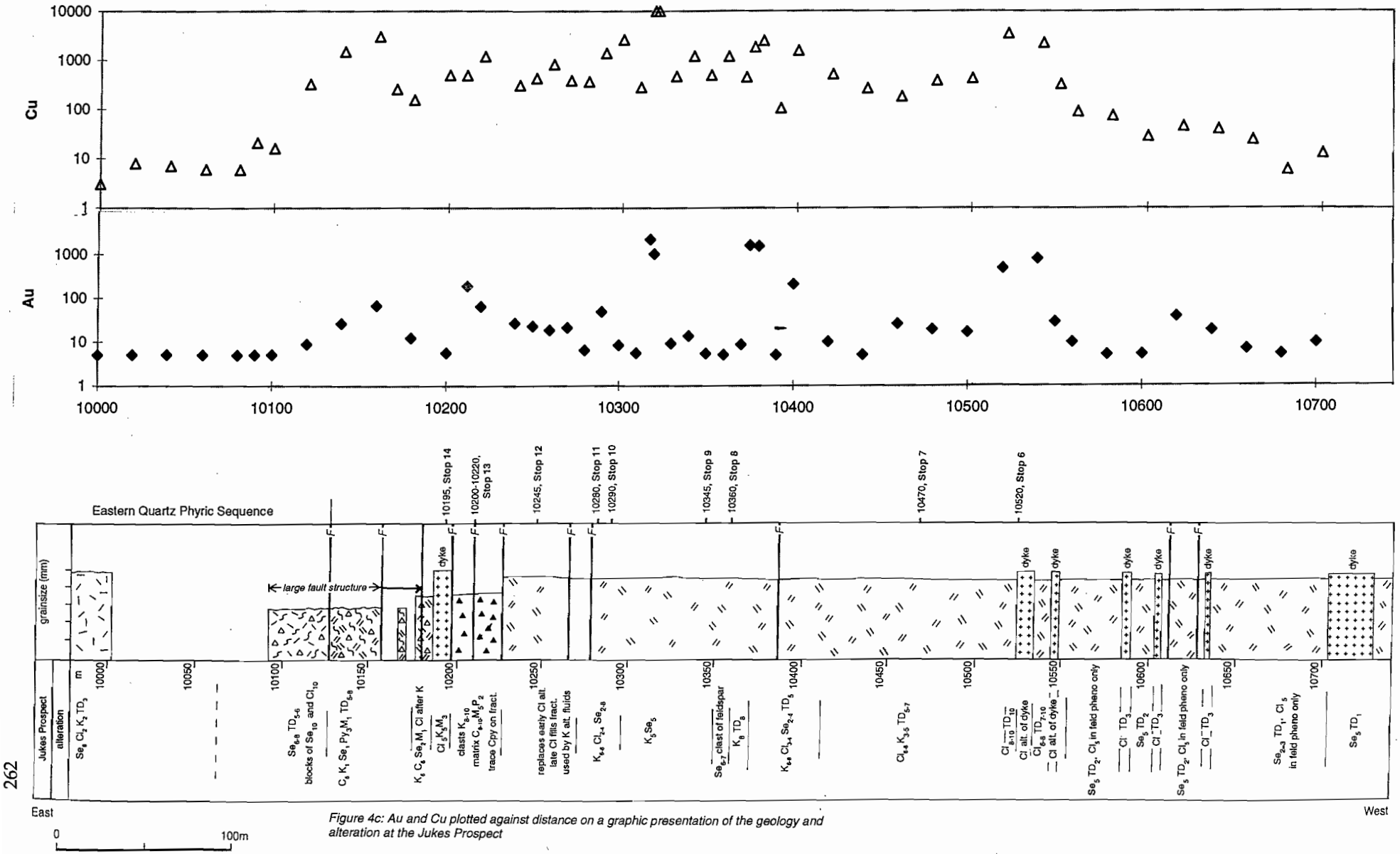

Figure 4c: Au and Cu plotted against distance on a graphic presentation of the geology and alteration at the Jukes Prospect

Plate 1
CVC Feldspar-Phyric Mass Flow Deposit. Large boulder amongst smaller boulders in a rhyolitic volcaniclastic mass flow deposit in the western part of the CVC.

Plate 2
12600 m. Pink and green banding in the Jukes Road Pumice Breccia. Excellent tube pumice breccia textures and altered pumice and lithic clasts are common. Pink bands are albite alteration and green bands are chlorite alteration. Banding appears to be parallel to bedding.

Plate 3
12600 m. Jukes Road Pumice Breccia. Relict pumice shards (A). The tube pumice is preserved as small wispy very fine-grained mosaics of quartz and feldspar with the long dimension of the tubes defined by alignment of small chlorite and sericite blebs and patches. Shards are randomly oriented in the sample. Notice carbonate alteration (B) that is believed to be post hydrothermal activity in origin. Plane polarized light, magnification is 2.5X.

Plate 4
12600 m. Jukes Road Pumice Breccia. Vesicular or spherulitic pumice/glass shard. Circular and semicircular spherulites or vesicles (A) are common and are filled with interlocking aggregates of recrystallised twinned feldspar (albite?) and quartz. Plane polarized light, magnification is 2.5X.

Plate 5
12600 m. Jukes Road Pumice Breccia. Albite has almost totally replaced and recrystallised the groundmass into fine to medium-grained aggregrates of interlocking crystals. Faint twinning (A) in groundmass sized feldspar crystals is common. Chlorite occurs as patches and blebs (C). The albite is clearly post sericite alteration as seen in feldspar phenocrysts where albite alteration halos occur around fractures within the feldspar phenocryst (B). Crossed polars, magnification is 10X.

Plate 6
12600 m. Jukes Road Pumice Breccia. Typical replacement of groundmass feldspars with chlorite and weak sericite alteration of the feldspar phenocrysts. Crossed polars, magnification is 2.5X.

Plate 7
11500 m. Thin tuffaceous ash horizons interbedded with thin tuffaceous sandstone and pumiceous volcaniclastic horizons. plane polarized light, magnification is 1.5X.

Plate 8
11500 m. Thin pumiceous volcaniclastic horizons. (A) is a chloritised relict glass/pumice shard. Plane polarized light, magnification is 1.5X.

Plate 1

Plate 2

Plate 3

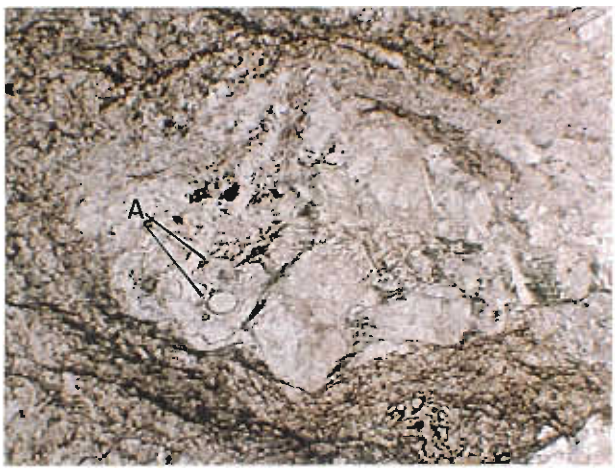

Plate 4

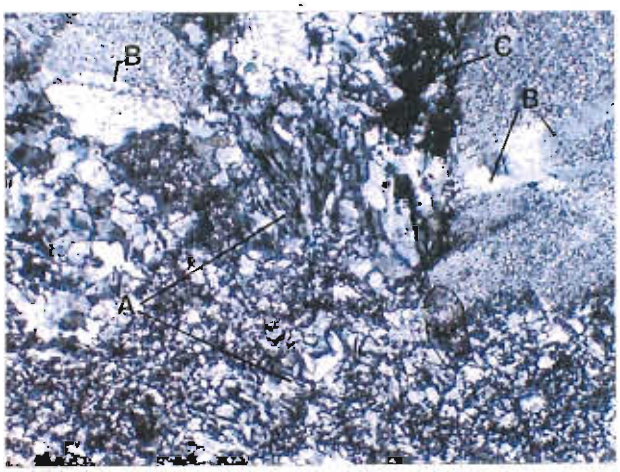

Plate 5

Plate 6

Plate 7

Plate 8

Plate 9
Relict spherulite (A) in the Columnar Jointed Feldspar–Phyric Rhyolite. This spherulite is replaced with quartz and feldspar and has a core of chlorite. The spherulite is 2 mm across. Plane polarized light, magnification is 1.5X.

Plate 10
Well developed columnar joints in the Columnar Jointed Feldspar–Phyric Rhyolite.

Plate 11a, b
Intergrown quartz and feldspar form distinct micropoikilitic texture in the Columnar Jointed Feldspar–Phyric Rhyolite. Plane polarized light, and crossed polars, magnification is 2.5X.

Plate 12
Granophyric texture between quartz and feldspar in the Columnar Jointed Feldspar–Phyric Rhyolite. The feldspar is now replaced by chlorite. Plane polarized light, magnification is 2.5X.

Plate 13a, b
11200 m. Columnar Jointed Feldspar–Phyric Rhyolite. Plagioclase phenocryst replaced with sericite (S), chlorite (CL) and carbonate. Plane polarized light, and crossed polars, magnification is 2.5X.

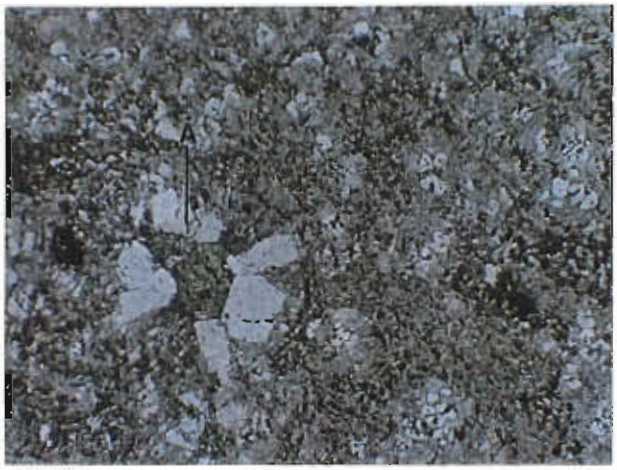

Plate 9

Plate 10

Plate 11a

Plate 11b

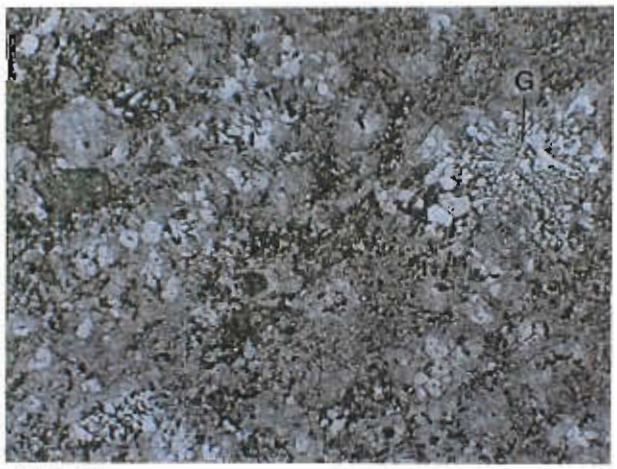

Plate 12

Plate 13a

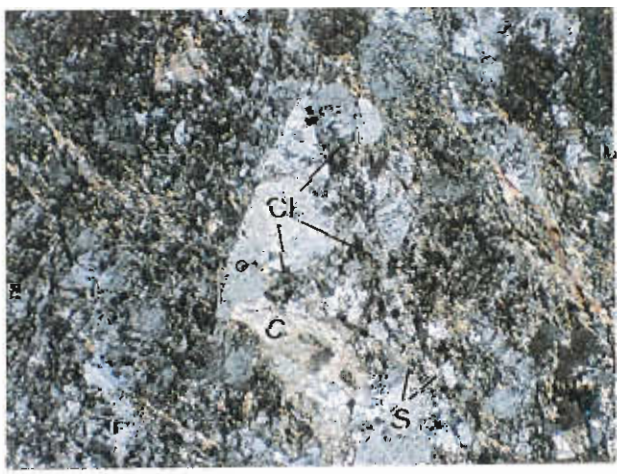

Plate 13b

Plate 14a, b
10420 m. Columnar Jointed Feldspar–Phyric Rhyolite. Sericite (S) has entirely replaced the feldspars in the microphyric texture. Feldspars form cores of the "birdseye" textures in micropoikilitic quartz. Plane polarized light, and crossed polars, magnification is 5X.

Plate 15a, b
Sericite replacement in feldspar phenocryst at 10390 m. Note relict feldspar shape. Plane polarized light, and crossed polars, magnification is 2.5X.

Plate 16a, b
Chlorite replacement in feldspar phenocryst at 10390 meters. Opaques are magnetite. Plane polarized light, and crossed polars, magnification is 2.5X.

Plate 14a

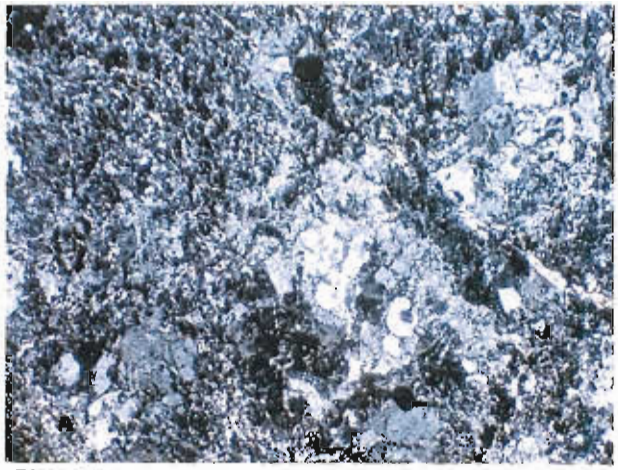

Plate 14b

Plate 15a

Plate 15b

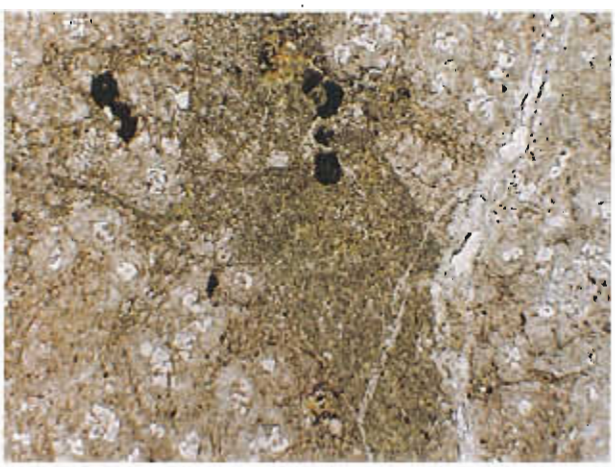

Plate 16a

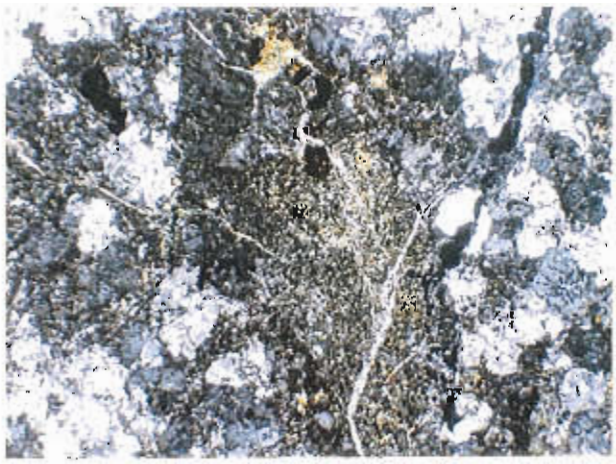

Plate 16b

Plate 17
Complex vein relationships at 10390. The major veining is caused by intrusion of magnetite/chlorite/tourmaline breccia veins (A) into pre-existing quartz veins (B). The earlier quartz veins formed stockworks (C) of small to micro-scale veinlets. Banding (D) within the breccia vein apparently indicates continued reuse of the vein by several fluid events. Plane polarized light.

Plate 18
Typical stockwork quartz veining at 10390. Notice the offsets. Plane polarized light, magnification is 1.5X.

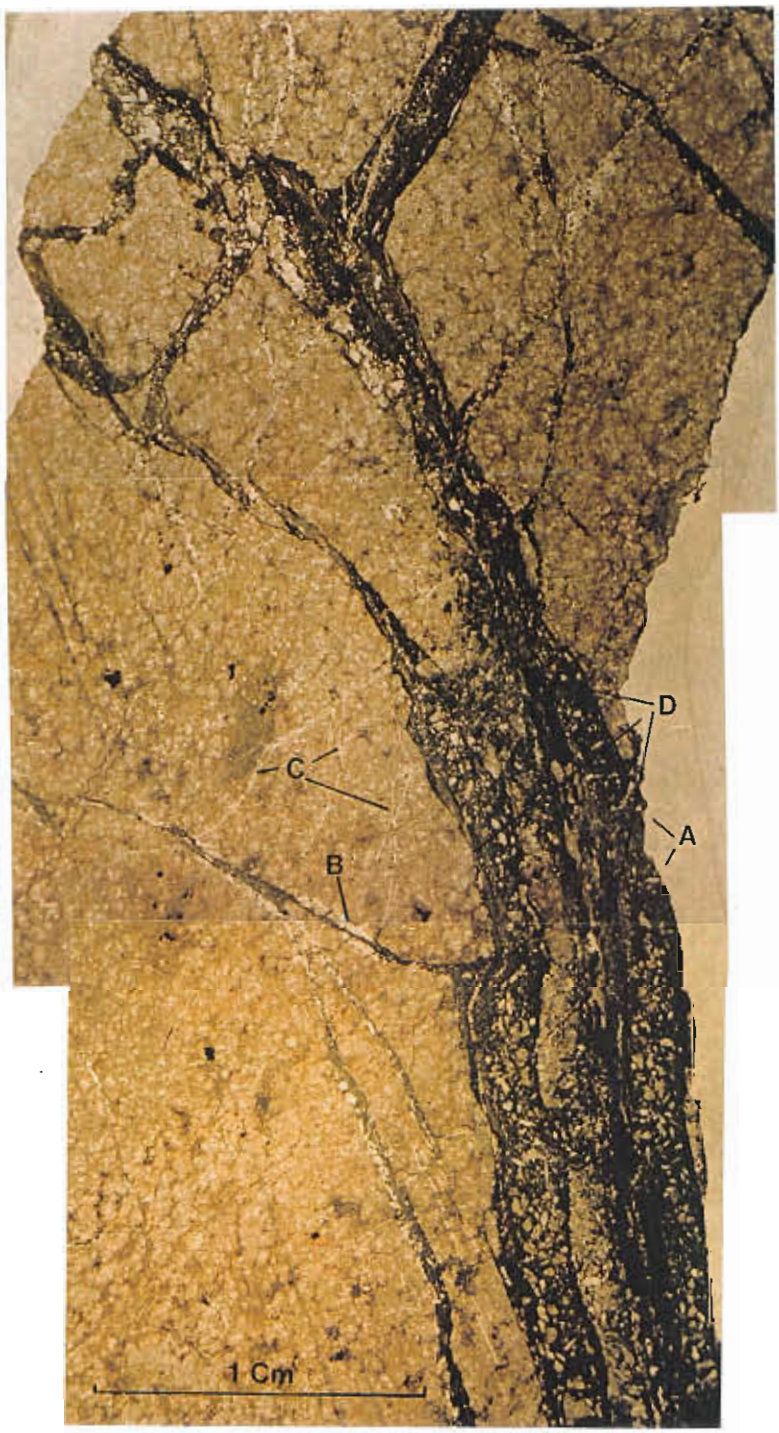

Plate 17

Plate 18

Plate 19a, b
At 10350 m. Feldspar phenocrysts are intensely altered to mosiacs of sericite and chlorite. This sample shows a fine mesh of interlocking sericite (70%) and chlorite (30%). Plane polarized light, crossed polars, magnification is 2.5X.

Plate 20a, b
At 10350 m. Feldspar phenocrysts are intensely altered to mosiacs of sericite and chlorite. This sample shows a fine mesh of interlocking chlorite (80–90%) and sericite (10–20%). Plane polarized light, and crossed polars, magnification is 2.5X.

Plate 21a, b
10310 m. Feldspar phenocrysts are 80–90% or more replaced buy fine grained sericite (S). Faint relict cleavage is visible. Chlorite (Cl) and magnetite (M) occur in association with the feldspar phenocrysts but do not appear to replace it. Note the small zircon (Z) next to the magnetite. Plane polarized light, and crossed polars, magnification is 2.5X.

Plate 22
10310 m. Alteration front with small chlorite altered groundmass feldspars and micropoikilitic feldspar on one side (A) and relatively unaltered groundmass feldspars on the other (B). Plane polarized light, magnification is 1.5X.

Plate 23
10310 m. Small chlorite altered groundmass feldspars and micropoikilitic feldspar (CL) on side (A) of Plate 22. Plane polarized light, magnification is 5X.

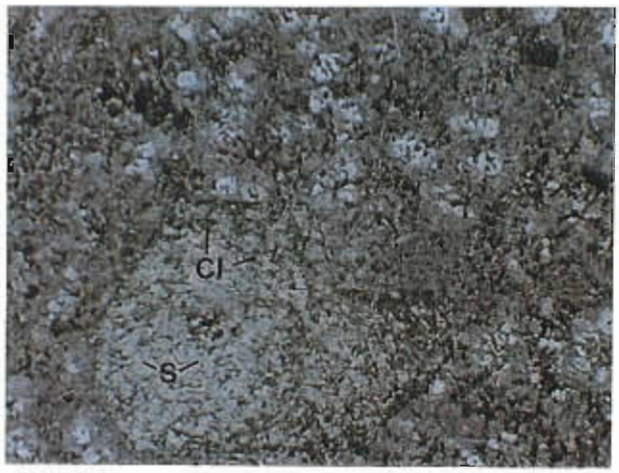

Plate 19a

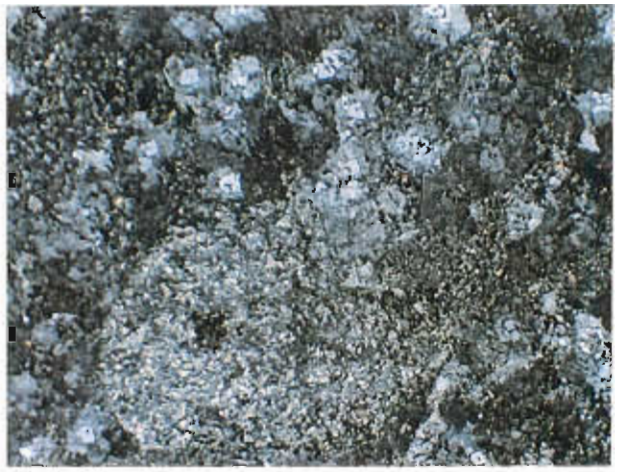

Plate 19b

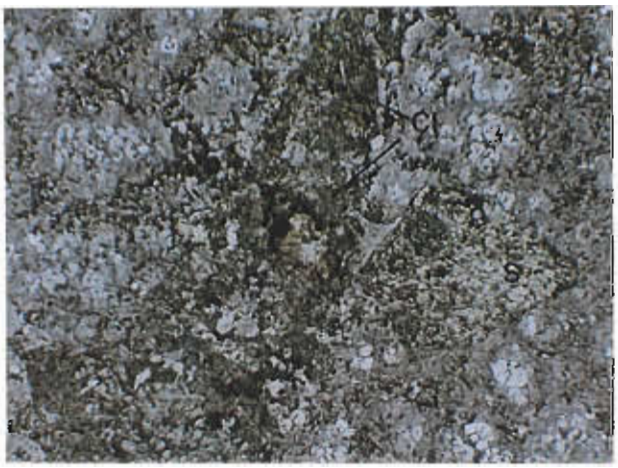

Plate 20a

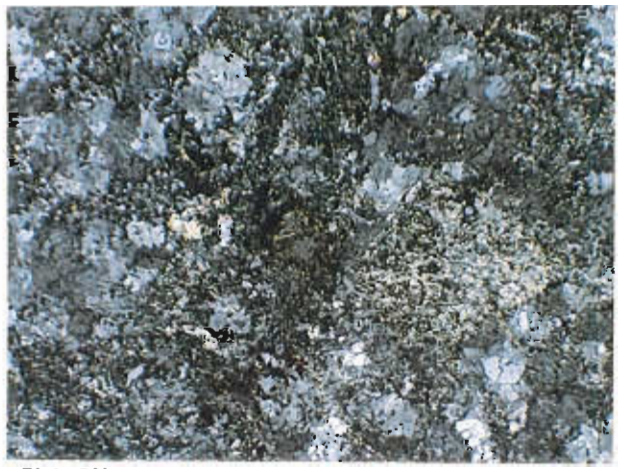

Plate 20b

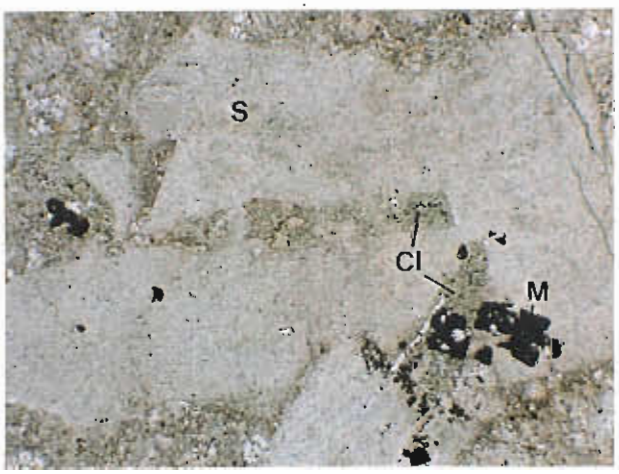

Plate 21a

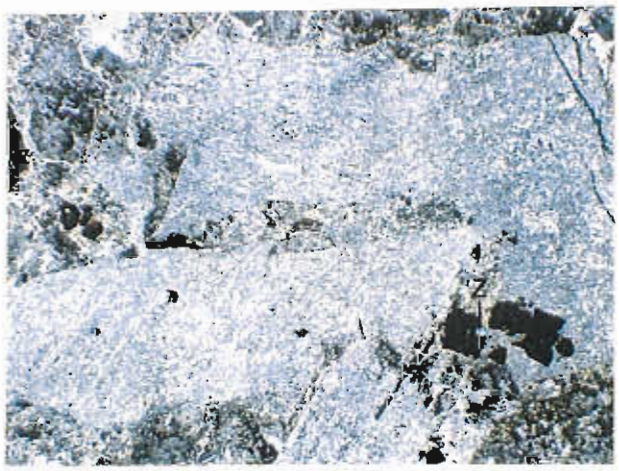

Plate 21b

Plate 22

Plate 23

Plate 24
10310 m. Small relatively unaltered groundmass feldspars and micropoikilitic feldspar (F) on side (B) of Plate 22. Plane polarized light, magnification is 5X.

Plate 25
This photo shows the fracture density at 10310 m where alteration fronts with small chlorite altered groundmass feldspars and micropoikilitic feldspar on one side and relatively unaltered groundmass feldspars on the other are seen as in Plate 22 Notice the earlier quartz vein (Q) without any alteration. The alteration halos are clearly related to the later chlorite veining that, in this case has reopened a pre-existing earlier quartz vein. Plane polarized light, magnification is 0.5X.

Plate 26a , b
10290 m, pinkish color in the groundmass micropoikilitic texture is due to K-feldspar alteration of the feldspars. Small groundmass feldspars are unaltered to weakly sericitised. Plane polarized light, and crossed polars, magnification is 5X.

Plate 27
10290 m, as part of a continuum of alteration from Plate 26a through Plate 28, groundmass feldspar and micropoikilitic feldspars are weakly chlorite altered. Polarized light, magnification is 5X.

Plate 28
10290 m, as part of a continuum of alteration from Plate 26a through Plate 27, groundmass feldspar and micropoikilitic feldspars are strongly chlorite altered. Polarized light, magnification is 5X.

Plate 29a, b
10250 m, sericite and K-feldspar alteration are the dominant alteration phases in the groundmass. Sericite (S) alteration of the plagioclases (F) has replaced along cleavage and preserved twinning. Plane polarized light, and crossed polars, magnification is 2.5X.

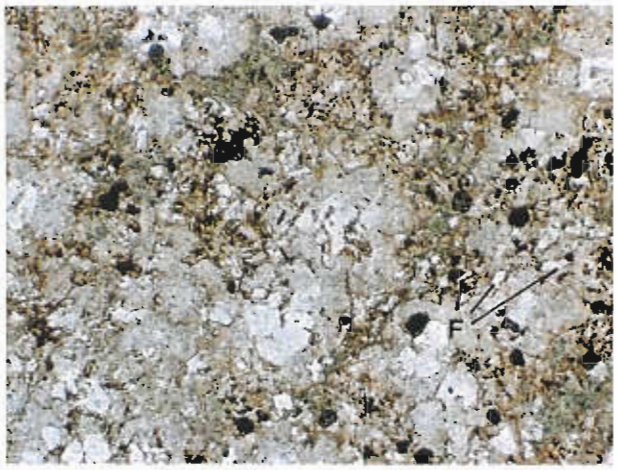

Plate 24

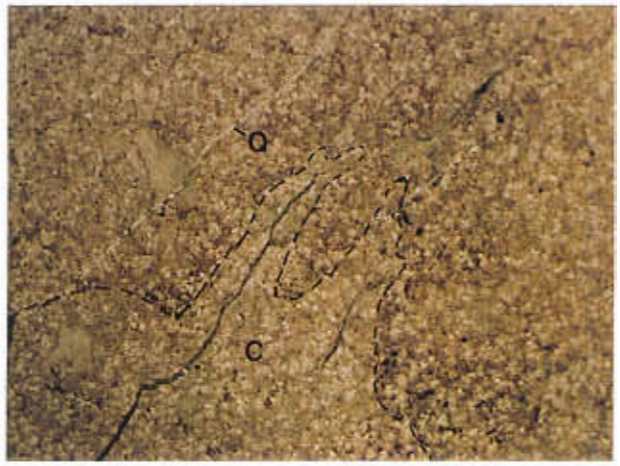

Plate 25

Plate 26a

Plate 26b

Plate 27

Plate 28

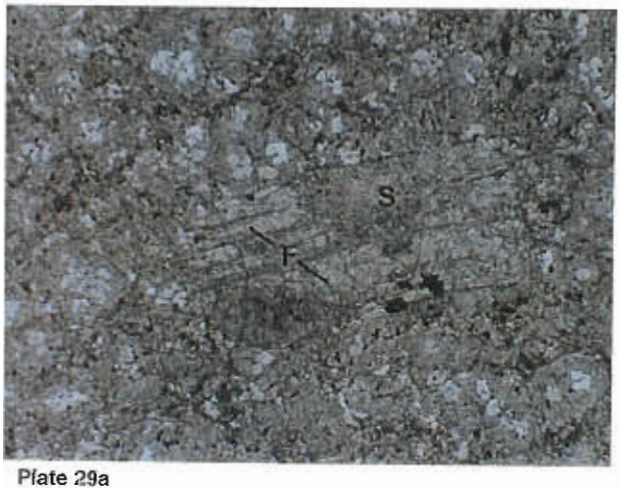

Plate 29a

Plate 29b

Plate 30
10230 m, ladder like quartz and bright green chlorite occur in a late vein. Many earlier quartz-feldspar veins have been broken by microfaults. This is typical fracture density as the alteration system is approached. Plane polarized light, magnification is 2.5X.

Plate 31a, b
10220 m, intense chlorite and minor sericite alteration of a feldspar phenocryst in a K-feldspar altered groundmass. Notice the increase in chlorite alteration around the cross-cutting quartz vein. Plane polarized light, and Crossed Polars, magnification is 2.5X.

Plate 32a, b
10220 m, pyrite (P) and chalcopyrite (Cpy) in a quartz–feldspar vein (Qv) in a K-feldspar altered groundmass. Plane polarized light, and Reflected Light, magnification is 2.5X.

Plate 33
10220 m, banded quartz vein (Q2) with pyrite (P) cross-cuts an earlier quartz vein (Q1) and is in turn cut by a later one (Q3). The groundmass is K-feldspar altered. Plane Light, magnification is 1.5X.

Plate 34
Type 1 Quartz–Feldspar ± Biotite Porphyry. Subhedral to anhedral quartz and feldspar phenocrysts make up fully 30–40% of the rock. Some show rounding of the grains and excellent embayed textures while others can be angular, the result of being broken. Both quartz and feldspar phenocrysts show a complete gradation in size from microphenocrysts through to their maximum size. Plane Light, magnification is 0.5X.

Plate 30

Plate 31a

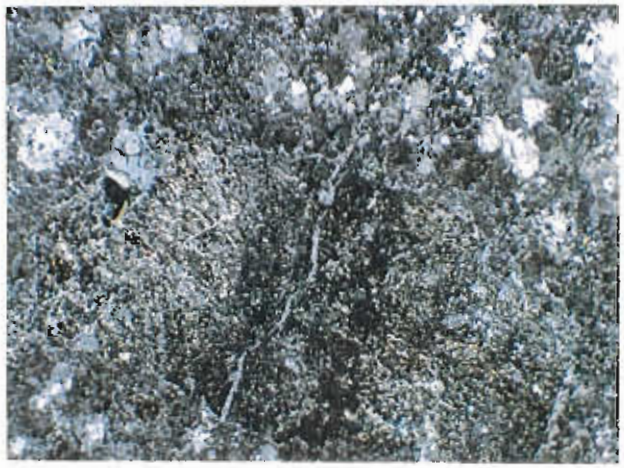

Plate 31b

Plate 32a

Plate 32b

Plate 33

Plate 34

Plate 35
'Type 2 Quartz-Feldspar ± Biotite Porphyry. The grainsize of the groundmass is much coarser than Type 1 averaging 0.01–0.1 mm. Quartz phenocrysts can be up to 5–10% of the rock and plagioclase phenocrysts (F) make up about 15%. Plane Light, magnification is 0.5X.

Plate 36a , b
Type 1 Quartz–Feldspar ± Biotite Porphyry. Cleavage controlled sericite (S) alteration of feldspar phenocrysts. Relict unaltered feldspar (F) is preserved. Plane polarized light, and Crossed Polars, magnification is 2.5X.

Plate 37a, b
Type 1 Quartz–Feldspar ± Biotite Porphyry. Sericite (S) replacement of K-feldspar (K) altered groundmass via well-developed fracture system. Plane polarized light, and Crossed Polars, magnification is 2.5X.

Plate 38a, b
Type 1 Quartz–Feldspar ± Biotite Porphyry. Two types of chlorite, one has typical green to greenish-brown interference colors (A) and the other has very distinctive blue–green interference colors (B). Plane polarized light, and crossed polars, magnification is 2.5X.

Plate 35

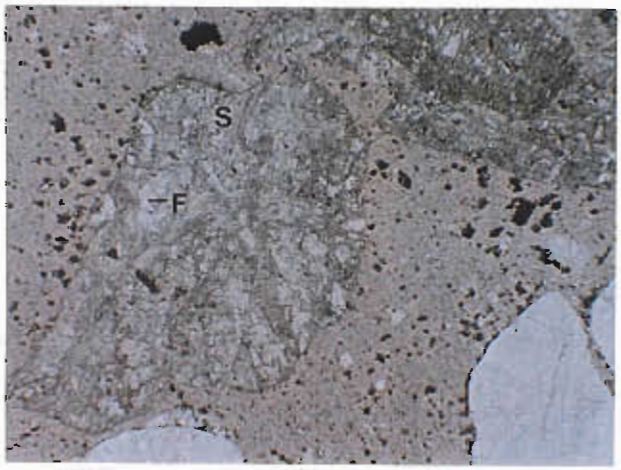

Plate 36a

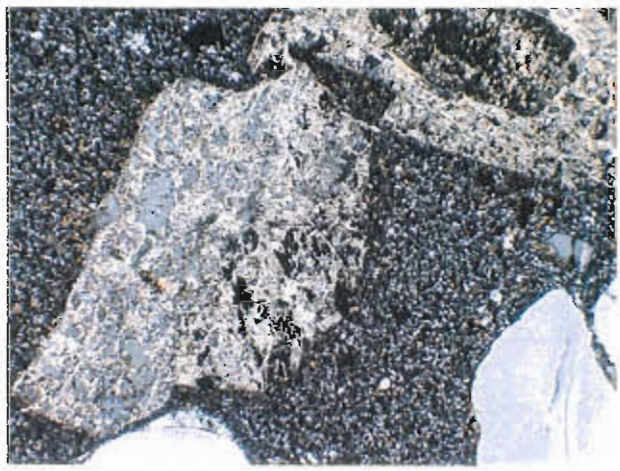

Plate 36b

Plate 37a

Plate 37b

Plate 38a

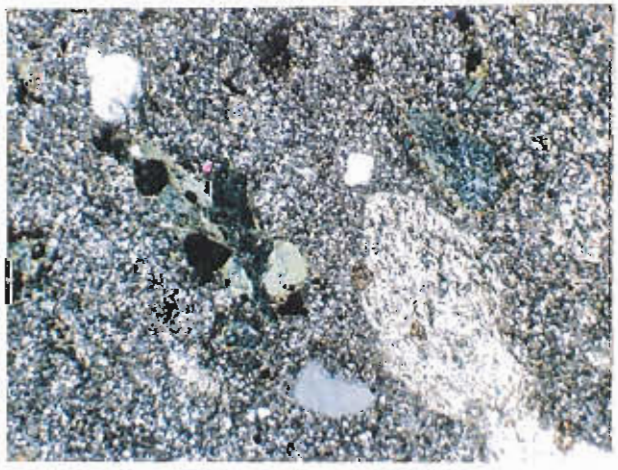

Plate 38b

Plate 39
Type 2 Quartz–Feldspar ± Biotite Porphyry. This photo shows typical replacement of feldspar phenocryst by sericite (S) and chlorite (Cl). The sericite replacement probably took place first leaving relict unaltered cores of feldspar as shown in Plate 36a, b. Later chlorite alteration then replaced the remaining feldspar preferentially. Crossed polars, magnification is 2.5X.

Plate 40
Typical magnetite–tourmaline breccia. Notice angularity of clasts and pseudo jigsaw fits on some. Clasts are intensely K-feldspar altered feldspar-phyric rhyolite. Plane polarized light, magnification is 1.5X.

Plate 41: Typical chlorite–tourmaline breccia with jigsaw fit texture. Clasts are intensely K-feldspar altered feldspar-phyric rhyolite. Plane polarized light, magnification is 1.5X.

Plate 42: Exsolution lamellae with magnetite and ilmenite. Reflected light, magnification is 40X.

Plate 43: Euhedral and subhedral tourmaline in magnetite–tourmaline breccia matrix. Notice excellent zoning in the tourmaline. Plane polarized light, magnification is 10X.

Plate 44: Late quartz veins cross-cut magnetite–tourmaline breccia matrix. These quartz veins are bent and deformed by later Devonian tectonism. Plane polarized light, magnification is 2.5X.

Plate 45a and 45b
Typical matrix of the chlorite–tourmaline breccia. Notice the abundance of tourmaline (T) that occurs as small euhedral to subhedral crystals throughout the matrix. Plane polarized light, and crossed polars, magnification is 10X.

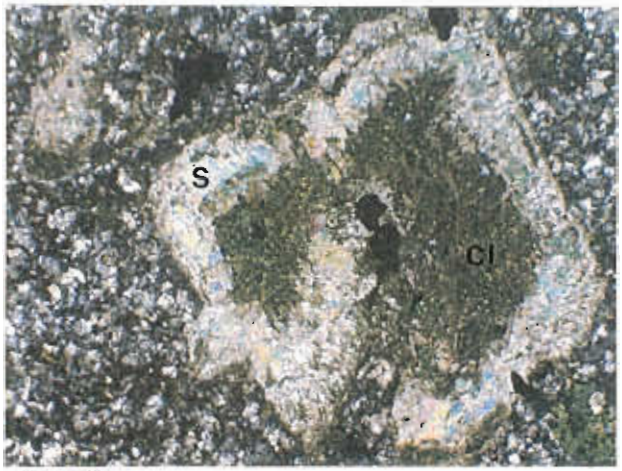

Plate 39

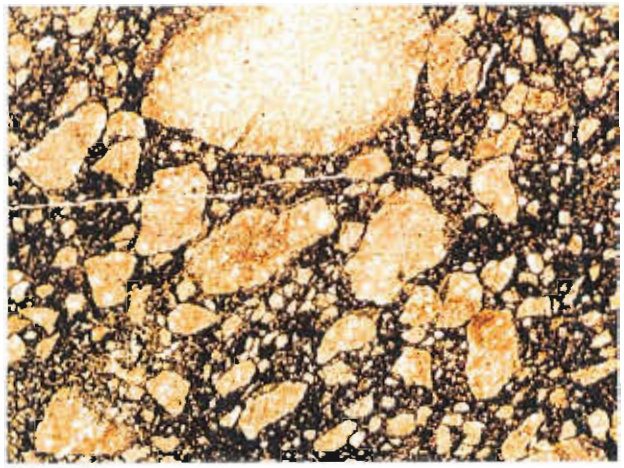

Plate 40

Plate 41

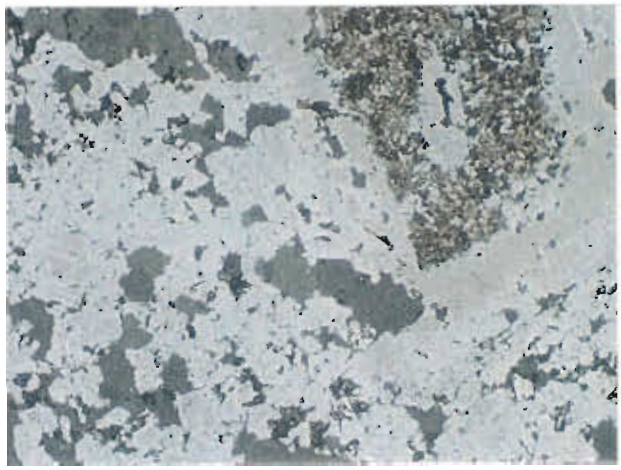

Plate 42

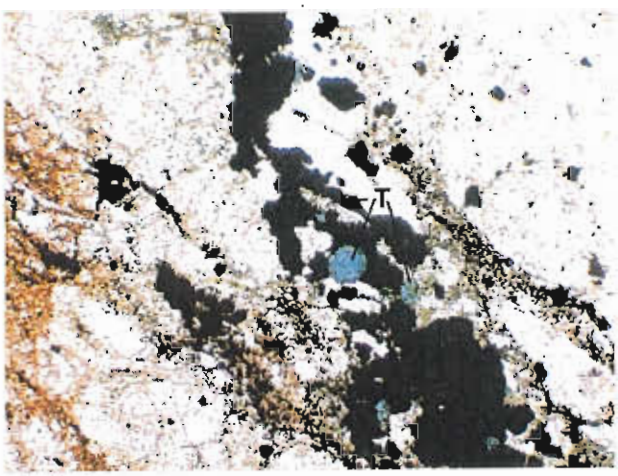

Plate 43

Plate 44

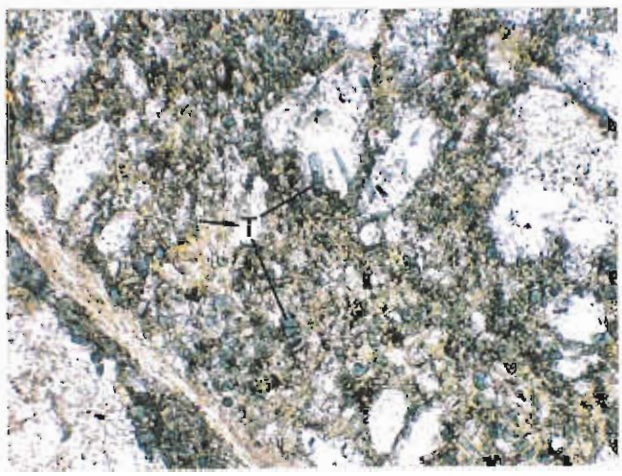

Plate 45a

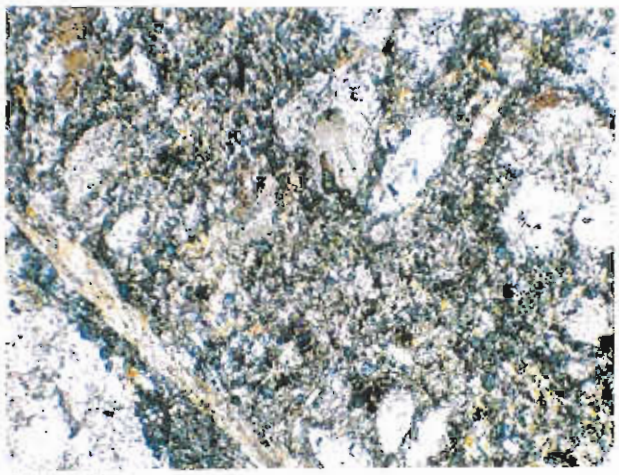

Plate 45b

Plate 46
Magnetite (M) pseudomorphs after an unknown bladed mineral in the groundmass of the chlorite–tourmaline breccia matrix. Plane polarized light, magnification is 2.5X.

Plate 47
Carbonate (C), probably ankerite, in the chlorite–tourmaline breccia. This carbonate may be related to later event and be unrelated to the hydrothermal event. Plane polarized light, magnification is 10X.

Plate 48
Quartz microveinlets cross-cut K-feldspar altered feldspar-phyric rhyolite clasts and predate the intrusion of the chlorite–tourmaline matrix. Notice that the chlorite–tourmaline matrix has reopened a pre-existing quartz vein (A) probably related to the microveinlets. Plane polarized light, magnification is 1.5X.

Plate 49: Chlorite–tourmaline breccia cross-cut by later quartz vein. Plane polarized light, magnification is 1.5X.

Plate 50
EQP Feldspar-Phyric Dacite. Relict glassy lithic clasts or recrystallised glassy shards form thin flattened and deformed rod and spine shapes (A). Some of the relict lithic clasts appear to have been pumiceous and are now replaced by sericite and chlorite. Iron oxides are common along cleavage surfaces. This unit is interpreted to be a volcaniclastic rock. Plane polarized light, magnification is 0.5X.

Plate 51a, b
EQP Feldspar-Phyric Dacite. Relict spherulites (S) are shown by radial growths of quartz and feldspar (now sericite) from a central point. Plane polarized light, and crossed polars, magnification is 5X.

Plate 46

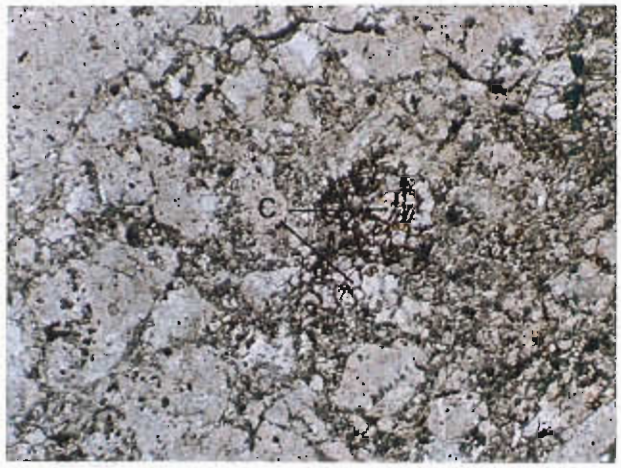

Plate 47

Plate 48

Plate 49

Plate 50

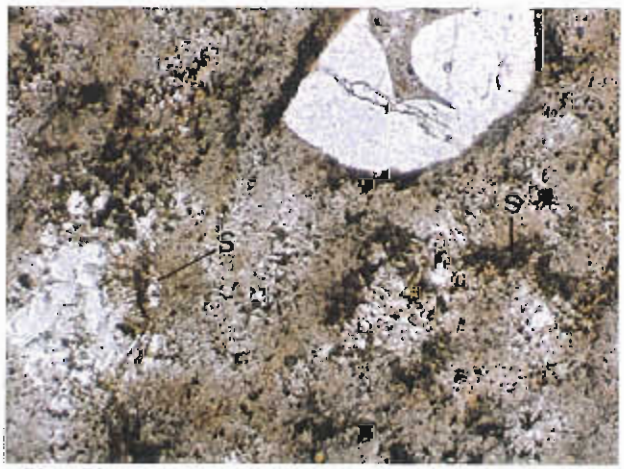

Plate 51a

Plate 51b

Plate 52a, b
EQP Feldspar-Phyric Rhyolite Porphyry. Tectonic cleavage is weakly developed but has dismembered many crystals and a weakly developed foliation is defined by sericite. Plane polarized light, and crossed polars, magnification is 0.5X.

Plate 53a, b
EQP Feldspar-Phyric Rhyolite Porphyry. Feldspar phenocrysts strongly altered by sericite (S) and chlorite (C). The groundmass is weakly altered by sericite and feldspar is preserved. Plane polarized light, and crossed polars, magnification is 2.5X.

Plate 54
EQP Feldspar-Phyric Rhyolitic Volcaniclastic. Large lithic clast in matrix with euhedral rounded or broken quartz phenocrysts. Lithic clasts can be of several types including former glassy shards and clasts with relict perlitic textures. This unit is interpreted to be a massive, moderately crystal rich volcaniclastic sediment or mass flow. Plane polarized light, magnification is 2.5X.

Plate 55a, b
EQP Feldspar-Phyric Rhyolitic Volcaniclastic. Moderately well developed foliation defined by sericite. Plane polarized light, and crossed polars, magnification is 2.5X.

Plate 52a

Plate 52b

Plate 53a

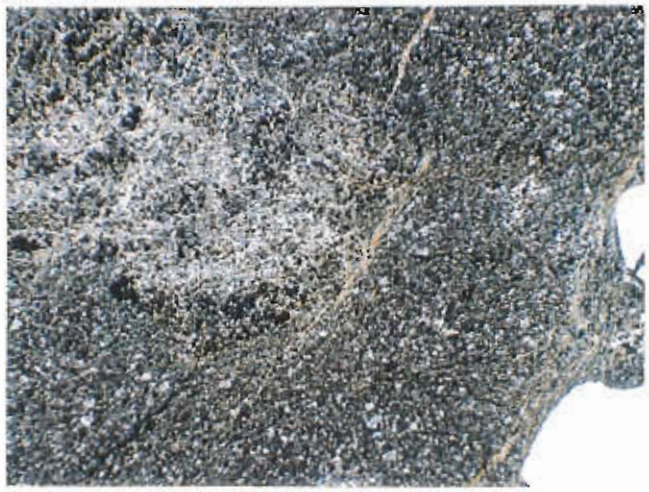

Plate 53b

Plate 54

Plate 55a

Plate 55b

Appendix A — Results of X-ray diffraction analysis

TASMANIA DEVELOPMENT AND RESOURCES

Industry Safety and Mines Division

Client: Bill Wyman
Sample Location: King River Tunnel, Queenstown
Analysis: Approximate Mineralogy
Method: X-Ray Diffraction

Results (approx wt %)

Sample	*>60%*	*40-60%*	*25-40%*	*15-25%*	*10-15%*	*5-10%*	*<5%*
8600		Quartz		Mica	Kaolinite		Chlorite, K-Feldspar
10140	Quartz			Chlorite	Mica	K-Feldspar	Hematite, Goethite
10330	Quartz			Mica	Chlorite	K-Feldspar	
10520		Quartz		Chlorite	Mica, K-Feldspar		
10550		Quartz	Mica	Chlorite			K-Feldspar, Hematite
10800		Quartz		Mica	Plagioclase	K-Feldspar	Chlorite
10850	Quartz			Mica		Plagioclase	K-Feldspar, Chlorite
10900		Quartz		Mica	Plagioclase	K-Feldspar	Chlorite
12450		Quartz		Plagioclase	Mica	Chlorite	
13800		Quartz	Mica		Kaolinite	Plagioclase	K-Feldspar
880329		Quartz	Mica			Plagioclase	Calcite, Chlorite
880333		Quartz		K-Feldspar	Mica	Chlorite	Siderite
880337	Quartz			K-Feldspar	Mica	Chlorite	Ankerite
880339		Quartz		Mica	K-Feldspar, Siderite	Chlorite	
880369	Quartz			Mica		Chlorite, K-Feldspar	
880375	Quartz			Mica	K-Feldspar	Chlorite	Ankerite, Plagioclase, ?Pyrite
880379	Quartz			Mica	K-Feldspar	Chlorite	
880380	Quartz				Mica	K-Feldspar, Plagioclase, Chlorite	Ankerite
880393		Quartz			Plagioclase, K-Feldspar, Mica	Chlorite	
880397		Quartz			Plagioclase, K-Feldspar, Mica	Chlorite	
880418		Quartz		Mica	Plagioclase, Chlorite	K-Feldspar	

Peak overlap may interfere with identification (e.g. secondary Mica peak overlaps major Siderite peak).
Minerals present in trace amounts may not be detected.

Appendix B — Whole-rock and trace element analytical results

(Sample Number corresponds to the meterage along Jukes Road)

Sample Number	8100	8600	9500	9550	9600	9650	9700	9760	9770	9780	9790	9800	9805	9820	9840	9860	9880	9900	9920	9940	9960	9980
SiO2	67.64	66.87	66.85	67.27	68.66	63.42	70.21	67.94	68.04	68.62	67.94	67.40	67.58	68.45	68.91	73.54	75.61	68.26	64.20	70.88	61.19	62.00
TiO2	0.51	0.57	0.60	0.53	0.55	0.87	0.41	0.41	0.45	0.48	0.48	0.50	0.44	0.38	0.40	0.26	0.22	0.53	0.84	0.42	0.79	0.83
Al2O3	17.81	17.46	17.76	16.24	15.98	16.38	15.00	15.07	16.11	15.82	16.05	16.04	15.72	14.03	15.19	13.48	12.17	14.04	15.62	14.33	16.97	16.04
Fe2O3	3.34	2.82	3.61	4.67	4.61	7.4	3.79	6.17	5.42	4.82	5.5	5.32	5.69	7.48	5.96	3.97	3.72	7.38	9.08	4.54	9.19	10.00
MnO	0.03	0.04	0.04	0.1	0.08	0.1	0.21	0.00	0.14	0.09	0.15	0.16	0.09	0.09	0.12	0.04	0.07	0.08	0.10	0.03	0.07	0.05
MgO	1.04	0.86	0.88	1.14	0.77	1.26	0.91	0.00	0.77	0.86	0.83	0.96	0.87	0.78	0.68	0.53	0.59	1.00	1.30	0.66	1.06	1.04
CaO	0.01	0.01	0.01	0.02	0.02	0.04	0.06	0.00	0.01	0.01	0.01	0.01	0.01	0.01	0.01	0.01	0.02	0.06	0.07	0.01	0.01	0.01
Na2O	0.03	0.03	0.03	0.27	0.39	0.59	0.28	0.00	0.06	0.03	0.06	0.09	0.05	0.06	0.14	0.26	0.60	0.46	0.04	0.13	0.04	0.04
K2O	5.26	3.72	3.95	4.04	4.26	4.44	4.05	0.00	3.66	4.35	4.06	4.33	4.35	3.85	4.15	4.37	4.35	5.01	4.76	5.70	4.23	4.51
P2O5	0.04	0.05	0.07	0.08	0.08	0.11	0.05	0.00	0.07	0.06	0.08	0.08	0.09	0.10	0.07	0.04	0.03	0.09	0.14	0.06	0.13	0.16
Loss	3.90	7.58	5.85	5.34	4.09	5.41	4.29	4.62	5.03	4.25	4.74	4.61	4.64	4.40	4.33	3.21	2.05	3.15	3.74	3.04	6.37	5.37
Total	99.66	100.06	99.76	99.7	99.60	100.02	99.41	99.69	99.76	99.53	99.9	99.67	99.67	99.75	100.10	99.82	99.54	100.22	99.97	99.96	100.13	100.14
S	<0.01	0	0	<0.01	<0.01	<0.01	<0.01	<0.01	0	0	<0.01	0	<0.01	0	<0.01	<0.01	<0.01	<0.01	<0.01	<0.01	0	0
Total C																						
Alt. Index	99.37	99.13	99.18	94.70	92.46	90.05	93.58		98.44	99.24	98.59	98.14	98.86	98.51	96.99	94.78	88.85	92.04	98.22	97.85	99.06	99.11
Sc																						
V																						
Cr																						
Co				5		4			5		3											
Ni																						
Cu	10	11	8	13	7	16	6	8	10	13	16	18	18	30	9	8	55	16	8	6	18	20
Zn	78	100	203	329	144	136	393	260	169	123	134	150	121	164	213	68	85	122	107	58	88	90
As				<3		<3			<3		<3											
Br				<1		5			<1		<1											
Rb	346	174	157	152	155	185	165	153	142	164	154	170	174	168	173	178	167	170	198	195	200	195
Sr	13	19	5	13	10	37	42	10	8	8	9	7	11	7	9	19	28	49	14	33	9	11
Y				28		33			11		17											
Zr	279	338	341	311	300	425	263	259	277	290	303	316	292	236	255	199	174	270	383	253	351	399
Nb				18		19			19		18											
Mo	1	1	2	2	2	2	1	2	<1	1	1	2	2	3	2	2	2	<1	2	1	2	3
Ag																						
Cd																						
Sn				3		4			4		4											
Sb																						
Cs																						
Ba	708	734	1025	1069	952	1064	1300	1389	1331	1251	1278	1535	1242	1044	1286	1012	940	1434	721	1398	711	762
La																						
Ce																						
Nd				46		32			13		13											
W				4		8			3		2											
Tl																						
Pb	18	92	179	137	52	29	41	109	34	31	59	74	173	55	21	19	17	30	16	21	32	39
Au(ppb)				5	5	9.8	5	5	5	5	5.3	5	5	5	5	5	5	5	7.5	8.1	5	5.5
Bi	<1.5	<1.5	<1.5	<1.5	<1.5	2	<1.5	<1.5	4	2	2	<1.5	4	2	2	2	3	3	3	<1.5	2	<1.5
Th	20	20	21	19	17	16	20	18	20	19	21	22	23	20	21	23	21	18	12	19	15	17
U	5	4	7	5	5	3	6	5	6	5	5	7	6	5	5	4	6	3	4	5	4	6

Analytical Results of the 1995 Chip Sampling by Nathan Duhig and Andrew Jones

(Sample Number corresponds to the meterage along Jukes Road)

Sample Number	10000	10020	10040	10060	10080	10090	10100	10120	10140	10160	10180	10200	10212	10220	10240	10250	10260	10270	10280	10290	10300	10310
SiO2	72.71	69.40	68.61	72.08	69.15	66.01	76.76	69.95	66.13	65.62	64.83	69.42	54.61	69.00	67.27	72.47	70.14	70.62	71.19	66.97	67.21	72.85
TiO2	0.47	0.44	0.46	0.46	0.43	0.54	0.29	0.27	0.14	0.24	0.35	0.36	0.24	0.28	0.29	0.29	0.30	0.29	0.29	0.29	0.31	0.33
Al2O3	14.85	15.69	15.82	15.21	16.51	17.72	12.29	12.39	11.06	10.53	11.14	12.28	10.51	11.99	11.86	12.46	13.32	12.34	12.56	12.72	13.09	13.22
Fe2O3	2.24	3.97	5.80	2.64	3.73	3.99	2.47	7.73	13.77	15.11	14.19	9.06	24.90	8.07	10.32	4.92	5.40	5.95	5.82	9.66	8.80	4.22
MnO	0.01	0.02	0.02	0.01	0.02	0.02	0.01	0.02	0.12	0.05	0.05	0.06	0.09	0.06	0.04	0.02	0.02	0.06	0.03	0.04	0.03	0.02
MgO	0.58	0.59	0.57	0.57	0.65	0.88	0.66	0.49	0.78	0.76	1.40	0.68	1.27	0.64	0.60	0.45	0.67	0.61	0.61	0.71	0.76	0.69
CaO	0.01	0.01	0.03	0.01	0.01	0.02	0.02	0.02	0.01	0.02	0.01	0.02	0.01	0.02	0.04	0.01	0.01	0.01	0.01	0.01	0.01	0.02
Na2O	0.08	0.34	0.65	0.05	0.13	0.15	0.11	0.04	0.08	0.02	0.10	0.06	0.04	0.10	0.18	0.19	0.17	0.14	0.13	0.11	0.04	0.18
K2O	4.66	4.31	3.61	4.41	4.31	5.52	4.54	5.44	4.33	2.84	3.80	5.01	1.45	6.79	7.42	7.88	7.74	7.76	6.88	6.34	5.98	6.51
P2O5	0.02	0.03	0.09	0.02	0.04	0.05	0.03	0.07	0.04	0.04	0.06	0.06	0.03	0.04	0.05	0.04	0.03	0.05	0.03	0.06	0.10	0.04
Loss	4.08	5.02	4.51	4.10	4.90	4.76	2.40	3.20	3.23	4.00	3.67	2.82	6.43	2.15	1.60	1.52	1.86	1.69	1.81	2.95	3.17	1.76
Total	99.79	99.93	100.24	99.65	100.00	99.66	99.67	99.82	100.02	99.67	99.86	100.05	99.66	99.53	100.00	100.3	100.05	99.57	99.67	100.04	99.99	99.88
S	<0.01	0	<0.01	<0.01	<0.01	<0.01	<0.01	0	0	0	0	0	4	4	1	1	0	0	<0.01	<0.01	0	<0.01
Total C																						
Alt. Index	98.31	93.33	86.01	98.81	97.25	97.41	97.56	99.00	98.27	98.90	97.93	98.61	98.19	98.41	97.33	97.66	97.90	98.24	98.17	98.33	99.26	97.30
Sc																						
V																						
Cr																						
Co						<2										6		6		28		7
Ni																						
Cu	3	8	7	6	6	21	16	321	1500	3040	156	491	491	1200	305	430	834	387	365	1400	2640	284
Zn	27	46	43	28	54	85	35	63	156	158	74	307	307	98	75	56	86	82	62	78	111	60
As						7										<3		<3		10		<3
Br						3										1		<1		<1		<1
Rb	174	146	145	166	155	201	168	146	100	109	134	59	59	158	156	172	176	165	160	162	178	183
Sr	13	18	21	12	18	23	21	31	27	9	41	6	6	44	51	55	58	53	43	32	27	42
Y						35										36		34		96		36
Zr	299	295	289	288	294	277	234	190	129	211	294	197	197	245	244	260	269	253	269	259	277	279
Nb						21										13		12		15		14
Mo	1	<1	<1	2	2	2	1	4	5	4	1	2	14	10	13	8	3	6	4	10	3	1
Ag																						
Cd																						
Sn						3										5		4		18		4
Sb																						
Cs																						
Ba	731	1014	590	808	1090	1190	808	1448	1161	536	1812	190	190	2088	2611	2689	2526	2818	2359	2101	1447	1957
La																						
Ce																						
Nd						42										50		52		58		44
W						5										22		19		33		25
Tl																						
Pb	5	10	12	7	18	31	21	45	13	19	12	137	137	44	16	11	14	28	16	71	67	47
Au(ppb)	5	5	5	5	5	5	5	8.8	26.2	67.4	12.2	5.6	184	63.2	26.5	22.3	18.4	20.8	6.5	47.6	8.4	5.5
Bi	<1.5	<1.5	<1.5	<1.5	<1.5	<1.5	6	2	7	3	3	2	21	11	3	3	2	3	<1.5	14	3	2
Th	10	17	16	13	16	22	16	20	22	18	13	18	18	17	17	17	21	19	20	19	21	20
U	3	3	5	3	3	4	3	8	12	10	5	10	10	9	23	12	13	13	10	16	21	6

Analytical Results of the 1995 Chip Sampling by Nathan Duhig and Andrew Jones

(Sample Number corresponds to the meterage along Jukes Road)

Sample Number	10318	10320	10330	10340	10350	10360	10370	10375	10380	10390	10400	10420	10440	10460	10480	10500	10520	10540	10550	10560	10580	10600
SiO2	48.20	61.49	71.08	70.67	72.51	70.52	71.3	50.98	61.83	72.67	69.47	70.91	71.63	72.34	71.83	67.52	62.46	63.97	64.69	71.56	67.96	74.42
TiO2	0.15	0.25	0.3	0.30	0.3	0.29	0.31	0.30	0.29	0.3	0.28	0.31	0.31	0.31	0.30	0.42	0.62	0.51	0.55	0.30	0.54	0.26
Al2O3	8.86	11.89	13.22	12.92	12.61	12.85	13.48	15.25	13.37	12.57	11.94	12.71	13.33	13.14	12.69	13.68	13.21	12.26	13.59	13.04	13.29	12.85
Fe2O3	19.04	14.04	5.55	5.65	5.66	6.23	4.9	21.60	13.89	4.24	8.03	5.16	4.15	4.02	4.24	6.89	13.27	13.37	11.42	5.40	8.71	3.68
MnO	0.00	0.00	0.03	0.04	0.03	0.06	0.03	0.03	0.03	0.03	0.03	0.02	0.02	0.01	0.03	0.02	0.05	0.12	0.12	0.03	0.08	0.14
MgO	0.00	0.00	1.04	0.99	0.97	0.77	0.54	1.98	1.13	0.59	0.67	0.56	0.59	0.61	0.51	0.65	1.38	1.34	1.41	0.78	1.46	0.78
CaO	0.00	0.00	0.02	0.02	0.03	0.02	0.02	0.16	0.07	0.01	0.01	0.01	0.05	0.02	0.02	0.03	0.12	0.09	0.10	0.03	0.15	0.04
Na2O	0.00	0.00	0.11	0.17	0.14	0.26	0.19	0.81	0.35	0.19	0.11	0.09	0.29	0.15	0.34	0.16	0.08	0.10	0.17	0.32	0.33	0.07
K2O	0.00	0.00	5.99	5.87	4.9	5.78	8.02	1.45	4.53	7.46	5.86	7.34	6.86	6.54	7.98	7.61	5.15	4.54	4.81	5.87	4.98	5.14
P2O5	0.00	0.00	0.03	0.04	0.03	0.05	0.05	0.05	0.04	0.04	0.10	0.06	0.04	0.04	0.05	0.10	0.14	0.13	0.13	0.06	0.11	0.05
Loss	8.39	5.21	2.45	2.65	2.62	2.74	1.73	3.35	3.35	1.79	2.71	1.95	2.43	2.34	1.55	2.42	2.93	3.33	3.10	2.32	2.41	2.51
Total	100.22	100.49	99.88	99.67	99.86	99.93	100.63	96.26	99.38	99.9	99.61	99.48	99.96	99.74	99.87	99.81	100.00	100.19	100.25	99.88	100.14	100.04
S	<0.01	6	1	<0.01	0	0	<0.01	0	0	0	0	0	0	0	<0.01	0	0	0	0	0	0	0
Total C																						
Alt. Index			98.18	97.30	97.19	95.90	97.61	77.95	93.09	97.58	98.20	98.75	95.64	97.68	95.93	97.75	97.03	96.87	95.84	95.00	93.06	98.18
Sc																						
V																						
Cr																						
Co			4		2		6			7												
Ni																						
Cu	[10.5%]	[2.32%]	469	1200	493	1195	454	1840	2480	104	1550	523	272	187	385	429	3510	2240	324	91	74	28
Zn	119	117	94	84	93	84	33	48	83	66	88	72	64	52	56	99	175	144	107	53	82	80
As			<3		<3		<3			<3												
Br			<1		<1		<1			<1												
Rb	95	151	176	181	166	179	183	43	109	196	157	179	21	192	179	193	151	150	178	174	178	188
Sr	4	13	30	28	21	34	47	72	45	45	31	47	46	39	56	49	34	24	20	30	24	10
Y			36		31		223			43												
Zr	91	194	276	269	271	266	286	240	256	270	242	268	287	277	267	291	308	300	331	278	312	239
Nb			12		14		15			13												
Mo	14	11	1	1	2	3	3	40	30	1	4	2	1	2	2	2	2	5	2	2	2	1
Ag																						
Cd																						
Sn			5		9		4			7												
Sb																						
Cs																						
Ba	500	1035	1961	1805	1323	1912	2698	576	1692	2750	1754	2625	2058	1668	2526	2285	1355	1267	1085	1462	996	893
La																						
Ce																						
Nd			42		38		30			51												
W			17		21		38			18												
Tl																						
Pb	199	207	11	14	11	20	17	20	24	19	46	9	7	5	6	4	11	16	9	5	3	11
Au(ppb)	2120	991	9.1	13.4	5.4	5	8.6	1530	1470	5	200	9.8	5	25.2	18.8	16.2	459	748	27.4	9.6	5	5
Bi	1156	557	4	<1.5	<1.5	<1.5	<1.5	29	25	<1.5	6	<1.5	<1.5	<1.5	3	<1.5	7	16	7	<1.5	<1.5	<1.5
Th	ot Determin	ot Determin	19	20	20	20	20	18	18	20	19	19	21	20	20	16	13	13	14	20	15	23
U	34	36	6	8	7	9	11	40	33	5	19	7	7	6	7	7	8	16	7	6	5	5

Analytical Results of the 1995 Chip Sampling by Nathan Duhig and Andrew Jones

(Sample Number corresponds to the meterage along Jukes Road)

Sample Number	10620	10640	10660	10680	10700	10750	10800	10850	10900	11400	11900	12450	12800	13300	13800
SiO2	70.95	73.45	73.88	72.64	72.34	74.2	73.94	74.5	73.14	68.37	70.98	72.3	77.02	72.19	68.99
TiO2	0.38	0.31	0.30	0.29	0.30	0.29	0.31	0.28	0.32	0.33	0.36	0.29	0.29	0.34	0.34
Al2O3	13.37	13.04	12.90	12.83	13.35	13.47	13.14	13.04	13.63	16.35	15.50	13	12.34	14.40	16.24
Fe2O3	5.89	3.15	3.13	3.80	4.10	3.08	3.31	3.84	2.67	4.05	3.39	3.89	2.48	2.98	3.13
MnO	0.34	0.13	0.13	0.13	0.09	0.01	0.07	0.21	0.10	0.02	0.05	0.06	0.02	0.03	0.02
MgO	1.17	0.82	0.81	1.15	0.94	0.72	0.70	0.68	0.58	1.26	0.66	1.1	0.67	1.22	0.81
CaO	0.08	0.03	0.07	0.28	0.02	0.03	0.15	0.24	0.24	0.01	0.01	0.93	0.03	0.02	0.05
Na2O	0.17	0.53	0.79	0.55	0.36	1.44	2.04	1.22	2.06	0.44	0.90	3.93	0.16	0.66	1.25
K2O	4.68	5.85	5.43	5.60	4.94	4.06	4.36	4.68	5.18	4.46	2.38	2.44	3.92	5.25	4.29
P2O5	0.08	0.05	0.05	0.05	0.05	0.04	0.05	0.05	0.05	0.05	0.06	0.06	0.03	0.03	0.04
Loss	2.98	2.11	2.14	2.39	2.98	2.66	1.96	1.38	1.48	5.31	5.88	2.16	2.72	3.16	4.35
Total	100.20	99.65	99.79	99.87	99.60	100	100.16	100.12	99.62	100.73	100.24	100.16	99.74	100.43	99.62
S	0	0	0	<0.01	0	<0.01	<0.01	<0.01	<0.01	<0.01	0	<0.01	<0.01	<0.01	<0.01
Total C															
Alt. Index	95.90	92.25	87.89	89.05	93.93	76.48	69.79	78.59	71.46	92.71	76.96	42.14	96.03	90.49	79.69
Sc															
V															
Cr															
Co						2		3				4			
Ni															
Cu	45	40	24	6	13	6	5	7	5	10	86	9	3	7	32
Zn	94	43	38	46	62	57	40	59	42	88	81	93	26	43	56
As						<3		<3				<3			
Br						<1		<1				<1			
Rb	184	200	188	185	183	145	143	165	159	187	96	100	150	157	151
Sr	13	20	22	21	13	18	29	20	45	11	21	60	5	43	44
Y						38		41				40			
Zr	309	278	280	274	284	291	289	274	298	336	340	257	241	331	355
Nb						14		13				12			
Mo	2	2	2	2	1	1	1	2	<1	1	2	1	<1	1	<1
Ag															
Cd															
Sn						5		4				3			
Sb															
Cs															
Ba	909	1498	1433	1485	1204	882		1141	1527	688	566	692	506	1353	966
La															
Ce															
Nd															
W						4		6				5			
Tl															
Pb	28	28	12	15	8	26	8	8	3	55	69	2	5	9	13
Au(ppb)	36.2	17.8	6.7	5	9.3	5									
Bi	2	3	<1.5	<1.5	<1.5	<1.5	2	<1.5	<1.5	<1.5	3	2	<1.5	<1.5	<1.5
Th	19	20	21	21	21	22	20	20	21	25	24	18	18	21	25
U	6	5	5	4	5	5	5	4	5	4	6	5	4	5	6

Geochemical Data for the 1996 Volcanic Facies Traverse

Sample Number	MJ96-1	MJ96-2	MJ96-4	MJ96-6	MJ96-8	MJ96-9	MJ96-10	MJ96-11	MJ96-12	MJ96-13	MJ96-14	MJ96-15	MJ96-16	MJ96-17	MJ96-18
SiO2	67.38	71.97	70.42	73.03	62.56	67.95	68.63	72.37	66.97	75.2	73.88	65.84	72.03	73.05	73.51
TiO2	0.5	0.38	0.34	0.33	0.77	0.86	0.29	0.34	0.39	0.31	0.3	0.37	0.3	0.3	0.27
Al2O3	13.92	13.46	12.09	13.4	14.1	14.4	13.82	12.88	14.23	13.29	12.85	15.59	12.84	13.7	12.63
Fe2O3	3.13	3.07	5.1	3.78	12.54	5.73	3.77	3.71	6.54	2.82	3.39	4.78	3.03	2.95	3.19
MnO	0.24	0.25	0.22	0.03	0.17	0.4	0.33	0.08	0.12	0.03	0.13	0.08	0.08	0.02	0.06
MgO	0.76	0.8	0.5	0.7	1.38	1.32	0.93	0.87	1.78	0.71	0.89	1.33	0.7	0.73	0.9
CaO	3.33	0.56	0.07	-0.01	0.22	0.48	1.41	-0.01	0.04	0.08	0.13	1.47	1.59	0.07	0.58
Na2O	2.52	2.64	0.17	0.08	0.1	1.51	0.51	0.11	0.1	5.42	4.22	2.59	4.81	3.28	1.61
K2O	3.58	4.08	8.18	6.37	5.16	4.05	6.34	8.02	7.3	2.1	3	4.84	2.43	4.41	5
P2O5	0.09	0.07	0.06	0.03	0.18	0.2	0.06	0.06	0.07	0.06	0.06	0.07	0.05	0.05	0.05
Loss	4.29	1.9	2.31	2.08	2.78	3.01	4.01	1.69	2.21	0.85	1.35	3.06	2.05	1.26	2.16
TOTAL	99.83	99.37	99.76	100.1	100.08	99.96	100.22	100.28	99.95	100.95	100.29	100.11	100	99.94	100.03
S	0.01	0.01	0.04	0.01	0.02	0.04	0.01	0.2	0.15	0.28	<0.01	<0.01	<0.01	0.01	0.01
Total C															
Alt Index	42.59	60.40	97.31	99.02	95.34	72.96	79.11	98.89	98.48	33.81	47.21	60.31	32.84	60.54	72.93
Sc	15	10	18	8	19	21	14	8	11	11	11	15	13	11	9
V	63	36	18	10	75	87	6	12	14	8	8	10	3	6	8
Cr	12	5	3	4	9	8	2	5	4	2	3	2	5	5	6
Ni	4	3	2	2	4	5	2	2	3	1	2	1	1	3	3
Cu	11	5	48	164	74	26	7	38	101	3	12	26	4	14	17
Zn	152	313	39	66	134	187	142	315	227	148	78	61	67	53	72
As	1	<1	1	<1	3	1	<1	4	2	<1	<1	<1	<1	<1	<1
Rb	144	142	158	196	203	162	269	209	240	53	109	204	79	145	157
Sr	75	136	111	30	25	34	33	35	26	68	57	56	107	84	65
Y	47	56	35	43	35	36	53	37	46	38	52	54	41	54	56
Zr	290	243	295	295	424	429	290	283	339	256	246	330	292	305	278
Nb	17.1	15.6	17.4	13.8	16.6	18.3	14.2	12.7	15.7	11.7	11.1	15.5	11.8	14.1	13
Mo	0.8	0.9	2.5	0.3	0.4	1.6	0.7	0.3	2.7	0.2	0.2	0.2	0.1	0.3	0.1
Ag	0.1	0.2	0.1	0.3	<0.1	0.1	<0.1	0.4	0.1	<0.1	0.4	<0.1	<0.1	<0.1	<0.1
Cd	0.4	0.2	0.1	<0.1	<0.1	0.2	0.4	0.6	0.1	0.1	<0.1	<0.1	<0.1	<0.1	<0.1
Sb	1.1	0.6	1.5	1.2	2.3	1	2	1.8	1.7	0.6	0.9	1.1	0.6	1	0.5
Cs	6.07	4.7	1.17	1.62	2.73	2.37	3.25	2.84	4.7	0.6	2.22	5.28	2.42	6.06	8.34
Ba	631	1588	2987	2592	1049	773	1160	1516	1480	1006	700	1096	714	1216	731
La	49	66	40	55	32	41	36	50	89	26	54	53	28	81	65
Ce	96	135	80	115	68	88	78	110	187	59	116	119	59	164	122
Nd	46	55	33	49	32	42	36	47	77	27	52	53	26	72	53
Tl	1	1	1	1	1	1	2	2	2	<0.5	1	1	<0.5	1	1
Pb	154	73	11	25	<1.5	7	23	49	9	2	25	4	<1.5	14	4
Bi (XRF)	<2	<2	<2	<2	<2	<2	<2	<2	<2	<2	<2	<2	<2	<2	<2
Bi (ICP)	<0.1	0.2	0.7	0.4	0.1	0.2	0.1	1.5	1.1	0.1	0.7	0.2	<0.1	0.2	0.1
Th (XRF)	16	19	14	23	14	13	23	19	25	19	17	24	17	21	19
Th (ICP)	17.4	20.5	14.8	23.8	15.2	14.4	22.8	19.5	25.7	18.9	19.3	23.3	17.4	22.5	20.2
U	3.53	4.69	3.57	6.5	4.33	3.46	5.53	4.8	5.71	4.21	4.43	5.33	4.18	5.53	4.41

Hellyer alteration study

Russell Fulton
Centre for Ore Deposit and Exploration Studies, Geology Department, University of Tasmania

Progress on the Hellyer hangingwall alteration study since the last meeting has concentrated on logging and sampling core, and attempting to map out the alteration from core logs provided by Aberfoyle. To date, the hangingwall basalt has been sampled in 11 holes with another three or four still to be looked at. Approximately 190 samples have been cut at 10 m intervals down through the basalt and at 5 m intervals near to the contact with the underlying hangingwall volcaniclastic suite (HVS). Samples are being used for whole rock geochemistry and thin sectioning for microprobe analysis of minerals. Holes have been chosen to sample both the most and least altered parts of the basalt and intermediate zones. For the Hellyer core shed visit, examples of intensely altered and relatively unaltered (hydrothermallly) basalt will be laid out and logs of the core are appended to this report.

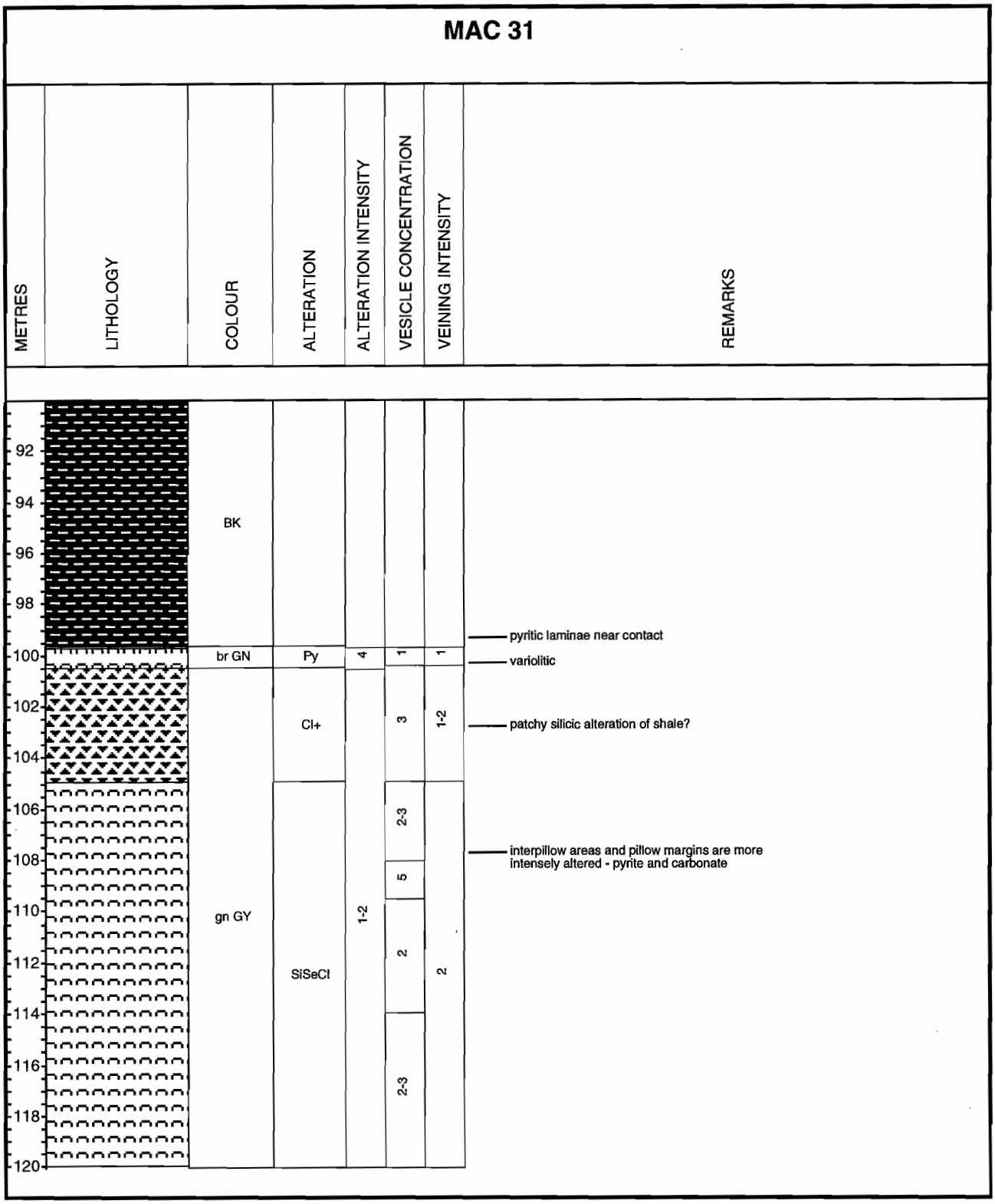
MAC 31
METRES
LITHOLOGY
COLOUR
ALTERATION
ALTERATION INTENSITY
VESICLE CONCENTRATION
VEINING INTENSITY
REMARKS
92
94
96
98
100
102
104
106
108
110
112
114
116
118
120
BK
br GN
gn GY
Py
Cl+
SiSeCl
4
1-2
1
3
2-3
5
2
2-3
1
1-2
2
pyritic laminae near contact
variolitic
patchy silicic alteration of shale?
interpillow areas and pillow margins are more intensely altered - pyrite and carbonate

MAC 31 (cont.)

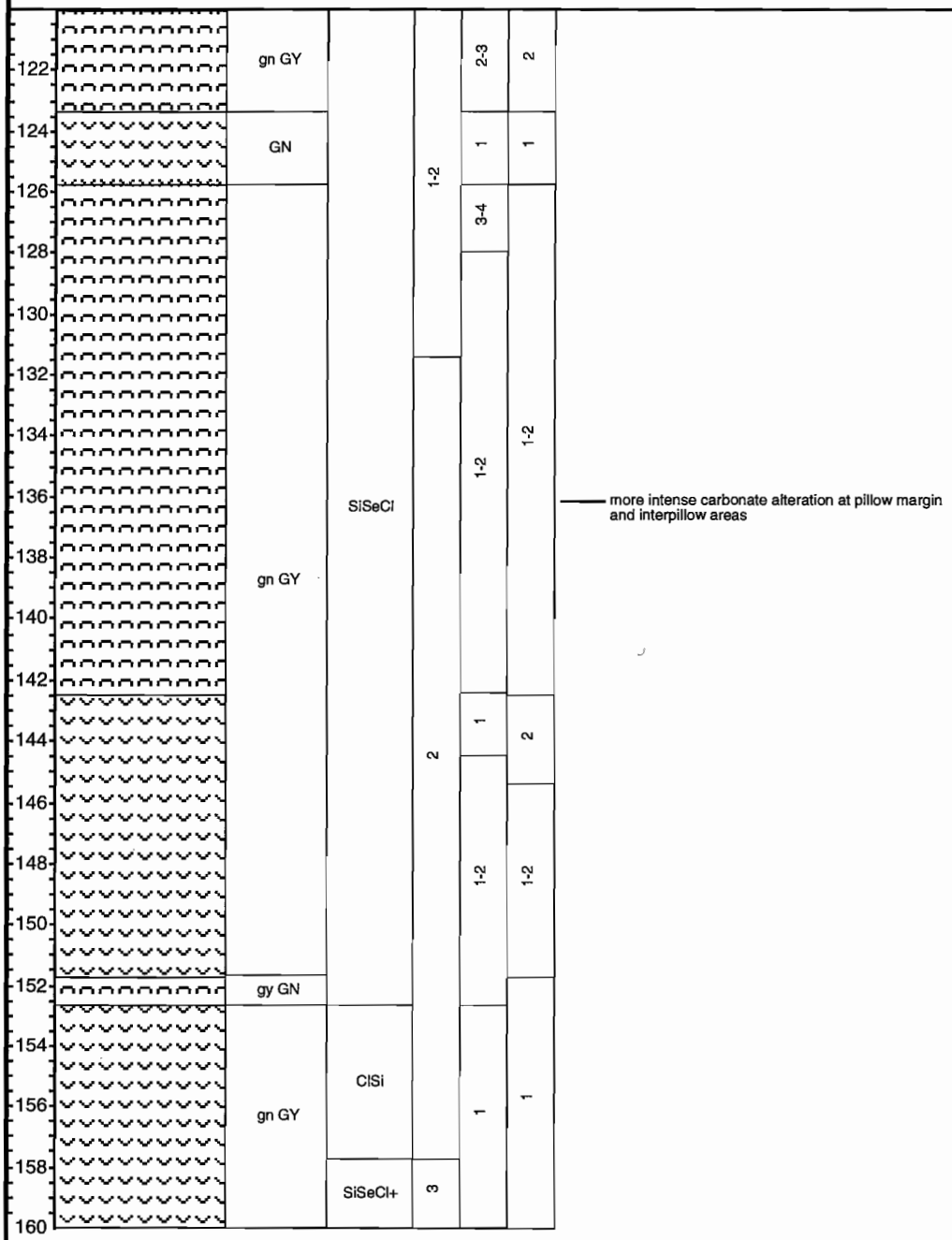
METRES
LITHOLOGY
COLOUR
ALTERATION
ALTERATION INTENSITY
VESICLE CONCENTRATION
VEINING INTENSITY
REMARKS
122
124
126
128
130
132
134
136
138
140
142
144
146
148
150
152
154
156
158
160
gn GY
GN
gn GY
gy GN
gn GY
SiSeCl
ClSi
SiSeCl+
1-2
2
3
2-3
3-4
1-2
1
1-2
1
1
2
1-2
1
2
1-2
1
1
more intense carbonate alteration at pillow margin and interpillow areas

MAC 31 (cont.)

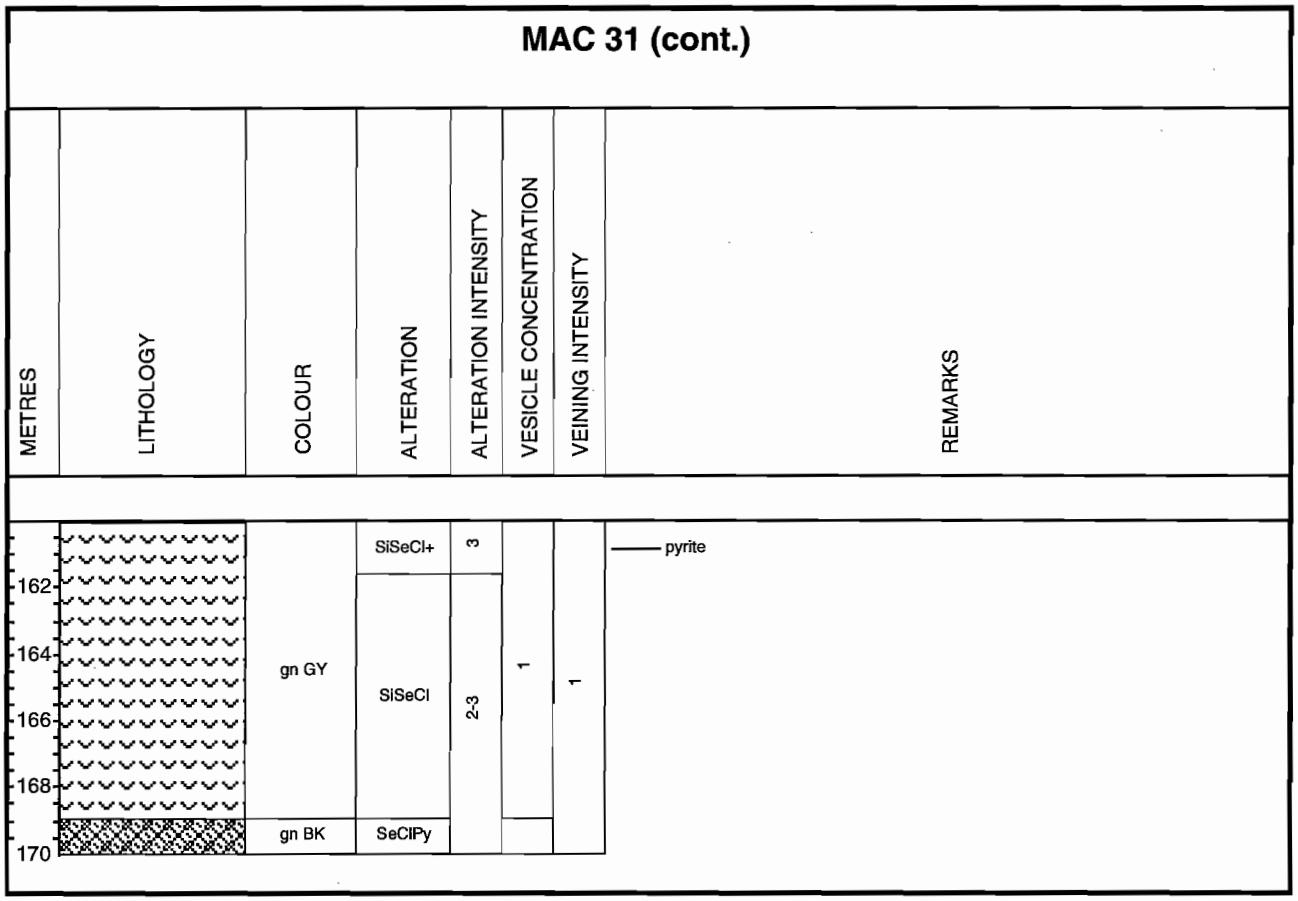
METRES
LITHOLOGY
COLOUR
ALTERATION
ALTERATION INTENSITY
VESICLE CONCENTRATION
VEINING INTENSITY
REMARKS
162
164
166
168
170
gn GY
gn BK
SiSeCl+
SiSeCl
SeClPy
3
2-3
1
1
pyrite

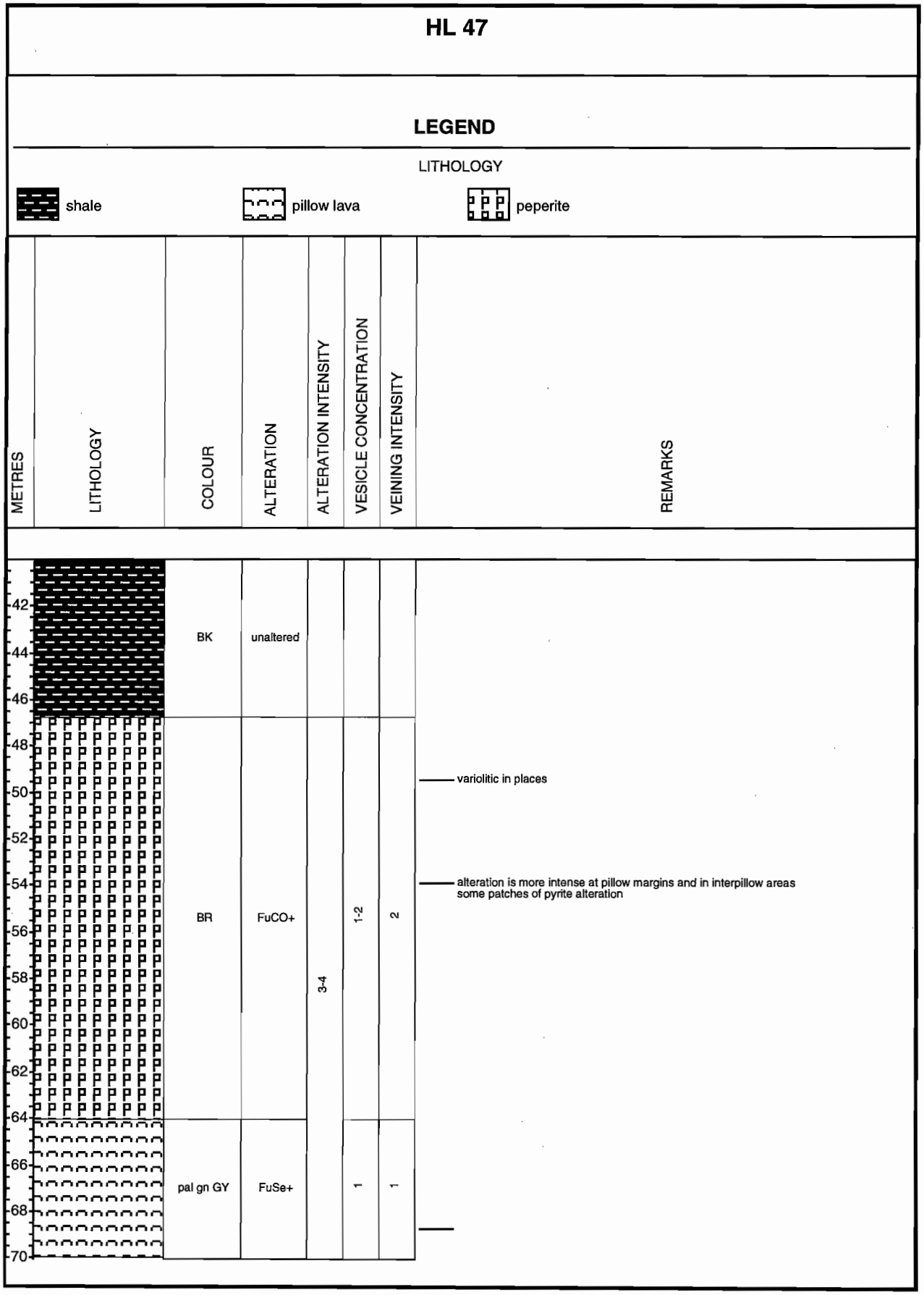
HL 47
LEGEND
LITHOLOGY
shale
pillow lava
peperite
METRES
LITHOLOGY
COLOUR
ALTERATION
ALTERATION INTENSITY
VESICLE CONCENTRATION
VEINING INTENSITY
REMARKS
42
44
46
48
50
52
54
56
58
60
62
64
66
68
70
BK
unaltered
BR
FuCO+
pal gn GY
FuSe+
3-4
1-2
2
1
1
variolitic in places
alteration is more intense at pillow margins and in interpillow areas
some patches of pyrite alteration

HL 47 (cont.)

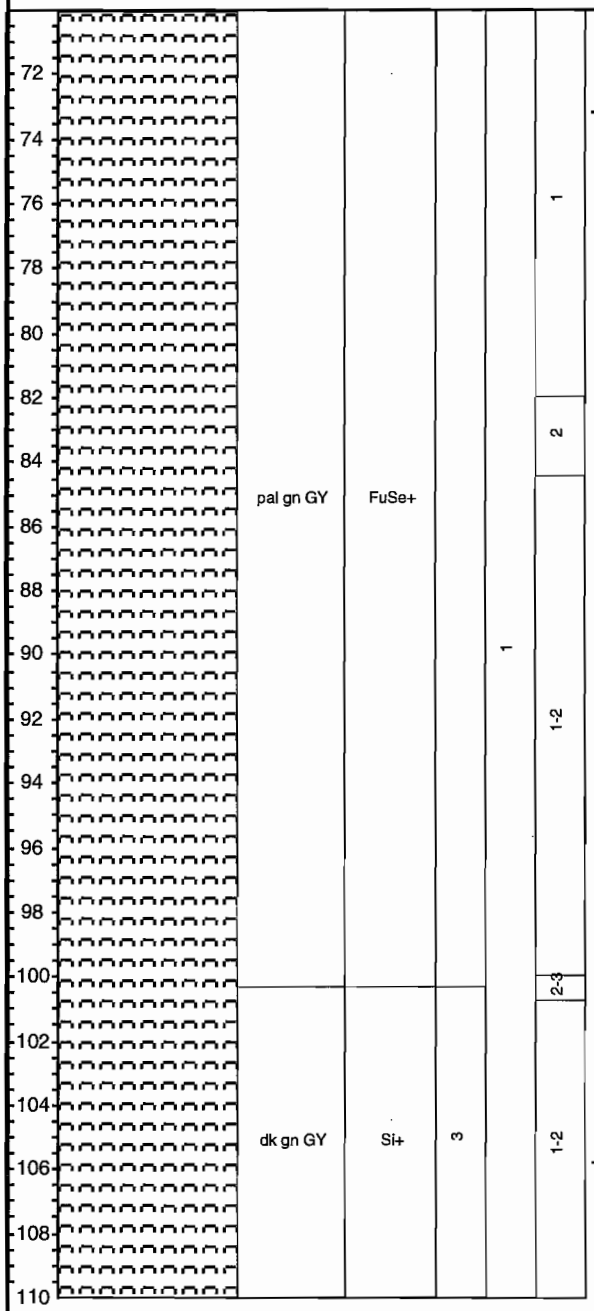
METRES
LITHOLOGY
COLOUR
ALTERATION
ALTERATION INTENSITY
VESICLE CONCENTRATION
VEINING INTENSITY
REMARKS
72
74
76
78
80
82
84
86
88
90
92
94
96
98
100
102
104
106
108
110
pal gn GY
FuSe+
dk gn GY
Si+
3
1
1
2
1-2
2-3
1-2
very hard shale margins - silicified?
alteration more intense at pillow margins and interpillow areas, some pyrite
dark green shale fragments - silicified and chloritised

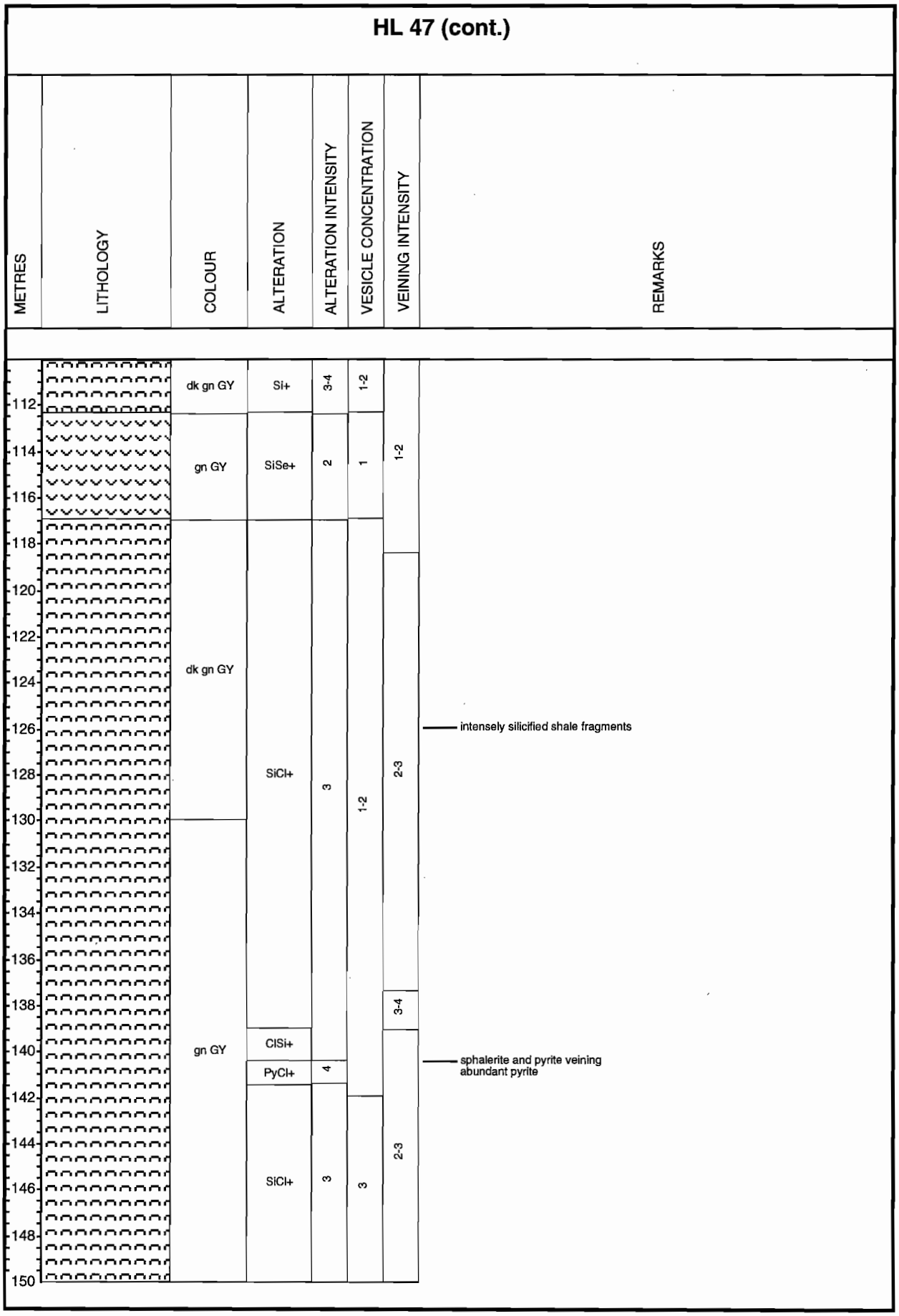
HL 47 (cont.)
METRES
LITHOLOGY
COLOUR
ALTERATION
ALTERATION INTENSITY
VESICLE CONCENTRATION
VEINING INTENSITY
REMARKS
112
114
116
118
120
122
124
126
128
130
132
134
136
138
140
142
144
146
148
150
dk gn GY
Si+
3-4
1-2
gn GY
SiSe+
2
1
1-2
dk gn GY
SiCl+
3
1-2
2-3
intensely silicified shale fragments
3-4
gn GY
ClSi+
PyCl+
4
sphalerite and pyrite veining
abundant pyrite
SiCl+
3
3
2-3

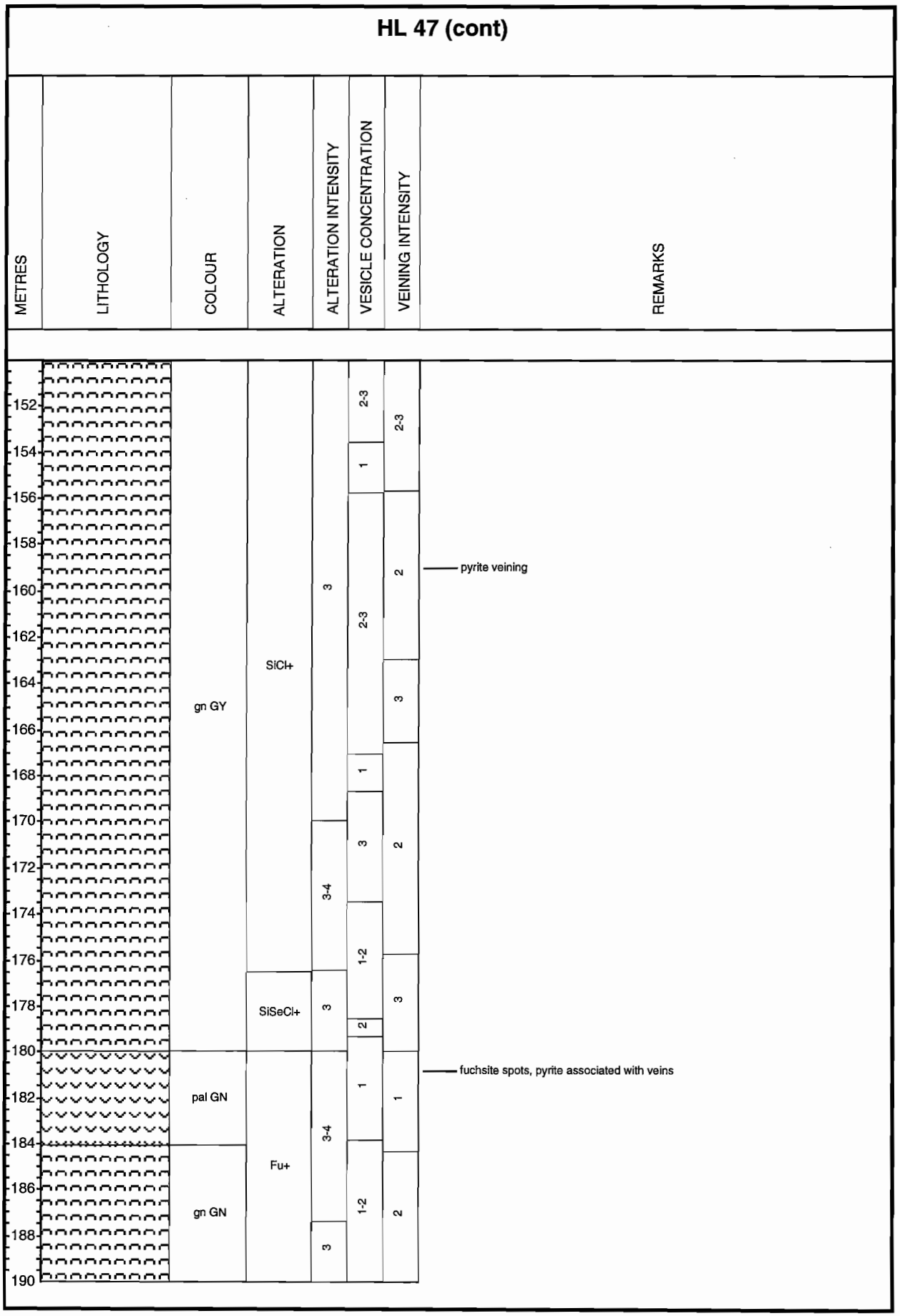
HL 47 (cont)
METRES
LITHOLOGY
COLOUR
ALTERATION
ALTERATION INTENSITY
VESICLE CONCENTRATION
VEINING INTENSITY
REMARKS
152
154
156
158
160
162
164
166
168
170
172
174
176
178
180
182
184
186
188
190
gn GY
pal GN
gn GN
SiCl+
SiSeCl+
Fu+
3
3-4
3
3-4
3
2-3
1
2-3
1
2
3
1-2
2
1
2-3
2
3
2
3
1
2
pyrite veining
fuchsite spots, pyrite associated with veins

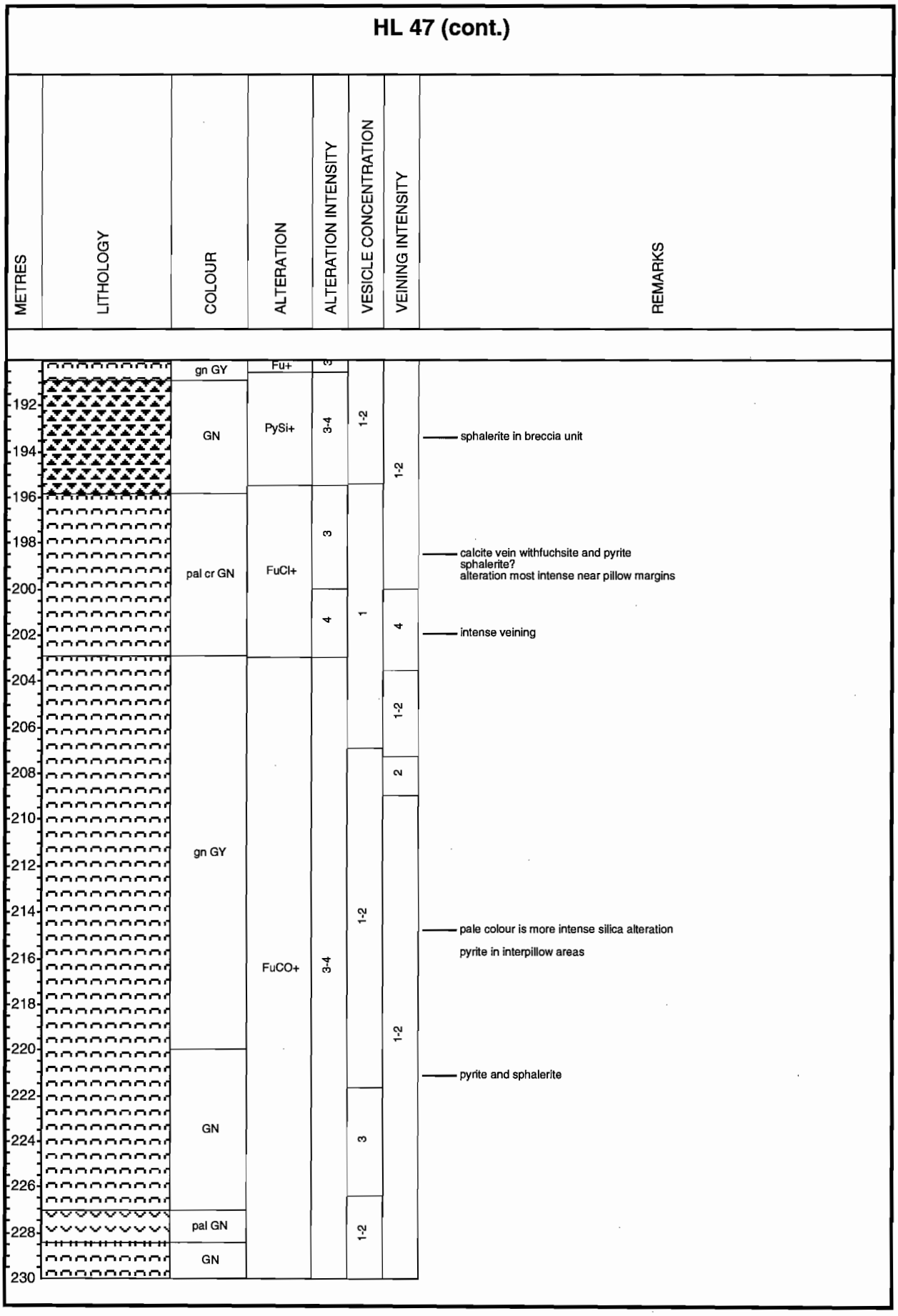
HL 47 (cont.)
METRES
LITHOLOGY
COLOUR
ALTERATION
ALTERATION INTENSITY
VESICLE CONCENTRATION
VEINING INTENSITY
REMARKS
192
194
196
198
200
202
204
206
208
210
212
214
216
218
220
222
224
226
228
230
gn GY
GN
pal cr GN
gn GY
GN
pal GN
GN
Fu+
PySi+
FuCl+
FuCO+
3
3-4
3
4
3-4
1-2
1
1-2
3
1-2
1-2
4
1-2
2
1-2
sphalerite in breccia unit
calcite vein withfuchsite and pyrite
sphalerite?
alteration most intense near pillow margins
intense veining
pale colour is more intense silica alteration
pyrite in interpillow areas
pyrite and sphalerite

HL 47 (cont.)

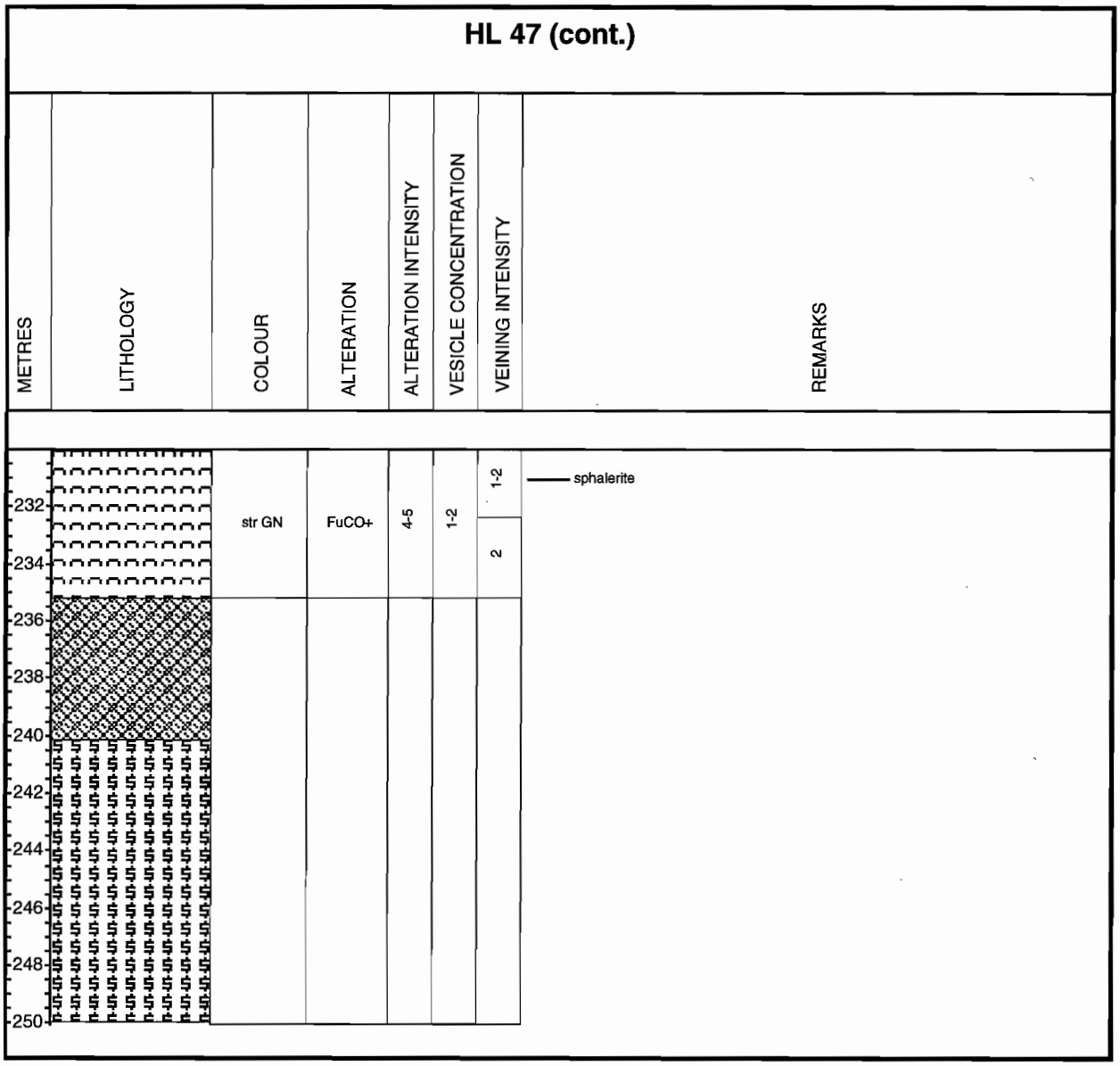
METRES
LITHOLOGY
COLOUR
ALTERATION
ALTERATION INTENSITY
VESICLE CONCENTRATION
VEINING INTENSITY
REMARKS
232
234
236
238
240
242
244
246
248
250
str GN
FuCO+
4-5
1-2
1-2
2
sphalerite

RGC (TASMANIA) LTD
HENTY GOLD PROJECT

Geology Visitors Guide

1. Introduction

The Henty Gold Project is located approximately 30 kilometres north of Queenstown at the head waters of the Henty River. The project is managed by RGC (Tasmania) Limited a wholly owned subsidiary of Renison Goldfields Consolidated Limited.

Exploration in the Henty area commenced in 1966 when EL 9/66 was pegged by the Mt Lyell Mining and Railway Company. Initial exploration was for Mt Lyell style mineralisation. The area was mapped, soil sampled, and tested using both ground magnetic and vertical loop EM surveys. In 1971-72, old copper working were discovered north of the current mine area. Follow up work around these old working were disappointing.

A major gradient array IP survey in 1972-73 identified 17 anomalies for further testing. This testing included soil geochemistry, costeaning, geophysics and diamond drilling. Most results were poor except for one costean on the site of the current Portal Pad which returned 2.4m of massive sulfide mineralisation assaying 1.8% Cu, 1.76% Pb, 0.2% Zn and 37.89% FeS_2. Two diamond drillholes were drilled to test the results from the costean. Poor results were returned for both holes, and the exploration focus shifted elsewhere.

Exploration activity around the Henty Gold Project was renewed in 1982-83 when EL 9/66 was due for reduction. The area was reinterpreted and the gold zone identified. It was not until 1982-83 that gold assaying was carried out. Assays from one of the initial two holes, HFZ5, returned a result of 6.7m @ 7 g/t Au.

From 1983 to 1987, a further 38 holes were drilled and identified a shallow gold resource over a strike length of 650m. Due to the nature of the mineralisation observed in drillcore, and the highly variable grade, further work was required to prove sufficient tonnes at sufficient grade to develop the deposit. The initial resource estimate in 1987 was 500,000 tonnes @ 10 g/t Au. This resource was tested in 1988/89 by an exploration decline into what is now called the Sill Zone. The exploration decline resolved several of the geological questions but unfortunately delineated insufficient mineable reserves for the project to proceed.

While the exploration decline was being developed, further diamond drilling located a deeper target some 400 to 500 metres below surface. HP096 drilled in September 1989 intersected 7.5m @ 107.1 g/t Au. During the next 3 years this area was drilled to its current spacing and a diluted resource of 506,000 tonnes @ 26.9 g/t identified.

The decision to develop a shaft access to this deep mineralisation was taken in 1992. Following negotiations with the then Joint Venture partner Little River (Resources) Pty Ltd, and the approval of the Department of Environmental Management work commenced in 1993.

2. Regional Geology

The Henty Gold Project lies in the Mt Read Volcanic Belt which also hosts the ore deposits of Hellyer, Que River, Rosebery, Hercules and Mt Lyell. The Mt Read Volcanics are a belt of Cambrian felsic to intermediate volcanic rocks with a strike length of over 200 km. These volcanics are normally divided into five litho-stratigraphic associations (Corbett 1992):

1. Sticht Range Beds - Siliciclastic sandstone and conglomerate.
2. Eastern Sequence - Quartz-feldspar phorphyitic felsic volcanic, volcaniclastic and intrusives.
3. Central Volcanic Complex - Feldspar phorphyritic lava rich volcanics.
4. Tyndall Group - Quartz phorphyritic volcaniclastics, epiclastics and breccias.
5. Western Sequence - Tuffaceous sandstone, siltstone and conglomerate.

Two major faults dominate the structure of the area. These are the Henty Fault and the Great Lyell Fault. The Henty Fault is a major break in the geology of western Tasmania and runs for over 60 km. The fault separates the younger Tyndall Group rocks from the older Central Volcanic Complex. Locally the Henty fault strikes 017 and dips 70° to the west. North and south of the project area, the Henty Fault divides into two branches. Several stages of movement are identifiable along the Henty Fault including pre-Devonian, Devonian and post-Devonian phases (Berry 1989). The Great Lyell Fault is sub-parallel to the Henty Fault and is represented by a branch locally termed CF3 (Cambrian Fault 3).

4. Local Geology

The local geology is dominated by the Henty Fault which separates younger Tyndall Group rocks from older Central Volcanic Sequence rocks, in turn the Tyndall Group is overlain by the Owen Conglomerate a coarse siliciclastic unit derived from Precambrian quartzites and schists.

To the west of the Henty Fault, the Central Volcanic Complex (CVC) consists of feldspar-phyric dacite lavas and coarse grained volcaniclastics. To the east of the Henty Fault, the Tyndall Group can be split into four stratigraphic units. These are;

- **ets** - Shales, siltstones, minor intermediate volcanics.
- **etl** - Massive quartz-phyric lavas and breccias.
- **ett** - Mixed quartz-phyric volcaniclastics, lavas and minor epiclastics.

etc - Very fine grained to blocky epiclastics.

The lower unit of the Tyndall Group includes a correlate of the Comstock Tuff a crystal rich volcaniclastic sandstone described by Corbett et al., (1974) which acts as a reliable marker unit.

The Tyndall Group shows a rapid change in thickness along strike, thickest in the south and thinning to the north. This facies change coincides with a swing in the strike from 340 to 020 - subparallel to the Henty Fault.

Gold mineralisation occurs in an asymmetric sequence of strongly altered rocks. The alteration zone is strongest adjacent to the Henty Fault and is a silica-sericite-pyrite alteration. Three main styles of mineralisation and alteration are identified with the alteration zone. These are;

MZ - Quartz, sericite, pyrite, base metal sulfide rock. Average Au grade 1 g/t.

MV - Quartz, sericite, sulfide poor, strongly foliated rock. Average Au grade 4g g/t.

MQ - Massive Quartz, late crosscutting pyrite, chalcopyrite, galena, gold, telluride fractures. Average Au grade 36 g/t.

The MQ hosts the main gold mineralisation and is enveloped in turn by MV and MZ. MQ varies in thickness generally decreasing to the north and upwards. In Zone 96, MQ averages 3m wide and in the Sill Zone, 0.6m wide. The MZ commonly has a relict fragmental texture and is probably a coarse epiclastic.

In the footwall of the alteration sequence, lenses of massive pyrite (MP) up to 2m thick occur. These pyrite beds contain relict colloform textures and typically include calcite gangue. Gold values in MP average 5.5 g/t.

In the hangingwall, an intense quartz-albite alteration occurs 20 to 30m above the pyrite horizon. This alteration has destroyed the textures of the original rhyolite lavas and volcaniclastics.

The MQ zone and surrounding rocks have been strongly effected by Devonian faulting associated with the regional Tabberabberan Orogeny. Most of the deformation is brittle with numerous small to medium scale faults developed. These faults have throws varying from negligible to 20+ metres. The frequency of faulting is extreme with upward of four small scale faults occurringg in the space of 3 metres. These faults will present the biggest challenge to the mining of the deposit.

5. Resource Estimation

The current insitu resource is 380,000 tonnes @ 35.4 g/t Au.

The current "Mineable Resource" is 506,000 tonnes @ 26.9 g/t Au. This figure includes 24.9% dilution.

The resource estimate is based on comparing and contrasting manual estimates (isocline), Indicator Kriged geostatisitcal estimates and 3D wireframed estimates using the Datamine mining software package. These 3 estimation techniques all

provide contained metal estimates within 5% of each other.

As well as local grade estimation with in the MQ horizon, mining performance will also be effected by the dilution mined on a round by round basis. While every attempt will be made to minimise dilution, it is expected some narrow areas will be mined at higher than average dilution. The initial sill along with an intense diamond drilling program from a drive 75 metres to the footwall wall is designed to provide as much information as possible to locate narrow or faulted zones. Once identified, these areas can be scheduled and mined in an appropriate manner.

6. Mining Method

Given the narrow width of the orebody, high frequency of small fault offsets, and foliated host rocks, the only mining method considered appropriate is cut and fill. Feasibility studies considered the options of cut and fill, shrinkage stoping, rill shrinkage stoping, sub-level open stoping and sub-level benching. All options except cut and fill were eliminated on the basis of maximum flexibility. Once mining experience is gained, other methods may be employed where possible.

The current mining rate is estimated to be around 100,000 tonnes per annum.

GOLDFIELDS (TASMANIA) LIMITED
HENTY GOLD MINE

Proposed Research Project for Master of Economic Geology

Tim Callaghan, 24/09/96

The Henty Gold Mine is hosted in Tyndall Group volcanics and sediments of the Cambrian Mt. Read Volcanics on the West Coast of Tasmania. The deposit is a high grade gold deposit with current resources of approximately 500, 000t @ 27g/t.

Two main resources have been delineated, Zone 96 and the Sill Zone. Several other areas of high exploration potential have been identified, the intermediate zone, Mt. Julia and south of Zone 96.

Although the deposit has been studied by company and external geologists during the last decade, new information is rapidly being accumulated through current development and exploration activities.

The importance of Devonian remobilisation had been noted by previous workers (eg. Halley and Roberts, *in press*, Taheri and Green, 1991), but the main conclusions led to a Cambrian origin for the mineralisation. However Devonian influences have been very much understated as is evident from recent exploration work and resource drilling. The study outlined below should document some observations recently made and clarify processes involved in mineralisation.

The research project I wish to undertake should involve:

1) Study/review of the mineralisation, stratigraphy and alteration of the existing resources (Sill Zone, Zone 96) and a comparison with Mt. Julia and other exploration areas..

2) Interpretation of local to regional stratigraphic and structural setting of Henty mineralisation.

3) Whole rock and trace element studies of alteration for Henty Style mineralisation. This will involve drillholes from Mt. Julia, Zone 96, Sill Zone and unaltered drillholes and a compilation of all existing data.

Through the exploration program proposed for the coming year and through observations of the development of the existing resources this research project should provide valuable information to the Henty Gold Mine and our understanding of this unique style of mineralisation.

PROPOSED RESEARCH PROJECT SUMMARY

GEOLOGY AND ALTERATION OF ZONE 96 OREBODY - HENTY

The following details objectives and work program to be undertaken as the research component of the M.Econ Geol.

Henty Gold comprises three zones of gold mineralisation. The Sill zone, Intermediate zone and Zone 96. Zone 96 comprises the Bulk of the 506,000t deposit. A grade of 26.9g/t is anticipated.

The aims of the research project are:

- Construction of a detailed stratigraphy of Zone 96; the main orebody of the Henty Mine, by analysis of host volcaniclastic sediments and volcanics in drillcore.
- An analysis of chemical and spatial variables between host lithologies, alteration and mineralisation. This analysis will be under taken using both geostatistical and possibly fractal analysis.
- To provide an empirical framework, based on the above analysis, for minesite exploration.
- To provide some insight into the genesis Henty mineralisation - Syngenetic, epigenetic, syntectonic.

To achieve these aims the following work program is proposed:

- A comprehensive literature review of previous work at Henty is underway to ensure no duplication of work. A short report detailing previous work will be submitted to CODES prior to the commencement of the next short course in November 1996. At this time an introductory talk will also be given on research aims and progress to date.
- Zone 96 will be drilled on a 20*20 metre pattern commencing August 1996. Standard logging and interpretation of rock relationships. Alteration assemblages will be compared for discrete lithologies adjacent to mineralised Massive Quartz (MQ).

- Multielement analysis of selected lithologies which have some continuity in the mine sequence.
- Petrographical analysis of selected samples.
- Possibly some electron microprobe work on phyllosilicate assemblages adjacent to Massive Quartz alteration to plot trace element distribution.

PIMA-II apectral analysis of hydrothermal alteration associated with the Hellyer VHMS deposit: Progress report

K. Yang*, J.F. Huntington*, J.B. Gemmell and R. Fulton

In collaboration with CSIRO/AMIRA Project P435 Mineral Mapping with Field Spectroscopy for Exploration

Introduction

AMIRA project P435 "Mineral Mapping with Field Spectroscopy for Exploration" (Project leader Jon Hunnington) is a multi-disciplinary research project focusing on the development of new, operational, field spectroscopic techniques for mapping mineral, soil and rock composition during exploration. The field portable spectrometer (PIMA-II) has brought the opportunity of applying this technology routinely to exploration programs. For example, the PIMA-II can determine, in situ, hematite, geothite, smectite varieties, kaolinite, dickite, halloysite, sericite/illite varieties, gibbsite, jarosite, alunite, gypsum, pyrophyllite, amphiboles, opaline silica, carbonate species, epidote, talc, tremolite, chlorite varieties, phlogopite, and biotite.

As part of project P435 several case studies of well documented alteration zones around mineral deposits are being undertaken. One of these case histories is the Hellyer VHMS deposit in Tasmania as the footwall alteration zonation (Gemmell and Large, 1992) and the hangingwall alteration (Jack, 1989) is well developed and preserved. AMIRA projects P435 and P439 started at roughly the same time and several companies are sponsors of both projects. These companies suggested that as the alteration at Hellyer was being investigated by both projects, we should collaborate. Both sponsor groups were approached and it was decided to combine research efforts to compare the spectral data from the PIMA-II generated from P435 with the detailed mineral chemistry and whole rock chemistry obtained from P439. Initial results from this study were given by Yang et al (1996) in Report 2 of P439 (May 1996). This paper reports some preliminary results from continuing the study of the Hellyer material.

The specific aims of the study at Hellyer are to:

- identify and (semi)quantify major phyllosilicate minerals and thus delineate alteration zoning.
- identify any chemical variations of a particular mineral species, and determine their relationship to mineralisation.

Samples from 10 diamond drill-holes, comprising 293 pulverised composite samples (most representing a 10-metre interval) and 21 core splits, were measured with the PIMA II portable infrared spectrometer (Table 1). Locations of the drill holes are given in Figures 1 and 2.

Samples analysed in this study cover both the hangingwall and the footwall, and include volcanic rocks both within and outside the Hellyer mineralising system.

Only phyllosilicates and, in some cases, carbonate minerals were interpreted from PIMA spectra.

Results

White mica

White mica is widespread in both the altered footwall and hangingwall rocks and is typically enriched near the margins of the system.

In light of the low grade metamorphism (prehnite grade) at Hellyer, significant white enrichment is expected only in rocks affected by hydrothermal activity.

*CSIRO, Division of Exploration and Mining

Table 1
Sample list

drill-hole	sample type	sample #	number of samples	comment
HL 014	Pulp	333969 to 333977	14	HW, in
HL 028	Pulp	334195 to 334206	12	HW, in
HL 055	Core	334010 to 334033*	21	HW, in
HL 057	Pulp	334207 to 334216	10	HW, in
HL 306	Pulp	209598 to 209647	49	FW, in
HL 840	Pulp	626260 to 626313	53	FW, in
HL 841B	Pulp	626324 to 626419	80	HW & FW, in
HL 850	Pulp	629017 to 629045	27	FW, in
MAC 19	Pulp	430563 to 430604	42	out
MAC 31	Core	622213 to 622219**	6	out

* not consecutive; ** 622214 missing; HW = hangingwall; FW = footwall; in = within Hellyer mineralisation system; out = outside Hellyer mineralisation system.

In H 840, there appears a gradation in the footwall from the unaltered or much less altered volcanics to the highly altered rocks within the alteration system.

At the northern end of the orebody, the eastern margin of the footwall alteration system appears to be more mica-rich than the western margin (e.g. drill-holes HL 840, 841B). These spectral abundance data confirm the asymmetric zoning pattern in the northern portion of the Hellyer alteration system (Gemmell & Large 1992).

White mica tends to concentrate in the upper (close to orebody) part of the footwall alteration system, although locally in the deeper sections high to very high mica content is still possible (HL 306).

In general white mica abundance increases with depth toward the contact with the footwall (or ore body) in the altered hangingwall (Fig. 4).

Composition variations in footwall

Wavelength of the AlOH absorption minima reflects the octahedral substitution between Al and other cations (mainly Fe and Mg), with longer AlOH indicating more octahedral Fe and Mg relative to Al (i.e. more phengitic) (Duke 1994; Cudahy et al. 1996).

In the footwall alteration system, changes in AlOH wavelength may cover a wide range, and are spatially either gradual or abrupt (Fig. 5).

Intensified stringer veining and sulpide enrichment is observed where increased mica AlOH wavelengths are observed.

Within the alteration system, (e.g. drill-hole HL 850), the AlOH wavelength was found to increase towards the centre of the alteration system (siliceous zone at 364–400 m), suggesting that white mica in the centre is more Fe and/or Mg-rich than that in the margins (Fig. 5c).

AlOH wavelength is related to metal contents of the altered volcanics. By comparing Figures 5 and 6, it can be seen that in HL 840, 841B and 850 elevated metal contents are observed in the intervals with longer AlOH. This important finding suggests that muscovites are relatively Fe and Mg-rich (more phengitic) in the mineralised zones and Fe and Mg-poor in the surrounding alteration zones.

Composition variations in hangingwall

AlOH wavelength of white mica in the altered hangingwall varies in in a similar range as the footwall mica (Fig. 7). This probably indicates a a downward increasing intensity of alteration in the hangingwall, suggested by the increasing whitemica abundance.

Hydrothermal white mica tends to contain more Fe and Mg with increasing alteration intensity.

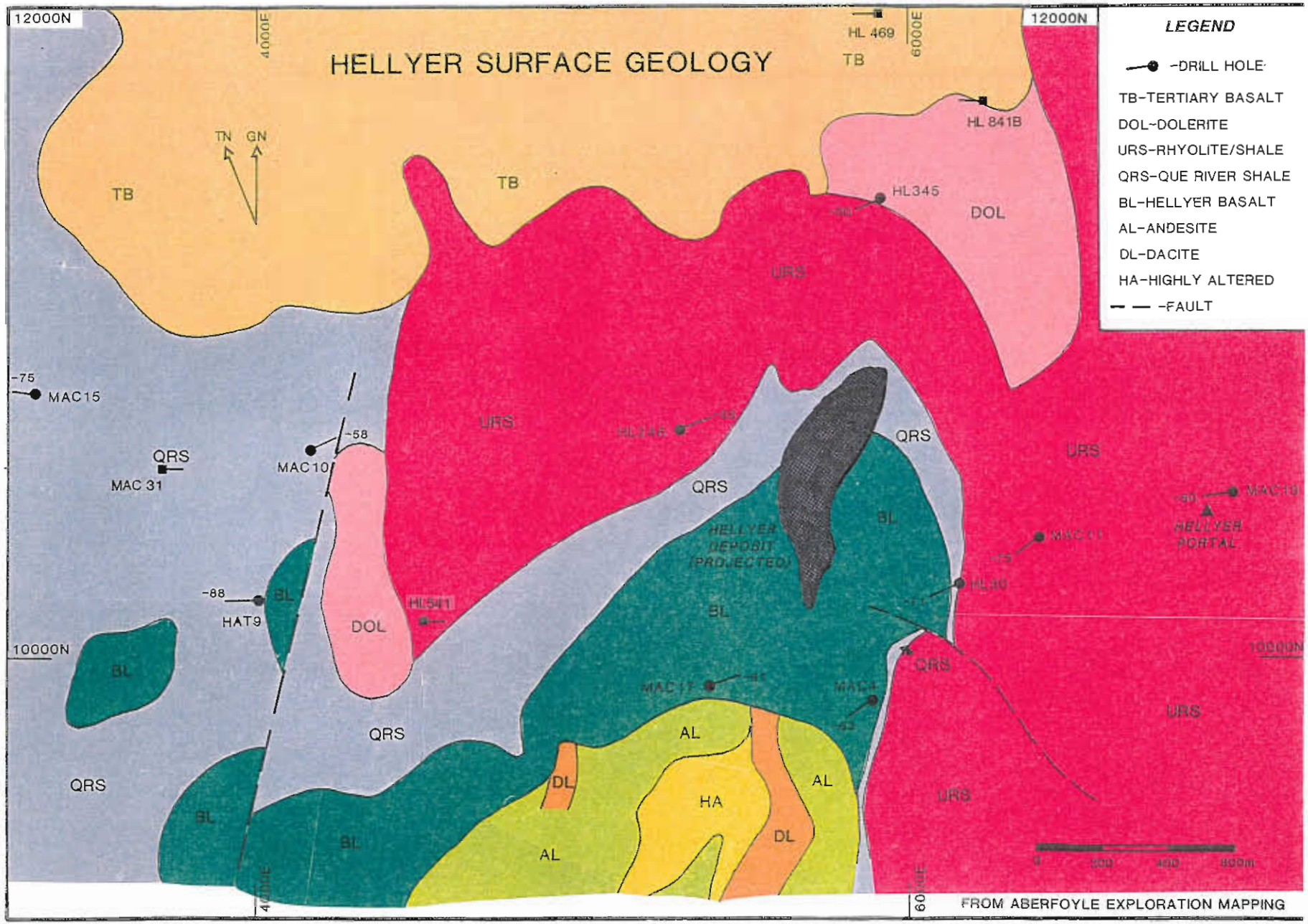

Fig. 1
Surface geology of the Hellyer area with collar locations of some of the drill holes used in this study.

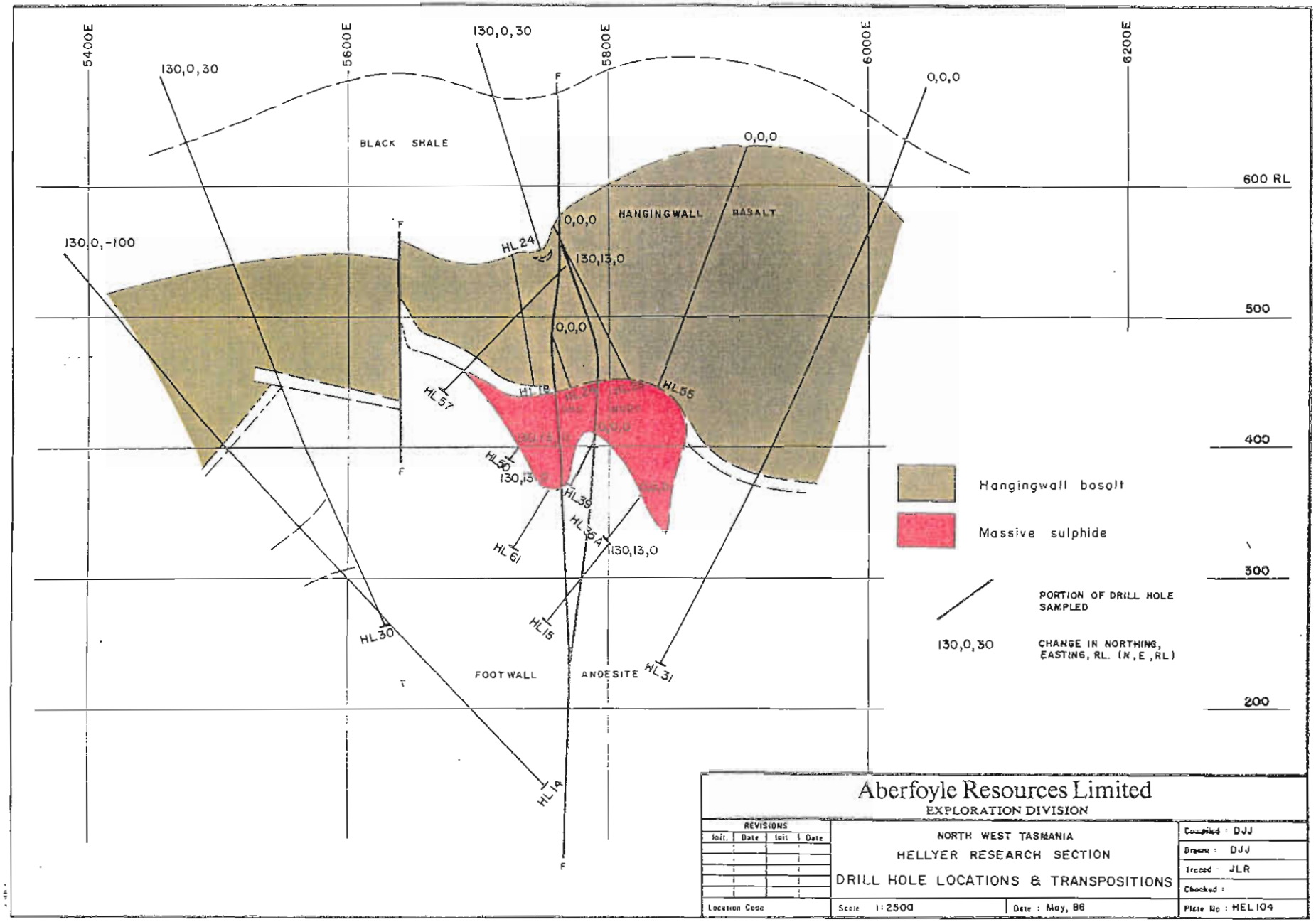

Fig. 2
Transposed cross section (pre-Jack Fault movement) showing location of some of the drill holes used in this study.

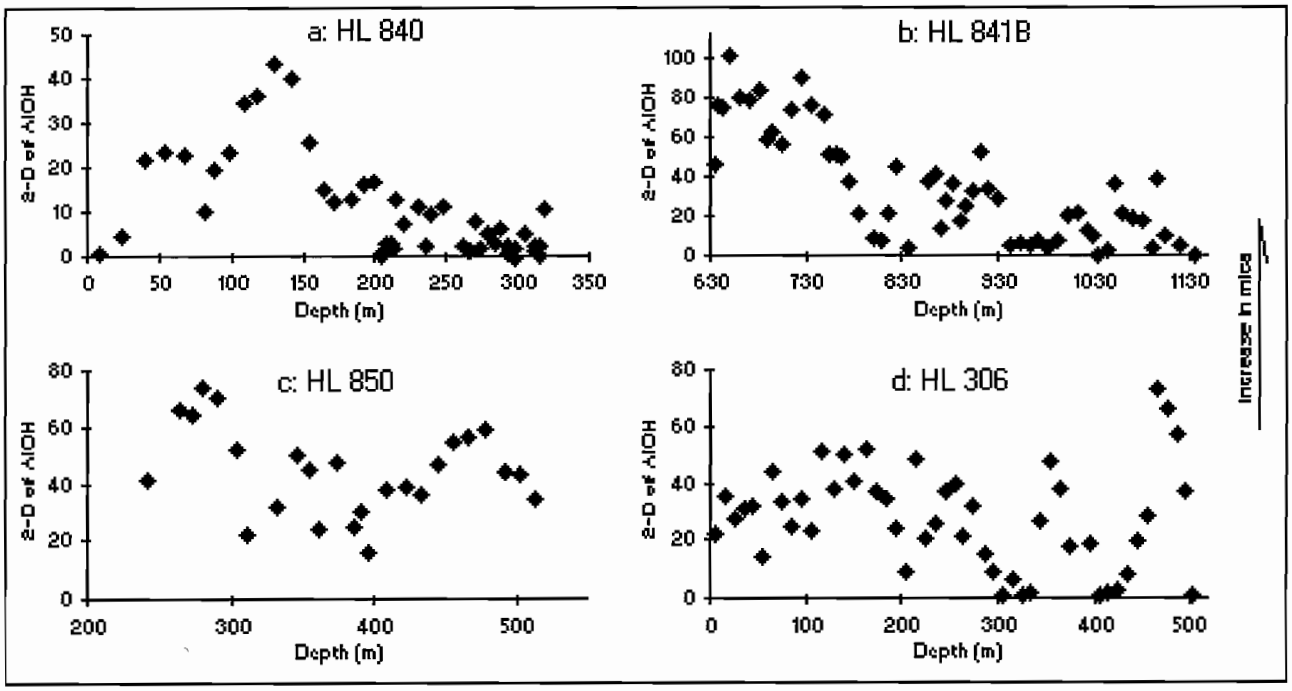

Fig. 3
Variations in second derivative (2-D) of mica AlOH feature in the altered footwall. Higher 2-D indicates higher white mica content. 2-D values < 0 indicate undetectable mica, and are not plotted.

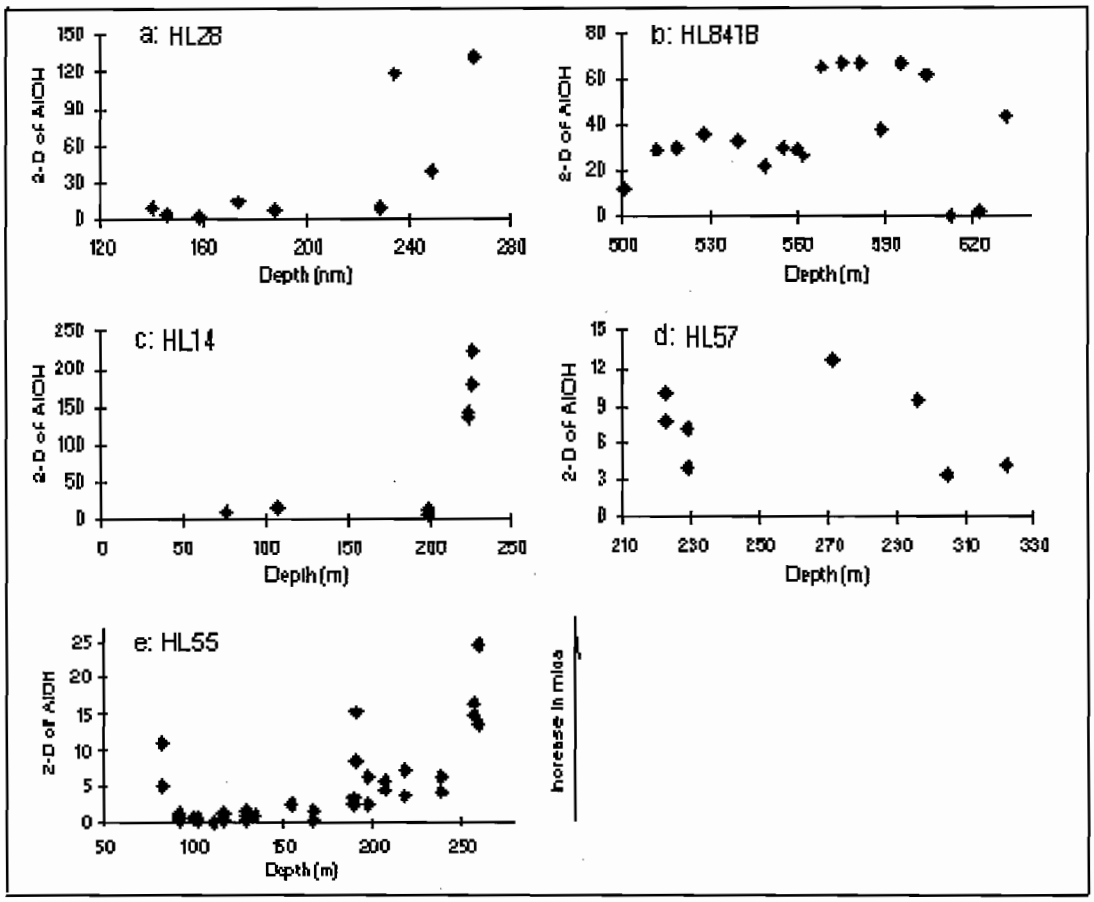

Fig. 4
Variations in second derivative (2-D) of mica AlOH feature in the altered hangingwall. Higher 2-D value indicates higher white mica content. 2-D values < 0 indicate undetectable mica and are not plotted. More than one datum point at a depth (e.g. HL 55) represents multiple measurements on a single sample.

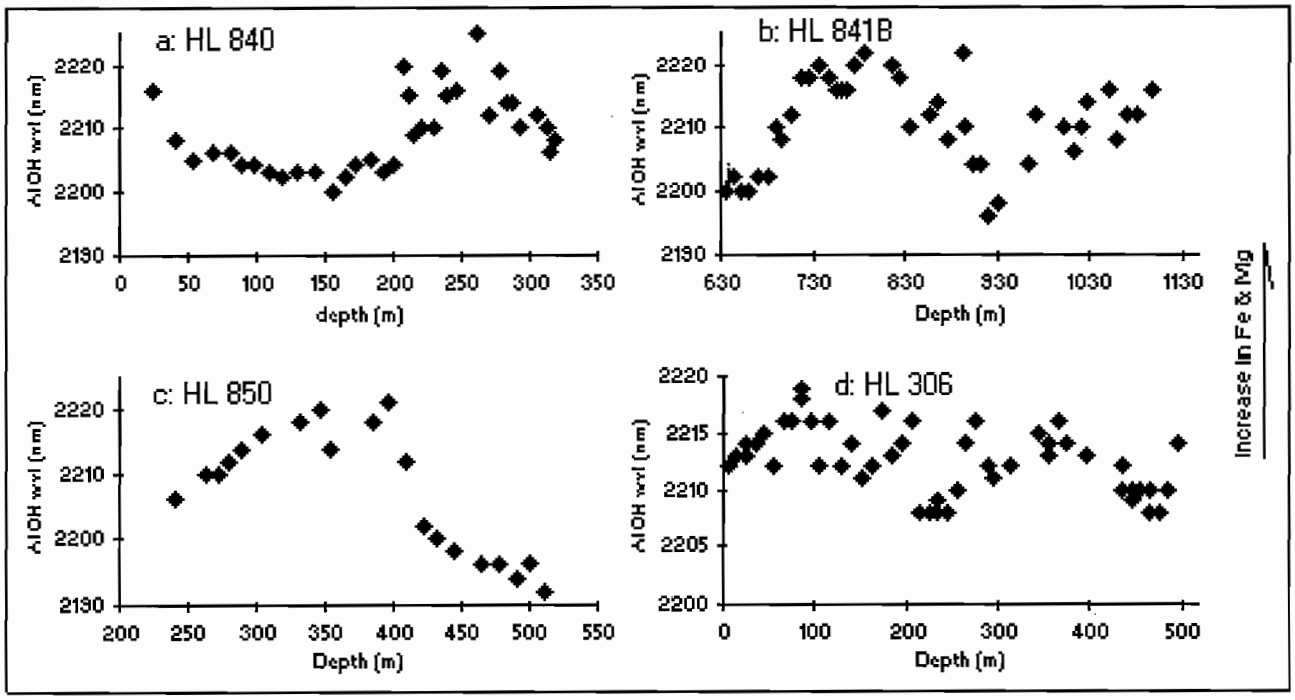

Fig. 5
Wavelength variations of AlOH for white mica in the altered footwall. Longer AlOH wavelength indicates higher octahedral Fe and Mg. Only those samples with identifiable mica AlOH feature are plotted.

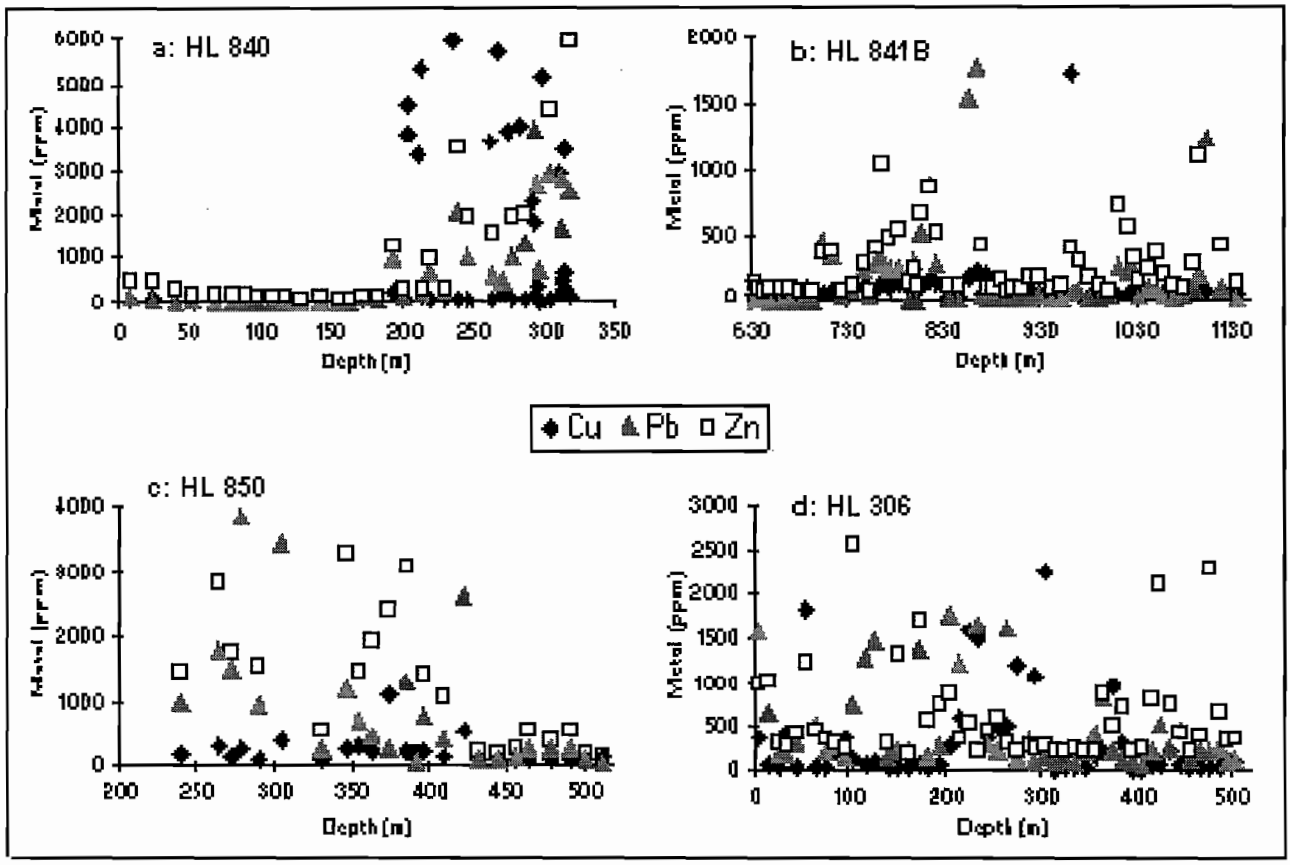

Fig. 6
Variations in metal abundance through drill-holes in footwall.

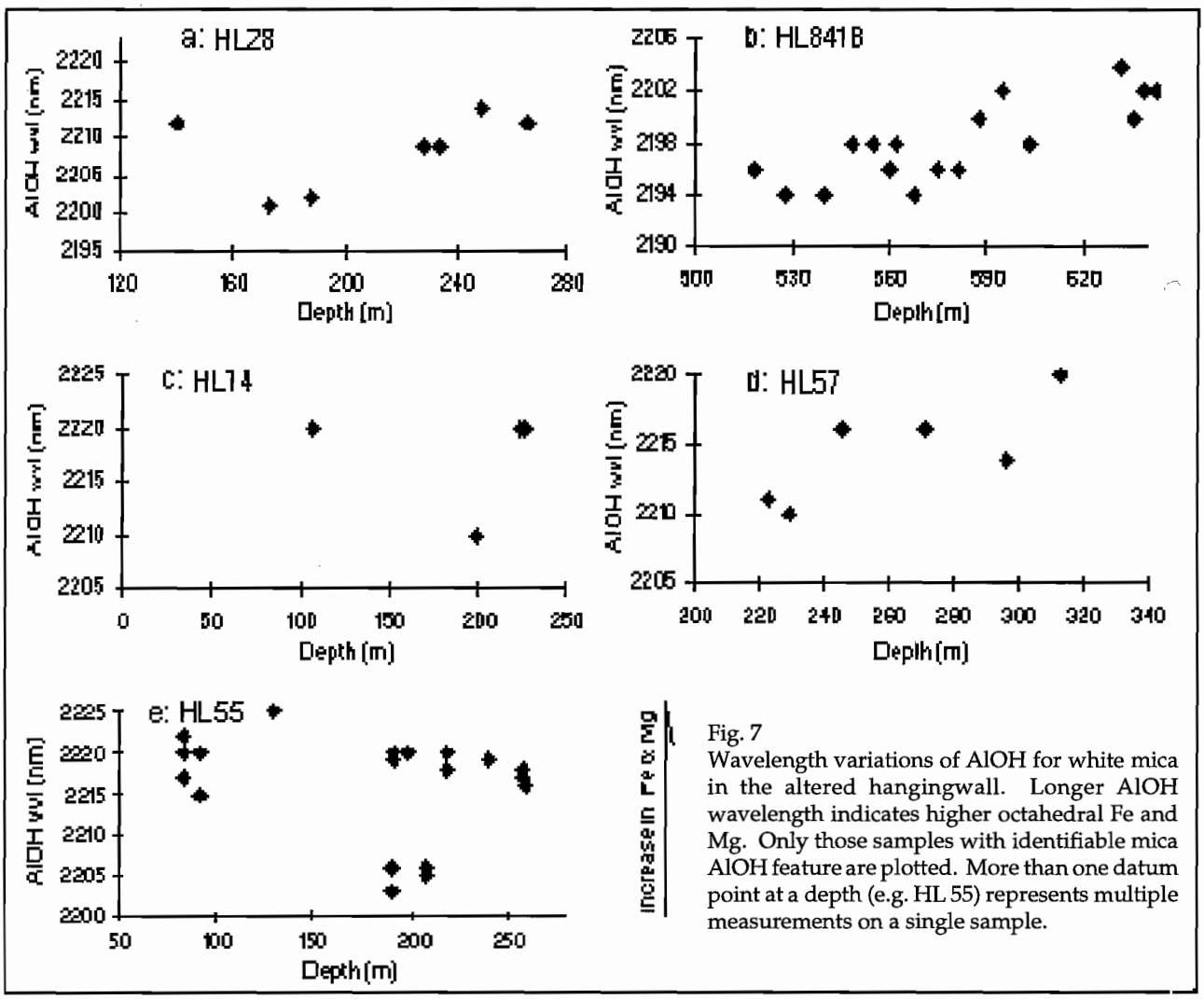

Fig. 7
Wavelength variations of AlOH for white mica in the altered hangingwall. Longer AlOH wavelength indicates higher octahedral Fe and Mg. Only those samples with identifiable mica AlOH feature are plotted. More than one datum point at a depth (e.g. HL 55) represents multiple measurements on a single sample.

Chlorite

Chlorite abundance can be semi-quantitatively indexed by the intensity of chlorite FeOH absorption. Variations of chlorite abundance in the footwall and the hangingwall alteration systems are illustrated in Figures 8 and 9.

In HL 840, chlorite abundance decreases gradually from the eastern margin of the alteration system toward the central siliceous zone at 200–250 m depth. A sharp increase in chlorite is evident from 270 m to the end of the sampled section, which marks the western margin of the alteration pipe. The semi-quantitative abundance data indicate, in a broad scale, that the assemblage of major phyllosilicates is sericite–chlorite and chlorite in the eastern and western margins of the alteration pipe, respectively, and confirms that the footwall alteration system is asymmetric in terms of both major mineral assemblage and abundances as described by Gemmell and Large (1992).

HL 306 shows very low chlorite at 0–200 m and very high chlorite at > 300 m. The chlorite abundance variation indicates a vertical transition within the alteration system at around 300 m depth from silica–sericite to chlorite or chlorite–sericite assemblages, as previously described by Gemmell and Large (1992).

Chlorite abundance in the altered hangingwall may reach a significant level. In HL 841B and 14, chlorite content tends to increase toward the contact with footwall, suggesting increasing alteration toward the footwall.

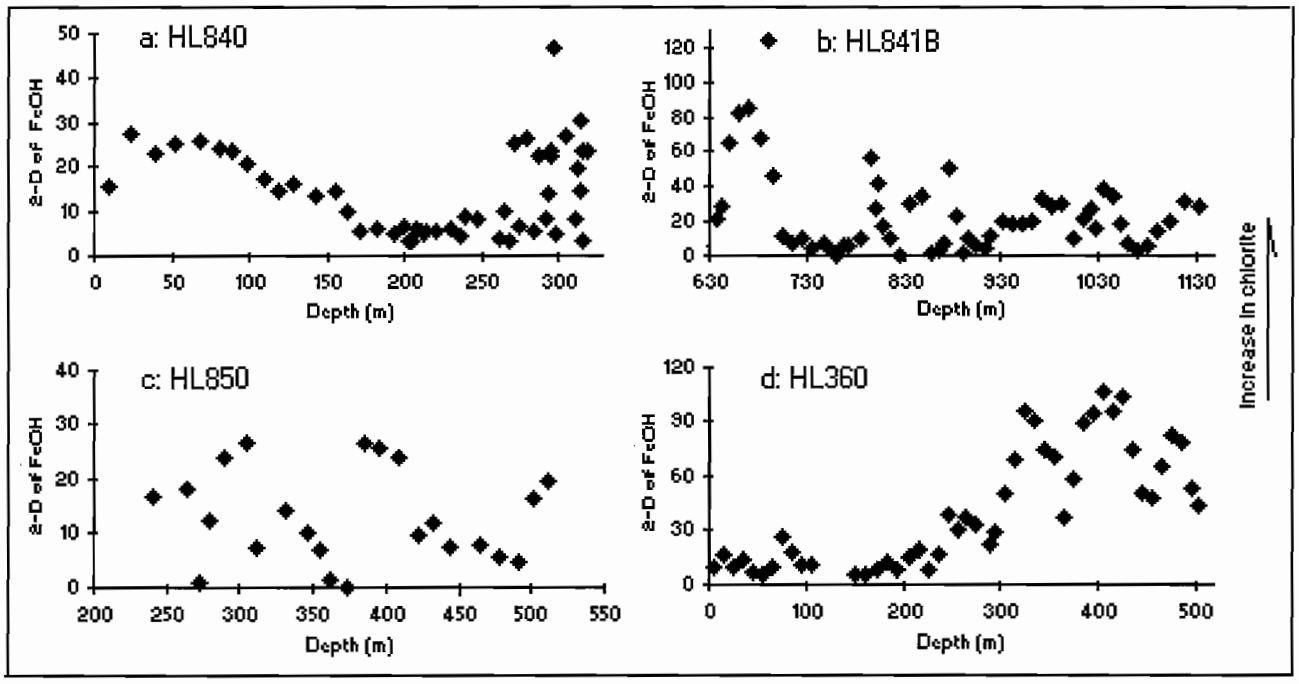

Fig. 8
Variations in second derivative (2-D) of chlorite FeOH in the altered footwall. Higher 2-D value indicates higher chlorite abundance. 2-D values £ 0 indicate undetectable chlorite and are not plotted.

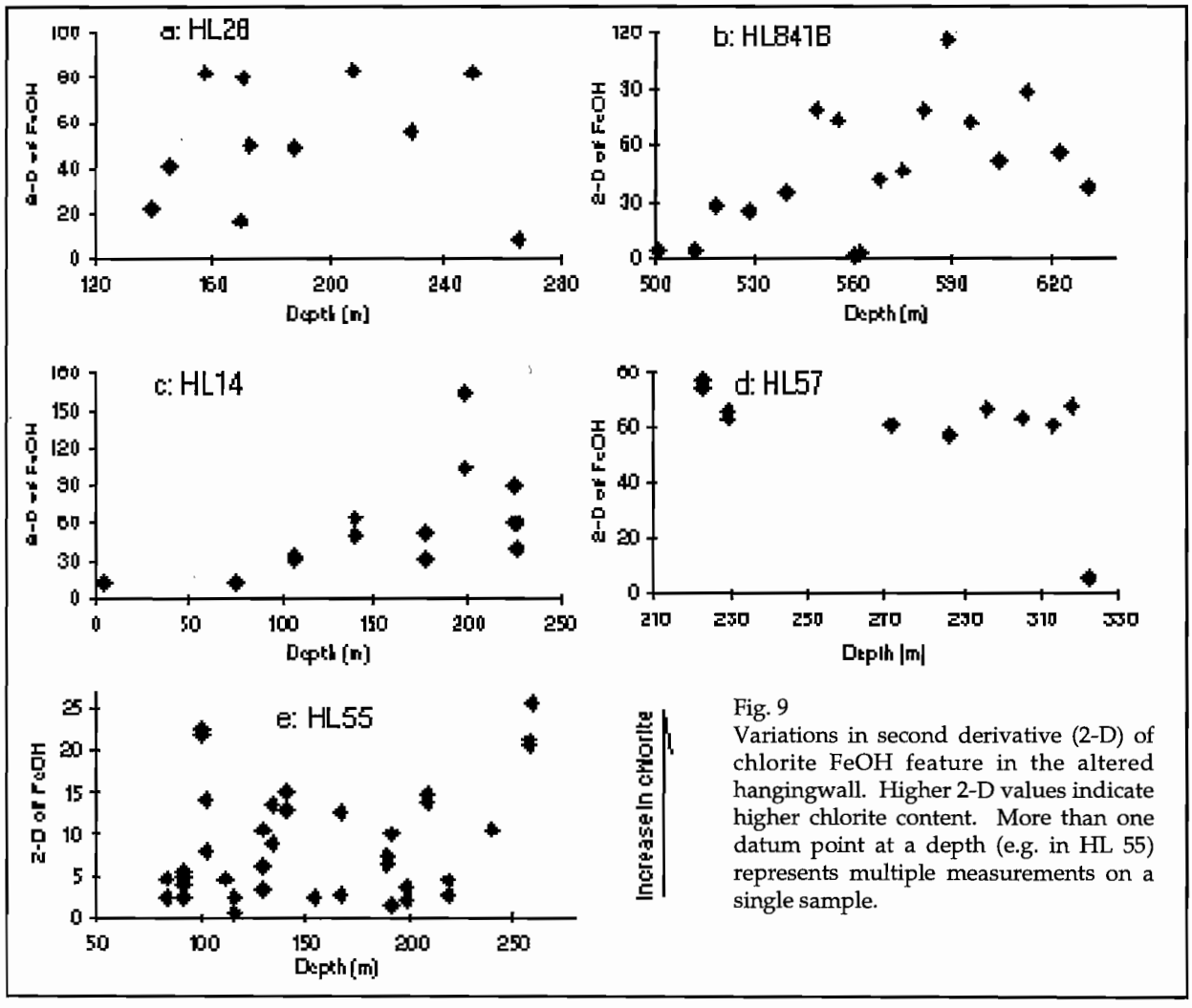

Fig. 9
Variations in second derivative (2-D) of chlorite FeOH feature in the altered hangingwall. Higher 2-D values indicate higher chlorite content. More than one datum point at a depth (e.g. in HL 55) represents multiple measurements on a single sample.

Composition variations

FeOH wavelength of chlorite is the spectral parameter for chlorite Mg# {Mg/(Mg+Fe)}, with the longer wavelength corresponding to lower Mg# (Pontual 1994; Yang et al. 1996). Wavelength variations for chlorite FeOH are shown in Figures 10 and 11.

In the altered footwall, there does not appear to be a consistent trend of wavelength variation for chlorite in relation to alteration zoning. For example, data from HL 840 show chlorite of more Fe-rich in the sulpide-rich, intensely altered siliceous zone (170–270 m) than in sericite and sericite–chlorite zones, whereas in HL 841B relatively Mg-rich chlorite tends to develop in the two sulphides-rich intervals. In HL 306, the chlorite in the siliceous core appears to be more Mg-rich than in the other zones (Fig. 10).

Similarly in the hangingwall, while chlorite in HL 14, 28 and 55 shows a decrease in FeOH wavelength toward the contact with the footwall, the chlorite in HL 57 appears to behave in an opposite manner (Fig. 11).

It appears that in a single drill hole the composition of chlorite (FeOH wavelength) in the hangingwall does not vary as much as in the footwall.

Chlorite Mg#, estimated from our data for Mg# – FeOH wavelength is 0.7–0.2 for the altered footwall, and 0.7–0.3 for the hangingwall rocks.

A limited number of electron microprobe analysis for chlorite fail to reveal the correlation between microprobe between FeOH wavelength and Mg# (Fig. 12).

Host Rocks

To be of practical use in exploration, it is necessary to document and understand the spectral signatures of the unaltered background volcanics. For this purpose, MAC 19 and MAC 31 were selected. The two drill-holes are located a few kilometres east and west, respectively, of the Hellyer mineralised system, and so may be taken as the less altered or unaltered rocks outside the mineralised system for comparison. Spectral data for MAC 19 are extracted and plotted in Figure 13.

There does not seem to be any difference in white mica composition between the mineralised and unmineralised systems.

Most MAC 19 samples contain a moderate amount of chlorite, with increasing abundance downhole. The chlorite composition also shows a downward trend of variation from more Fe-rich to less Fe-rich. The abundance of chlorite is significant and comparable to that of many samples from the Hellyer deposit.

Samples from MAC 31, all from the Pillow Lava, contain chlorite. Also, carbonate minerals are the major (dominant?) component of the samples analysed.

Based on MAC 31 data, calcite enrichment, association of calcite and chlorite and rare to no white mica may be characteristic of the country rocks of the Pillow Lava Sequence.

Samples of MAC 19 are not suitable as the unaltered volcanics, as the moderate to high abundance of both white mica and chlorite, and their similar compositions to those from the mineralised system, suggest that they formed in a similar processes as their counterparts from the Hellyer system.

However, it is still not certain if the rocks encountered in MAC 31 are representative of unaltered host rocks. The common presence of chlorite, and in places white mica, neither of which are common minerals in prehnite–pumpelliyte facies metamorphism, makes it hard to confidently conclude that these rocks are unaltered.

Conclusions

From the spectral data obtained in this portion of the study:

- Alteration zoning in the footwall can be better characterised than the hangingwall by the PIMA spectral data.

- White mica composition is a good index for mineralisation, with the Fe and/or Mg-rich mica being within or proximal, whereas the relatively Fe and Mg-poor mica peripheral, to the orebody.

- Chlorite composition, though also highly variable, does not appear to have a particular relationship with mineralisation, and therefore is less significant in directly indicating the mineralisation. The estimated Mg# of chlorite ranges from 0.7–0.2 for the altered footwall and 0.7–0.3 for hangingwall volcanics.

- Carbonate with minor chlorite could be the spectral signatures of the immediate host volcanics.

References

Cudahy, T., Yang, K., Mason, P., Gray, D., Scott, K. & Huntington, J. 1996. Kalgoorlie field spectral workshop manual. CSIRO Exploration and Mining Report 301R.

Corbett, K.D. 1992. Stratigraphic-volcanic setting of massive sulfide deposits in the Cambrian Mount Read Volcanics, Tasmania. Econ Geol 87, 564–586.

Duke, E.F. 1994. Near infrared spectra of muscovite, Tschermak substitution, and metamorphic reaction progress: implications for remote sensing. Geology 22, 621–624.

Gemmell, J.B. & Large, R.R. 1992. Stringer system and alteration zones underlying the Hellyer volcanic-hosted massive sulfide deposit, Tasmania, Australia. Econ Geol 87, 620–649.

Jack, D.J. 1989. Hellyer host rock alteration. M.Sc. Thesis, Department of Geology, University of Tasmania.

Large, R.R. 1992. Australian volcanic-hosted massive sulfide deposits: features, styles, and genetic models. Econ Geol 87, 471–510.

McGoldrick, P J and Large, R R, 1992. Geologic and geochemical controls on gold-rich stringer mineralisation in the Que River deposit, Tasmania, Econ. Geol., 87:667–685.

Offler, R. & Whitford, D.J. 1992. Wall-rock alteration and metamorphism of a volcanic-hosted massive sulfide deposit at Que River, Tasmania: petrology and mineralogy. Econ Geol 87, 686–705.

Pontual, S., 1994. Influence of composition on the spectral response in the chlorite and biotite-phlogopite mineral groups. Internal CSIRO DEM Consultancy Report. Summary Report: Phase 3C.

Waters, J.C. & Wallace, D.B. 1992. Volcanology and sedimentology of the host succession to the Hellyer and Que River volcanic-hosted massive sulfide deposits, northwestern Tasmania. Econ Geol 87, 650–666.

Yang, K., Huntington, J.F., Scott, K.M. & Mason, P. 1996. Pilot spectral analysis of samples from the Ardlethan tin deposit, NSW. CSIRO Exploration and Mining Report 136 R, 33 p.

Whitford, D.J., Creelman, R.A. & Ramsden, A.R. 1984. Petrological, geochemical and mineragraphic studies at Que River and Hellyer, Part 6. CSIRO Division of Mineralogy Report 1544R, 38 p.

Yang, K., Gemmell, J.B. and Fulton, R., 1996, PIMA-II spectral analysis of alteration associated with the Hellyer VHMS deposit: preliminary results, AMIRA Project P439, Second Report, May 1996, p. 171–178.

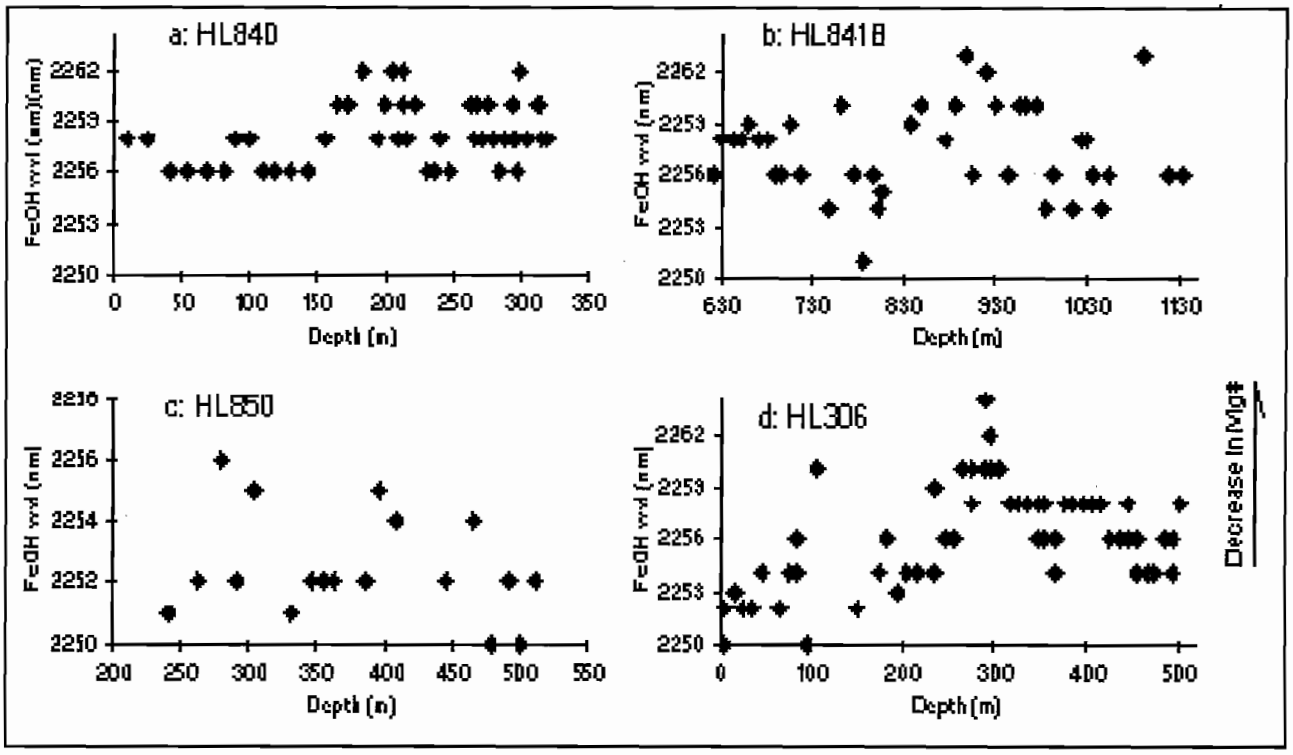

Fig. 10
Wavelength variations of chlorite FeOH in the altered footwall. Longer FeOH wavelength indicates higher Mg/(Mg+Fe). Only those samples with an identifiable FeOH feature are plotted.

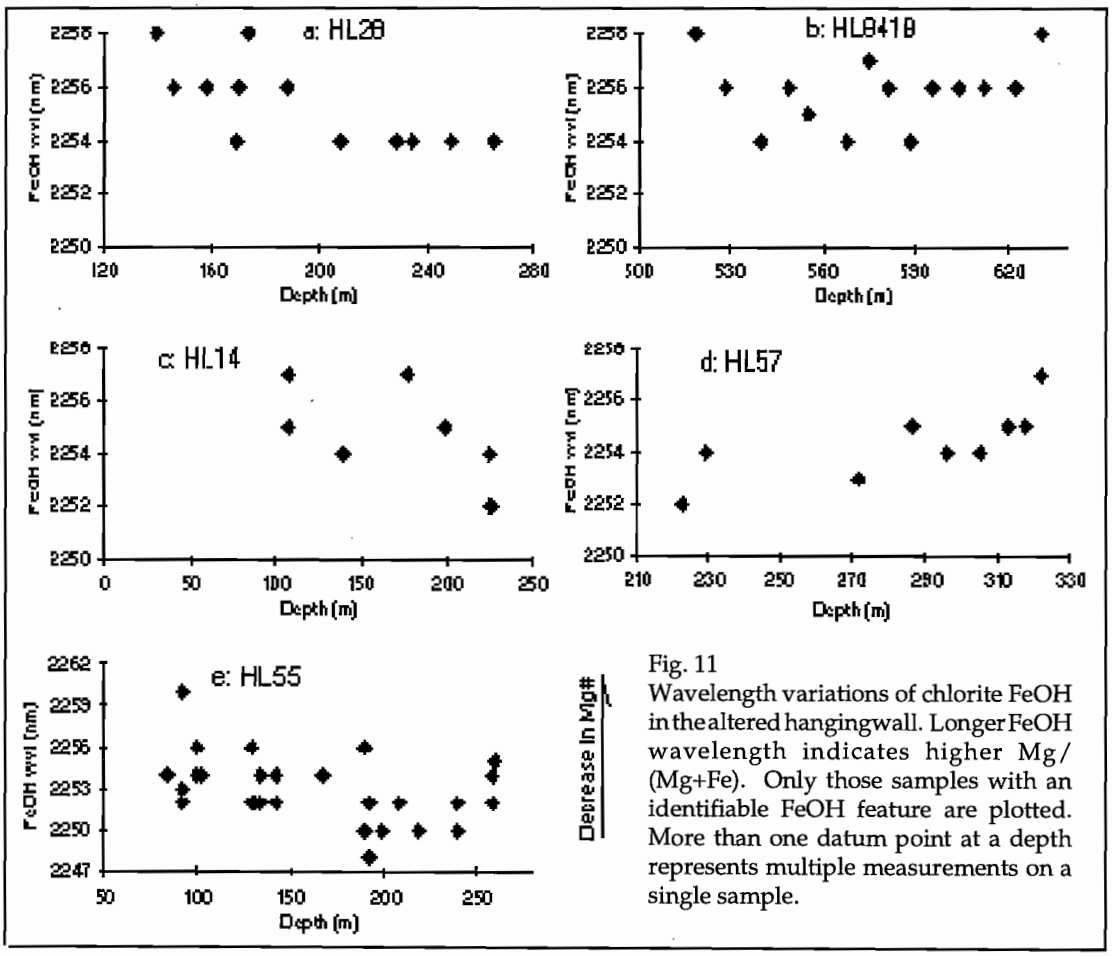

Fig. 11
Wavelength variations of chlorite FeOH in the altered hangingwall. Longer FeOH wavelength indicates higher Mg/(Mg+Fe). Only those samples with an identifiable FeOH feature are plotted. More than one datum point at a depth represents multiple measurements on a single sample.

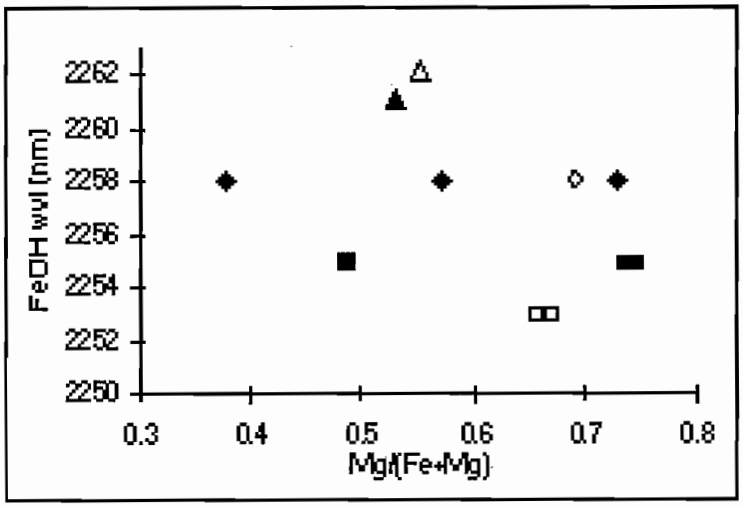

Fig. 12
Relationship between FeOH wavelength and Mg# for chlorite. Each datum point is the average of 1-4 analyses on a single sample. Datum points with same a pattern belong to a same sample.

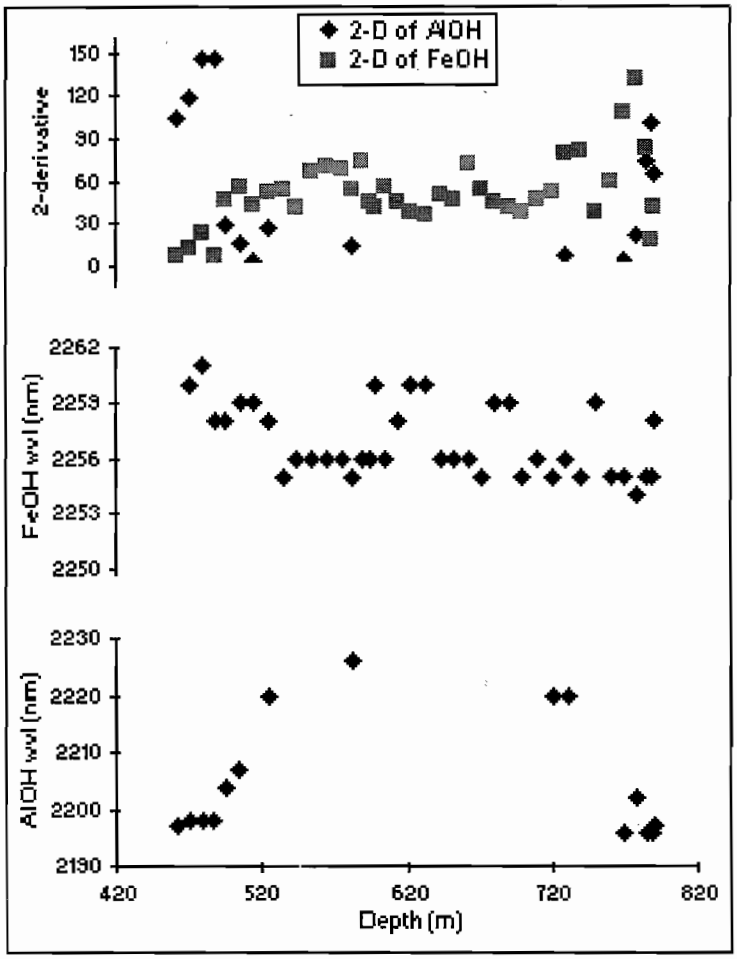

Fig. 13
Variations of spectral parameters with depth for MAC 19. Second derivatives of AlOH < 0 indicate no detectable mica and are not plotted. Similarly, only the samples with measurable AlOH wavelengths are plotted.

Mount Black Volcanics: Preliminary volcanic facies and alteration, petrography and geochemistry

Cathryn C Gifkins
Centre for Ore Deposit and Exploration Studies, Geology Department, University of Tasmania

Introduction

The Mount Black Volcanics (MBV) are located to the east of Rosebery, in the Mount Read Volcanics, western Tasmania. Occurring between the Henty Fault Zone and the Rosebery–Hercules sequence, the MBV extend northwards from Mount Read to Pieman Road and Lake Rosebery (Fig. 1). Road cuttings along the Murchison highway and the Mount Black summit 4WD track provide a good opportunity to examine a variety of volcanic facies and alteration assemblages within the MBV. As part of an on going Phd project and in conjunction with the AMIRA project P439, 132 samples were collected along the Mount Black summit and Murchison highway sections during 1995 and 1996. From these 67 thin sections were prepared for petrography and 52 samples were analysed for major and trace elements using XRF whole rock geochemistry and ICPMS.

This paper aims to provide descriptions of the volcanic facies and alteration assemblages observed in the MBV and the Sterling Valley Volcanics (SVV). These descriptions are based on the results of detailed field and petrographic examinations and preliminary analysis of the geochemical data. The paper is organised into a regional description of the MBV and the SVV, followed by detailed facies descriptions, including both the petrography and geochemistry. The final section is devoted to the main alteration assemblages, a description of their distribution and style and related geochemistry. All this work is complimented by a series of figures which show the facies in association with alteration assemblage, alteration index and mobile element chemistry.

Previous work in the MBV and SVV has been limited and is reported by Allen (1994), Allen (1995), Anderson (1972), Brathwaite (1969), Gifkins et al. (1996a), Gifkins (1995), Green (1983(, Lees (1987) and Warmeant (1990).

Geology of the Mount Black Volcanics

The rocks of the MBV are part of the northern Central Volcanic Complex (CVC). They are a several-kilometre-thick package of feldspar-phyric massive, flowbanded and flow-brecciated lavas and sills of generally dacitic composition with minor rhyolite and andesite. The western side of Mount Black is dominated by flowbanded and brecciated rhyolites and pumice-rich rhyolitic breccias intruded by thick feldspar-hornblende porphyritic dacitic sills. Conversely the eastern side of Mount Black is dominated by massive red-brown to grey feldspar-hornblende porphyritic dacitic to andesitic lavas and sills with minor rhyolite. Variable proportions of pumiceous sediment, volcaniclastic breccias, sandstones and siltstones are also present throughout the Mount Black Volcanics.

Conformably underlying the MBV to the east is a package of basalts to andesites, locally known as the Sterling Valley Volcanics. These are composed of numerous monomictic and polymictic basaltic and andesitic mass-flow breccias, basaltic to dacitic lavas and sills and rare tuffaceous siltstones. The Sterling Valley Volcanics and Mount Black Volcanics are in stratigraphic contact and appear to petrographically and chemically related. The conformable and gradational nature of this contact allows the rocks

exposed in these two groups to be discussed as a single package of volcanics.

Both the MBV'S and SVV have been intruded by a series of mafic dykes known as the "Henty Dyke Swarm".

The Rosebery–Hercules sequence which unconformably underlies the Mount Black Volcanics to the west and hosts both the Rosebery and Hercules ore deposits, dips and faces towards the east. The Mount Black Volcanics also dip and face east at their western margin, however towards the east they dip and face west. The Sterling Valley volcanics dip steeply west, and also face west.

These changes in structural orientation are interpreted to indicate that the Rosebery sequence and western Mount Black Volcanics are the eastern limb of a NNE trending regional anticline which extends for 20 km from Hercules in the south to Pinnacles in the north (Fig. 1). The Mount Black Volcanics represent a large open syncline. The Sterling Valley Volcanics occur in the core and on the western limb of a regional anticline which extends from the north of Mount Block and is truncated to the south by the Henty Fault. This suggests that the Sterling Valley Volcanics are the lowest exposed stratigraphic component of the CVC.

Two major faults; the Mount Black Fault and the Henty Fault; form the boundaries of the package of volcanics being described here. The Mount Black Fault on the western side of the package can be seen in drill core, but is not exposed in either of the sections. It is a brittle thrust fault forming the contact between the quartz-phyric volcaniclastic mass-flow units of the Rosebery–Hercules Hangingwall and the feldspar-phyric Mount Black Volcanics. A 2–10 m zone of intense ductile shearing and silicification exists either side of the brittle fault.

The Henty Fault which binds the eastern margin of the Mount Black–Sterling Valley volcanic package is a complex relatively brittle fault forming the contact between the Sterling Valley Volcanics and the Farrell Slates. It is a major reverse fault dipping westward under the Sterling Valley Volcanics and comprises several metres of intensely broken and sheared, quartz veined rock within a strong zone of silicification. The fault is slightly oblique to bedding in both cross section and map view. In map view (Fig. 1) this discordance is reflected in the southward truncation of both the Farrell Slates and Sterling Valley Volcanics. This structural discordance and change in facies either side of the fault indicate that there has been major displacement on the Henty Fault. The original stratigraphic relationships between the Rosebery–Hercules hangingwall and the MBV and the SVV and Farrell Slates are uncertain.

Volcanic facies

The principal volcanic facies within this package vary in composition from rhyolitic to basaltic and include both coherent lavas and sills and volcaniclastics. The distribution and contact relationships of these facies can be quiet complex reflecting the high proportion of intrusive bodies. These intrusions, with the exception of the basaltic dykes associated with the Henty Dyke Swarm, are interpreted to be shallow sills which were coeval with the continuing volcaniclastic activity and extrusion of lavas. The lavas and intrusions have similar mineralogy, geochemistry and primary volcanic textures and are best differentiated based on their contact relationships. It is also worth noting that it is a reasonable possibility that many of these coherent bodies may be both partly intrusive and vary along strike to extrusive.

The distribution of the facies discussed here can be observed in Figures 2 and 3, where a schematic graphic log of the facies has been constructed on a west to east cross-section for the Mount Black summit track and the Murchison Highway respectively. This log is not a stratigraphic log, structural complications have not been removed.

Feldspar-phyric, spherulitic, rhyolites, rhyodacites and autobreccias

Samples MB96-35, MB96-39, M37, M78, M103, M105, M112, M116, MB96-41(pumiceous autobreccia)

The feldspar-phyric spherulitic rhyolites and rhyodacites are commonly massive to flowbanded and flow-brecciated. Spherulites consist of radial bundles of alkali feldspar and/or quartz crystal fibre's

Figure 1
Mount Black and Sterling Valley volcanics showing samples MB96-35 to MB96-46 along the Mount Black summit track and M-series samples along the Murchison Highway.

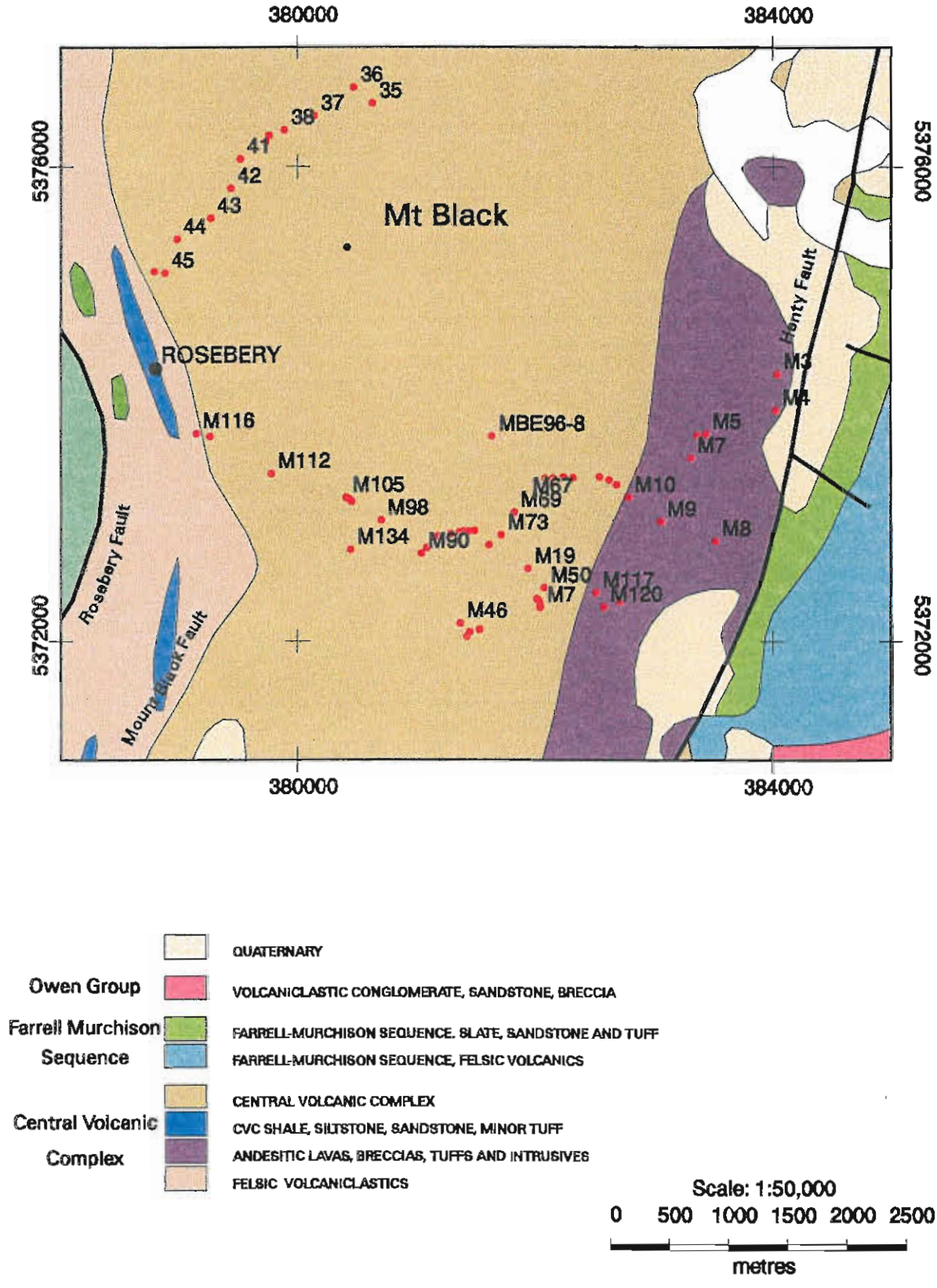

Volcanic facies


Plagioclase porphyritic rhyolite or rhyodacite


Crystal-rich plagioclase porphyritic rhyolite or rhyodacite


Plagioclase±hornblende porphyritic dacite


Crystal-rich plagioclase porphyritic dacite


Aphyric or weakly plagioclase porphyritic andesite


Plagioclase porphyritic andesite


Basalt


Feldspar-phyric sandstone


Crystal-rich feldspar-phyric sandstone


Breccia


Spherulites


Flow banding


Pumice clasts

Alteration assemblages


Chlorite±magnetite

Sericite


Feldspar-quartz

Sericite+chlorite


Epidote±chlorite


Silica


Feldspar alteration in or around clasts


Patchy chlorite alteration


Albite replacement of plagioclase crystals


Chlorite replacement of phenocrysts


Carbonare alteration


Patchy feldspar+quartz alteration


Patchy epidote alteration

Key to figures 2 and 3; volcanic facies symbols and alteration assemblages.
Alteration index: $\frac{100\ (K_2O + MgO)}{(K_2O + MgO + Na_2O + CaO)}$ (Ishikawa et al, 1976).

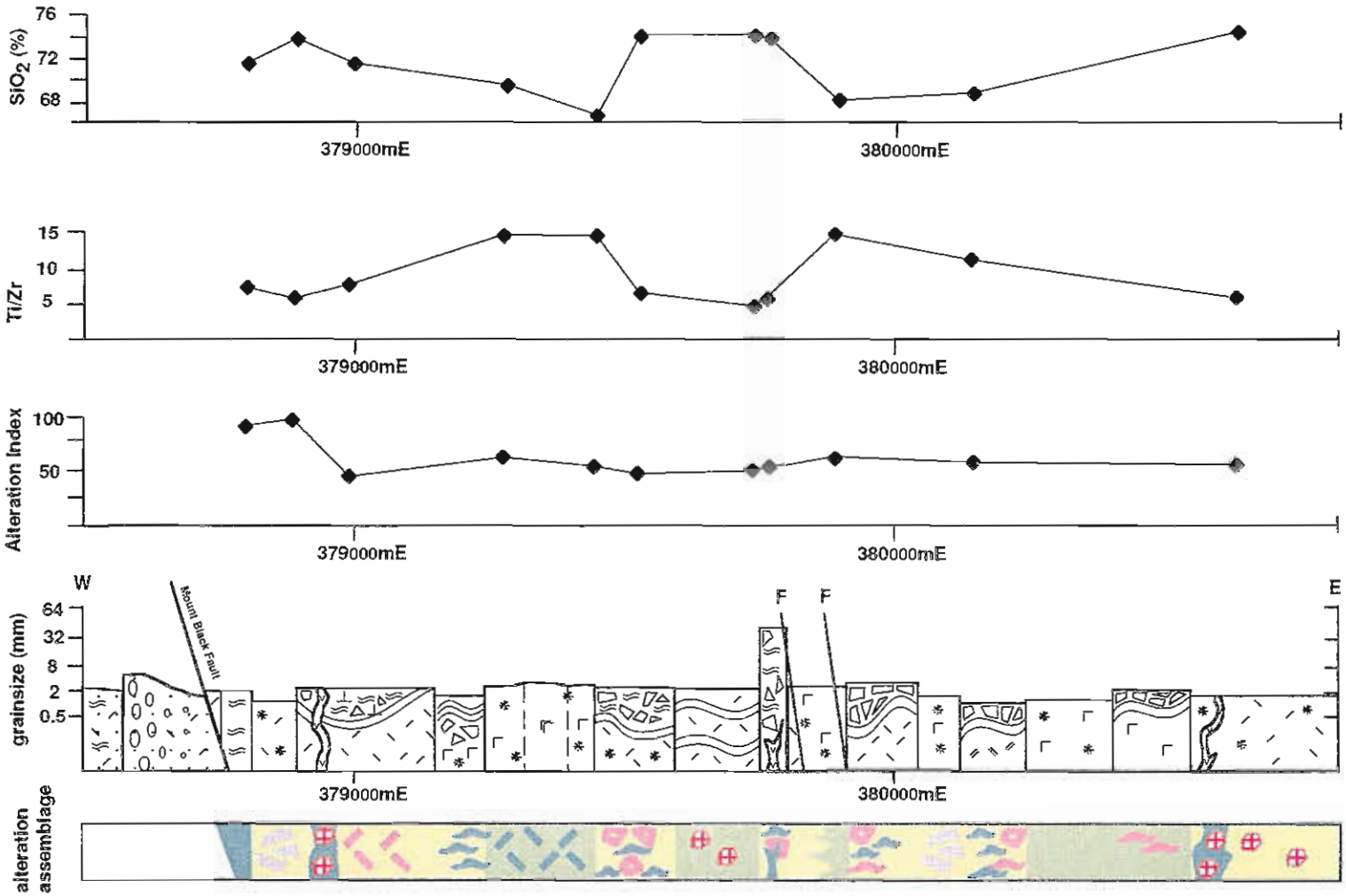

Figure 2; Mount Black summit section. Graphic log of the distribution of volcanic facies, alteration styles, Alteration index (Ishikawa, et al 1976), and major element geochemistry. See key to facies symbols and alteration styles.

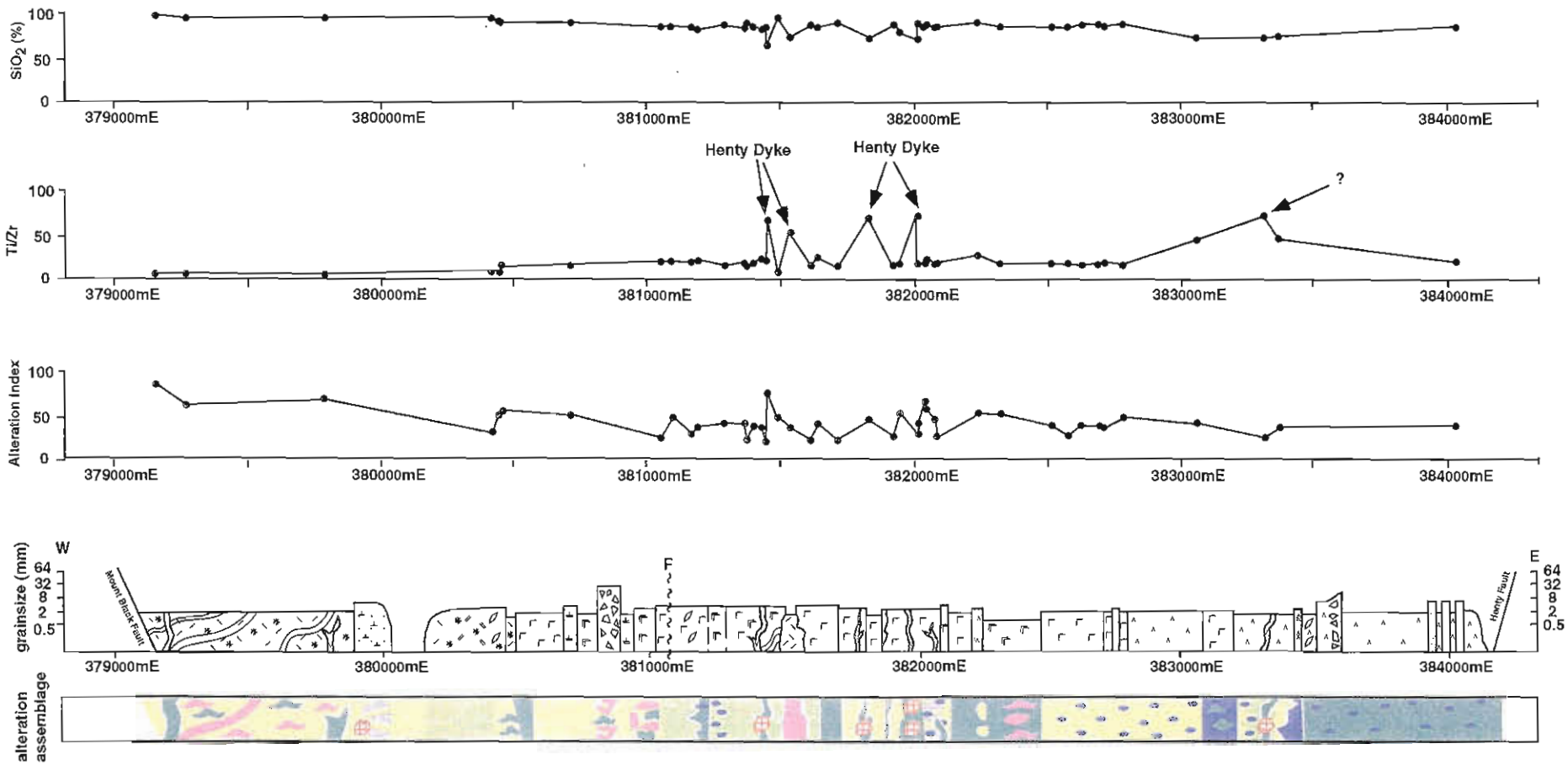

Figure 3; Murchison Highway Section; Mount Black Volcanics and Sterling Valley Volcanics, volcanic facies, alteration styles, Alteration Index and major element geochemistry plotted along the traverse. See key for facies symbols and alteration assemblages.

(McPhie et al., 1993). Most of the spherulites visible in these rocks have been partially or completely recrystallised during the subsequent metamorphic event. These rhyolites and rhyodacites are densely microspherulitic and in outcrop appear blocky with a fine sandy texture. The rhyolites typically have 3–10% euhedral plagioclase phenocrysts of 1–2 mm in diameter and 1–3% quartz phenocrysts. In thin section the flowbands are defined by coarse granophyric textured layers and microspherulitic-rich or micropoikolitic-like layers. The micropoikolitic texture or 'snowflake texture' consist of small irregular quartz crystals which completely enclose very fine laths of feldspar (Lofgren, 1971). The presence of spherulites and micropoikolitic textures which are the product of high temperature devitrification indicate that these bands were originally coherent volcanic glass (McPhie et al., 1993). There is also a weak alignment of the plagioclase phenocrysts parallel to the flowbanding. Where observed large spherulites (0.5–2 cm) are elongated and aligned in the direction of flow. The morphology of the microspherulites is not always spherical and can be bow-tie shaped. The interstitial originally glassy areas between the microspherulites are now granophyric aggregates of quartz and feldspar and the core of the spherulites are dusted with sericite. The plagioclase phenocrysts often form glomeroporphyritic aggregates in a siliceous groundmass with interstitial carbonate and chlorite. The plagioclase is commonly dusted with sericite or partially replaced by chlorite. Chlorite alteration occurs in the core of some of the plagioclase and not the rims suggesting a chemical zonation in the phenocrysts. The groundmass is generally pervasively weakly sericite altered with patchy feldspar and chlorite±magnetite alteration and rare patchy carbonate alteration. Stronger chlorite alteration occurs along fractures which are related to the later Devonian deformation. The margins of units may be marked by peperite textures, rare inclusions of fine grained buff coloured siltstone which have mixed with the lava as it flowed over or intruded into wet sediment. Clasts of flowbanded and vesicular lava are also rarely included within the massive feldspar-phyric rhyolite bodies.

Associated with many of the rhyolites and rhyodacites are feldspar-phyric autobreccias and hyaloclastite. These are syn-eruptive volcaniclastic deposits formed by passive or non-explosive fragmentation. Autobreccias are the product of flow fragmentation. As parts of lavas that are cooler or more viscous flow, they are subjected to locally higher strain rates (McPhie et al., 1993). They may respond to the stress created by strain gradients by plastically deforming and/or by brittle fragmentation (Cas and Wright, 1987). Hyaloclastite is produced when a hot coherent magma body suddenly comes into contact with cold water or water saturated sediment. As quenching occurs thermal stresses cause contraction of the magma and this may in turn fragment the magma body producing clasts with distinctive curviplanar margins. Aggregates of quench-fragmented debris are often called hyaloclastite (Pichler, 1965; Cas and Wright, 1987; McPhie et al., 1993). The blocks produced by flow brecciation and quenching may be enclosed within the non-fragmented magma, deposited on the flanks of a moving flow, or are free to be redeposited by sedimentary processes.

The feldspar-phyric autobreccias and hyaloclastite deposits in the Mount Black Volcanic package are typically massive, poorly sorted and vary from matrix supported aggregates of rotated clasts to clast supported breccias with jigsaw fit textures. Locally the deposits can be very coarse with 1–2m blocks. The deposits are dominated by non-vesicular massive to flowbanded clasts, however there are examples of pumiceous autobreccia associated with adjacent pumiceous margins of lavas (MB96-41). The pumice breccias are composed of poorly sorted aggregate of plagioclase porphyritic tube pumice, shards and broken angular plagioclase fragments. The close spatial and textural association between the coherent lava, pumiceous lava and pumiceous breccia and the recognition of areas of jig saw fit textured clasts in the pumice breccias has led to the interpretation that the many of the monomictic pumice and/or fiamme bearing breccias on the western side of Mount Black may be highly vesicular autobreccia deposits at the margins of lavas, domes or shallow intrusions similar

to those in the Kuroko district, Japan (Gifkins et al., 1996b). The margins of many of the flowbanded rhyolites and rhyodacites contain highly vesicular or pumiceous bands which have undergone strong compaction and phyllosilicate alteration producing chlorite rich foliated bands and lenses. The pumice-breccias have also undergone compaction and commonly contain streaky phyllosilicate-rich fiamme.

Aphyric, rhyolite lava and pumice breccia

Sample MB96-45 (lava) and MB96-46 (pumice breccia).

The fine grained aphyric rhyolite lavas are rare and occur mostly in the western part of the MBV. They may contain weak flowbanding or be vesicular however they are commonly massive uniform bodies which are pervasively altered. The associated pumice and shard-rich breccia, MB96-46 which outcrops on the Mount Black summit track, contains large chloritic wisps or fiamme which are interpreted to be compacted and altered pumice clasts greater than 1 cm in length. There are two possible interpretations of this pumiceous unit: (i) that it represents a pumiceous autobreccia at the base of the overlying aphyric rhyolite lava or (ii) that it is the result of a pyroclastic eruption of aphyric magma immediately prior to the passive effusion of the overlying lava body.

Feldspar-hornblende porphyritic, spherulitic dacites

Samples MB96-38, MB96-42, MB96-43, M10, M24, M25, M26, M46, M73, M98.

Feldspar-hornblende phyric, spherulitic, dacites are massive, blocky, medium brown with 5–10%, 1–2 mm euhedral plagioclase phenocrysts and 2–5%, 1 mm prismatic hornblende crystals, rare quartz and accessory sphene. The hornblende phenocrysts are commonly replaced by epidote, magnetite or chlorite and form 2–6 mm aggregate intergrowths with plagioclase crystals (glomeroporphyritic clusters). These clusters contain interstitial chlorite±magnetite. The plagioclase crystals are dusted with fine grained white muscovite and disseminated epidote. The fine muscovite alteration is concentrated along the crystal cleavage. The groundmass has a fine sandy texture reflecting the high density of microspherulites and/or micropoikolitic quartz. Between the microspherulites and micropoikolitic quartz is fine grained chlorite. The groundmass is pervasively weakly sericite±chlorite altered. The feldspar-hornblende phyric dacites are occasionally flowbanded or contain flow alignment of phenocrysts and often have sharp intrusive contacts.

Vesicular, feldspar crystal-rich dacites

Samples M79, M80, M81, M85, M86, M89, M90A, MBE-4

Feldspar crystal-rich dacites are the dominant facies type in the MBV and SVV. They are typically thick, massive, weakly vesicular and red-brown to grey in colour. They contain 10–25% 1–3 mm zoned euhedral plagioclase phenocrysts which often form glomeroporphyritic aggregates upto 5mm in diameter in the siliceous groundmass. The glomeroporphyritic clusters commonly contain interstitial chlorite, magnetite, epidote and sphene and rarely carbonate. Accessory ilmenite which is replaced by leucoxene occurs in the groundmass. The plagioclase phenocrysts are generally partially replaced by epidote, sericite or have secondary feldspar overgrowths. The groundmass is recrystallised granophyric and occasionally contains microspherulites but more commonly contains arcuate perlitic fractures which are defined by secondary minerals (quartz + feldspar or chlorite±epidote), both microspherulites and perlitic fractures reflect the originally glassy nature of the groundmass. The cores of the microspherulites contain blebs of clear quartz about 100μ in diameter. Some samples display a continuous gradation from microspherulites to 'micropoikolitic-like' texture in the groundmass. The amygdales are mostly filled with chlorite, calcite and/or granophyric textured quartz and are elongated in the direction of flow indicating that they exsolved prior to final emplacement of the dacite.

Massive, feldspar crystal-poor dacites

Samples M29B, M67, M77, M84, M100

Feldspar crystal-poor dacites are the second most significant facies in the volcanic package. There appearance in outcrop is similar to the crystal-rich dacites, typically massive, blocky and red-brown to grey-green in colour. However the phenocryst population is significantly less averaging 3–8%, 1–1.5mm plagioclase crystals and rare <6mm glomeroporphyritic clusters of plagioclase + chlorite ± magnetite ± quartz. Epidote alteration is localised around these glomeroporphyritic clusters. The groundmass is micropoikolitic and generally weak to moderately pervasively altered. Stronger patchy chlorite±sericite alteration occurs interstitial to the micropoikolitic quartz. Micropoikolitic quartz is generally 200μ across and contains micro-feldspar laths and blebs and fine grained white muscovite. Sample M100 is good example of the gradational change between microspherulites through to 'micropoikolitic-like' quartz. It contains abundant close packed spherulites which show progressive degrees of recrystallisation to quartz and feldspar. Commonly arcuate perlitic fractures are highlighted by dark phyllosilicate-rich alteration assemblages in many of these dacites.

Feldspar porphyritic, coarse grained, andesites and basalts

Samples M5, M7, M29A, M9

Andesitic to basaltic lavas and sills are coarse grained (2–2.5mm), blue-green and massive, with 10–20% plagioclase and minor hornblende phenocrysts and abundant fine grained opaques. The hornblende is largely replaced by epidote and lesser biotite and chlorite. The plagioclase crystals are partially replaced by sericite±epidote or chlorite. The dark groundmass is composed of interlocking needles of plagioclase and hornblende or actinolite ("felt textured") and is strongly pervasively altered by chlorite±magnetite and epidote. Sample M5 contains irregular clasts of silicified diffusely laminated and massive siltstone which were probably incorporated into the andesite as it flowed over or intruded into a siltstone unit. As only the lower contact was observed the distinction between extrusion or intrusion can not be made.

Fine grained, aphyric andesite

Samples M3A and M6.

Fine grained aphyric andesites are limited to the eastern portion of the Mount Black Volcanic package. They form massive, strongly weathered, dark green outcrops. In thin section fine interlocking laths of feldspar and actinolite are visible. They are pervasively altered by epidote, chlorite and sphene.

Aphyric, weakly vesicular basalt

Fine grained samples M69B, M39; coarse grained M30, M34, M42

The aphyric equigranular weakly vesicular basalts are generally fine to medium grained, massive and often form irregular branching dark green bodies, rarely more than one metre wide. They have sharp irregular contacts interpreted to be intrusive and have been previously described as basaltic dykes of the *Henty Dyke Swarm*. They commonly contain calcite–chlorite–quartz filled amygdales. They are intensely chlorite ± magnetite ± carbonate altered with overprinting patchy epidote. The groundmass is "felt textured" interlocking feldspar laths and prismatic chlorite altered needles.

Feldspar crystal-rich sandstone

Sample M19

The crystal-rich sandstones are one of the most common clastic units within the MBV package. The total crystal content averages 30% and in hand-specimen the distribution of the crystals appears uneven. The outcrop is usually a blue-grey to buff coloured. The crystal-rich sandstones are composed of predominantly euhedral and angular plagioclase crystal fragments and lesser proportions of broken quartz crystals, fine plagioclase porphyritic pumice clasts and dense glassy lithics. The crystal-rich sandstones, are commonly massive bodies upto tens of metres in thickness and are occasionally observed to be normally graded. This is typical of deposits formed by mass transport processes, ie. mass flows.

Feldspar-porphyritic pumice-rich rhyolitic to rhyodacitic breccias, sandstones and siltstones

Samples MB96-40 (breccia), MB96-44 (sandstone), MX (siltstone)

Pumiceous feldspar porphyritic rhyolitic breccias, sandstones and siltstones are dominated 3–10% plagioclase porphyritic pumice, plagioclase crystal fragments and shards. They also contain dense clasts which include; dense glassy fragments which are often spherulitic and flowbanded to massive plagioclase porphyritic and aphyric rhyolite. Plagioclase phenocrysts and crystal fragments are dusted with sericite but only weakly altered. The groundmass has a granophyric texture and is moderately pervasively sericite altered with patchy chlorite±magnetite and fracture controlled chlorite alteration. The breccias in handspecimen contain dark lenticular patches, 1–5 cm long aligned roughly in the plane of regional bedding. These lenses comprise of compacted pumice which resemble fiamme in welded ignimbrites. These phyllosilicate-rich (chlorite–sericite) lenses are set in paler quartz–feldspar rich domains. The quartz-feldspar domains contain relic uncompacted tube pumice indicating that the deposits were originally unwelded and that the feldspar alteration occurred very early, prior to compaction. In areas of strong deformation the flattened tube pumices become stretched and transposed in the cleavage resulting in a foliated fabric which resembles eutaxitic texture in welded primary pyroclastic deposits (Allen, 1988).

On an outcrop scale the breccia deposits are normally graded with sharp bases and finely stratified tops suggesting deposition by mass flow. The sandstones are massive to diffusely bedded and may represent the tops of unrecognised pumice-rich breccias or reworked pumiceous deposits. The tuffaceous siltstones are commonly siliceous, pale grey to buff coloured and weakly laminated or cross bedded. Sedimentary structures within the siltstones are typical of turbidite deposits and indicate the below wave base environment of deposition for parts of the Mount Black Volcanics.

Polymictic and monomictic andesitic to basaltic breccias and sandstones

Sample MB96-8 (andesitic breccia) M60 (andesitic sandstone)

The mafic breccias and sandstones vary from monomictic to polymictic and comprise of angular, feldspar-hornblende porphyritic lava clasts ranging from basaltic to dacitic in composition. The clasts range in texture from highly vesicular or scoriaceous to dense quenched lava, trachytic clasts and coarsely porphyritic clasts. These deposits also contain abundant angular and broken feldspar crystals and very rare quartz fragments in a chlorite-rich matrix. In drill core they are normally graded thick deposits suggesting that they were deposited by mass flow (Allen, 1995). Extensive moderate to strong pervasive chlorite±magnetite and epidote alteration and patchy sericite alteration occur in the mafic volcaniclastic deposits.

Primary geochemistry

The entire Mount Black Volcanic package has undergone regional Greenschist facies metamorphism and variable degrees of hydrothermal alteration (McNeill and Corbett, 1989). Under metamorphic conditions the least mobile elements are most likely to be Ti, Zr, Nb and the rare earth elements (Whitford et al., 1989). Rocks which have been subjected to hydrothermal alteration may show substantial mobility of most elements although Ti, Zr, Al and the heavy rare earth elements appear to remain essentially immobile (McLean and Barett, 1993). Figure 4 shows a number of plots for the trace element data analysed from Table 1. Essentially they define linear trends with only minor scatter. Some of the scatter observed is due to the inclusion of the Henty Dyke suite into the data set rather than mobility of Zr or Ti. Y does however appear to be partially mobile with a broader scatter noticeable in the Y versus Zr plot. The option that Zr is mobile can be eliminated as the Nb versus Zr plot shows that Zr is immobile. Hence the immobile elements Ti, Zr and Nb and relatively immobile Y can be used as a guide to the primary volcanic compositions. A plot of Zr/TiO_2 versus Nb/Y (Fig. 5) for the analysed samples

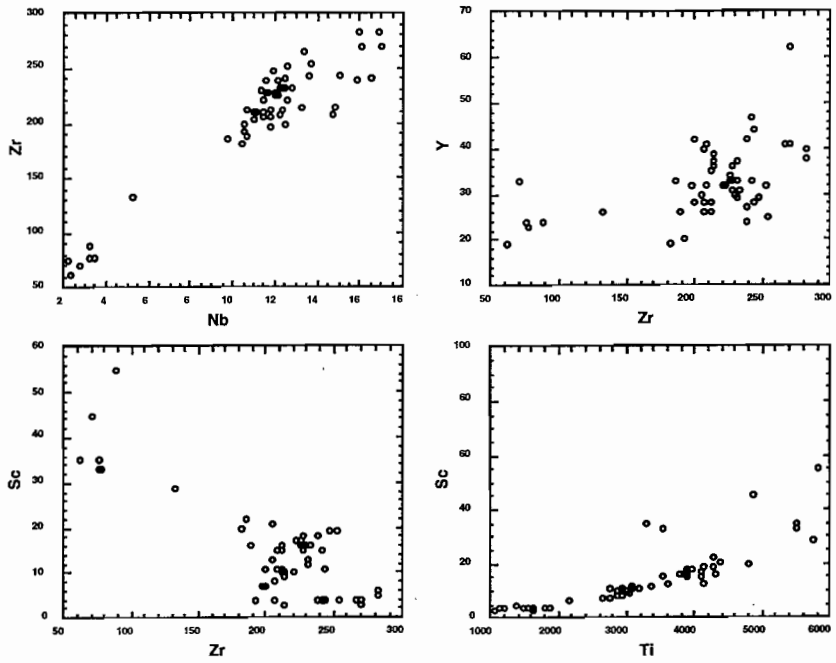

Figure 4: Plots of trace element data for the Mount Black Volcanic package including samples of the Henty Dyke Swarm. See table 1 for trace element data.

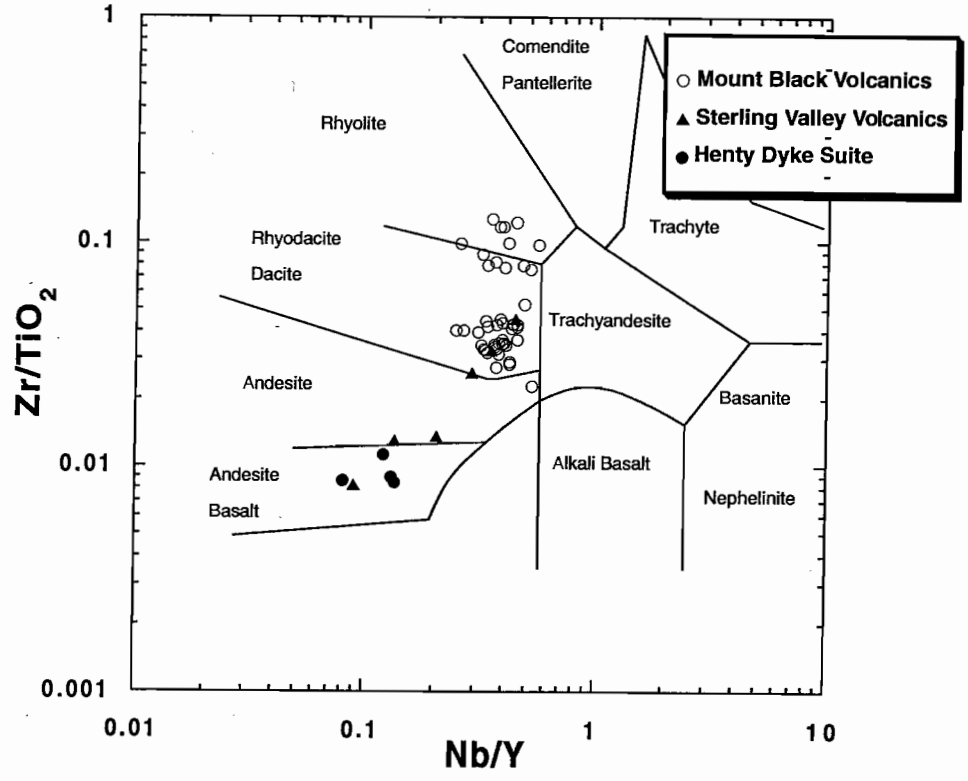

Figure5: Plot of Nb/Y versus Zr/TiO2 (after Winchester and Floyd, 1977) for the Mount Black Volcanic package.

indicates that the Mount Black Volcanic package spans a broad range of compositions from basalt to rhyolite, while the Henty Dyke suite is composed only of basalts. The Volcanic package generally shows a linear trend of increasing TiO_2 with decreasing SiO_2 (Fig. 6) which suggests that the silica mobility has been quiet limited. However the percentage of SiO_2 of many of the samples is higher than would be predicted for the composition according to the Ti/Zr ratios. Such that many of the dacites have SiO_2 contents over 68% which would suggest that they were rhyolites. In handspecimen the samples often appear silicified and this may account for the apparent increase in the silica content of many of the Mount Black samples.

The Mount Black Volcanics have petrographically been divided into five broad facies which can be described now in terms of their geochemistry:

1. The rhyolite and rhyodacites are typified by very low (<0.5%) TiO_2, low Ti/Zr ratios of 5–8 and high silica (71–78% SiO_2). The rhyolites and rhyodacites of the Mount Black package show affinities with the Suite I Crawford et al (1992). They have silica values greater than 58% and Ti/Zr ratios between 5 and 35. However the low, medium or high K affinintes of the any of the Mount Black package have not been determined due to the high mobility of K_2O. Figure 7 shows the broad scatter of K_2O versus SiO_2.
2. The feldspar-hornblende dacites are characterised by moderate TiO_2 values (0.44–0.53%) , moderate Ti/Zr ratios of 13–15 and high silica 66–70% SiO_2. These rocks share affinities with Suite I and Suite II rocks of Crawford et al. (1992). They have higher P_2O_5 contents than the rhyolites, rhyodacites and feldspar-porphyritic dacites.
3. The crystal-poor dacites also have moderate TiO_2 values between (0.5–0.6%) and Ti/Zr ratios between 13–17. The SiO_2 is 67–68%.
4. The crystal-rich dacites have moderately high TiO_2 (0.63–0.72%) and Ti/Zr 16–19. They have lower silica values than the two other dacite suites around 60–64.5% SiO_2. Both the crystal-poor and crystal-rich dacites are Suite I (Crawford et al., 1992).
5. Only one Mount Black andesite sample was analysed and it has high TiO_2 0.8% and Ti/Zr ratio of 26 however the silica is also relatively high at 70%. From this one sample it is difficult to determine the geochemical characterisitics of the Mount Black andesites and assign them to a particular geochemical suite.

The Sterling Valley Volcanics appear to define a linear trend in composition from basaltic to dacitic. They are comparatively high TiO_2, ranging from 0.6–0.96% and the SiO_2 from 50.5 to 70%. The Ti/Zr ratios vary from 18–46 which overlaps with the MBV but is still significantly lower than the Henty Dyke suite.

The Henty Dyke suite is characterised by high TiO_2 values greater than 81%, Ti/Zr 66–72, low Nb < 3ppm and low SiO_2 49–50%. These are Suite IV rocks of Crawford et al (1992) and are considered to be similar to suprasubduction zone basalts erupted during the early stages of arc splitting and back-arc basin development. Hence the deposition of the Mount Black Volcanic package has been followed by a period of tension and rifting.

Plots of immobile elements in Figure 8, with the exception of Ti/Zr versus Y, show a linear trend which may suggest that the range in compositions from basaltic to rhyolitic in the Mount Black and Sterling Valley volcanics is due to magmatic fractionation of a single parent magma.

Alteration petrography and geochemistry

Devitrification, hydration, hydrothermal and diagenetic alteration, diagenetic compaction and metamorphism have all acted to modify the primary volcanic facies. The characteristics of each of these processes are not satisfactorily understood to be able to infer which process was involved in the changes in chemistry and/or texture evident. No attempt to distinguish between diagenetic alteration, regional metamorphism and hydrothermal alteration will be made. However, the characteristics of each alteration phase will be discussed below. The distribution of the alteration assemblages relative to the principal

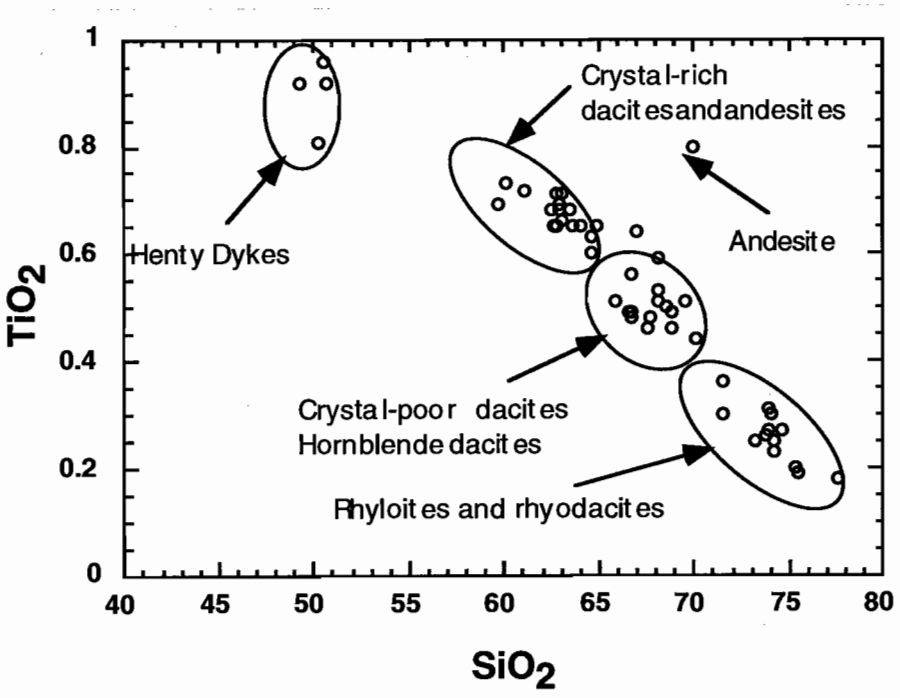

Figure 6: SiO_2 vs TiO_2 for the samples from the Mount Black Volcanic package. Showing the compositional suites based on petrograpgy, Nb/Y versus Zr/TiO_2 and Zr/Ti ratios.

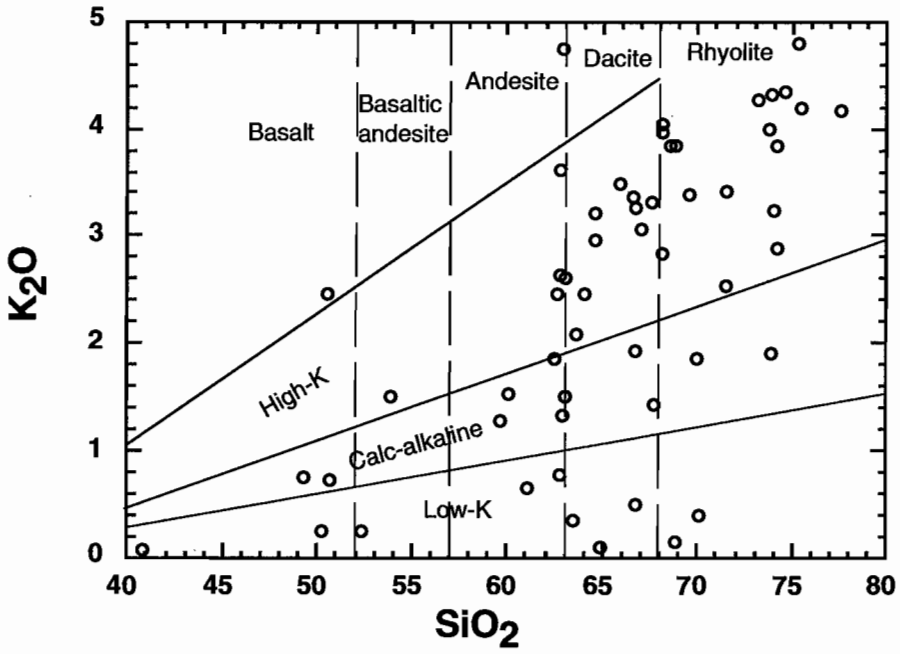

Figure 7: Plot of SiO2 versus K2O for the Mount Black Volcanic package

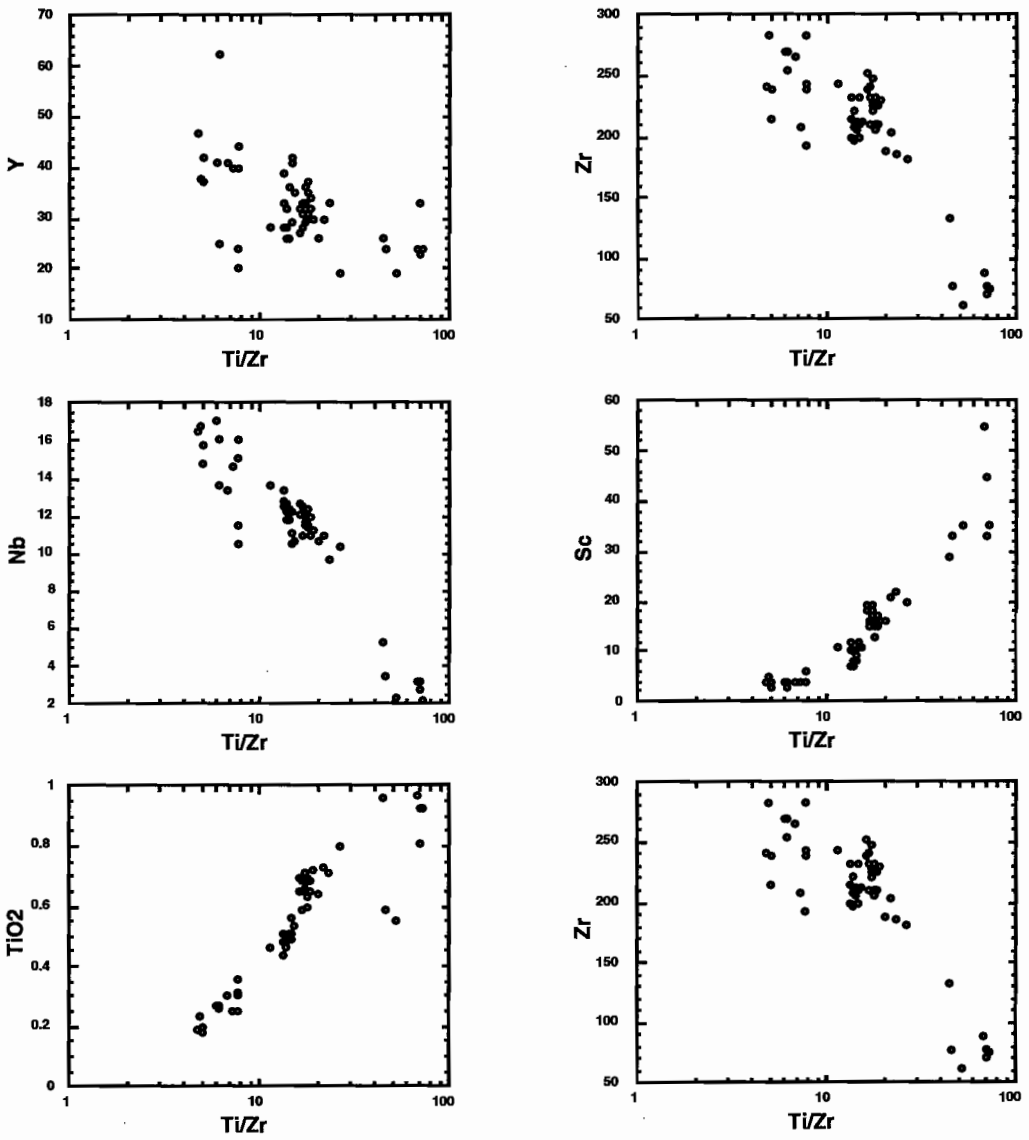

Figure 8: Plots of immobile elements defining a linear trends reflecting possible fractionation from asingle magma.

volcanic facies is presented graphically in figures 2 and 3, which shows the distribution of volcanic facies, their alteration mineralogy and major element chemistry plotted along the path of the traverse. The intensity of alteration is also expressed on these logs as a plot of the Alteration Index (AI) of Ishikawa et al (1976) versus distance.

The Alteration Index [AI = $(100(K_2O+MgO)/(K_2O+MgO+Na_2O+CaO)]$ for the majority of the samples falls in a narrow window of 40–60. Unaltered arc-related rocks are assigned a window of 20–50 (Stolz et al., 1996) which suggests that the bulk of the Mount Black Volcanics are only weakly altered. By comparing the AI to the major element trends it is possible to qualify the alteration mineralogy. Samples with AI values lower than the unaltered window (20–50, high Na_2O and low K_2O probably represent strongly albitised samples. This reflects the decrease in Ca and increase in Na as plagioclase breaks down to form albite. Figure 7 of SiO_2 versus K_2O shows a broad scatter in the K_2O values probably reflecting both primary geochemical variation and mobility of K_2O during the alteration. The common mineral phase in the Mount Black volcanic package which is most likely to contain high K_2O is sericite while low K_2O samples are likely to be dominated by chlorite or albite. Hence samples with high AI and high K_2O are strongly sericite altered and low K_2O samples are chlorite altered. It is important to remember that this alteration index does not account for carbonate alteration and hence strongly carbonate altered rocks will plot in the unaltered window.

The principal alteration assemblages are:

Silicification is weak, widespread and pervasive occurring most notably within the high level intrusions (dacitic sills) of the Mount Black and Sterling Valley Volcanics. Silicification is also associated with major faults and shear zones throughout the sequence.

Quartz-feldspar alteration appears to be the most common throughout the transect. It is regionally extensive and significant. It is characterised by a pink colouration due to the presence of albite dusted with hematite or fine grained muscovite and varies in intensity and texture. Albite may partially replace primary plagioclase phenocrysts or form albite overgrowths around the originally euhedral crystal. Albite also occurs as fine euhedral laths in the groundmass however most commonly the feldspar alteration is fine grained and domainal, forming pink quartz-feldspar rich zones in the groundmass or matrix. The quartz is usually fine grained. It is commonly associated with chlorite-sericite or sericite alteration producing a distinctive pink and green mottled pattern. This occurs in both coherent and volcaniclastic deposits. In the massive, coherent units pink-green alteration is patchy, forming a contrasting green and pink mottled pattern on a scale of 2–20 cm, while in the flowbanded units the pink and green alteration is confined to individual bands where sericite-chlorite defines the originally glassy flowbands and quartz-feldspar the spherulitic flowbands. In many of the autobreccias and hyaloclastite quartz-feldspar alteration forms pink halos or rinds around lithic clasts set in a green sericite-chlorite groundmass. The pumice-rich units are also pink-green altered, with original pumice textures being preserved in the pale quartz-feldspar altered domains while in the sericite-chlorite domains only the porphyritic nature of the original pumice clasts can be determined. Quartz-feldspar is also a very common vein assemblage, particularly on the western side of Mount.

Hematite occurs dominantly as fill in fractures and replaces existing minerals most notably magnetite.

Muscovite is one of the most common minerals in these rocks and is probably the result largely of the metamorphism rather than hydrothermal alteration. Fine grained white muscovite is a pervasive weak disseminated phase in most of the volcanic package. Commonly fine grained muscovite dusts or partially to completely replaces the primary plagioclase crystals. It also rims feldspar phenocrysts, spherulites and micropoikolitic quartz. Although this alteration phase is widespread in the Mount Black and Sterling Valley Volcanics it is rarely strong enough to mask primary volcanic. Muscovite also commonly forms along cleavage and fracture surfaces.

Sericite–quartz–chlorite±carbonate alteration

occurs in coherent flowbanded lavas and sills, autobreccias, hyaloclastite and pumiceous breccias. Pale green variably silicified and chloritised, it is often non-homogenous alteration producing patches or lenses of dark green chlorite–sericite in a paler quartz-rich composition. These dark lenses typically form in pumiceous debris with carbonate–sericite altered feldspar phenocrysts but they can also form in individual flowbands of a coherent unit or the flowbanded clasts of autoclastic deposits. This is common in the Mount Black rhyolites.

Sericite–chlorite alteration is pervasive in the dacitic to basaltic coherent units. Weak pervasive chlorite–sericite±magnetite alteration occurs in the groundmass of feldspar–hornblende dacites of the Mount Black Volcanics while more intense chlorite–sericite alteration is common in the mafic dykes of the Henty Dyke Swarm. Partial to complete pseudomorphing of the ferromagnesian phases by chlorite is also common. In the more rhyolitic units sericite–chlorite alteration tends to be patchy set in quartz-feldspar rich domains. Within the chlorite–sericite rich domains the phenocrysts are preserved but other primary volcanic textures are largely destroyed.

Carbonate alteration is fine grained, either disseminated, partially replacing or rimming feldspar phenocrysts as well as occurring as vein and vesicle fill material. Carbonate alteration is generally weak, however more intense carbonate alteration often masks the presence of primary phenocrysts leaving a fine grained massive homogenous pale grey rock. It is often observed to be moderately strong in mafic dykes and decrease in strength in the wall rock away from the dyke.

Chlorite alteration has more than one recognisable phase. In outcrop and thin section at least two types of chlorite can be determined. A dark blue-green chlorite ± magnetite and paler brown-green chlorite. The dark chlorite ± magnetite alteration is very widespread occurring in almost all units in a number of different forms. Most commonly as patchy to pervasive disseminated fine grained aggregates in the groundmass of the rocks throughout the volcanic package. It also occurs commonly as fibrous and fine grained material interstitial to the crystals in glomeroporphyritic clusters and between microspherulites and micropoikolitic quartz in the groundmass of coherent lavas and sills. It can rim individual feldspar phenocrysts in many of the coherent units. In the hornblende porphyritic rocks chlorite ± magnetite commonly pseudomorphs the hornblende crystals. Less commonly chlorite ± magnetite alters the primary plagioclase crystals, often only replacing the core of zoned crystals or altering along the crystal cleavage. It occurs as pervasive fine grained aggregates between the feldspar and hornblende laths in the basalts of the Sterling Valley Volcanics. Chlorite -rich assemblages also commonly fill vesicles or vugs. Chlorite ± magnetite occurs in the pumice-rich volcaniclastics as styolitic textures parallel to the compaction foliation. Chlorite alteration halos are also associated with mafic dykes and sills and with brittle fractures and faults throughout the region. Chlorite commonly highlights both early syn-volcanic fractures, ie, perlitic fractures, and later hydraulic and tectonic fractures. The magnetite associated with this alteration phase occurs as blebs or euhedral pseudomorphs in the groundmass. These blebs are often concentrated along grain boundaries.

The brown-green chlorite appears to be an earlier phase regularly being overprinted by the blue-green chlorite±magnetite. It is fine grained and disseminated and often associated with weak sericite alteration.

Chlorite–carbonate±sericite alteration is most common as vesicle fill, hydraulic fracture or vein assemblages. It also occurs as moderately strong pervasive alteration in the basaltic lavas, sills and dykes of the Sterling Valley Volcanics and the Henty Dyke Swarm.

Epidote alteration is largely associated with the more basic rocks of the Mount Black volcanics and the Sterling Valley Volcanics. It completely replaces hornblende and partially alters primary plagioclase. It also occurs as weak fine grained irregular patches in the groundmass of many of the coherent dacites, andesites and basalts. Epidote filled fractures are less common.

Sphene is a weak alteration phase in fine grained irregular patches which often concentrate along grain boundaries. Sphene is commonly replaced by leucoxene.

Discussion

The MBV and SVV are a conformable suite of rocks which span a broad range of compositions from basaltic to rhyolitic. This range of primary compositions shows a linear trend and may reflect the magmatic fragmentation of a single parent magma. This would imply that the SVV, which are at the stratigraphic base of the sequence, were erupted first as a series of basaltic lava flows and associated volcaniclastic breccias. As the parent magma fractionated more silicic volcanics were erupted. These were dominated by the MBV dacites and rhyolites. Post-dating the deposition of the MBV and SVV was the intrusion of the basaltic dykes of the Henty Dyke Swarm.

The present alteration assemblages reflect the combined effects of different post-depositional processes — devitrification, hydration, hydrothermal and diagenetic alteration, diagenetic compaction and metamorphism — on the primary mineralogies and textures. Thus the composition and texture of the volcanic facies evolves by a series of steps, however the steps are not necessarily discrete and many overlap making the recognition of individual phases complicated. Despite the complex series of steps, the current mineral assemblage in many of the volcanics reflects primary variations in composition. The silicic volcanics are dominated by sericite > chlorite > feldspar-rich alteration assemblages while more mafic rocks are typically chlorite > epidote >carbonate altered.

Work to date on the petrology and geochemistry of the alteration in the Mount Black Volcanic package suggests that the majority of the package is weakly altered. Alteration assemblages are dominated by chlorite ± magnetite, sericite + chlorite, albite–quartz, weak silicification and epidote ± chlorite. Although fine grained white muscovite (sericite) is one of the most common and widespread secondary minerals in these rocks it is a typical product of Greenschist facies metamorphism and diagenetic alteration of silicic rocks. The widespread occurrence of weak disseminated sericite suggests that it is the product of a regional event rather than localised hydrothermal activity. Furthermore from the geochemistry it is observed that for a large proportion of the rocks analysed the amount of potassium compared with that in unaltered arc related rocks does not show a significant increase. Hydrothermal sericite alteration is normally associated with the addition of potassium and this only evident in the more intensely altered samples.

Less extensive alteration phases include carbonate alteration which usually occurs as disseminated patches of replaces primary plagioclase crystals. The intensity of the carbonate alteration is not expressed in the AI however weak increases in the whole rock CaO and Fe_2O_3 are observed. Hematite is strongly fracture controlled and appears to be late in the alteration history.

Many of the alteration styles in the rhyolites to dacites are texturally enhancing. The patterns of permeability and competence contrasts in the silicic rocks have a marked effect on the alteration patterns. Both chlorite and sericite dominated alteration assemblages appear to be strongly controlled by fluid pathways, except in areas of intense alteration. The dominant fluid pathways include volcaniclastic deposits, originally glassy bands in flowbanded lavas, insitu breccia (autobreccia and hyaloclastite), perlitic fractures, hydraulic breccias and fractures or joints. This permeability controlled alteration enhances the both primary and secondary textures in the volcanics. For example chlorite±sericite assemblages commonly occur in perlitic fractures in the groundmass of the massive rhyolite and dacites while the enclosed core has been altered by paler quartz–feldspar ± sericite ± carbonate. The alteration has enhanced the fractures creating a contrast in composition and colour between the fractures and the areas that they enclose. The more advanced that the prominent fracture controlled alteration becomes the more a clastic texture is resembled where pale round clasts are supported in the dark chloritic–matrix.

However, the albite–quartz dominated alteration

assemblage is not as clearly controlled by the permeability. It forms irregular patches or domains in both the volcaniclastic and coherent facies but is usually more in intense in the volcaniclastics. There is often a marked increase in the amount of albite in the autobrecciated facies of a lavas compared with the massive coherent body of the flow.

The alteration of the andesites and basalts is more uniformly pervasive although varying in intensity. They generally have pervasively altered groundmass and partial to complete replacement of the primary phenocrysts. Although they appear intensely altered, the AI suggests that they are relatively unaltered and the present mineral assemblage, plagioclase + chlorite + epidote ± sphene ± actinolite may be largely the result of the Greenschist facies metamorphism.

Destruction of primary volcanic textures by the post depositional processes occurs in areas of intense alteration, clearly showing the effects of hydrothermal alteration, either early in the geological history or late hydrothermal alteration related to the over-printing deformational features such as hydraulic breccias and fractures. Although most of the Mount Black Volcanic package is weakly altered there are areas of more intense alteration. Alteration intensity appears to be strongest near the faulted contact with the Rosebery–Hercules hangingwall. Other areas with high AI values correspond to samples of the Henty Dyke Swarm which are strongly chlorite + carbonate ± magnetite altered.

Future work

This report has presented the preliminary geochemical analysis and further work will be continued on the primary volcanic geochemistry and on the geochemistry of the principal alteration assemblages. An attempt will be made to better understand the changes in whole rock geochemistry in relation to the petrography of the alteration styles, hence to identify the geochemical effects of the defined alteration assemblages. It is hoped that by defining the chemical changes which occur we can distinguish between diagenetic alteration, regional metamorphism and hydrothermal alteration.

References

Allen, R.L., 1995. Geological Transect across the Sterling Valley and Murchison Volcanics, Tasmania. Unpubl Pasminco Exploration Rep.

Allen, R.L., 1994. Volcanic Facies analysis indicates large pyroclastic eruptions, sill complexes, synvolcanic grabens, and subtle thrusts in the Cambrian "Central Volcanic Complex" volcanic centre, western Tasmania. Contentious issues in Tasmanian geology. Ed by Cooke, D.R. and Kitto, P.A. in Geol Soc of Aust Abstracts 39, 31–34.

Allen, R.L., 1988. False pyroclastic textures in altered silicic lavas, with implications for volcanic-associated mineralisation. Econ. Geol. 83: 1424–1446.

Anderson, W.B., 1972. The Mount Read Volcanics in the Rosebery–Tullah area, petrology, geochemistry, and possible tectonic significance. Unpub Hons Thesis, University of Tasmania.

Brathwaite, R.L., 1969. The geology of the Rosebery ore deposit. Unpubl. Phd Thesis. University of Tasmania.

Cas, R.A.F. and Wright, J.V., 1987. Volcanic successions: modern and ancient: a geological approach to processes, products and successions. Allen and Unwin. p487.

Crawford, A.J., Corbett, K.D. and Everard, J.L., 1992. Geochemistry of the Cambrian volcanic-hosted massive sulfide-rich Mount Read Volcanics, Tasmania, and some tectonic aimplications. Econ Geol v.87, 597–619.

Gifkins, C.C., Allen, R.A., Stolz, A.J. and Duhig, N.,1996a. Mount Black to Murchison Gorge: Preliminary volcanic facies analysis and alteration styles. AMIRA Project P439 Report 2, May 1996. Unpubl.

Gifkins, C.C., Allen, R.A. and McPhie, J, 1996b. Fiamme associated with silicic lavas and intrusions.EOS, Transactions, AGU v.77, No.22, p W125

Gifkins, C.C., 1995. Subaqueous silicic volcanism in the Mount Black Volcanics, western Tasmania. AMIRA Project P439 1st report. Unpubl.

Green, G.R., 1983. The geological setting and formation of the Rosebery volcanic-hosted massive sulphide orebody, Tasmania. Unpubl. Phd Thesis, Univ. Tasmania.

Lees, T.C., 1987. Geology and mineralisation of the Rosebery–Hercules area, Tasmania. Unpubl MSc Thesis. University of Tasmania.

Lofgren, G., 1971. Experimentally produced devitrification textures in natural rhyolitic glass. Geol Soc Am Bull. v. 82:111–124.

McLean, W.H. and Barrett, T.J., 1993. Lithogeochemical techniques using immobile elements. Journal of Geochemical Exploration. v.48. 109–133.

McNeill, A.W. and Corbett, K.D., 1989. Geology of the Tullah-Mt Block area. Mt Read Volcanics Project Geological Report 2.

McPhie, J., Doyle, M. and Allen, R.L., 1993. Volcanic Textures: a guide to the interpretation of textures in volcanic rocks. p198.

Pichler, H., 1965. Acid Hyaloclastites. Bull. Volcanol. 28, 293–310.

Stolz, A.J., Large, R. and Duhig, N., 1996. Progress report on the utilisation of the Mount Read Volcanics database. AMIRA Project P439 Report 2, May 1996. Unpubl.

Warmeant, P.J., 1990. The Geology, Geochemistry and Mineralisation of the Mount Black Volcanics. Unpubl. Hons. thesis. University of Tasmania.

Whitford, D.J., McPherson, W.P.A. and Wallace, D.B., 1989. Geochemistry of the host rocks to the volcanogenic massive sulfide deposit at Que River, Tasmania. Economic Geology, v. 84, p1–21.

Winchester, J.A. and Floyd, P.A., 1977. Geochemical discrimination of different magma series and their diferentation products using immobile elements. Chemical Geology, v. 20, p. 325–344.

Table 1. Major and trace element analyses of volcanic rocks from the Mt Black traverse.

	M4	M6	M7	M9	M10	M19	M24	M25	M29B	M3O	M33	M39
SiO2	62.51	53.86	50.66	50.49	65.89	59.68	66.52	67.63	68.15	49.22	62.93	52.39
TiO2	0.68	0.59	0.92	0.96	0.51	0.69	0.49	0.46	0.59	0.92	0.68	0.55
Al2O3	15.66	16.34	18.32	18.39	15.70	16.59	15.30	14.87	14.09	19.56	16.28	14.87
Fe2O3#	6.54	7.79	10.00	10.36	4.70	8.76	4.36	4.33	4.66	11.74	5.83	10.30
MnO	0.10	0.13	0.19	0.16	0.08	0.09	0.06	0.07	0.11	0.18	0.07	0.21
MgO	2.74	6.02	4.38	4.73	1.35	4.58	1.22	1.33	1.66	4.01	3.10	7.29
CaO	4.61	8.73	8.64	6.46	0.77	1.11	2.17	3.04	3.03	7.60	1.15	6.09
Na2O	1.78	2.90	4.03	2.19	3.81	3.30	3.78	3.48	2.70	2.28	1.96	5.07
K2O	1.85	1.50	0.73	2.46	3.49	1.29	3.35	3.30	2.83	0.76	4.74	0.24
P2O5	0.10	0.06	0.10	0.11	0.13	0.12	0.12	0.13	0.08	0.09	0.12	0.05
LOI	3.39	2.47	2.61	3.70	2.88	4.04	1.90	1.43	2.05	4.00	3.23	2.83
Total	99.96	100.39	100.58	100.01	99.33	100.25	99.27	100.07	99.95	100.36	100.09	99.89
S	<0.01	<0.01	0.04	0.09	0.06	0.03	0.11	0.03	0.02	0.03	0.10	0.06
Total C	0.07	0.03	0.03	0.11	0.09	0.08	0.07	0.03	0.04	0.04	0.08	0.14
CO2	0.26	0.11	0.11	0.40	0.33	0.29	0.26	0.11	0.15	0.15	0.29	0.51
Alteration Index	41.8	39.3	28.7	45.4	51.3	57.1	43.4	41.5	43.9	32.6	71.6	40.3
Trace Elements (ppm)												
Sc	17	33	35	29	9	19	8	7	15	33	15	35
V	129	176	292	271	65	159	60	54	114	300	133	201
Cr	43	67	83	61	4	50	5	5	46	107	28	67
Ni	9	34	54	31	2	11	2	2	7	47	5	36
Cu	11	73	163	112	4	6	5	3	17	123	8	48
Zn	104	81	82	118	63	95	47	38	67	104	58	119
As	5	2	10	1	1	3	<1	1	3	2	6	3
Rb	84	69	28	84	97	79	90	88	88	27	224	5
Sr	263	268	385	267	134	115	214	265	233	360	128	228
Y	34	24	24	26	36	32	26	32	28	23	33	19
Zr	225	77	76	132	213	253	206	197	211	78	242	62
Nb	12.0	3.4	2.2	5.3	12.4	12.6	11.8	11.8	11.0	3.2	12.5	2.3
Mo	0.9	0.5	0.9	0.5	0.4	0.4	0.3	0.5	0.3	0.4	0.3	0.6
Ag	0.2	0.1	0.2	0.1	<0.1	0.1	<0.1	<0.1	0.1	<0.1	0.2	<0.1
Cd	0.1	0.4	0.1	0.2	<0.1	<0.1	0.1	0.2	<0.1	0.1	<0.1	0.1
Sb	1.2	1.2	1.5	1	0.4	3.2	0.7	0.7	1.3	0.7	1.8	0.9
Cs	1.32	2.79	1.44	1.56	1.29	4.56	0.93	0.94	1.28	1.07	3.3	0.33
Ba	429	410	285	1017	968	88	755	878	813	423	1175	85
La	40	15	9	15	46	35	30	34	26	8	25	11
Ce	81	33	19	33	81	69	63	73	63	24	61	22
Nd	35	13	10	15	38	31	29	30	26	12	24	12
Tl	0.7	<0.5	<0.5	<0.5	<0.5	<0.5	<0.5	<0.5	0.7	<0.5	1	<0.5
Pb	147	10	16	20	4	6	13	11	10	7	13	5
Bi	0.1	<0.1	<0.1	<0.1	0.3	<0.1	<0.1	<0.1	0.1	<0.1	<0.1	<0.1
Th	13.4	4.39	3.37	6.81	16	15.6	15.3	14	12.6	3.46	15.1	3.97
U	3.24	1.07	1.18	1.86	3.54	3.76	3.56	3.33	3.04	1.14	3.86	1.18

Total Fe as Fe2O3; LOI = loss on ignition; Alteration Index = 100(MgO+K2O)/(MgO+K2O+CaO+Na2O)

Table 1. continued

	M45	M46	M50	M59	M60	M63	M67	M69B	M73	M77	M78	M79
SiO2	60.15	70.08	64.10	63.06	69.98	64.92	67.73	50.29	68.85	66.65	74.18	63.48
TiO2	0.73	0.44	0.65	0.71	0.80	0.65	0.48	0.81	0.49	0.48	<0.5	0.68
Al2O3	16.55	14.49	14.69	16.39	12.65	15.50	15.14	19.29	14.96	16.41	13.65	15.60
Fe2O3#	7.43	3.82	6.41	6.85	5.79	5.64	4.95	11.66	3.93	4.15	2.12	6.03
MnO	0.12	0.06	0.09	0.13	0.10	0.09	0.10	0.21	0.06	0.03	0.02	0.08
MgO	3.08	1.68	2.78	3.00	2.46	3.12	1.58	6.42	2.01	2.03	0.50	2.15
CaO	4.47	1.04	2.96	0.85	0.59	1.30	1.59	0.77	0.34	0.24	0.40	5.59
Na2O	2.58	5.54	2.27	3.44	2.60	5.91	5.09	5.77	6.54	7.07	3.66	3.49
K2O	1.53	0.40	2.45	2.62	1.86	0.10	1.42	0.25	0.16	0.50	3.85	0.36
P2O5	0.08	0.09	0.10	0.13	0.12	0.10	0.12	0.10	0.10	0.12	0.04	0.10
LOI	3.44	2.22	3.64	3.08	2.90	2.51	1.87	4.48	1.97	1.95	1.30	2.38
Total	100.16	99.86	100.14	100.26	99.85	99.84	100.07	100.05	99.41	99.63	99.97	99.94
S	0.11	<0.01	0.01	<0.01	<0.01	<0.01	<0.01	<0.01	<0.01	<0.01	<0.01	<0.01
Total C	0.14	0.04	0.24	0.04	0.04	0.06	0.08	0.06	0.06	0.05	0.10	0.04
CO2	0.51	0.15	0.88	0.15	0.15	0.22	0.29	0.22	0.22	0.18	0.37	0.15
Alteration Index	39.5	24.0	50.0	56.7	57.5	30.9	31.0	50.5	24.0	25.7	51.7	21.7
Trace Elements (ppm)												
Sc	21	7	16	19	20	18	8	45	10	10	4	15
V	158	45	120	149	147	136	61	318	61	63	13	139
Cr	37	5	49	24	227	49	4	11	6	5	5	30
Ni	12	2	10	5	43	10	2	29	3	2	2	10
Cu	52	3	10	6	3	3	4	10	3	2	4	8
Zn	104	64	61	162	147	108	75	280	87	68	32	60
As	4	<1	3	<1	2	2	2	<1	<1	<1	<1	5
Rb	47	21	62	119	69	4	46	19	7	20	118	16
Sr	377	325	192	141	111	160	253	152	147	94	121	406
Y	30	28	31	29	19	27	28	33	26	39	20	31
Zr	204	200	233	247	182	238	207	70	212	214	192	228
Nb	11.0	12.5	12.5	11.9	10.4	12.1	12.2	2.8	11.8	13.3	10.5	11.6
Mo	0.6	0.3	0.3	0.3	1.9	1	0.6	0.4	0.5	0.3	0.2	1
Ag	<0.1	<0.1	0.1	0.1	<0.1	<0.1	<0.1	<0.1	<0.1	<0.1	<0.1	<0.1
Cd	0.1	<0.1	<0.1	2.9	0.1	<0.1	0.2	<0.1	0.1	0.2	<0.1	<0.1
Sb	1.8	1	0.5	2.4	0.9	0.6	1	2.2	1	0.4	0.6	1.4
Cs	0.96	0.91	0.87	2.47	1.31	0.27	1.64	1.54	0.47	0.68	2.24	0.9
Ba	562	123	664	761	483	42	362	78	71	91	942	102
La	25	37	25	26	21	27	28	47	22	53	23	27
Ce	59	71	55	56	40	56	63	104	42	110	50	64
Nd	26	33	25	22	17	26	26	47	21	47	16	29
Tl	<0.5	<0.5	<0.5	0.7	0.9	<0.5	<0.5	<0.5	<0.5	<0.5	<0.5	<0.5
Pb	16	5	8	29	10	9	11	34	12	8	11	30
Bi	0.1	<0.1	<0.1	<0.1	<0.1	<0.1	0.1	<0.1	<0.1	<0.1	<0.1	0.1
Th	12.5	16.1	14.1	14.2	9.05	14.5	16	5.97	16.6	16	19.3	14.2
U	3.15	3.18	3.48	3.47	2.02	3.49	3.25	2.06	3.23	2.41	3.84	3.47

Total Fe as Fe2O3; LOI = loss on ignition; Alteration Index = 100(MgO+K2O)/(MgO+K2O+CaO+Na2O)

Table 1. continued

	M81	M84	M85	M86	M89	M90	M98	M103	M105	M112	M114	M116
SiO2	62.58	66.77	61.05	62.81	64.53	62.98	68.53	73.19	73.93	75.30	75.48	77.62
TiO2	0.65	0.56	0.72	0.65	0.63	0.69	0.50	<0.5	0.31	0.20	0.19	0.18
Al2O3	15.18	14.83	15.89	15.34	14.87	15.32	14.76	13.72	13.72	13.02	13.49	12.54
Fe2O3#	6.20	5.32	7.59	6.33	6.08	5.60	4.34	2.40	2.66	1.61	1.45	2.01
MnO	0.09	0.07	0.10	0.09	0.09	0.10	0.06	0.04	0.11	0.01	0.00	0.01
MgO	2.82	2.56	3.57	3.03	2.75	2.21	1.38	0.52	0.61	0.35	0.42	0.60
CaO	3.53	2.02	2.69	4.92	1.73	5.62	1.09	0.18	0.18	0.03	0.03	0.01
Na2O	2.66	3.52	3.66	3.42	3.42	3.61	3.33	3.71	4.63	1.70	2.11	0.42
K2O	2.46	1.92	0.66	0.77	2.97	1.33	3.83	4.26	1.91	4.79	4.20	4.16
P2O5	0.11	0.08	0.10	0.11	0.11	0.13	0.12	0.05	0.05	0.03	0.02	0.02
LOI	2.79	2.50	4.04	2.36	2.77	2.22	1.76	1.08	1.60	1.85	2.31	2.15
Total	99.07	100.15	100.07	99.83	99.95	99.81	99.70	99.40	99.71	98.89	99.70	99.72
S	<0.01	<0.01	<0.01	<0.01	<0.01	0.01	<0.01	<0.01	<0.01	0.01	<0.01	<0.01
Total C	0.07	0.04	0.17	0.02	0.04	0.11	0.02	0.01	0.07	0.16	0.35	0.05
CO2	0.26	0.15	0.62	0.07	0.15	0.40	0.07	0.04	0.26	0.59	1.28	0.18
Alteration Index	46.0	44.7	40.0	31.3	52.6	27.7	54.1	55.1	34.4	74.8	68.3	91.7
Trace Elements (ppm)												
Sc	17	12	16	15	16	13	10	4	4	4	4	3
V	132	109	145	132	143	113	68	8	6	<1.5	3	2
Cr	55	29	64	40	45	27	7	2	2	2	2	2
Ni	11	6	11	8	8	6	2	1	0	2	2	1
Cu	8	5	5	5	5	6	5	3	35	14	30	10
Zn	86	71	86	92	71	99	91	33	33	18	26	28
As	<1	6	6	6	<1	5	3	<1	2	17	<1	1
Rb	86	76	22	36	77	44	150	122	78	298	153	171
Sr	240	188	205	283	226	305	157	142	152	41	56	10
Y	32	29	30	32	35	37	32	40	44	42	47	37
Zr	222	231	230	209	211	231	220	207	244	238	241	214
Nb	11.5	12.2	11.3	11.0	11.4	12.4	12.6	14.7	15.1	15.8	16.5	14.8
Mo	0.2	0.5	0.4	0.6	0.2	0.9	0.2	0.7	1.1	0.3	0.3	0.4
Ag	<0.1	<0.1	<0.1	<0.1	<0.1	<0.1	<0.1	<0.1	<0.1	0.1	0.4	0.1
Cd	<0.1	<0.1	<0.1	<0.1	<0.1	0.2	0.2	<0.1	<0.1	<0.1	<0.1	<0.1
Sb	0.6	0.7	0.5	1	0.5	1.4	1.3	0.5	1.3	2.1	1	1
Cs	1.27	1	0.49	0.93	1.18	1.32	3.94	3.43	2.04	3.84	2.05	2.5
Ba	595	499	213	223	871	400	889	1133	551	932	1613	858
La	27	23	24	29	30	30	37	50	42	43	41	32
Ce	59	58	55	62	63	68	78	91	89	94	92	71
Nd	26	25	23	30	30	32	33	43	37	39	37	31
Tl	<0.5	<0.5	<0.5	<0.5	<0.5	<0.5	0.6	0.6	<0.5	1.7	1	0.9
Pb	19	16	18	18	11	30	34	11	19	17	13	12
Bi	<0.1	0.1	<0.1	<0.1	<0.1	<0.1	<0.1	<0.1	<0.1	0.4	1.9	<0.1
Th	8.57	15.3	13.5	13.5	13.3	14.2	18.4	20.1	18.4	21.6	21.2	16.9
U	1.9	3.89	3.36	3.31	3.32	3.56	4.08	4.07	4.65	4.8	4.71	4.35

Total Fe as Fe2O3; LOI = loss on ignition; Alteration Index = 100(MgO+K2O)/(MgO+K2O+CaO+Na2O)

Table 1. continued

	M120	M121	M134	MBE96-8	MY	MB96-1	MB96-2	MB96-3	MB96-4	MB96-5	MB96-6	MB96-7
SiO2	63.11	63.67	68.17	62.71	66.94	59.69	63.98	61.82	59.90	72.66	61.20	61.50
TiO2	0.66	0.65	0.51	0.71	0.64	0.72	0.74	0.75	0.65	0.29	0.68	0.80
Al2O3	14.95	15.12	15.04	15.01	14.11	14.61	16.39	16.36	14.90	13.47	14.20	16.76
Fe2O3#	6.12	5.92	4.83	5.96	5.82	12.46	4.99	8.61	12.13	2.18	7.57	7.97
MnO	0.10	0.12	0.03	0.10	0.08	1.03	0.20	0.06	0.68	0.06	0.53	0.03
MgO	2.43	2.61	1.67	2.62	2.81	2.88	1.97	1.40	3.46	0.75	2.32	1.51
CaO	6.29	4.19	0.36	4.29	1.74	0.18	0.14	0.19	0.24	0.42	3.03	0.35
Na2O	2.66	3.18	3.24	3.46	1.64	0.05	0.19	0.18	0.08	2.33	1.83	0.19
K2O	1.51	2.08	3.97	3.61	3.05	3.25	7.45	7.21	3.51	5.99	4.55	7.70
P2O5	0.09	0.10	0.12	0.11	0.10	0.18	0.18	0.19	0.18	0.06	0.19	0.27
LOI	2.40	2.29	1.71	1.77	3.18	4.14	3.41	2.91	3.86	1.76	3.47	2.46
Total	100.32	99.93	99.65	100.35	100.11	99.19	99.64	99.68	99.59	99.97	99.57	99.54
S	<0.01	<0.01	<0.01	0.13	<0.01	0.68	0.01	0.01	0.02	<0.01	0.19	<0.01
Total C	0.04	0.04	0.04	0.06	0.17	0.04	0.10	0.05	0.06	0.06	0.36	0.06
CO2	0.15	0.15	0.15	0.22	0.62	0.15	0.37	0.18	0.22	0.22	1.32	0.22
Alteration Index	30.6	38.9	61.0	44.6	63.4	96.4	96.6	95.9	95.6	71.0	58.6	94.5
Trace Elements (ppm)												
Sc	18	16	12	22	16	22	22	23	20	6	17	23
V	126	124	73	157	143	172	179	139	119	42	142	133
Cr	47	47	9	31	46	37	41	36	33	9	26	30
Ni	8	9	2	8	10	11	10	16	8	4	8	27
Cu	5	4	3	37	22	74	68	9	37	4	140	6
Zn	64	92	63	47	68	1447	165	168	956	67	390	119
As	8	<1	<1	1	4	20	9	2	1	<1	2	2
Rb	39	56	136	115	127	321	446	314	201	186	218	337
Sr	352	315	170	205	131	8	124	100	10	278	220	96
Y	33	36	33	33	26	27	24	30	21	15	29	31
Zr	228	227	231	186	188	200	225	188	168	116	187	211
Nb	12.0	11.7	12.8	9.7	10.7	14	14.9	13.7	12.9	14.2	14.7	14.9
Mo	0.3	0.2	0.5	0.2	0.3	1	0.7	0.5	0.4	0.4	0.5	0.5
Ag	<0.1	<0.1	<0.1	0.1	0.1	1.7	7.7	0.3	0.4	0.2	8.5	0.3
Cd	0.2	<0.1	<0.1	0.1	0.2	12.7	0.7	0.4	0.3	<0.1	1.2	<0.1
Sb	1.1	0.9	1.1	1	0.5	2	1.9	1.8	1.9	1.3	4.5	2.8
Cs	0.41	0.82	4.46	1.14	1.71	5	9.41	17.5	14.1	3.57	11.5	28.5
Ba	515	568	1176	809	742	492	1455	964	844	798	1151	1023
La	31	34	42	27	25	51	49	69	38	43	54	55
Ce	70	70	88	62	47	99	98	125	71	84	101	101
Nd	32	33	35	28	20	39	39	52	30	29	38	41
Tl	<0.5	<0.5	0.7	0.6	0.6	3.7	5.6	2.7	2	2.2	3.8	2.3
Pb	22	5	8	20	29	361	406	104	105	140	791	19
Bi	<0.1	<0.1	<0.1	<0.1	0.3	2.4	5.7	0.4	5.3	0.1	28.8	0.4
Th	13.9	13.6	17.9	10.3	11.4	26.2	23.7	22.6	21.2	44.4	25	21.6
U	3.41	3.34	4.25	2.64	3.36	6.52	4.97	1.8	3.21	8.84	6.26	3.41

Total Fe as Fe2O3; LOI = loss on ignition; Alteration Index = 100(MgO+K2O)/(MgO+K2O+CaO+Na2O)

Table 1. continued

	MB96-9	MB96-10	MB96-11	MB96-12	MB96-13	MB96-13B	MB96-14	MB96-15	MB96-17	MB96-18	MB96-19	MB96-20
SiO2	63.31	62.77	72.41	58.14	66.88	63.89	69.67	69.76	76.51	76.51	69.93	65.53
TiO2	0.84	0.68	0.28	0.62	0.56	0.62	0.50	0.49	0.33	0.33	0.44	0.54
Al2O3	16.44	13.19	12.95	13.82	14.02	14.43	12.56	12.32	12.35	12.52	13.77	14.05
Fe2O3#	5.53	7.54	3.97	10.77	7.23	8.74	7.23	6.42	1.38	1.78	3.58	4.77
MnO	0.09	0.72	0.09	0.17	0.19	0.16	0.10	0.23	0.06	0.05	0.13	0.16
MgO	2.09	2.85	1.62	3.10	2.03	2.71	2.15	1.53	0.80	0.90	1.46	1.97
CaO	0.82	2.19	0.12	2.61	0.86	0.41	0.38	0.22	1.94	0.28	0.46	2.02
Na2O	5.54	2.33	0.67	1.35	2.35	0.69	0.06	0.12	3.31	4.67	0.86	1.86
K2O	3.67	4.37	6.43	5.09	3.09	5.00	4.57	6.17	1.83	1.25	7.17	5.86
P2O5	0.21	0.17	0.05	0.14	0.10	0.13	0.10	0.09	0.05	0.03	0.10	0.11
LOI	1.71	3.07	1.80	3.82	2.47	2.89	2.57	1.99	1.33	1.39	2.01	2.73
Total	100.25	99.88	100.55	99.63	99.78	99.67	99.89	99.34	99.89	99.71	100.17	99.60
S	0.04	0.03	0.03	0.05	<0.01	0.04	0.08	0.03	0.02	<0.01	0.22	0.06
Total C	0.03	0.31	0.03	0.45	0.07	0.05	0.08	0.09	0.13	0.03	0.07	0.32
CO2	0.11	1.14	0.11	1.65	0.26	0.18	0.29	0.33	0.48	0.11	0.26	1.17
Alteration Index	47.5	61.5	91.1	67.4	61.5	87.5	93.9	95.8	33.4	30.3	86.7	66.9
Trace Elements (ppm)												
Sc	22	17	10	28	24	28	13	14	9	9	11	13
V	173	141	14	187	113	180	69	65	25	23	77	95
Cr	35	29	2	20	15	18	26	24	3	3	15	20
Ni	9	8	4	7	4	5	5	5	8	3	5	7
Cu	28	21	6	13	5	12	15	13	2	2	7	4
Zn	95	934	102	134	138	211	96	111	66	90	136	203
As	11	2	3	8	<1	2	1	2	1	<1	33	3
Rb	121	147	247	192	154	224	137	168	124	68	290	250
Sr	107	88	130	125	137	81	36	49	151	90	101	188
Y	24	27	46	33	43	33	37	38	47	34	29	32
Zr	174	187	269	163	232	189	280	276	258	254	167	195
Nb	13.6	11.2	19.3	10.9	12.5	13.2	14.1	13.5	13.9	13.9	13.6	14.4
Mo	2.1	3	0.7	1.6	0.3	0.9	2.2	3.2	1.3	0.5	1.2	2
Ag	0.1	0.6	0.1	<0.1	<0.1	0.1	<0.1	<0.1	0.2	<0.1	0.3	0.1
Cd	0.1	2.8	0.2	<0.1	<0.1	0.8	<0.1	<0.1	0.1	<0.1	0.3	<0.1
Sb	1.6	1	2	0.6	0.5	0.7	0.9	1	0.6	0.3	1.1	0.6
Cs	3.72	3.09	4.86	9.65	5.2	11.2	9.49	8.72	8.5	3.81	18.2	17.5
Ba	605	886	1485	1922	879	1440	1947	2097	353	496	2735	2342
La	36	37	126	31	51	38	39	39	39	35	42	47
Ce	72	72	269	61	96	74	91	84	95	88	91	99
Nd	32	30	92	24	39	30	40	36	41	36	30	37
Tl	1.3	1.7	2.3	2.3	1.2	1.9	1.2	1.3	1	0.6	2.9	2.1
Pb	20	112	31	10	9	25	23	10	64	7	98	70
Bi	0.9	3.9	0.6	0.3	0.1	0.2	0.1	0.4	<0.1	<0.1	<0.1	0.1
Th	15.6	13.6	29.9	10.9	15	12.3	19.6	18.9	20.9	20.8	24	21
U	3.12	2.38	4.33	2.72	4.26	2.88	4.93	5.54	5.2	4.43	5.65	5.11

Total Fe as Fe2O3; LOI = loss on ignition; Alteration Index = 100(MgO+K2O)/(MgO+K2O+CaO+Na2O)

Table 1. continued

	MB96-22	MB96-23	MB96-24	MB96-25	MB96-26	MB96-27	MB96-27B	MB96-28	MB96-29	MB96-30	MB96-31	MB96-32
SiO2	72.39	67.55	51.31	61.41	65.16	68.76	67.29	73.56	73.06	74.43	44.12	77.14
TIO2	0.34	0.56	0.56	0.54	0.58	0.52	0.56	0.29	0.32	0.30	0.79	0.19
Al2O3	13.09	13.79	15.10	15.38	14.21	15.07	14.07	12.91	13.46	12.89	17.11	10.05
Fe2O3#	2.30	4.44	14.34	8.54	6.86	3.97	5.34	4.77	3.13	2.45	21.49	2.99
MnO	0.06	0.08	0.39	0.11	0.09	0.11	0.06	0.05	0.05	0.03	0.22	0.07
MgO	1.14	2.50	8.22	2.87	3.04	1.78	2.44	1.23	1.34	0.82	4.90	0.60
CaO	1.48	2.45	0.39	0.40	0.34	0.26	0.16	0.04	0.10	0.16	0.17	0.05
Na2O	3.52	2.47	0.48	0.67	2.02	2.50	0.73	0.06	2.32	3.92	0.13	0.18
K2O	3.27	4.06	3.94	8.10	4.78	5.45	4.88	4.90	4.23	3.82	6.33	7.38
P2O5	0.05	0.09	0.10	0.11	0.10	0.11	0.09	0.05	0.05	0.05	0.13	0.04
LOI	1.51	2.01	4.65	2.46	2.47	2.17	3.71	2.18	1.76	0.94	3.45	0.82
Total	99.15	100.00	99.48	100.59	99.65	100.70	99.33	100.12	99.82	99.81	98.84	99.51
S	<0.01	0.02	0.39	0.81	0.07	0.43	1.40	0.05	<0.01	0.01	0.11	0.12
Total C	0.12	0.16	0.04	0.03	0.03	0.04	0.04	0.03	0.06	0.02	0.03	0.05
CO2	0.44	0.59	0.15	0.11	0.11	0.15	0.15	0.11	0.22	0.07	0.11	0.18
Alteration Index	46.9	57.1	93.3	91.1	76.8	72.4	89.2	98.4	69.7	53.2	97.4	97.2
Trace Elements (ppm)												
Sc	7	13	35	16	20	14	16	12	9	7	36	6
V	36	87	231	117	101	42	92	3	10	8	279	3
Cr	24	104	558	101	124	20	74	2	4	4	6	2
Ni	8	26	105	31	29	11	31	3	3	3	12	3
Cu	4	6	11	48	5	23	28	50	3	3	285	56
Zn	72	73	259	162	153	546	216	112	107	79	511	58
As	<1	<1	8	5	<1	9	40	2	<1	<1	2	4
Rb	149	206	478	209	141	193	229	231	211	78	257	150
Sr	139	150	39	66	73	98	37	10	47	95	45	94
Y	38	39	15	98	26	20	33	32	39	36	26	43
Zr	221	265	100	254	277	370	175	281	295	276	114	174
Nb	13.1	13.2	9.4	12.6	13.1	12	14.4	12.4	13.2	13.3	9.2	8.8
Mo	0.4	0.6	0.3	0.5	1.9	1.5	7.2	1.3	0.3	0.6	1.1	0.3
Ag	<0.1	<0.1	<0.1	0.3	0.1	0.9	1.4	<0.1	<0.1	<0.1	0.4	0.1
Cd	0.2	0.2	0.2	<0.1	<0.1	3.4	1.4	<0.1	<0.1	<0.1	0.3	<
Sb	0.4	0.4	0.5	0.8	1	2.1	3	0.8	0.9	0.4	1.9	1
Cs	4.52	8.6	32.9	5.97	3.95	5.78	9.91	6.46	6.57	1.36	8.45	2.21
Ba	620	827	215	3197	1346	1835	1226	719	840	1277	1684	3271
La	43	41	19	55	42	25	30	35	54	54	32	63
Ce	95	93	34	111	91	61	68	72	110	110	62	137
Nd	40	40	14	49	38	22	28	32	46	46	24	59
Tl	1.3	1.8	4.6	1.3	0.8	3.2	2.8	1	1.4	0.5	1.5	0.8
Pb	14	15	45	16	11	768	625	14	11	9	60	13
Bi	<0.1	0.1	<0.1	0.4	0.5	0.3	1	<0.1	<0.1	<0.1	0.2	0.4
Th	19.9	18	7.89	17.9	19.8	17	20.5	19.8	24.3	22.6	8.23	15.5
U	3.7	3.98	3.61	4.42	4.08	4.58	7.82	5.09	5.6	5.15	4.65	3.55

Total Fe as Fe2O3; LOI = loss on ignition; Alteration Index = 100(MgO+K2O)/(MgO+K2O+CaO+Na2O)

Table 1. continued

	MB96-34	MB96-35	MB96-37	MB96-38	MB96-39	MB96-40	MB96-41	MB96-42	MB96-43	MB96-44	MB96-45	MB96-46
SiO2	76.03	74.58	68.89	68.13	73.89	74.24	74.03	66.68	69.50	71.51	73.78	71.55
TiO2	0.15	0.27	0.46	0.53	0.27	0.23	0.30	0.49	0.51	0.36	0.26	0.30
Al2O3	13.09	13.85	15.12	14.98	13.70	13.93	13.74	14.21	14.95	15.00	13.10	13.87
Fe2O3#	1.43	2.08	4.11	5.50	2.22	2.15	2.38	6.09	4.60	3.15	4.79	5.74
MnO	0.02	0.01	0.02	0.10	0.02	0.01	0.01	0.37	0.14	0.02	0.02	0.12
MgO	0.53	0.38	1.23	1.18	0.37	0.49	0.46	1.34	1.42	0.89	0.64	1.06
CaO	0.02	0.13	0.08	0.25	0.41	0.04	0.04	0.90	0.21	0.06	0.00	0.02
Na2O	1.50	3.54	3.66	2.83	3.46	3.21	3.95	2.94	2.62	3.80	0.06	0.48
K2O	5.17	4.34	3.83	4.04	4.31	2.88	3.24	3.27	3.39	2.53	3.98	3.40
P2O5	0.03	0.03	0.09	0.14	0.04	0.02	0.05	0.13	0.13	0.05	0.03	0.04
LOI	1.44	1.11	2.12	2.22	1.25	2.71	1.79	3.23	2.42	2.23	3.09	2.94
Total	99.41	100.32	99.61	99.90	99.94	99.91	99.99	99.65	99.89	99.60	99.75	99.52
S	<0.01	<0.01	<0.01	<0.01	<0.01	0.02	<0.01	0.01	0.02	0.02	<0.01	0.01
Total C	0.03	0.03	0.05	0.07	0.09	0.17	0.10	0.40	0.11	0.08	0.09	0.08
CO2	0.11	0.11	0.18	0.26	0.33	0.62	0.37	1.47	0.40	0.29	0.33	0.29
Alteration Index	78.9	56.3	57.5	62.9	54.7	50.9	48.1	54.6	63.0	47.0	98.7	89.9
Trace Elements (ppm)												
Sc	5	4	11	11	3	5	4	11	11	6	4	4
V	6	4	60	83	3	3	12	77	81	12	7	18
Cr	3	2	11	8	2	3	3	7	7	3	2	4
Ni	2	1	3	3	2	2	1	3	3	1	1	1
Cu	4	2	3	18	4	3	3	6	7	6	35	14
Zn	39	17	36	32	19	23	21	75	40	38	33	70
As	1	<1	<1	<1	<1	<1	1	<1	<1	<1	4	2
Rb	256	136	138	157	140	121	112	135	129	103	170	154
Sr	29	96	122	103	104	78	112	100	78	98	4	8
Y	35	41	28	35	62	38	41	42	41	40	25	24
Zr	125	270	243	212	269	282	266	199	209	282	254	238
Nb	13.7	17	13.6	10.7	16.1	16.8	13.4	10.6	11.1	16	13.7	11.6
Mo	0.2	0.5	0.4	1.7	0.6	0.7	0.8	0.9	0.2	0.4	1	0.2
Ag	0.9	<0.1	<0.1	<0.1	<0.1	<0.1	<0.1	<0.1	<0.1	<0.1	<0.1	0.1
Cd	0.2	<0.1	<0.1	0.3	0.2	<0.1	<0.1	0.1	0.4	<0.1	<0.1	<0.1
Sb	1.5	0.4	0.7	0.5	0.5	0.6	0.9	0.7	0.9	0.4	0.9	1.4
Cs	5.82	1.98	2.98	2.9	2.35	1.99	2.36	4.06	2.57	1.17	1.46	1.53
Ba	1138	988	817	876	947	787	942	696	711	606	931	703
La	56	57	38	54	174	47	54	47	49	41	32	41
Ce	122	102	80	113	289	82	107	95	101	74	72	82
Nd	46	45	31	47	131	42	44	39	45	37	29	32
Tl	1.9	<0.5	0.5	<0.5	<0.5	<0.5	<0.5	<0.5	<0.5	<0.5	0.9	0.9
Pb	94	3	3	2	3	8	7	4	2	3	5	7
Bi	0.8	<0.1	0.3	<0.1	<0.1	<0.1	0.1	<0.1	<0.1	0.3	2.6	2.1
Th	28.2	22	21.4	19.6	22	23.3	22.3	18.4	19.3	20.6	25.1	18.4
U	5.9	5.4	5.01	4.59	5.05	5.21	5.73	4.35	4.66	4.98	5.79	3.91

Total Fe as Fe2O3; LOI = loss on ignition; Alteration Index = 100(MgO+K2O)/(MgO+K2O+CaO+Na2O)

Lithogeochemical exploration for metasomatic alteration zones using Pearce element ratios: Hellyer case study

Clifford R. Stanley* **and J. Bruce Gemmell**

Mineral Deposit Research Unit (MDRU), Department of Geological Sciences, The University of British Columbia; and Centre for Ore Deposit and Exploration Studies, Geology Department, University of Tasmania

Many mineral deposits have associated hydrothermal alteration zones that envelop the mineralisation and thus are larger than the deposits themselves. As a result, these zones constitute ideal intermediate exploration targets that may be used as guides to mineralisation. This study intends to improve lithogeochemical exploration methods to enhance a geologist's ability to locate, identify and understand these hydrothermal alteration zones, and thus improve their chances of discovering associated mineral deposits. This will be accomplished by: i) developing a numerical methodology, founded on simple yet sound theory, that may be used to quantify the metasomatism that accompanied the hydrothermal reactions responsible for the alteration zones and ii) investigate the Hellyer alteration system in order to test the lithogeochemical exploration methodology. In short, the goal of this project is to provide an improved exploration tool for the AMIRA participants, supply them with the means to use this tool, and equip them with the geological criteria and knowledge to effectively direct its use.

Background

The principal sources of geochemical variation observed in host rocks of VHMS deposits are: (i) measurement error, including error during sampling (nugget effect) and analysis, (ii) closure, a mathematical artefact caused by the requirement that a rock composition sum to 100%, preventing the manifestation of differences in rock composition from directly reflecting the actual changes that have occurred in the rock, (iii) fractionation, systematic geochemical variations produced by crystal or volatile separation from a melt, and by crystal sorting; present before mineralising fluids alter these rocks, (iv) compositional mixing, mechanical mixing of rocks of different genesis and composition (e.g. volcaniclastics with exotic clasts) and (v) metasomatism, material transfer associated with chemical reactions between mineralising fluids and host rocks.

Lithogeochemistry has traditionally been used in mineral exploration to locate hydrothermal alteration zones associated with volcanic-hosted massive sulphide (VHMS) deposits. Examples include the numerous *Na* and *Ca* depletion anomalies identified in the volcanic footwalls to many VHMS deposits. In many cases, these anomalous zones contributed to the discovery of the deposits. Unfortunately, these lithogeochemical anomalies may sometimes be difficult to identity. This is because: (i) the processes that produce these lithogeochemical anomalies are not restricted to only those responsible for hydrothermal mineral deposits, (ii) pre-existing lithogeochemical variations in the host rocks can obscure these anomalous patterns and prevent their identification, (iii) many elements do not necessarily display consistent lithogeochemical patterns in the alteration zones (e.g. K in VHMS footwalls), and (iv) the effect of closure, a mathematical peculiarity that introduces spurious numerical variations to concentration data. can obscure any real lithogeochemical pattern that does exist. All of these factors can make it difficult to confidently identity anomalous lithogeochemical patterns associated with the alteration zones related to hydrothermal mineral deposits.

A number of numerical approaches, all of which avoid the spurious effects of closure in concentration data, have been developed to quantity the effects of metasomatism (Akella 1966; Gresens 1967; Grant

1986; MacLean and Barrett 1993). Recently, theoretical advances in Pearce element ratio (PER) analysis (Russell and Stanley 1990; Stanley and Madeisky 1993) have also allowed its use to study various types of material transfer processes, including metasomatic processes associated with hydrothermal alteration and mineral deposit genesis. Whereas PER were originally used to study fractionation processes in igneous systems (e.g. Russell and Stanley 1990), Stanley and Madeisky (1993) have demonstrated how PER can also be used effectively in lithogeochemical exploration for several types of hydrothermal mineral deposits. One of their significant discoveries was that the magnitude of pre-existing lithogeochemical variability in VHMS deposit host rocks (i.e. the background variations caused by phenocryst sorting in the host volcanics) may, in many cases. be as large as the variations produced by the metasomatism that accompanied deposit genesis. Previous numerical approaches that lack the ability to model and remove the pre-existing lithogeochemical variability are unable to accurately quantity the effects of metasomatism because of this background 'noise'. The ability to avoid the effects of closure and to model and remove the effects of pre-existing lithogeochemical variations (fractionation) make PER analysis a superior tool in lithogeochemical exploration for igneous rock-hosted hydrothermal mineral deposits. With this methodology, even subtle metasomatic effects that would otherwise be obscured by the background lithogeochemical variability can readily be identified.

Preliminary application of the PER methodology to VHMS deposits has already resulted in several new observations with significant exploration import. in the Rio Tinto VHMS camp, the most evolved portions of the footwall rhyolite appear to be spatially associated with the deposits, and are the most metasomatized. This suggests that the degree of petrologic evolution, along with the degree of metasomatism, may constitute important exploration parameters for VHMS deposits (Stanley and Madeisky 1993). Furthermore, explanations for common observations made during lithogeochemical exploration have also been discovered using PER. In VHMS footwalls, K is known to generally be a less effective exploration tool for discovering footwall alteration zones to VHMS deposits than Na or Ca (personal communication, Dr Steve Juras, 1993). This is because K can be added or lost during the formation of a quartz-muscovite-pyrite alteration zone. PER analysis has demonstrated that this variable lithogeochemical behaviour is dependent on the original feldspar composition and (Na+K)/Al ratio of the volcanic host rocks (Stanley and Madeisky, unpublished work). Because it is unlikely that these discoveries could be made using a numerical methodology that could not remove the effects of pre-existing background lithogeochemical variation, significant advantages can be gained through use of the PER technique in lithogeochemical exploration.

The theoretical basis for PER analysis requires that (1) al least one conserved element be present (an element that is "incompatible" during igneous fractionation and "immobile" during hydrothermal alteration), (2) the rocks be related to a common parent that was at one time homogeneous (at least with respect to the conserved element) and (3) at least one material transfer process has acted to create the geochemical variability observed in these rocks. The PER approach uses a ratio formulation (computer spreadsheet) where the material transfer equation is expressed in molar terms using a conserved constituent (element) in the ratio denominator. This causes the PER to be directly proportional to the amount of material transfer in the numerator element. By using a mole instead of mass concentrations in PER analysis the resulting material transfers can be related directly to mineral formulae and chemical reactions (Stanley and Madeisky, 1993). This allows solid-solution mineral composition variations to be accommodated and allows development of linear fractionation models which can represent the geochemical heterogeneity in volcanic rocks before the advent of hydrothermal alteration. PER analysis overcomes the effects of closure and also allows geochemical variations associated with fractionation and crystal sorting to be recognised and accommodated. It has been demonstrated that the magnitude of pre-existing lithogeochemical variability in VHMS deposit host rocks (i.e. background variations caused by phenocryst sorting in host volcanics) may, in many

cases, be as large as the variations produced by the alteration).

A study of alteration in a variety of felsic hosted VHMS deposits (Archean to Mesozoic, zeolite to middle amphibolite metamorphic grades) by PER analysis by Madeisky and Stanley (1994) concluded that the patterns of metasomatic additions and losses in both quartz-sericite and quartz-chlorite alteration zones are surprisingly consistent among deposits. Fluid-rock (buffered) reactions include the common Na and Ca metasomatic losses as well as the addition of K, an often erratic behaviour that is controlled by the primary K/Na ration (alkali feldspar) and Al budget of the host rocks, and the stability of sericite. The behaviours of chalcophile elements (Cu, Pb, Zn, Ag, Au) can be explained in terms fluid only (unbuffered) reactions within specific alteration mineral stability fields, and the mass transfer of other trace elements (Sr, Rb, Ba, Cr, Ni, Mn) corresponds with camouflaging major element behaviour. Environments where Al is mobile in the hydrothermal fluids appear to be restricted (Madeisky and Stanley, 1994). To date there has not been a study using PER to a VHMS system hosted by intermediate to mafic volcanics, this is why Hellyer was chosen and will make an excellent case study. The recent development of the above numerical methodologies to study material transfer processes provides a unique opportunity to (i) study metasomatic processes at a level of rigour previously unattainable, leading to a better geological and geochemical understanding of hydrothermal mineral deposits and the processes that formed them, and (ii) develop effective, theoretically-based strategies, methodologies and models for use in lithogeochemical exploration for hydrothermal mineral deposits. The ability of PER analysis to avoid the effects of closure and to model and remove the effects of pre-existing lithogeochemical variations (fractionation) make PER analysis a superior tool in lithogeochemical exploration for igneous rock-hosted VHMS deposits (Stanley and Madeisky, 1993).

Research

This research project can be divided into three basic objectives. These are (i) to develop a new, effective lithogeochemical exploration methodology, (ii) to produce dedicated computer software with which to implement this methodology, and (iii) to test this methodology, expand its application, improve its results, and identify sound strategies for its use in exploration.

Hellyer Case Study

As the lithogeochemical signature of the footwall (Gemmell and Large, 1992) and hangingwall (Jack, 1989) alteration at Hellyer has previously been investigated and is well characterised this study will concentrate on the lithologies surrounding the deposit to detect a regional lithogeochemical signature. At Hellyer, data from Jack (1989), Gemmell (1990), Gemmell and Large (1992), Sinclair (1994) and unpublished Aberfoyle data will be used in conjunction with new analyses for the Pearce Element lithogeochemical study. This project will be broken down into two parts: (i) previous data from both the footwall and hangingwall alteration zones will be interpreted to determine the systematics of the intense alteration and (ii) new samples and previous data from the immediate footwall and hangingwall lithologies away from the alteration zones will be analysed to determine vectors towards the alteration and mineralisation.

Ninety new samples have been collected from the Hellyer basalt, Que River Shale and the footwall andesite in drill holes up to 4 km away surrounding Hellyer. The location of the drill holes used in this study is shown in Figure 1 of Yang et al. (this volume, p. 307). For the purpose of this investigation no footwall polymict debris flow material was analysed.

These samples have been crushed in a W carbide pulverizer and will be analysed by lithium mets borate frisioll XRF whole rock analysis for SiO_2, TiO_2, Al_2O_3, Fe_2O_3, MnO, MgO, CaO, Na_2O, K_20, P_20_5 and LOI and by pressed pellet or fused disk for Ni, Cr, V, Zr, Y, Sc, La, Sr, Rb, Ba, Cu, Pb, Zn, Au, Ag, Nb, TI, Se, Sb, Cd and Mo. The samples were analysed at the University of Tasmania. In addition both H_2O+ and CO_2 contents will be determined. Geochemical data for unaltered samples of the Hellyer basalt, Que River Shale and the footwall andesite are given in Table 1.

Footwall andesite

Figure 1
Plot of Zr against Nb demonstrates that orientation samples collected JBG and CRS in 1995 from plagioclase phyric footwall andesite to the Hellyer VHMS deposit are cogenetic (derived from common parent that was at one time homogeneous) and that Zr and Nb are conserved elements (did not participate in material transfer processes (e.g. igneous fractionation and metasomatism) that have affected these rocks). This is supported by fact that the data lie on single line that passes through the origin. Although the 2 SD error ellipses do not all include this single line, these error estimates were derived from well blended pulp replicate analyses and thus represent only analytical error. They do not accommodate sampling error. As a result, these samples are interpreted to be collinear because their deviations from this line are readily attributable to sampling error.

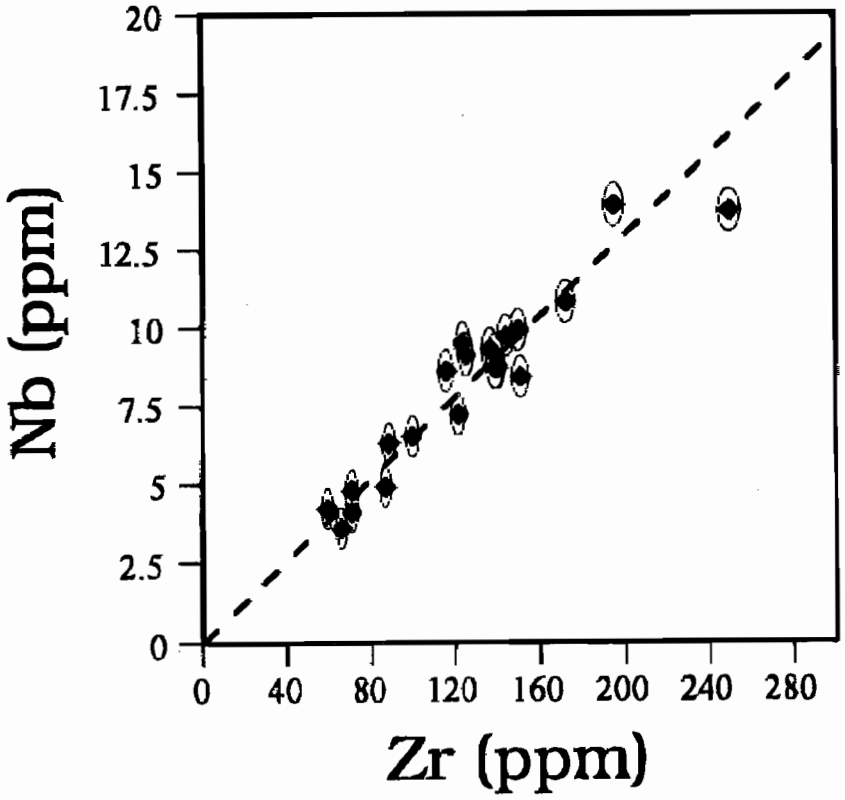

Figure 2
Plot of Si/Zr against (2Ca+3Na+K)/Zr Pearce element ratio diagram. The Zr in the denominator is used to standardize these ratios and avoid the effects of changes in size of the rocks due to material transfer. Fractionation (crystal sorting) of plagioclase (in any composition) and clinopyroxene (in any composition), in any modal proportion, will displace these rock compositions along a line with unit slope because the stoichiometry of these minerals dictates that the (for example) addition of one mole of any or all of the end-member minerals in plagioclase and clinopyroxene (albite and anorthite; diopside and hedenbergite) will cause the addition of the same number of moles of Si as of (2Ca+3Na+K), and thus displace the rock compositions the same distance in the abscissa direction as the ordinate direction. Hydrolysis of pyroxene and feldspar will likely involve at least the partial loss of alkali and alkali earth elements, displacing the rock compositions downward on this plot, whereas the addition of silica will displace rock compositions to the right. However, the presence of cross-cutting Ca-bearing carbonate veins will displace the rock compositions upward on these plots. Hydrolysis of these rocks produced two major phyllosilicate minerals (muscovite and chlorite) and rocks containing only these minerals would plot on the lines indicated. Clearly, most rocks consist of mixtures of these two hydrolysis products and the plagioclase and clinopyroxene that comprise the bulk of the fresh mineral assemblage.

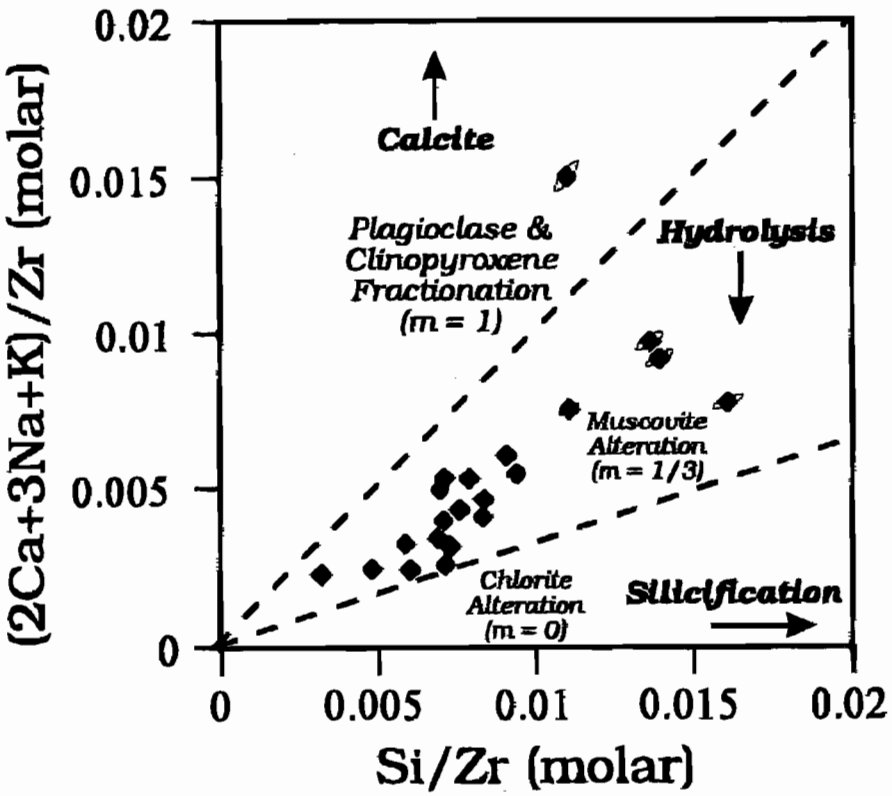

Figure 3
Plot of Ca/Zr against CO_2/Zr Pearce element ratio diagram. On this plot, if all of the Ca in a rock is contained in the mineral calcite, the rock will plot on a line with unit slope that passes through the origin. All rocks plot to the right of this line (although this line acts as a left/upper limit of the data), indicating that in many samples, other Ca-bearing minerals (plagioclase, clinpyroxene) are present. Nevertheless, the control of calcite on the Ca budget in many of these rocks is strong.

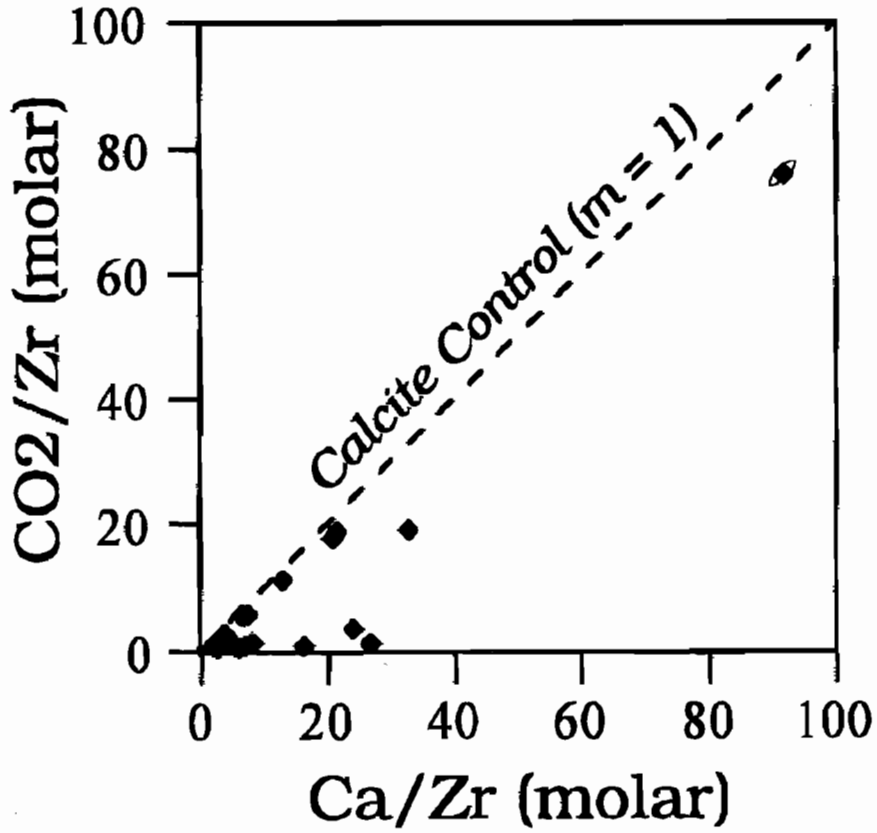

Figure 4
Plot of Si/Zr against (2Ca+3Na+K-2CO_2)/Zr Pearce element ratio diagram, that is similar to CDR #2 but has 2CO_2 subtracted from the ordinate numerator. This causes this diagram to be a projection from calcite, and thus to be unaffected by the addition of calcite (as veins) to the rocks, but to have all of the same other attributes. Consequently, this diagram is affected by only two of the three metasomatic processes affecting #2 (silicification and hydrolysis) and the residual of the samples from the line with unit slope (which corresponds to a plagioclase-clinopyroxene fractionation model for these rocks) represents a measure of how much hydrolysis and silicification has taken place.

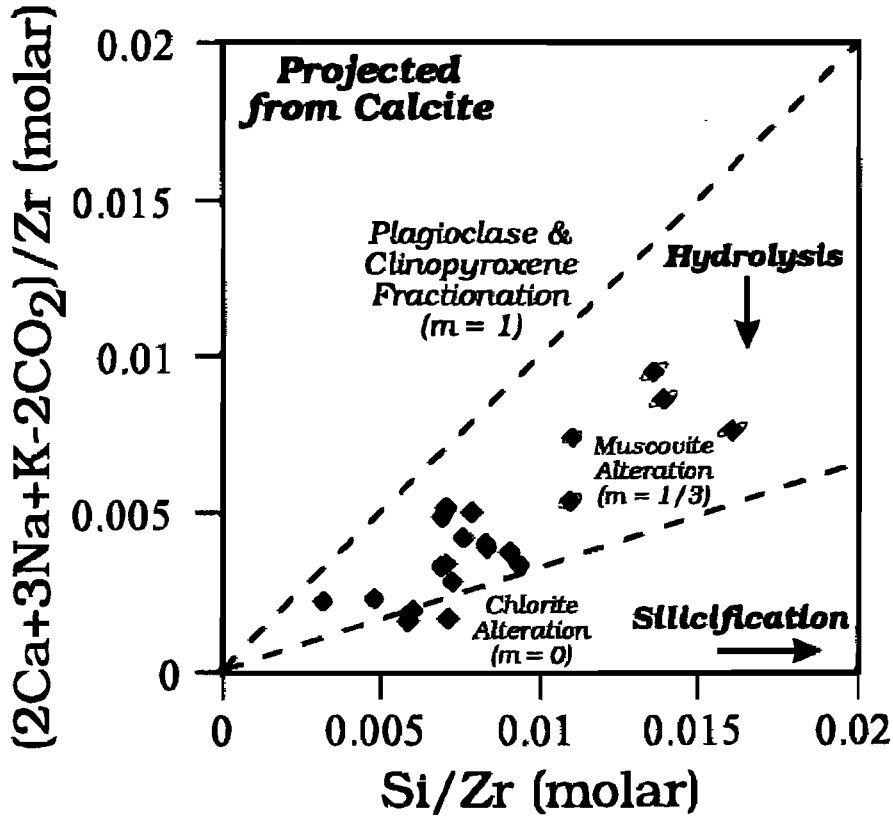

Figure 5
Plot of Al/Zr against (2Ca+Na+K)/Zr Pearce element ratio diagram. This is analogous to # 2 as it is not a projection from calcite, but has otherwise different fractionation properties. Plagioclase fractionation displaces rock compositions along a line with unit slope but clinopyroxene fractionation displaces rock compositions along a line with vertical slope. Consequently, if both plagioclase and clinopyroxene fractionation has taken place in these rocks (a likely scenario given the observed phenocryst assemblage in these andesites), then background compositional variations should be displaced along a line with slope between one and infinity. The upper edge of the data cloud plots along a line with slope of 5/2 and this determines the plagioclase/clinopyroxene fractionation ratio if the plagioclase composition is know (and assuming that the ratio and composition are the same for all rocks). Given a plagioclase composition 'A' in terms of mole fraction anorthite, the mole fraction of clinopyroxene involved in fractionation 'B' can be calculated from : B = (3+3A)/(7+3A). In other words, for this fractionation slope of 5/2, if it is anorthite that fractionated, then the mole fraction of clinopyroxene fractionating is 3/5 (albite => 3/7) and the PL/CP fractionation ratio is 2/3 (albite => 4/3). You can insert the average mole fraction anorthite composition of plagioclase at Hellyer to determine just what this fractionation ratio is in the andesites.

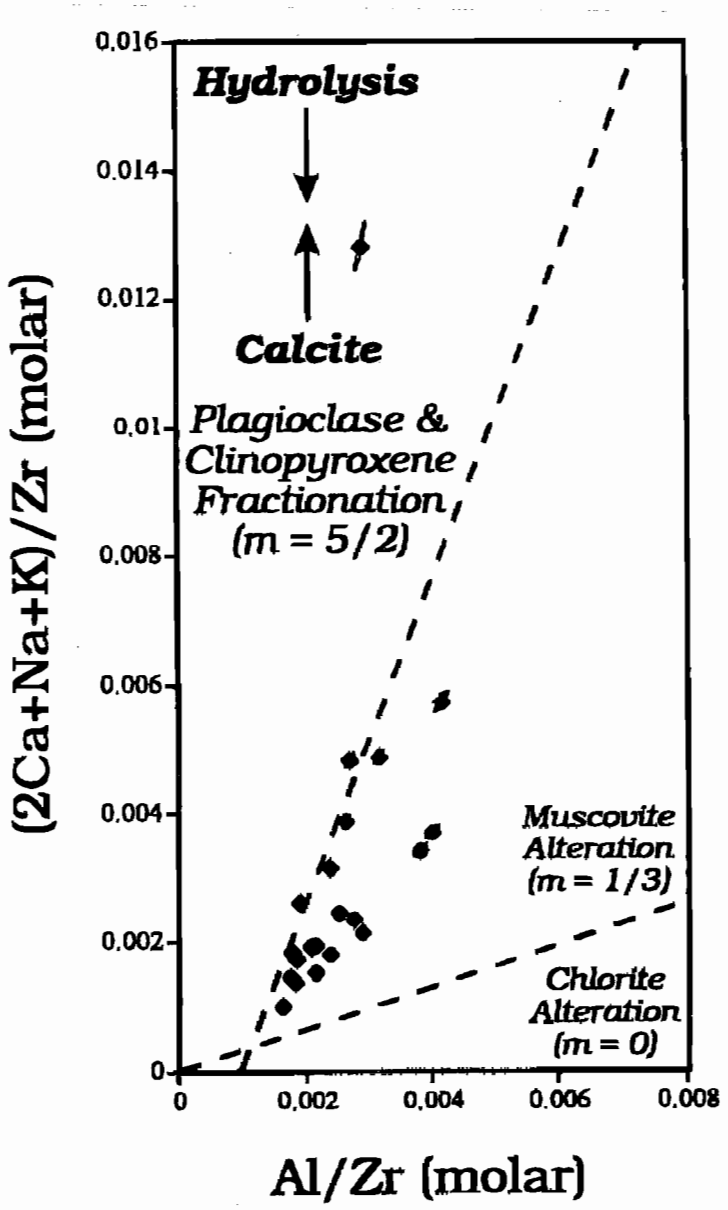

Figure 6
Plot of Al/Zr against (2Ca+Na+K-2CO_2)/Zr Pearce element ratio diagram. This diagram is projected from calcite and thus is analogous to # 4. Silicification does not influence the diagram so the vertical residual from the line with slope of 5/2 is a direct measure of the amount of hydrolysis each sample has undergone and could be used as an exploration parameter. Once these hydrolysis scores have been determined from this diagram, the amount of hydrolysis + silicification derived from # 4 can be decomposed using vector algebra to determine the amount of silicification in each sample. This measurement can also be used as an exploration parameter.

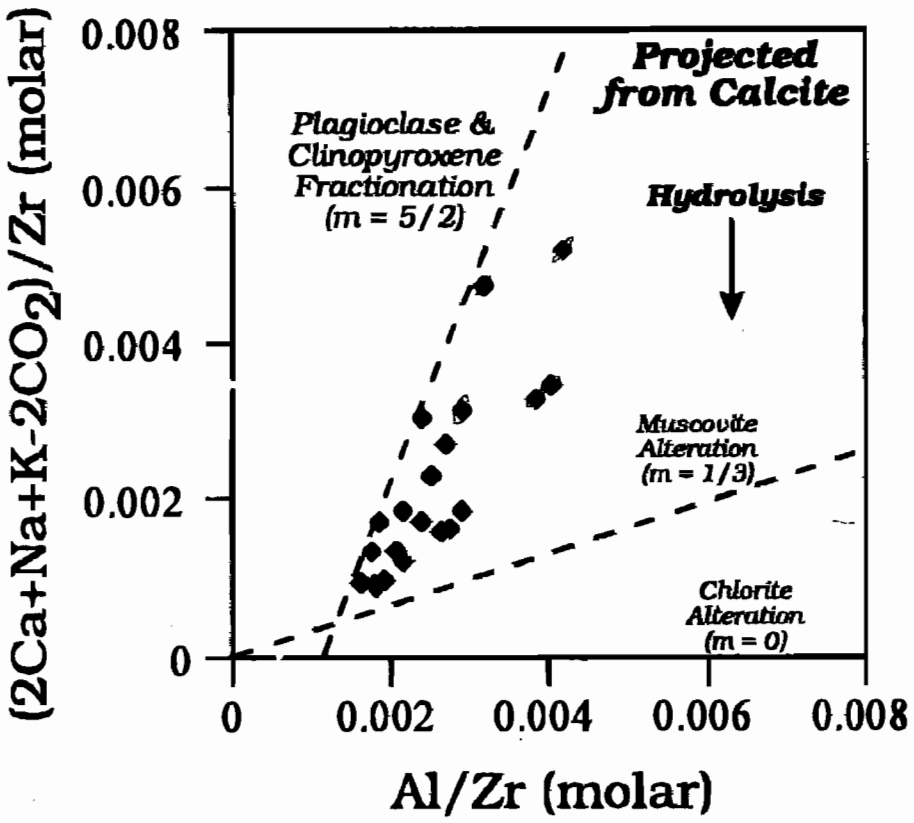

Figure 7
Plot of Al/Zr against K/Zr Pearce element ratio diagram. On this plot, fresh rocks would plot close to the abscissa because of the generally low amount of K present in fresh andesite. With hydrolysis, muscovite is produced, and the rocks undergo K addition and their compositions move up toward the muscovite alteration (control) line with slope of 1/3, corresponding to the K/Al ratio in muscovite. The K/Al molar ratio in these rocks is thus indicative of the amount of sericitization that has taken place in each rock and thus is a more specific measure of not only the degree, but type of hydrolysis that has taken place. By subtracting these scores from those of the total hydrolysis scores derived from Figure 6, the amount of chlorite sample can be determined and used as another exploration parameter.

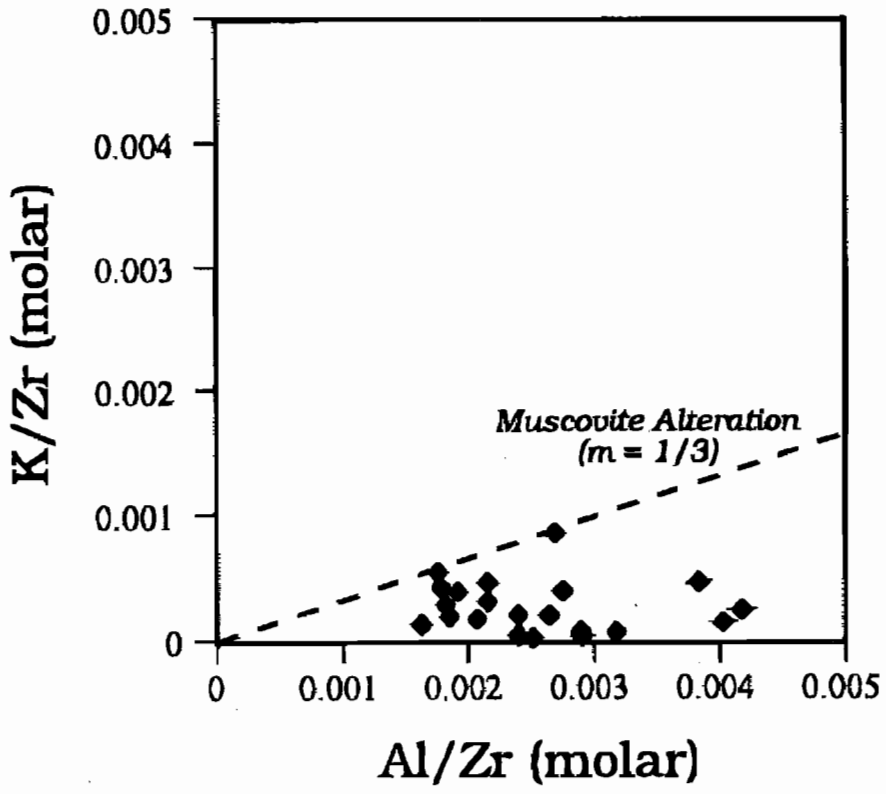

Figure 8
Plot of Fe/Zr against S/Zr Pearce element ratio diagram. This diagram is analogous to # 3 except that pyrite control of the Fe budget is investigated instead of calcite control of the Ca budget. Clearly only a few of these orientation samples contain significant pyrite, and most contain other Fe-bearing minerals (clinopyroxene, chlorite, etc.). Using data from Gemmell (open squares) and Jacks (filled circles), several plots from above have been reproduced. As these data sets are more proximal to mineralisation, these datasets contain more highly altered samples and thus exhibit significantly different trends on these plots. Note that because these samples do not have CO2 determinations, we cannot avoid the interferring effects of carbonate veins on these plots.

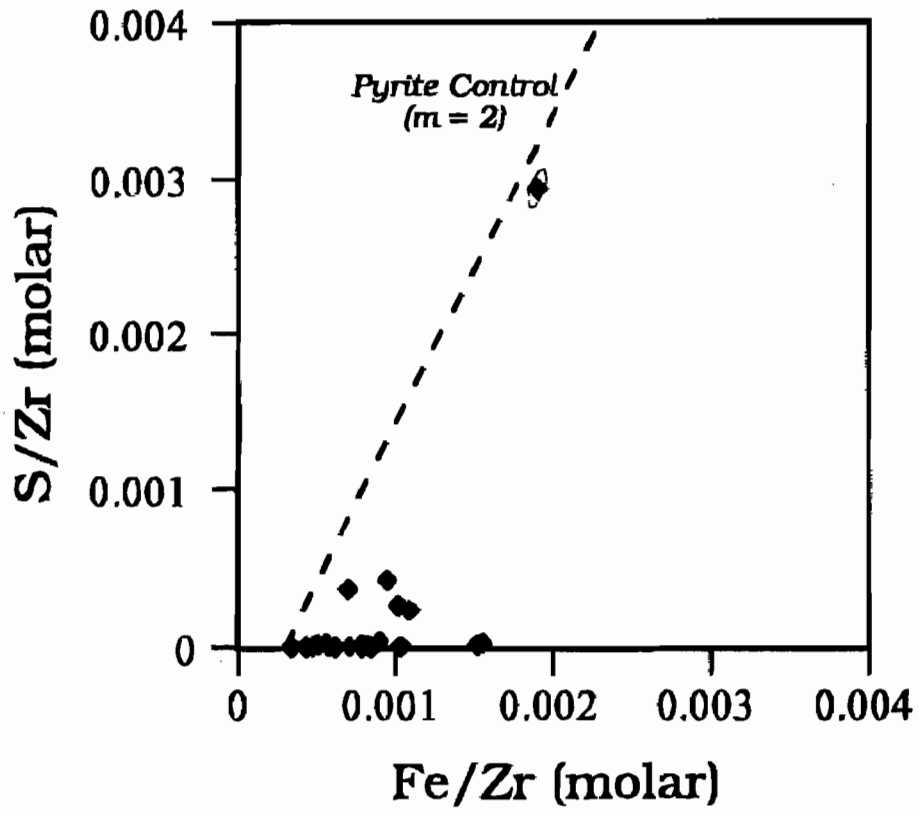

Figure 9
Analogous to Figure 1. Samples with high Zr plotting off of the line through the origin are largely from the SEZ and would normally be omitted from further consideration because they do not satisfy the conserved element-cogenetic parent assumptions. The fan of scatter at low concentrations is due to degrading analytical quality close to the detection limit, and might illustrate improvements made to the analytical regimes at CODES for Zr and Nb analyses (my interpretation and only a conjecture at this point - was there a change in methodology ?).

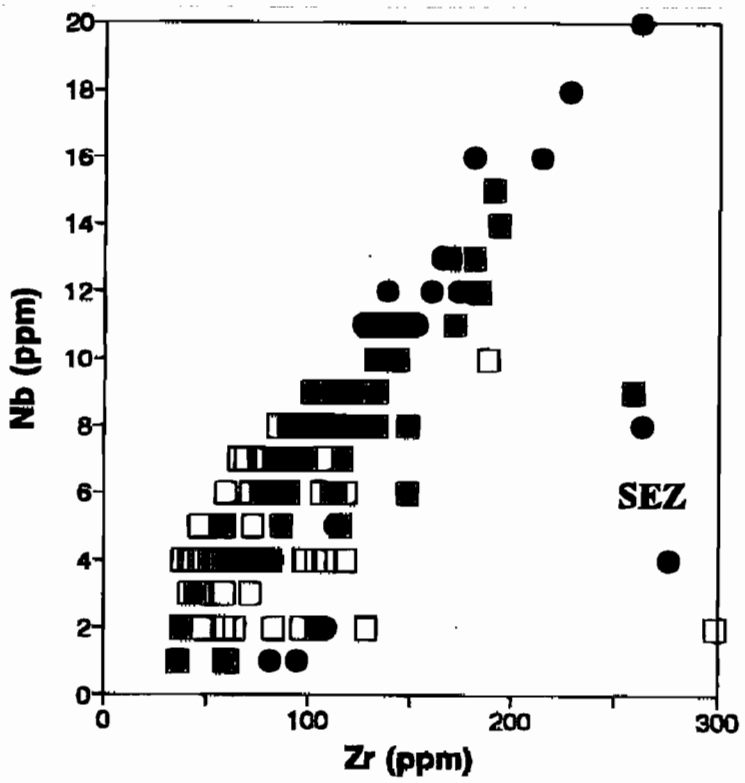

Figure 10
Analogous to Figure 2. Sample cloud limited on top by line with a unit slope (with one, presumably high calcite, exception), but a lot of samples plot down and to the right, suggesting that significant amounts of both hydrolysis and silicification have taken place in these samples.

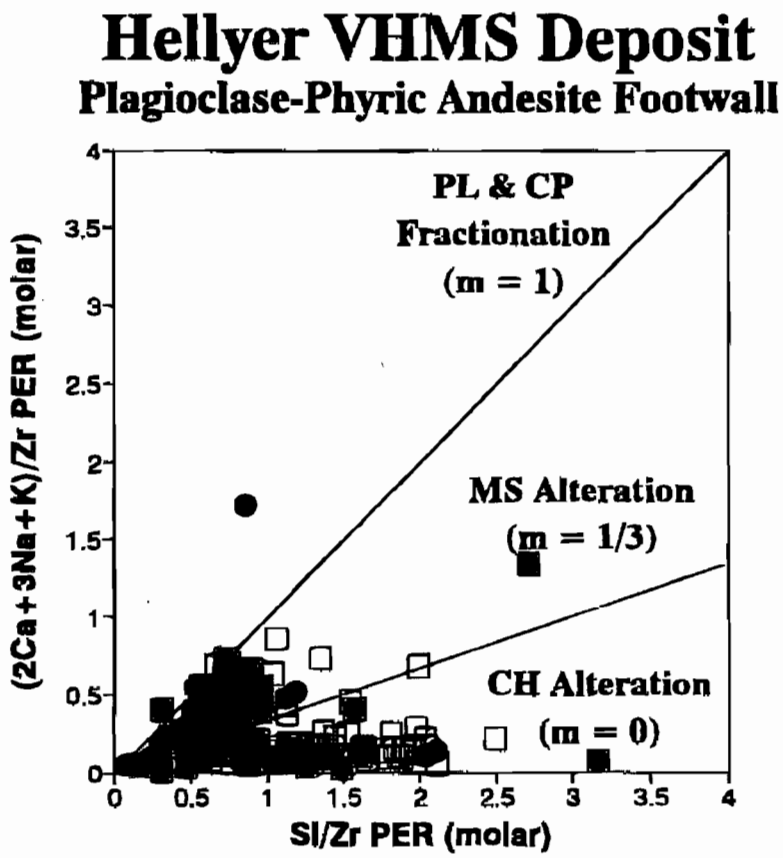

Figure 11
Analogous to Figure 5. Sample could limited on top by line with slope of 5/2 and data occurs all of the way down to the abscissa indicating that very large (almost complete) amounts of hydrolysis have taken place in these samples.

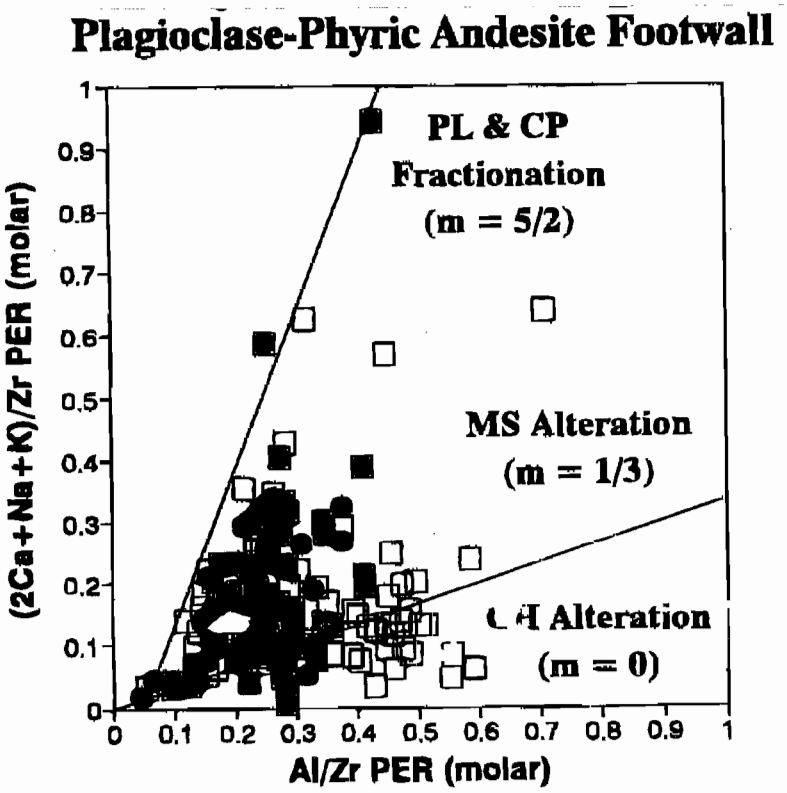

Figure 12
Analogous to Figure 7. Samples limited on top by sericite alteration line and span space down to abscissa. On this plot, both fresh and fully chloritized samples would plot along the abscissa and fully sericitized samples would plot along the line with slope of 1/3.

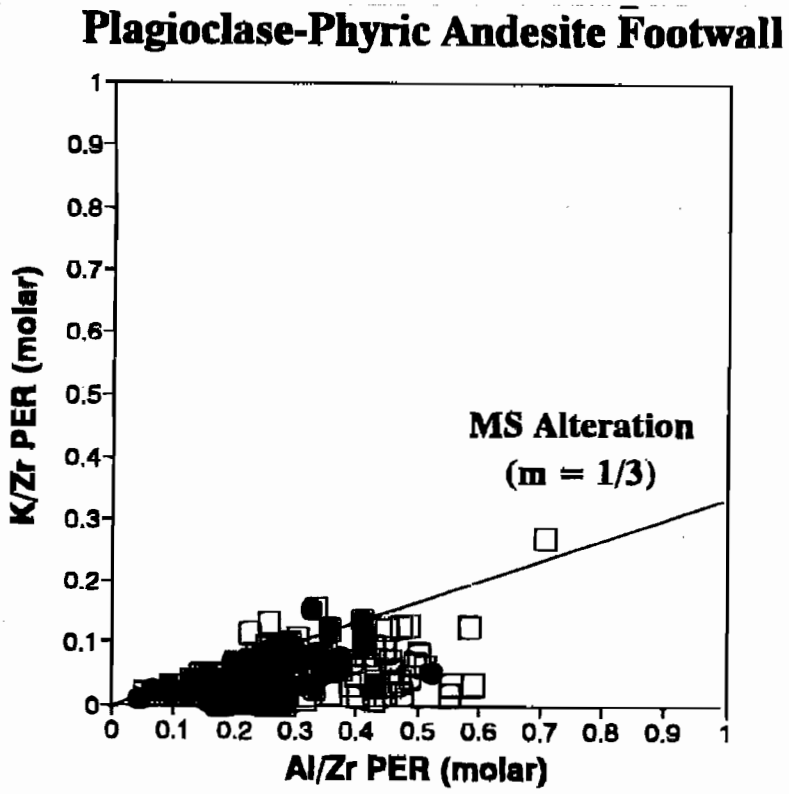

Figure 13
Analogous to Figure 8. Samples exhibit contain more sulphur and the Fe and S budgets are also controlled by pyrite, as would be expected in samples that have undergone more alteration and would presumably contain more sulphides.

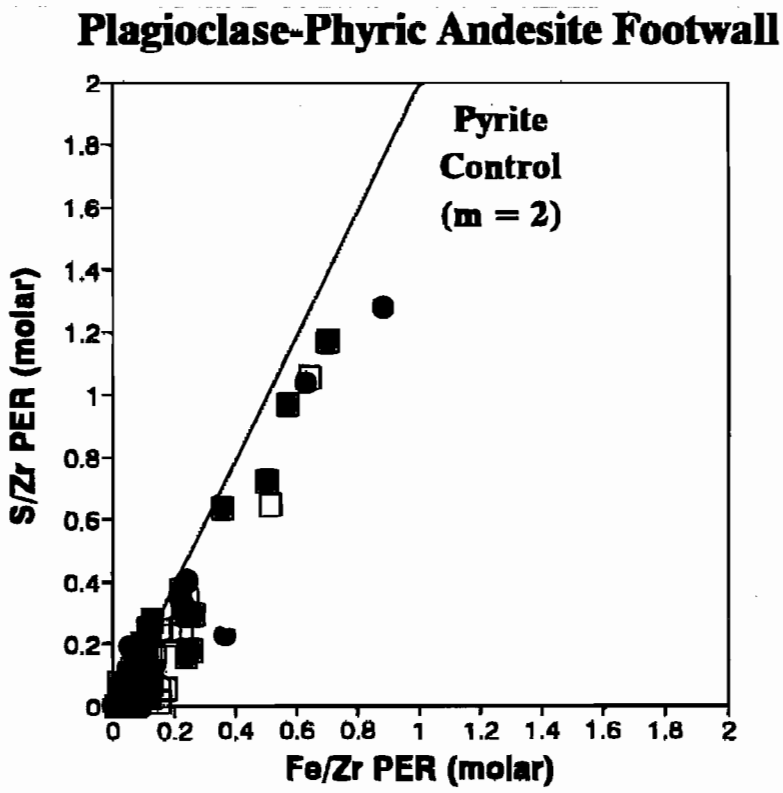

Que River Shale

An initial analyses of the Que River Shale whole rock geochemical data was made from the data contained in Jack (1989) and Sinclair (1994). There are no systematic errors between the data sets. XRD data from Sinclair (1994) indicate that the essential mineralogy (that set of minerals that comprise - 95 % of the rock) of these samples is quartz, muscovite, chlorite, calcite and pyrite. These minerals are thus considered in the analysis below.

Figure14

Much of the data plot on a single line passing through the origin, these data exhibit constant P_2O_5/TiO_2 ratios, possibly indicating that these element are conserved in material transfer processes that have affected these rocks, and that these rocks are cogenetic (they derive from a common parent that was at one time homogeneous, i.e. the sediment source composition didn't change over time). The range in $Ti0_2$ concentration of samples that lie along this 'constant ratio' line is from about 0.13 to 0.80, a factor of over 3 fold. This may suggest that significant material transfer has taken place among these samples in order to dilute (or enrich) these conserved elements so drastically, This material transfer may merely be the sorting of minerals that do not contain TiO_2 and P_2O_5 (quartz, muscovite, etc.), and may be a primary sedimentological process rather than something related to mineral deposit genesis. By contrast, samples that lie along this line may have had different starting compositions, or these elements are not conserved within them (possibly due to hydrothermal alteration).

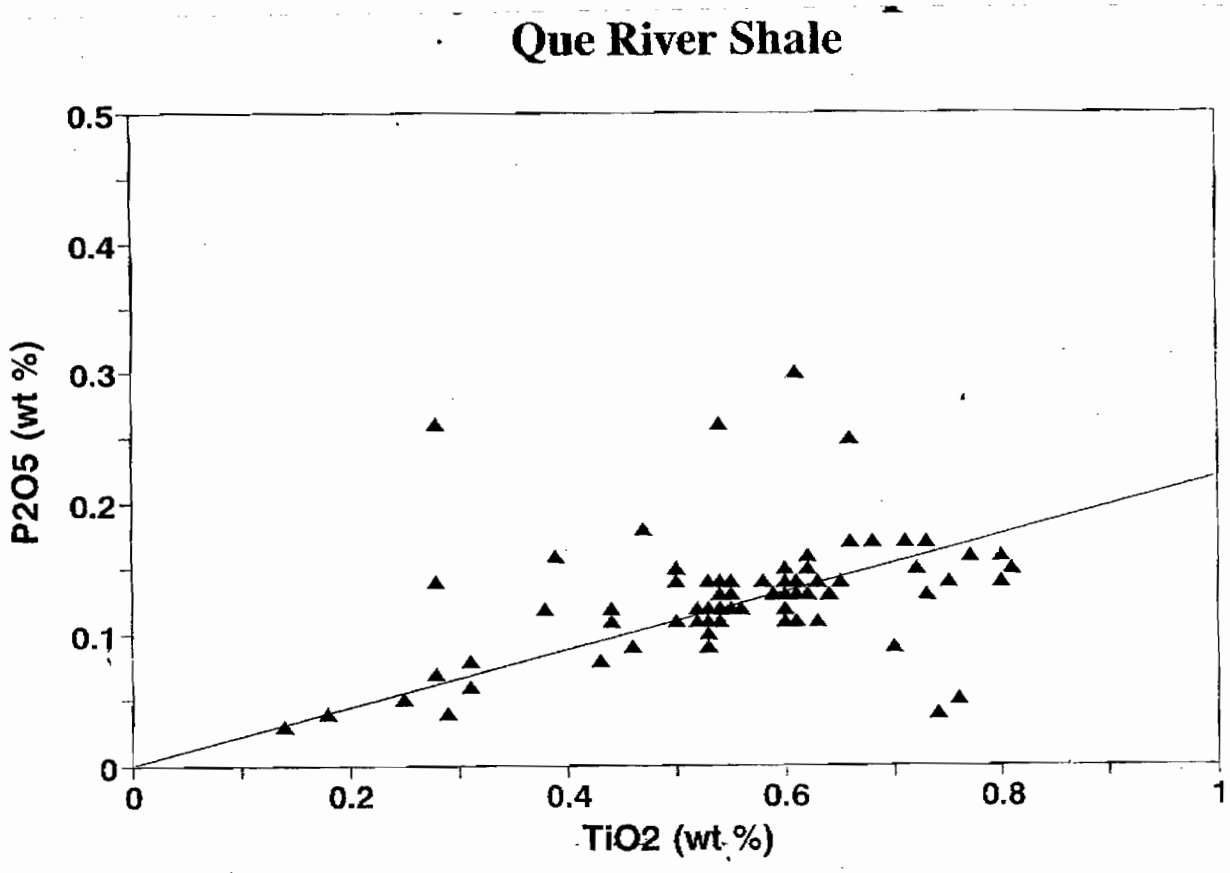

Figure 15

All of these data essentially lie on muscovite control line (it has a slope of 1/3 reflecting the K/A molar stoichiometry in muscovite). Thus, the location of data points on this diagram can be interpreted to represent the relative amount of muscovite in each sample. Samples to the right will have more muscovite than those to the left. However, this is not true for those samples that do not fall on the constant ratio line of Figure 1, even though these same samples do fall on the muscovite control line of Figure 2. This is because these 'off but on' samples may have undergone Ti02 addition or loss (in order to plot off of the constant ratio line on Figure 1) and the effect of this denominator material transfer on Figure 2 is' to displace the composition toward or away from the origin. Consequently, the representation of the relative amount of muscovite in these sample has been altered by TiO_2 material transfer, which has displaced the composition along the muscovite control line to some other location, Consequently, the amount of muscovite can accurately be determined only in those samples that plot on the constant ratio line of Figure 1. This metric might reflect hydrothermal processes that resulted in extra muscovite in these samples, but which didn't affect TiO_2.

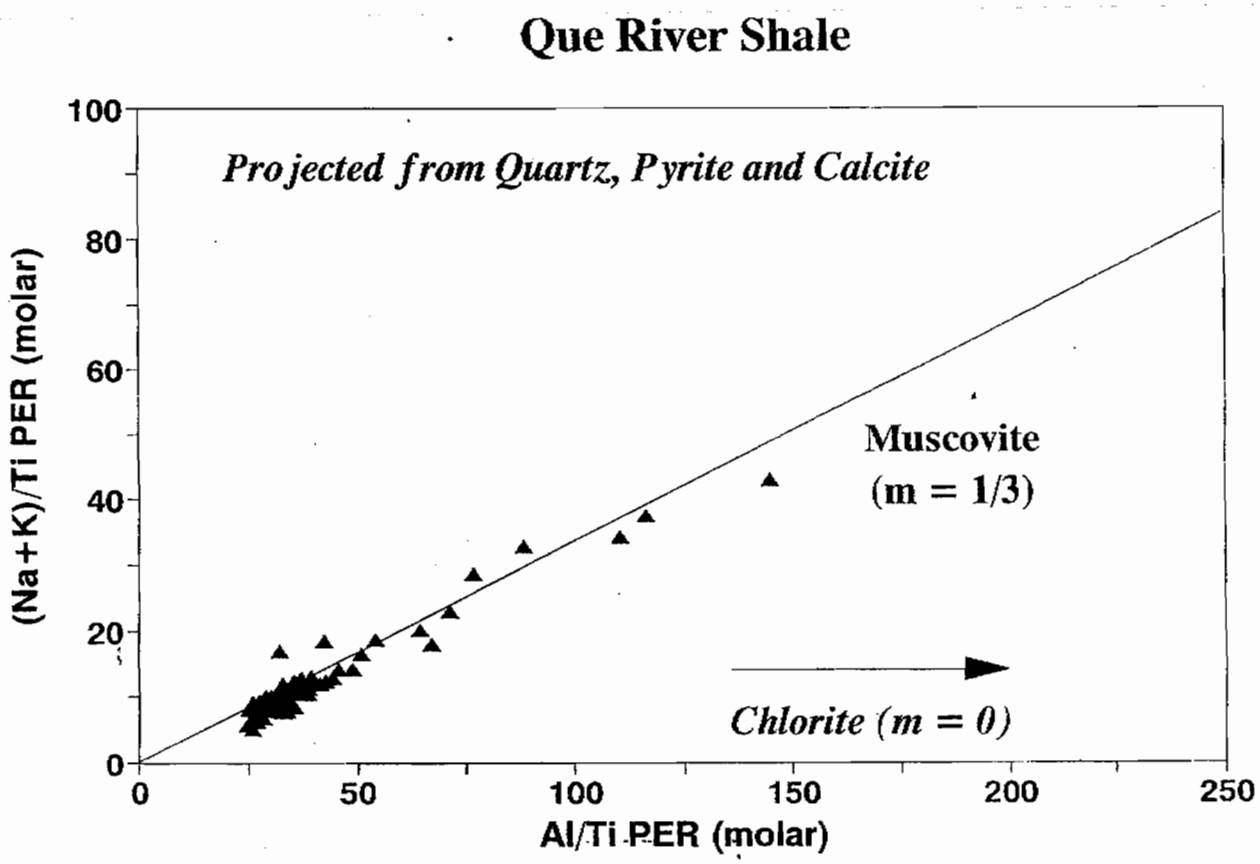

Figure 16
Samples on this plot are affected by the presence of quartz (m = 0), muscovite (m = 1) and chlorite (clinochiore; m = 2/3). Note that the slope of the data is about 1/5, and thus must correspond to some linear combination of quartz (mostly), muscovite and chlorite (clinochiore; the two arrows on this plot depict the direction of the effect of compositional variations within chlorite–tschermak exchange [Al_2MgSi) and di-tri exchange [Al_2Mg_3]). Note that whereas most of the data plot on a single tine, suggesting a constant ratio of quartz : muscovite : chlorite, some do not. Those that fall off of the line may have more or less any of these minerals (i.e. there may be some fractionation during the sorting of these minerals, or — let's hope — hydrothermalism may be responsible).

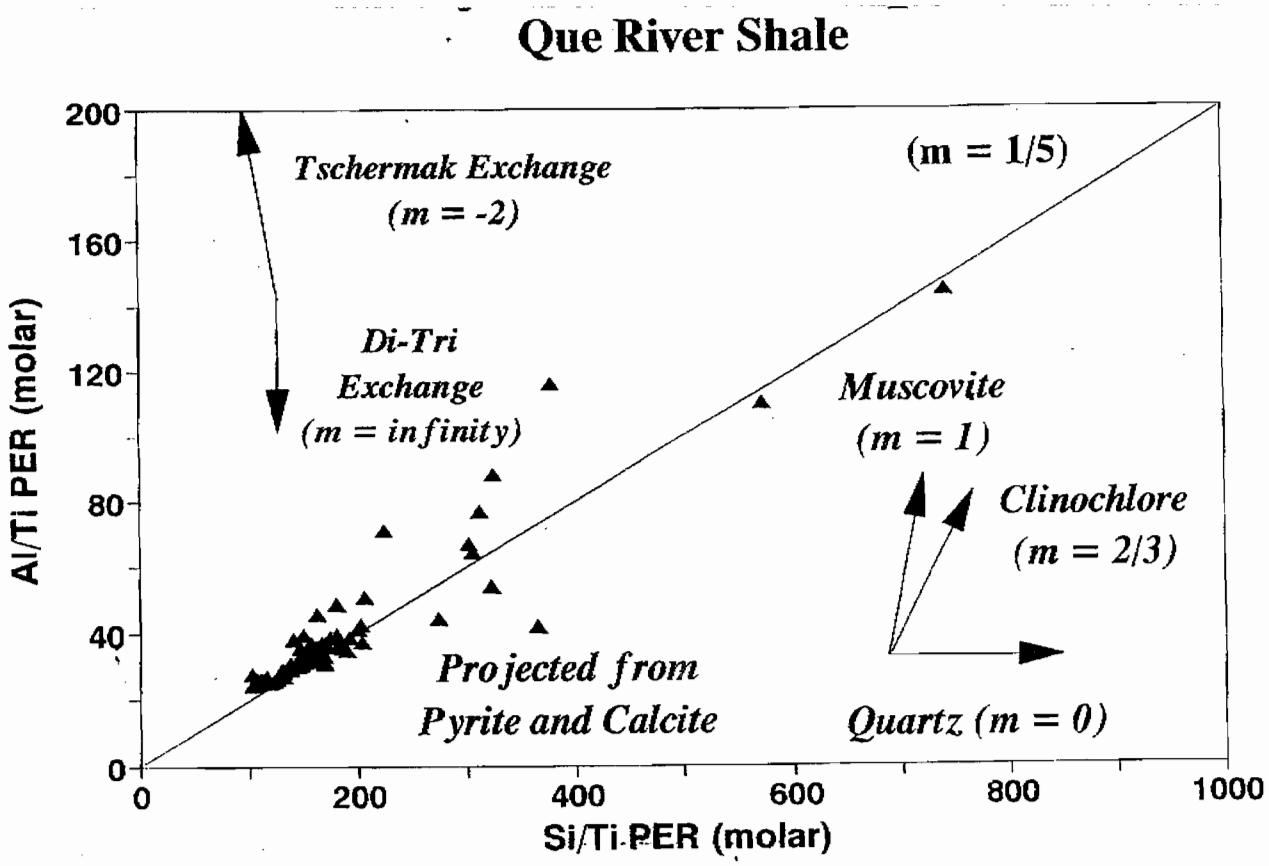

Figure 17
Many of these data plot on a pyrite control line (m = 2). Those that do not may be displaced to the right from this line due to an 'over-abundance' of chlorite (possibly introduced hydrothermally), or the presence of Fe-bearing carbonates (also possibly introduced hydrothermally). When we obtain C02 analyses from these samples, we can evaluate whether the amount of CO2 is commensurate with the amount of Ca, or whether carbonate minerals other than calcite (possibly Fe-bearing) are present.

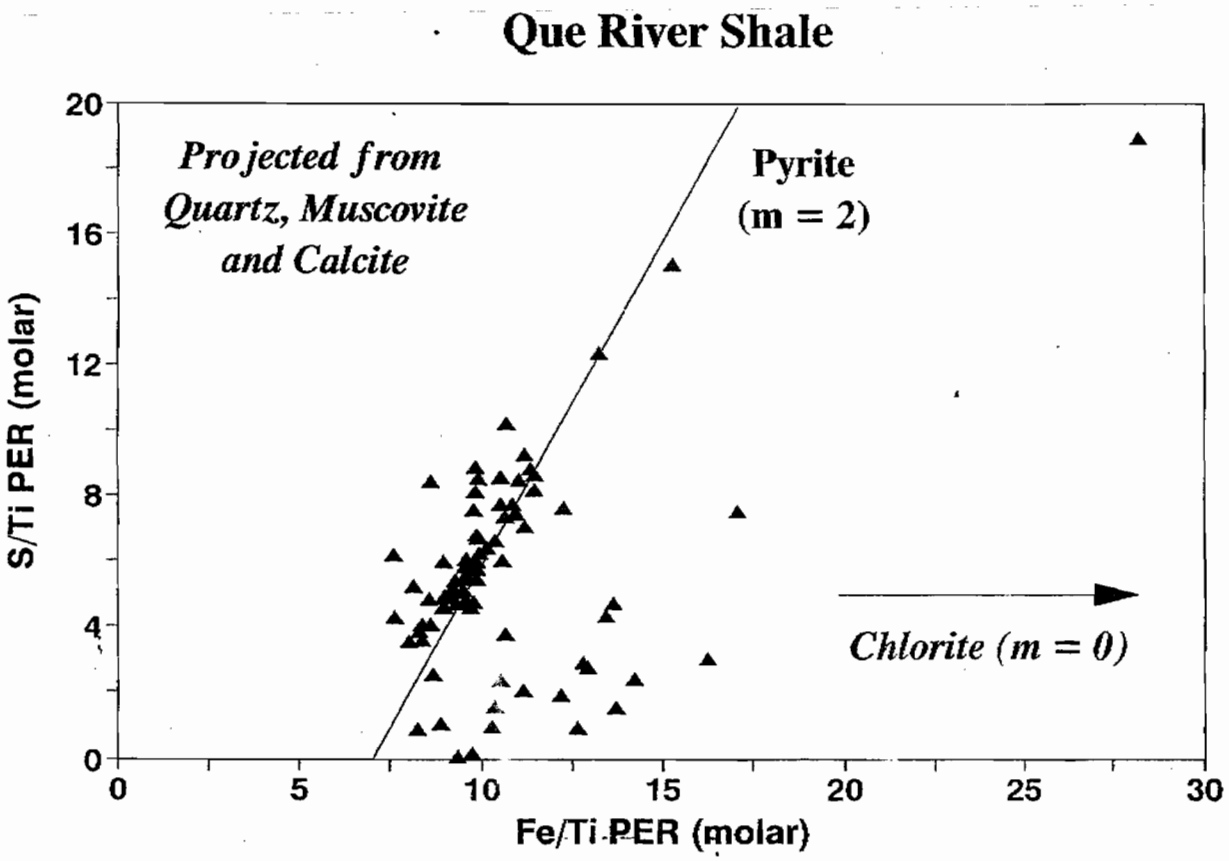

Figure 18
This diagram is sensitive only to the presence of chlorite (clinochlore; m = 5/2; see explanation above for exchange vectors). Clearly, more is going on here than that, but this may be due to measurement error.

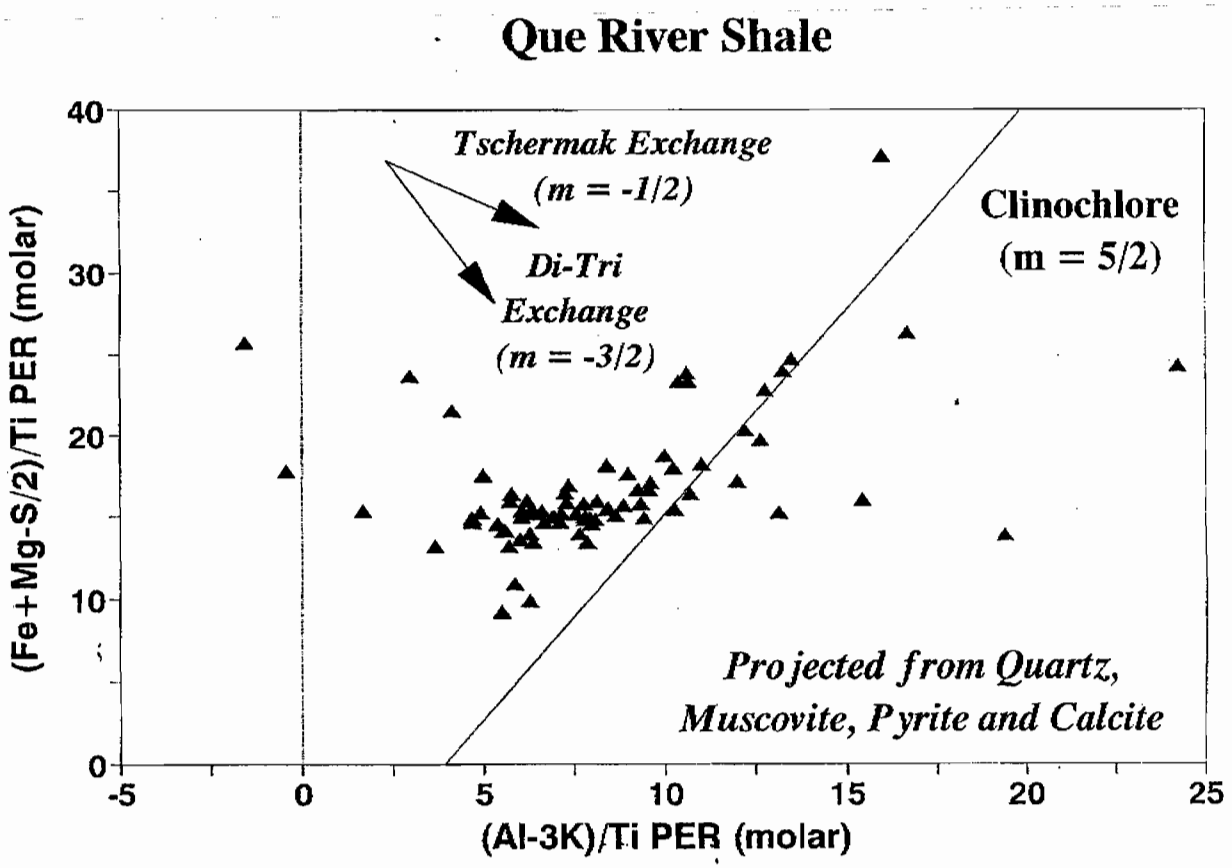

Figure19

On this plot the effect of the presence" of both muscovite and chlorite (clinochlore) is the same (m = 1, see explanation above for exchange vectors). This plot looks almost identical to that of Figure 2 in terms of tile relative position of the points, suggesting that the amount of chlorite present in these samples is small relative to muscovite (this is consistent with Sinclair's (1994) observations, and may explain why Figure 5 is so squirrelly, i.e. it is significantly affected by measurement errors).

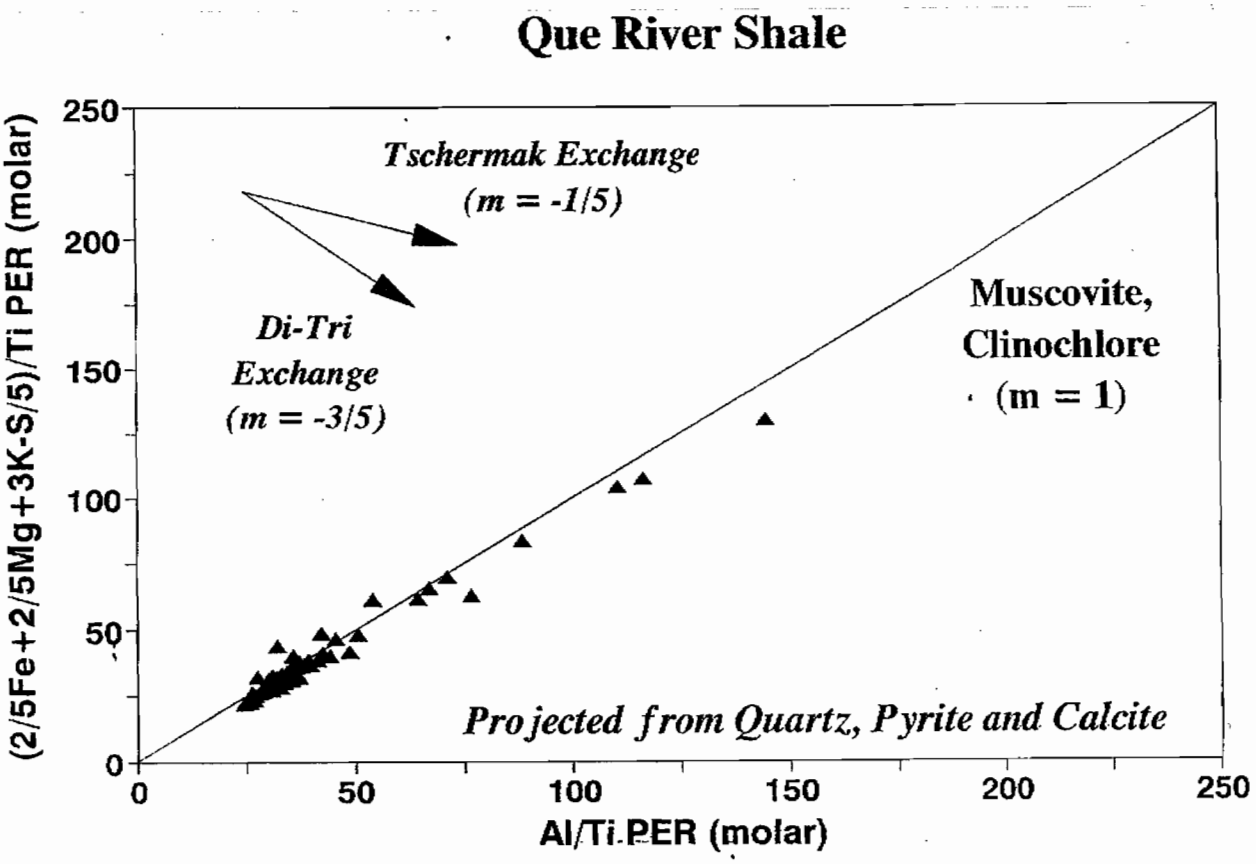

Summary

1. The new analyses of the unaltered footwall andesite and Que River Shale ("orientation data") are co-linear and plot along a background model lines. These data indicate the plagioclase phyric footwall andesite are cogenetic (derived from common parent that was at one time homogeneous). The data for the Que River Shale also indicates that they are cogenetic (they derive from a common parent that was at one time homogeneous, i.e. the sediment source composition didn't change over time).

2. The altered samples show substantial variation from the background model lines. The deviation of the altered data from these lines indicates the degree of alteration and the direction of the deviation gives evidence as to the type and extent of the alteration processes.

3. Pearce element ratio analysis of the altered andesites in the immediate footwall indicate that they conatin significant amounts of both hydrolysis (sericite and chlorite) products and silicification (quartz).

4. Pearce element ratio analysis of the Que River Shale indicates a constant ratio of quartz: muscovite: chlorite for the majority of samples. Some samples have a over or under abundance of these minerals which may be due to some fractionation during the sorting of these minerals, or hydrothermalism may be responsible.

5. CO_2 measurments are needed for proper evaluation of the role of carbonate altereation. Splits of the various samples sets have been set to the University of British Columbia and these analyses will be done shortly.

References

Akella, J. (1966): Calculation of Material Transport in Some Metasomatic Processes: Neues *Jahrbuch ftr Mineralogische Abhandlungen* 104: 316-329.

Gemmell, J.B., 1990, Hellyer Stringer Zone Project: Progress Report No. 3, Aberfoyle Resources Ltd. (Australia): 76 p.

Gemmell, J.B. and Large, R.R., 1992, Stringer system and alteration zones underlying the Hellyer volcanogenic massive sulphide deposit, Tasmania, Australia, *Economic Geology* 87: 620-649.

Grant, J.A. (1986): The Isocon Diagram — A Simple Solution to Gresens' Equation for Metasomatic Alteration. Economic Geology 81: 1976-1982.

Gresens, R.L. (1967): Composition-Volume Relationships in Metasomatism. *Chemical Geology* 2: 47-55.

Jack, D.J., 1989, Hellyer host rock alteration: Unpub. Masters thesis, University of Tasmania: 182 p.

MacLean, W.H. and Barrett, T.J. (1993): Lithogeochemical Techniques Using Immobile Elements. *Journal of Geochemical Exploration* 48: 109-133.

Russell, J.K. and Stanley, C.R. (1990): Theory and Application of Pearce Element Ratios to Geochemical Data Analysis. (editors) Geological Association of Canada, Short Course No. 8, Vancouver, British Columbia, May: 310 p.

Sinclair, B.J., 1994, Geology and geochemistry of the Que River Shale, western Tasmania. Unpubl. BSc (Hons) thesis, University of Tasmania.

Stanley, C.R. and Madeisky, H.E. (1993): Pearce Element Ratio Analysis : Applications in Lithogeochemical Exploration. Mineral Deposit Research Unit, Dept. of Geological Sciences, Univ. of British Columbia, Short Course No. 13 Notes, Vancouver, British Columbia, March: 540p.

Sample Name	SiO2	TiO2	Al2O3	Fe2O3	MnO	MgO	CaO	Na2O	K2O	P2O5	LOI	Total	ALT INDEX	Ti/Zr	S	Total C	Sc	V	Cr	Ni	Cu	Zn	Se	Rb
	%	%	%	%	%	%	%	%	%	%	%	%			%	%	ppm	ppm	ppm	ppm	ppm	ppm	ppm	ppm
MBX-1A (Standard)	58.29	0.47	17.19	3.86	0.07	2.15	3.75	5.20	4.68	0.25	3.87	99.78	43.3	28	0.24	0.68	9	189	57	5.9	379	28	<1	82
MBX-1B (Standard)	58.85	0.48	17.42	3.90	0.07	2.13	3.77	5.16	4.74	0.24	3.90	100.66	43.5	29	0.25	0.73	9	187	53	6.6	395	31	<1	82
MBX-1C (Standard)	57.87	0.47	17.38	3.91	0.07	2.17	3.77	5.18	4.70	0.24	3.86	99.62	43.4	28	0.24	0.68	10	190	53	6.4	388	29	<1	83
WP-1A (Standard)	64.40	0.50	16.63	4.34	0.08	2.70	4.99	4.33	1.59	0.17	0.07	99.80	31.5	24	<0.01	0.01	11	83	70	38	18	54	<1	22
WP-1B (Standard)	64.27	0.50	16.63	4.36	0.08	2.72	4.99	4.31	1.58	0.17	0.07	99.68	31.6	24	<0.01	0.01	11	83	70	38	18	54	<1	22
WP-1C (Standard)	64.51	0.49	16.61	4.36	0.08	2.72	4.99	4.34	1.58	0.18	0.08	99.94	31.5	23	<0.01	<0.01	12	83	69	38	19	55	<1	22
QUA-1A (Standard)	66.08	0.46	15.53	4.33	0.08	2.56	4.08	4.07	1.37	0.13	1.26	99.95	32.5	27	0.07	0.06	10	79	52	23	36	54	<1	23
QUA-1B (Standard)	65.82	0.46	15.44	4.33	0.08	2.56	4.07	4.02	1.39	0.12	1.29	99.58	32.8	28	0.07	0.06	9	76	51	23	35	53	<1	23
QUA-1C (Standard)	65.85	0.45	15.52	4.35	0.08	2.55	4.08	4.07	1.37	0.13	1.32	99.77	32.5	27	0.09	0.05	12	75	51	22	34	53	<1	23
CUL-1A (Standard)	51.45	0.86	14.09	9.74	0.13	2.13	6.82	2.47	0.70	0.17	10.31	98.86	23.3	101	2.03	2.01	40	321	30	27	112	107	<1	13
CUL-1B (Standard)	51.62	0.87	14.17	9.77	0.13	2.14	6.83	2.47	0.71	0.17	10.19	99.05	23.4	102	2.04	2.00	41	320	30	26	112	104	1.1	13
CUL-1C (Standard)	51.68	0.86	14.11	9.73	0.13	2.12	6.84	2.45	0.70	0.15	10.28	99.05	23.3	100	1.99	2.02	40	318	30	27	110	103	<1	13
ALB-1A (Standard)	54.97	0.61	18.82	1.59	0.03	2.89	10.14	5.82	0.81	0.29	3.52	99.49	18.8	51	0.24	0.40	17	191	41	46	1790	10	1	18
ALB-1B (Standard)	54.92	0.61	18.83	1.55	0.03	2.91	10.11	5.81	0.81	0.29	3.52	99.39	18.9	52	0.23	0.41	15	189	41	45	1750	10	1.3	19
ALB-1C (Standard)	54.79	0.60	18.79	1.57	0.04	2.91	10.11	5.87	0.81	0.29	3.52	99.30	18.9	50	0.23	0.40	17	191	40	47	1730	11	<1	19
CHI-1A (Standard)	21.98	0.12	1.30	0.93	0.04	4.97	37.14	0.08	0.10	0.07	32.63	99.36	12.0	28	0.55	7.98	Ca int.	27	20	5.5	9	19	<1	1.7
CHI-1B (Standard)	21.98	0.12	1.28	0.92	0.04	4.99	37.19	0.09	0.10	0.07	32.54	99.32	12.0	27	0.54	8.04	Ca int.	27	19	4.3	9	17	<1	1.6
CHI-1C (Standard)	21.74	0.12	1.25	0.92	0.04	4.95	37.10	0.07	0.10	0.07	32.57	98.93	12.0	28	0.56	8.04	Ca int.	26	19	4.7	8	19	<1	1.7
P-1A (Standard)	70.44	0.38	14.43	3.69	0.08	1.12	3.47	3.89	2.09	0.08	0.40	100.07	30.4	19	<0.01	0.02	11	59	150	3	10	42	<1	46
P-1B (Standard)	70.37	0.38	14.46	3.76	0.08	1.12	3.47	3.87	2.09	0.07	0.40	100.07	30.4	18	<0.01	0.02	12	58	149	3.2	11	42	<1	46
P-1C (Standard)	70.55	0.38	14.46	3.71	0.08	1.12	3.48	3.87	2.10	0.08	0.42	100.25	30.5	19	<0.01	0.01	12	60	152	3.5	9	42	<1	46
MAC10-130 (Basalt)	44.26	0.91	12.13	8.23	0.20	8.12	12.37	2.90	1.71	0.77	8.03	99.63	39.2	13	0.1	1.23	31	270	856	279	119	78	<1	30
MAC10-164 (Basalt)	45.02	0.48	12.43	9.42	0.21	10.18	11.79	3.20	0.48	0.50	5.87	99.58	41.6	22	0.03	0.73	37	278	725	175	104	60	<1	10
MAC10-200 (Basalt)	49.32	0.77	10.22	7.39	0.28	9.33	8.89	1.10	1.42	0.66	10.45	99.83	51.8	13	0.02	1.45	29	244	696	234	64	80	<1	31
MAC11-239 (Andesite)	47.86	0.91	20.76	12.13	0.13	5.24	1.64	4.96	1.46	0.68	4.46	100.23	50.4	22	<0.01	0.08	42	387	8	48	8	195	<1	55
MAC11-250 (Shale)	64.73	0.42	10.16	4.52	0.13	2.46	4.66	0.11	2.90	0.14	9.62	99.85	52.9	24	0.82	2.43	16	102	139	37	10	20	1.9	103
MAC11-388 (Basalt)	43.91	0.54	13.65	7.17	0.13	5.43	9.53	0.46	2.72	0.15	15.09	98.78	44.9	29	0.56	3.28	35	261	344	63	46	48	<1	95
MAC11-502 (Basalt)	46.18	0.37	15.71	7.58	0.09	9.35	7.20	2.43	0.52	0.09	9.89	99.41	50.6	17	0.25	1.31	40	236	808	188	70	81	<1	20
MAC11-641 (Andesite)	58.24	0.44	13.19	3.26	0.08	2.10	15.67	0.81	0.03	0.24	6.48	100.54	11.4	24	0.51	0.76	28	176	486	76	30	363	<1	1
MAC11-766 (Andesite)	52.98	0.56	14.76	6.06	0.09	3.47	8.14	1.44	2.72	0.32	8.84	99.38	39.3	22	0.08	1.48	42	316	263	52	79	90	<1	91
MAC11-823 (Andesite)	61.89	0.59	15.97	6.43	0.06	2.07	2.79	2.74	2.27	0.19	4.67	99.67	44.0	21	0.03	0.49	23	59	4	4	5	99	<1	82
MC12-82(Shale)	67.14	0.55	12.16	5.33	0.04	2.79	2.44	0.41	2.53	0.13	6.55	100.07	65.1	25	0.97	1.49	18	165	152	60	60	99	2	103
MC12-124(Shale)	62.89	0.54	11.59	8.23	0.04	2.52	3.15	0.31	2.40	0.54	7.45	99.66	58.7	26	2.92	1.32	18	195	161	69	62	104	6.8	95
MC12-346(Andesite)	48.85	0.39	11.96	7.54	0.18	8.88	8.93	0.86	3.49	0.26	8.04	99.38	55.8	27	0.66	1.11	42	295	899	199	129	69	<1	68
MAC19-492(Basalt)	50.20	0.43	15.87	7.88	0.12	7.72	5.55	2.54	0.73	0.08	8.82	99.94	51.1	23	0.02	1.05	37	234	680	137	10	236	<1	26
MAC19-661(Basalt)	45.34	0.40	15.22	9.08	0.19	11.07	6.76	3.29	0.85	0.12	7.53	99.85	54.3	20	0.01	0.71	26	215	707	221	35	122	<1	26
MAC19-760(Basalt)	50.67	0.53	13.77	7.28	0.20	7.09	9.45	4.40	0.06	0.19	6.44	100.08	34.0	22	0.02	0.95	27	201	444	135	79	97	<1	1
MAC19-812(Andesite)	61.05	0.64	17.12	5.35	0.05	1.82	2.84	4.30	2.25	0.19	4.47	100.08	36.3	31	0.09	0.54	41	273	294	34	18	65	<1	102
MAC19-860(Andesite)	64.01	0.49	13.65	5.07	0.11	1.59	4.39	1.71	2.95	0.16	5.91	100.04	42.7	20	<0.01	0.82	20	57	4	3	6	72	<1	107
MAC19-913(Andesite)	56.04	0.84	17.50	8.84	0.15	2.70	2.38	2.92	5.00	0.21	3.14	99.72	59.2	26	<0.01	0.15	25	109	33	6	12	418	<1	110
MAC21-72(Andesite)	55.10	0.42	14.07	8.17	0.25	6.59	7.07	3.47	0.74	0.13	3.55	99.56	41.0	38	0.06	0.22	31	231	228	53	113	436	<1	18
MAC21-321(Andesite)	58.97	0.47	14.41	6.40	0.17	3.89	8.76	3.63	0.26	0.10	2.51	99.57	25.1	32	0.11	0.08	23	187	105	26	154	1199	<1	5
MAC21-354(Andesite)	54.28	0.49	13.48	8.24	0.21	3.58	7.31	3.34	0.93	0.11	8.38	100.35	29.7	29	0.02	1.38	31	211	129	26	12	81	<1	32
MAC21-436(Andesite)	56.41	0.72	15.18	8.14	0.20	4.70	8.19	2.26	1.17	0.16	2.99	100.12	36.0	35	0.04	0.08	27	190	128	93	108	345	<1	30
MAC25-112(Andesite)	38.84	0.30	8.74	7.14	0.36	6.18	19.26	2.04	0.10	0.10	16.86	99.92	22.8	31	0.03	3.42	40	226	1097	200	117	185	<1	2
MAC25-152(Basalt)	46.51	0.41	14.78	9.15	0.44	6.81	9.66	3.33	1.78	0.19	6.91	99.97	39.8	42	0.22	0.95	42	397	1055	276	161	443	<1	44
MAC31-47(Shale)	66.28	0.77	13.37	5.99	0.03	3.10	0.70	0.29	3.02	0.14	5.73	99.39	86.1	30	1.56	0.80	22	282	158	78	51	48	3.7	121
MAC31-78(Shale)	64.70	0.69	11.77	6.18	0.05	2.89	2.82	0.09	2.72	0.16	7.34	99.37	65.9	30.13	1.92	1.28	21	138	139	72	59	109	1.9	110
MAC31-90(Shale)	65.63	0.68	12.04	5.88	0.04	2.69	2.37	0.37	2.78	0.14	6.83	99.42	66.6	27	1.71	1.19	20	131	130	64	54	117	1	114
MAC31-103(Basalt)	34.38	0.31	9.88	5.94	0.24	6.64	21.78	3.00	0.23	0.22	17.07	99.69	21.7	26	0.03	3.55	34	232	713	147	63	40	<1	4
MAC31-147(Basalt)	56.35	0.38	11.79	6.43	0.12	6.34	9.63	2.51	0.71	0.33	5.11	99.70	36.7	26	0.24	0.55	30	216	600	132	123	91	<1	14
MAC31-168(Basalt)	48.38	0.41	11.79	8.02	0.15	7.36	10.31	2.29	1.46	0.36	9.01	99.54	41.2	24	0.91	1.45	35	249	707	138	48	70	<1	34
HAT4-141(Shale)	66.73	0.59	12.83	6.91	0.21	2.50	0.33	0.31	3.16	0.11	6.24	99.92	89.8	25	1.22	1.29	18	212	131	72	49	122	2.7	133

HAT4-148(Shale)	69.80	0.43	13.34	5.02	0.14	2.34	0.20	0.40	3.46	0.08	4.69	99.90	90.6	18	0.95	0.51	10	91	61	33	24	71	<1	146
HAT4-223(Basalt)	48.85	0.67	12.21	8.23	0.11	5.97	9.98	0.15	2.03	0.42	11.06	99.68	44.1	25	0.02	1.71	39	276	386	50	51	75	<1	78
HAT4-323(Basalt)	46.20	0.56	12.42	8.49	0.27	7.46	13.04	3.07	1.06	0.61	6.51	99.69	34.6	20	0.09	1.00	37	275	733	149	108	174	<1	29
HAT4-462(Basalt)	49.65	0.60	12.21	8.12	0.21	6.83	11.94	2.06	0.55	0.29	7.25	99.71	34.5	29	0.01	1.07	32	249	403	86	24	278	<1	14
HAT8-139(Basalt)	57.40	0.43	14.32	7.07	0.18	6.50	6.55	4.46	1.22	0.15	2.19	100.47	41.2	40	<0.01	0.05	34	270	189	38	38	108	<1	32
HAT8-179(Basalt)	52.15	0.48	16.21	9.20	0.18	5.69	9.47	3.17	0.53	0.17	3.18	100.43	33.0	41	<0.01	0.15	33	271	106	26	65	81	<1	17
HAT8-207(Andesite)	68.41	0.42	13.88	4.80	0.14	2.15	1.58	4.76	1.54	0.10	1.86	99.64	36.8	17	<0.01	0.06	17	57	39	7	7	184	<1	31
HAT8-313(Andesite)	71.53	0.37	13.65	3.84	0.16	1.35	1.57	5.22	1.24	0.10	1.28	100.31	27.6	17	0.02	0.03	14	42	15	5	6	591	<1	28
HAT8-361(Basalt)	55.76	0.46	15.13	8.32	0.14	5.63	8.92	1.59	1.39	0.14	2.46	99.94	40.0	41	<0.01	0.06	34	257	146	32	54	70	<1	39
HAT9-65(Basalt)	56.80	0.69	9.38	5.02	0.33	3.66	9.88	3.19	0.32	0.65	9.42	99.34	23.3	13	0.51	1.70	28	230	690	206	109	2258	<1	6
HAT9-96(Basalt)	41.67	0.93	12.41	9.63	0.34	7.95	11.09	2.56	0.21	0.78	12.11	99.68	37.4	13	0.04	1.97	40	329	952	258	46	197	<1	7
HAT9-118(Dacite)	73.86	0.23	13.04	2.31	0.03	0.48	1.57	3.32	2.32	0.05	2.97	100.18	36.4	7	0.79	0.30	11	7	4	2	5	12	<1	73
HL26-136(Shale)	69.74	0.53	10.83	5.25	0.04	2.18	1.80	0.07	2.62	0.11	6.28	99.44	72.0	25	1.97	1.39	16	140	132	68	44	159	1.9	101
HL26-159(Shale)	72.95	0.28	12.29	2.60	0.05	1.62	1.93	0.22	3.23	0.06	4.39	99.62	69.3	11	0.68	0.43	7	55	48	17	14	85	<1	105
HL26-197(Basalt)	41.17	0.48	13.71	8.69	0.16	8.32	10.86	2.40	0.85	0.16	12.97	99.77	40.9	37	0.62	1.97	46	288	816	187	83	135	<1	28
HL26-211(Basalt)	41.20	0.48	14.30	8.14	0.16	10.27	11.02	2.64	0.42	0.18	10.78	99.59	43.9	38	0.04	1.50	46	311	949	244	86	68	<1	12
HL26-228(Basalt)	36.77	0.43	12.79	7.81	0.21	8.26	15.17	2.86	0.59	0.18	14.50	99.57	32.9	36	0.06	2.55	44	304	889	202	66	95	<1	11
HL26-286(Andesite)	58.02	0.58	14.58	10.70	0.03	1.06	1.14	6.60	0.47	0.13	5.74	99.05	16.5	20	6.7	0.11	13	63	5	2	27	60	<1	19
HL80-103(Basalt)	52.10	0.49	12.21	6.64	0.09	4.75	9.20	1.16	1.59	0.17	10.89	99.29	38.0	19	1.24	1.68	33	230	550	102	72	53	<1	56
HL80-225(Basalt)	50.65	0.52	12.92	17.25	0.26	7.64	2.93	0.28	0.37	0.16	7.13	100.11	71.4	23	0.15	0.50	30	220	498	96	7	210	<1	15
HL80-332(Basalt)	53.43	0.52	14.04	7.58	0.18	7.41	4.93	3.50	0.44	0.24	7.20	99.47	48.2	19	0.03	0.86	34	246	418	92	73	857	<1	17
HL246-96(Shale)	65.71	0.61	12.82	5.15	0.04	2.73	1.84	0.80	3.01	0.12	6.95	99.78	68.5	24	1.17	1.55	18	188	147	71	44	40	2.1	119
HL246-168(Shale)	67.63	0.61	12.26	5.11	0.04	2.56	1.89	0.26	2.83	0.12	6.22	99.53	71.5	25	1.1	1.35	19	210	139	68	47	225	2.1	114
HL246-204(Shale)	69.18	0.21	10.48	3.34	0.04	2.18	4.73	0.34	2.44	0.04	6.73	99.71	47.7	10	0.8	0.97	7	64	46	18	15	60	<1	81
HL246-244(Basalt)	35.48	0.44	10.04	6.82	0.15	5.90	19.39	1.15	1.01	0.42	17.48	98.28	25.2	20	1.57	3.62	47	289	619	85	100	58	<1	35
HL246-262(Basalt)	48.72	0.47	10.92	7.07	0.16	4.96	11.79	3.71	0.59	0.31	9.77	98.45	26.4	20	2.32	1.74	34	231	360	61	53	102	<1	10
HL246-282(Andesite)	58.24	0.67	17.13	7.76	0.10	3.91	0.86	6.80	0.24	0.14	3.86	99.71	35.1	32	1.65	0.09	39	269	185	33	81	85	<1	9
HL246-314(Andesite)	53.22	0.63	16.18	9.56	0.22	5.30	3.54	5.58	0.14	0.13	4.92	99.40	37.3	32	1.71	0.12	32	227	131	26	30	106	<1	3
HL246-348(Andesite)	54.66	0.69	17.12	9.41	0.21	5.12	1.66	5.66	0.37	0.13	4.89	99.92	42.9	31	0.99	0.21	39	247	144	28	30	165	<1	15
HL541-284(Shale)	67.04	0.48	10.23	7.92	0.17	3.23	2.50	0.22	1.63	0.15	6.07	99.64	64.1	23	0.57	1.35	13	98	126	52	81	59	1	67
HL541-306(Shale)	64.67	0.56	11.46	7.37	0.07	2.75	2.71	0.12	2.57	0.14	6.97	99.35	65.3	27	1.89	1.25	16	220	152	62	81	181	6.8	106
HL541-322(Shale)	66.09	0.51	15.08	4.52	0.03	2.51	0.93	0.61	3.89	0.10	5.33	99.60	80.6	17	1.3	0.63	14	137	103	48	35	41	1.7	153
HL541-414(Basalt)	55.31	0.36	11.52	6.62	0.12	9.31	6.92	2.30	2.23	0.16	4.91	99.76	55.6	18	0.01	0.37	23	174	825	217	33	38	<1	50
HL541-424(Basalt)	48.68	0.58	13.01	8.86	0.19	8.37	9.89	3.24	1.69	0.33	4.73	99.57	43.4	22	0.02	0.56	33	268	287	73	134	156	<1	34
HL541-543(Shale)	65.59	0.76	12.21	5.75	0.05	2.78	2.15	0.21	2.95	0.17	6.17	98.77	70.8	34	1.49	1.06	20	144	138	73	25	3091	<1	121
HL541-577(Basalt)	61.81	0.44	15.38	5.82	0.07	3.21	2.78	4.15	1.41	0.13	4.48	99.68	40.0	19	0.1	0.47	24	74	27	5	6	72	<1	62
HL541-715(Andesite)	57.33	0.62	15.26	8.70	0.29	4.86	3.01	3.14	2.98	0.15	3.27	99.61	56.0	27	0.01	0.09	23	178	82	24	34	310	<1	79
HL541-784(Andesite)	59.50	0.61	15.11	8.58	0.15	4.52	1.56	3.43	1.99	0.15	4.03	99.63	56.6	26	0.07	0.25	27	190	66	25	7	132	<1	68
HL541-828(andesite)	58.87	0.57	14.70	7.82	0.18	4.13	2.92	4.38	1.08	0.13	4.83	99.61	41.6	29	0.03	0.49	33	233	151	32	39	126	<1	33
DETECTION LIMIT (ppm)	0.002	0.006	0.008	0.004	0.004	0.011	0.001	0.024	4E-04	0.003	0.01				0.01	0.005	2	2	1	1	1	1	1	1

Alt Index = (MgO+K2O)/(MgO+K2O+CaO+Na2O)*100, Ca int. = Ca interference, < = less than detection limit

Sample Name	Sr	Y	Zr	Nb	Ba	La	Ce	Nd	Pb	Th (XRF)	Th (ICP)	U	Ag	As	Bi	Mo	Cd	Sb	Cs	Tl	
	ppm	ppm	ppm	ppm	ppm	ppm	ppm	ppm	ppm	ppm	ppm	ppm	ppm	ppm	ppm	ppm	ppm	ppm	ppm	ppm	
MBX-1A (Standard)	528	15	101	9.9	701	11	24	10	3	2	2.29	0.35	0.2	6	0.1	4.2	0.2	3.2	2.66	0.7	
MBX-1B (Standard)	525	15	100	10.3	697	11	26	12	3.5	3	2.34	0.3	0.2	5	0.1	4	0.1	2.9	2.61	0.7	
MBX-1C (Standard)	525	16	100	9.9	707	12	26	13	2.5	3.5	2.31	0.29	0.2	5	0.1	6.6	0.1	3.2	2.61	0.7	
WP-1A (Standard)	719	14	127	3.9	610	13	30	16	6	2	1.91	0.79	<	<	<	1.2	0.1	0.3	0.47	<	
WP-1B (Standard)	717	14	127	3.6	616	14	30	17	7	2	1.89	0.77	<	<	<	1.1	0.1	0.2	0.47	<	
WP-1C (Standard)	718	14	127	3.8	613	12	29	14	6	2	1.83	0.74	<	<	<	1.1	0.2	0.2	0.46	<	
QUA-1A (Standard)	608	12	101	3.9	700	11	27	13	7	2	2	0.74	0.1	19	0.2	1.5	0.2	1.8	0.54	<	
QUA-1B (Standard)	605	12	99	3.1	694	12	27	12	7	2	2.22	0.8	0.1	20	0.3	1.5	0.9	1.8	0.51	<	
QUA-1C (Standard)	606	12	99	3.5	700	13	29	13	8	2	2.11	0.8	0.1	27	0.2	1.4	0.2	1.8	0.53	<	
CUL-1A (Standard)	279	21	51	1.8	689	7	12	8	3	<1.5	0.45	1.52	<	19	0.2	5.7	0.3	1.4	0.76	1.2	
CUL-1B (Standard)	279	21	51	2.3	691	6	13	7	2.5	<1.5	0.48	1.51	0.1	20	0.2	5.6	0.3	1.3	0.74	1.3	
CUL-1C (Standard)	279	21	52	2	688	8	9	9	2	<1.5	0.47	1.41	0.1	19	0.2	5.8	0.3	1.4	0.77	1.2	
ALB-1A (Standard)	809	20	72	3	257	5	15	11	<1.5	<1.5	1.22	0.9	0.2	6	<	2	0.1	0.3	0.28	<	
ALB-1B (Standard)	810	20	71	2.5	260	5	14	10	<1.5	<1.5	1.14	0.87	0.3	4	<	1.4	0.1	0.3	0.25	<	
ALB-1C (Standard)	814	20	72	3.1	259	5	15	9	<1.5	<1.5	1.22	0.88	0.2	5	<	1.3	0.1	0.3	0.28	<	
CHI-1A (Standard)	268	16	26	1	43	5	8	4	4	2	0.25	1.01	<	6	<	1.2	0.3	0.8	0.13	<	
CHI-1B (Standard)	269	16	26	2.4	43	4	7	6	3	<1.5	0.27	1.05	0.4	7	<	1.2	0.3	0.8	0.13	<	
CHI-1C (Standard)	269	16	26	1	44	4	8	4	4	<1.5	0.24	1.13	<	9	<	1.2	0.3	0.8	0.12	<	
P-1A (Standard)	222	20	117	3.3	726	9	25	10	7	4	3.95	1.13	<	<	<	0.6	<	0.3	1.22	<	
P-1B (Standard)	222	20	126	3.4	728	11	24	13	8	5	3.71	1.15	<	<	<	0.6	0.1	0.3	1.17	<	
P-1C (Standard)	222	20	119	3.2	720	9	22	11	9	5	3.77	1.1	<	<	<	0.6	<	0.3	1.17	<	
MAC10-130 (Basalt)	365	31	423	13.1	2716	148	295	120	3	56	48.2	11.9	0.1	11	0.4	0.4	0.1	1	0.98	<	
MAC10-164 (Basalt)	588	23	130	5.4	918	139	275	119	<1.5	34	28.8	6.06	<	<	0.1	0.2	<	0.8	1.05	<	
MAC10-200 (Basalt)	450	26	364	12	1598	148	281	115	16	47	26.2	6.9	<	1	<	0.3	<	0.4	2.55	<	
MAC11-239 (Andesite)	233	29	250	13.7	432	92	183	83	3	31	41.6	10.1	0.3	<	0.2	0.4	<	1.2	3.5	<	
MAC11-250 (Shale)	84	20	105	9.2	415	26	47	21	30	11	9.68	3.11	0.5	14	0.3	0.8	<	3.3	4.02	0.8	
MAC11-388 (Basalt)	215	19	111	6.8	742	37	71	31	5	9	8.52	2.26	0.1	3	0.1	0.4	<	1.5	3.53	1.1	
MAC11-502 (Basalt)	342	18	129	7.1	382	55	102	37	4	16	14.5	3.98	<	3	<	0.4	<	0.6	4.24	<	
MAC11-641 (Andesite)	158	20	111	7.1	42	44	85	37	116	12	10.3	4.54	0.4	15	0.1	0.9	3.1	1.2	0.09	<	
MAC11-766 (Andesite)	174	22	151	8.4	1055	86	172	72	3	19	17.3	5.71	<	1	0.2	0.6	<	0.8	2.12	0.7	
MAC11-823 (Andesite)	176	34	172	10.8	758	38	76	34	3	18	14.2	4	<	<	<	0.8	<	0.5	2.27	0.6	
MC12-82(Shale)	95	24	131	11	1232	28	51	23	12	12	10.5	3.16	0.2	9	0.3	2	0.4	1.2	6.38	0.8	
MC12-124(Shale)	75	31	124	10.7	824	32	67	31	43	12	9.59	3	0.4	44	0.3	1	0.8	5.4	4.94	0.8	
MC12-346(Andesite)	323	16	87	4.9	4084	66	147	62	13	18	16.7	3.83	0.2	11	0.2	1.7	0.1	2.1	2.56	0.8	
MAC19-492(Basalt)	148	16	113	7.3	295	30	52	21	5	14	12.7	3.32	<	<	<	0.2	<	0.3	1.45	<	
MAC19-661(Basalt)	439	19	121	7.4	1078	31	67	27	2	15	14.2	3.76	<	<	<	0.4	<	1.4	1.59	<	
MAC19-760(Basalt)	661	21	147	8.6	309	37	77	34	23	13	12.9	3.54	0.3	2	0.2	0.4	<	1.7	0.48	<	
MAC19-812(Andesite)	150	21	122	7.2	660	40	77	33	5	12	8.59	2.25	<	<	<	0.4	<	0.7	2.16	0.6	
MAC19-860(Andesite)	163	30	150	9.9	730	42	83	37	10	15	12.5	3.37	<	<	0.1	1.1	<	0.5	2.86	0.7	
MAC19-913(Andesite)	288	41	195	13.9	3466	48	102	37	9	17	16.6	4.33	<	2	<	1	0.3	0.6	1.9	0.8	
MAC21-72(Andesite)	505	15	66	3.6	1118	23	51	23	321	7	7.74	1.85	0.3	5	0.2	1	1.5	1.3	0.72	<	
MAC21-321(Andesite)	508	20	89	6.3	165	20	46	20	1877	6	7.22	1.86	0.8	16	<	1	5.4	1.7	0.14	1.8	
MAC21-354(Andesite)	203	19	100	6.5	305	24	51	23	10	9	7.57	2.23	<	<	<	1.1	0.1	0.6	0.7	<	
MAC21-436(Andesite)	471	25	124	9.5	626	23	50	22	117	9	8.19	2.07	0.1	6	0.7	1.3	0.9	0.8	0.78	<	
MAC25-112(Andesite)	230	11	59	4.2	113	21	41	20	<1.5	6	5.49	1.73	0.2	3	<	0.3	0.3	1.4	0.55	<	
MAC25-152(Basalt)	182	16	59	3.3	1511	29	63	27	13	9	7.33	2.32	0.6	18	0.3	0.4	0.9	1.3	1.54	<	
MAC31-47(Shale)	31	26	154	12.8	777	28	57	25	42	12	10.2	3.7	0.4	16	0.4	2.6	<	3	6.39	0.9	
MAC31-78(Shale)	65	26	136	12.1	628	25	57	28	50	12	12	10.5	3.79	0.2	36	0.5	5.6	0.5	3.4	5.97	0.9
MAC31-90(Shale)	55	26	151	12	638	33	65	29	38	11	11.1	4.87	0.3	30	0.5	6.1	0.8	3	5.77	1	
MAC31-103(Basalt)	413	13	71	4.7	650	56	108	46	5	14	12.4	3.03	<	8	0.1	0.6	<	0.5	0.72	<	
MAC31-147(Basalt)	405	17	89	5.8	1555	76	146	63	37	20	18.7	3.86	0.2	11	0.4	0.3	0.3	1	0.52	<	
MAC31-168(Basalt)	381	19	102	6.3	1553	94	182	74	37	24	19.6	4.55	0.2	4	0.2	0.4	0.2	1.1	1.67	<	
HAT4-141(Shale)	21	26	141	12.5	1228	30	64	28	43	14	12.2	4.53	0.4	22	0.8	4.9	0.9	3.6	6.03	1	

HAT4-148(Shale)	20	28	142	12.8	1497	46	87	32	26	23	19.5	5.93	0.2	13	0.5	2.2	0.5	1.8	5.06	0.9
HAT4-223(Basalt)	181	25	159	11.1	400	72	148	68	5	16	14	3.25	<	<	0.1	0.8	0.1	0.1	2.77	<
HAT4-323(Basalt)	646	26	165	11.1	1109	90	181	80	53	20	20.5	5.56	0.3	<	0.3	1.2	0.6	0.6	0.52	<
HAT4-462(Basalt)	746	21	123	8.1	452	59	120	52	77	16	14.8	3.42	0.1	<	0.2	0.5	1	1.3	1.19	<
HAT8-139(Basalt)	314	14	65	3.7	993	22	44	19	27	8	7.63	1.87	0.2	9	0.2	1.1	0.1	1.6	0.68	<
HAT8-179(Basalt)	467	19	71	4.1	328	22	45	18	9	7	6.19	1.68	<	1	0.2	0.5	0.1	0.6	1.24	<
HAT8-207(Andesite)	241	21	144	9.7	888	25	53	20	2	13	12	2.89	<	<	<	0.2	<	0.4	0.3	<
HAT8-313(Andesite)	243	20	131	8.5	770	31	61	26	2	13	10.5	2.25	<	<	<	0.2	1.6	0.4	0.25	<
HAT8-361(Basalt)	499	16	68	3.4	681	22	45	20	5	6	5.73	1.53	<	6	0.1	0.8	0.1	0.5	1.16	<
HAT9-65(Basalt)	213	24	314	10	208	134	246	105	914	42	36.7	9.15	0.7	10	0.5	1.1	8.1	2.9	0.47	<
HAT9-96(Basalt)	275	32	425	14.7	101	155	292	126	18	56	50.1	11.6	0.2	5	0.2	0.9	0.2	1.9	1.19	<
HAT9-118(Dacite)	154	29	206	14.9	370	56	116	47	3	25	17.9	7.3	0.1	35	<	0.9	<	1.4	1.97	<
HL26-136(Shale)	51	22	127	11.1	553	23	49	20	73	11	10	4.54	0.6	53	0.5	10.5	0.8	12.7	4.14	1.9
HL26-159(Shale)	41	23	154	10.9	874	43	83	30	25	26	22.5	6.46	0.2	19	0.3	2.3	0.5	4.3	3.91	2.6
HL26-197(Basalt)	327	16	79	6.9	872	36	71	27	20	8	7.04	1.72	0.3	9	0.1	0.6	0.3	4.3	3.22	1.1
HL26-211(Basalt)	401	16	75	4.2	1287	34	73	31	5	9	7.2	1.83	0.1	3	<	0.2	0.1	6.8	2.43	<
HL26-228(Basalt)	564	16	71	4.8	2751	29	68	25	<1.5	7	6.38	2.09	<	33	<	0.2	0.1	6.5	1.98	0.9
HL26-286(Andesite)	463	27	170	11.4	383	35	76	33	30	19	8.64	3.29	0.1	31	0.2	12.7	0.2	10.1	0.38	1.1
HL80-103(Basalt)	174	18	153	9.8	447	43	85	37	13	13	11.9	3.36	0.4	10	<	1.4	<	2.3	3.02	0.6
HL80-225(Basalt)	35	17	136	9.8	87	33	64	27	9	14	11.3	2.99	<	1	<	0.3	0.1	0.5	2.51	<
HL80-332(Basalt)	255	20	160	8.7	326	47	96	42	468	14	12.3	3.11	0.4	<	0.2	0.3	2	1.9	1.35	<
HL246-96(Shale)	63	27	151	11.7	671	30	59	28	38	14	11	4.04	0.4	23	0.4	5.8	0.1	2.6	5.14	0.9
HL246-168(Shale)	58	31	146	12.1	580	31	63	29	98	12	11.1	4.11	0.6	31	0.5	5.5	1	6.8	5.07	1.5
HL246-204(Shale)	80	29	121	12.2	614	43	87	37	16	20	17.3	4.95	0.2	25	0.3	2.3	0.3	7.4	3.64	1.6
HL246-244(Basalt)	274	17	133	7.7	626	42	89	43	7	9	9.11	4.59	<	8	0.2	1.4	0.1	2.3	2.36	0.6
HL246-262(Basalt)	474	16	140	8.7	1844	54	106	48	48	11	10.2	3.76	0.3	51	<	0.4	0.4	5.7	0.69	<
HL246-282(Andesite)	256	19	126	9.1	224	25	55	24	308	11	7.39	2.27	0.8	55	0.1	0.6	<	3.1	0.62	<
HL246-314(Andesite)	287	23	116	8.6	293	33	64	27	42	10	10.4	2.55	0.2	85	0.2	0.8	0.2	3.2	0.71	<
HL246-348(Andesite)	284	25	136	9.5	280	30	61	27	41	13	11.7	2.81	0.3	24	<	0.8	0.3	2	0.65	<
HL541-284(Shale)	65	22	124	10.4	387	32	64	26	19	10	10.7	2.61	0.3	22	0.5	1	<	1.2	3.21	<
HL541-306(Shale)	70	26	125	11.3	533	28	58	27	100	11	11.6	3.22	0.7	28	0.4	1.3	0.7	4.9	5.04	0.8
HL541-322(Shale)	36	28	176	15	903	55	101	43	46	23	24.4	7.44	0.8	28	0.5	4.7	0.1	4.5	6.32	1.3
HL541-414(Basalt)	293	17	121	7.6	1057	53	102	41	2	16	16.5	3.74	<	<	<	0.3	<	0.6	2.13	<
HL541-424(Basalt)	378	21	156	8.4	1134	50	108	47	12	14	13.6	3.5	0.2	<	0.1	0.7	0.5	1.1	0.76	<
HL541-543(Shale)	37	21	133	11.9	493	14	34	17	729	10	11.7	4.27	0.6	22	0.5	5.4	12.1	3.1	5.12	1.3
HL541-577(Basalt)	436	26	139	8.7	509	38	70	28	9	15	14.1	3.59	0.1	7	0.1	4.5	0.2	0.6	2.02	<
HL541-715(Andesite)	388	29	137	9.3	1730	30	62	25	16	14	14.3	3.78	<	2	<	1.6	<	0.8	0.8	<
HL541-784(Andesite)	178	25	139	9.1	735	27	53	22	<1.5	14	13.5	3.13	<	<	<	0.3	<	0.3	0.8	<
HL541-828(andesite)	179	24	116	8.3	548	29	57	25	3	10	10.5	2.54	<	<	<	0.5	<	0.3	0.52	<
DETECTION LIMIT (ppm)	1	1	1	1	4	2	4	2	1.5	1.5	0.05	0.05	0.1	1	0.1	0.1	0.1	0.1	0.05	0.5

Alt Index = (MgO+K2O)/(MgO

Petrographic and geochemical characteristics of alteration from the Hall Rivulet Canal–Mt Read–Red Hills–Anthony Dam traverse, Mt Read Volcanic Belt

Joe Stolz, Rod Allen, Cathryn Gifkins, Garry Davidson, Jocelyn McPhie and Michael Blake

Centre for Ore Deposit and Exploration Studies, Geology Department, University of Tasmania

Summary

Petrographic and geochemical studies of the samples from the Hall Rivulet Canal–Mt Read–Red Hills–Anthony Dam traverse indicate that diagenetic alteration of siliceous volcaniclastic sandstones involving albitisation and, less commonly, K-feldspar alteration is widespread. These styles of alteration produce distinctive chemical characteristics which are readily distinguishable from the more important and restricted hydrothermal alteration which produces the assemblage sericite ± pyrite ± chlorite. The chemical and mineralogical characteristics of the granitoid-related K–feldspar ± magnetite ± chlorite at Red Hills and Lake Selina are also documented and discussed.

Introduction

One of the principal objectives of undertaking the regional traverses in the Mt Read Volcanic belt was to characterise the 'background' alteration effects in the volcanics i.e. those attributable to processes other than mineralising hydrothermal convection cells. These processes may include immediate post-depositional effects related to devitrification of glass, diagenetic modification by interaction with low-temperature seawater and rock-buffered fluids, as well as subsequent regional metamorphism.

Samples collected along the Hall Rivulet Canal–Mt Read–Red Hills–Anthony Dam traverse (Fig. 1) during January 1996 have been examined petrographically and analysed for major elements and a wide range of trace elements. The results and interpretation of these data are presented in this report with the exception of the host sequence to the Hercules deposit. The mineralogy and geochemistry of those rocks (samples MR96-45 to MR96-70) are discussed in a separate report (Large, this volume).

Lithofacies variation

Descriptions of field observations, principal lithofacies and field logs for this traverse were provided by McPhie (1996). The traverse was undertaken in four sections which encompassed the following important lithostratigraphic units of the Mt Read Volcanic Belt.

1. Hall Rivulet Canal: White Spur Formation and Central Volcanic Complex (CVC).
2. Hercules–Mt Read: Central Volcanic Complex, including the Hercules mineralisation and Mt Black Volcanics on Mt Read.
3. Henty Fault–Red Hills: Tyndall Group and Central Volcanic Complex.
4. Anthony Dam: Owen Conglomerate and Tyndall Group.

The principal lithofacies distinguished from handspecimen observations of White Spur Formation units exposed along the Hall Rivulet Canal (Fig. 2) include pumice breccia, pumice-lithic breccia, crystal-rich sandstone, pumiceous sandstone, mud-matrix pumice breccia, mudstone, and volcanolithic sandstone (McPhie, 1996). Thin section observations confirm this range of lithofacies and the general absence of coherent units in this sequence.

Within the underlying Central Volcanic Complex and in CVC rocks from the Mt Read and Red Hills areas (Fig. 3) pumiceous sandstones and breccias are

abundant, but syn-volcanic dacitic to rhyolitic intrusives and lavas are also locally important. The CVC sandstones and coherent rocks are typically feldspar-phyric with only minor quartz, whereas volcaniclastic rocks from the White Spur Formation generelly contain abundant quartz and feldspar.

Tyndall Group rocks on the traverse immediately east of the Henty Fault are predominantly quartz-feldspar-phyric rhyolites with associated insitu breccia facies, whereas Tyndall Group rocks from the Anthony Dam section of the traverse (Fig. 4) include both coherent and volcaniclastic quartz-feldspar-phyric rocks. Porphyritic microgranitic rocks are also represented in the latter section of the traverse.

Styles of alteration

All of the rocks examined have experienced some alteration. As expected for volcaniclastic or coherent rocks that were erupted subaqueously or intruded into wet sediments, glass is a major component of the rocks and as it is metastable, it has reacted readily with seawater.

For the purpose of characterising the alteration types and intensities, and how these parameters relate to the various lithofacies, the samples have been grouped on the basis of their present mineralogical assemblages and with regard to the likely precursor lithofacies. Five major styles of alteration have been distinguished on the basis of the traverse samples:

1. Albite ± epidote ± sericite
2. K-feldspar
3. Sericite + pyrite ± chlorite
4. Carbonate
5. K-feldspar ± magnetite ± chlorite

In general, the coherent rocks are less altered than volcaniclastic units regardless of the style of alteration. The least altered samples (chemically and mineralogically) are rhyolitic lavas and intrusives from the CVC and Tyndall Group. For example, a feldspar-phyric dacite from the CVC in the Hall Rivulet Canal (HRC96-37, Fig. 5) contains unaltered plagioclase, hornblende and magnetite phenocrysts in a fine grained groundmass of quartz, albite, minor chlorite, epidote and sphene. There are also some feldspar-phyric pumiceous sandstones (e.g. HRC96-18, Fig. 6) that contain fresh detrital hornblende and plagioclase, and which show only minor evidence of secondary hydrous phases such as chlorite and sericite.

Albite ± Epidote ± Sericite Alteration

This is best developed in the volcaniclastic sandstones from the White Spur Formation and Central Volcanic Complex in the Hall Rivulet Canal. In handspecimen this style of alteration is commonly characterised by a distinctive patchy or banded pink and green colouration (e.g. HRC96-38, Fig. 6), but the pink colour may be more pervasive (e.g. HRC96-18, Fig. 6) or may be absent (e.g. HRC96-5 and HRC96-17, Fig. 7). The albite occurs as overgrowths on the margins of plagioclase grains and as a replacement along fractures in the feldspar grains (Figs 6D, F; 7B, D). These overgrowths are generally evident from the ragged nature of the margins, or due to the preferential partial alteration of the cores of the grains to sericite or clays. Albite also occurs in aggregates of decussate laths of varying grain size adjacent to plagioclase grains (e.g. Fig. 7B), scattered through the matrix, or replacing pumice fragments (e.g. Fig. 6F). The volcaniclastic rocks commonly also have a matrix composed of very fine grained aggregates of albite, quartz and minor chlorite which frequently retains textural evidence of the pumiceous, shard-rich nature of the glassy precursor materials (Fig. 5A).

Many of the sandstones display albite alteration without epidote. This most likely reflects a control by whole-rock chemistry where the sandstones with rhyolitic compositions had very low CaO contents in the primary glass and hence did not have the capacity to crystallise epidote at any stage. All of the albite–epidote-bearing samples examined have more dacitic (and CaO-rich) bulk compositions. The epidote occurs as aggregates of small grains through the matrix commonly with fine granular sphene (e.g. HR96-17, Figs. 7C & D) and, less commonly, as tiny aggregates partially replacing plagioclase grains (Fig. 6D).

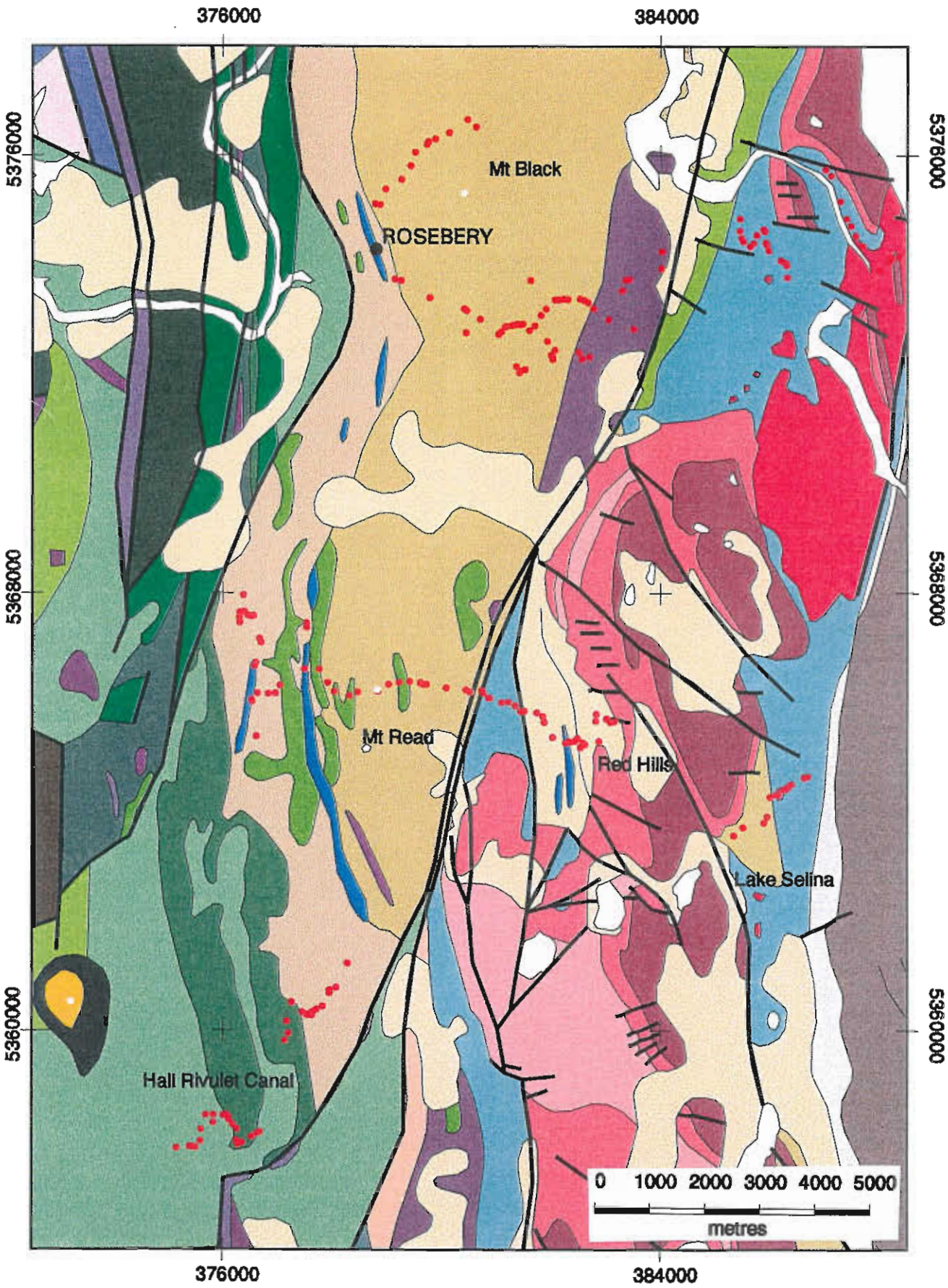

Figure 1
1:100,000 geological map of the Mt Read Volcanics showing the positions of the Mt Black–Murchison Gorge, and Hall Rivulet Canal–Mt Read–Red Hills–Anthony Dam traverses.

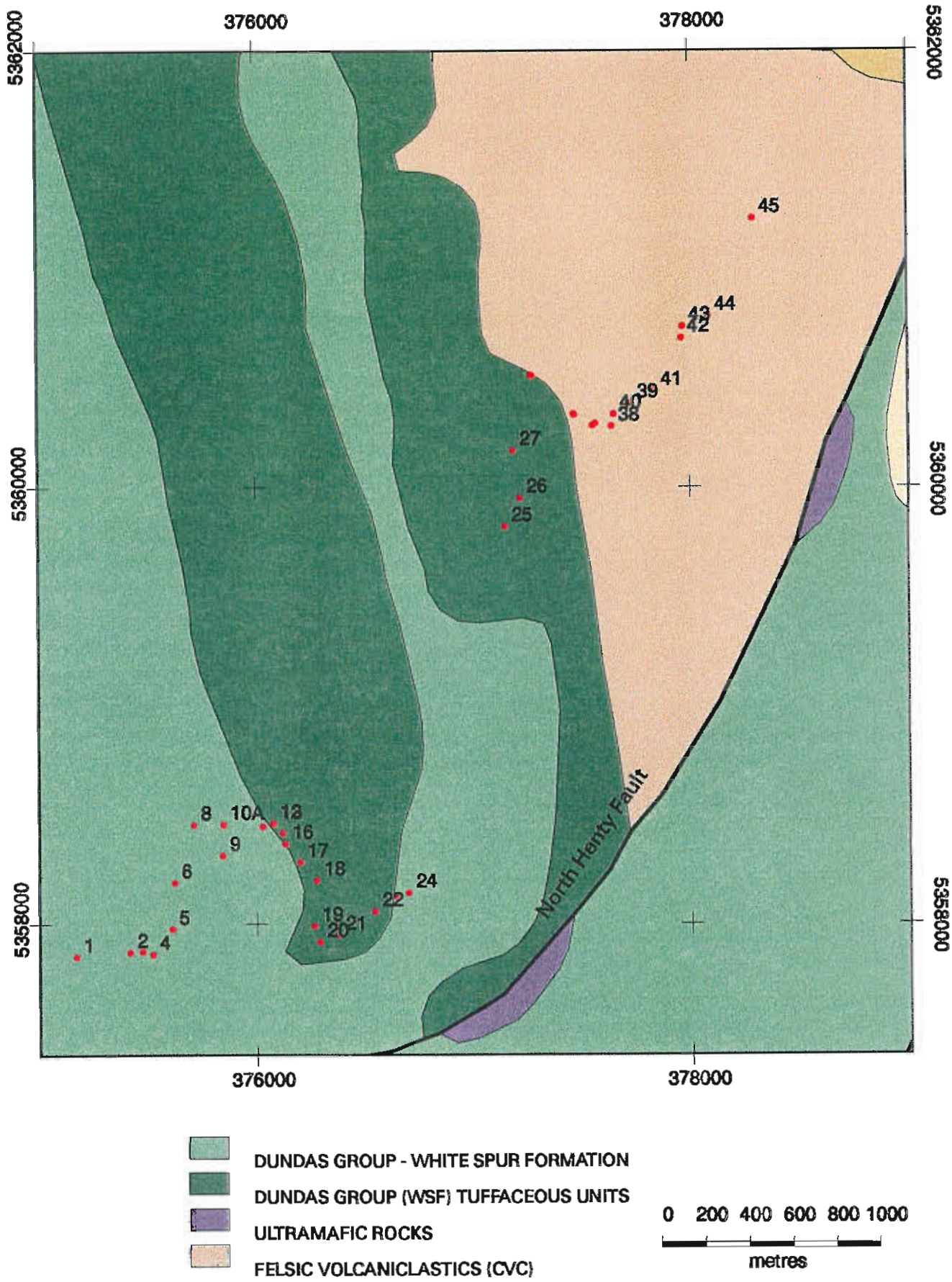

Figure 2
Detailed map of the sample locations along the Hall Rivulet Canal traverse.

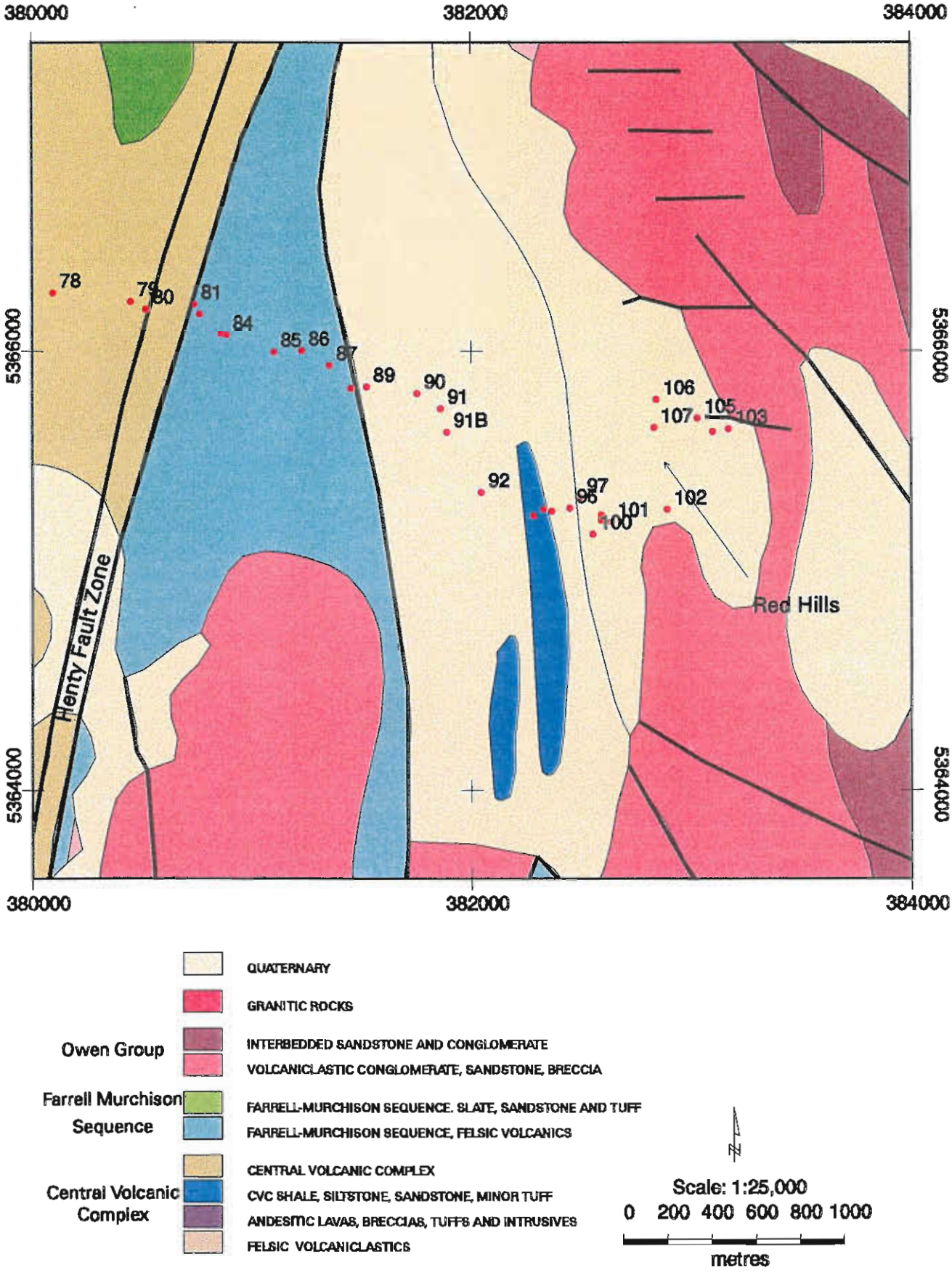

Figure 3
Detailed map of the sample locations between the Henty Fault and Red Hills.

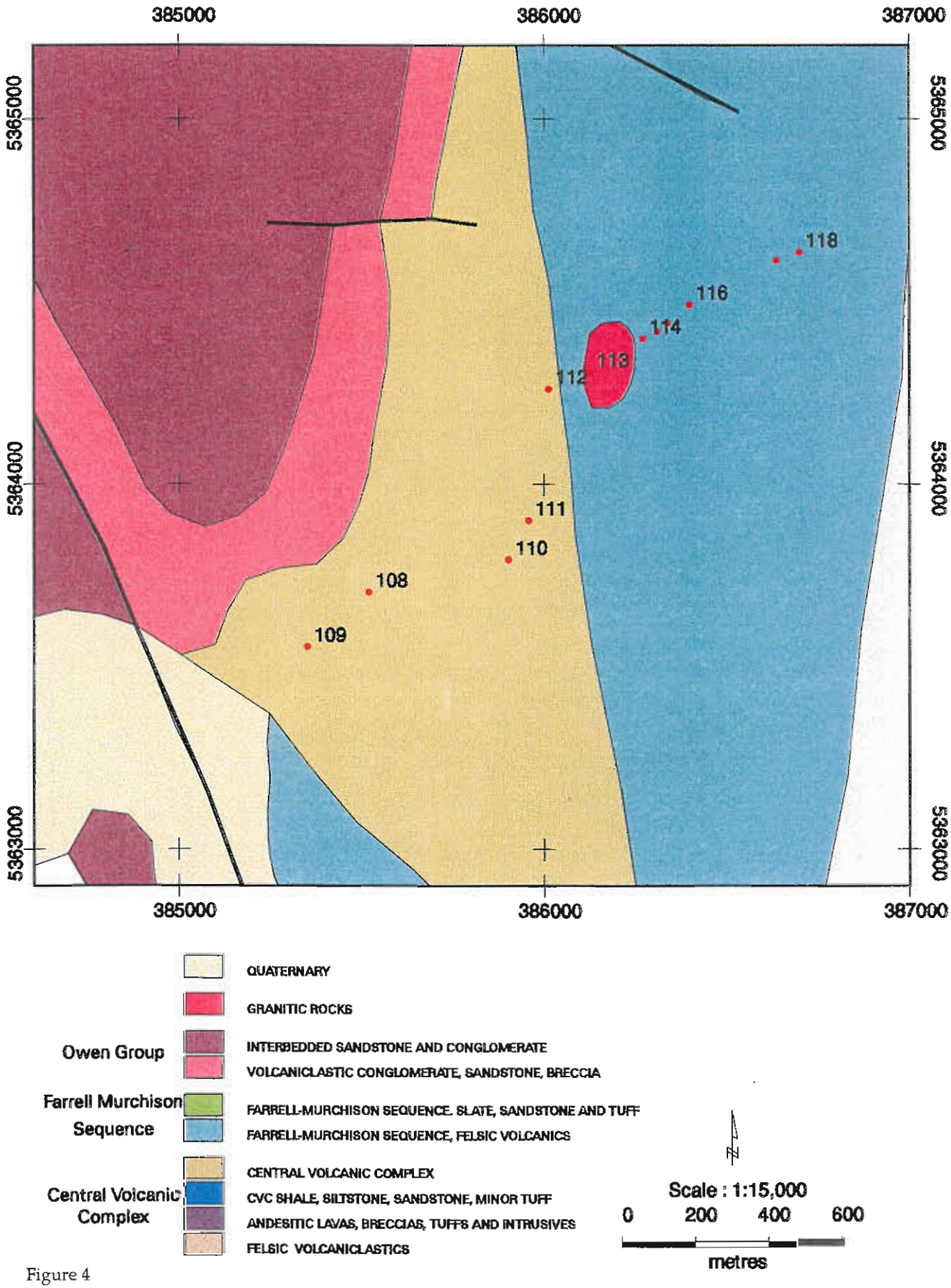

Figure 4
Detailed map showing the location of samples from the Anthony Dam section of the traverse.

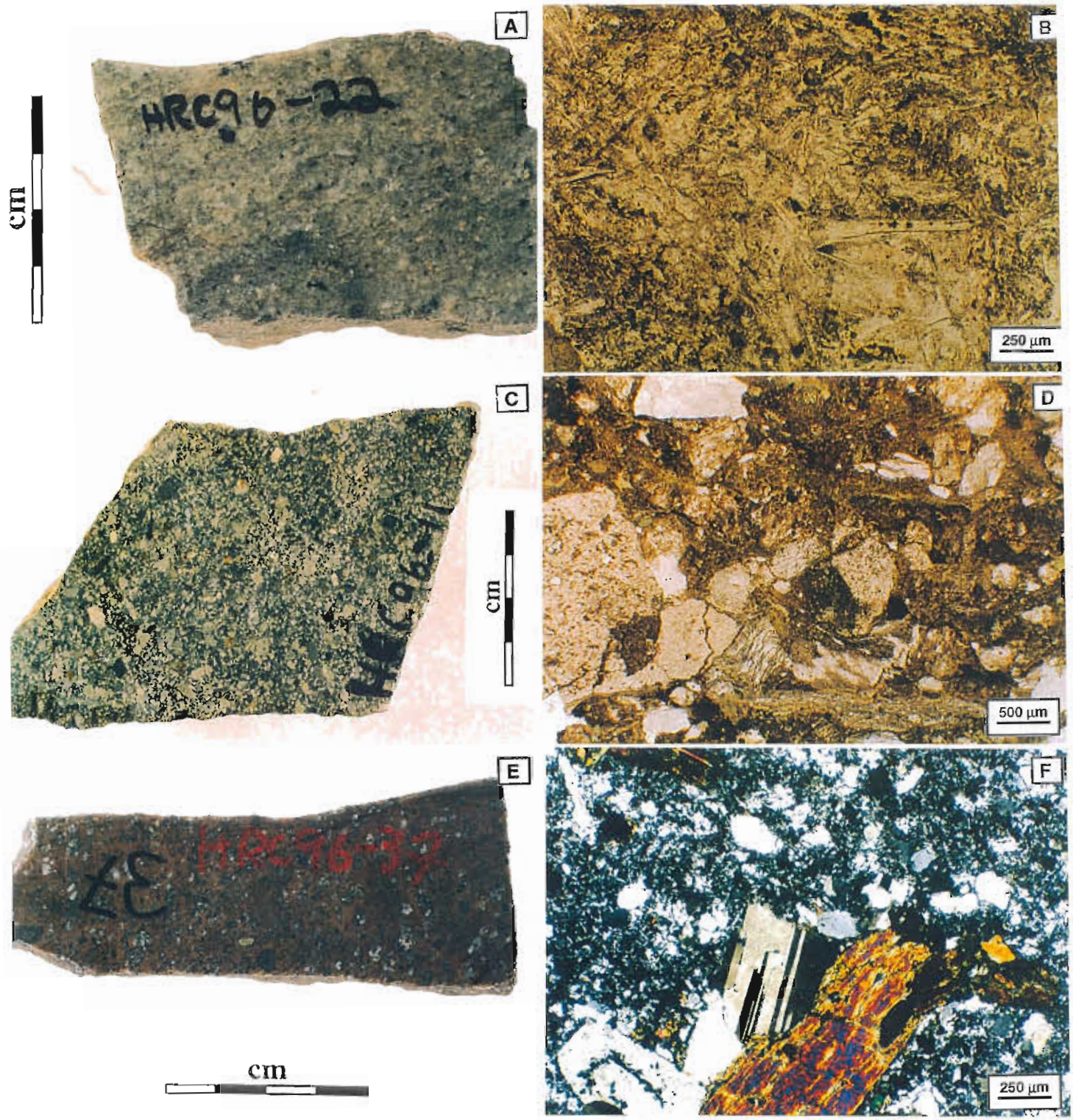

Figure 5
(A) Pumiceous sandstone HRC96-22 from White Spur Formation, Hall Rivulet Canal. (B) Photomicrograph showing relict shard textures in the albite–quartz-rich matrix of HRC96-22. (C) Lithic breccia HRC96-11 from White Spur Formation, Hall Rivulet Canal. (D) Photomicrograph showing the diversity of lithic fragments in HRC96-11.

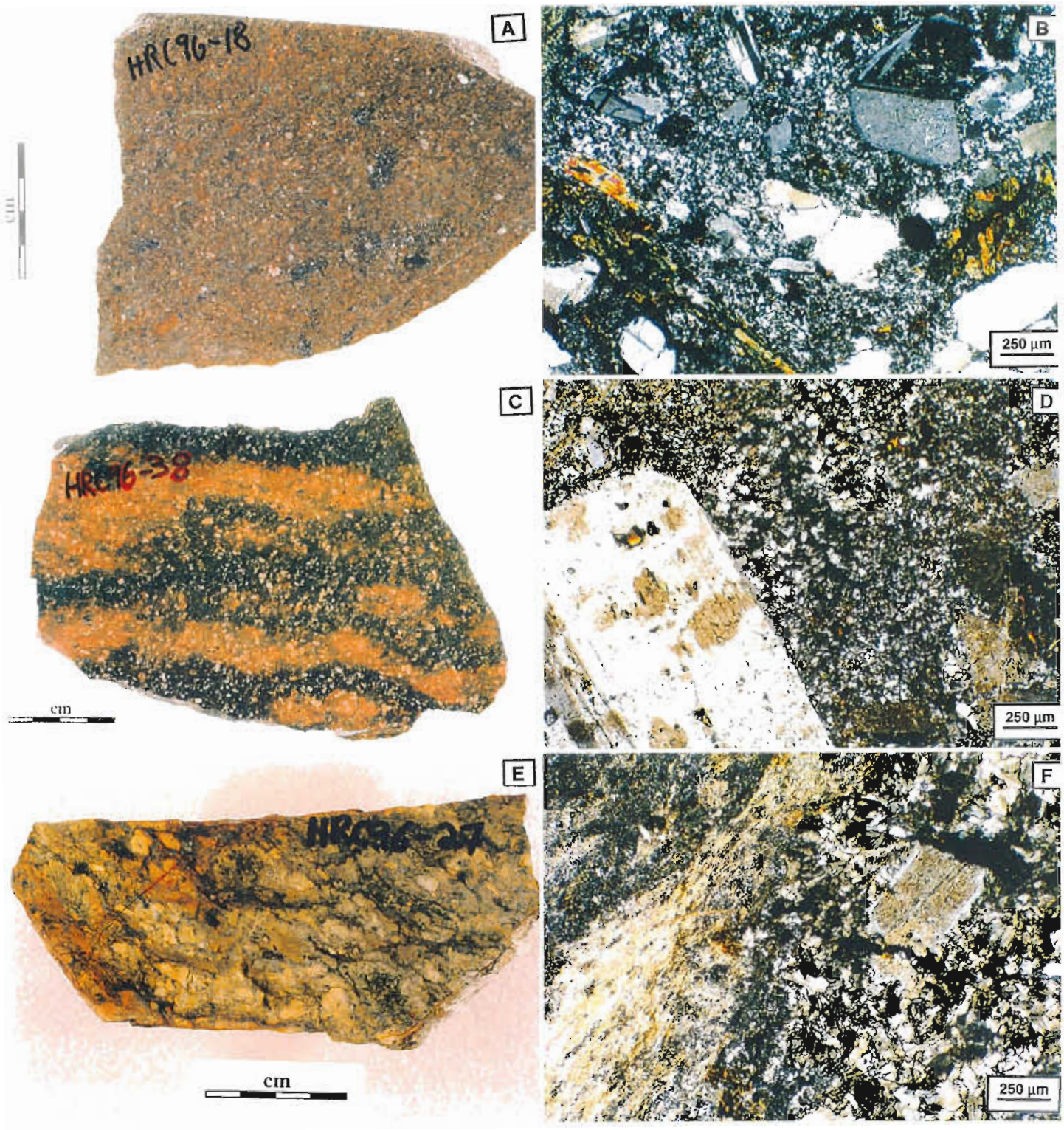

Figure 6
(A) Volcaniclastic sandstone HRC96-18 (White Spur Formation) with distinctive pink colour reflecting pervasive albitic alteration. (B) Photomicrograph of HRC96-18 showing fresh hornblende and plagioclase preserved in an albite-quartz-rich matrix with minor chlorite. (C) Albite-altered volcaniclastic sandstone HRC96-38 from the Central Volcanic Complex showing irregular pink banding and patches. (D) Photomicrograph of HRC96-38 showing a plagioclase crystal with weak clay and epidote alteration in a variable grainsize matrix of albite, quartz and minor chlorite. (E) Pumiceous breccia HRC96-27. (F) Photomicrograph of HRC96-27 showing a pumice fragment replaced by relatively coarse grained albite laths, and containing a plagioclase phenocryst with an unaltered albite rim and sericitised core. The finer albite-rich matrix displays preferential sericite alteration.

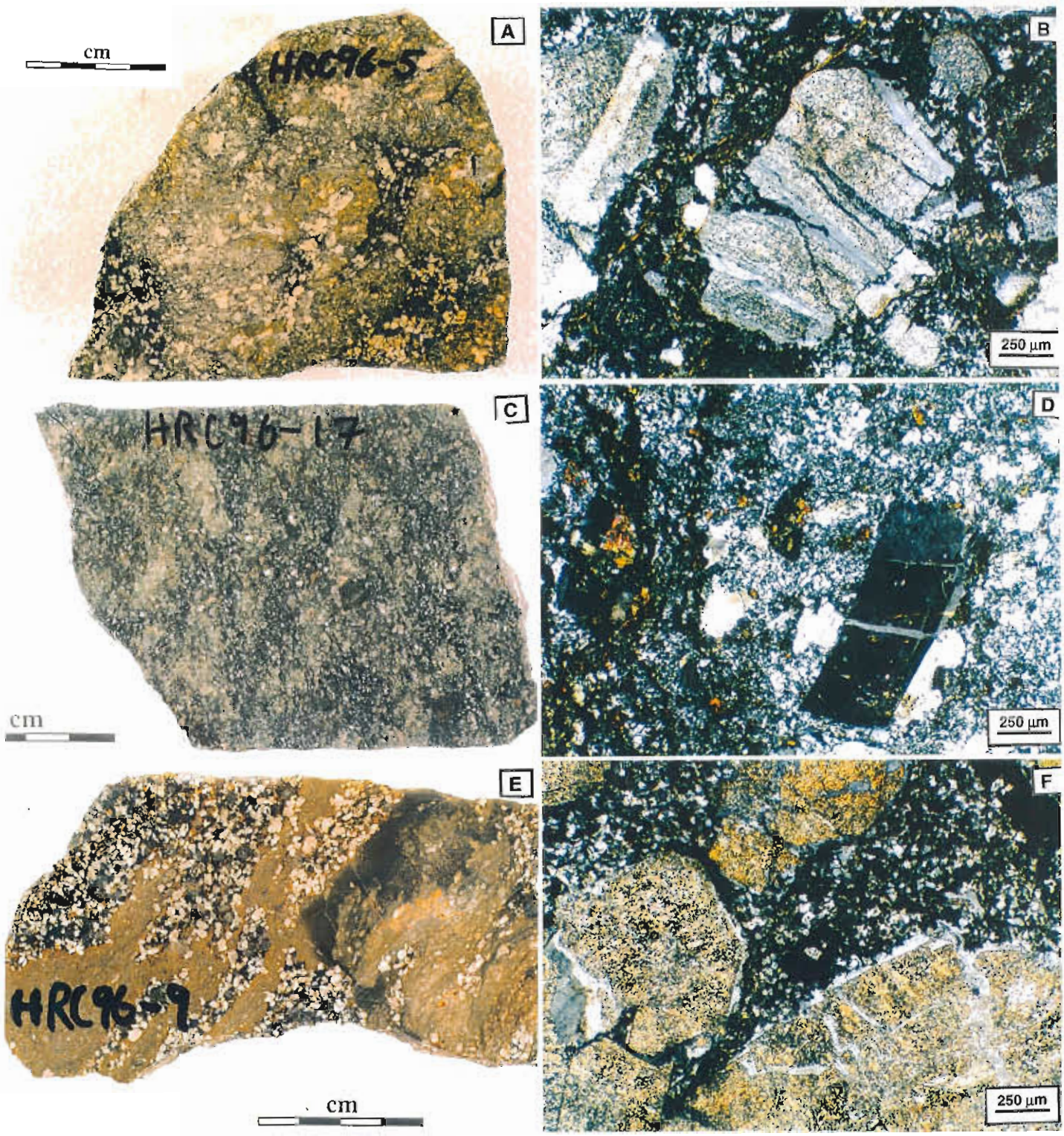

Figure 7
(A) Albite and patchy chlorite alteration in volcaniclastic sandstone HRC96-5 from the White Spur Formation. (B) Photomicrograph showing albite occurring around rims and along fractures of plagioclase grains in HRC96-5. (C) Volcaniclastic sandstone HRC96-17 from the White Spur Formation. (D) Photomicrograph of HRC96-17 showing albite overgrowths on plagioclase grains and disseminated aggregates of fine epidote in an albite and quartz-rich matrix. (E) HRC96-9, the mud-matrix-rich base of a crystal-rich sandstone unit from the White Spur Formation. (F) Photomicrograph showing K-feldspar overgrowths and fracture filling in sericite altered feldspar grains set in a fine grained K-feldspar-rich matrix.

Many of the volcaniclastic rocks with albitic alteration display varying amounts of sericite which is usually concentrated in the matrix, but also occurs partly replacing plagioclase grains (Figs. 8B & D, 9D). The amount of sericite typically varies from a trace to about 10–15% for this type of alteration, but in practise there is complete gradation between this type and the sericite–pyrite–chlorite alteration. Nevertheless the distinction is made because the presence of small amounts of sericite in these rocks does not necessarily reflect interaction of the rocks with hydrothermal fluids. The presence of sericitised cores of plagioclase grains with unaltered albitic rims indicates that sericite and albite were in equilibrium during the most recent thermal event which was the Devonian regional metamorphism.

The coherent rhyolitic and dacitic units rarely show evidence of substantial albite–epidote–sericite alteration through the development of albite overgrowths on plagioclase phenocrysts. However, their originally glassy groundmass has typically recrystallised to fine spherulitic or granular aggregates of albite, quartz and K-feldspar with minor chlorite and sericite. Without knowledge about the composition of the original glassy groundmass it is difficult to precisely determine the extent of any albitic alteration.

K-Feldspar Alteration

Several of the volcaniclastic sandstones from the Hall Rivulet Canal show substantial alteration by K-feldspar that petrographically is very similar to the more widespread albite alteration. The K-feldspar occurs as rims on feldspar grains and replacing these grains along fractures as well as fine grained aggregates in the matrix (Fig. 7F). The cores of feldspar grains may also display sericite alteration. Recognition of this style of alteration was facilitated by the whole-rock chemical data which indicated a high K_2O/Na_2O coupled with an obviously feldspar-rich assemblage. This type of alteration has not been recognised in the coherent rocks from the traverses undertaken in the Mt Read Volcanic belt, but has been recognised in coherent rhyolitic rocks from the Mt Windsor Volcanics (Stolz et al., this report).

Sericite + Pyrite ± Chlorite

This alteration type overlaps in characteristics with the albite ± epidote ± sericite alteration, but is generally characterised by more extensive development of sericite initially in the matrix and also ultimately replacing the plagioclase crystals (Fig. 8F, 9B), whereas feldspar destruction is clearly not associated with the albitic alteration. Feldspar crystals have also been replaced by quartz in the more intensely altered examples. An increase in sericite abundance coincides with a significant cleavage identification, although this is surprisingly poorly developed in the sericite-altered samples from adjacent to the Henty Fault (e.g. Fig. 9B). Chlorite is subordinate to sericite in the great majority of the samples displaying this style of alteration.

Carbonate Alteration

Weak, patchy, partial alteration of the albite–quartz–chlorite matrix and plagioclase grains is a common feature of both volcaniclastic, coarse clastic and coherent silicic rocks from this traverse. Carbonate also commonly occurs in veins that appear to have been remobilised during the Devonian metamorphism. The most carbonate-rich rocks from this traverse are black shales/siltstones (e.g. HRC96-1 and HRC96-10) in which the carbonate occurs concentrated in calcite-rich layers up to 10 cm or so thick, but disseminated with muscovite and quartz in the shale layers.

More intense carbonate alteration is generally associated with the inner zones of hydrothermal alteration systems directly underlying massive sulphide deposits, and aspects of this style of alteration at Hercules and Rosebery are discussed by Large (this report) and Allen (this report), respectively.

K-feldspar ± Magnetite ± Chlorite Alteration

This alteration style occurs at a number of localities within the MRVB including Red Hills and Lake Selina (on this traverse), Murchison Gorge (on the Mt Black traverse), Mt Sedgwick and the Jukes–Darwin area (Eastoe et al., 1987; Doyle, 1990; Wyman, this report). Jenkins (1991) mapped the alteration at Red Hills

and argued for a roughly circular pipe shaped alteration zone with a core dominated by K-feldspar and chlorite alteration and a sericite–pyrite–chlorite-rich outer zone. He further argued that the chlorite–magnetite alteration (with associated weak Cu mineralisation) post-dated and overprinted the K-feldspar alteration assemblage.

The K-feldspar alteration is commonly characterised by an orange colour (Fig. 10A) in handspecimen. In thin section the K-feldspar typically occurs as very fine grained aggregates that have pervasively replaced the rock. There may rarely be some preservation of primary textures such as feldspar phenocryts (Fig. 10B) or original breccia textures (Fig. 10C, D) although some of the latter may be hydrothermal breccias in which the chlorite-rich matrix alteration has overprinted the earlier K-feldspar alteration. There is widespread evidence in the K-feldspar altered rocks of retrogressive alteration of feldspar to sericite in veins that also commonly have chlorite and magnetite (Fig. 10F), and less commonly there is more complete replacement of some K-feldspar altered clasts by sericite.

Geochemistry

Major and trace element analyses for the samples from this traverse are presented in Table 1. Details of the analytical methods and accuracy and precision of the data are provided by Stolz et al. (this report). The geochemical data have been assessed with the objectives of:

- determining the chemical changes which characterise the different alteration types,
- distinguishing any differences in the intensity and styles of alteration in volcaniclastic and coherent rock types, and
- determining the distribution of the different alteration types along the traverse and how this relates to the geology.

No attempt has been made at this stage to rigorously quantify the chemical changes associated with the major alteration types (e.g. isocon analysis) in part because of the limited time available to assess the data, and also because of the difficulties associated with selecting a representative least-altered precursor for heterogeneous volcaniclastic rocks, and the pervasively K-feldspar–chlorite altered rocks. In the following discussion of the chemical characteristics of the various alteration types the major and trace elements (as well as some ratios) have been plotted as functions of the alteration Index ($100(MgO+K_2O)/(MgO+K_2O+CaO+Na_2O)$) of Ishikawa et al. (1976). The various chemical groupings were chosen to correlate closely with the different alteration assemblages from the two major sectors of the traverse discussed in this report and are as follows:

>5 wt% K_2O (Red Hills section)
= K-feldspar ± magnetite ± chlorite alteration
<2 wt% Na_2O & <5 wt% K_2O (Red Hills)
= sericite ± pyrite ± chlorite alteration
2–5 wt% Na_2O (Red Hills)
= generally least altered samples

<2 wt% Na_2O (Hall Rivulet Canal)
= sericite ± pyrite ± chlorite alteration
2–5 wt% Na_2O (Hall Rivulet Canal)
= generally least altered samples
>5 wt% Na_2O (Hall Rivulet Canal)
= albite ± epidote ± sericite alteration

Albite ± Epidote ± Sericite Alteration

The most obvious chemical change associated with this alteration type is an increase in the Na_2O content above concentrations that would be regarded as the normal upper limit for unaltered modern volcanics of similar bulk composition. Petrographic evidence for albitic alteration has been noted in rhyolitic rocks with > 4.5 to 5 wt.% Na_2O and hence rocks with >5 wt.% Na_2O have been generally designated as albite-altered (see also Stolz et al., this report). There are some samples with < 4.5 wt.% Na_2O that still display albite overgrowths on plagioclase grains (e.g. HRC96-13, Fig. 8B), but these rocks invariably exhibit substantial sericite alteration of their matrix which has resulted in albite breakdown and some loss of Na_2O. The enrichment in Na_2O is reflected in low values for the alteration index, and accompanied by substantial decreases in the K-group elements (K_2O, Rb, Cs, Ba; Fig. 11) compared with the least altered

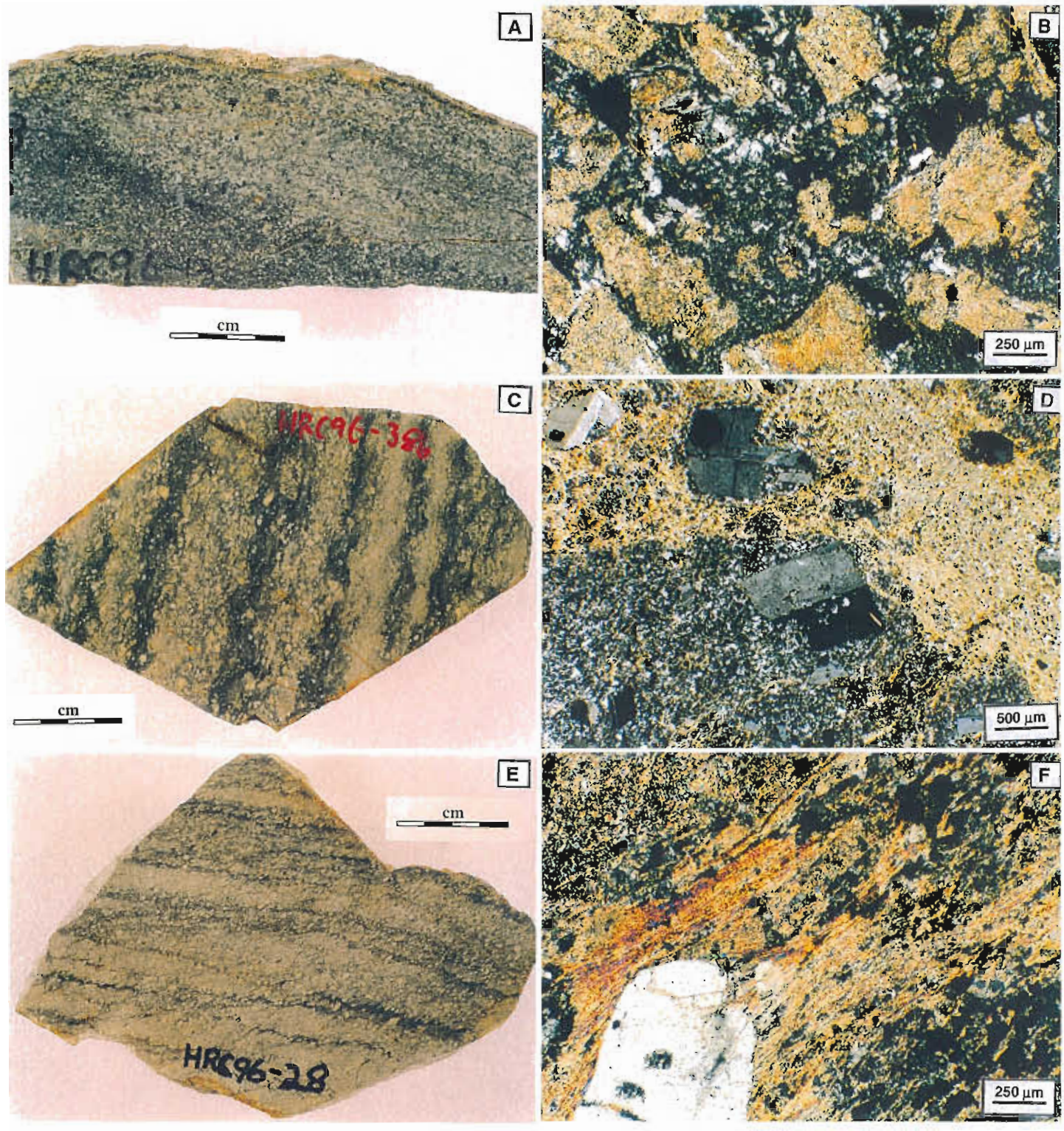

Figure 8
(A) Volcaniclastic sandstone HRC96-13 from the White Spur Formation. (B) Photomicrograph of HRC96-13 showing sericite-altered feldspar grains in a sericite-poor, albite-rich matrix. (C) Crystal-rich sandstone HRC96-38B from the Central Volcanic Complex showing alternating chlorite-rich and chlorite-poor layers which are approximately parallel to bedding as indicated by variations in crystal content (and grainsize. (D) Photomicrograph of HRC96-38B showing unaltered plagioclase crystals in a partly sericitised albite and quartz -rich matrix. (E) Weakly cleaved volcaniclastic sandstone HRC96-28. (F) Photomicrograph of HRC96-28 showing more intense pyrite ± sericite ± chlorite alteration of the matrix and strongly altered feldspar grain (top left).

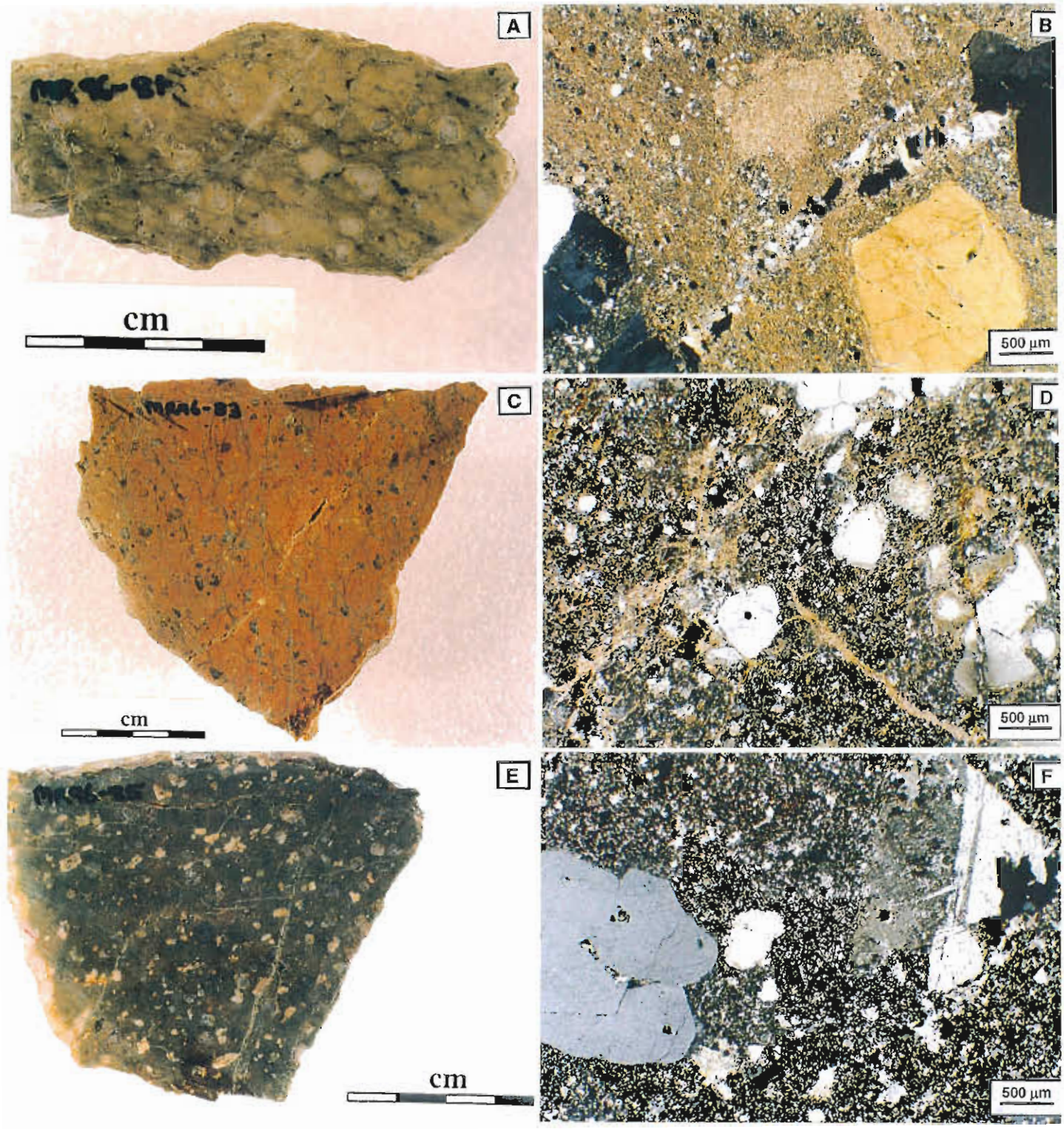

Figure 9
(A) Strongly altered quartz-feldspar–phyric rhyolite MR96-81 from the Tyndall Group directly adjacent to the Henty Fault. (B) Photomicrograph of MR96-81 showing strong sericite alteration of feldspar phenocrysts and groundmass, and cross-cutting quartz veins. (C) MR96-83, weakly altered quartz-feldspar–phyric rhyolite from further east in the Tyndall Group. (D) Photomicrograph of MR96-83 showing strongly resorbed quartz phenocrysts with 'spongy' margins and partly sericitised feldspar phenocrysts in a silicic groundmass with sericite veinlets. (E) Least altered example of the Tyndall Group rhyolites (MR96-85). (F) Photomicrograph of MR96-85 showing unaltered plagioclase phenocrysts set in a sericite-poor, albite and quartz-rich groundmass.

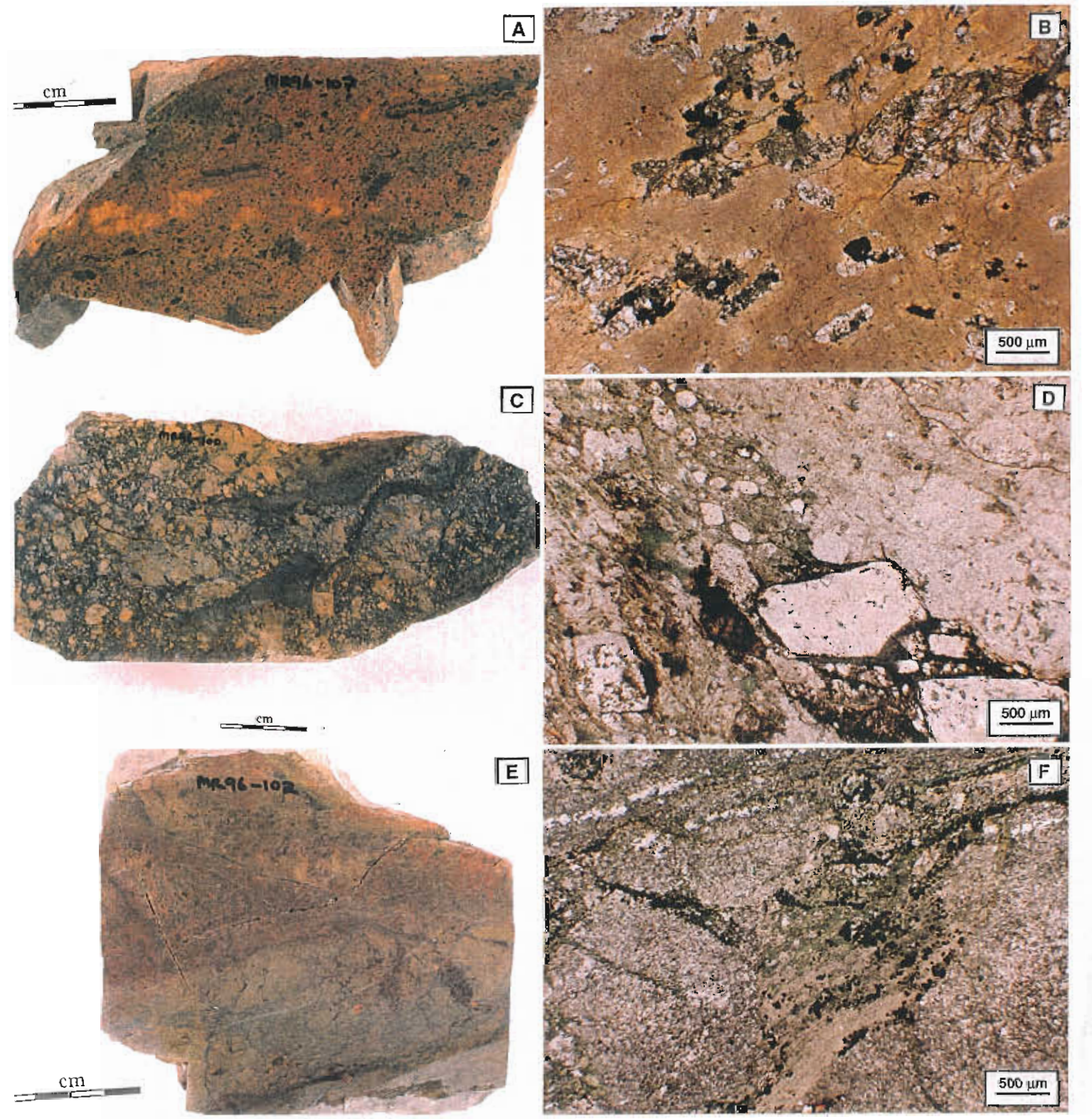

Figure 10
(A) Intensely K-feldspar altered feldspar-phyric dacitic lava, Red Hills (MR96-107. (B) Photomicrograph showing relict porphyritic texture of a probable dacitic lava now competely altered to fine grained K-feldspar with some coarse disseminated magnetite. (C) K-feldspar–chlorite altered dacitic or rhyolitic breccia, Red Hills (MR96-100). (D) Photomicrograph of MR96-100 showing clasts of fine grained K-feldspar, some of which have been partly retrogressed to sericite. The matrix to the clasts is mostly chlorite with subordinate magnetite. (E) Intensely K-feldspar altered rock, Red Hills (MR96-102). (F) Photomicrograph of MR96-102 showing fine grained K-feldspar that is cut by veins of chlorite and maguetite, and also of sericite.

coherent rocks with similar SiO_2 contents and more normal Na_2O/K_2O values. There is no significant enrichment in CO_2, S, Cu, Zn, Pb, As, Mo, Ag, Cd, Sb, Tl or Bi associated with the albitic alteration (Figs 12, 13), although S concentrations in the albitised rocks tend to be slightly higher than unaltered or weakly sericite altered samples. The Rb/Sr (Fig. 14) and K/Ba values for the albitised rocks are among the lowest for any of the rocks reflecting the stronger leaching of K_2O and Rb relative to Ba and Sr even though these elements have also been decreased compared with their original concentrations.

K-feldspar Alteration

As there is only one sample (Table 1, HRC96-9) in our dataset that definitely displays this style of alteration, it is difficult to generalise about chemical changes. However, in this sample the enrichment in K_2O is associated with strong enrichments in Rb, Ba, Cs and Mo, and a moderate enrichment in Tl relative to inferred background values in unaltered precursor rocks. Other trace elements such as Cu, Pb, Zn, As, Ag, Cd, Sb, Bi, as well as CO_2 and S appear to be unmodified by the alteration (Table 1, Figs 11–14).

Sericite + Pyrite ± Chlorite Alteration

As there is a wide range in the intensity of this alteration style among the traverse samples, the geochemical changes accordingly show substantial variation. The effects of this alteration style also appear to have been superimposed on the albitic alteration resulting in transitional chemical characteristics between the two groups. Alteration index values for samples in which this style of alteration is significant range from about 55 to 99 (Fig. 11). The progressive increase in the alteration index accompanies depletion of CaO, Na_2O and Sr, and general enrichments in S, Cs, Mo, Tl and Rb/Sr. In addition, there are sporadic marked enrichments in As, Ag, Cd, Bi, Sb and U in some of the the sericite ± pyrite ± chlorite altered rocks (Figs 11–14). Associated with the relative enrichment of U is a decrease in the Th/U value which appears to be an important indicator of strong hydrothermal alteration. Strong enrichment in Ba is not a feature of the sericitic alteration in general and only occurs close to the mineralised horizon at Hercules suggesting it may be present in baryte rather than muscovite (Large, this report).

K-feldspar ± Magnetite ± Chlorite Alteration

The chemical changes associated with this alteration style vary depending on the relative abundance of chlorite and K-feldspar. Strong enrichment in K_2O (up to 10.5 wt.%, Table 1, MR96-107) reflecting K-feldspar-rich assemblages is typically accompanied by higher ΣFe as Fe_2O_3, Ba and Rb, and strong depletion of CaO, Na_2O resulting in consistently very high values for the alteration index (generally >98). These rocks generally have very low CO_2, S and loss on ignition, and concentrations of Pb, Zn, Bi, As, Ag, Cd, Mo, Tl and Sb that are only occasionally elevated above background values. Several samples display elevated Cu concentrations, but the remainder have <10 ppm Cu. The chlorite-rich samples (e.g. Table 1, MR96-106) are relatively enriched in ΣFe as Fe_2O_3, MnO, MgO, Cu, Zn, Ni, As, Mo and U, and depleted in Al_2O_3, K_2O, Rb, Sr, Zr, Nb, Ba and Tl compared with the K-feldspar-rich rocks (Figs 11–14).

Chemical alteration along the Hall Rivulet Canal sector

As the traverses were undertaken in a broadly E–W orientaton across the MRV belt, the geographical variability of the geochemical data has been evaluated by plotting the various elements as functions of easting (Figs 15–18). With regard to Ti/Zr values most of the volcaniclastic sandstones fall into two groups, one with Ti/Zr ~ 4–6 (rhyolitic), and another with values of ~10–17 which are broadly dacitic in composition. The samples with higher Ti/Zr values are shaly sedimentary units. The rocks display a wide range of Na_2O, K_2O and Alteration Index values (Fig. 15) which reflect in part variation in the lithofacies, and partly the different types of alteration. The trace element data are much more useful in delineating zones of potential interest for VHMS exploration. For example there are several significant spikes in the Ba, Pb, As, Ag, Mo, Sb and Tl data which on closer examination appear to correlate with zones of Na_2O depletion and enrichment in S. One of

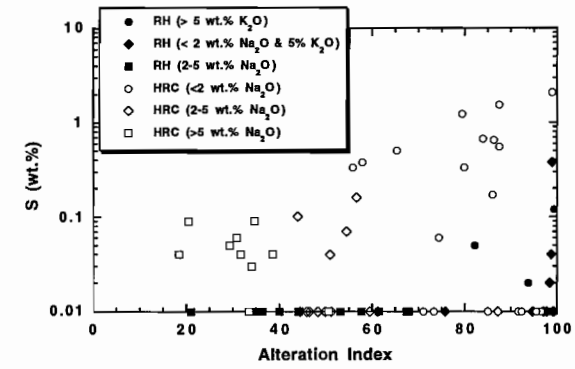

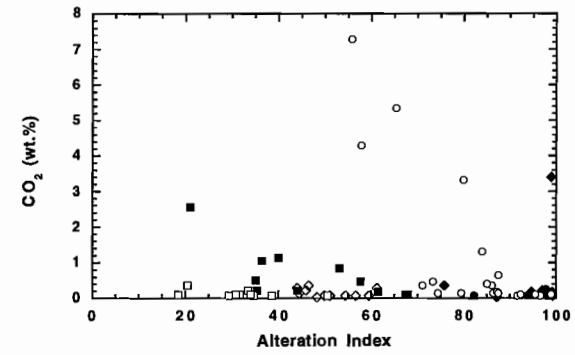

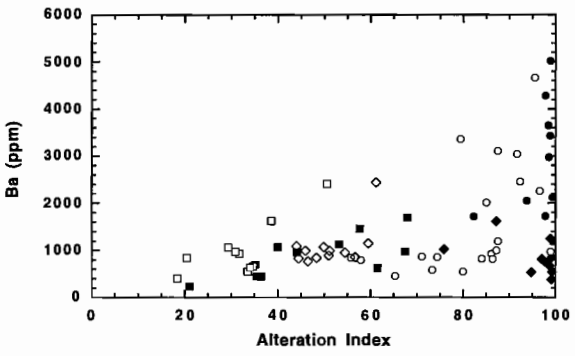

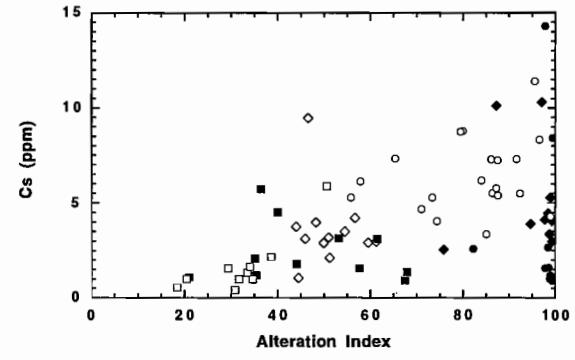

Figure 11.
Plots of S, CO_2, Ba and Cs against Alteration Index for the rocks from the Hall Rivulet Canal (HRC) and Mt Read–Red Hills (RH) sectors of the traverse. See text for correlation between chemical groupings and alteration types.

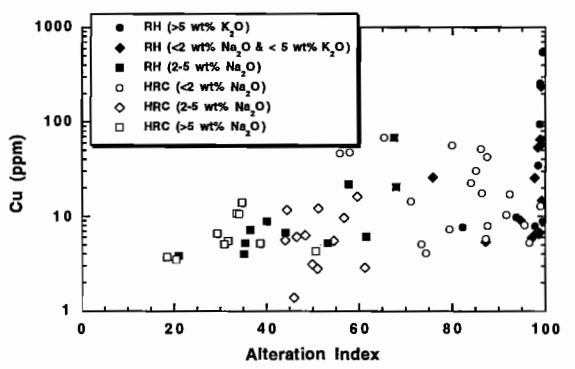

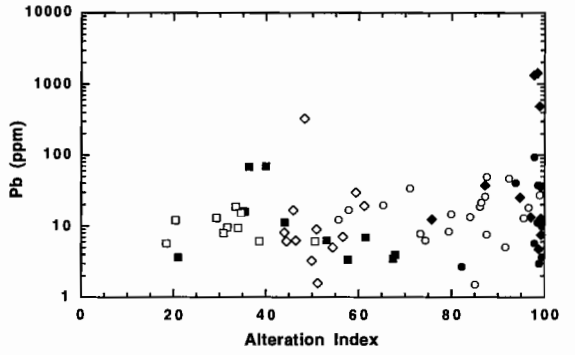

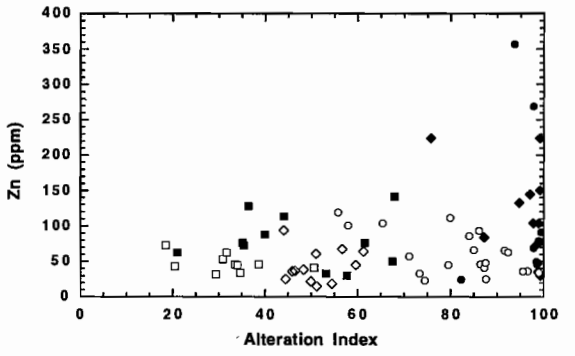

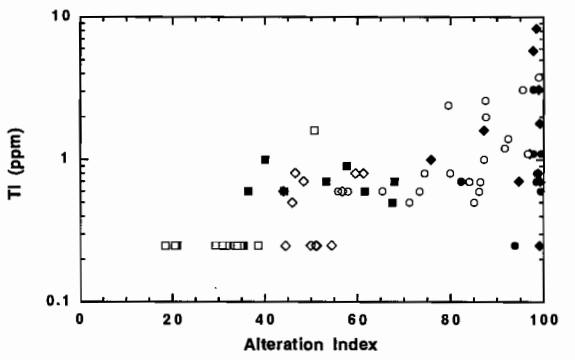

Figure 12
Plots of Cu, Pb, Zn and Tl versus Alteration Index.

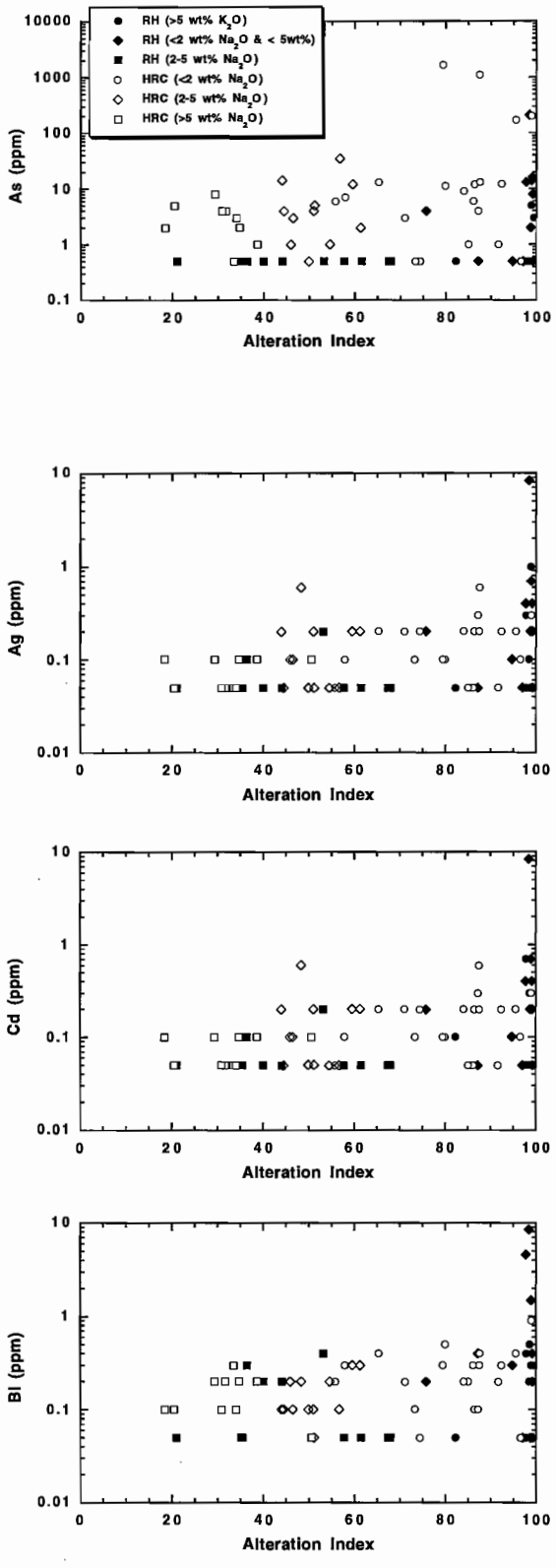

Figure 13
Plots of As, Ag, Cd and Bi versus Alteration Index.

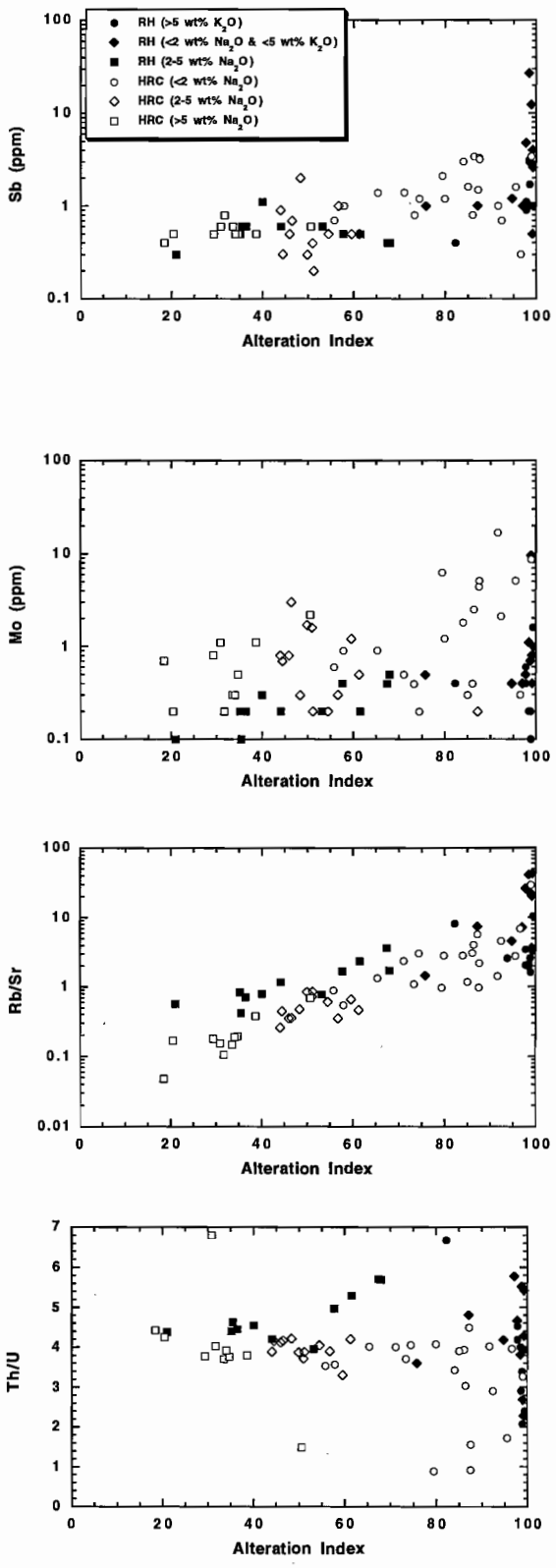

Figure 14
Plots of Sb, Mo, Rb/Sr and Th/U versus Alteration Index.

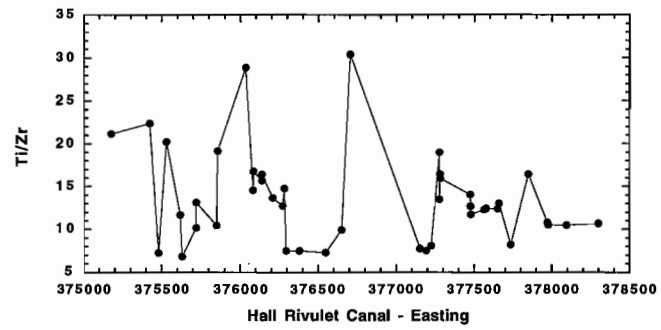

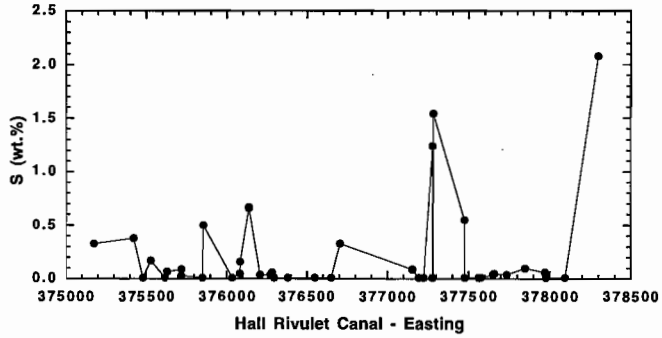

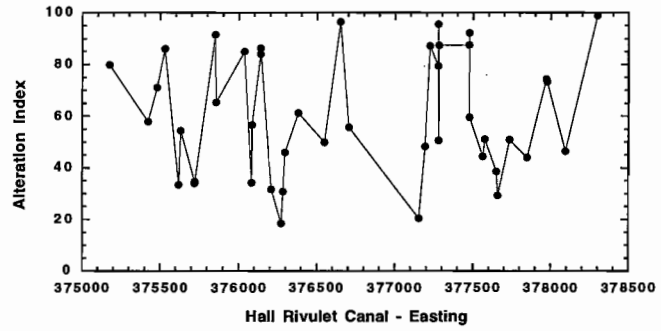

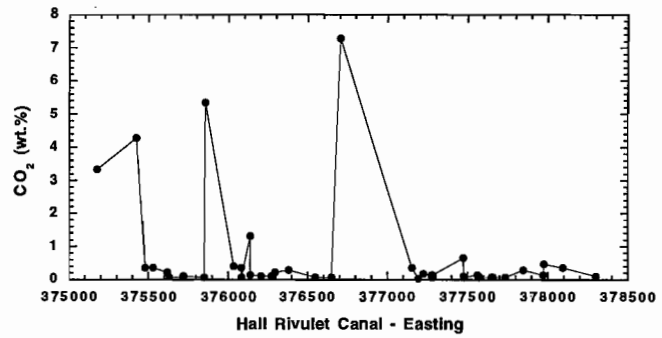

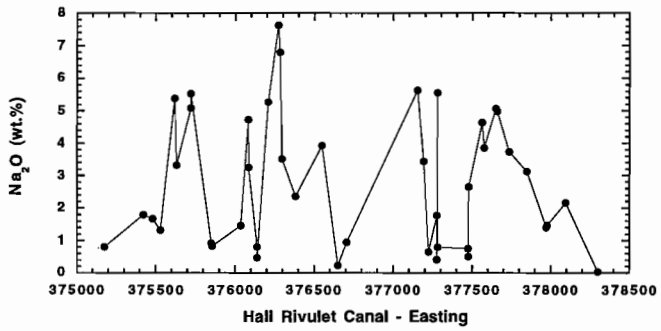

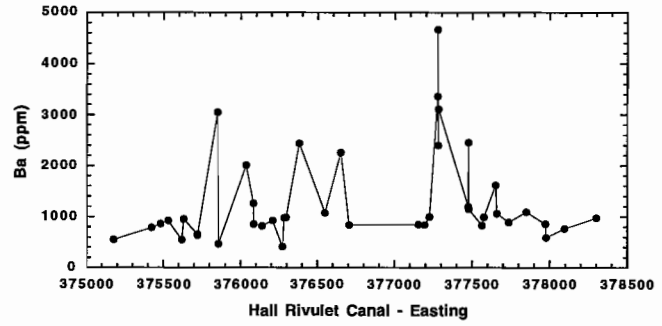

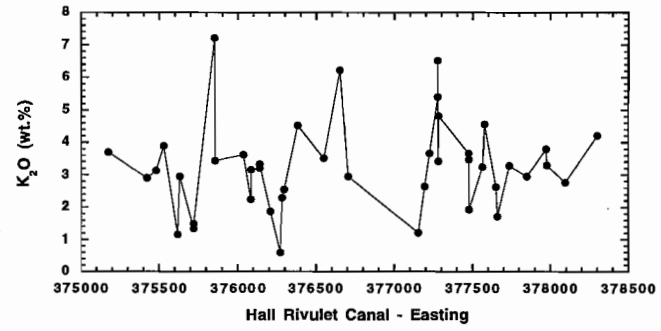

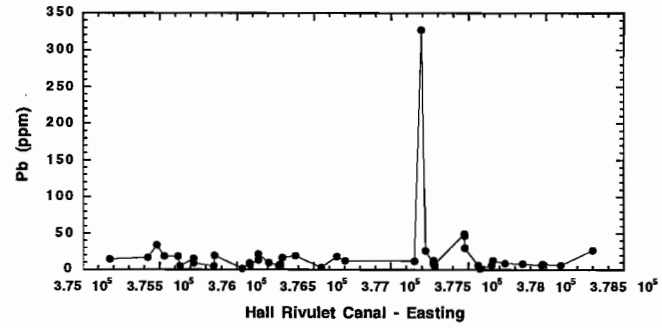

Figure 15
Variation of Ti/Zr, Alteration Index, Na_2O and K_2O as functions of easting for the samples from the Hall Rivulet Canal.

Figure 16
Variation of S, CO_2, Ba and Pb as functions of easting for the samples from the Hall Rivulet Canal.

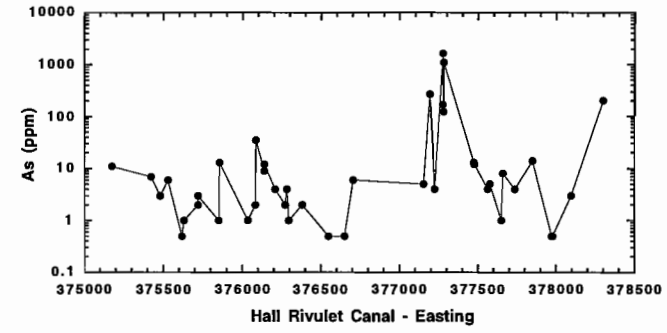

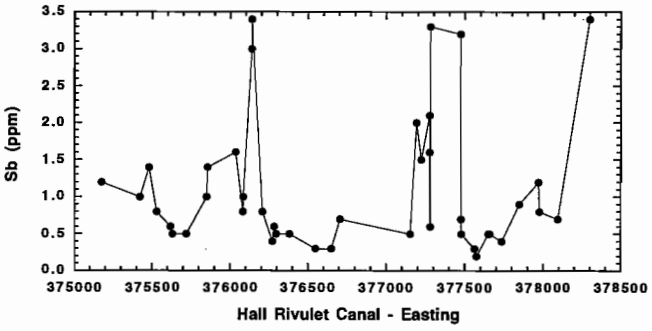

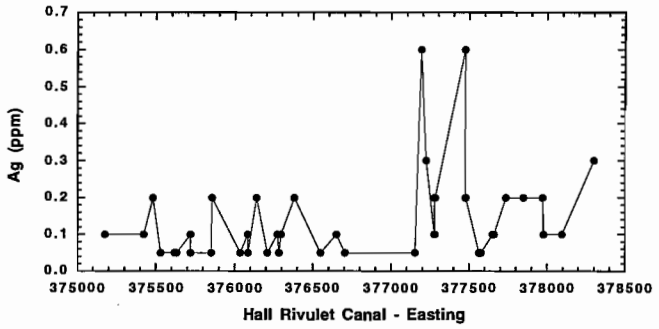

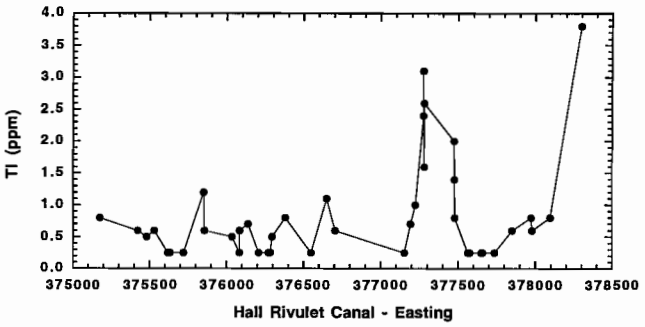

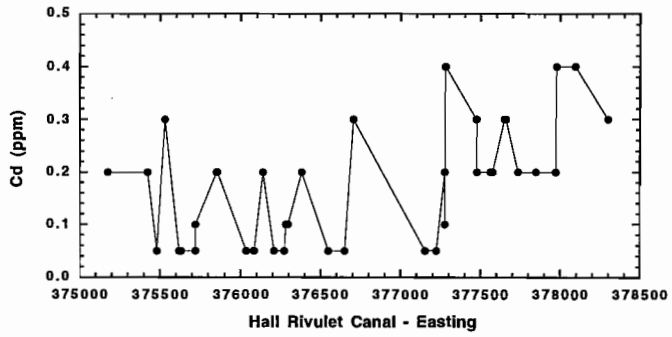

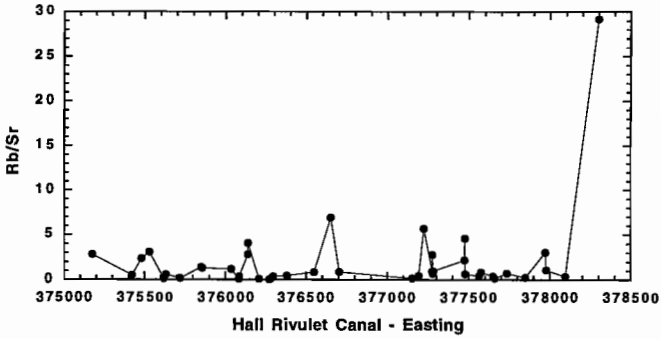

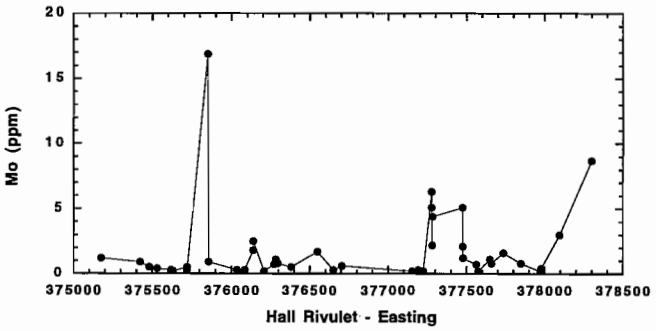

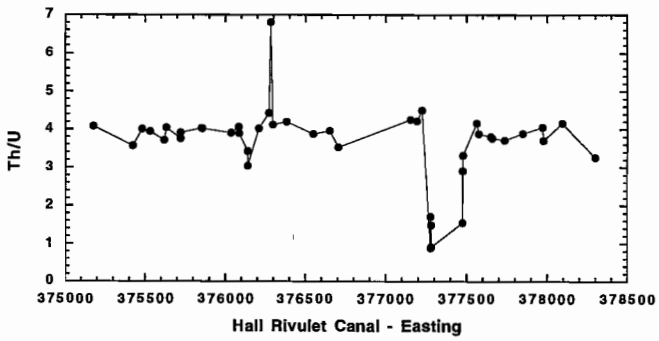

Figure 17
Variation of As, Ag, Cd and Mo as functions of easting for the samples from the Hall Rivulet Canal.

Figure 18
Variation of Sb, Tl, Th/U and Rb/Sr as functions of easting for the samples from the Hall Rivulet Canal.

these anomalous zones in particular displays a coincident reduction in Th/U values (Fig. 18) which is also a feature of the Hercules footwall alteration. However, only one of the samples from this zone displays a Pb concentration that is elevated above the general background, and both Zn and Cu remain at background concentrations. Arsenic appears to be the most strongly enriched and potentially useful element, but the other elements above are also substantially enriched above their normal concentration range for diagenetic or background alteration effects.

Chemical variation along the Henty Fault–Red Hills sector

The data for this sector identified a narrow zone of intense sericite alteration in Tyndall Group rhyolites immediately to the east of the Henty Fault (Figs 19–23). This passed quite rapidly into weakly sericite-altered and unaltered rocks within several hundred meters. This zone is characterised by strong Ca and Na depletion, and high Rb/Sr, K/Ba and Alteration Index values. However, the only evidence of anomalous metal concentrations is provided by a very slight enrichment in S, Sb and As.

The other major alteration zone is at Red Hills where there is an inner core of K-feldspar ± magnetite ± chlorite alteration surrounded by a zone of sericite ± pyrite ± chlorite alteration. These rocks have consistently higher Ti/Zr values than the very uniform rhyolitic rocks of the Tyndall Group which is consistent with the interpretation that they are altered equivalents of dacitic rocks from the Central Volcanic Complex. All of the samples from the immediate vicinity of Red Hills show profound depletion of CaO and Na_2O coupled with enrichment in K_2O, Fe_2O_3 and very high values for the Alteration Index. The only elevated CO_2 and S values in this area are for a shale unit (Table 1, HRC96-93). The significant enrichment in Pb, Tl, As, Ag, Mo, Sb and Bi is focussed in the sericite-altered rocks and only weakly developed in the adjacent K-feldpar–magnetite–chlorite altered samples. The K-feldspar altered rocks are also distinguished from the sericite-altered rocks by higher Ba, and lower K/Ba, Th/U and Rb/Sr (Fig. 23).

Significance and timing of different alteration styles

The earliest alteration appears to be related to diagenesis and reflected by the present assemblage albite ± epidote ± sericite. As these rocks have recrystallised under prehnite–pumpellyite or lower greenschist facies conditions during the Devonian metamorphism, there is some uncertainty whether these phases were produced during diagenetic alteration or are the recystallised metamorphic equivalents. Studies in Japan of diagenetic alteration in currently forming volcaniclastic sandstones derived from rhyolitic or dacitic rocks indicate that rhyolitic glass may be altered initially to Na-smectite and subsequently at depths > 600m and temperature >70°C to analcite + quartz (Masuda et al., 1992). Analcite will recrystallise to albite at temperatures >120°C. It is unclear if the albite forming overgrowths on plagioclase grains and filling fractures would have initially formed perhaps as a smectite, then re-crystallised to analcite and susequently albite with increasing depth of burial and temperature. The textural character of the overgrowths tends to support a very early timing for this alteration in contrast to the decussate aggregates of albite laths, which seem more typical of the effects expected from metamorphic recrystallisation.

Additional studies of diagenetic alteration in modern sediments indicate that illite may also form as a diagenetic phase in the matrix of sandstones of similar composition (Boggs and Seyedolali, 1992), and illite will recrystallise to sericite at higher temperatures. As most rhyolitic rocks probably have about 2–3 wt.% K_2O in the glass, there is sufficient K_2O present to form 20–25 % sericite without adding any K from seawater, although some H_2O is obviously required. Albite and sericite may coexist over a significant P/T range at moderate pH and relatively high Na/K values. Albite becomes unstable and will break down at the expense of sericite with decreasing pH. The coexistence of albite and sericite is indicated by the unaltered albite rims surrounding partly sericitised cores of plagioclase grains. The implication is that the cores of the feldspars were slightly more calcic than the rims and experienced some alteration,

perhaps initially to illite, which recrystallised as sericite or muscovite during the metamorphism, whereas the albitic rims were stable under the range of diagenetic and metamorphic conditions.

Albite–epidote alteration has also been proposed as a potential hangingwall alteration assemblage where Na_2O and CaO leached from the footwall volcanic package are added to hangingwall volcanic units by the hydrothermal system during the period it continues to operate after these units have been emplaced over the massive sulphide deposit. This alteration style is well developed in the hangingwall dacites immediately above the Thalanga massive sulphide deposit in the Mt Windsor Volcanic belt (Stolz, 1991). A distinctive, patchy, pink-green, albite–epidote-rich assemblage occurs up to at least 60m above the mineralisation with an upward decrease in intensity. Stolz (1991) noted increases in CaO, Sr, Cu and Na_2O concentrations in the altered dacite relative to the unaltered dacite along strike. This alteration appears to have been quite a localised feature at Thalanga possibly due to the coherent, impermeable nature of the hangingwall dacites, and a broader zone of alteration may perhaps be expected for example in the hangingwall pumice breccia to the Hercules deposit.

The occurrence of K-feldspar as an overgrowth on detrital felspar grains in the volcaniclastic rocks is less common, but is also permitted by the phase equilibria at low temperature if the Na/K of the fluid is appropriate and the fluid is neutral or slightly alkaline. The strong enrichment of K_2O in HRC96-9 (and some Mt Windsor rocks) is unusual, and if it occurred at low temperature suggests equilibration with a rock-buffered fluid which had reacted with a lot of glass resulting in a high K/Na. This coupled with a relatively high $aSiO_2$ in the fluid may have been responsible for the precipitation of K-feldspar rather than albite.

The sericite ± pyrite ± chlorite alteration generally overprints earlier diagenetic alteration although it is not always clear where diagenetic alteration ends and hydrothermal alteration begins. A rough approximation would be that a silicic volcaniclastic rock with up to about 25% sericite concentrated in the matrix, but which exhibits only minor sericitisation of plagioclase grains (and paricularly if the feldspar has albite rims), could be simply a product of diagenetic alteration involving relatively small volumes (i.e. low water/rock values) of low temperature, near neutral fluids. Interaction with larger volumes of hotter and more acid fluids will result in increasing replacement by sericite + pyrite + chlorite, first of the matrix, and subsequently of the plagioclase grains. The feldspar grains may also be replaced by quartz in some cases. The final breakdown of the feldspar grains is the best indicator of intense alteration and is reflected chemically by the strong depletion of Na_2O and CaO (unless carbonate is an associated alteration product).

The depletion of Na_2O, which is a common characteristic of many altered footwall volcanic packages to massive sulphide deposits, is frequently used as an exploration vector to ore. However, this should be exercised with some caution given that low-temperature diagenetic K-feldspar alteration effectively results in depletion of Na_2O through cation exchange processes rather than breakdown of primary Na-bearing phases by interaction with high temperature hydrothermal fluids. Very large zones of Na_2O depletion and K_2O enrichment produced in this manner have been described from the Sturgeon Lake area, Bergslagen and the Iberian Pyrite Belt (Galley, 1995).

The lower porosity and permeability of coherent units is generally reflected in less intense alteration compared with volcaniclastic rocks in the same sequence. A rhyolite with ~2.5 wt.% K_2O is capable of developing 20–25 % sericite during regional metamorphism if sericite is the only K-bearing phase and sufficient H_2O is added, but few of the coherent rocks display anything near this amount unless they are close to a significant hydrothermal system.

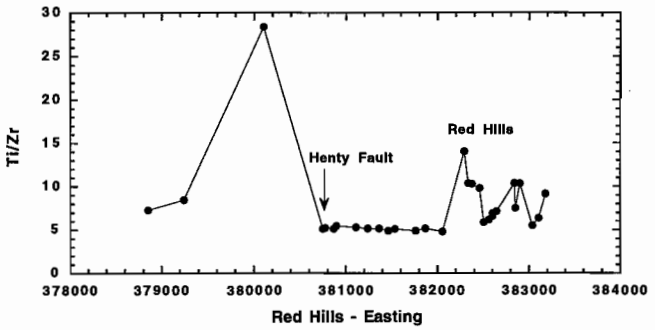

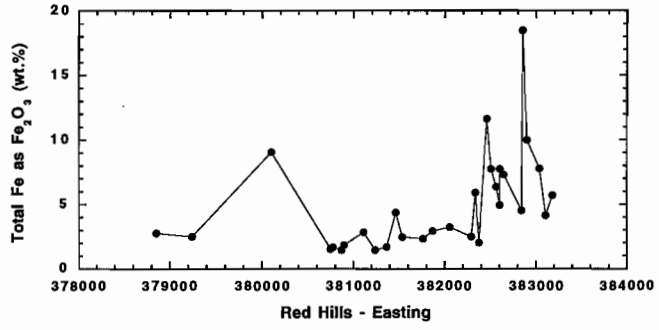

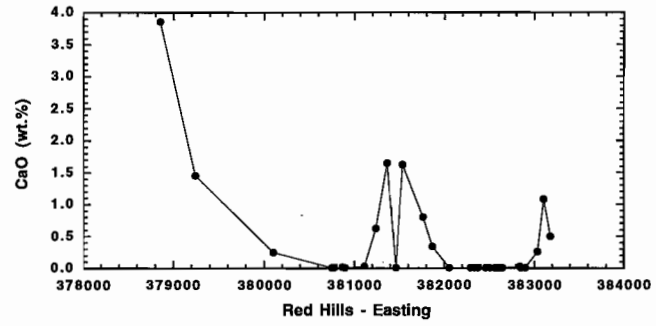

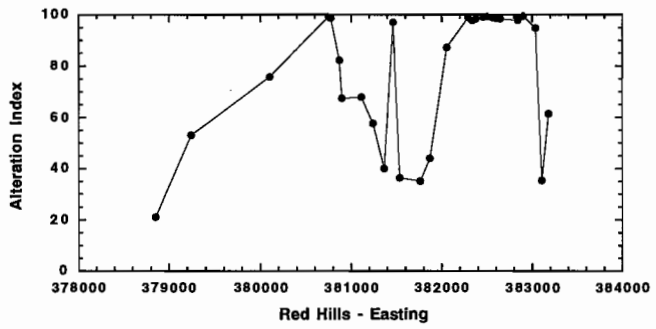

Figure 19
Variation of Ti/Zr, Total Fe as Fe_2O_3, CaO and Alteration Index as functions of easting for the samples from the Henty Fault–Red Hills sector of the traverse.

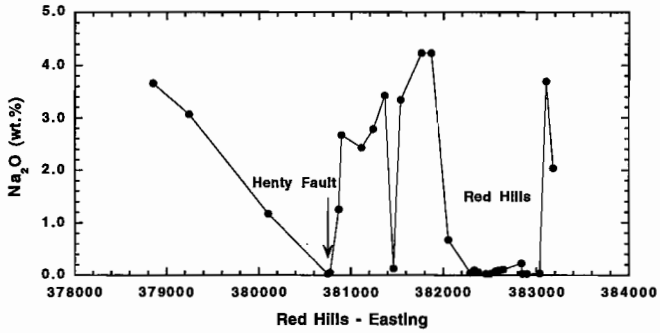

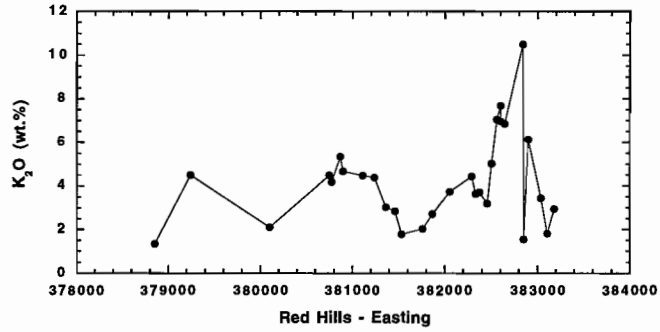

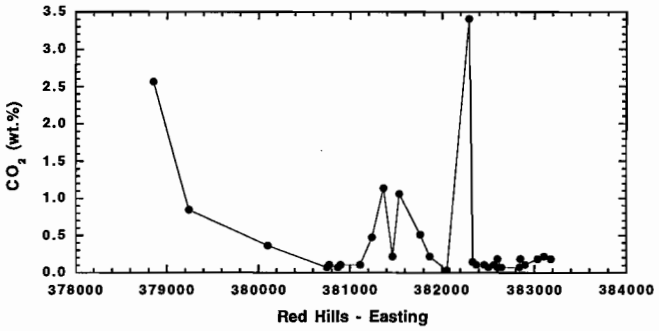

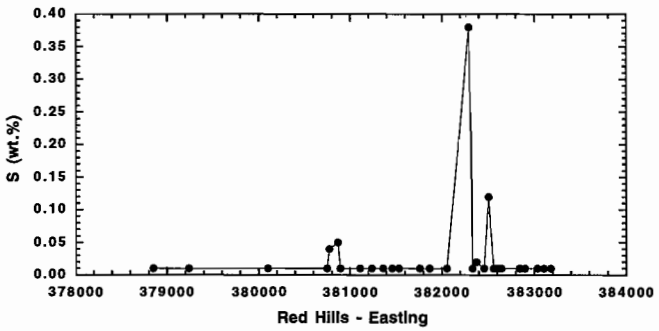

Figure 20
Variation of Na_2O, K_2O, CO_2 and S as functions of easting for the samples from the Henty Fault–Red Hills sector of the traverse.

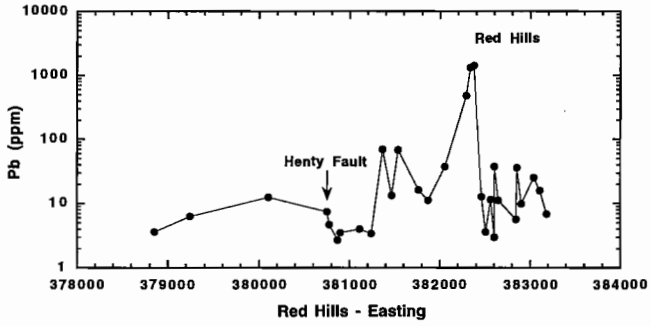

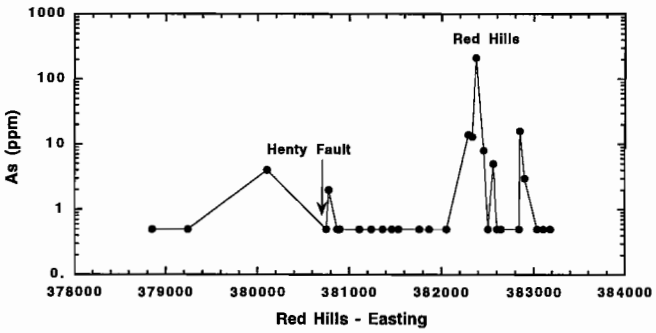

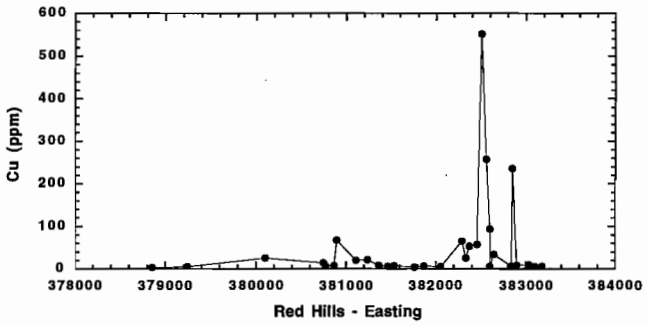

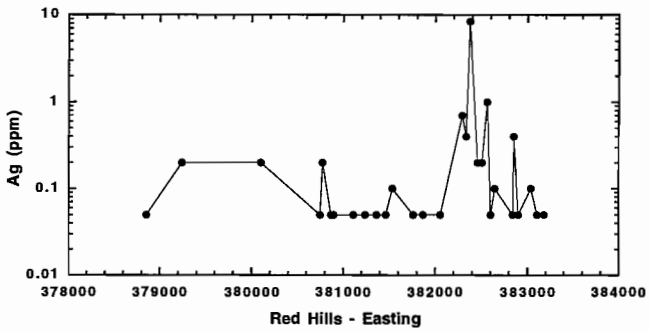

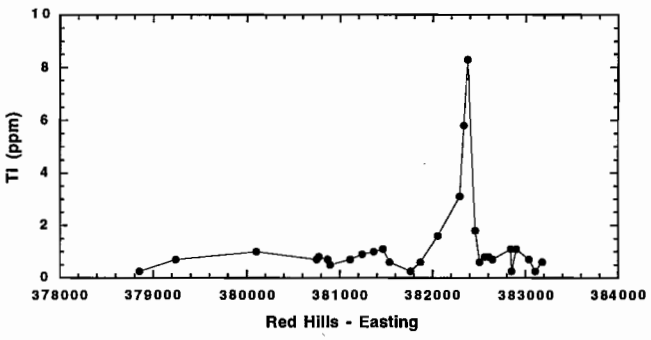

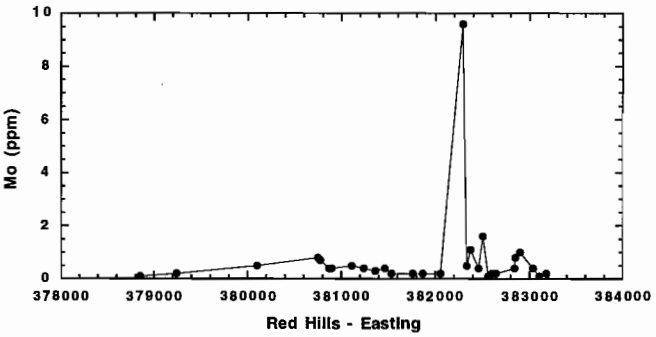

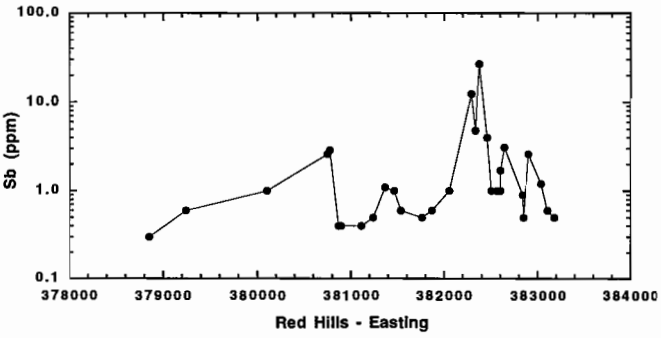

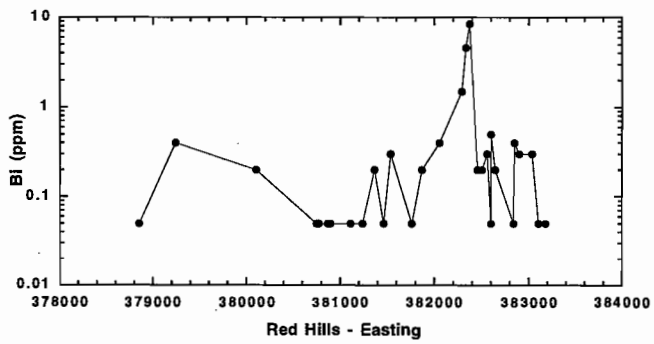

Figure 21
Variation of Pb, Cu, Tl and Sb as functions of easting for the samples from the Henty Fault–Red Hills sector of the traverse.

Figure 22
Variation of As, Ag, Mo and Bi as functions of easting for the samples from the Henty Fault–Red Hills sector of the traverse.

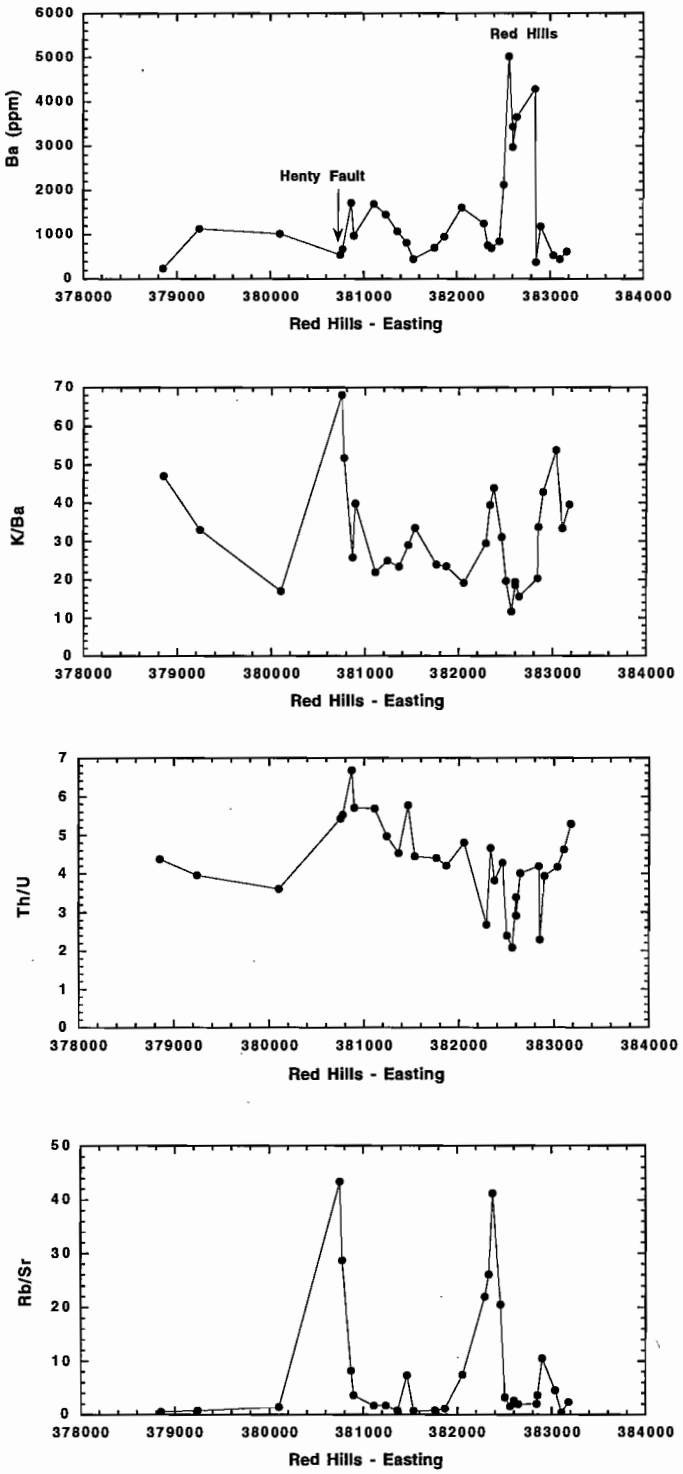

Figure 23
Variation of Ba, K/Ba, Th/U and Rb/Sr as functions of easting for the samples from the Henty Fault–Red Hills sector of the traverse.

Conclusions

- Petrographic and chemical data for the samples from the Hall Rivulet Canal–Mt Read–Red Hills–Anthony Dam traverse indicate five major styles of alteration. Two of these (albite ± epidote ± sericte and low-temperature K-feldspar alteration) are regarded as the result of diagenetic processes that may have been modified by subsequent greenschist facies regional metamorphism. An important facet of this alteration is the presence of significant sericite in some samples (up to 20–25%) which may be of diagenetic origin rather than related to hydrothermal fluid activity.

- There is negligible enrichment of base or precious metals associated with the diagenetic albitic alteration, but these rocks have distinctive compositions characterised by $Na_2O > 5$ wt% and substantial depletion of K_2O, Rb, Cs and Ba compared with unaltered equivalents.

- Diagenetic K-feldspar alteration is much less common in the traverse samples and is indicated by high K_2O/Na_2O, Rb, Ba and Cs, but negligible enrichment in base metals, S and CO_2.

- The effects of sericite ± pyrite ± chlorite hydrothermal alteration commonly overprint and are gradational to the albite ± epidote ± sericite alteration. The more intense variants of this alteration style are characterised by strong depletion of CaO, Na_2O and Sr, and commonly display significant enrichment of a wide range of trace elements including As, Mo, Ag, Sb, Tl, Pb and Bi. High Rb/Sr and low Th/U values are additional distinctive features. Arsenic appears to be the most sensitive indicator of metal enrichment associated with this alteration type. However, additional assessment in the deposit studies is required to see if it produces broader dispersion haloes than Cu, Pb and Zn, for example.

- K-feldspar ± magnetite ± chlorite alteration at Red Hills is characterised by strong depletion of Na_2O and CaO, coupled with high K_2O and Ba in the feldspar-rich rocks, and high Fe_2O_3, MnO, MgO together with lower K_2O and Ba in the chlorite-rich assemblages. The feldspar-rich alteration appears to be the earliest phase and is overprinted by chlorite–magnetite-rich veins and sericite-rich veins.

References

Boggs, S. and Seyedolali, A., 1992, Diagenetic albitization, zeolitization and replacement in Miocene sandstones, Sites 796, 797, and 799, Japan Sea. Proc. ODP Scientific Results, 127/128, 131–149.

Doyle, M.G., 1990, The geology, mineralisation and alteration of the Jukes Proprietry prospect, Tasmania. Unpubl. BSC Hons Thesis, University of Tasmania, 114p.

Eastoe, C.J., Solomon, M. and Walshe, J.L., 1987, District-scale alteration associated with massive sulfide deposits in the Mt Read Volcanics, western Tasmania. Economic Geology, 82, 1239–1258.

Galley, A.G., 1995, Target vectoring using lithogeochemistry: Applications to the exploration for volcanic-hosted massive sulphide deposits. CIM Bulletin, 88, No. 990, 15–27.

Ishikawa, Y., Sawaguchi, T., Iwaya, S. and Horiuchi, M., 1976. Delineation of prospecting targets for Kuroko deposits based on modes of volcanism of underlying dacite and alteration haloes. Mining Geology, 26, 105–117.

Jenkins, D.R., 1991, Volcanology, mineralisation and alteration of the Red Hills, western Tasmania. Unpubl. Bsc Hons. Thesis, University of Tasmania, 90p.

Masuda, H., Tanaka, H., Gamo, T., O'Neil, J.R., Peacor, D.R. and Jiang, W.-T., 1992, Formation of authigenic smectite and zeolite and associated major element behaviour during early diagenesis of volcanic ash in the Nankai Trough, Japan, ODP leg 131, in, Kharaka and Maest (eds.) Water-Rock Interaction, Balkema, Rotterdam, p1659–1662.

Stolz, J., 1991, Stratigraphy and geochemistry of the Mt Windsor Volcanics and associated exhalites. Mt Windsor Project Research Report No. 2, 23–83.

Table 1. Major and trace element analyses of rocks from the Hall Rivulet Canal-Mt Read-Red Hills-Anthony Dam Traverse

	HRC96-1	HRC96-2	HRC96-3	HRC96-4	HRC96-5	HRC96-6	HRC96-7	HRC96-8	HRC96-9	HRC96-10	HRC96-11	HRC96-12
SiO2	52.95	55.29	73.81	59.23	69.95	76.28	74.56	70.18	58.52	50.43	62.27	63.72
TiO2	0.81	0.65	0.33	0.69	0.44	0.24	0.35	0.47	0.49	0.79	0.64	0.73
Al2O3	16.47	14.28	14.27	17.82	15.25	12.56	12.90	14.98	19.37	15.37	15.64	16.04
Fe2O3#	7.79	6.72	2.73	7.27	3.41	1.40	2.73	3.62	4.98	6.92	6.71	5.07
MnO	0.25	0.14	0.01	0.03	0.01	0.01	0.02	0.03	0.03	0.10	0.03	0.09
MgO	6.76	5.58	1.00	4.81	1.66	1.27	1.44	1.52	3.76	7.29	4.95	1.67
CaO	1.82	4.38	0.01	0.08	0.20	0.20	0.16	0.30	0.08	4.85	0.05	2.79
Na2O	0.81	1.80	1.68	1.33	5.39	3.33	5.09	5.54	0.92	0.83	1.47	4.73
K2O	3.70	2.90	3.13	3.90	1.16	2.94	1.35	1.49	7.21	3.44	3.63	2.25
P2O5	0.10	0.15	0.05	0.10	0.07	0.06	0.06	0.09	0.10	0.10	0.11	0.14
LOI	7.65	7.95	3.11	4.64	2.34	1.50	1.35	1.68	4.01	9.86	4.42	2.06
Total	99.17	99.85	100.14	99.91	99.88	99.79	100.01	99.89	99.49	100.00	99.93	99.30
S	0.33	0.38	0.01	0.17	0.01	0.07	0.09	0.03	0.01	0.50	0.01	0.05
Total C	0.91	1.17	0.10	0.10	0.06	0.02	0.02	0.03	0.02	1.46	0.11	0.10
CO2	3.33	4.29	0.37	0.37	0.22	0.07	0.07	0.11	0.07	5.35	0.40	0.37
Alteration Index	79.9	57.8	71.0	86.1	33.5	54.4	34.6	34.0	91.6	65.4	85.0	34.2
Trace Elements (ppm)												
Sc	28	24	12	25	11	5	9	12	11	27	24	16
V	171	149	27	165	56	16	38	56	53	172	161	52
Cr	340	190	19	139	15	11	14	13	17	266	53	7
Ni	280	104	17	88	12	6	8	6	18	175	32	3
Cu	56	48	14	52	11	6	14	11	10	69	30	7
Zn	111	101	57	93	46	19	34	45	66	104	66	61
As	11	7	3	6	<1	1	2	3	1	13	1	2
Rb	176	115	120	148	35	111	33	47	255	159	107	59
Sr	62	211	51	48	233	181	167	248	178	118	90	631
Y	38	43	43	32	32	33	30	30	46	39	24	43
Zr	230	175	273	205	227	211	207	215	282	249	133	302
Nb	19.5	13.0	14.9	13.3	10.2	10.4	9.7	8.7	15.1	17.8	7.8	10.9
Mo	1.2	0.9	0.5	0.4	0.3	0.2	0.5	0.3	16.9	0.9	0.3	0.2
Ag	0.1	0.1	0.2	<0.1	<0.1	<0.1	0.1	<0.1	<0.1	0.2	<0.1	0.1
Cd	0.2	0.2	<0.1	0.3	<0.1	<0.1	<0.1	0.1	0.2	0.2	<0.1	<0.1
Sb	1.2	1	1.4	0.8	0.6	0.5	0.5	0.5	1	1.4	1.6	0.8
Cs	8.78	6.13	4.7	7.29	1.34	3.5	0.98	1.66	7.32	7.35	3.37	2.12
Ba	556	794	870	928	549	957	658	638	3047	467	2008	1264
La	32	28	50	34	31	51	36	34	71	34	21	38
Ce	69	59	102	76	70	103	76	72	138	73	49	83
Nd	32	25	41	32	31	36	31	29	50	33	18	40
Tl	0.8	0.6	0.5	0.6	<0.5	<0.5	<0.5	<0.5	1.2	0.6	0.5	<0.5
Pb	15	17	34	19	19	5	15	9	5	20	2	9
Bi	0.5	0.3	0.2	0.3	0.3	0.2	0.2	0.1	0.2	0.4	0.2	0.1
Th (XRF)	13.0	12.0	22.5	12.9	19.1	25.4	19.3	15.1	30.8	14.6	6.6	15.3
Th (ICP)	12	9.14	20	11.4	15.9	24	16.3	13.4	28.3	12.3	7.07	13.2
U	2.94	2.56	4.99	2.89	4.28	5.93	4.33	3.42	7.02	3.06	1.81	3.25

Total Fe as Fe2O3; LOI = loss on ignition; Alteration Index = 100(MgO+K2O)/(MgO+K2O+CaO+Na2O)

Table 1. continued

	HRC96-13	HRC96-15	HRC96-16	HRC96-17	HRC96-18	HRC96-19	HRC96-20	HRC96-21	HRC96-22	HRC96-23	HRC96-24	HRC96-25
SiO2	66.36	68.75	76.72	64.47	65.30	66.22	74.35	73.93	73.99	65.84	55.25	78.82
TIO2	0.80	0.60	0.55	0.72	0.72	0.69	0.36	0.34	0.29	0.47	0.79	0.14
Al2O3	16.49	13.01	12.44	16.06	16.06	16.20	14.04	13.23	14.17	19.69	12.45	12.35
Fe2O3#	5.16	5.93	1.59	5.21	4.81	4.83	1.97	2.27	2.24	2.67	6.77	1.23
MnO	0.04	0.16	0.01	0.10	0.10	0.15	0.02	0.08	0.04	0.01	0.14	0.04
MgO	1.59	2.33	0.92	1.65	1.28	1.27	0.56	0.64	0.53	1.07	4.88	0.29
CaO	0.37	0.24	0.20	2.33	1.22	0.59	0.15	0.91	0.13	0.02	5.26	0.22
Na2O	3.26	0.81	0.47	5.28	6.80	7.64	3.52	2.36	3.93	0.24	0.95	5.64
K2O	3.16	3.22	3.33	1.88	2.30	0.59	2.55	4.53	3.51	6.22	2.95	1.22
P2O5	0.16	0.14	0.17	0.14	0.13	0.13	0.05	0.04	0.04	0.08	0.16	0.01
LOI	2.36	4.45	3.06	1.81	1.00	1.43	2.18	1.45	1.25	3.45	10.34	0.81
Total	99.75	99.64	99.46	99.65	99.72	99.74	99.75	99.80	100.12	99.77	99.96	100.76
S	0.16	0.67	0.66	0.04	0.06	0.04	0.01	0.01	0.01	0.01	0.33	0.09
Total C	0.02	0.36	0.04	0.03	0.03	0.03	0.06	0.08	0.02	0.02	1.99	0.10
CO2	0.07	1.32	0.15	0.11	0.11	0.11	0.22	0.29	0.07	0.07	7.29	0.37
Alteration Index	56.7	84.0	86.3	31.7	30.8	18.4	45.9	61.2	49.9	96.5	55.8	20.5
Trace Elements (ppm)												
Sc	24	15	18	15	18	17	8	7	8	9	23	2
V	64	51	47	50	54	50	10	8	14	39	198	3
Cr	7	10	10	5	5	5	2	2	3	5	145	3
Ni	3	7	11	3	3	3	2	2	1	3	53	2
Cu	10	22	18	6	5	4	1	3	3	5	46	4
Zn	68	86	46	63	53	73	36	64	22	37	119	44
As	35	9	12	4	4	2	1	2	<1	<1	6	5
Rb	123	129	131	48	46	11	97	147	118	210	127	39
Sr	348	45	32	451	297	229	275	311	140	30	142	232
Y	33	45	42	49	42	102	43	49	43	35	34	29
Zr	287	230	202	317	294	327	288	273	239	285	157	109
Nb	10.7	11.9	9.5	12.7	11.4	13.3	14.4	14.0	12.0	13.9	14.1	12.2
Mo	0.3	1.8	2.5	0.2	1.1	0.7	0.8	0.5	1.7	0.3	0.6	0.2
Ag	<0.1	0.2	0.2	<0.1	<0.1	0.1	0.1	0.2	<0.1	0.1	<0.1	<0.1
Cd	<0.1	0.2	0.2	<0.1	0.1	<0.1	0.1	0.2	<0.1	<0.1	0.3	<0.1
Sb	1	3	3.4	0.8	0.6	0.4	0.5	0.5	0.3	0.3	0.7	0.5
Cs	4.22	6.17	5.52	0.97	0.42	0.55	3.12	2.96	2.9	8.32	5.29	1
Ba	858	826	821	930	978	410	992	2444	1077	2263	843	852
La	40	49	33	44	38	125	52	52	63	69	24	60
Ce	80	92	70	94	83	198	120	112	127	132	52	111
Nd	42	42	32	45	39	93	49	45	51	50	23	37
TI	0.6	0.7	0.7	<0.5	<0.5	<0.5	0.5	0.8	<0.5	1.1	0.6	<0.5
Pb	7	13	22	10	8	6	17	19	3	18	12	12
Bi	0.1	0.2	0.1	0.2	0.1	0.1	0.2	0.3	0.1	<0.1	0.2	0.1
Th (XRF)	10.5	18.4	11.9	16.9	14.7	18.8	23.6	22.4	23.5	24.0	10.6	32.9
Th (ICP)	9.44	14.6	10.8	14.4	7.01	8.86	20.9	21	20.2	21.5	8.72	28.6
U	2.42	4.26	3.55	3.58	1.03	2	5.07	5	5.21	5.42	2.47	6.72

Total Fe as Fe2O3; LOI = loss on ignition; Alteration Index = 100(MgO+K2O)/(MgO+K2O+CaO+Na2O)

Table 1. continued

	HRC96-26	HRC96-27	HRC96-28	HRC96-29	HRC96-30	HRC96-31	HRC96-33	HRC96-34	HRC96-35	HRC96-36	HRC96-37	HRC96-38
SiO2	75.66	75.66	51.54	56.08	54.01	59.64	71.29	67.30	72.27	72.31	72.89	68.29
TiO2	0.18	0.17	0.89	0.89	0.71	0.60	0.53	0.60	0.54	0.43	0.39	0.55
Al2O3	14.52	13.80	25.73	25.11	25.64	21.49	15.32	15.91	13.29	14.22	13.21	15.33
Fe2O3#	1.15	1.24	4.43	2.90	2.87	4.25	1.98	3.85	3.23	2.82	2.82	3.95
MnO	0.00	0.01	0.03	0.02	0.02	0.02	0.02	0.04	0.03	0.03	0.04	0.07
MgO	0.89	0.69	2.92	2.93	2.60	2.09	1.91	3.25	2.47	0.77	0.76	1.36
CaO	0.02	0.13	0.39	0.03	0.34	0.19	0.04	0.05	0.34	0.39	1.22	1.25
Na2O	0.65	3.44	1.77	0.41	5.56	0.80	0.75	0.51	2.65	4.64	3.86	5.07
K2O	3.67	2.64	5.41	6.52	3.43	4.82	3.67	3.48	1.93	3.25	4.56	2.62
P2O5	0.02	0.03	0.32	0.13	0.35	0.17	0.08	0.12	0.13	0.11	0.09	0.13
LOI	3.71	1.95	5.66	4.51	4.20	5.33	4.19	4.52	2.68	1.42	0.78	1.43
Total	100.47	99.76	99.41	99.97	99.74	99.71	99.79	99.62	99.56	100.48	100.71	100.05
S	0.01	0.01	1.24	0.01	0.01	1.54	0.55	0.01	0.01	0.01	0.01	0.04
Total C	0.05	0.01	0.04	0.03	0.02	0.04	0.18	0.03	0.02	0.04	0.02	0.02
CO2	0.18	0.04	0.15	0.11	0.07	0.15	0.66	0.11	0.07	0.15	0.07	0.07
Alteration Index	87.1	48.3	79.4	95.6	50.5	87.5	87.5	92.3	59.5	44.4	51.2	38.6
Trace Elements (ppm)												
Sc	3	4	29	22	20	22	14	10	11	9	8	12
V	13	8	184	435	190	152	213	84	75	47	39	37
Cr	8	4	26	79	24	24	43	67	83	4	3	3
Ni	4	5	23	13	17	20	11	8	11	3	2	2
Cu	6	6	7	8	4	42	8	17	16	12	12	5
Zn	42	38	45	36	41	48	25	63	45	25	15	46
As	4	270	1650	171	124	1100	13	12	12	4	5	1
Rb	197	127	226	295	159	195	195	200	110	75	110	83
Sr	34	264	230	105	228	197	88	43	166	169	128	217
Y	28	27	33	30	36	38	32	29	49	32	29	42
Zr	134	136	281	395	260	225	227	285	277	209	188	267
Nb	14.1	10.8	16.2	19.6	14.6	11.0	12.6	19.0	17.0	11.6	10.4	14.4
Mo	0.2	0.3	6.3	5.1	2.2	4.4	5.1	2.1	1.2	0.7	0.2	1.1
Ag	0.3	0.6	0.1	0.2	0.1	0.2	0.6	0.2	0.2	<0.1	<0.1	0.1
Cd	<0.1	<0.1	0.2	0.1	0.4	0.4	0.3	0.3	0.2	0.2	0.2	0.3
Sb	1.5	2	2.1	1.6	0.6	3.3	3.2	0.7	0.5	0.3	0.2	0.5
Cs	5.77	3.98	8.76	11.4	5.86	7.24	5.39	5.51	2.91	1.06	2.11	2.18
Ba	1000	844	3362	4667	2403	3109	1195	2460	1153	834	996	1616
La	59	48	45	39	52	49	76	63	69	45	36	43
Ce	114	96	121	107	122	126	143	126	140	100	76	94
Nd	40	34	47	43	54	50	63	52	59	42	32	41
Tl	1	0.7	2.4	3.1	1.6	2.6	2	1.4	0.8	<0.5	<0.5	<0.5
Pb	26	327	8	13	6	8	50	47	30	6	2	6
Bi	0.1	0.2	0.3	0.4	<0.1	0.3	0.4	0.3	0.3	0.1	<0.1	0.2
Th (XRF)	30.9	31.1	15.9	27.7	14.0	12.6	16.3	35.1	29.2	22.4	19.3	21.1
Th (ICP)	27.3	28.5	12.8	24	7.25	13.1	18	33.5	28.5	22.5	21	22.3
U	6.07	6.76	14.5	14	4.86	14.3	11.6	11.5	8.6	5.41	5.4	5.86

Total Fe as Fe2O3; LOI = loss on ignition; Alteration Index = 100(MgO+K2O)/(MgO+K2O+CaO+Na2O)

Table 1. continued

	HRC96-39	HRC96-40	HRC96-41	HRC96-42	HRC96-43	HRC96-44	HRC96-45	MR96-46	MR96-47	MR96-48	MR96-49	MR96-50
SiO2	72.71	71.26	64.31	74.46	76.82	72.27	74.10	74.85	67.93	73.04	72.46	76.19
TiO2	0.36	0.52	0.56	0.37	0.35	0.34	0.30	0.32	0.42	0.29	0.30	0.22
Al2O3	14.03	14.19	15.29	14.20	12.06	13.63	11.82	14.22	16.78	12.76	13.42	8.55
Fe2O3#	2.51	3.45	5.52	2.59	2.53	2.87	4.71	1.09	2.71	2.32	2.46	5.03
MnO	0.03	0.06	0.10	0.01	0.01	0.06	0.01	0.01	0.03	0.27	0.62	0.09
MgO	1.02	0.97	2.19	0.40	0.98	1.02	0.51	1.36	1.38	1.14	2.19	1.11
CaO	0.41	1.49	3.43	0.04	0.09	2.20	0.01	0.01	0.02	1.40	0.10	0.03
Na2O	3.74	4.98	3.12	1.41	1.47	2.16	0.04	0.07	0.21	0.96	0.03	0.05
K2O	3.29	1.71	2.95	3.80	3.30	2.76	4.21	5.41	7.25	4.33	4.87	3.08
P2O5	0.07	0.12	0.15	0.08	0.05	0.08	0.04	0.02	0.05	0.05	0.05	0.04
LOI	1.70	1.34	2.12	2.28	2.17	2.17	3.53	2.30	2.56	3.26	3.03	3.78
Total	99.87	100.09	99.75	99.64	99.83	99.57	99.28	99.62	99.34	99.82	99.53	97.94
S	0.04	0.05	0.10	0.06	0.01	0.01	2.08	0.01	0.01	0.29	0.24	3.26
Total C	0.02	0.02	0.08	0.04	0.13	0.10	0.03	0.02	0.05	0.31	0.20	0.02
CO2	0.07	0.07	0.29	0.15	0.48	0.37	0.11	0.07	0.18	1.14	0.73	0.07
Alteration Index	51.0	29.3	44.0	74.4	73.3	46.5	98.9	98.8	97.4	69.8	98.2	98.1
Trace Elements (ppm)												
Sc	5	11	11	8	7	8	8	5	7	5	4	2
V	15	34	91	35	32	33	39	6	16	10	10	4
Cr	2	3	11	5	5	5	4	2	2	2	2	2
Ni	1	1	4	2	2	2	7	2	2	2	2	1
Cu	3	7	6	4	5	6	13	3	4	5	5	1093
Zn	61	32	94	24	34	37	34	49	51	54	403	11667
As	4	8	14	<1	<1	3	202	3	4	3	8	33
Rb	131	55	113	160	138	139	172	227	278	215	258	150
Sr	182	303	437	52	126	390	6	4	20	40	5	2
Y	31	36	30	31	26	28	20	34	34	32	32	26
Zr	263	241	205	207	200	195	169	263	312	221	225	130
Nb	13.0	12.1	10.7	10.4	10.0	10.6	9.1	13.3	14.2	11.9	12.3	7.0
Mo	1.6	0.8	0.8	0.2	0.4	3	8.7	0.2	0.3	0.2	1.1	7.4
Ag	0.2	0.1	0.2	0.2	0.1	0.1	0.3	0.5	0.3	0.4	0.2	9.2
Cd	0.2	0.3	0.2	0.2	0.4	0.4	0.3	0.2	0.2	0.2	0.8	39.1
Sb	0.4	0.5	0.9	1.2	0.8	0.7	3.4	0.9	1.2	1.1	1.5	1.7
Cs	3.2	1.57	3.77	4.05	5.28	9.48	4.29	2.26	5.53	3.98	3.78	1.99
Ba	896	1065	1090	865	592	769	976	1267	1047	1308	908	1072
La	37	40	32	37	35	34	29	45	34	41	42	25
Ce	82	90	72	79	74	73	64	98	72	88	89	58
Nd	36	42	29	34	29	32	26	41	30	36	37	21
Tl	<0.5	<0.5	0.6	0.8	0.6	0.8	3.8	1	1.3	1	1.3	1.2
Pb	9	13	8	6	8	6	27	30	3	20	67	999
Bi	0.1	0.2	0.1	<0.1	0.1	0.1	0.9	<0.1	0.1	0.3	<0.1	22.9
Th (XRF)	22.2	18.8	17.6	21.0	19.6	18.9	15.5	23.4	22.2	19.2	19.3	11.7
Th (ICP)	22.3	18.9	19.7	20.3	18.9	19.2	16.3	23.6	24.1	20.4	20.6	12.1
U	6	5.01	5.06	5.01	5.1	4.61	4.99	5.7	5.96	5.23	5.42	4.21

Total Fe as Fe2O3; LOI = loss on ignition; Alteration Index = 100(MgO+K2O)/(MgO+K2O+CaO+Na2O)

Table 1. continued

	MR96-51	MR96-52	MR96-53	MR96-54	MR96-55	MR96-56	MR96-57	MR96-58	MR96-59	MR96-60	MR96-61	MR96-62
SiO2	72.42	57.91	72.58	70.47	73.45	44.31	29.42	81.26	61.94	75.81	73.97	13.27
TiO2	0.30	0.32	0.29	0.39	0.35	0.51	0.34	0.33	0.55	0.30	0.31	0.26
Al2O3	12.22	11.34	12.95	15.81	14.09	14.87	10.12	9.41	17.39	12.44	14.36	7.86
Fe2O3#	5.70	18.57	5.86	2.65	2.36	1.77	2.82	2.07	3.39	2.86	2.02	6.27
MnO	0.18	0.82	0.17	0.04	0.04	0.92	2.66	0.02	0.62	0.21	0.05	20.70
MgO	1.39	4.43	1.10	1.30	0.96	8.14	14.87	0.65	2.87	1.24	0.60	3.43
CaO	0.01	0.01	0.01	0.76	0.62	10.52	17.24	0.13	1.59	0.04	0.17	4.88
Na2O	0.03	0.05	0.03	2.76	3.89	0.11	0.03	0.03	0.47	2.62	3.28	0.05
K2O	3.67	0.65	3.67	3.49	2.31	3.28	0.06	3.10	4.17	2.38	2.92	2.01
P2O5	0.04	0.02	0.05	0.06	0.05	0.12	0.12	0.08	0.11	0.04	0.05	0.09
LOI	3.23	5.77	2.83	2.28	1.56	15.23	21.61	2.59	5.71	1.82	1.75	23.95
Total	99.14	99.88	99.50	100.01	99.69	99.78	99.30	99.64	98.81	99.76	99.48	97.98
S	1.53	2.68	0.72	0.01	0.01	0.45	0.27	1.72	1.69	0.01	0.12	9.42
Total C	0.02	0.02	0.02	0.03	0.01	2.79	4.16	0.03	0.40	0.05	0.04	4.50
CO2	0.07	0.07	0.07	0.11	0.04	10.22	15.24	0.11	1.47	0.18	0.15	16.49
Alteration Index	99.2	98.8	99.2	57.6	42.1	51.8	46.4	95.9	77.4	57.6	50.5	52.5
Trace Elements (ppm)												
Sc	4	4	4	6	4	14	13	8	14	5	5	4
V	9	10	9	14	11	38	30	14	100	11	7	11
Cr	2	3	3	3	3	4	4	2	18	2	3	3
Ni	2	1	1	1	1	1	1	1	30	1	1	1
Cu	55	248	608	6	15	12	7	231	17	10	5	*3500*
Zn	155	651	111	53	60	79	139	2848	3676	187	31	*87000*
As	25	23	6	3	2	45	77	51	77	<1	4	577
Rb	191	35	194	171	105	176	3	151	193	127	122	105
Sr	5	3	8	228	228	172	253	9	110	32	216	12
Y	26	52	33	51	57	40	48	20	56	31	33	
Zr	230	232	230	296	267	286	192	150	278	227	261	112
Nb	11.6	12.8	11.7	14.9	12.8	14.5	10.2	6.7	15.1	11.3	13.7	3.3
Mo	6.3	1.3	0.5	0.2	0.2	0.8	0.4	9	4.5	1.7	0.2	19.9
Ag	2	1.8	3.9	0.2	0.1	2.6	1.6	0.9	1.9	1.1	0.3	92.3
Cd	0.7	0.5	0.3	0.4	0.4	0.4	0.2	6.3	2	0.2	0.3	203
Sb	1.2	1.7	1.2	1.1	1.5	8.9	13.4	7.3	20.1	1	1.5	315
Cs	1.74	0.39	1.82	5.37	3.78	3.37	0.48	3.11	4.5	1.89	3.37	2.4
Ba	1018	220	1284	1017	721	2317	117	2103	2320	1168	1095	2514
La	37	23	35	56	61	52	36	14	68	39	60	30
Ce	77	48	75	111	97	116	74	41	150	77	124	84
Nd	32	20	31	54	67	46	32	14	64	33	49	5
Tl	1.6	<0.5	1.5	1	0.8	16.7	8	6.8	17	0.7	0.6	53.1
Pb	52	54	94	7	13	109	28	1457	58	155	7	*35000*
Bi	7.3	4.7	10.5	0.3	0.2	0.2	0.2	0.1	0.4	3.1	0.1	0.7
Th (XRF)	19.4	21.4	20.1	26.2	22.2	21.7	16.5	10.8	22.4	20.8	23.8	
Th (ICP)	17.8	20.9	18.4	23.7	19.8	20.3	13.7	12.6	23	21.6	23.7	12.2
U	4.5	3.9	5.06	5.81	4.32	5.35	5.56	3.95	18.8	5.26	6.21	5.71

Total Fe as Fe2O3; LOI = loss on ignition; Alteration Index = 100(MgO+K2O)/(MgO+K2O+CaO+Na2O)

Table 1. continued

	MR96-63	MR96-64	MR96-65	MR96-66	MR96-67	MR96-68	MR96-69	MR96-70	MR96-71	MR96-72	MR96-73	MR96-74
SiO2	75.49	71.22	62.55	76.27	69.14	71.43	73.51	76.37	70.81	71.37	79.55	76.17
TiO2	0.31	0.33	0.71	0.26	0.43	0.47	0.27	0.23	0.40	0.35	0.17	0.16
Al2O3	13.29	13.74	16.48	12.40	15.08	14.54	13.39	11.65	14.21	14.18	11.47	11.63
Fe2O3#	1.91	4.11	5.34	1.80	4.36	3.55	1.79	2.02	3.33	2.90	1.66	2.08
MnO	0.08	0.47	0.12	0.05	0.16	0.07	0.04	0.15	0.10	0.06	0.02	0.07
MgO	0.45	0.97	1.89	0.36	1.00	0.81	0.36	0.49	1.06	0.55	0.47	0.73
CaO	0.71	0.66	1.69	0.49	0.14	0.08	1.03	1.35	0.15	0.89	0.04	1.55
Na2O	3.64	1.37	3.64	4.57	2.91	1.98	3.80	3.84	3.48	3.79	3.72	1.29
K2O	2.51	4.01	3.26	2.32	3.00	4.42	3.71	1.71	3.65	3.68	1.71	3.17
P2O5	0.04	0.06	0.21	0.04	0.09	0.09	0.04	0.04	0.09	0.07	0.01	0.02
LOI	1.49	2.62	3.44	1.21	2.66	2.13	1.82	2.10	1.93	1.90	1.19	2.72
Total	99.97	99.56	99.32	99.78	98.99	99.58	99.86	99.95	99.19	99.75	100.01	99.58
S	0.02	0.27	0.02	0.01	0.02	0.01	0.01	0.01	0.01	0.01	0.01	0.01
Total C	0.05	0.16	0.26	0.09	0.05	0.06	0.20	0.24	0.02	0.14	0.06	0.30
CO2	0.18	0.59	0.95	0.33	0.18	0.22	0.73	0.88	0.07	0.51	0.22	1.10
Alteration Index	40.5	71.1	49.1	34.6	56.8	71.8	45.7	29.8	56.5	47.5	36.7	57.9
Trace Elements (ppm)												
Sc	5	5	15	4	10	11	4	2	8	5	2	3
V	10	11	74	7	64	42	7	7	46	11	1.5	1.5
Cr	2	2	11	2	6	3	3	2	3	2	2	2
Ni	1	1	4	1	1	2	1	1	2	1	1	1
Cu	7	139	7	3	28	4	4	2	4	7	2	5
Zn	107	124	194	28	198	94	28	46	54	23	27	46
As	3	3	<1	<1	<1	3	<1	<1	<1	2	<1	3
Rb	113	222	155	79	107	162	105	77	120	116	69	137
Sr	272	31	130	107	114	76	118	68	118	131	94	88
Y	40	36	40	33	29	41	33	32	38	42	31	40
Zr	237	260	227	240	181	247	260	227	205	264	214	209
Nb	12.3	12.4	12.7	13.1	10.2	13.5	14.6	12.2	11.6	15.1	13.7	13.9
Mo	0.5	0.2	0.3	0.3	0.3	1.3	0.2	0.2	0.2	0.7	0.1	0.5
Ag	1.1	0.5	0.2	<0.1	0.2	<0.1	0.2	0.1	<0.1	<0.1	<0.1	0.2
Cd	0.2	0.6	0.4	0.3	1.1	0.4	0.4	0.4	0.3	0.3	0.3	<0.1
Sb	5.3	1.5	0.8	0.8	0.6	1	0.9	0.4	1.2	0.8	0.4	0.6
Cs	2.65	2.76	1.76	1.21	2.07	3.16	1.08	1.02	2.32	3.21	1.35	2.7
Ba	786	933	1011	665	1291	1184	1092	302	987	1149	496	713
La	47	42	77	67	41	44	36	74	66	52	24	44
Ce	89	81	101	81	80	95	78	83	105	100	60	80
Nd	46	37	62	47	33	41	30	52	55	46	21	34
Tl	1.5	1.5	1.2	0.5	0.8	1	0.6	<0.5	0.6	0.7	<0.5	0.6
Pb	66	31	18	5	3	9	8	6	14	4	3	15
Bi	0.2	1.5	0.2	<0.1	0.3	<0.1	<0.1	<0.1	<0.1	<0.1	<0.1	0.1
Th (XRF)	20.6	22.8	22.3	20.4	19.1	21.7	21.5	19.1	21.4	21.5	18.9	21.2
Th (ICP)	18.5	20.5	19.4	19.4	17.5	20.9	18.5	17.7	20	19.8	17.5	17.6
U	4.76	5.42	5.09	5.53	3.99	3.76	4.45	4.42	3.38	4.49	4.48	4.72

Total Fe as Fe2O3; LOI = loss on ignition; Alteration Index = 100(MgO+K2O)/(MgO+K2O+CaO+Na2O)

Table 1. continued

	MR96-75	MR96-77	MR96-78	MR96-79	MR96-80	MR96-81	MR96-82	MR96-83	MR96-84	MR96-85	MR96-86	MR90-87
SiO2	71.78	72.08	63.18	50.83	53.72	77.31	78.79	77.78	77.89	75.53	77.71	75.36
TiO2	0.34	0.21	0.87	2.51	0.60	0.18	0.18	0.16	0.16	0.17	0.14	0.17
Al2O3	13.33	10.95	16.24	16.77	14.70	12.91	12.19	11.31	11.07	11.85	10.96	11.24
Fe2O3#	2.50	2.77	9.07	14.34	9.89	1.54	1.68	1.46	1.85	2.84	1.46	1.69
MnO	0.05	0.14	0.06	0.27	0.18	0.01	0.01	0.01	0.02	0.03	0.04	0.08
MgO	0.64	0.65	2.37	4.26	6.84	0.61	0.48	0.55	0.88	0.74	0.26	0.35
CaO	1.46	3.86	0.25	3.37	10.00	0.01	0.01	0.02	0.01	0.03	0.62	1.65
Na2O	3.07	3.66	1.18	3.34	2.20	0.03	0.05	1.26	2.67	2.43	2.78	3.43
K2O	4.50	1.35	2.10	0.22	0.76	4.49	4.19	5.35	4.67	4.47	4.38	3.03
P2O5	0.06	0.04	0.29	0.15	0.08	0.02	0.02	0.03	0.02	0.02	0.01	0.02
LOI	2.03	4.06	3.96	3.95	1.39	2.05	1.90	1.16	0.83	1.25	1.17	2.23
Total	99.78	99.78	99.58	100.02	100.36	99.14	99.55	99.08	100.08	99.37	99.54	99.25
S	0.01	0.01	0.01	0.01	0.05	0.01	0.04	0.05	0.01	0.01	0.01	0.01
Total C	0.23	0.70	0.10	0.05	0.04	0.02	0.03	0.02	0.03	0.03	0.13	0.31
CO2	0.84	2.56	0.37	0.18	0.15	0.07	0.11	0.07	0.11	0.11	0.48	1.14
Alteration Index	53.2	21.0	75.8	40.0	38.4	99.2	98.7	82.2	67.4	67.9	57.7	40.0
Trace Elements (ppm)												
Sc	6	4	16	44	42	8	7	6	5	6	6	8
V	10	7	76	386	249	5	5	4	2	4	2	2
Cr	2	3	3	2	129	2	2	2	2	2	1	1
Ni	1	1	4	2	80	2	1	1	1	1	1	1
Cu	5	4	26	33	87	15	7	8	68	20	22	9
Zn	33	63	224	171	80	30	35	24	50	141	30	88
As	<1	<1	4	4	7	<1	2		<1	<1	<1	<1
Rb	144	63	71	7	20	169	155	145	83	112	102	95
Sr	185	111	49	307	153	4	5	18	23	65	61	119
Y	37	36	46	42	24	29	48	30	24	45	42	50
Zr	241	173	185	76	97	210	206	187	176	193	163	198
Nb	12.9	12.5	6.4	3.4	5.0	19.5	19.0	16.8	15.0	17.3	14.7	14.7
Mo	0.2	0.1	0.5	0.3	0.3	0.8	0.7	0.4	0.4	0.5	0.4	0.3
Ag	0.2	<0.1	0.2	0.3	0.2	<0.1	0.2	<0.1	<0.1	<0.1	<0.1	<0.1
Cd	0.2	0.2	0.6	0.3	0.3	<0.1	0.4	0.1	0.1	0.1	0.2	<0.1
Sb	0.6	0.3	1	1.1	1.2	2.6	2.9	0.4	0.4	0.4	0.5	1.1
Cs	3.14	1.09	2.54	0.43	0.87	2.97	3.37	2.59	0.91	1.36	1.57	4.53
Ba	1131	237	1023	115	240	547	672	1719	974	1692	1456	1075
La	47	28	49	17	16	55	57	42	36	73	71	52
Ce	93	51	91	28	25	122	113	91	77	113	147	110
Nd	40	22	45	22	13	54	51	38	34	62	63	48
Tl	0.7	<0.5	1	<0.5	<0.5	0.7	0.8	0.7	0.5	0.7	0.9	1
Pb	6	4	13	29	5	8	5	3	4	4	3	70
Bi	0.4	<0.1	0.2	<0.1	<0.1	<0.1	<0.1	<0.1	<0.1	<0.1	<0.1	0.2
Th (XRF)	22.1	19.8	19.2	5.5	4.1	23.2	22.0	20.0	19.6	21.7	22.1	20.3
Th (ICP)	20.3	16.3	17.1	4.29	3.66	21.5	19.5	19.3	17.7	20.2	20.9	19.2
U	5.12	3.72	4.74	0.85	0.92	3.96	3.53	2.89	3.1	3.55	4.2	4.23

Total Fe as Fe2O3; LOI = loss on ignition; Alteration Index = 100(MgO+K2O)/(MgO+K2O+CaO+Na2O)

Table 1. continued

	MR96-88	MR96-89	MR96-90	MR96-91	MR96-92	MR96-93	MR96-94	MR96-95	MR96-96	MR96-97	MR96-98	MR96-99
SiO2	72.88	74.92	76.59	74.61	74.37	71.92	70.60	78.68	64.93	71.17	71.00	72.17
TiO2	0.23	0.21	0.20	0.21	0.23	0.53	0.46	0.35	0.42	0.26	0.33	0.27
Al2O3	13.78	11.56	11.65	12.59	13.72	13.95	14.61	11.63	13.90	11.67	13.44	10.36
Fe2O3#	4.37	2.46	2.32	2.92	3.24	2.49	5.90	2.01	11.64	7.76	4.94	7.75
MnO	0.01	0.08	0.08	0.07	0.19	0.01	0.15	0.05	0.30	0.08	0.04	0.01
MgO	1.78	1.04	0.69	0.88	0.91	1.19	1.10	0.60	1.63	1.24	0.85	0.63
CaO	0.01	1.63	0.80	0.34	0.01	0.01	0.01	0.01	0.01	0.01	0.01	0.01
Na2O	0.13	3.35	4.23	4.23	0.67	0.05	0.10	0.06	0.03	0.03	0.09	0.10
K2O	2.85	1.80	2.03	2.71	3.74	4.44	3.63	3.71	3.20	5.02	7.69	6.97
P2O5	0.04	0.03	0.03	0.03	0.03	0.08	0.10	0.08	0.09	0.04	0.05	0.05
LOI	4.09	2.64	1.56	1.35	2.56	4.14	2.94	2.17	3.34	2.09	1.67	0.98
Total	100.16	99.71	100.18	99.95	99.65	98.95	99.78	99.53	99.43	99.34	100.10	99.29
S	0.01	0.01	0.01	0.01	0.01	0.38	0.01	0.02	0.01	0.12	0.01	0.01
Total C	0.06	0.29	0.14	0.06	0.01	0.93	0.04	0.03	0.03	0.02	0.02	0.05
CO2	0.22	1.06	0.51	0.22	0.04	3.41	0.15	0.11	0.11	0.07	0.07	0.18
Alteration Index	97.1	36.4	35.1	44.0	87.2	98.9	97.7	98.4	99.2	99.4	98.8	98.6
Trace Elements (ppm)												
Sc	11	10	9	9	12	16	13	10	14	7	9	7
V	2	3	2	1.5	1.5	103	58	47	62	7	9	12
Cr	2	2	1	2	2	96	6	4	5	3	4	4
Ni	1	1	2	2	2	12	3	1	4	12	2	1
Cu	6	7	4	7	5	65	26	54	57	552	94	6
Zn	145	128	76	113	84	104	104	73	150	78	48	46
As	<1	<1	<1	<1	<1	14	13	212	8	<1	<1	<1
Rb	149	108	75	93	195	211	193	215	191	134	210	161
Sr	20	152	89	79	26	10	7	5	9	41	80	75
Y	42	49	55	44	61	37	30	26	28	58	39	48
Zr	282	247	245	245	289	226	266	204	258	266	302	234
Nb	13.8	12.0	11.4	11.9	13.4	13.3	10.9	8.6	11.6	12.1	12.0	7.3
Mo	0.4	0.2	0.2	0.2	0.2	9.6	0.5	1.1	0.4	1.6	0.2	0.2
Ag	<0.1	0.1	<0.1	<0.1	<0.1	0.7	0.4	8.4	0.2	0.2	<0.1	<0.1
Cd	0.2	0.2	0.1	<0.1	0.2	0.5	0.2	0.3	<0.1	<0.1	<0.1	0.3
Sb	1	0.6	0.5	0.6	1	12.4	4.8	26.9	4	1	1	1.7
Cs	10.3	5.72	2.08	1.78	10.1	5.28	4.12	4.46	4.06	0.88	1.01	1.6
Ba	817	446	704	958	1614	1250	763	701	852	2123	3437	2974
La	39	51	67	66	49	32	38	38	57	86	47	32
Ce	84	104	110	132	168	82	84	91	111	173	103	76
Nd	40	50	61	64	50	34	35	35	46	71	42	28
Tl	1.1	0.6	<0.5	0.6	1.6	3.1	5.8	8.3	1.8	0.6	0.8	0.8
Pb	13	69	16	11	38	487	1330	1427	13	4	3	38
Bi	<0.1	0.3	<0.1	0.2	0.4	1.5	4.6	8.5	0.2	0.2	<0.1	0.5
Th (XRF)	22.8	19.0	19.5	19.9	23.2	19.3	20.9	14.2	20.1	21.0	21.2	16.2
Th (ICP)	20.5	17.2	17.5	18	21.3	17.9	18.9	15.4	18.5	19	19.9	16.3
U	3.55	3.86	3.97	4.28	4.43	6.68	4.05	4.03	4.32	7.92	5.86	5.6

Total Fe as Fe2O3; LOI = loss on ignition; Alteration Index = 100(MgO+K2O)/(MgO+K2O+CaO+Na2O)

Table 1. continued

	MR96-100	MR96-101	MR96-102	MR96-103	MR96-104	MR96-105	MR96-106	MR96-107	MR96-108B	MR96-113	MR96-114	MR96-115
SiO2	68.90	68.61	64.04	72.30	73.03	69.50	62.87	66.32	67.62	60.92	69.23	65.74
TiO2	0.31	0.33	0.44	0.33	0.32	0.23	0.21	0.45	0.63	0.57	0.64	0.37
Al2O3	13.35	12.92	14.78	12.35	13.09	12.83	9.67	14.81	15.02	13.45	14.41	13.13
Fe2O3#	6.37	7.31	9.99	5.72	4.16	7.78	18.48	4.52	4.81	10.84	4.93	10.66
MnO	0.06	0.01	0.01	0.09	0.05	0.10	0.24	0.03	0.03	0.16	0.08	0.35
MgO	0.93	0.56	1.27	1.11	0.80	1.94	3.08	1.03	1.31	2.77	1.22	1.63
CaO	0.01	0.01	0.01	0.50	1.09	0.26	0.01	0.03	0.01	0.44	0.13	0.01
Na2O	0.08	0.11	0.03	2.04	3.70	0.04	0.03	0.23	0.08	0.10	0.74	0.03
K2O	7.05	6.86	6.13	2.94	1.82	3.45	1.56	10.50	7.90	5.32	6.31	4.14
P2O5	0.06	0.06	0.06	0.05	0.04	0.07	0.05	0.11	0.04	0.33	0.11	0.06
LOI	2.24	2.87	2.95	2.33	2.00	3.84	3.66	1.70	2.20	2.58	2.50	3.36
Total	99.36	99.64	99.68	99.76	100.10	100.04	99.82	99.74	99.66	97.5	100.31	99.49
S	0.01	0.01	0.01	0.01	0.01	0.01	0.01	0.01	0.01	0.02	0.02	0.24
Total C	0.03	0.02	0.03	0.05	0.06	0.05	0.05	0.02	0.03	0.02	0.13	0.06
CO2	0.11	0.07	0.11	0.18	0.22	0.18	0.18	0.07	0.11	0.07	0.48	0.22
Alteration Index	98.9	98.4	99.5	61.4	35.4	94.7	99.1	97.8	99.0	93.7	89.6	99.3
Trace Elements (ppm)												
Sc	7	8	13	8	8	20	11	11	22	23	16	10
V	5	9	54	28	36	32	37	54	98	162	65	21
Cr	3	5	5	20	4	2	2	5	17	22	7	7
Ni	9	9	11	14	8	19	46	5	7	5	3	5
Cu	258	35	9	6	5	9	236	7	6	10	22	154
Zn	79	50	91	76	73	133	224	69	206	357	103	393
As	5	<1	3	<1	<1	<1	16	<1	36		2	32
Rb	168	150	280	149	68	187	62	223	516	203	258	174
Sr	104	76	27	63	161	41	17	108	41	78	59	17
Y	102	37	38	38	51	25	36	31	16	26	27	42
Zr	301	277	256	217	301	251	168	261	201	178	391	300
Nb	15.0	11.7	12.1	14.2	14.8	3.4	7.0	11.0	12.8	14.4	17.6	11.1
Mo	0.1	0.2	1	0.2	0.1	0.4	0.8	0.4	0.4		1.7	1.3
Ag	1	0.1	<0.1	<0.1	<0.1	0.1	0.4	<0.1	<0.1		0.1	1.5
Cd	<0.1	<0.1	<0.1	<0.1	0.2	<0.1	<0.1	<0.1	<0.1		0.1	0.7
Sb	1	3.1	2.6	0.5	0.6	1.2	0.5	0.9	51.5		1	1
Cs	1.18	2.67	8.42	3.12	1.2	3.91	1.13	1.57	111		6.46	2.81
Ba	5023	3651	1187	618	452	533	384	4284	1246	2047	1295	973
La	62	37	46	55	62	155	108	40	40	43	47	87
Ce	134	87	94	107	126	350	212	94	80	91	100	174
Nd	50	34	40	47	55	131	86	34	30	36	38	76
Tl	0.8	0.7	1.1	0.6	<0.5	0.7	<0.5	1.1	5.7		1.8	0.9
Pb	12	11	10	7	16	26	36	6	21	41	24	211
Bi	0.3	0.2	0.3	<0.1	<0.1	0.3	0.4	<0.1	<0.1		0.3	1.2
Th (XRF)	22.7	16.1	18.8	22.8	25.7	30.2	17.8	19.4	13.1	9.1	19.2	20.6
Th (ICP)	21	16.8	18.6	21.7	21.8	26.5	15.2	18.6	11.8		16.9	16.7
U	10.1	4.19	4.72	4.1	4.71	6.35	6.65	4.44	1.52		3.2	4.18

Total Fe as Fe2O3; LOI = loss on ignition; Alteration Index = 100(MgO+K2O)/(MgO+K2O+CaO+Na2O)

Table 1. continued

	MR96-116	MR96-117	MR96-118
SiO2	72.13	70.39	63.97
TiO2	0.36	0.43	0.62
Al2O3	13.53	14.11	13.96
Fe2O3#	3.09	3.58	5.56
MnO	0.16	0.12	0.19
MgO	1.12	1.65	2.09
CaO	0.05	0.15	3.09
Na2O	0.13	2.01	1.88
K2O	6.93	4.65	4.45
P2O5	0.05	0.09	0.14
LOI	1.90	2.59	4.27
Total	99.65	99.76	100.22
S	0.01	0.01	0.01
Total C	0.07	0.10	
CO2	0.26	0.37	
Alteration Index	97.8	74.5	
Trace Elements (ppm)			
Sc	10	12	
V	28	59	
Cr	3	9	
Ni	1	3	
Cu	8	5	
Zn	269	178	
As	<1	<1	10
Rb	336	188	
Sr	96	116	
Y	28	21	
Zr	253	231	
Nb	14.6	14.5	
Mo	0.6	0.1	1.4
Ag	0.3	<0.1	<0.1
Cd	0.7	<0.1	0.1
Sb	1.1	0.9	1.1
Cs	14.3	7.62	8.81
Ba	1722	1230	
La	38	27	
Ce	86	57	
Nd	33	24	
Tl	3.1	1.3	0.8
Pb	94	13	
Bi	0.4	0.2	0.4
Th (XRF)	16.0	16.7	
Th (ICP)	14.8	14.6	11.3
U	3.27	2.42	2.78

Total Fe as Fe2O3; LOI = loss on ignition; Alteration Index = 100(MgO+K2O)/(MgO+K2O+CaO+Na2O)